A Wideband Spectropolarimetry Study of the Spatially Resolved Radio Galaxies: Cygnus A & Hydra A

A Thesis Presented

by

Makhuduga Lerato Lydia Sebokolodi

To

The Department of Physics and Electronics

For the Degree of

Doctor of Philosophy

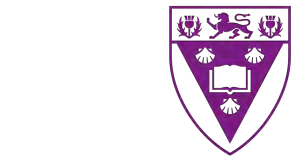

RHODES UNIVERSITY

Where leaders learn

Rhodes University

Grahamstown, Eastern Cape, South Africa

2021

Name of Advisor and Affiliation

Oleg Smirnov, *Rhodes University and South African Radio Astronomical Observatory.*

Rick Perley, *Rhodes University and National Radio Astronomy Observatory.*

Jean Eilek, *National Radio Astronomy Observatory and New Mexico Tech.*

Chris Carilli, *National Radio Astronomy Observatory.*

Abstract

This study presented results from our deep, wideband, high-spectral and high-spatial-resolution polarisation observations of the two most powerful radio galaxies, namely Cygnus A and Hydra A, with the Jansky Very Large Array (JVLA). The high surface brightness and strong polarisation of these radio sources enabled detailed polarimetric imaging, providing images at $0.75''$ resolution across $2-18$ GHz and 2000 independent lines-of-sight across Cygnus A, and images at $1.5''$ ($2-12$ GHz) and 600 lines-of-sight across Hydra A.

Our data revealed significant depolarisation and depolarisation structure, as well as deviations from a λ^2-law. We also found complicated structures in the Faraday spectra ranging from single-peaked to blended/resolved double- and multiple-peaked. The Faraday spectra of Hydra A were more multiple-peaked than Cygnus A. The fractional polarisation increased monotonically with increasing resolution, as expected. However, there were numerous lines-of-sight with complicated behaviour. We also found that the structure and complexity in the depolarisation increased at lower resolutions, suggesting substantial spatial structures across the lobes/tails.

We fitted the $0.3''$ ($6-18$ GHz) and $0.50''$ ($6-12$ GHz) images of Cygnus A and Hydra A, respectively, with a simple model incorporating random, unresolved fluctuations in the cluster magnetic field to determine the high-resolution, high-frequency properties of the sources and the cluster. We found rotation measures (RM) between -5000 rad m^{-2} and $+6400$ rad m^{-2} across Cygnus A, and -2000 rad m^{-2} and $+11900$ rad m^{-2} across Hydra A, consistent with previous studies. From these derived properties, we generated predicted polarisation images of the sources at lower frequencies (< 6 GHz), convolved to $0.75''$ for Cygnus A and $1.5''$ for Hydra A. The predictions were remarkably consistent with the observed emission in both sources, providing strong support for the depolarisation being a result of unresolved fluctuations in the magnetic fields.

We fitted various analytical models to the wideband data. We found that the data for both sources were inconsistent with a wholly mixed gas of thermal and synchrotron gas, particularly for regions with $RM > 1000$ rad m^{-2}. Instead, the data required a dominant Faraday rotating screen in the foreground of the radio sources. The wideband modelling also showed preference towards models with at least two or more unresolved Faraday rotating patches. Single depolarising models fail to describe the data. This implies the presence of more than one depolarising screen in the vicinity of these sources.

The observations were consistent with the lower-frequency depolarisation due to unresolved fluctuations on scales $\gtrsim 300-700$ pc in the magnetic field or the electron density superposed on a partially ordered field component. Both the large-scale magnetic fields and unresolved magnetic field fluctuations are external to the radio emission. The magnetic fields around Cygnus A are located in the ambient cluster gas, the shocked gas in the boundary of the lobes or both, while the magnetic fields around Hydra A are most likely located in the ambient cluster gas.

*This work is dedicated to **Jesus**, my family and God-fearing future generations.*

"In the beginning, God created the heavens and the earth." Genesis 1:1

Acknowledgments

I would like to thank my advisors: Oleg Smirnov, Rick Perley, Jean Eilek and Chris Carilli for the support you provided for the past four years. You have helped me in many different ways, and I will forever be grateful. I was indeed privileged to have had the opportunity to work with you. Thank you for working with me in patience, understanding, and sacrifice. May the Lord God, the God of Abraham, Isaac, and Jacob, whom I serve, bless you and your loved ones.

I am grateful to Eric Greisen, Larry Rudnick and Robert Laing for all the useful discussions. A special thanks to Eric for always being available to help with AIPS, and for patiently enduring my many questions.

Secondly, I give thanks to the following organisations for providing financial support: the South African Radio Astronomy Observatory, the National Aeronautics and Space Administration through Chandra Award Number GO5-16117B issued by the Chandra X-ray Centre, the National Radio Astronomy Observatory (NRAO), and the South African Research Chairs Initiative of the Department of Science and Technology and the National Research Foundation.

Thirdly I thank the NRAO for hosting me for the duration of my PhD study. I feel blessed to have been part of this great organisation. I want to give a special thanks to Allen Lewis for ensuring that all my travel arrangements and residency status are up to date. I know that many people were working behind the scenes to make sure that my stay here is comfortable, to name a few: Skip Lagoyda, Lori Appel, Jim Braatz, Dale Frail, Jessica Utley, Sarah Gibson, and Nancy Ortiz. I am grateful for all your contributions and efforts. May the Lord bless you.

I want to thank the new friends I made in Socorro, New Mexico: Bethany Carillo, Lois-Ann, Tristan Griego, Tina Griego and her husband Saul, Martha and her husband, and Jodie. You guys made my stay here worth it. I will forever cherish all the moments I have spent with you. All the praising, praying, eating, laughing, and dancing together. You guys are my family. I also thank my friends Paul Harden and his wife Jan, and Clifford, for the exciting 4-wheel drives to see historic areas around New Mexico. My other friends who made my stay here memorable include Paula Nielsen, Flor Perez, Robert (Bob), Sis Dorothy Ampomah, PK Djaba, Kofi and Monique Rasmussen, and many others. I was honoured to be part of many families in Socorro. Special thanks to Bethany's parents: Carlos Carillo and Raina.

To Bethany, Lois-Ann, and Tristan. You and I had some of the most blessed experiences ever. Serving God with you was the best thing for the past four years. I know God has even greater plans for us. May He take us deeper into Himself, and use us to bring many to the knowledge of Him. I pray that God will help us to complete this race in faith. May He cause His name, glory and power be known through us.

I thank my church members at Family Christian Centre, for providing a home and safe place for me to grow in the Lord. Special thanks to my Pastor Randy Corley and his wife, Jeanne. Thanks for being my

parent, a covering and shepherd. I have grown a lot under your care, and I am thankful to God to have provided me with his best. I will forever remember the Thursday prayer meetings, as well as the spirit-filled Sunday services. God is indeed moving in His church (His bride), and I cannot wait to see the new things He is about to do. Thanks to Jan for the beautiful, long, heart-warming hugs. I also thank Allen Lewis parents, and Debra Baca for making tasteful cookies/cakes for me. I also thank Pastor Shaun and mama Deana for the encouragements during cell group meetings during the lockdown.

Now to my family. I am thankful for you guys always. I thank God more for the mercies He has bestowed towards me for keeping you in all areas of life. To my mom, Joyce Kgabo Clementina Sebokolodi, I will forever be grateful for you. I remember how you have always been by my side—accompanying me to interviews, to register for school, etc. Your daughter has made it, mamzo. May the Lord grant you the desires of your heart according to His purposes. My grandma, Lydia Nene, you are a woman with the most beautiful heart. Your giving and beautiful spirit I will cherish forever. Thank you for having been our pillar for all these years, your efforts are not in vain. May the Lord reward you, and remember you in light of His lovingkindness. To my dad, Tshidi Sebokolodi, I wouldn't have asked for a better father but you. I am grateful for your life, May the Lord shine His light upon you. My siblings Tebogo Sebokolodi and Keneilwe Sebokolodi, you guys are the best. No words can describe my love for your two – my wrestling partners. May the Lord bless and prosper you, and keep you, and expand your territory. To my beautiful nieces: Bokamoso Maropefela and Resego Sebokolodi, you guys are the future doctors and preachers. A special thanks to Edmund Baidoo, thank you for the support and encouragement, You are God-sent. May the Lord keep us, establish us, and use us for His Kingdom and purposes.

Finally, all glory to God, the Father of our Lord Jesus Christ. The God of peace, an everlasting Father. The One who was from the beginning, the One who has no beginning nor end. The God who spoke and things became, to Him be all honour and glory. May Your Kingdom come, may Your will be done on earth as it is in heaven. You are the ruler of all. There is no like You, and there will never be anyone like You. Your wisdom and knowledge are unsearchable. Lord, thank you for saving my soul and for loving me, for being my Father and my Friend. You are indeed a sure Foundation. Thank you that it pleased You to call me Your own. Thank you that it pleases You to bless me, to love me, to care for me, to commune with me, to live inside of me, and to share Your inheritance with me. May all praise, and honour be unto You: the Father, the Son and the Holy Spirit. Amen.

Contents

List of Figures

List of Tables

List of Acronyms

AGN	Active Galatic Nucleus
ATCA	Australia Telescope Compact Array
ASKAP	Australian Square Kilometre Array Pathfinder
CC	Cool-Core
CF	Cooling Flow
FR	Fanaroff-Riley
FDR	Frequency Depolarisation Ratio
FWHM	Full Width Half Maximum
IGM	Intergalactic Medium
ICM	Intracluster Medium
ISM	Interstellar Medium
lnBF	ln Bayes Factor
JVLA	Jansky Very Large Array
LOFAR	Low-Frequency Array
LoTSS	LOFAR Two-Metre Sky Survey
MHD	Magneto-Hydrodynamic
Mpc	Mega-Parsecs
NCC	Non-Cool Core
NAT	Narrow-Angle Tailed
RDR	Resolution Depolarisation Ratio
RM	Rotation Measure(s)
RMTF	Rotation Measure Transfer Function
RUFD	Random and Uniform Foreground Depolarising
RUID	Random-Uniform Internal Depolarising
RUID+F	Random-Uniform Internal Depolarising with Foreground Screen
SKA	Square Kilometre Array
SMBH	Supermassive Black hole
UFD	Uniform Foreground Depolarising
VLA	Very Large Array
WAT	Wide-Angle Tailed

CHAPTER 1

Introduction

"And God made the two great lights – the greater light to rule the day (the Sun) and the lesser light to rule the night (the Moon) – and the stars."
Genesis 1:16

1.1 A Problem Statement

It is now well-established that the intracluster gas in clusters of galaxies is magnetised. However, we still do not understand their structure, how they evolve or where they originate. What is currently known is that magnetic fields play a crucial role in the Universe. For example, magnetic fields affect the formation, evolution and dynamics of galaxies and galaxy clusters, regulate heat conduction and have the ability to trap or accelerate cosmic particles. It thus appears that to understand the Universe, we need to understand the magnetic fields.

We infer cluster magnetic fields using two main approaches: i) by studying large-scale, cluster-associated synchrotron emitting sources such as radio halos and radio relics, ii) and Faraday rotation study of background/cluster-embedded linearly polarised sources. Faraday rotation is the most commonly used of the two, primarily because the emission of most radio sources is linearly polarised. Additionally, radio halos and relics are usually very faint, so very few are detected (or known). Moreover, Faraday rotation offers the opportunity to study both the strength and structure of the magnetic fields. The latter is possible when using spatially extended radio sources to study cluster magnetic fields. A drawback of this approach is that the estimated field strength is an average along a specific line-of-sight and has no information about the gas's location. It is most likely that there are multiple magnetised emission regions along the signal path, particularly for extragalactic polarised sources. Thus, the major challenge is disassociating the contributions from different Faraday rotating gas regions. Figures 1.1 and 1.2 show the Cygnus A field, with the radio emission from radio observations shown in green contours and the ambient intracluster gas from X-ray observations shown in colour. The X-ray brightness is enhanced around the radio source, suggesting the two are interacting. It is safe to assume that if the two interact so noticeably, then it is also possible that the global intracluster gas and X-ray enhanced region "may" contribute to the overall Faraday rotation. Furthermore, X-ray gas can intermix with radio emission either within the entire volume or edges of the radio galaxy. In such situations, we would also expect the radio source itself to produce its own internal Faraday rotation, which we need to disentangle from the rest of the contributions. Thus, the question is "where is the Faraday rotation located for cluster-embedded sources" - cluster-wide, local or internal to the radio galaxy? Moreover, the structure of the magnetic fields is still far from understood. Some of the current assumptions are that the fields are

uniform across the cluster, tangled on single scales and/or turbulent.

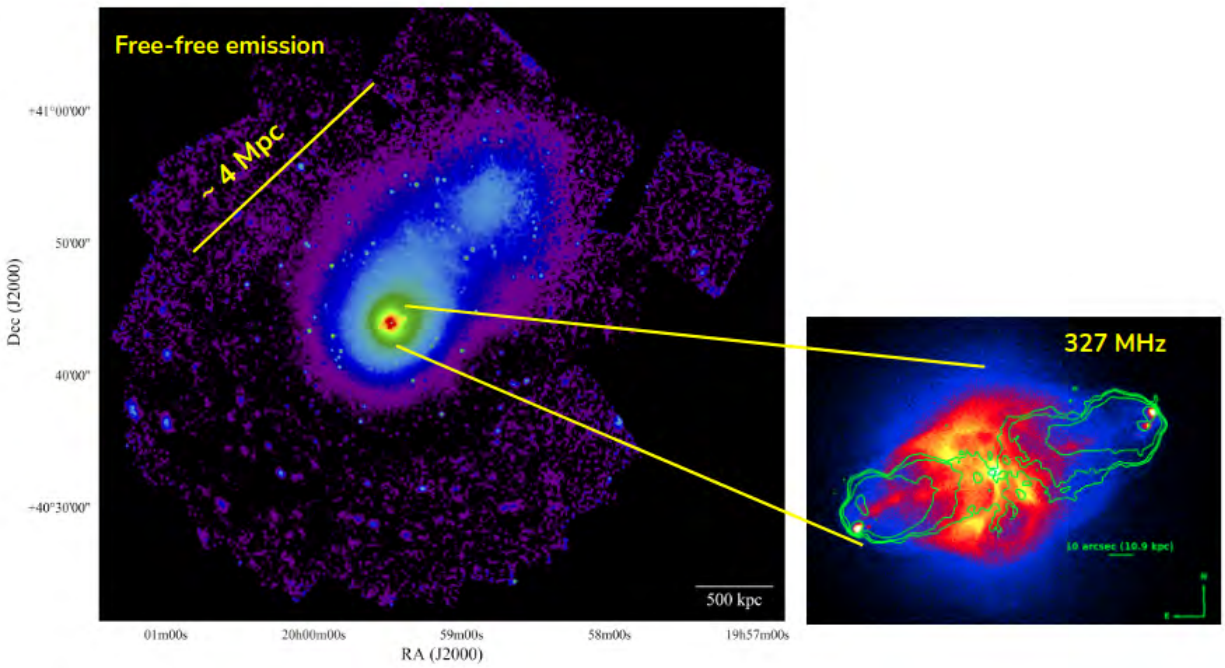

Figure 1.1: *Cygnus A field as seen in the radio and X-ray frequencies.* Radio data were obtained using the Very Large Array (green contours) and the X-ray using Chandra telescope (thermal emission shown in colour). Purple to red represent faint to brightest X-ray emission. X-ray brightness enhancement near the radio lobes suggests some form of interaction between the radio galaxy and its ambient intracluster gas. Image credit: Michael Wise 2019 private communication (left) and Duffy et al. (2018) (right).

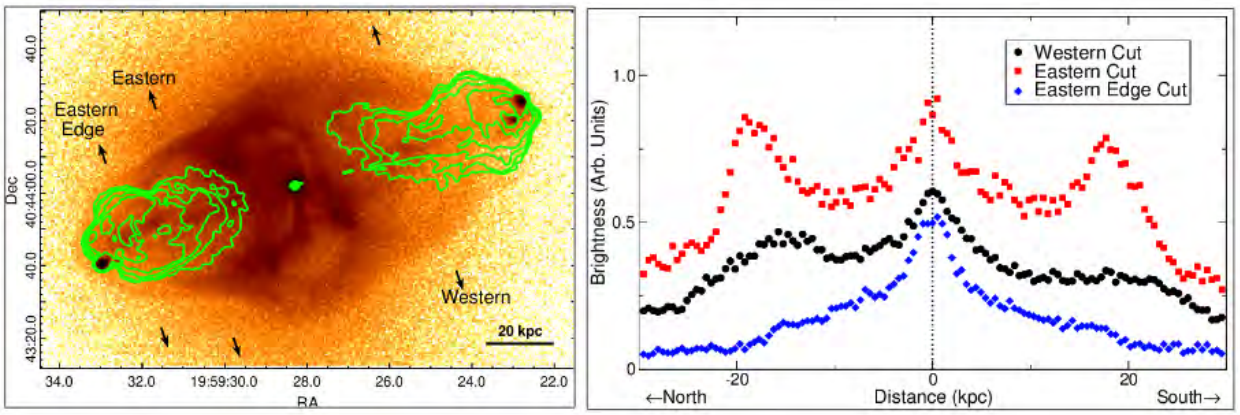

Figure 1.2: *Shocked X-ray compressed gas surrounding the Cygnus A radio lobes.* Left plot: Radio emission in contours and the X-ray surface brightness in orange. Right plot: X-ray surface brightness profiles for three cuts across the lobes – the arrows on the left figure show the location of the cuts. The peaks on each profile mark the enhanced X-ray emission due to the shock driven by the expanding lobes. This is particularly visible for the red points. Image credit: Snios et al. (2018).

1.2 Magnetic Fields Study Using Faraday Rotation

Whenever a linearly polarised emission passes through a region consisting of ionised gas and magnetic fields, its plane of polarisation is rotated by this gas. This effect is known as Faraday rotation. In practice, we observe Faraday rotation by a change in the degree of polarisation and polarisation angle (orientation) as a function of wavelength squared. In the absence of Faraday rotation, we expect both the degree of polarisation and polarisation angle to remain constant as a function of wavelength-squared. However, very early radio observations using two or three frequencies revealed that the observed polarisation angle has the tendency to vary linearly with wavelength squared, and the degree of polarisation tends to decrease as you go to longer wavelengths (for example, Cooper and Price 1962; Slysh 1966; Mitton 1971; Dreher et al. 1987; Taylor et al. 1990; Perley et al. 1997). The change in the observed polarisation properties of a source with frequency implies that there is a Faraday rotating gas along the line-of-sight.

From a theoretical point of view, it is shown that the different physical situations result in unique Faraday rotation behaviour (for example, Burn 1966; Tribble 1991; Sokoloff et al. 1998) – which can then enable us to differentiate (or even locate) the different gases along the line-of-sight. A simple case is that of uniform magnetic fields within a purely ionised gas. The observed degree of polarisation remains constant across frequency and polarisation angle varies linearly with λ^2. The gradient of polarisation vs λ^2 gives a quantity known as the rotation measure, RM, which is proportional to the product of the gas' electron density and line-of-sight magnetic field strength, integrated along the pathlength across the Faraday rotating gas region.

Suppose there is a region of intermixed gas – thermal gas that can cause Faraday rotation mixed with the synchrotron emitting relativistic plasma. In that case, the degree of polarisation will decrease with increasing λ^2 and the polarisation angle may deviate from linearity as a function of λ^2. The former is known as 'depolarisation' and the latter as 'nonlinearities'. How the emission depolarises reveals the nature of the magnetic field structure. There are two extremes: i) uniform ii) and random magnetic fields. For uniformly structured magnetic fields, the observed depolarisation shows $\sin(x)/x$ decaying behaviour, where $x \propto \lambda^2$. When the magnetic fields' structure is entirely random, the depolarisation decays smoothly as $\sim e^{-y}$, where $y \propto \lambda^4$. It is also possible that the uniform and random magnetic fields are superimposed – this will lead to intermediate decaying behaviour. These two situations are idealistic, since real-life magnetic field are probably non-Gaussian and not completely random (for example, the interstellar gas, Armstrong et al. 1995; Haverkorn et al. 2008; Hollins et al. 2017). **Unfortunately, a similar depolarisation behaviour as that from a mixed gas region can result from unresolved turbulent magnetic fields** (Tribble 1991).

The point made here is that Faraday rotation remains a useful tool for investigating the gas's location responsible for Faraday rotations (as either external or internal). It also allows us to probe magnetic field structures' uniformity or turbulence.

1.3 Previous and Future Observing Capabilities

The capabilities of the observing instruments hindered much progress in Faraday rotation studies of radio galaxies. Besides improving noise sensitivity and spatial resolution, the Faraday rotation study's ideal obser-

vation covers both the short wavelengths ($\lambda^2 \approx 0$ m^2) and long wavelengths ($\lambda^2 \approx 1$ m^2). The wavelength space should be finely sampled – high-spectral resolution combined with continuous sampling. First, short wavelengths are essential because Faraday rotation effects are negligible in this wavelength-regime (assuming that the intrinsic degree of polarisation is independent of frequency); this allows probing of polarised source' intrinsic properties. The depolarisation and Faraday rotations, on the other hand, are most dominant and apparent at long wavelengths. The high-spectral resolution allows us to see small changes in the observed polarisation measurements as a function of λ^2. This is important because the presence or absence of deviations have physical implication.

Building instruments with the above observing capabilities is challenging and expensive. At most, one can have one or two of these capabilities: for example, short wavelengths and high spectral resolution, either (or both) short and long wavelengths with sparsely sampled wavelength-space. Before the Very Large Array (the VLA) was upgraded into 'Karl Jansky' VLA (the JVLA, Perley et al. 2011), the VLA's correlator limited the observations to a narrow bandwidth, which then prevented any chance of finding non-linearities in the polarisation angle dependence on λ^2. The previous observations include Dreher et al. (1987), Taylor et al. (1990), Perley et al. (1997), and Taylor et al. (2009).

Thankfully, we are now in an era where instruments are beginning to catch up with the observing capabilities desired for Faraday rotation studies. For example, the upgraded VLA in New Mexico, United States is now able to observe at short and long wavelengths at a high-spectral resolution of 1 MHz and large bandwidths of up to 2 GHz with an 8-bit sampler, or using a 3-bit system which gives a full 8 GHz bandwidth with 2 MHz spectral resolution. The MeerKAT in Cape Town, South Africa has spectral resolution of 16.6 or 132.8 kHz at the UHF band (580 - 1015 MHz) and 26.1 kHz or 208.9 kHz at L-band (900 - 1670 MHz) [1]. Other instruments with similar observing capabilities include the Australian Square Kilometre Array Pathfinder (ASKAP) in Perth, Australia with bandwidth 1200 - 1800 MHz with 1 MHz channel width, the upgraded Australia Telescope Compact Array (ATCA) covering $1100 - 3100$ MHz and $4500 - 6500$ MHz, sampled at 1 MHz channel width (see Wilson et al. 2011) and ultimately the future international project the Square Kilometre Array (SKA).

The study of magnetic fields through Faraday rotation of background/cluster-embedded polarised sources forms a significant part of science goals for these instruments, for example, for the SKA see Heald et al. (2020). Currently, there are on-going polarisation surveys that use some of the above instruments. These include the MeerKAT International GHz Tiered Extragalactic Exploration survey (MIGHTEE, Jarvis et al. 2016), POlarisation Sky Survey of the Universe's Magnetism with the ASKAP (POSSUM, Gaensler et al. 2010) and the JVLA Sky Survey using frequency range 2000 - 4000 MHz (VLASS, Lacy et al. 2020).

1.4 Previous Faraday Rotation Studies

Before late 2000, observations were made using at least two to five frequencies at most. Faraday rotation studies at that time would fit a linear function to polarisation angle vs λ^2 to estimate RM from the slope – and then magnetic field strengths. These studies led to significant findings; however, their physical interpretation

[1] https://science.ska.ac.za/meerkat

was limited to a purely magnetised ionised gas due to the perfect linearity in polarisation vs λ^2 (for example, Dreher et al. 1987; Laing 1988; Taylor et al. 1990; Taylor et al. 2009; Guidetti et al. 2010).

We now know that the linearity might have been an observational limitation, in that high-frequencies may have prevented one from probing any significant Faraday rotation effects that are apparent at low-frequencies. Also, the sparse sampling may have prevented noticing any small changes between neighbouring frequencies. See Section 7.5 of Anderson et al. (2016) for a consideration on the effect of bandwidth coverage.

These previous studies also observe depolarisation with decreasing frequency. The majority interpreted the depolarisation as coming from unresolved magnetic field fluctuations within the foreground gas (for example, Laing et al. 2008a). However, later work by Rudnick and Blundell (2003), Guidetti et al. (2011), and Guidetti et al. (2012) argued that the same depolarisation and Faraday rotations could result from a highly-dense, compressed thin-skin encompassing the radio lobes.

Knuettel et al. (2019), using wider VLA bandwidth between $1-4$ GHz and complex polarisation modelling, derived that the Faraday rotations associated with Coma A radio galaxy are a result of a turbulent magnetic field around the lobes. The same interpretation was reached by Pasetto et al. (2018) after studying 12 radio sources using $1-2$ GHz and $4-12$ GHz VLA data. Other studies suggesting thin-skin around the lobes and jets include Kaczmarek et al. (2018), using ATCA $1.3-3.1$ GHz observations of NGC 612 and O'Sullivan et al. (2012), using $1.1-3.1$ GHz ATCA observations of PKS B1610-771 and PKS B1039-47. Some studies claim internal mixing within the lobes or the jets; Anderson et al. (2018) explain the low fractional polarisation patches in Fornax A as coming from an intermixing with the ambient ionised gas. Knuettel et al. (2019) attribute a highly depolarised region within the southern lobe of Coma A radio galaxy to internal mixing with the ambient Hα gas. O'Sullivan et al. (2013) used RM residuals to suggest internal mixing.

There is currently a wide range of claims for the origin of Faraday rotation for different environments. It is believed that wider bandwidths, high-spectral resolution, and high-spatial resolution observations will make it possible to properly distinguish between internal mixing and turbulent magnetic fields.

1.5 This Study

In this dissertation, we conduct a wideband study of two well-known radio galaxies; Cygnus A and Hydra A. These radio galaxies are of different morphology: Cygnus A is an Fanaroff-Riley (FR) II radio galaxy and Hydra A is an FR I (Fanaroff and Riley 1974). Both of them are nearby, Cygnus A is at redshift 0.056 (Spinrad and Stauffer 1982), and Hydra A at 0.054 (Dwarakanath et al. 1995). They are the most luminous radio galaxies of their morphological class. Due to their proximity and high surface brightness, these radio galaxies can be studied at exceptionally high spatial resolution and high signal-to-noise ratio. Moreover, these radio galaxies are situated in centrally dense environments with core electron density $\sim 10^{-2}$ cm^{-3} (Smith et al. 2002; McNamara et al. 2000). For these reasons, these two radio galaxies are considered the best candidates for studying environmental effects.

Cygnus A and Hydra A are also associated with very large rotation measures, ranging between -4000 and $+3000$ rad m^{-2} for Cygnus A and between 3000 rad m^{-2} and -12000 rad m^{-2} for Hydra A. The RM change sign across Cygnus A's lobes on scales of $5-20$ kpc (Dreher et al. 1987) and about $3-20$ kpc across

Hydra A (Taylor et al. 1990; Taylor and Perley 1993). Moreover, the RM gradients across the lobes of both galaxies range between typical values of 300 rad m^{-2} arcsec^{-1} and few regions with gradients as high as 1000 rad m^{-2} arcsec^{-1}. Previous studies of these radio galaxies claim that the large RM and gradients result from a foreground Faraday rotating gas – either the cluster gas, thin-skin or both. Internal mixing within the lobes was ruled out by arguing that the observed depolarisation between 15 GHz and 5 GHz is too small to come from the observed large Faraday RM. The perfect linearity in the polarisation as a function of λ^2 supports an external gas.

The last detailed study of these radio galaxies dates back to 1987 for Cygnus A (Dreher et al. 1987; Perley and Carilli 1996), and 1993 for Hydra A (Taylor and Perley 1993). These were observed extensively with the VLA at frequency $5-15$ GHz. These observations were made at four/five sparsely sampled frequencies. As already mentioned above, with such sparsity in frequency, perfect linearity claims are still open for scrutiny. Moreover, high-frequencies alone do not provide a full expression of the depolarisation involved.

The VLA wideband extension to include frequencies below < 5 GHz and increased spectral resolution to ~ 1 MHz, presented an opportunity to revisit these radio galaxies. We observed Cygnus A from 2014 Nov to 2015 Nov and Hydra A from 2013 Dec to 2014 Dec. We used all the array configurations of the JVLA for both sources: A (36 km), B (11 km), C (3 km) and D (1 km) to obtain both high spatial resolution and sensitivity. Cygnus A was initially observed at four frequency bands, namely: the S-band ($2-4$ GHz), C-band ($4-8$ GHz), X-band ($8-12$ GHz) and Ku-band ($12-18$ GHz) but later (in 2018) was also observed also at L-band ($1-2$ GHz) and P-band ($236-492$ MHz). Hydra A, on the other hand, was observed at L, S-, C- and X-band giving a total bandwidth of $1-12$ GHz. However, in this dissertation, we only present $2-18$ GHz (S-, C-, X- and Ku-band) for Cygnus A and $2-12$ GHz for Hydra A. The reason for excluding the low-frequency data is that the resolution is too low, which when combined with the large RM gradients in these sources and the turbulent structures, results in too great a depolarisation to be useful.

These wideband data allows us to study these radio galaxies at a spatial resolution of $0.75'' \times 0.75''$ for Cygnus A and $1'' \times 1.50''$ for Hydra A. The ellipticity in the beam for Hydra A observations is due to the low declination of the source. These observations provide the widest continuous frequency coverage and the highest spatial resolution data of this kind. Moreover, since these radio galaxies are exceptionally luminous, they provide the highest signal-to-noise data possible. We plan to address the following research questions using these wideband data: i) which gas along the line-of-sight is responsible for the observed Faraday rotations and depolarisation? ii) where is this gas located? iii) and what is the structure of its magnetic fields?

1.6 Dissertation Outline

This dissertation is arranged into seven chapters, including the introduction. Chapter 2 gives a general introduction on clusters, cluster magnetic fields, radio galaxies and radio galaxy-cluster gas interaction. Chapter 3 provides a detailed discussion on Faraday rotation – our methodology for studying magnetic fields. We also introduce the two Faraday rotation techniques used for our study: RM-Synthesis and QU-fitting. Chapter 4 presents our wideband data of Cygnus A and high-frequency, high-spatial resolution Faraday rotation

study. The majority of this chapter is published in Sebokolodi et al. (2020). Chapter 5 characterises different RM-Synthesis spectra across Cygnus A and also models the wideband data. Chapter 6 presents a wideband polarisation study of Hydra A. Chapter 7 summarises our findings and provides recommendations for future observing and studies.

CHAPTER 2

Scientific Background

"The heavens declare the glory of God; and the expanse of heaven sheweth the work of His hands."
Psalms 19:1

The purpose of this chapter is to provide an overview of galaxy clusters, cosmic magnetic fields and radio galaxies which are most relevant to this dissertation. We refer the reader to Sarazin (1986) for a detailed review on X-ray emission and Carilli and Taylor (2002), Govoni and Feretti (2004), and Beck and Wielebinski (2013) on cosmic magnetic fields. Regarding radio galaxy physics we refer the reader to Begelman et al. (1984) for a broader and detailed overview, and Carilli and Barthel (1996) as pertaining to Cygnus A radio galaxy.

2.1 Galaxy Clusters

Galaxy clusters span a few mega-parsecs (Mpc) across the sky, making them the largest gravitationally bound structures in the Universe. Typical clusters consist of possibly hundreds to thousands of luminous galaxies, thousands of dwarf galaxies, hot gas and dark matter. Clusters typically have masses ranging between 10^{14} and 10^{15} $M_{\odot}$ – with the observable matter (such as galaxies and hot gas) making up only 20% and the rest of the mass is attributed to dark matter.

2.1.1 Morphology

Clusters of galaxies are categorised into two morphologies: regular and irregular (Abell 1958; Abell 1965; Abell et al. 1989). Regular clusters are spatially smooth and spherically symmetric, similar to globular clusters, while irregulars do not have a well-defined morphology, or symmetry, similar to open star clusters. Figure 2.1 shows an example of a regular cluster on the left (Hydra) and irregular cluster on the right (Virgo). Regular clusters are centrally concentrated and tend to be relatively more massive, hot, rich and luminous than irregular clusters. These two types of clusters also differ in galaxy content: regulars predominantly contain the elliptical (E) and lenticular (S0) galaxies, while irregulars have both kinds of galaxies, as well as a significant fraction of spiral (S) galaxies. The distribution density of galaxies tends to increase towards the cluster centre in regulars and is relatively uniform in irregulars.

Abell (1958) classified clusters of galaxies based on the number of galaxies within Abell radius ($1.72/z$ in arcminutes where z is the cluster redshift) with apparent magnitude in the range m_3 and m_3+2, where m_3 is the magnitude of the 3rd brightest cluster galaxy member. Clusters with about 30 to 49 galaxies are called

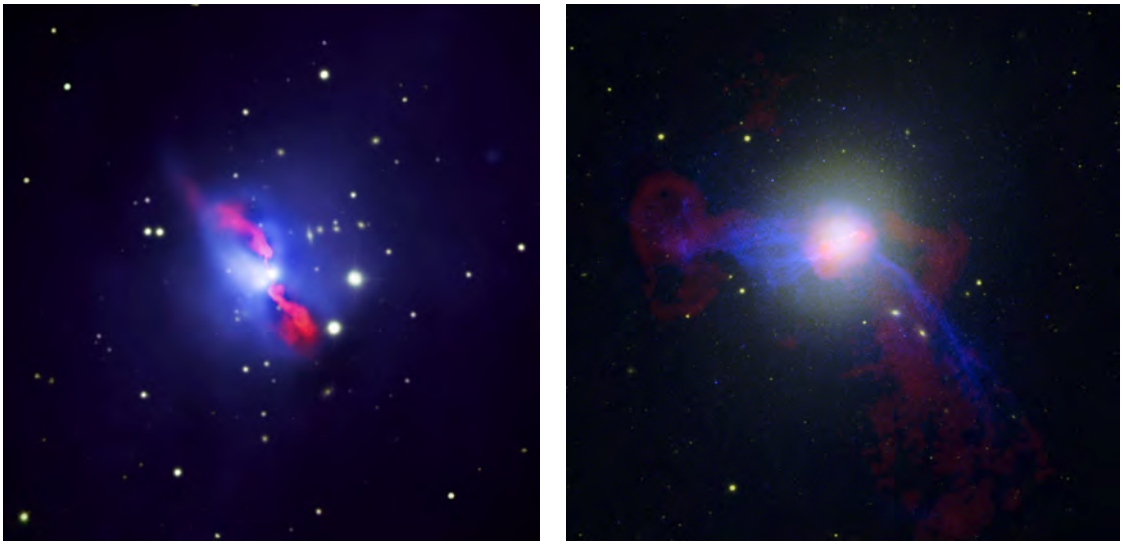

Figure 2.1: *An example of a regular and an irregular cluster*. Left: An example of a regular cluster (Hydra A cluster). Right: An example of an irregular cluster (Virgo cluster). Red shows the radio, blue the X-rays and yellow the optical data. Image credit: chandra.harvard.edu

clusters of *richness* 0, 50 - 79 galaxies are of *richness* 1, 80 - 129 of *richness* 2, 130 - 199 of *richness* 3, 200 - 299 of *richness* 4 and $\gtrsim 300$ are of *richness* 5. The majority of clusters tend to have a brightest (dominant) member at their centre – either a giant elliptical galaxy (the D-type) and supergiant (cD-type). Using this key observation, Bautz and Morgan (1970) developed a classification scheme based on the dominant cluster member, namely type I, II and III. Type I clusters have a cD galaxy at the centre, type II clusters have dominant member intermediate in appearance to a cD galaxy or a giant elliptical and type III clusters do not contain a dominant galaxy at their centre. There is also an intermediate form-type of the three, referred to as type I-II and II-III. Furthermore, Oemler (1974) classified clusters based on their galaxy content ratio, E:S0:S, i) cD clusters are clusters with a dominant supergiant galaxy with galaxy ratio 3:4:2, and are generally regular, ii) spiral-rich clusters have content ratio 1:2:3 and tend to be irregular, iii) and spiral-poor clusters are the intermediate class with content ratio 1:2:1.

2.1.2 Cooling and Non-Cooling Clusters

In between galaxies in a cluster is hot X-ray gas, the intracluster medium (ICM). This ICM gas is detected by thermal bremsstrahlung radiation and is found to have X-ray luminosities ranging between 10^{43} and 10^{45} ergs s^{-1}, temperatures of $\sim 10^7$ - 10^8 K and electron densities, $n_e \sim 10^{-3}$ - 10^{-5} cm^{-3}. Figure 2.1 shows two examples: the X-ray ICM gas is shown in blue. The Hydra A cluster shown on the left is studied in this dissertation, see Section 6.

Clusters are also classified into cool-core (CC) and non-cool core (NCC) based on the properties of their respective ICM. It was during 1970s that studies of the ICM via X-ray observations began to notice that the surface brightness of some clusters peaks steeply towards the centre, and that the temperature decreases significantly in the core (for example, Fabian, Nulsen, et al. 1981; Fabian, Hu, et al. 1981; Allen et al. 1993).

The estimated cooling time due to radiative losses was estimated to be less than the Hubble time (for example, Mathews and Bregman 1978). This led to the cooling flow (CF) model which hypothesises that cool gas at the centre of the cluster will be compressed gravitationally by the surrounding warm gas and ultimately this warm gas will begin to flow inwardly to replace the cool compressed gas. However, later X-ray studies showed that this model overestimates the cooling rates and cannot explain the lack of star formation. It was shortly afterwards that these clusters were referred to CC and NCC rather than CF (Molendi and Pizzolato 2001). CC clusters are generally associated with temperature drop towards the core (Sanderson et al. 2006; Hudson et al. 2010), short central cooling times of $\lesssim 1$ Gyr assuming Hubble constant $H_0 = 71$ km s^{-1} Mpc^{-1} (Sanderson et al. 2006; Burns et al. 2008; Hudson et al. 2010), uniformity in temperature and cooling time distribution (Sanderson et al. 2006), less entropy at the centre (Hudson et al. 2010), a brightest cluster galaxy at the X-ray peak (Hudson et al. 2010), as well as mini-halos (Govoni et al. 2009; Kale et al. 2015; Giacintucci et al. 2017; Savini et al. 2018) and they also undergo minor mergers (Bauer et al. 2005; Mazzotta and Giacintucci 2008). The NCC are the opposite of CC: i) the temperature profiles are relatively flat (Hudson et al. 2010), ii) cooling times are longer $\lesssim 5$ Gyr (Hudson et al. 2010), iii) they are highly non-uniform (Sanderson et al. 2006), iv) have high central entropy (Hudson et al. 2010), v) are associated with giant radio halos (Hudson et al. 2010), vi) and are associated with major mergers (see Feretti 2000, and references therein).

2.2 Cosmological Magnetic Fields

The Universe is permeated by magnetic fields. Magnetic fields are observed in different cosmic objects, for example, stars, planets, interstellar medium (ISM) and galaxies. One thing that is already obvious is that magnetic fields tend to be much stronger in more compact and dense objects, than in larger and less dense objects. For example, compact objects such as pulsars and neutron stars (with roughly 20 km diameters and density 10^{14} g cm^{-3}) have field strengths of up to $\sim 10^{12}$ G. Normal stars, on the other hand, such as our Sun have field strengths of 10 G at the poles and 10^3 G at the equatorial regions, and our planet Earth has field strengths of ~ 0.5 G. Spiral galaxies have field strengths of ~ 5 μG to 30 μG within their arms and ~ 1 mG at the bulge (central regions). Spatially larger and low-density objects such as the ISM, intergalactic medium (IGM) and ICM have field strengths in the order of a few μG.

2.2.1 Importance of Magnetic Fields

Though magnetic fields are known to be important in the Universe, they are not yet well understood. For instance, it is still not clear what their structure is, how they evolve or even where they originate (for example, whether or not they are primordial). However, what is currently well-known is that the magnetic field plays a significant role in the formation and evolution of galaxies, as well as in clusters of galaxies (Beck and Wielebinski 2013). Magnetic fields are known to be able to regulate star formation, feedback and heat conduction. Moreover, magnetic fields are essential in understanding non-thermal processes by accelerating/trapping cosmic rays particles – this is possible when the magnetic fields are coupled to plasma motions, for example, through reconnection layers, magneto-hydrodynamic (MHD) turbulence Eilek (2002). They also play an essential part in AGN jet collimation and can inhibit the spatial mixing of gases.

Moreover, magnetic fields can affect the dynamics of the cluster by providing an additional external pressure term, the magnetic pressure:

$$\mathcal{P}_{\mathcal{B}} = \frac{\langle \mathcal{B} \rangle^2}{8\pi}, \tag{2.1}$$

where $\mathcal{B}$ is the magnetic field.

In clusters of galaxies, for example, the magnetic pressure from free-free emission adds to the thermal pressure:

$$\mathcal{P}_T = n k_B T, \tag{2.2}$$

where n is the total particle number density – related to the electron density, n_e, as $n \simeq 1.93\, n_e$.

These two pressures act against the gravitational force. The importance of magnetic pressure relative to thermal pressure is usually quantified using pressure ratio (the β-parameter):

$$\beta = \frac{\mathcal{P}_{\mathcal{B}}}{\mathcal{P}_T} \tag{2.3}$$

with $\beta \ll 1$ implying the fields are not important and $\beta \sim 0.1 - 1$ implying the fields are dynamically important. For example, Vogt and Enßlin (2003) found dynamically important magnetic fields associated with 3C 75, 3C 465 and Hydra A radio galaxies – with β ranging 0.01 - 0.2.

2.2.2 Origin of Magnetic Fields

There are currently a large number of theories attempting to explain the origin of magnetic fields in the ICM. However, the subject is still of great debate, but what is currently accepted is that the strength and large-scale order ($\gtrsim 1$ Mpc) of the observed magnetic fields cannot be produced by any known process/effect, for example, the battery effect. Thus, the general idea of these theories is that the field started as a small seed magnetic field sometime during the formation and early evolution of the Universe (primordial origin, Dolag et al. 1999; Dolag et al. 2002), or was injected by the galactic or active galactic nucleus (AGN) during the structure formation or evolution of the cluster itself (Rephaeli 1988; Ruzmaikin et al. 1989; Colgate and Li 2000; Furlanetto and Loeb 2001; Kronberg et al. 2001; Xu et al. 2009; Donnert et al. 2009). Cho (2014) presupposes that primordial magnetic fields should already be permeating large-scales before any large-scale structure formation occurs, while the galactic injected fields are initially localised. The seed fields, of whatever origin, are likely amplified to the observed strengths and spatial scales by turbulent dynamo processes that are driven by hierarchical cluster mergers (Dolag et al. 2002; Xu et al. 2009). The only requirement for producing a cluster-wide magnetic field is that the seed field injection should occur before the major merger (Xu et al. 2010).

The MHD simulations of the cluster magnetic field origin and evolution find that the final magnetic configuration, for example, the strength, energy and the degree of homogeneity does not depend strongly on the initial magnetic field configuration but more on the properties of the turbulence (Dolag et al. 1999; Xu et al. 2010). As a result, multiple magnetic field seed injections from on-going galactic or AGN activities after the cluster field is established would not change the strength, the configuration or the energy of the

final magnetic fields significantly (Xu et al. 2010; Xu et al. 2012). The initial seed magnetic field strength of $\gtrsim 10^{-11}$ G for primordial and $\gtrsim 10^{-9}$ G for galactic/AGN origin can produce the observed strengths by dynamo effects if the turbulence has the right dissipative properties (for example, Cho 2014).

2.2.3 Synchrotron Emission Basics

Synchrotron radiation results from centripetal acceleration of relativistic electrons by the local, strong magnetic fields. In the presence of a uniform magnetic field, the electron will move in a spiral along the field lines with constant velocity. Since the electrons have relativistic speeds, the radiation will be confined to a cone of opening angle, $\sim 2/\gamma$, where $\gamma = 1/\sqrt{1-(v/c)^2}$ is the Lorentz factor and v is the velocity of the relativistic electrons. For an optically thin emission region, an electron will result in a continuum spectrum which peaks at the following critical frequency:

$$\nu_{\text{critical}} \simeq 16.1\,\mathcal{B}\sin\theta\varepsilon^2, \tag{2.4}$$

in MHz, $\mathcal{B}$ is the magnetic field in micro-Gauss (μG) and ε is the energy of an electron in GeV. The relativistic electron's radiative power:

$$-\frac{d\varepsilon}{dt} \simeq 6\times10^{-15}(\mathcal{B}\sin\theta)^2\varepsilon^2, \tag{2.5}$$

in ergs s^{-1} and where θ is the angle between velocity and magnetic field – also known as the pitch angle (Govoni and Feretti 2004). The frequency at which we detect the peak synchrotron radiation depends on both the strength of the magnetic field and the Lorentz factor. Assuming $\theta = 90°$, magnetic field strengths of 1 μG and relativistic electron of $\gamma = 5000$, the synchrotron radiation spectrum will peak at 100 MHz, and for $\mathcal{B} = 10$ μG, the spectrum will peak at 1000 MHz.

The radiation itself comes from the acceleration of a population of relativistic electrons. Assuming a homogeneous and an isotropic population, the electron energy density will take the form:

$$N_\varepsilon d\varepsilon = N_0\varepsilon^{-\delta}d\varepsilon, \tag{2.6}$$

for electrons with energies between $\varepsilon_1 = \varepsilon$ and $\varepsilon_2 = \varepsilon + d\varepsilon$. The observed spectral distribution of radio sources is a power-law. Thus, a power-law energy distribution is generally used to describe the spectral energy of radio sources. The energy distribution in an optically thin region is defined as follows:

$$I_\nu = I_0\Big(\frac{\nu}{\nu_0}\Big)^{-\alpha}, \tag{2.7}$$

where ν_0 is the reference frequency and I_0 is the intensity of the source at the reference frequency, and α is the spectral index – which is related to the power-law index in Equation 2.6 as $(\delta-1)/2$.

The emission from radio sources is generally linearly polarised. Le Roux (1961) showed that in a uniform magnetic field, the intrinsic degree of polarisation of the wave is related to the spectral index:

$$p_i = \frac{3\alpha+3}{3\alpha+5}. \tag{2.8}$$

Typical spectral indices for radio sources range between 0.6 to 1, giving a degree of polarisation of up to 75%. In the presence of irregularities (non-uniformities) in the magnetic fields, the degree of polarisation is reduced significantly. Assuming a uniform magnetic field $\mathcal{B}_u$ superimposed on a random magnetic field, $\mathcal{B}_r$, Burn (1966) showed that p_i will be reduced as follows:

$$p_i = p_u \frac{\mathcal{B}_u^2}{\mathcal{B}_u^2 + \mathcal{B}_r^2}, \tag{2.9}$$

where p_u is p_i in uniform fields (Equation 2.8). Suppose that $\mathcal{B}_u = \mathcal{B}_r = 1$ µG, the degree of polarisation of a source with $\alpha = 1$ will be $\sim 40\%$ instead of the expected 75% in the absence of random fields. As $\mathcal{B}_u \gg \mathcal{B}_r$, the reduction in the degree of polarisation becomes slight and in the reverse situation, $\mathcal{B}_u \lesssim \mathcal{B}_r$, the degree of polarisation approaches zero.

It is also important to note here that fractional polarisation is not a function of frequency. As such, any variation in fractional polarisation with frequency is a direct indication of effects coming from the medium itself and not the emission process.

Equations 2.8 and 2.9 mainly describe the degree of polarisation. However, an electric field vector of a linearly polarised source also has an orientation – the polarisation angle, ψ_i. Therefore, the linear polarisation of a source is defined as follows in an optically-thin case described above:

$$p = p_i e^{2i\psi_i}. \tag{2.10}$$

The electric field vectors are orthogonal to the projected magnetic fields ($\psi_i + \pi/2$). In terms of the observables – the Stokes parameters, the linearly polarised intensity of a source is:

$$P = \sqrt{Q^2 + U^2}, \tag{2.11}$$

where Q and U are Stokes parameters that represent the linear polarisation of a radio signal. The polarisation angle is:

$$\psi = \frac{1}{2} \arctan\left(\frac{U}{Q}\right). \tag{2.12}$$

The degree of polarisation (hereinafter, fractional polarisation) defined in Equation 2.10 as p_i is:

$$p = P/I = \sqrt{q^2 + u^2}, \tag{2.13}$$

where $q = Q/I$ and $u = U/I$ and I is the total intensity.

The high linear polarisation in extended synchrotron emitting astrophysical objects is generally argued to suggest uniformity in the magnetic fields. However, Laing (1980) argued that the magnetic fields need not be uniform and showed that even if the fields were random, the high linear polarisation would still result when the object's surface boundaries are tangentially compressed. This compression (as well as shearing) re-aligns the magnetic field vectors into a single plane. The linear polarisation is then highest when the magnetic field vectors lie parallel to the lines-of-sight. This model was motivated by the observations at the

time (for example, Burch 1979; Hogbom 1979): which found that the magnetic field vectors tend to follow the object's boundaries, and the degree of polarisation tends to be higher at the boundaries and decreases towards the centre.

2.2.4 Magnetic Field Probes

There are two methods used to probe and study magnetic fields in the ICM, and these are: i) synchrotron radiation from large scale diffuse emission, ii) and Faraday rotation effect. These two phenomena are described below.

2.2.4.1 Diffuse Synchrotron Emitting Volume

Observing synchrotron emission provides a direct inference of the presence of a magnetic field. Cluster-scale (500 kpc - 1 Mpc), low-surface brightness, diffuse synchrotron emitting objects have been observed close to the centre of clusters (radio halos, for example, Giovannini et al.), as well as close to the periphery of clusters (radio relics, for example, Bonafede et al.; van Weeren et al.). Both the radio halos and relics are not seen to be associated with any galaxy in the cluster, as a result, it is believed that they are associated with the cluster itself (Willson 1970; Feretti et al. 1999).

The total energy of a population of electrons is given by:

$$\mathcal{U}_e = V \int_{\varepsilon_1}^{\varepsilon_2} N_\varepsilon d\varepsilon, \tag{2.14}$$

where V is the volume of a synchrotron emitting region. The magnetic field energy is defined as:

$$\mathcal{U}_\mathcal{B} = \frac{\mathcal{B}^2}{8\pi} V. \tag{2.15}$$

The total energy density, $\mathcal{U}_{\rm tot}$, of a synchrotron emitting volume is then a sum of energy from relativistic electrons and protons, $\mathcal{U}_e + \mathcal{U}_p$, as well as magnetic field, $\mathcal{U}_\mathcal{B}$. In most cases, $\mathcal{U}_p \approx K\mathcal{U}_e$, where K is the ratio of energy in the relativistic protons to that in relativistic electrons.

One way in which magnetic fields are estimated is by assuming a minimum energy condition in which $\mathcal{U}_e(1+K) \simeq \mathcal{U}_\mathcal{B}$ (Burbidge 1959), such that

$$\mathcal{U}_{\rm tot}(\min) \simeq (1+K)\mathcal{U}_e = \mathcal{U}_\mathcal{B}. \tag{2.16}$$

The resulting magnetic field strength is referred to as "equipartition magnetic field" and it takes the form:

$$\mathcal{B}_{eq} = \left(\frac{24\pi\, \mathcal{U}_{\rm tot}(\min)}{7V} \right)^{1/2}. \tag{2.17}$$

For a detailed derivation of final expression in Equation 2.17, see Govoni and Feretti (2004), and Miley (1980) for a detailed review on this subject. The estimated magnetic field strengths from these approaches range between 0.1 μG and 1 μG for radio halos (for example, Feretti and Giovannini 1996; Feretti et al.

1999; Bacchi et al. 2003; Giovannini et al. 2009; Giacintucci et al. 2009), and 0.2 µG - 2.7 µG for radio relics (Ensslin et al. 1998).

2.2.4.2 Faraday Rotation Effect

The presence of magnetic fields within an ionised plasma causes the plane of polarisation of an incident linearly polarised wave to become rotated as the wave propagates through the plasma. This effect is known as Faraday rotation. We discuss this phenomenon in more detail in Chapter 3. Figure 2.2 shows a schematic diagram of this phenomenon. A linearly polarised wave is a sum of two opposite circularly-polarised waves: the right- and left-circularly polarised waves. The right- and left- circularly-polarised waves propagate across a magnetised plasma at different phase velocities, $v = \omega/k$, where $\omega = 2\pi\nu$ is the angular frequency, ν is the frequency, and k is the wave number:

$$k_{R,L} = \frac{\omega}{c}\sqrt{1 - \frac{\omega_P^2}{\omega(\omega \mp \omega_G)}}, \tag{2.18}$$

where R and L represents right- and left-circular polarisation, respectively, c is the speed of light, ω_P is the plasma frequency:

$$\omega_P = \sqrt{\frac{4\pi n_e\, e^2}{m_e}}, \tag{2.19}$$

ω_G is cyclotron frequency:

$$\omega_G = \frac{e\,\mathcal{B}_{||}}{m_e c}, \tag{2.20}$$

where n_e is the electron density, e electron charge, m_e electron mass and $\mathcal{B}_{||}$ is the component of the magnetic field along our line-of-sight. The two oppositely circularly-polarised waves will propagate out of phase, resulting in a net rotation of the plane of polarisation.

The net angle of rotation of the linear polarisation due to the difference in phase velocity between two circularly polarised modes is:

$$d\psi = \frac{1}{2}(k_L - k_R)dl. \tag{2.21}$$

Taking the limit $\omega \gg \omega_P$ and $\omega \gg \omega_G$, we find:

$$\int d\psi = \frac{\lambda^2\, e^3}{8\pi^2 c^3 \epsilon_0 m_e^2} \int_{\text{source}}^{\text{observer}} n_e\, \mathcal{B}_{||} dl = \lambda^2 RM, \tag{2.22}$$

where RM is the rotation measure. Using astronomical units, RM is:

$$RM = 812 \int_{\text{source}}^{\text{observer}} n_e\, \mathcal{B}_{||} dl \quad [\text{rad m}^{-2}], \tag{2.23}$$

where $\mathcal{B}$ is in µG, n_e in cm^{-3} and dl is kpc. If n_e and RM are known, the average line-of-sight magnetic field strengths can be estimated. The sign of RM indicates the orientation of the magnetic field along the line-of-sight – positive RM means magnetic fields are pointing towards the observer, and vice versa.

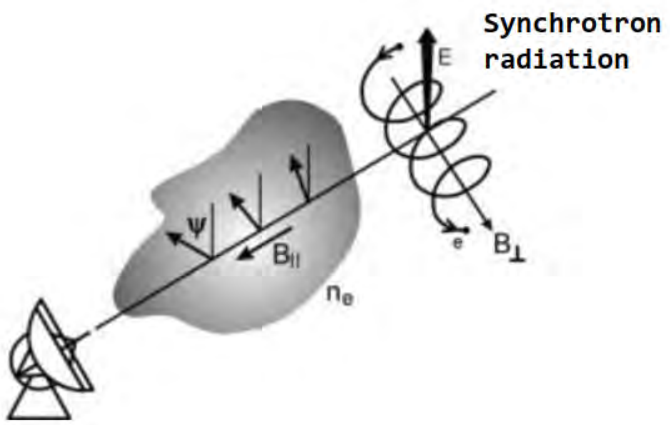

Figure 2.2: *Schematic diagram showing Faraday rotation effect.* In the far left is the observing telescope ("us"), midway is the Faraday rotating gas and far right is the source of polarised emission. Image credit: Beck and Wielebinski (2013).

2.2.5 Faraday Rotation Studies

Faraday rotation studies of extragalactic magnetic fields can be categorised into two, namely i) a statistical study of polarised unresolved sources, ii) and the study of individually extended radio galaxies.

2.2.5.1 Statistical Approach

The statistical approaches study a statistically sufficient sample of polarised radio sources to infer cluster magnetic fields. The sample must consist of sources situated at different radii across and behind the cluster. Ideally, we wish to probe multiple polarised sources across a given cluster – unfortunately, that is usually not possible due to poor sensitivity of the observing instruments. Current statistical studies are performed by probing multiple polarised sources across different clusters. However, a precaution is taken by ensuring that the clusters considered have similar characteristics. The requirement of this approach is that the polarised sources cover a wide range of impact parameters across the cluster and that the overall sample must be statistically significant and must consist of both cluster-embedded sources, non-cluster and background sources. The different impact parameters across the clusters allow the probing of different distances from the cluster-centres, thus, radial properties of the cluster can be probed. Control sources are those sources that are situated beyond the X-ray detectable emission and these are used to determine the contribution from our Galaxy in the direction of each cluster. Background sources are sources situated along the lines-of-sight of the cluster but are at higher redshift with respect to a cluster in question. These are used to remove local effects on the cluster-embedded sources. However, other studies reveal that the IGM itself is permeated by magnetic fields (Lee et al. 2009), as such, even background sources are subject to their own local effects which must be properly accounted for.

Figure 2.3 shows the results from Clarke et al. (2001) (shown in circles) combined with those from Kim et al. (1991) (shown in squares). Control sources are shown in black, embedded in red and background in blue.

It is immediately obvious that sources at small impact parameters have high RM – with RM excess out to impact parameters of more than 500 kpc. Moreover, RM for embedded and background sources are similar, indicating that the majority of the RM excess comes from the ICM themselves. Clarke (2004) estimates field strengths of 0.5 - 3 μG assuming uniform fields. A limitation of this approach is that unresolved data can underestimate the true RM (Eilek and Owen 2002).

Bonafede et al. (2011) proposed an alternative approach to the statistical study: the use of fractional polarisation to probe magnetic fields. The general idea in this work is that fractional polarisation of sources close to the cluster centre (small impact parameters) is lower compared to those situated away from the centre. The low fractional polarisation at the centre of a cluster is attributed to differential rotation occurring across the observing synthesised beam – beam depolarisation. A very weak trend is observed in agreement with this hypothesis.

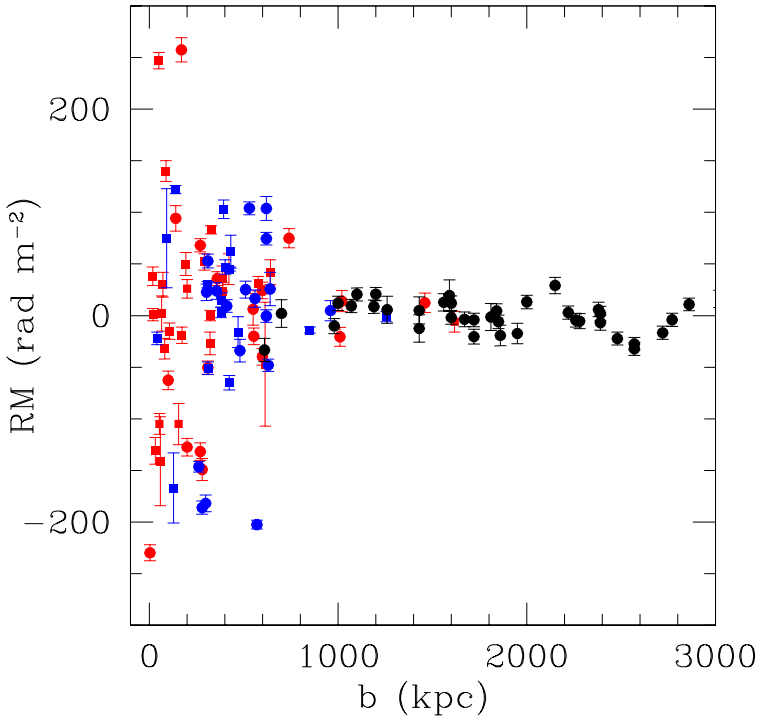

Figure 2.3: *RM as a function of cluster impact parameter*. Red: Cluster-embedded sources. Blue: Background sources. Black: Control sources. Data in circles came from Clarke et al. (2001) and squares from Kim et al. (1991). High RM values occur at small impact parameters – indicating cluster-associated magnetic fields. Image credit: Clarke (2004).

2.2.5.2 Extended (Resolved) Emission

Statistical study of unresolved, compact sources is perhaps the best method for probing magnetic field strengths as a function of cluster radii, as well as the location of the Faraday rotating medium. However, magnetic field structures cannot be inferred through this approach. To probe a projected topology of the magnetic fields, resolved radio sources are usually considered. Studying the spatial distribution of RM

across a source can be used to constrain magnetic field coherence scale (scale length).

Using spatial distribution of Faraday depths across radio galaxies, field strengths of a few μG are found for sources situated in NCC, ordered on scales of 2 - 15 kpc (Feretti et al. 1995; Feretti et al. 1999; Taylor et al. 2001; Eilek and Owen 2002). Much higher magnetic field strengths are observed in CC ranging from a few 2 μG up to 40 μG ordered on scales 5 - 30 kpc (Dreher et al. 1987; Taylor and Perley 1993; Perley and Taylor 1991; Ge and Owen 1993). More specifically, Hydra A radio galaxy shown in Figure 2.4 consists of very high RM with absolute values of a few 1000 rad m^{-2} and up to 12000 rad m^{-2} ordered on 5 - 10 kpc-scales. Taylor and Perley (1993) estimates uniform magnetic fields of $\sim$ 7 μG and tangled magnetic fields of 40 μG.

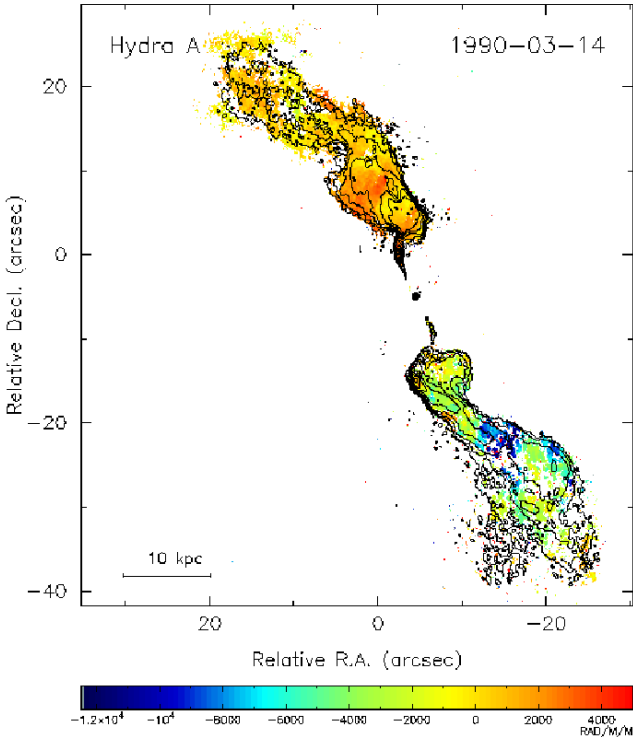

Figure 2.4: *RM across an extended radio source (Hydra A radio galaxy).* The spatial distribution of RM across the extended sources is able to give insight to the magnetic field coherence scale. Image credit: Taylor and Perley (1993).

A more detailed study of extended sources is also possible in situations where multiple extended, cluster- and non-cluster embedded radio galaxies are seen across the cluster. Such situations are extremely rare because i) there are usually few (mostly just one) bright radio galaxies close to the cluster-centre, ii) their emission is below the detection limit and iii) the central radio galaxy is so bright that it obscures the rest of the field. Feretti et al. (1999) was able to carry one such study in Abell 119 with three extended polarised sources located within the cluster impact parameters of 115 kpc (0053-015), 300 kpc (0053-016) and 1010 kpc (3C 29). They found that the magnitude of the RM, the RM dispersions and the depolarisation when observed at low-frequencies decreases with increasing distance from the centre of the cluster. Estimating the coherence length scale to be $\lesssim$ 4 kpc, they derived a tangled magnetic field in the range of 12 - 17 μG.

2.2.6 Galactic and Extragalactic Magnetic Fields

The ionised ISM within our Galaxy is permeated by magnetic fields. Galactic magnetic fields are of interest for two reasons: primarily because they influence the dynamics of our Galaxy itself and secondly because all extragalactic emission in our line-of-sight eventually passes through our Galaxy. RM of extragalactic sources, for example, encapsulate a contribution from our Galaxy, the Earth ionosphere, the ambient ICM and within the extragalactic radio source. Thus, studies of extragalactic magnetic fields need knowledge of the Galactic Faraday rotations in order to remove its contribution from the observed RM. Survey studies of Faraday rotation of compact extragalactic sources and pulsars across the entire sky have been used to probe Galactic and extragalactic magnetic fields. Figure 2.5 shows a sky map of RM of compact, extragalactic sources observed through the NRAO VLA Sky Survey (NVSS) covering a sky area north of declination -40° (Taylor et al. 2009). The RM were determined using only two frequencies: 1364.9 MHz and 1435.1 MHz each with 42 MHz channel width, for a total of $37,543$ sources. The map shows large-scale structure ordering of the RM, as well as an increase in RM amplitude towards the Galactic plane – towards strong Hα and HII regions (see also Schnitzeler et al. 2019).

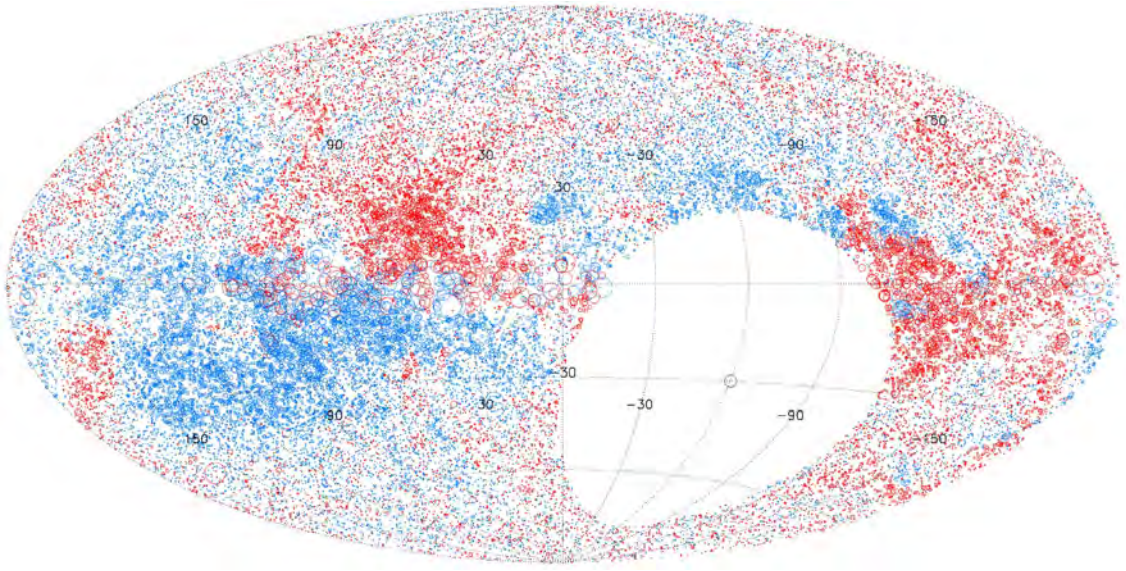

Figure 2.5: *All-sky RM map.* Red: Positive RM. Blue: Negative RM. The size of the circles increases linearly with the magnitude of RM. The RM values are of 37543 compact sources over the sky north of -40°, observed by the NRAO VLA Sky survey (NVSS). Image credit: Taylor et al. (2009).

Though this map can provide an estimate of Galactic contribution towards specific directions, the data are sparse: there is roughly a single measurement per square degree – thus, more data are required. Taylor et al. (2009) attempted a simple interpolation procedure by taking the median values of neighbouring pixels (see Fig 4 of the paper) but the resolution was still very poor; $\simeq 8^{\circ}$. Other more sophisticated methods using Information Field Theory have been proposed for interpolating for missing information by taking advantage of the spatial correlations (see Oppermann et al. 2012; Oppermann et al. 2015; Hutschenreuter and Enßlin 2020, for details). Figure 2.6 shows the result of this interpolation obtained by Hutschenreuter and Enßlin (2020).

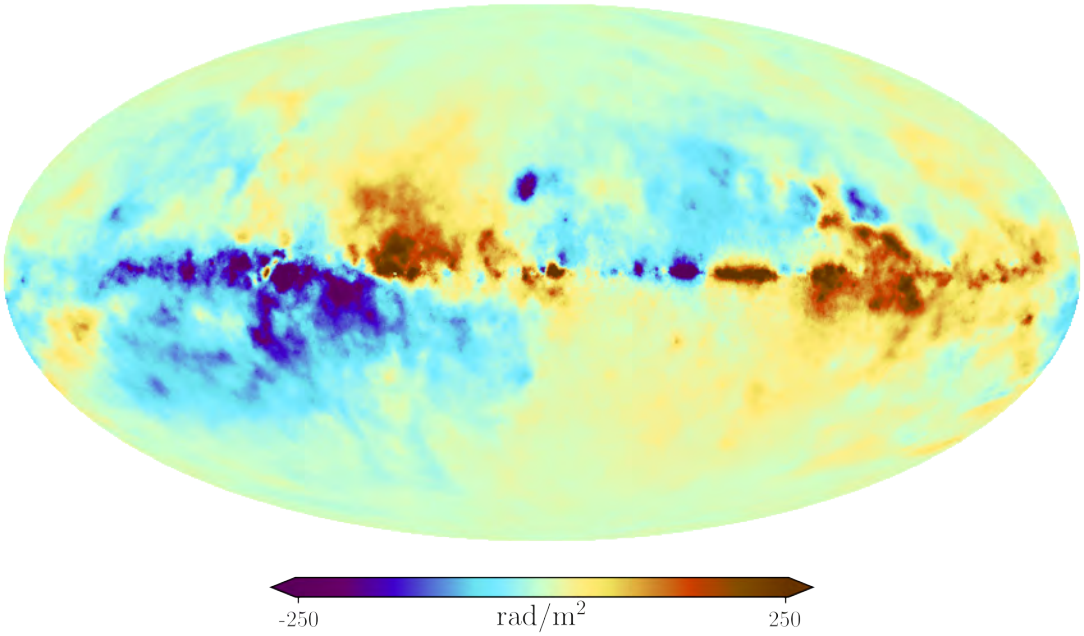

Figure 2.6: *Galactic RM interpolation obtained using information field theory.* Image credit: Hutschenreuter and Enßlin (2020)

In statistical studies such as those presented in Section 2.2.5.1, Galactic contribution is generally estimated using control sources (non-cluster sources). See for example Clarke (2000) and Clarke et al. (2001). However, the goal of a map such as that shown in Figure 2.6 is to provide a template of sky RM. This template is generally used for Galactic removal. For example, Johnston-Hollitt (2004) used an interpolated RM map from Johnston-Hollitt et al. (2004) to remove Galactic contributions towards Abell 3667 cluster.

2.2.7 Computing Magnetic Field Strengths

Computing magnetic field strength and deriving its structure, is one of the most difficult tasks – partly because of our limited knowledge of the 3D structure of the magnetic fields. In this section, we summarise the currently used approaches, and highlight the limitations in each.

2.2.7.1 Unidirectional Magnetic Fields

Using radio observations at two or more frequencies, the RM values can be derived from the slope of ψ vs λ^2 (see Equation 2.22). Combining this estimate with measurements of n_e from X-ray observations, the average line-of-sight magnetic field can be determined from Equation 2.23. However, the difficulty arises when solving for $\mathcal{B}_{||}$ in Equation 2.23 from the fact that the field geometry must be assumed – which affects the final estimate of the magnetic field strength (for example, Dreher et al. 1987). There are at least two simple geometries generally assumed in the literature. The first one assumes a region of uniform magnetic fields such that the field strength is constant across the cluster and is unidirectional. The second approach is

similar to the first but assumes that the magnetic field strengths scales with electron density $\propto n_e^{\gamma}$; see results from MHD simulations in Dolag et al. (2002). For cases where flux-conservation is assumed $\gamma = 2/3$ and for situations were the magnetic energy density scales with thermal energy density $\gamma = 1/2$. For all the above assumptions, the derived magnetic field strengths represent the lower-limit of cluster field strength since the field reversals are not taken into account.

2.2.7.2 Single-Scale Random Magnetic Fields

RM maps of spatially resolved radio sources show structure in the RM distribution with scale length, Λ_{RM}, less than the size of the source. In practice, the value of Λ_{RM} is commonly taken to represent field reversal scale-length, $\Lambda_{\mathcal{B}}$. However, Enßlin and Vogt (2003) argue that in typical astrophysical situations $\Lambda_{RM} > \Lambda_{\mathcal{B}}$. Thus, studies that use $\Lambda_{RM} \approx \Lambda_{\mathcal{B}}$ ultimately underestimate the strength of the magnetic field. Vogt and Enßlin (2003) estimate Λ_{RM} to be a factor of 2 to 4 larger than the actual magnetic field length scale for Abell 400, Abell 2634 and Hydra A, respectively. The field reversals are usually modelled by assuming a tangled magnetic field geometry consisting of an array of cells along the line-of-sight with each cell having a constant field strength and electron density. Meanwhile, the direction of the magnetic fields across the cells is assumed to be random, such that the RM distribution is a Gaussian with zero mean and dispersion:

$$\langle RM^2 \rangle^{1/2} = 812\, n_c\, \mathcal{B}_c\, N^{1/2}\, \Lambda_c \quad [\mathrm{rad\ m^{-2}}], \tag{2.24}$$

where $N = L/\Lambda_c$ is the number of cells along the line-of-sight, L is the total pathlength across the cluster, and Λ_c is the cell size (constant for all the cells) and n_c and $\mathcal{B}_c$ is the cell electron density and magnetic field, respectively (for example, Taylor and Perley 1993). Assuming statistically isotropic magnetic fields, Enßlin and Vogt (2003) estimate $\Lambda_c = 3/2\Lambda_B$.

However, this model is generally opposed (for example, Enßlin and Vogt 2003; Vogt and Enßlin 2003) since it predicts a non-zero magnetic field divergence – contradicting Maxwell's equation. Moreover, it is more likely that there exists a wide range of scales rather than just a single scale. As such, assuming a single-scale magnetic field will ultimately overestimate field strength (Newman et al. 2002). The existence of multiscale magnetic fields is suggested through a detailed MHD simulations (see Dolag et al. 2002).

2.2.7.3 Power-Spectrum/Structure Function:

Attempts have been made in the past years to incorporate the multiscale nature of the magnetic fields, while ensuring that $\nabla \cdot \mathcal{B} = 0$ is not violated. This has been done through the study of the magnetic power-spectrum (Enßlin and Vogt 2003; Vogt and Enßlin 2003; Murgia et al. 2004), tension force power spectrum (Waelkens et al. 2009), auto-correlation function (Enßlin and Vogt 2003; Vogt and Enßlin 2003), or structure function (see Laing et al. 2008b, and references therein). It should be noted that the power-spectrum (the first two methods) and the functions (last two) are related; the former is in the Fourier space (wavenumber, $k = 2\pi/r$) and the latter is in real space (spatial, r). Based on Wiener-Khinchin theorem, the same information is present in both spaces, however, the results obtained in the k-space are shown to be more precise (see Vogt and Enßlin 2003). The basic assumption made for power-spectrum analysis is that the fields are

statistically isotropic when averaged over a large volume and they obey Gaussian statistics. In this case, the magnetic power spectrum takes the form (Waelkens et al. 2009):

$$M(k) = 4\pi k^2 \langle |\mathcal{B}(k)|^2 \rangle. \tag{2.25}$$

The average is taken over all k, and the resulting $M(k)$ provides the magnetic power at a given wavenumber. It should be noted that phase information is completely lost in this expression, as such one can only derive the strength of the fields but cannot constrain the structure of the fields themselves. For this reason, different magnetic field structures with the same power spectrum shape cannot be distinguished. Waelkens et al. (2009) demonstrated this particular issue by comparing magnetic field structures of the same power spectrum obtained using MHD simulations, as well as synthetic divergence-free Gaussian random field. See Figure 2.7 for the field structure. In this study, they proposed using magnetic tensor force spectrum, to distinguish between completely random fields (right plot in Figure 2.7), and fields with organised structures such as folded flux sheets and filaments – such as those seen on the left of Figure 2.7 and also those seen in real observations (for example, Dreher et al. 1987; Taylor and Perley 1993; Taylor et al. 2001; Eilek and Owen 2002; Guidetti et al. 2011). For details, we refer the reader to Waelkens et al. (2009) and references therein.

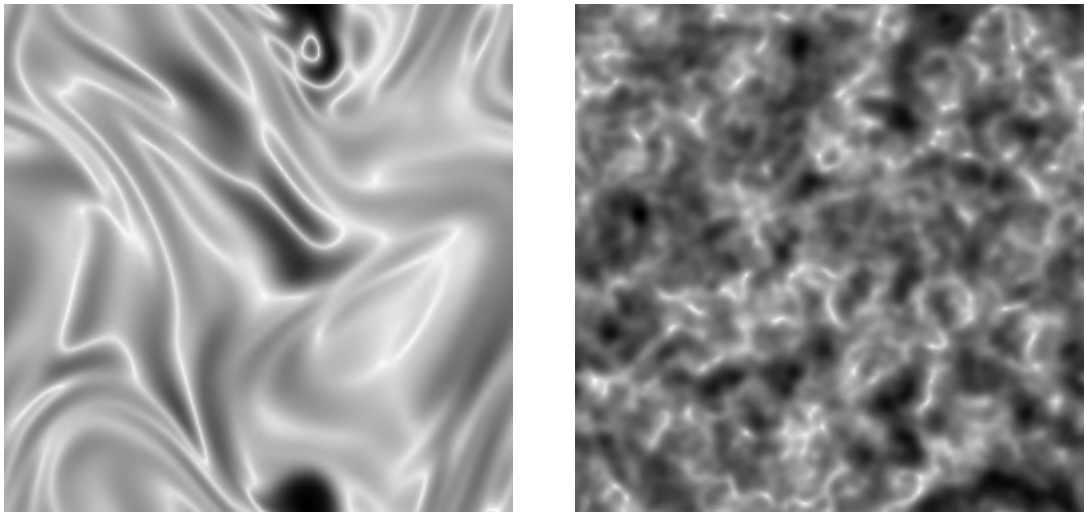

Figure 2.7: *Magnetic structure realisation of the same power spectrum*. Left: Magnetic field realisation obtained from MHD simulations. Right: Magnetic field realisation from a synthetic divergence-free Gaussian random magnetic field simulation. The same power spectrum can result from two different magnetic field structures. Image credit: Waelkens et al. (2009).

2.3 Radio Galaxies

2.3.1 Radio Galaxy Morphology

Radio galaxies are one of the most remarkable and most powerful radio objects in the sky. Radio galaxies are active galaxies with bright extended radio emission. The morphology of a typical radio galaxy consists of

a central AGN which harbours the supermassive black hole (SMBH), jet(s), lobes (or plumes) and hotspots. There are two main classes of radio galaxies based on their morphology, namely Fanaroff-Riley (FR) of type I and II (Fanaroff and Riley 1974). Figure 2.8 shows these two classes. The extended emission in FR I is normally referred to as plumes/tails, and as lobes for FR II radio galaxies. FR I sources have the brightest surface brightness emission close to the core and are generally associated with the jets, while the high brightness emission regions are near the extreme edges of the (bounded) lobes in FR II galaxies. These high surface brightness regions are referred to as hotspots in FRIIs. FR II interestingly tend to have a one-sided jet. Fanaroff and Riley (1974) found that FR I are relatively less luminous compared to FR II and as a result FR I are referred to as low-luminosity radio galaxies and FR II as high-luminosity radio galaxies. They estimated a dividing luminosity threshold of the two classes (known as FR I - FR II break) to be $\sim 10^{24.5}$ W Hz^{-1} at 1.4 GHz. However, larger and less biased survey studies of radio galaxies show that there isn't a clear distinction: although FR II are generally more luminous than FR I, there is a large overlap – there are low-luminosity FR II radio galaxies comparable to FR I (for example, Best 2009; Miraghaei and Best 2017; Mingo et al. 2019).

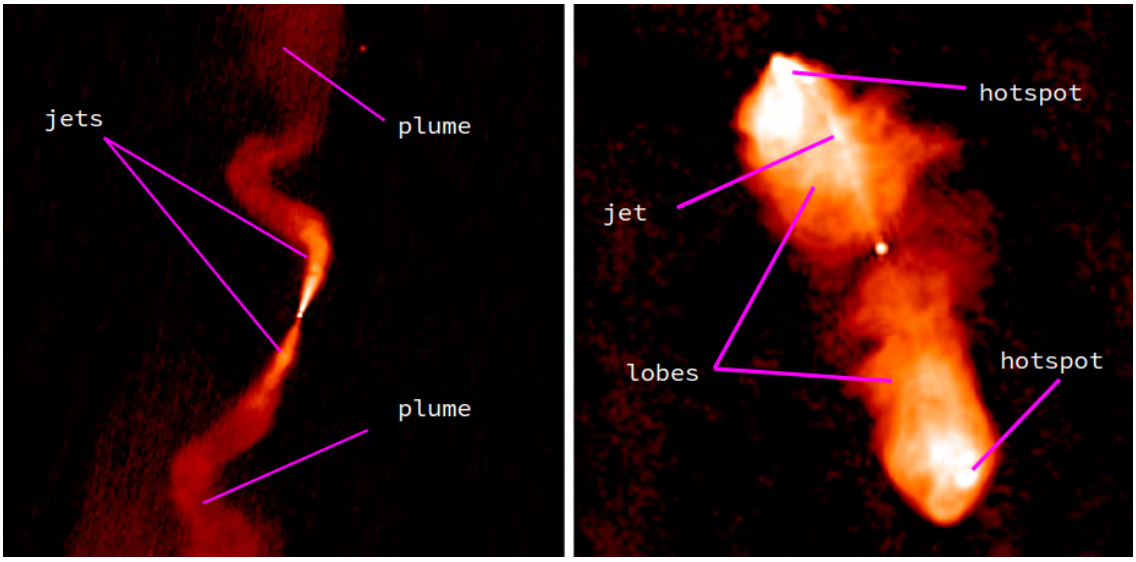

Figure 2.8: *Two types of radio galaxies morphologies: FR I (left) and FR II (right).* The FR I shown is 3C 31 and FR II is 3C 98. Image credit: Hardcastle and Croston (2020).

There is another type (sub-class) of radio galaxy morphology: the wide-angle tailed (WAT) and narrow-angle tailed (NAT) radio galaxies. Figure 2.9 shows examples of tailed radio galaxies. These two sub-classes have bent jets (hence tailed), and the main difference between the two is the degree of bending of the tails; the tails of NAT radio galaxies are bent significantly and are so close together that sometimes the jets are unresolved and can be misclassified as one-sided tailed source (Terni de Gregory et al. 2017), and WAT tails are slightly open making a "C"-like shape (Sakelliou and Merrifield 2000). The morphology of these tailed radio galaxies is interpreted as indicating that the radio galaxy is moving across the ICM and the tails are left behind by ram pressure (Rudnick and Owen 1976). One main observational evidence in support of this picture is that tailed sources are mostly found in clusters compared to other types of radio galaxies (Thorat et al. 2013; Mingo et al. 2019). Moreover, tailed sources are generally found in the outskirts of galaxy clusters

and their tails tend to point directly towards or away from the cluster centre – suggesting that they are radially orbiting about the cluster centre (Sakelliou and Merrifield 2000).

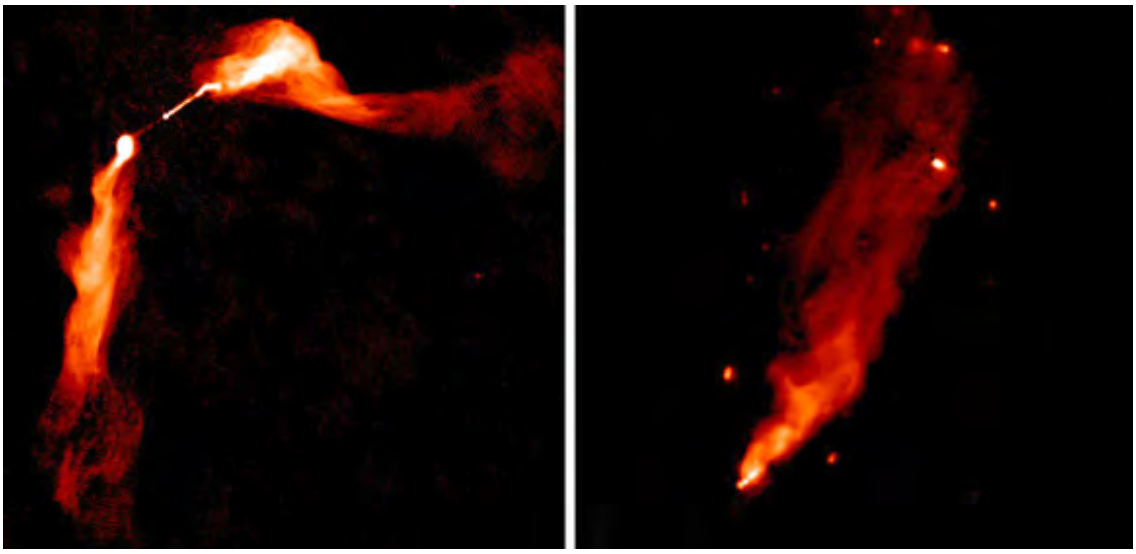

Figure 2.9: *Two types of tailed radio galaxies*. Left plot: WAT radio galaxy known as 3C 465. Right plot: NAT radio galaxy known as NGC 6109. Image credit: Hardcastle and Croston (2020).

There is yet another set of radio galaxy morphology: the hybrid radio galaxies. These show FR I on one side and FR II on the other (Gopal-Krishna and Wiita 2000; Kapińska et al. 2017; Mingo et al. 2019). Figure 2.10 shows two examples of hybrid galaxies from Kapińska et al. (2017).

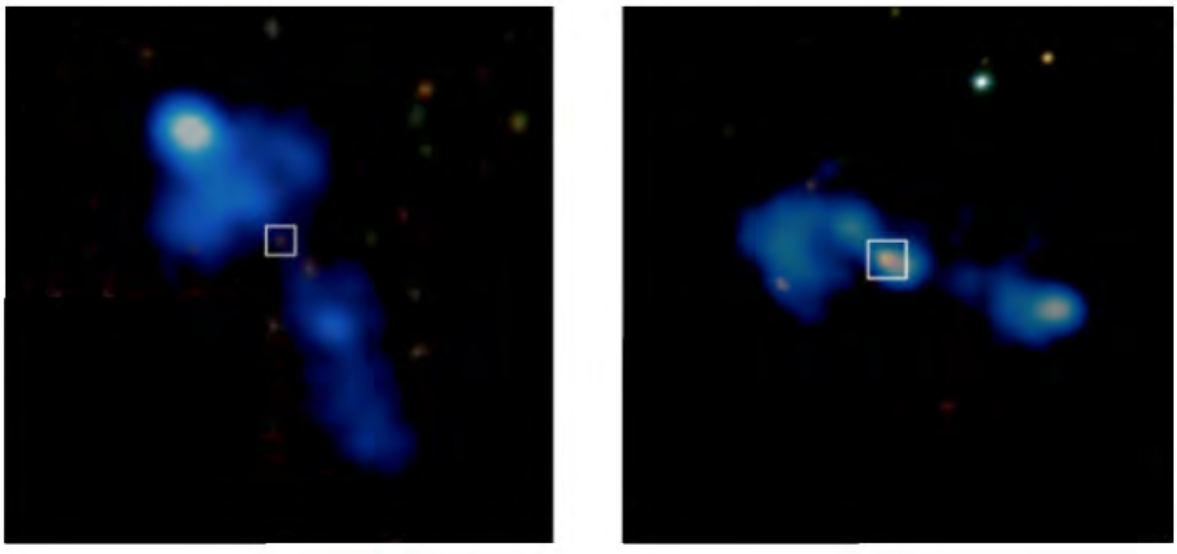

Figure 2.10: *Examples of hybrid radio galaxies*. The white box indicates the optical host. Image credit: Kapińska et al. (2017).

2.3.2 FR I - FR II Dichotomy

One of the important astrophysical questions is the origin of the two morphologies: the FR I - FR II dichotomy. This topic has been of much scientific interest for many years. The key goal is understanding whether the dichotomy is a result of the differences in the intrinsic properties of central SMBHs such as the accretion mechanism, black hole spin, or jet kinetic power and content (Baum et al. 1995; Meier et al. 1997; Ghisellini and Celotti 2001), or due to external effects such as the deceleration and disruption of jets upon interacting with the ICM (Bicknell 1995; Kaiser and Alexander 1997; Kaiser and Best 2007; Best 2009; Kawakatu et al. 2009; Thorat et al. 2013; Miraghaei and Best 2017; Mingo et al. 2019). Owen and Ledlow (1994) and Ledlow and Owen (1996) found a separation of the two morphologies on a plot of radio luminosity vs optical absolute magnitude. Figure 2.11 shows their results on the left. The interpretation of the observed correlation is that the optical magnitude is indicative of the ISM density, with bright galaxies found in dense ISM and vice versa. This means for a given jet power, a source will likely become FR I radio galaxy in a rich environment (bright host), or FR II in a relatively poor environment. A jet in FR I sources gets disrupted very early on its journey by a dense ISM (Bicknell 1995), while FR II jets are able to travel large distances undisturbed. Conversely, assuming that radio luminosity translates to jet power, for a given ISM density, we would expect a more powerful jet to travel far distances without interruption than a less powerful jet. Bicknell (1995), Kaiser and Best (2007), and Best (2009) argued that all sources begin as FR II – with relativistic and collimated jets – but weaker jets are eventually disrupted by the dense environment forming FR I radio galaxies. The result from Best (2009) shown on the right of Figure 2.11 using a less biased sample found a large overlap in the distribution: there are low-radio power FR II radio galaxies in environments that are conducive for FR I sources. Mingo et al. (2019) using data from LoTSS (a more complete survey) found a similar overlap and also found that these low-radio power FR II are associated with fainter host galaxies – consistent with the jet power - environment picture which predicts that less powerful jets "may" remain undisrupted in low-density environments.

The jet power - environment picture is the well-accepted model. The evidence that is usually used to support this picture and disprove the intrinsic differences picture is the existence of hybrid radio galaxies (Gopal-Krishna and Wiita 2000; Kapińska et al. 2017). However, it should be noted that hybrid radio galaxies may not be a separate class altogether, however could simply be FR I/FR II affected by projection effects (for example, Kapińska et al. 2017). Supposing that there are indeed hybrid sources, intrinsic factors alone would fail to explain these differing morphologies in the lobes belonging to the same source. Thorat et al. (2013) also observed asymmetries in the lobes of radio galaxies (for example, one lobe being longer than the other) and found that these are related to environmental anisotropies; with shorter lobes associated with higher galaxy density regions.

2.3.3 Radio Galaxy Formation and Evolution: The Jet Model

The question of how radio galaxies form dates back to the early 1960s. The major areas of interest were understanding: i) the source of energy, ii) the origin of the radio emission in the lobes, iii) the source of confinement of the lobes (to reduce radiative losses or prevent the lobes from floating into space) and iv) the

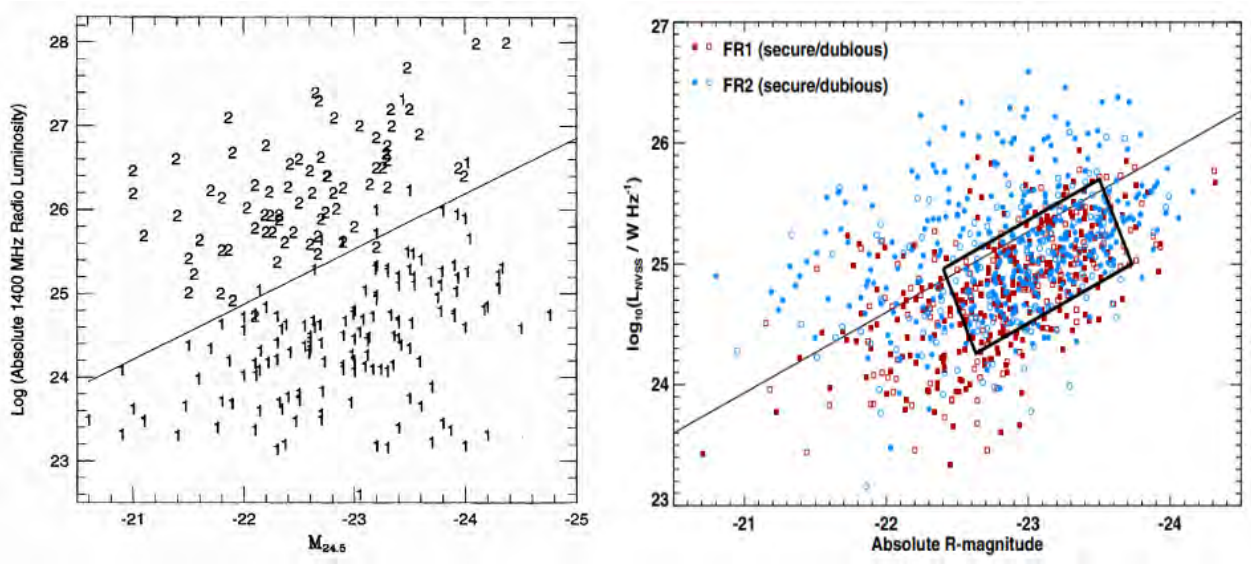

Figure 2.11: *Radio luminosity as a function of optical luminosity for a sample of FRI and FR II radio galaxies.* Red: FR I radio galaxies. Blue: FR II radio galaxies. A straight line shows the FR I - FR II break. Image credit: Owen and Ledlow (1994) and Ledlow and Owen (1996) (left) and Best (2009) (right).

form of energy transportation and efficiency to large distances.

2.3.3.1 Source of Energy Supply

Various methods were proposed over the years, for example: the AGN as a source of energy supply became apparent when observations revealed the evidence of violent activities (for example, explosions) at the centre, significant variability in the optical emission and double structures merging from the AGN (Ryle and Longair 1967; Longair et al. 1973; Scheuer 1974). Rees (1971) suggested that the emitted energy results from a differential rotation of collapsing and colliding normal stars, pulsars and neutron stars occurring at the galactic centre. Another hypothesis proposed in the literature was the existence of a more massive phenomenon: SMBH accreting matter into itself. Black holes cannot be observed directly but have been inferred through: i) Keplerian motions of mega-masers (Miyoshi et al. 1995), ii) reverberation mapping (Blandford and McKee 1982; Netzer and Peterson 1997; Peterson and Wandel 2000) and iii) a shadow (EHT 2019).

2.3.3.2 Means of Transportation

The energy from the central SMBH was initially thought to be transported by means of either low-frequency electromagnetic waves (Rees 1971), a beam (Scheuer 1974), clouds (Ryle and Longair 1967), bubbles of relativistic particles (Gull and Northover 1973), or massive objects such as quasi-pulsars (Burbidge 1967). How is the energy sustained for such large distances without dissipation? Hargrave and Ryle (1974), using Cygnus A' radio observation data, found that the radiative lifetime of the electrons in the hotspots is far less than the travel time from the AGN to the hotspots, thus, we would expect the hotspot to have faded away for the estimated source age. However, that is not what is happening, as a result, it was

concluded that this must be an indication of a continuous supply and outflow of energy. The magnetic fields close to the AGN are suggested to be the agency that collimates the relativistic particles into a beam-like structure and sustains them for large distances.

2.3.3.3 Lobe Confinement

Various possible sources for confining radio lobes have been proposed, namely i) the inertial model assumes the presence of cold matter (heavy particles) which traps both the relativistic particles and fields by slowing them down, ii) ram pressure exerted by the IGM (De Young and Axford 1967), iii) thermal pressure from the surrounding hot gas (Gull and Northover 1973) and iv) magnetic pressure.

2.3.3.4 The Jet Model

The current well-accepted model is called the jet or beam-model (Longair et al. 1973; Hargrave and Ryle 1974; Scheuer 1974). See Begelman et al. (1984) for an extensive review. In this model, the central SMBH is the source of energy, the jets/beams are tunnels by which energy is transported and the lobes are waste-tanks for decelerated jet materials. A SMBH is actively accreting matter unto itself; some of the material cannot escape once it crosses the event horizon (a region around the black hole with an escape velocity exceeding the speed of light), while others within the accreting disk get expelled (closely) along the black hole rotation axis in the form of highly beamed, supersonic relativistic particles and magnetic fields – the jets. For FR I sources, the jets get disrupted very early on their path due to the entrainment of external gas but for FR II the jet travels uninterrupted for large distance and terminates in a strong shock at a point of contact with the external gas. Most of the jet's bulk kinetic energy gets converted to relativistic particles and magnetic fields forming high brightness regions called hotspots. Some of the decelerated, high pressured material from the jets expands sideways from the hotspot creating a cigar-shape (Scheuer 1974) and fills this 'waste' plasma into cavities – the radio lobes.

The jet model also has a further implication. At the shock, two shocks are predicted to form: i) the beam shock and ii) the bow-shock. The beam-shock stops the continually incoming jet, while the bow-shock propagates into the unshocked gas and accelerates and heats the gas. The two beam-shock materials meet in pressure balance along the boundary surface layer, referred to as a layer of contact discontinuity.

2.3.4 Radio Galaxy and ICM Interaction

Radio galaxies interact with their ambient ICM. Below we consider some of the relevant physical implications resulting from this interaction.

2.3.4.1 Shocked Displaced Gas

Jets are expected to push the surrounding gas away from its path as it propagates through the ICM – creating cavities – inferred in X-ray studies as a reduction of X-ray surface brightness emission. These cavities are filled with radio galaxy plasma – radio lobe emission. For example, such cavities are observed in

the Perseus cluster (Boehringer et al. 1993), Cygnus A cluster (Carilli et al. 1994), Abell 2052 (Blanton et al. 2001), Abell 4059 (Heinz et al. 2002) and Hydra A (McNamara et al. 2000; David et al. 2001; Nulsen et al. 2002). The displaced gas is observed as a region of compressed gas of enhanced X-ray brightness surrounding the lobes. Figure 2.12 shows an example of the Hydra A cluster – the enhanced gas is most notable on the western side of the source, the right side of the figure. This compressed region around Hydra A (seen beyond the radio emission at 330 MHz) is interpreted as a weak shock of Mach number ~ 1.3. Similar weak shocks are also observed in the Perseus cluster (Fabian et al. 2003), M87 (Young et al. 2002) and Cygnus A (Snios et al. 2018).

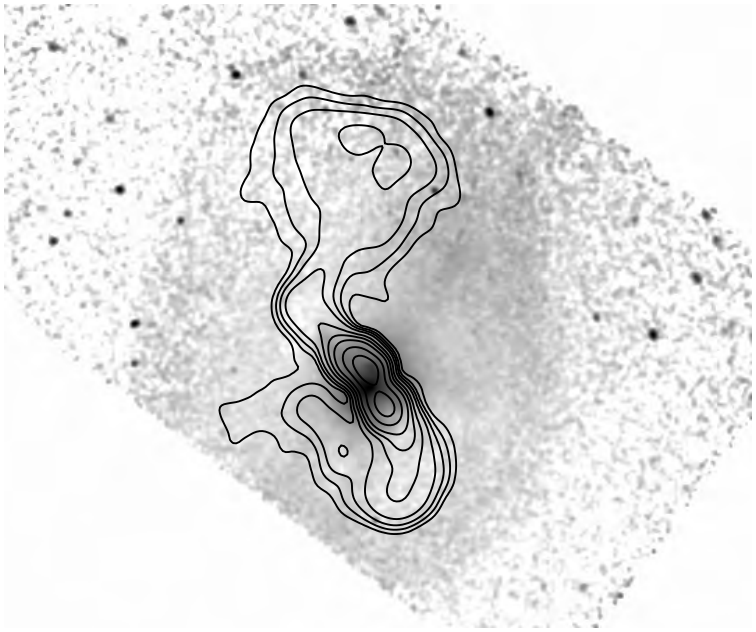

Figure 2.12: *Shocked compressed gas at the boundary of Hydra A radio emission.* Grey: X-ray cluster emission. Contours: Hydra A Radio emission at 330 MHz. Image credit: Nulsen et al. (2005a).

2.3.4.2 Feedback: Core-Cooling Problem

One of the things mentioned in Section 2.1.2 about CC and NCC clusters was the inability of the standard CF model to explain the much longer cooling rates, as well as lack of star formation at the centre of these clusters. It was then suggested that there has to be a heating mechanism occurring at the centre of the cluster which prevents both the cooling and star formation. Amongst the mechanisms proposed is heating by AGN (known as AGN feedback) – through depositing energy via jets into the ICM (see Bîrzan et al. 2004; Dunn and Fabian 2006; Rafferty et al. 2006; McNamara and Nulsen 2007).

2.3.4.3 Lobe-ICM Surface Layer Instabilities

It has been postulated that a mixing of gases can occur due to instabilities at the boundary surface layer (contact discontinuity layer) between the radio lobe and the external ICM. Scheuer (1974) suggested that such mixing can occur by means of convection, or diffusion. Bicknell et al. (1990) expanded on the diffusion-type

of mixing by demonstrating that a layer undergoing Kelvin-Helmholtz instabilities is prone to mixing and also suggested that the surface-wave like structures in the lobes of Cygnus A are indicative of this phenomenon.

2.4 Connection to the Dissertation

In this dissertation, we study two radio galaxies: Cygnus A and Hydra A. Cygnus A is an FR II radio galaxy and is hosted by a cD galaxy. Hydra A has the same type of parent galaxy but is an FR I. Both of these radio galaxies are situated at the centre of CC dense cluster systems. Enhanced surface brightness X-ray emission is observed at the lobes' boundaries, revealing that these radio galaxies interact with their environment, as shown in Figure 2.12 and 1.2

Studies of Faraday rotation show extremely large RM associated with these radio galaxies. Figure 2.4 shows RM across Hydra A, ranging between 3000 and -12000 rad m^{-2} with gradients of a few 100 rad m^{-2} arcsec^{-1} up to 1000 rad m^{-2} arcsec^{-1}. The RM of Cygnus A ranges between -4000 and $+3000$ rad m^{-2}, with similar gradients. The occurrence of Faraday rotation indicates the presence of a thermally magnetised gas region along the galaxy's line-of-sight. The possible locations along the path line include our Galaxy, the ambient cluster gas, shocked compressed gas surrounding the lobes, or mixed gas at the boundaries of or inside the lobes. Our Galaxy should contribute no more than 300 rad m^{-2} (see typical sky RM in Figure 2.5). A mixing of gas in the lobes is argued against based on the observed amount of depolarisation between 5 and 15 GHz, which is far less than those expected from such large Faraday rotations (Dreher et al. 1987; Taylor et al. 1990). Moreover, these observations infer perfect linearity between ψ and λ^2. This linearity indicates an external origin for the observed Faraday rotations. However, these conclusions were made using four sparsely sampled frequencies beyond > 5 GHz. At such sparsity, it is impossible to see any polarisation variations with λ^2. Additionally, the depolarisation is most dominant at lower frequencies, below 5 GHz.

Our study of these radio galaxies uses the new wideband observations taken with the JVLA covering $2 - 12$ GHz for Hydra A and $2 - 18$ GHz for Cygnus A at high spectral resolutions ~ 1 MHz and sub-arcsecond spatial resolution. These observations allow us to investigate the origin of the observed Faraday rotations, RM gradients, depolarisation and the structure of the magnetic fields in detail.

CHAPTER 3

Methodology: Faraday Rotation

"He counts the number of the stars; He calls them all by name. Great is our Lord, and mighty in power; His understanding is infinite."
Psalms 147:4-5

3.1 Faraday Rotation

The Faraday rotation effect occurs when a linearly polarised wave is rotated as it propagates through an ionised-magnetised gas. We first introduced this concept in Section 2.2.4.2. This chapter provides a detailed description of this topic by considering the different astrophysical situations and their implications to the observed polarised emission and the techniques used to interpret Faraday rotation observation data. The concepts are introduced more generically and later narrowed down to those applicable to this dissertation.

3.1.1 Rotation Measure vs. Faraday-Depth

There are likely multiple polarised sources and Faraday rotating gases along a particular propagation line in real life. For example, an extragalactic source's emission will pass through gas emission regions such as the IGM, the ISM in our Galaxy and Earth's ionosphere. Thus, the observed polarised emission is a sum of all possible contributions along the signal path (Burn 1966):

$$p(\lambda^2) = \int_{-\infty}^{\infty} f(\phi) e^{2i\phi\lambda^2} d\phi, \tag{3.1}$$

where λ is the observation wavelength [in meter], ϕ is the Faraday depth [in rad m^{-2}]:

$$\phi = \int_{0}^{L} n_e \mathcal{B}_{||} dl, \tag{3.2}$$

where 0 is at the site of the Faraday rotating emission region furthest from the observer and L is the site of the emission region closest to the observer, and $f(\phi)$ is the intrinsic complex fractional polarisation at ϕ – hereinafter, Faraday spectrum. Equation 3.1 relates two spaces: λ-space which is the "observation space" and ϕ-space that represents the "real space".

In an ideal situation whereby there is only a single Faraday rotating gas permeated by uniform magnetic fields in the foreground of a single polarised source, the Faraday depth in Equation 3.1 is equivalent to the

RM in Equation 2.23. Equation 3.1 reduces to:

$$p(\lambda^2) = p_i e^{2i\psi_i} e^{2iRM\lambda^2}, \tag{3.3}$$

where p_i and ψ_i are the intrinsic fractional polarisation and polarisation angle, respectively. The Faraday spectrum is a delta function:

$$f(\phi) = p_i e^{2i\psi_i} \delta(\phi - \phi_0). \tag{3.4}$$

Thus, "RM" is used to denote an ideal case of a single, uniform, foreground Faraday rotating screen. The RM for this situation is identified with Faraday depth, ϕ_0.

3.1.2 Rotation Measure Synthesis

RM synthesis, hereinafter RM-Synthesis, is a technique that was first introduced by Burn (1966) and later developed for implementation by Brentjens and de Bruyn (2005). This technique utilises the Fourier relation in Equation 3.1 to obtain the emission in real-space, $f(\phi)$. **The spectrum from RM-Synthesis gives important information – it is able to show us the number and the strengths of emission components in the data as a function of their Faraday depth – essentially, the amount of rotation each component experiences by passing from "there" to "here".**

However, performing the inverse Fourier transform of Equation 3.1 is made difficult by the fact that we only measure $p(\lambda^2 > 0)$, at discretely (and sometimes sparsely) sampled channels. To solve these two problems, Brentjens and de Bruyn (2005) treated them similarly to the issue of incomplete uv-coverage in aperture synthesis, by assuming that the observed polarised emission, p_{Obs}, is:

$$p_{\text{Obs}}(\lambda^2) = p(\lambda^2) W(\lambda^2), \tag{3.5}$$

where $p(\lambda^2)$ is the true emission ("complete/continuous") and $W(\lambda^2)$ is the sampling function (or weighting function). The idea is that $W(\lambda)$ takes a non-zero value at λ^2 where measurements are made and zero elsewhere. For example, when we assume a uniform weighting, then $W(\lambda^2)$ is 1, where there are measurements and 0 elsewhere. This immediately implies that $W(\lambda^2)$ is 0 at $\lambda^2 < 0$. The resulting inverse FT takes the form:

$$f_{\text{Obs}}(\phi) = K \int_{-\infty}^{\infty} p_{\text{Obs}}(\lambda^2) e^{-2i\phi(\lambda^2 - \lambda_0^2)} \mathrm{d}\lambda^2, \tag{3.6}$$

where

$$K = \left(\int_{-\infty}^{\infty} W(\lambda^2)\, \mathrm{d}\lambda^2 \right)^{-1}. \tag{3.7}$$

Equation 3.6 can be expressed in short as:

$$f_{\text{Obs}}(\phi) = f(\phi) * R(\phi), \tag{3.8}$$

where $*$ is a convolution and $R(\phi)$ is the RM transfer function (RMTF) – similar to the point spread function, PSF in aperture synthesis:

$$R(\phi) = K \int_{-\infty}^{\infty} W(\lambda^2) e^{-2i\phi(\lambda^2 - \lambda_0^2)} \mathrm{d}\lambda^2. \tag{3.9}$$

Equation 3.6 and 3.9 can be approximated as sums under the assumption that $\phi\delta\lambda^2 \ll 1$ for all channels:

$$f_{\mathrm{Obs}} = K \sum_{n=1}^{N} p_{\mathrm{Obs},n} e^{-2i\phi(\lambda_n^2 - \lambda_0^2)} \tag{3.10}$$

$$R(\phi) = K \sum_{n=1}^{N} W_n e^{-2i\phi(\lambda_n^2 - \lambda_0^2)} \tag{3.11}$$

where n is the channel.

Brentjens and de Bruyn (2005) introduced an additional derotation term λ_0^2 to reduce large phase variations/rotations within the main beam of the RMTF. For illustration purposes, we will show a few examples using simulated data. We generated these data by assuming a frequency range between 300 MHz ($\lambda = 1.0$ m) and 30 GHz ($\lambda = 0.01$ m). These are sampled equally in λ-space (not λ^2) to give a total of 1000 channels. The Faraday space, on the other hand, is restricted to ± 150 rad m^{-2}. Figure 3.1 shows examples of the RMTF with and without the derotation. Left plots are without derotation $\lambda_0^2 = 0$ and those on the right are with derotation – λ_0^2 is equal to the mean of λ^2. We show results for different wavelength range: 0.01 m to 0.95 m (first row), 0.3 m to 0.95 m (second), 0.6 m to 0.95 m (third), and 0.8 m to 0.95 m (fourth). The large phase variations occur at longer wavelengths. Thus, the derotation is only necessary for observations with narrower bandwidth at longer wavelengths. These rapid phase variations have the potential to prevent us from accurately determining the polarisation angle (Brentjens and de Bruyn 2005).

3.1.2.1 RM-Clean

The derived f_{Obs} is "dirty" – it is the true spectrum, $f(\phi)$ convolved by the dirty beam, the RMTF. One way in which the dirty spectrum is deconvolved is by using the technique called RM-Clean (Heald 2009). The RM-Cleaning procedure is as follows:

1) Identify a peak in $|f_{\mathrm{Obs}}|$ and locate ϕ that corresponds to the peak, hence ϕ_{peak}.
2) Multiply the extracted component by gain factor: $f_{\mathrm{Obs,\ peak}} \times$ gain.
3) Store Step 2 as a clean component.
4) Shift and scale the RMTF: $f_{\mathrm{Obs,peak}} \times$ gain $\times\ R(\phi - \phi_{\mathrm{peak}})$
5) Subtract Step 4 from the f_{Obs} to get the residual, f_{res}.
6) Then repeat Step 1 to 5 using the resulting residual at each iteration until reaching some threshold or a given total number of iterations.
7) Once the number of iterations/threshold is reached, convolve the clean components by an Gaussian of width equation to that of the RMTF. The resulting spectrum is the cleaned spectrum.

All the spectra presented in this work are cleaned using this technique, otherwise we explicitly state that the spectra shown are dirty or undeconvolved.

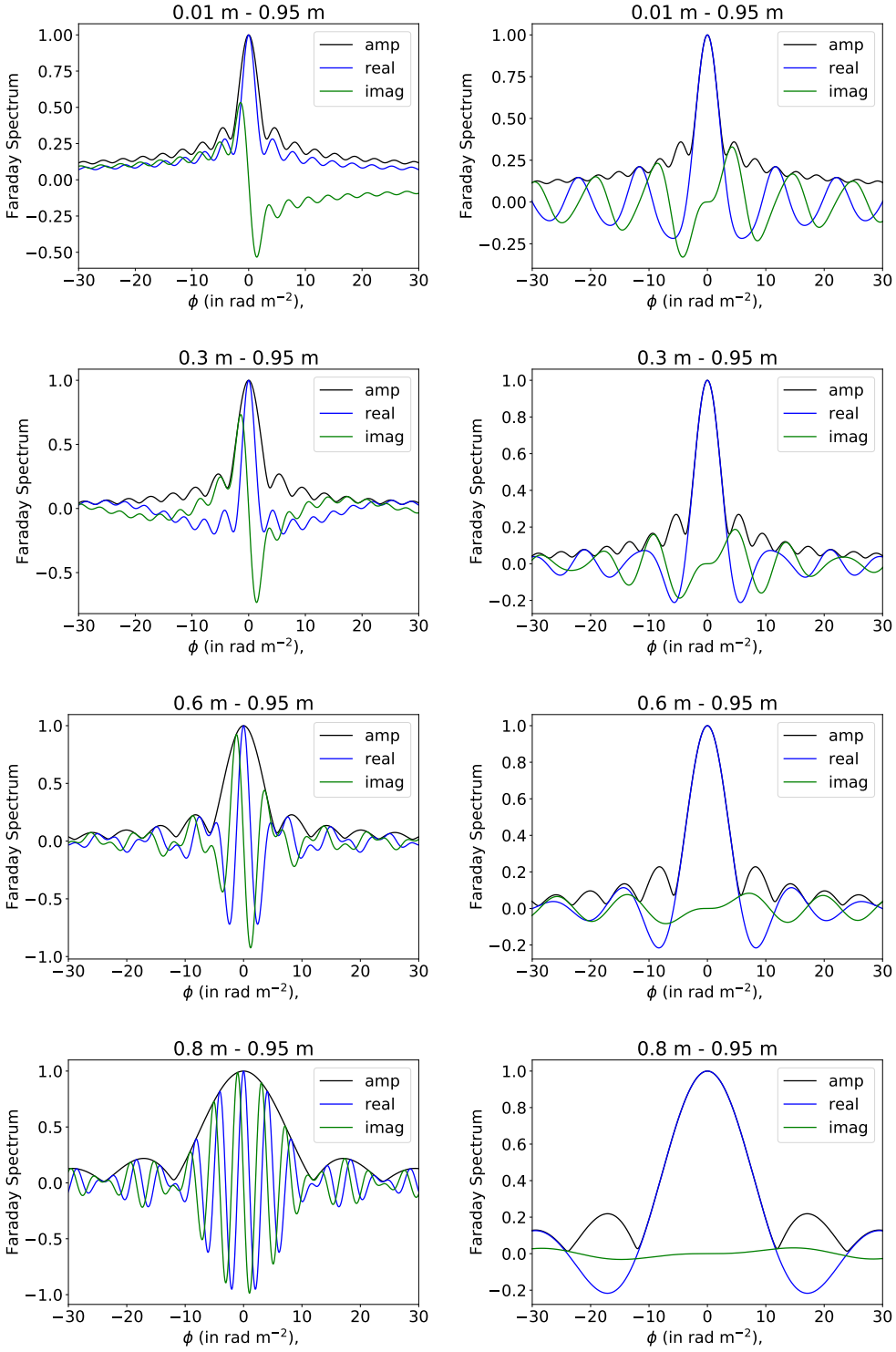

Figure 3.1: *RMTF at different minimum wavelengths with and without derotation.* Left: RMTF at $\lambda_0^2 = 0$ (without derotation). Right: RMTF at λ_0^2 equal to the average of λ^2 (with derotation). Black: Amplitude. Blue: Real part. Green: Imaginary. The derotation is most needed for narrower bandwidths at longer wavelengths.

3.1.2.2 Limitations

The wavelength coverage of the observations limits the results from RM-Synthesis. First, the bandwidth $\Delta\lambda^2$ of the observation determines our resolution in Faraday depth space – the full-width-half-maximum (FWHM) of the RMTF (Brentjens and de Bruyn 2005; Schnitzeler et al. 2009):

$$\delta\phi = \frac{3.8}{\Delta(\lambda^2)}, \tag{3.12}$$

where $\Delta(\lambda^2) = \lambda^2_{\rm max} - \lambda^2_{\rm min}$. In large bandwidths, the resolution is determined predominantly by longer wavelengths such that $\delta \sim 3.8/\lambda^2_{\rm max}$. Faraday components separated by a width $\leq \delta\phi$ will not be resolved, and vice versa. Figure 3.2 demonstrates this limitation. A left plot shows two components in Faraday space located at -75 rad m^{-2} and -67 rad m^{-2} respectively and a plot on the right shows a convolution of these two components by the RM-Cleaned RMTF at three wavelength ranges, namely: 0.01 m - 0.90 m (shown in green), 0.01 m - 0.70 m (blue) and 0.01 m - 0.50 m (red). These bandwidths result in $\delta\phi$ of ~ 5 rad m^{-2}, ~ 8 rad m^{-2} and ~ 15 rad m^{-2}, respectively. These results show the importance of a large bandwidth, especially the longer wavelengths.

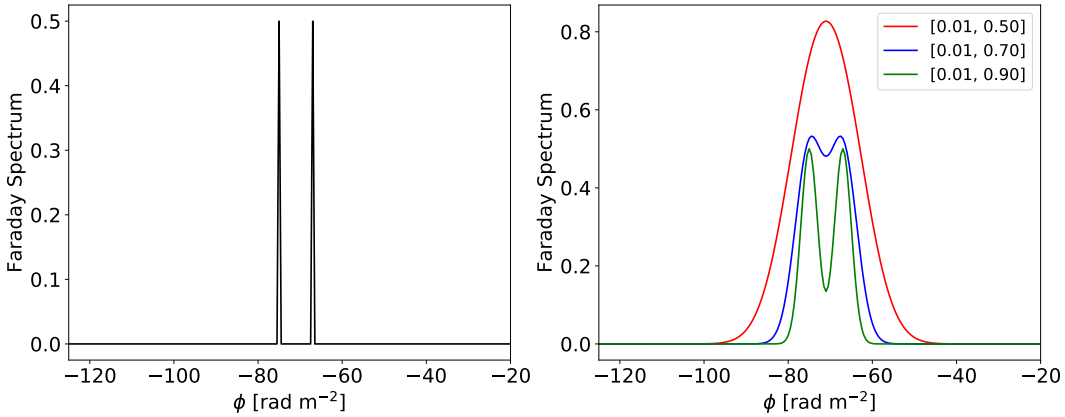

Figure 3.2: *Effects of the bandwidth on the RMTF resolution.* Left plot: Two real-valued components situated at -75 rad m^{-2} and -67 rad m^{-2}. Right plot: Two components convolved with the RM-Cleaned RMTF. The wavelength ranges show are 0.01 m - 0.90 m (green), 0.01 m - 0.70 m (blue) and 0.01 m - 0.50 m (red). Longer wavelengths and larger bandwidths are important to obtain a higher resolution in Faraday space.

The second limitation is the maximum Faraday depth we can probe, $\phi_{\rm max}$. This value depends on the channel width/spectral resolution, $\delta\lambda^2$:

$$\phi_{\rm max} = \frac{1.9}{\delta(\lambda^2)}. \tag{3.13}$$

The plane of polarisation of the emission with Faraday depths larger than $\phi_{\rm max}$ rotates rapidly across the channel, causing the emission to depolarise. Brentjens and de Bruyn (2005) approximated $\delta\lambda^2$ as:

$$\delta\lambda^2 = \frac{2c^2\delta\nu}{\nu_c^3}\left(1 + \frac{1}{2}\left(\frac{\delta\nu}{\nu_c}\right)^2\right), \tag{3.14}$$

where ν_c is the central frequency and $\delta\nu$ the channel width. The inner term in the parenthesis is negligible for high frequencies in which $\delta\nu \ll \nu_c$, so that the term in the outer parenthesis goes to 1. Suppose we observe at central frequency $\nu_c = 300$ MHz with a spectral resolution of $\delta\nu = 2$ MHz, any emission with Faraday depths greater than 140 rad m^{-2} will depolarise by more than 50%. This quantity is generally used to determine the observable range of Faraday depths.

The third limitation is our sensitivity to extended structures in Faraday space. The sensitivity to Faraday extended structure depends on our shortest wavelength, λ^2_{min} (our highest frequency):

$$\Delta\phi = \frac{\pi}{\lambda^2_{\text{min}}}. \tag{3.15}$$

Figure 3.3 shows examples of this limitation for λ_{min}: 0.01 m, 0.1 m and 0.30 m. These correspond to $\Delta\phi \approx 31500$, 320 and 35 rad m^{-2}, respectively. On the left is the input Faraday spectra with resolution 0 rad m^{-2} (first row) and ~ 5 rad m^{-2} (second row). We inverse Fourier transformed these input spectra using Equation 3.1 as follows:

$$p_{\text{model}}(\lambda^2) = \mathcal{K}\sum_{i=1}^{M} f_i e^{2i\phi_i\lambda^2}, \tag{3.16}$$

where $\mathcal{K}$ is the normalisation constant. We set this constant to 1. Thus, the resulting amplitudes do not have physical meaning. However, what matters here is the relative amplitudes. We then obtain the output spectra shown on the right panel of Figure 3.3 by performing RM-Synthesis using Equation 3.10 on $p_{\text{model}}(\lambda^2)$ restricted to $0.01 - 0.95$ m, $0.1 - 0.95$ m and $0.30 - 0.95$ m, respectively. Notice that the resolution for these frequency intervals is relatively similar ~ 5 rad m^{-2}. Therefore, the only factor that is affecting the results is λ^2_{min}. For a delta Faraday spectrum, the amplitude is unaffected by the value of λ_{min} – since a delta function has no width. An extended structure in Faraday space, on the other hand, is depolarised – the amplitude of the Faraday spectrum is reduced.

Figures 3.4 and 3.5 demonstrate another limitation to RM-Synthesis technique at two different wavelength ranges. The left column shows the model Faraday spectra, the middle column shows $p_{\text{model}}(\lambda^2)$ obtained using model spectra (the left column) and the right column shows the Faraday spectra obtained using RM-Synthesis on $p_{\text{model}}(\lambda^2)$. We show three situations: the top row shows a simple delta Faraday spectrum, the middle row is a Gaussian Faraday spectrum and the bottom row is a box Faraday spectrum. The input Faraday spectra are real-valued functions and the output are RM-Cleaned. The bandwidth used in Figure 3.4 is $0.02 - 0.3$ m (1 - 15 GHz) and in Figure 3.5 is $0.3 - 0.42$ m ($700 - 1000$ MHz). In both examples, we did not apply any derotation, $\lambda^2_0 = 0$.

For both frequency intervals, a simple Faraday spectrum is well reproduced – the real component equals the amplitude and the imaginary is zero. The same is true for a Gaussian spectrum except that the imaginary component is small but not zero. On the other hand, the reconstructed spectrum of a box-function is affected significantly by the frequency interval. For the 1 to 15 GHz frequency interval, the real component is boxy, while the imaginary component is non-zero and shows sharp edges. These sharp edges manifest themselves in the amplitude as “ear-like” structures. The ears become extreme at longer wavelengths (see Figure 3.5). In some cases, the ears can get so deep that they can easily be mistaken as two separate components.

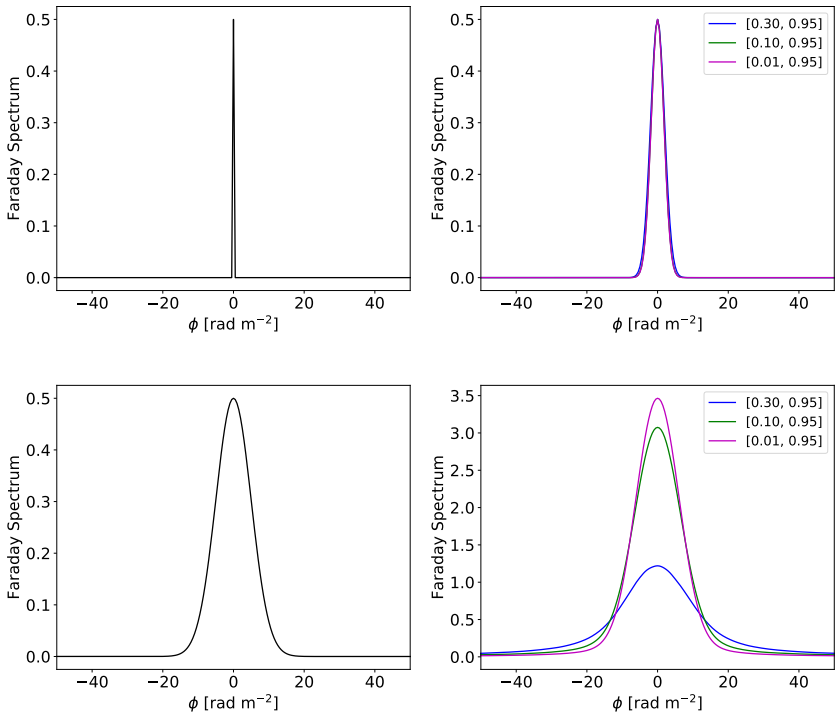

Figure 3.3: *RM-Synthesis limitation to extended structures in Faraday space*. Left: Input Faraday spectra. Right: Output Faraday spectra. Top: Delta spectra. Bottom: Gaussian spectra with the FWHM of 5. The amplitude of the Faraday extended structure is reduced by 50%, since its extension in Faraday space is $> \Delta\phi$.

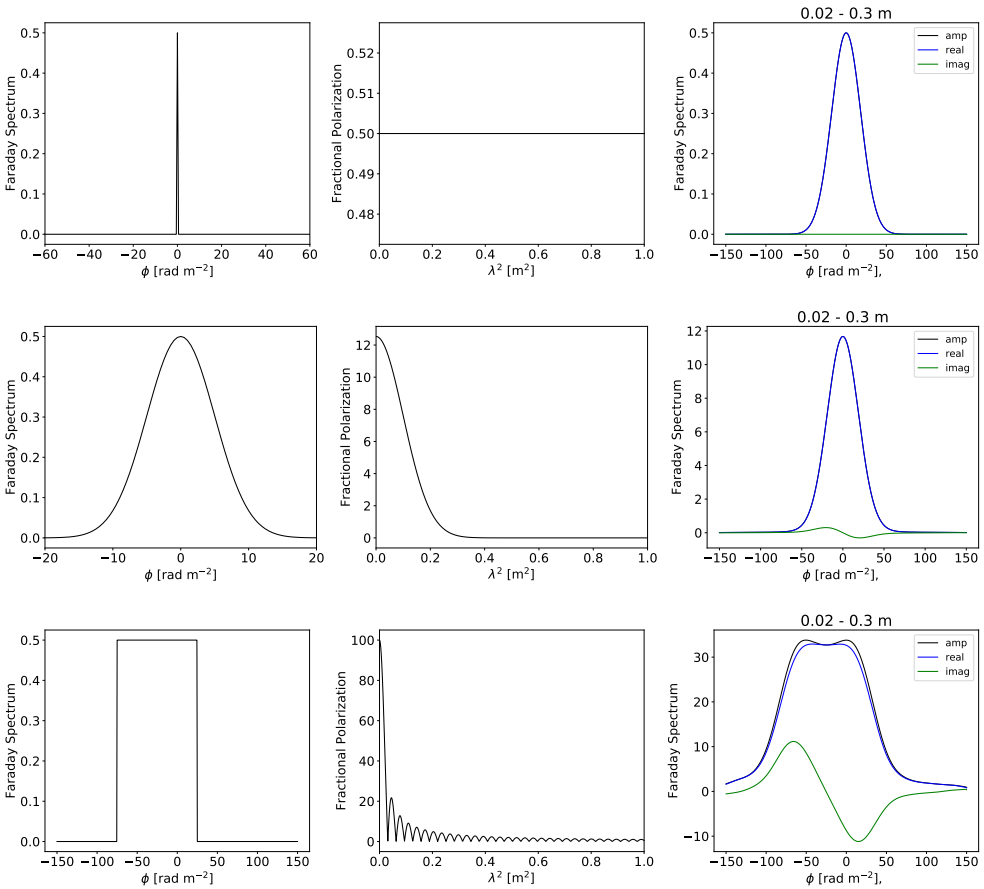

Figure 3.4: *RM-Synthesis limitation due to missing $\lambda^2 < 0$ for $0.02 - 0.3$ m wavelength range.* No derotation ($\lambda^2 = 0$). Left column: Input Faraday spectrum (real-valued function). Middle column: $p_{\text{model}}(\lambda^2)$ (see Equation 3.16). Right column: RM-Synthesis and RM-Clean results. Top row: Delta Faraday spectrum. Middle row: Gaussian. Bottom row: Box spectrum. For the last two spectra, the imaginary component is small but not zero, unlike the input spectra. For the box function, this non-zero imaginary component manifests itself as an "ear-like" structure in the amplitude.

This ear-problem results from the fact that measurements are only made at positive λ^2 (Frick et al. 2010). This effect appears particularly for functions with sharp edges such as a top-hat. Therefore, the relatively smooth functions deconvolve reasonably well. The ear-problem is an ill-posed inverse Fourier transform problem in which there is an infinite number of Faraday spectrum models that satisfy the measured data, $p(\lambda^2)$. To solve this problem requires that we impose some prior knowledge of the spectrum in Faraday space, ensuring that we select a unique model from an infinite number of models matching the data. Burn (1966) assumed that $f(\phi)$ is strictly real so that $p(\lambda^2)$ is Hermitian. This assumption is far from being an accurate representation of the sky – $f(\phi)$ is complex. Frick et al. (2010) proposed a method for predicting measurements in $\lambda^2 < 0$ by assuming that $f(\phi)$ is symmetric about a peak of interest, ϕ_0. Thus, $p(\lambda^2 < 0)$ is chosen to ensure this symmetry. The drawback of this method is its locality – it ignores the rest of the Faraday spectrum structures. However, the author introduced wavelets to solve for each peak locally and separately, see Frick et al. (2010), for details. So far, there has not been a satisfactory solution to this problem and it still researched by the community. However, as we have already demonstrated, this effect is less significant at high-frequency intervals. For this reason, we argue that the observations used in this dissertation (using $2 - 12$ GHz) are unlikely to be unaffected by this limitation, while observations with telescopes such as the MeerKAT ($900 - 1670$ MHz) and ASKAP ($700 - 1800$ MHz) need to factor this issue into their spectrum analysis. Moreover, there is good evidence that the problem has minimal effect on the presented data, as the observed Faraday spectral structures are not of the type which has been shown to cause problems.

3.1.3 Faraday Structure

Faraday situations are generally classified as Faraday-simple or Faraday-complex depending on the nature of $f(\phi)$ as a function of ϕ, $p(\lambda^2)$ as a function of λ^2, and $\psi(\lambda^2)$ as a function of λ^2 (Anderson et al. 2016). For example, a Faraday-simple source is a delta function in Faraday space, and Faraday-complex source has a spread (or width) in Faraday depth space.

3.1.3.1 Faraday-Simple

In a most straightforward physical situation of a single, purely synchrotron polarised source situated behind or embedded within a uniformly magnetised plasma, the complex polarised emission takes the form described by Equation 3.3. Note that for this situation, $\phi = RM$. Nevertheless, to define the Faraday spectrum, we will use ϕ rather than RM.

If we suppose that a uniform screen has Faraday depth of ϕ_0, the observed Faraday spectrum is simply a delta function with amplitude $|f(\phi)| = |p_0|\delta(\phi - \phi_0)$. The observed $p(\lambda^2)$ is unchanged by the screen, while the observed ψ will vary linearly with λ^2. We demonstrated this in the top row of Figure 3.4 and 3.5. The resolution of RMTF sets a limit to the observed Faraday spectrum (right plot) – the width of the RMTF being ~ 45 rad m^{-2} in both cases.

Suppose there are two or more consecutive Faraday rotating screens along the lines-of-sight without any intervening polarised emission and single background polarised source. In that case, the resulting Faraday depths will be the sum of the individual Faraday depths: $\phi = \phi_1 + \phi_2 + \ldots$. The resulting Faraday spectrum,

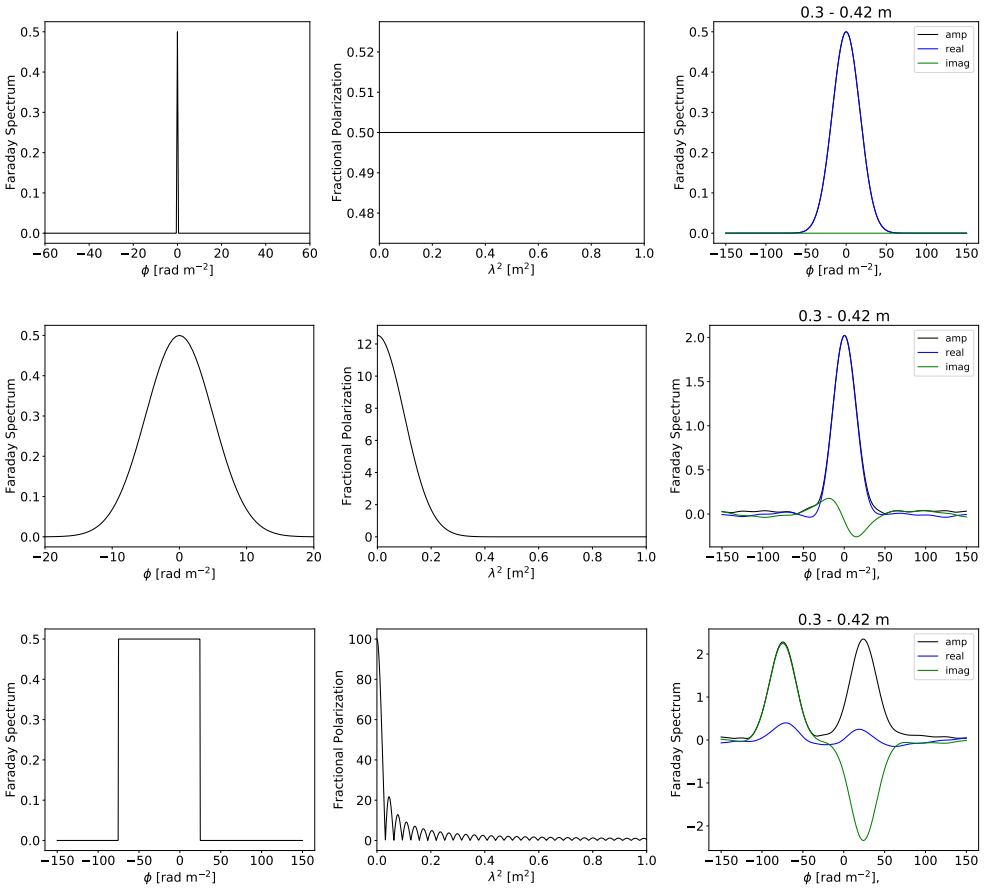

Figure 3.5: *RM-Synthesis limitation due to missing $\lambda^2 < 0$ for $0.3 - 0.42$ m wavelength range.* The simulation is similar to Figure 3.4 but for a different wavelength range. The real and imaginary components vary noticeably across the main beam and the ear-like structures are extreme – and likely to be misinterpreted as separate Faraday components.

$f(\phi)$, will remain a delta function and the fractional polarisation, $p(\lambda^2)$, will remain constant across λ^2 and the observed ψ will vary linearly with λ^2. Thus, it will not be possible to distinguish a single screen situation from a presence multiple screens situation (without intervening polarised emission).

3.1.3.2 Faraday-Complex: Multiple-Screens

When there is an intervening polarised emission between the multiple Faraday rotating screens, the situation becomes Faraday complex. The resulting Faraday spectrum will take the form:

$$f(\phi) = f_0(\bar{\phi}_0) + f_1(\bar{\phi}_1) + f(\bar{\phi}_2) + \cdots + f_S(\bar{\phi}_S), \tag{3.17}$$

where f_0 is a source furthest from the observer and f_S is the closest, and $\bar{\phi}_0$ denotes $\phi_0 + \phi_1 + \phi_2 + \cdots + \phi_S$, $\bar{\phi}_1$ is $\phi_1 + \phi_2 + \cdots + \phi_S$ and so forth. The resulting $f(\phi)$ is the sum of the delta functions peaking at $\bar{\phi}_0$, $\bar{\phi}_1$, $\ldots \bar{\phi}_S$. Figure 3.6 shows an example of this situation. The left plot is the input Faraday spectrum consisting of three polarised emissions at different Faraday depths. The middle plot is $p(\lambda^2)$ obtained by taking the Fourier transform of the input spectrum using Equation 3.16. The right plot is the output Faraday spectrum for wavelengths ranging between 0.02 m and 0.3 m. The fractional polarisation is a complicated function of λ^2. The three components are resolved in Faraday space for this wavelength range observation. This plot demonstrates the importance of the results from RM-Synthesis: they allow a simple and more practical way to determine the structure and strength of the emission, particularly when the emissions are resolved. On the other hand, the emission as seen in wavelength-space lets us know that components are beating against each other. Also, since there is no global decrease in fractional polarisation with increasing wavelength, the individual emission components involved are Faraday simple (not extended in Faraday space).

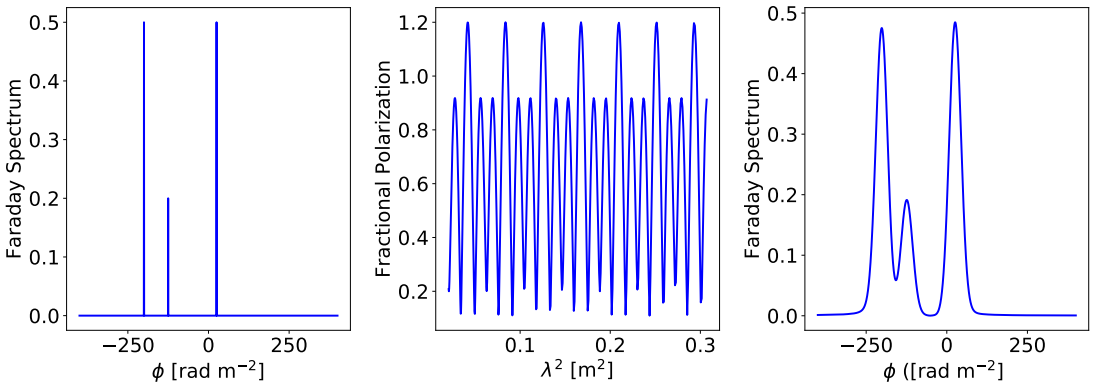

Figure 3.6: *Polarisation structure from multiple Faraday rotating screens with intervening polarised emission*. Left plot: Input Faraday spectrum. Middle plot: $p_{\text{model}}(\lambda^2)$ (see Equation 3.16). Right plot: The "observed" RM-Cleaned Faraday spectrum for observing wavelength range of 0.02 m - 0.3 m, with $\lambda_0^2 = 0$. The fractional polarisation is a complicated function of λ^2. For this wavelength-range, the multiple screens are resolved.

3.1.3.3 Faraday-Complex: Intermixed Gases

Ionised gas can also mix with polarised emissions. The process by which this can occur is still not well-known or understood. For example, Bicknell et al. (1990) proposed a mixing in the lobes of Cygnus A due to Kelvin-Helmholtz instabilities at the contact surface layer between the lobes and the external cluster gas. Another proposed process for the mixing of gases is when the material coming from the AGN moving along the jet already contain a mixture of thermal gas and radio-loud relativistic gas. Assuming that gases have mixed within some volume, we would expect different physical depths of the emission region to undergo different Faraday rotation, hence "differential rotation". In the presence of uniform magnetic fields within a uniform slab-like emission region, Burn (1966) showed that the observed fractional polarisation will take the form:

$$p(\lambda^2) = p_0\, e^{2i\psi_0}\, \frac{\sin \phi_0 \lambda^2}{\phi_0 \lambda^2}\, e^{2i\, \frac{1}{2}\phi_0 \lambda^2}, \tag{3.18}$$

where ϕ_0 is the Faraday depth from a layer closest to us (as the emission exits the mixed region). This situation is generally referred to as a uniform "Burn-slab". Figure 3.7 shows one realisation of this model: ϕ_0 is 50 rad m^{-2} and ψ_0 is $\pi/3$.

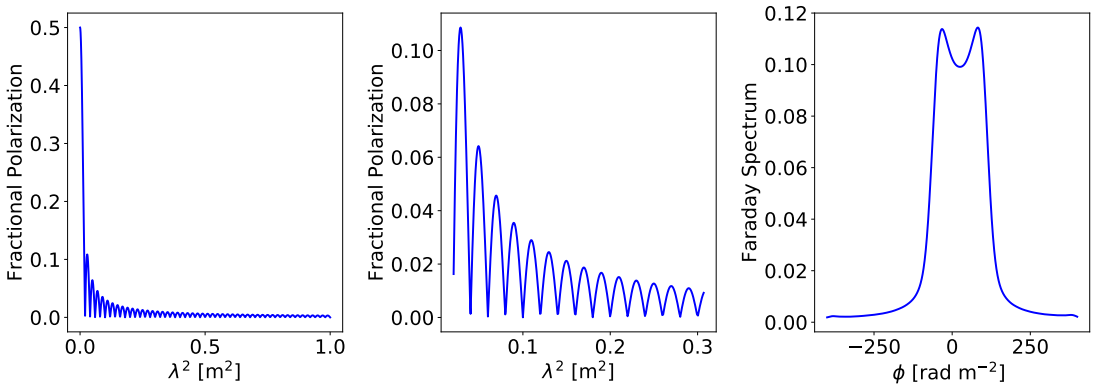

Figure 3.7: *Internally mixed region of thermal and synchrotron emitting gas in the presence of uniform magnetic fields*. Left plot: $p(\lambda^2)$ obtained using Equation 3.18 for wavelength ranges between 0.01 m and 1.0 m. Middle plot: The $p(\lambda^2)$ extracted between 0.02 m and 0.3 m. Right plot: Faraday spectrum of $p(\lambda^2)$ for $0.02-0.3$ m range. No derotation $\lambda_0^2 = 0$ was applied. Ideally, the Faraday spectrum should resemble a box-function but instead, we see ear-like structure described in Section 3.1.2.2.

It is also possible that the intermixed gas consists of both the uniform and random magnetic fields. In this situation, differential Faraday rotation will occur due to both the uniform and random fields. Burn (1966) derived an analytical expression for describing this phenomenon and showed that the fractional polarisation assuming that the source is a uniform-slab (see also Sokoloff et al. 1998):

$$p(\lambda^2) = p_0 e^{2i\psi_0} \left(\frac{1 - e^{-\eta}}{\eta} \right), \tag{3.19}$$

where $\eta = 2\sigma_0^2\lambda^4 - 2i\phi_0\lambda^2$, ϕ_0 is the Faraday depth due to the source's mean magnetic field and σ_0 is the

dispersion in the Faraday depths from randomly oriented cells of magnetised thermal gas:

$$\sigma_0 = 812\, n_0\, \mathcal{B}_0\, d\sqrt{N} \qquad [\text{rad m}^{-2}], \tag{3.20}$$

where n_0 is the electron density of the cell [cm^{-3}], $\mathcal{B}_0$ is the magnetic field of the cell [µG] and $N = L/d$ is the number of turbulent cells of size d [kpc] lying along the path length L.

This "random magnetic field" is modelled in terms of cells of uniform electron density and magnetic field strength, but random field direction – similar to a random walk problem. The resulting Gaussian distribution has a mean of zero and a non-zero dispersion, σ_0. This formulation of a Gaussian random field is used extensively in the literature. However, it does not provide the best physical picture as described in Section 2.2.7.2 (see also Equation 2.24).

The behavior of the function in Equation 3.19 depends on the ratio of the real (σ_0-term) and imaginary (the ϕ_0-term) parts. The two limiting cases are of interest:

- The real part dominates: $\sigma_0^2\lambda^2 \gg \phi_0$. There is no rotation in the plane of the polarisation and the resulting emission is highly depolarised: $p \longrightarrow p_0\sigma_0^{-2}\lambda^{-4}$.
- The imaginary part dominates: $\sigma_0^2\lambda^2 \ll \phi_0$. In this case, the depolarising effect of the fluctuations is negligible and the fractional polarisation behaves like a uniform Burn-slab: $p \longrightarrow p_0 \sin\phi_0\lambda^2/\phi_0\lambda^2$.

Figure 3.8 shows an example of this situation. The values of $p(\lambda^2)$ and the corresponding Faraday spectrum for situations whereby both σ_0 and ϕ_0 are important (top row) and also where σ_0-term (random component) dominates (middle row), and ϕ_0 (uniform component) dominates (bottom row). For regions where neither dominates, we would expect a complicated (less defined) Faraday spectrum. This represent a more realistic situation than the two extreme limits. See Burn (1966) and Sokoloff et al. (1998) for other model approximations such as a spherically mixed emission region, symmetry and asymmetry configurations, as well as non-uniformities.

3.1.3.4 Faraday-Complex: Spatially Unresolved Fluctuations

In real-life, the observing instruments have limited spatial resolution. Thus, sometimes the resolution beam may not be sufficient to resolve transverse fluctuations in the magnetic fields/electron density within the Faraday rotating gas. In such situations, the beam will encompass multiple polarised vectors, which will beat against each other. Thus, the resultant polarised emission will be the average of all the vectors within the beam. We refer to this situation as an 'artificial' Faraday-complexity or beam depolarisation since the occurrence of complexity results from the limitation of our instrument, not lines-of-sight effect as in Section 3.1.3.1.

Consider two adjacent screens, both within the same resolution element of the telescope. We denote the polarised fluxes, total fluxes and Faraday depths of the two adjacent screens by P_1, I_1, ϕ_1 and P_2, I_2, ϕ_2, respectively. The total flux within the beam is $I = I_1 + I_2$. The Faraday spectrum is $f(\phi) = (P_1\delta(\phi - \phi_1) + P_2\delta(\phi - \phi_2))/I$ – the two adjacent screens provide two separate spectral components, with strengths proportional to the polarised flux in each. The observed fractional polarisation flux

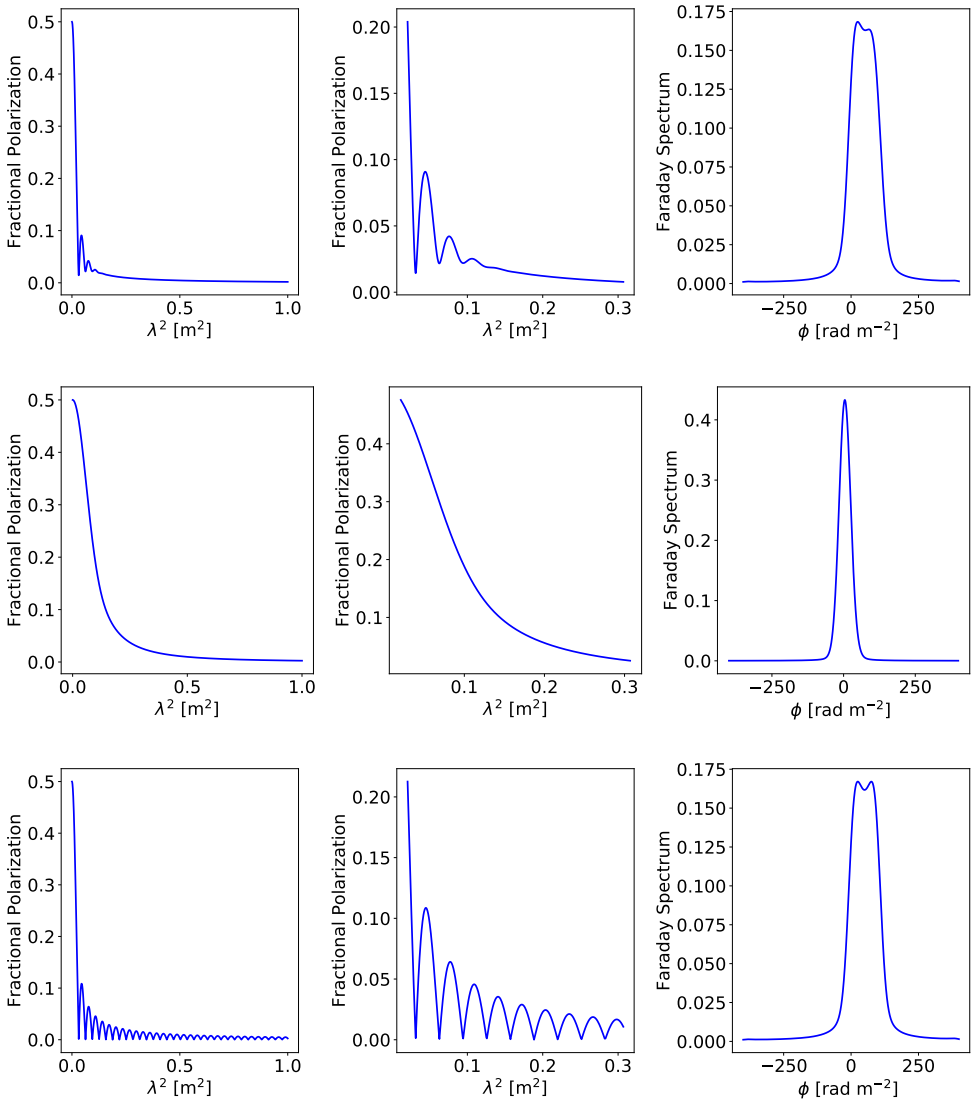

Figure 3.8: *Internally mixed region of thermal and synchrotron emitting gas in the presence of both uniform and random magnetic fields.* Left column: $p(\lambda^2)$ for wavelength range $0.01 - 1$ m. Middle column: $p(\lambda^2)$ restricted to $0.02 - 0.3$ m. Right column: Faraday spectra of the restricted $p(\lambda^2)$. We show different realisations obtained using Equation 3.19 for different values of σ_0 and ϕ_0. Top row: Both random and uniform fields are important ($\sigma_0 = 10$ and $\phi_0 = 100$ rad m^{-2}). Middle row: Random fields dominate ($\sigma_0 = 10$ and $\phi_0 = 10$ rad m^{-2}). Bottom row: Uniform fields dominate ($\sigma_0 = 0.1$ and $\phi_0 = 100$ rad m^{-2}). Uniform fields results in oscillatory structure in $p(\lambda^2)$ and ear-like structure in the Faraday spectra. Random magnetic fields result in smooth decaying $p(\lambda^2)$ and Gaussian Faraday spectra.

is:

$$p = (P_1 e^{2i\phi_1\lambda^2} + P_2 e^{2i\phi_2\lambda^2})/I \tag{3.21}$$

that represents an oscillating function with amplitude:

$$p = \sqrt{P_1^2 + 2P_1P_2\cos(2\Delta\phi\lambda^2) + P_2^2}/I \tag{3.22}$$

where $\Delta\phi$ is the difference in the Faraday depth of the two patches. The Fourier transform has two separated components beating in the polarised emission. Identifying the two components is possible if their separation $\Delta\phi$ is greater than the resolution in Faraday space. In general, there could be M number of screens across the resolution beam and the polarised vector takes the form:

$$p(\lambda^2) = \sum_j^M P_{0,j} e^{2\,i\,\psi_{0,j}} e^{2i\phi_j\lambda^2}/I, \tag{3.23}$$

where $P_{0,j}$ and $\psi_{0,j}$ are the polarised intensity and intrinsic polarisation angle of an jth component within the beam.

Figure 3.6 illustrates beam depolarisation for a situation with three polarised components within the beam. As we have already noted earlier, the resulting $p(\lambda^2)$ becomes a complicated function of λ^2. For multiple screens within the beam, $p(\lambda^2)$ can be approximated to a well-known function, depending on the distribution of ϕ within the beam. Supposing that there are linear gradients across the beam, with a slope in Faraday depth of $\Delta\phi/D$:

$$\phi = \phi_0 + \Delta\phi\,(x/D), \tag{3.24}$$

where ϕ_0 at the centre of the beam and D is the FWHM of the beam. First, we assume a square beam, such that:

$$w(x) = \begin{cases} 1/D, & \text{if } -D/2 < x < D/2. \\ 0, & \text{otherwise.} \end{cases} \tag{3.25}$$

The observed fractional polarisation will the take the form:

$$\begin{aligned} p(\lambda^2) &= p_0 e^{2i\psi_0} \frac{1}{D} \int_{-D/2}^{D/2} e^{2i\phi_0\lambda^2} e^{2i\Delta\phi(x/D)\lambda^2} dx \\ &= p_0 e^{2i\psi_0} e^{2i\phi_0\lambda^2} \frac{\sin(\Delta\phi\lambda^2)}{\Delta\phi\lambda^2}. \end{aligned} \tag{3.26}$$

In this scenario, the fractional polarisation is a decaying oscillatory function. The Faraday spectrum will be a top-hat function whose width is the span of the Faraday depths, $\Delta\phi$ across the square beam. Note that due to the limitation of RM-Synthesis we described above, the Faraday spectrum will consist of "ears" rather than a perfect top-hat function. The polarisation behaviour will be similar to that of Burn-slab in the presence of uniform magnetic fields shown in Figure 3.7.

The synthesised beam in real telescopes is approximately Gaussian. Thus, considering the same Faraday

depth distribution, such as a uniform gradient, but now distributed across a Gaussian beam of FWHM $\sim D$, such that $\sigma_{\rm FWHM} = D/2\sqrt{2\ln 2}$:

$$w(x) = \frac{1}{\sqrt{2\pi D}} e^{-4\ln 2 \frac{x^2}{D^2}}, \tag{3.27}$$

the observed fractional polarisation will be:

$$\begin{aligned} p(\lambda^2) &= p_0 e^{2i\psi_0} e^{2i\phi_0\lambda^2} \frac{1}{\sqrt{2\pi D}} \int_{-\infty}^{\infty} e^{-4\ln 2(x^2/D^2)} e^{2i\Delta\phi(x/D)\lambda^2} dx \\ &= p_0 e^{2i\psi_0} e^{2i\phi_0\lambda^2} e^{-\Delta\phi\lambda^4/\ln 2}. \end{aligned} \tag{3.28}$$

The corresponding Faraday spectrum is a Gaussian with a width proportional to Faraday depths' spread within the beam.

It can also happen that the magnetic field structure within the beam is non-uniform. Such situations are difficult to model. An extreme situation is that of unresolved random fluctuations. Various authors (such as Sokoloff et al. 1998; Tribble 1991; Burn 1966; Gardner and Whiteoak 1966) have modelled this depolarisation mechanism by assuming the foreground medium comprises of unresolved, randomly oriented cells; with each cell having a constant electron density, n_t, and constant magnetic field strength, $\mathcal{B}_t$, but random magnetic field direction. The observed fractional polarisation, in this case, is given by:

$$p(\lambda^2) = p_0 e^{2i\psi_0} e^{2i\phi\lambda^2} e^{-2\sigma_t^2\lambda^4}, \tag{3.29}$$

where σ_t is the dispersion with the same representation as Equation 3.20.

3.2 Complex Faraday Rotations

It is also possible that the situation is a bit more complicated than those described in Section 3.1.3. Real observations already reveal the presence of complex polarisation structures and Faraday rotations (see for example O'Sullivan et al. 2012; Anderson et al. 2016; Van Eck et al. 2017; Ma et al. 2019; Wolleben et al. 2019; Riseley et al. 2020; Sebokolodi et al. 2020; Stuardi et al. 2020). We do not, however, have a mathematical formulation for complex situations. In this section, we consider a few examples to demonstrate such situations. For example, there are likely multiple emission regions (with or without mixing) along the lines-of-sight. These regions may consist of very different Faraday rotation structures.

Figure 3.9 shows a few examples. The left column shows the input Faraday spectra, middle column the fractional polarisation $p_{\rm model}(\lambda^2)$ and right column the output Faraday spectra. The wavelengths are sampled between $0.02 - 0.3$ m, without derotation. The output spectra are RM-Cleaned. The top row shows three emission regions along a line-of-sight with similar Faraday depth distribution; the random magnetic fields. The second row shows a similar situation but for uniform fields. Note that the number of emission regions is unlimited. Thus, using three emission regions was mainly for illustration purposes. Additionally, the

emission distribution itself need not be Gaussian nor box-like.

The behaviour of $p(\lambda^2)$ is complicated for both cases. Nevertheless, the global decay of the fractional polarisation with increasing wavelength indicates that the components involved are extended in Faraday space. Besides this point, very little can be said about the data based on the fractional polarisation. This is a situation where RM-Synthesis comes in handy – since it reveals to us the different emission regions across the Faraday-space. Thus, it is advisable to use the information from these two spaces: λ^2-space and ϕ-space to derive a physical picture.

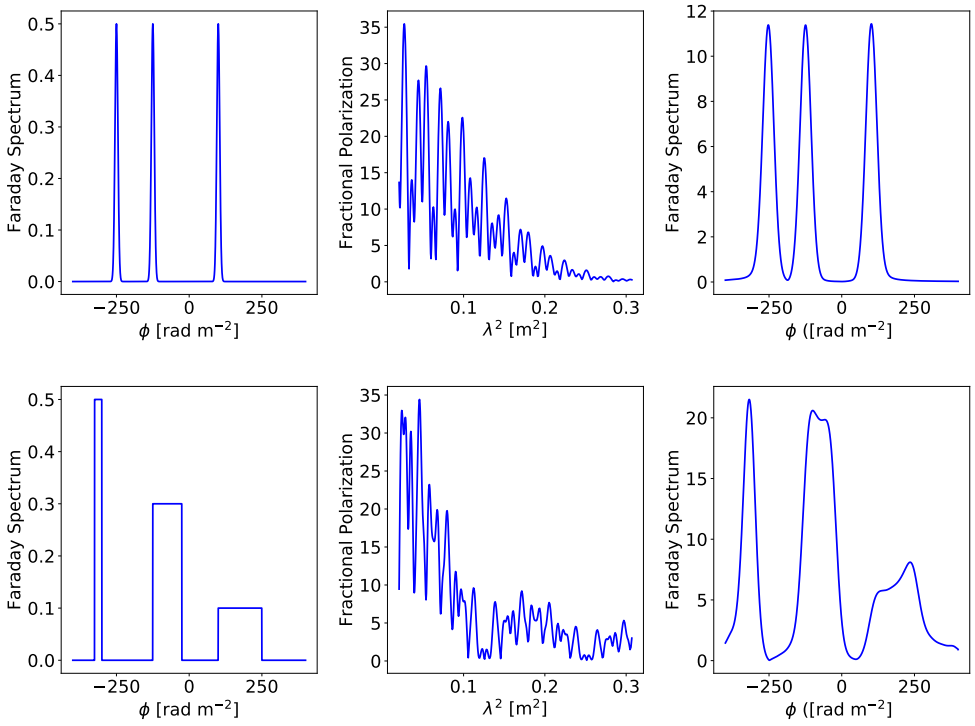

Figure 3.9: *Complicated polarisation structures resulting from multiple Faraday rotating and depolarising regions with intervening polarisation emission regions*. Left column: Simulated input Faraday spectra. Middle column: $p_{\text{model}}(\lambda^2)$ obtained from Equation 3.16. Right column: RM-Synthesis output Faraday spectra for $p_{\text{model}}(\lambda^2)$. The wavelength range used is from 0.02 m to 0.3 m, without derotation. Top row: Multiple random depolarising screens. Bottom row: Multiple uniformly depolarising screens. The behaviour of $p(\lambda^2)$ is complicated.

The models considered in Figure 3.9 are still limited: they inherently assume Gaussianity and uniformity and uncorrelated spatial structures in the magnetic fields. Studies of the diffuse emission from Galactic ISM (Armstrong et al. 1995; Haverkorn et al. 2008; Hollins et al. 2017) already reveal non-Gaussianity and spatial correlations in the ISM magnetic fields.

Basu et al. (2019) considered a "more realistic" case by incorporating both spatial correlations and non-Gaussianity of the field and electron density distribution. They generated these synthetic data using MHD simulations, which assumes an isothermal, transonic and compressible turbulent plasma. Furthermore, the plasma is assumed to consist of both synchrotron emitting gas and thermal magnetised gas – there is internal depolarisation (see Section 3.1.3.3). Figure 3.10 shows an example of the total synchrotron emissivity (left) and intensity (right) at 1 GHz from these simulations. The z-axis is the direction of our line-of-sight. The

emissivity was integrated along this direction to obtain synchrotron intensity for each pixel in the 2D plane.

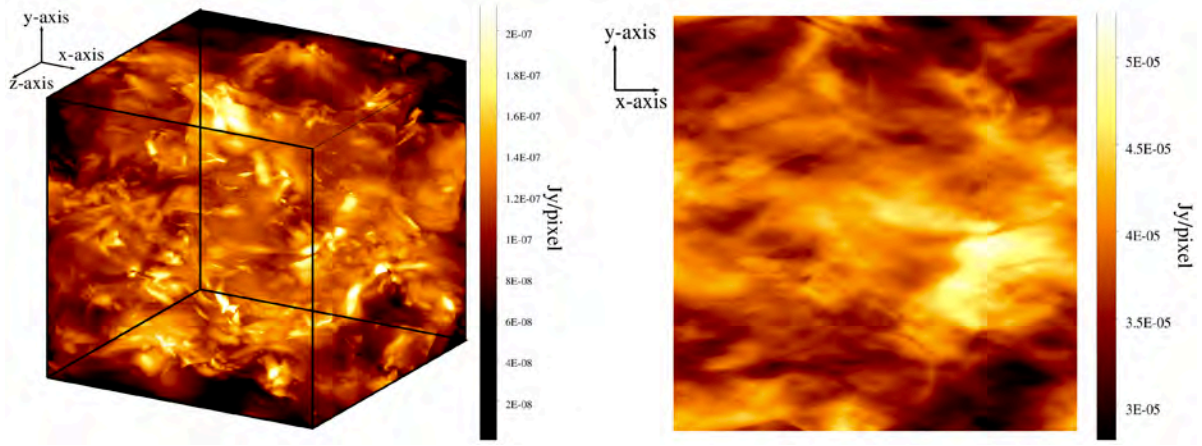

Figure 3.10: *MHD simulated synchrotron emissivity and intensity at* 1 *GHz.* Left: Total synchrotron emissivity. Right: Synchrotron intensity integrated along the z-axis. Image Credit: Basu et al. (2019)

The synthetic polarisation data were extracted assuming mock observations with a frequency range between 0.5 GHz (0.6 m) and 6 GHz (0.05 m) split into 500 frequency planes – resulting in Faraday depth resolution of 10 rad m^{-2}. Figure 3.11 shows the result of the spatially correlated, non-Gaussian magnetic field and electron density MHD simulation, which is a realistic situation. The Faraday spectra from a realistic situation are very complicated. We would expect to see such complexity in the real-life data provided that we have enough resolution in Faraday space. Seeing such complexities indicates the presence of very complex magnetic field structures and electron density distributions.

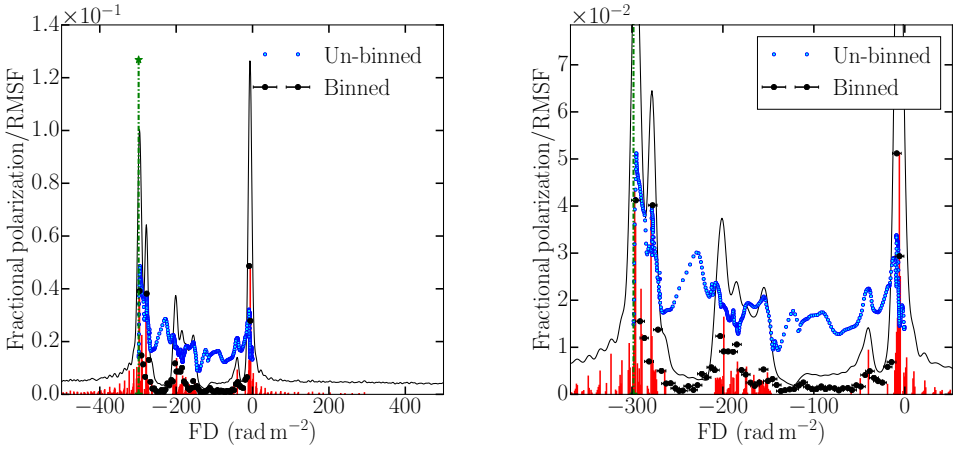

Figure 3.11: *Example Faraday spectrum from MHD simulations.* The simulations incorporate non-Gaussian, spatially correlated magnetic fields and electron density. Right: A zoomed version of the left plot. Red: RM-Clean components. Black solid: Convolved RM-Cleaned spectrum. Blue dots: Faraday spectrum model extracted directly from the polarisation cubes. Black dots: Binned version of blue dots. Image credit: Basu et al. (2019)

Although the above examples describe the situation for the lines-of-sight effect, the same complexities can occur due to beam depolarisation. Even worse, the two can occur at once: the lines-of-sight effect combined with spatially unresolved fluctuations. The spectrum from RM-Synthesis including $p(\lambda^2)$ cannot

distinguish these two possibilities (internal/external). Moreover, the spectrum contains no information on the location of the emission regions, let alone the order of occurrence along the lines-of-sight. Therefore, these measurements must be complemented with other external information to describe the physics at play.

However, these extremely complicated scenarios shown above likely do not apply to Cygnus A or Hydra A. They are relevant to (for example) galactic plane emission, which is truly messy. Cygnus A and Hydra A are isolated systems, where we believe (for the most part) that the emission and rotation are taking place in different physical regions.

3.3 Linear-Fitting to Polarisation Angle

Until now, we have only focused on the amplitude of the fractional polarisation and nothing on polarisation angle $\psi(\lambda)$. During Faraday rotation, the plane of polarisation rotates according to equation Equation 3.30.

$$\psi = \psi_0 + RM\lambda^2, \tag{3.30}$$

where ψ_0 is the source (intrinsic) polarisation angle.

By measuring ψ at two or more frequencies, it is possible to estimate ψ_0 and RM – the former is the y-intercept and the latter is the slope. The estimate of RM combined with measurements of n_e from X-ray observations allows us to estimate the strength of the line-of-sight magnetic field using Equation 2.23.

One challenge with this approach is called the $n\pi$-ambiguity problem. The solution to Equation 2.12 takes the form:

$$\psi = \psi \pm k\pi \tag{3.31}$$

where k is a positive integer. Polarisation angle itself is a pseudo-vector that lies between $0 < \psi < \pi$. However, ψ may experience many turns between successive frequencies. Therefore, proper care is needed to avoid erroneous fit estimates. The $n\pi$-ambiguity is generally dealt with by observing with very closely spaced frequencies, so that (Ruzmaikin and Sokoloff 1979):

$$|\lambda_2^2 - \lambda_1^2| < \frac{\pi}{2RM}. \tag{3.32}$$

For example, suppose we observe at two wavelengths: $\lambda_1 = 0.075$ m and $\lambda_2 = 0.06$ m, the observed RM must not exceed 1330 rad m^{-2}. Otherwise ψ will experience multiple turns – thus, requiring even more closer frequencies. For example, the sky RM of 37543 compact polarised sources shown in Figure 2.5 were obtained by fitting a linear model in Equation 3.30 to two VLA frequency measurements: 1364.9 MHz and 1435.1 MHz (Taylor et al. 2009). $RM \lesssim 680$ rad m^{-2} can be determined accurately without $n\pi$-ambiguities.

A second major challenge is that for Faraday complex situations where $\psi(\lambda^2)$ may vary non-linearly with λ^2. Previous studies had often assumed linearity, however, the new high spectral resolution and wideband observations are beginning to reveal departures from this linear behaviour, for example, Figure 10 and 13 of O'Sullivan et al. (2012) and see Anderson et al. (2016).

3.4 Direct QU-Fitting to Stokes Q and U

Direct QU-fitting is a technique for fitting well-defined analytical models such as those defined in section 3.1.3 directly to the observed Stokes *Q* and *U*, simultaneously. The fitting is usually done in λ^2-space (for example, O'Sullivan et al. 2012; O'Sullivan et al. 2013; Anderson et al. 2018; Pasetto et al. 2018; Kaczmarek et al. 2018; Knuettel et al. 2019; Schnitzeler et al. 2019; Ma et al. 2019) and less often in Faraday-space (Anderson et al. 2016). The advantage of QU-fitting is that it is parametric and considers the uncertainties in the measurements. More importantly, the results are much easier to interpret since a fitted model describes a specific physical situation. However, the latter is also a disadvantage since our analytical models are generally very simplified, are approximations (Gaussianity and uniformity) and are not suitable for describing complicated physical situations (real-life). For this reason, a common practice for characterising real data is by linearly combining different models (O'Sullivan et al. 2012; Anderson et al. 2015). A problem with this practice is that we may over-fit the data under the disguise of a "best model". Therefore, model selection criteria such as the Bayesian information criterion (BIC) and Akaike information criterion (AIC) are often used to choose the best model. These criteria take the complexity of the dimensionality model into account.

Compared to other Faraday rotation analysis techniques (for example, RM-Synthesis, linear fitting), QU-fitting is shown to characterise polarisation structures better. Sun et al. (2015) found that the different techniques, in general, can characterise a simple single Faraday screen– as we would expect – since the Faraday spectrum is a single peak, and $p(\lambda^2)$ is constant across λ^2 and $\psi(\lambda^2)$ varies linearly with λ^2. QU-fitting outperforms all the other techniques for Faraday complex models, such as two Faraday rotating screens, particularly, when the two components are unresolved in Faraday space. For example, RM-Synthesis often fails to recognise two unresolved Faraday components (Sun et al. 2015; Miyashita 2019). Sun et al. (2015) also found that when the two components are largely separated in Faraday space, the curves of $q(\lambda^2)$ and $u(\lambda^2)$ are very similar across the bandwidth (1100 - 1400 MHz). As such, many realisations can fit the data. At this point, QU-fitting is unable to derive unique physical properties of the input model. Miyashita (2019) pointed out this same issue for 700 - 1800 MHz bandwidth — but to a lesser extent (20% probability). With larger bandwidths, this issue may be less problematic.

QU-fitting forms a significant part of this dissertation. For this, we will briefly demonstrate its capability as it pertains to our wavelength coverage of 2 - 12 GHz for simple analytical models. The QU-fitting provides a proper way to map the possible physical situation.

3.4.1 Modelling Procedure

3.4.1.1 Basic Definitions: Probability Theory

This section gives brief definitions of probability theory, primarily the notations used to represent different types of probabilities. Most of the material in this section was taken from the 'Towards data science' website [1]. There are three types of probabilities, namely, the marginal, joint, and conditional probability. Marginal probability defines a probability of an event happening and is denoted by $\mathcal{P}(A)$, where "A" is an event. For

[1] https://towardsdatascience.com/

example, when throwing a fair die (fair means all sides have equal probabilities), the probability of finding a "4" ($A = 4$), for example, is $1/6$.

On the other hand, the joint probability describes a probability for an event "A" to occur together with event "B". The joint probability is denoted as $\mathcal{P}(A \cap B)$ or $\mathcal{P}(A,\ B)$. The $\cap$ or comma denotes an intersection ("and"). Consider, for example, playing cards: each card is described by both a colour (black/red) and a number (2 to 10) or four alphabetic symbols. One may ask what the probability of picking a black-coloured card with a number 6? In this case, black and 6 are two events such that $\mathcal{P}(\text{black}, 6)$. There are 52 playing cards of which 26 are red and 26 are black, and of this only 2 have a number 6 (a spade and a club), thus, $\mathcal{P}(\text{black}, 6) = 2/52$. Had we asked the question differently such as $\mathcal{P}(6, \text{black})$ the answer would still be the same because the joint probability is commutative: $\mathcal{P}(A, B) = \mathcal{P}(B, A)$. The joint probability is also associative: $\mathcal{P}(A, B, C) = \mathcal{P}([A, B], C) = \mathcal{P}(A, [B, C])$, where C is another event.

Events can be dependent or independent. The above example represents a case where the events are dependent. An example of independent events is that of rolling two fair dice, the probability of finding any number (say 4) on one dice is not dependent/affected by the result of the other dice. In this situation, the joint probability is a product of the individual marginal probabilities: $\mathcal{P}(A, B) = \mathcal{P}(A)\mathcal{P}(B)$. So the probability of finding a "4" on both dice is $1/6 \times 1/6$.

A conditional probability is a probability of an event (say A) occurring after one has already occurred (say B) and is denoted by $\mathcal{P}(A|B)$. The conditional probability is somewhat similar to joint probability except that one event has already taken place. For example, from the playing cards example above, we can assume that we already know that the card is black (event B has occurred) and then we ask what is $\mathcal{P}(6|\text{black})$? In this case, we no longer consider all the 52 cards but rather only 26 that are black and we find that of this 26 only two have a number 6 giving us $\mathcal{P}(6|\text{black}) = 2/26$.

These three types of probabilities can be related using a multiplication rule as follows:

$$\mathcal{P}(A|B) = \frac{\mathcal{P}(A, B)}{\mathcal{P}(B)}. \tag{3.33}$$

For a playing cards example, $\mathcal{P}(\text{black}, 6) = 2/52$ and $\mathcal{P}(\text{black}) = 26/52$, which results in $\mathcal{P}(6|\text{black}) = 2/52 \times 52/26 = 2/26$. Similar to Equation 3.33, $\mathcal{P}(B|A) = \mathcal{P}(B, A)/\mathcal{P}(A)$ and since the joint probability is commutative we find that:

$$\mathcal{P}(A|B) = \frac{\mathcal{P}(B|A)\,\mathcal{P}(A)}{\mathcal{P}(B)}. \tag{3.34}$$

Equation 3.34 is what is known as the Bayes' theorem. The marginal $\mathcal{P}(B)$ can be obtained from a joint probability $\mathcal{P}(B, A)$ through a process called marginalising, which sums over a variable of no interest, which happens to be A in our example:

$$\mathcal{P}(B) = \sum_A \mathcal{P}(B, A) = \sum_A \mathcal{P}(B|A)\mathcal{P}(A). \tag{3.35}$$

Equation 3.35 describes a situation for a discrete random variable. The term within the sum is called the probability mass function. When we assume that A and B are continuous random variables, a similar relation

is obtained:

$$\mathcal{P}(B) = \int_A \mathcal{P}(B, A)\, dA = \int_A \mathcal{P}(B|A)\mathcal{P}(A)\, dA. \tag{3.36}$$

The function $\mathcal{P}(B, A)$ is now called the probability density function.

3.4.1.2 Bayesian Inference

Bayesian inference is a method that uses Bayes' theorem. These methods are generally concerned with estimating a model's parameter values and selecting the best model for the given data. To estimate parameter values of a hypothesis (or model), H, the Bayes' theorem takes the form:

$$\mathcal{P}(\Theta|D) = \frac{\mathcal{P}(D|\Theta)\mathcal{P}(\Theta)}{\mathcal{P}(D)}, \tag{3.37}$$

where Θ denotes a set of parameters, D are the data, and $\mathcal{P}(\Theta|D)$ is the probability of Θ given D – and is normally referred to as the posterior probability. $\mathcal{P}(D|\Theta)$ is the probability of observing D given Θ and is equal to $\mathcal{L}(\Theta|D)$ – the likelihood of Θ given D, and $\mathcal{P}(\Theta)$ the prior probability and $\mathcal{P}(D)$ is the evidence (often denoted as $\mathcal{Z}$). The $\mathcal{Z}$ is the marginalised probability over Θ (for example, Equation 3.36):

$$\mathcal{Z} = \int \mathcal{L}(\Theta|D)\mathcal{P}(\Theta)\, d^K\Theta, \tag{3.38}$$

where K is the dimensionality of the parameter space. The role of the $\mathcal{Z}$ is to normalise the posterior probability – such that the area under the posterior is unity. The way in which $\mathcal{Z}$ is computed is described in section 3.4.1.3.

A prior probability is a probability distribution incorporating a piece of information known before the current experiment. This prior knowledge may come from various sources such as a personal experience and the current knowledge in the field. As such, the prior probability distribution may take any form depending on how confident one is about the best Θ, from now on Θ_{max}. For example, if we are entirely sure about the best fitting parameters, a prior distribution to use would be a delta function centred on Θ_{max} and peak given by $\mathcal{P}(\Theta_{\text{max}})$. However, that is generally never the case; instead, if Θ_{max} is known, it is usually within a margin of error. Thus, the prior distribution is best chosen as a function of some width, for example, a Gaussian or box function of some width, σ_Θ. The difference between these two example prior distributions is the probability given to each parameter value. For example, for Gaussian prior distribution, the parameter values closest to the mean have higher probability than those further away from the mean, while for a box prior distribution, all the parameter values within the range defined by the box are equally probable. However, what matters most is that the parameter interval mapped by the prior distribution includes the parameters of the largest likelihood. The process of choosing the maximum posterior is iterative and in each step, the Bayes' theorem narrows the posterior until it converges to the correct parameters.

For parameter estimation problems, $\mathcal{Z}$ is a constant since it is not dependent on Θ. As a result, Equation

3.37 reduces to:

$$\mathcal{P}(\Theta|D) \propto \mathcal{L}(\Theta|D)\mathcal{P}(\Theta). \tag{3.39}$$

Parameter values are sometimes estimated using the Maximum Likelihood Estimate (MLE). MLE searches for a set of parameters, say $\Theta = \{\theta_1, \theta_2, \dots\}$ of H, that maximises $\mathcal{L}$. Bayesian inference approach, on the other hand, uses the Maximum A Posterior (MAP) for estimating parameter values by incorporating priors in finding the global peak in the posterior. In this dissertation, we use MAP for parameter estimation. The advantage of using the MAP Bayesian approach over MLE is that it takes into account any prior information, which improves the convergences to a global maximum likelihood.

To obtain MLE, let us assume that the data, $D = \{x_1, x_2, \dots, x_N\}$, are generated from a Gaussian random process defined by the mean, μ, and the standard deviation, σ. Such that the likelihood for a single data point, x_1 takes the form:

$$\mathcal{L}(\mu, \sigma; x_1) = \frac{1}{\sigma\sqrt{2\pi}} \exp\left(\frac{(x_1 - \mu)^2}{2\sigma^2}\right). \tag{3.40}$$

The likelihood for N data points will then be $\mathcal{L}(\mu, \sigma; x_1, x_2, \dots, x_N)$. To simplify this rather complicated joint probability, an assumption of independence is made – the data are generated independently from random Gaussian distribution. In this case, the likelihood will simply be a product of the individual marginal probabilities:

$$\mathcal{L}(\mu, \sigma; x_1, x_2, \dots) = \frac{1}{\sigma\sqrt{2\pi}} \exp\left(\frac{(x_1 - \mu)^2}{2\sigma^2}\right) \times \frac{1}{\sigma\sqrt{2\pi}} \exp\left(\frac{(x_2 - \mu)^2}{2\sigma^2}\right) \times \dots \tag{3.41}$$

Equation 3.41 can then we simplified by taking natural logarithm:

$$\ln \mathcal{L}(\mu, \sigma; x_1, x_2, \dots) = \frac{1}{\sigma\sqrt{2\pi}} - \frac{(x_1 - \mu)^2}{2\sigma^2} + \frac{1}{\sigma\sqrt{2\pi}} - \frac{(x_2 - \mu)^2}{2\sigma^2} + \dots \tag{3.42}$$

From Equation 3.42 the parameters μ and σ that maximise the likelihood are solved for by taking $\partial \ln \mathcal{L}/\partial\mu = 0$ and $\partial \ln \mathcal{L}/\partial\sigma = 0$.

To obtain MAP, the same approach is followed except that now we find the maximum of $\mathcal{L}(\Theta|D)\mathcal{P}(\Theta)$. From the MAP, we can then derive the mode, mean, median, standard deviation, covariances.

For best model selection, the $\mathcal{Z}$ becomes important. The $\mathcal{Z}$ is the average likelihood of a hypothesis over its prior parameter space (Mackay 2003; Gregory 2005). As a result, the evidence can be used to assign probabilities to different hypotheses. A measure of relative $\mathcal{Z}$ will allow us to select a best model. For example, suppose we have two hypotheses, say H_1 and H_2, the relative probabilities can be obtained by taking the ratio of their posteriors as follows:

$$\mathrm{BF}_{12} = \frac{\mathcal{P}(H_1|D)}{\mathcal{P}(H_2|D)} = \frac{\mathcal{P}(D|H_1)\mathcal{P}(H_1)}{\mathcal{P}(D|H_2)\mathcal{P}(H_2)}, \tag{3.43}$$

where BF is the Bayes factor. The notation is reversed since we are now investigating the probability of H given D. The ratio of the priors $\mathcal{P}(H_1)/\mathcal{P}(H_2)$ is often equated to 1 to show that there is no preference to

the priors for one hypothesis over the other. Equation 3.43 becomes:

$$\mathrm{BF}_{12} = \frac{\mathcal{P}(H_1|D)}{\mathcal{P}(H_2|D)} = \frac{\mathcal{P}(D|H_1)}{\mathcal{P}(D|H_2)} = \frac{\mathcal{Z}_1}{\mathcal{Z}_2}. \tag{3.44}$$

An important characteristic of the $\mathcal{Z}$ is that it obeys Occam's razor theorem which states that a simple model (one with few parameters) will have a large $\mathcal{Z}$ compared to a complicated model (large number of parameters), unless the latter explains the data significantly better. Thus, if a hypothesis has a large $\mathcal{Z}$ it is preferred over the other. The BF is often expressed in terms of natural logarithm:

$$\ln \mathrm{BF}_{12} = \ln \mathcal{Z}_1 - \ln \mathcal{Z}_2. \tag{3.45}$$

Table 3.1 shows the selection criterion using BF for discriminating against two hypotheses (Kass and Raftery 1995).

Table 3.1: *Model selection criterion using BF as derived by Kass and Raftery (1995)*

$\ln \mathrm{BF}_{12}$	BF_{12}	Evidence against hypothesis 2
$0-1$	$1-3$	Weak
$1-3$	$3-20$	Positive
$3-5$	$20-150$	Strong
>5	>150	Very strong

3.4.1.3 The Evidence via Nested Sampling

Computing the $\mathcal{Z}$ in Equation 3.38 can be very computationally intensive, especially for high dimensional parameter space. Current methods for evaluating the $\mathcal{Z}$ include: thermodynamic integration, nested sampling (Skilling 2004) and Savage-Dickey density ratio (Trotta 2007). Of these three methods, nested sampling has been shown to be efficient in that it requires fewer posterior evaluations (Mukherjee et al. 2006). An extension to the original nested sampling technique was made by Shaw et al. (2007) and Feroz and Hobson (2008) to handle multimodal posteriors.

For consistency with the common literature, we let $\mathcal{L}(\Theta|D) = \mathcal{L}(\Theta)$ and $\mathcal{P}(\Theta) = \Pi(\Theta)$, such that Equation 3.38 becomes:

$$\mathcal{Z} = \int \mathcal{L}(\Theta)\,\Pi(\Theta)\,d^K\Theta. \tag{3.46}$$

Nested sampling method resolves a multi-dimensional problem by converting Equation 3.46 to a 1-dimensional problem. It does this by defining a prior volume, $\mathcal{V}(\varsigma)$:

$$\mathcal{V}(\varsigma) = \int_{\mathcal{L}(\Theta)>\varsigma} \Pi(\Theta)\,d^K\Theta. \tag{3.47}$$

This prior volume contains all prior combinations whose $\mathcal{L}(\Theta) > \varsigma$. The volume is enclosed by an

iso-likelihood contour $\mathcal{L}(\Theta) = \varsigma$. Equation 3.46 reduces to a 1D integral:

$$\mathcal{Z} = \int_0^1 \mathcal{L}(\mathcal{V})\,\Pi(\mathcal{V})\,d\mathcal{V}. \tag{3.48}$$

The prior volume is sequence of decreasing values: $\{\mathcal{V}_0, \mathcal{V}_2, \ldots, \mathcal{V}_M\}$, such that:

$$\mathcal{V}_0 = 1 > \mathcal{V}_1 > \mathcal{V}_2 \ldots \mathcal{V}_M > 0. \tag{3.49}$$

The likelihood, on the other hand, decreases monotonically as a function of $\mathcal{V}$ (Feroz and Hobson 2008) so that $\mathcal{L}(\mathcal{V}_{i+1}) > \mathcal{L}(\mathcal{V}_i)$. Figure 3.12 demonstrates this point better (Feroz and Hobson 2008). On the left is an example of a 2D posterior with iso-likelihood contours and on the right is the transformed $\mathcal{L}(\mathcal{V}_i)$. Note that from here onwards we will use $\mathcal{L}_i$ to denote $\mathcal{L}(\mathcal{V}_i)$.

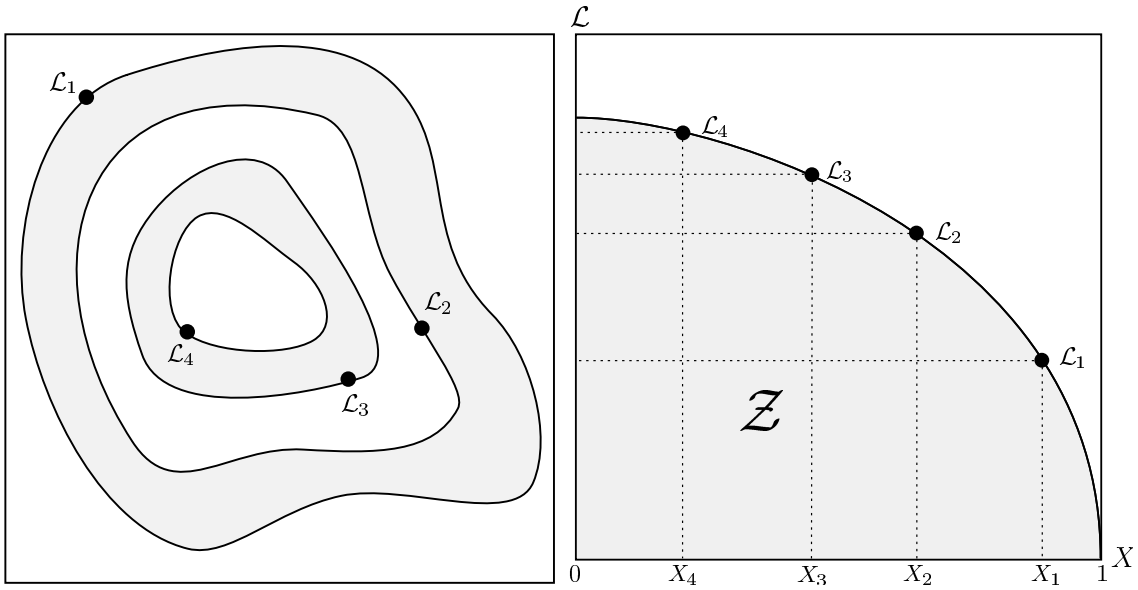

Figure 3.12: *Cartoon demonstrating a relationship between the likelihood and prior volume*. Left: 2D posterior showing four iso-likelihood regions as contours. Right: Transformed $\mathcal{L}(\mathcal{V}_i)$. Image credit: Feroz and Hobson (2008).

The $\mathcal{Z}$ is then the weighted sum of all the $\mathcal{L}_i$:

$$\mathcal{Z} = \sum_{i=1}^{M} \mathcal{L}_i w_i, \tag{3.50}$$

where w_i is the weight defined according to the trapesium rule as:

$$w_i = \frac{1}{2}(\mathcal{V}_{i-1} - \mathcal{V}_{i+1}). \tag{3.51}$$

The sum is done iteratively until reaching a specified $\mathcal{Z}$ precision. To begin with the process, the counter, i, is set to 0 and a total of N number of active points are drawn (or sampled) from the entire prior range $\Pi(\Theta)$. This sampled prior volume corresponds to $\mathcal{V}_0$. The likelihood of all the active points are then evaluated and ordered. The smallest likelihood, $\mathcal{L}_0$ is then removed from the active sample and is placed in an inactive

sample and is replaced by a randomly generated data point whose $\mathcal{L} > \mathcal{L}_0$. It can be seen that in each iteration, the prior volume is continually reduced while only the largest likelihoods are selected. This process is repeated until the entire prior volume is transversed (Feroz and Hobson 2008). Details on how the data points during the replacement are done efficiently can be found in Feroz and Hobson (2008) and references therein.

3.4.1.4 PyQUfit

We use MULTINEST for modelling our data (Feroz and Hobson 2008; Feroz et al. 2009). MULTINEST is a Bayesian inference that employs a nested sampling technique for computing the $\mathcal{Z}$ and also provides the maximum likelihood estimate (hence, the parameters) as a by-product. We used a python version of MULTINEST called pyMULTINEST (Buchner et al. 2014). We developed a more user-friendly and ready-to-use software package called PyQUfit[2] for fitting. PyQUfit inputs Stokes *Q* and *U*, frequency and noise text file. It then pre-processes the data, executes pyMULTINEST and outputs the best fitting parameters and other fitting statistics.

For our modelling, we assume a Gaussian probability density function for our likelihood function:

$$\mathcal{L} = \prod_{i=1}^{n} \frac{1}{\pi \sigma_{u_i} \sigma_{q_i}} \exp\left(\frac{-(q_i - q_{\text{mod},i})^2}{2\sigma_{q_i}^2} - \frac{-(u_i - u_{\text{mod},i})^2}{2\sigma_{u_i}^2} \right) \tag{3.52}$$

where q_i and u_i are the data points, $q_{\text{mod},i}$ and $u_{\text{mod},i}$ are model data.

For prior distributions, we chose uniform distribution. The intrinsic source polarisation prior is ranged between $[0, 1]$, polarisation angle $[-\pi/2, \pi/2]$ radians, Faraday depth between $[-1500, 1500]$ rad m^{-2} and Faraday dispersion and RM gradient $[0, 300]$ rad m^{-2}.

To qualitatively determine whether a model fits the data well or not, we use the reduced chi-square, χ_r^2 of the fit:

$$\chi_r^2 = \frac{1}{N-k} \sum_i \left(\frac{q - q_i}{\sigma_{q_i}} \right)^2, \tag{3.53}$$

where N is the number of data points and k is the number of free parameters. When χ_r^2 close to 1, the fitting is considered good, $\chi_r^2 \gg 1$ a "bad fit" and $\chi_r^2 < 1$ an overfit. The χ_r^2 values that we report are the average of χ_q^2 and χ_u^2 of Stokes q and u, respectively. We do note that a reduced chi-square is not always optimal for non-linear problems (Andrae et al. 2010). Also, the value of χ_r^2 is in itself subject to the noise. Thus, in addition to using χ_r^2, we will also evaluate the fits by eye to ensure that the results are consistent.

3.4.2 Simulated Data

We consider a mock observation covering a frequency bandwidth between 2 and 12 GHz. The frequency range choice is motivated by our real observation data presented in this dissertation for Cygnus A is 2 - 18 GHz and Hydra A is 2 - 12 GHz. We sampled frequencies between 2 - 3 GHz in steps of 4 MHz bandwidth channels, 3 - 8 GHz in 16 MHz and 8 - 12 GHz in 64 MHz – resulting in a total of 626 frequency planes. At

[2] https://github.com/Sebokolodi/PyQUfit

this bandwidth, the RMTF resolution is ~ 180 rad m^{-2}, minimum λ^2 of 6×10^{-4} m^2 gives $\Delta\phi = 5000$ rad m^{-2} and spectral resolution of 4 MHz at 2 GHz gives $\phi_{\rm max} = \pm 20000$ rad m^{-2}.

For modelling purposes, we restrict the RM between ± 1200 rad m^{-2}, polarisation angle between $\pm\pi/2$ and fractional polarisation between 0 and 1. We generate Stokes I using Equation 2.7, with $\nu_0 = 2$ GHz, I_0 at this frequency to be 0.2 Jy pixel^{-1} and ν is the above 626 frequency planes. To make the simulation seem realistic, we added the noise, N_I, to I. The noise is generated randomly over a normal distribution with the mean of zero and standard deviation of 2×10^{-3} Jy pixel^{-1}. The "observed" $I_{\rm Obs}$ is then $I + N_I$.

Figure 3.13 shows an example of Stokes I model (top row). To generate Stokes Q and U, we first generate fractional q and u, for a specific model and then convert them to Q and U, so that we add the noise to intensity and not to fractional polarisation:

$$\begin{aligned} Q &= q(\lambda^2) I_{\rm Obs} + N_Q \\ U &= u(\lambda^2) I_{\rm Obs} + N_U, \end{aligned} \tag{3.54}$$

where N_Q and N_U are noise in Stokes Q and U respectively.

The values of N_U and N_Q were generated similar to N_I but with standard deviation of 1×10^{-3} Jy pixel^{-1}. For a given realisation, we only change q and u by changing the different Faraday depths, intrinsic fractional polarisation, polarisation angle, Faraday dispersion and noise. However, we use the same I for all realisations. We generated 100 realisations in total. The bottom row of Figure 3.13 shows q and u from a single realisation using a model of a single polarised emission behind a uniformly magnetised screen (see Equation 3.3).

3.4.3 Modelling Results

3.4.3.1 Single Uniform Component

We generate the mock data by first considering a simple Faraday situation described in Equation 3.3 – a single polarised source behind a uniform Faraday rotating gas along the line-of-sight. We then fit the same analytical expression ("model 1") to these mock data, as well as a two-component model ("model 2"):

$$p(\lambda^2) = p_1 e^{2i\psi_1} e^{2iRM_1\lambda^2} + p_2 e^{2i\psi_2} e^{2iRM_2\lambda^2}. \tag{3.55}$$

The idea here is to see: i) whether BF is able to select a correct model (we use the word "correct" in this context mainly because we know the true answer, however, in real-life, the most appropriate wording is "the most probable"), ii) whether χ^2_r is able to determine if the model describes the data well or not and iii) whether QU-fitting is able to reproduce the correct parameters. We generate a total of 100 realisations. Figure 3.14 shows two examples from a single component fitting. The two components also result in the same fit so we decided not to show the plots.

Figure 3.15 shows the derived χ^2_r and $\ln$ BF. Both models fit the data well, based on the values of $\chi^2_r \approx 1$ – with slight overfitting. The $\ln$ BF suggests that a single component model is the most preferred of the two models (see Table 3.1). It is also immediately apparent that χ^2_r cannot be used to select the best model since

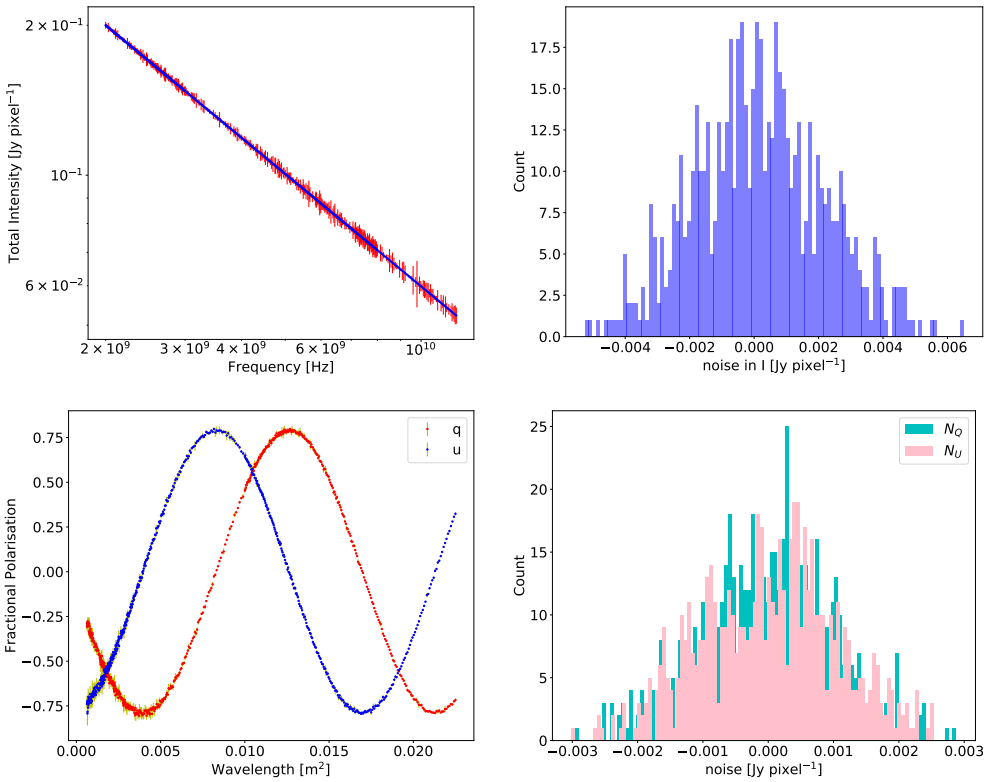

Figure 3.13: *Simulated Stokes I, fractional Q and U examples.* Top left: Stokes I. Top right: Noise distribution in Stokes I. Bottom left: Fractional Q and U. Bottom right: Noise distribution in Stokes Q and U. I_0 is set to 0.2 Jy pixel^{-1} at 2 GHz and spectral index -0.75. The noise was generated randomly to have a normal distribution with the mean of zero and the standard deviation of 2×10^{-3} Jy pixel^{-1} for I and 1×10^{-3} Jy pixel^{-1} for Q and U.

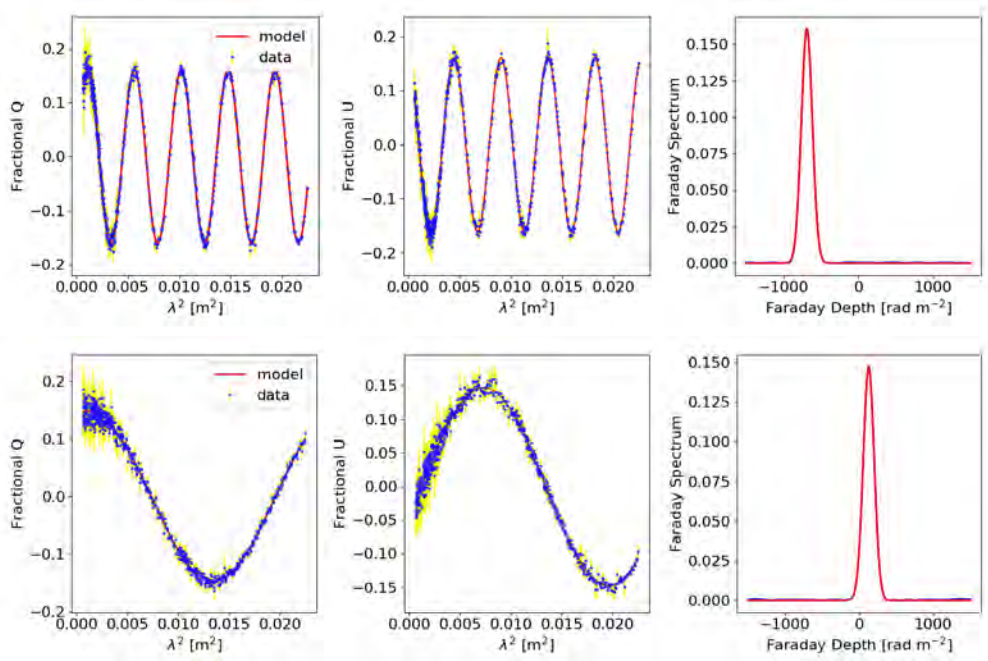

Figure 3.14: *Example QU-fitting of single component model to single component input data*. Left and middle column: Fractional Q and U respectively. Right column: Amplitude of the Faraday spectrum. The single component model fits the simulated data well. We find that the two-component model also fits the simulated data in the same way as the single component.

both models result in similar χ^2_r values.

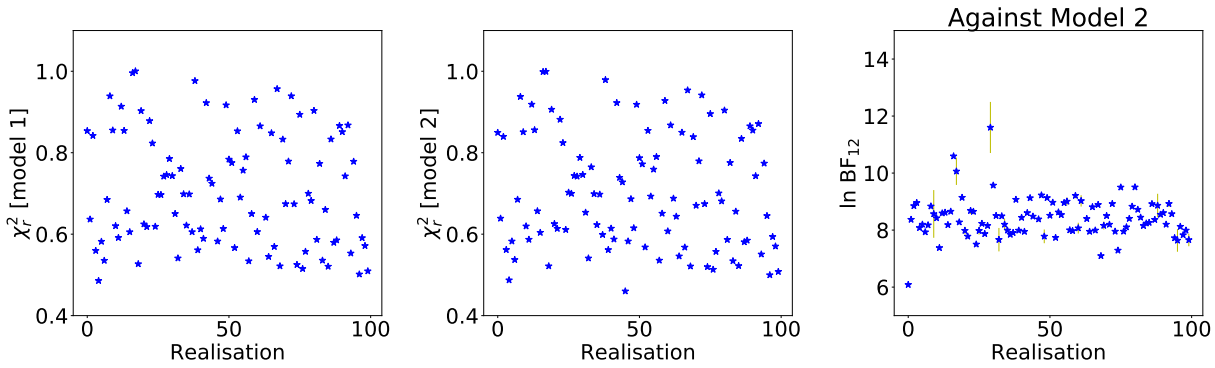

Figure 3.15: χ^2_r *and* $\ln$ *BF of model 1 and 2 fitted to a single purely Faraday rotating screen.* Left plot: χ^2_r of model 1. Middle plot: χ^2_r of model 2. Right plot: $\ln$ BF of model 1 and 2. According to χ^2_r, both models describe the data relatively well. The $\ln$ BF strongly favours a single uniform component hypothesis over a two-component model for all realisations (see Table 3.1). The $\ln$ BF was able to choose the correct model.

We looked into the residuals to check whether the estimated parameters are consistent with the input model parameters. Table 3.2 shows the mean and standard deviation of the residuals of the difference between the fitted parameter and input model parameter. The errors shown in this table are estimated mainly from the fitting errors; the input parameters for the simulated data had no errors. We show the result of the single

component model in the second column and the two-component model in the last two columns. The two-component model results were sorted based on the value of p_0 into a "strong" and "weak" component. The estimated parameters for the single-component model is consistent with that of the input data. The same is true for the strong component of the two-component model except that estimated parameters are associated with large fitting errors. On the other hand, the weak component is inconsistent with the input data for all parameters. This weak component's intrinsic polarisation is very small, therefore it indicates that this component may not be necessary.

This example shows that if we have the data of a simple Faraday situation, the $\ln$ BF can discriminate against fitting a complex model. We also find an incorrect model may tend to be associated with large fitted parameter errors, which can be used as another diagnostic for discriminating between two models.

Table 3.2: *Residuals of two fitted models to the single uniform Faraday rotating screen*

Parameter	Single-Comp		Two-Comp strong		Two-Comp weak	
residuals	mean	std	mean	std	mean	std
p_0	2×10^{-3}	1×10^{-2}	1×10^{-6}	2×10^{-4}	5×10^{-1}	3×10^{-1}
p_0-err	1×10^{-4}	6×10^{-5}	2×10^{-1}	2×10^{-1}	2×10^{-1}	2×10^{-1}
ψ_0	5×10^{-4}	7×10^{-3}	3×10^{-2}	3×10^{-1}	1×10^{-1}	1×10^{0}
ψ_0-err	3×10^{-4}	7×10^{-4}	5×10^{-1}	3×10^{-1}	8×10^{-1}	2×10^{-1}
RM	3×10^{-2}	4×10^{-1}	2×10^{-4}	9×10^{-2}	2×10^{2}	1×10^{3}
RM-err	3×10^{-2}	5×10^{-2}	5×10^{2}	3×10^{2}	7×10^{2}	2×10^{2}

3.4.3.2 Depolarising Single Component

We now consider a different situation whereby a single polarised emission is behind a turbulent Faraday screen. The emission will now depolarise. We assume random fluctuations within the screen described using Equation 3.29. The value of σ_t is generated uniformly between 10 and 100 rad m^{-2}. We fit the same analytical expression ("model 3") to the data, as well as two-depolarising Faraday components ("model 4"):

$$p(\lambda^2) = p_1 e^{2i\psi_1} e^{2iRM_1\lambda^2 - 2\sigma_1^2\lambda^4} + p_2 e^{2i\psi_2} e^{2iRM_2\lambda^2 - 2\sigma_2^2\lambda^4}. \tag{3.56}$$

We refer the reader to Table 3.3 for the different models.

Figure 3.16 shows the results of the χ^2_r and $\ln$ BF of model 3 and 4. We find that both models fit the data well based on χ^2_r. However, $\ln$ BF favours model 3 (the single depolarising screen) over model 4. The results of the $\ln$ BF are once again consistent with the correct model.

Table 3.3: *Models used for testing QU-fitting technique*

Model no.	Definition	Equation no.
1	single uniform screen	Equation 3.3
2	two uniform unresolved patches	Equation 3.55
3	single random screen	Equation 3.29
4	two random unresolved patches	Equation 3.56

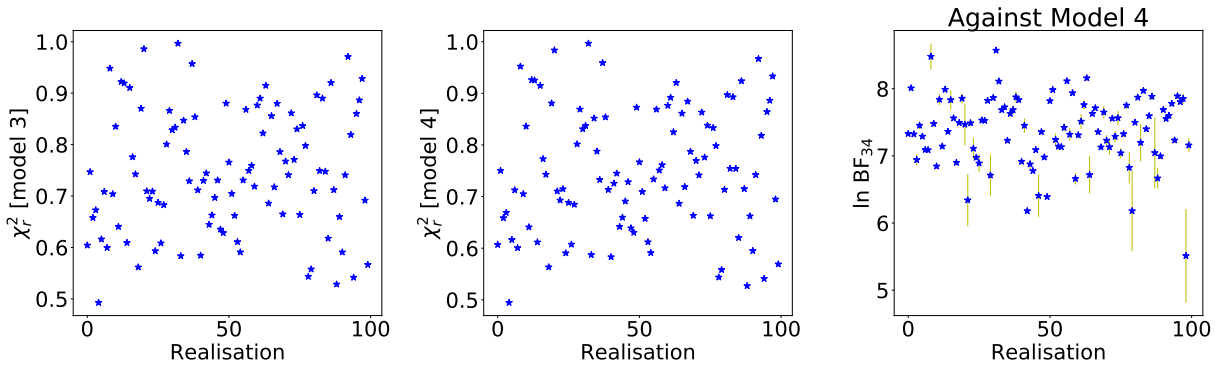

Figure 3.16: χ^2_r *and* $\ln$ *BF of model 3 and 4 fitted to a single randomly depolarising Faraday rotating screen.* Left plot: χ^2_r of model 3. Middle plot: χ^2_r of model 4. Right plot: $\ln$ BF of model 3 and 4. According to χ^2_r, both models fit the data well. The $\ln$ BF, on the other hand, strongly favours a single depolarising screen (model 3) – consistent with the truth.

3.4.3.3 Two Purely Faraday Rotating Patches

We now consider a situation of two unresolved/partially resolved purely (non-depolarising) Faraday rotating components, such that their separation is less than the RMTF width ~ 180 rad m^{-2} (are unresolved in Faraday space). We generate the input data using Equation 3.55 – the intrinsic p_0 and ψ_0 are determined similarly to the single component simulated data above. The RM of the first component, RM_1, is determined randomly between ± 1200 rad m^{-2}, while the RM of the second component is $RM_1 + \delta RM$, where δRM is any random number between ± 150 rad m^{-2}. We fit these data with model 1 to 4 (see Table 3.3). Note that model 2 is the correct model.

Figure 3.17 shows the fitting results of model 1 and model 2. Model 2 fits the data relatively well with $74/100$ having $\chi^2_r \lesssim 1$ and $10/100$ with $\chi^2_r \gtrsim 10$. The χ^2_r of model 1, on the other hand, is $\lesssim 1$ for $8/100$ and $\gtrsim 10$ for $77/100$. Model 1 fails to describe the majority of the data as expected – the model is too simple for the data. The $\ln$ BF correctly selects model 2 as the best model. However, unlike the above examples, the $\ln$ BF has huge values. These large values seem to be the result of complex input data. We find that only four realisations shown in red are in favour of model 1. These four realisations are associated with relatively small $\ln$ BF – indicating a weak evidence against model 2, the input p_1 and p_2 are either very small, or the component separation in Faraday space is small < 50 rad m^{-2} (see Figure 3.18). Thus, when one or both of the components have small fractional polarisation, combined with small separation, our modelling would not be able to notice the second component.

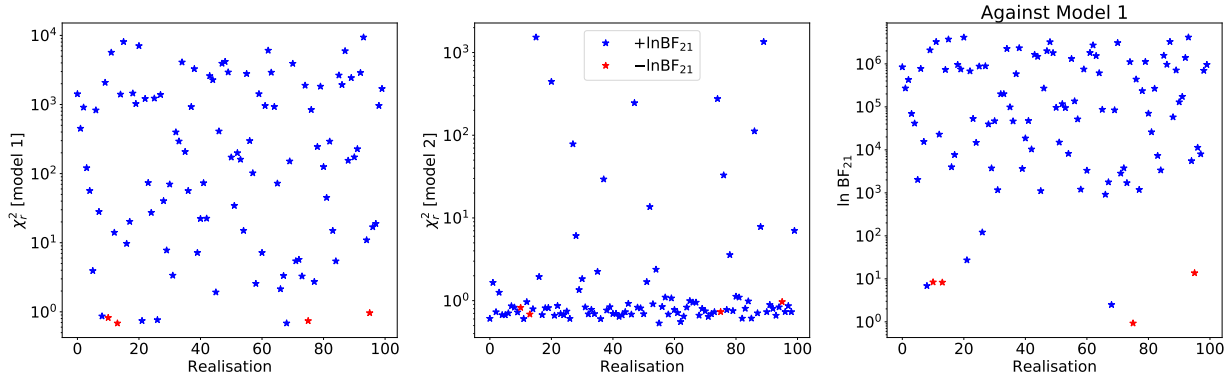

Figure 3.17: χ^2_r *and* $\ln$ *BF of model 1 and 2 fitted to a two purely Faraday rotating patches*. Left plot: χ^2_r of model 1. Middle plot: χ^2_r of model 2. Right plot: $\ln$ BF of model 1 and 2. Model 2 fits the data relatively well with 90% having $\chi^2_r \lesssim 10$. The $\ln$ BF strongly favours model 2 over model 1 – in agreement with the truth. Four realisations shown in red are in favour of model 1. We find that these four data points are associated with $|\ln \text{BF}| < 15$ (a relatively weaker evidence against model 2), the input p_1 and p_2 are either very small and/or their separation in Faraday space is small (see Figure 3.18).

Figure 3.19 compares the results of model 3 and model 4. None of these models are true but the modelling suggests that model 4 is more favourable than 3 – with four realisations in favour of model 3. We find that this is so for the same reason as the one above: that either the input p_0 is very small for one or both components, or the components are separated by no more than 50 rad m^{-2}. We find that the latter is true for all the four realisations (small separations) and only two realisations have $p_w < 10^{-2}$.

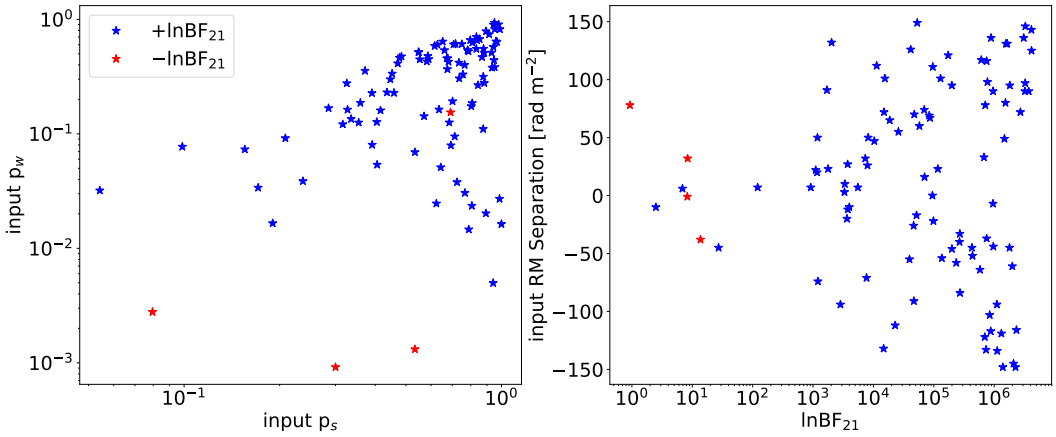

Figure 3.18: *Input parameters for two purely Faraday rotating patches.* Left plot: Input p_s (strong component) vs p_w (weak component). Right plot: Separation of the components in Faraday space. Blue points: Realisations in favour of model 2 (the true model). Red points: Realisations in favour of model 1. We find that the latter are associated with small intrinsic polarisation, and/or their separation is small < 50 rad m^{-2}. A realisation in red with large p, actually has a separation of -1 rad m^{-2}. At such separation, it is not surprising the modelling cannot recognise the second component. The same is true when the input p_w (and sometimes p_s) is extremely small.

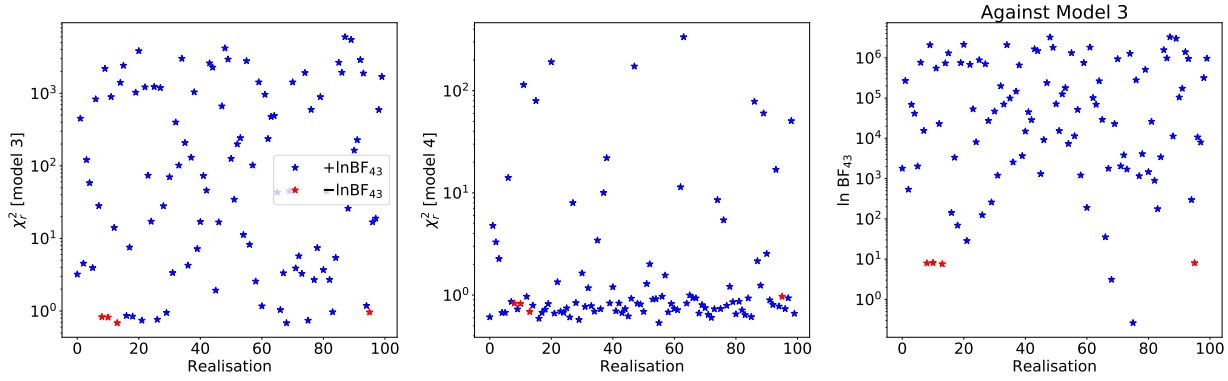

Figure 3.19: χ^2_r *and* $\ln$ *BF of model 3 and 4 fitted to two purely Faraday rotating patches.* Left plot: χ^2_r of model 3. Middle plot: χ^2_r of model 4. Right plot: $\ln$ BF of model 3 and 4. Blue points: Positive $\ln$ BF in favour of model 4. Red points: Negative $\ln$ BF in favour of model 3. The $\ln$ BF is strongly in favour of model 4.

Figure 3.20 shows the result of model 2 and 4. Note that model 2 is the correct model. According to the χ^2_r, both models fit the majority of the realisations well with $\chi^2_r \sim 1$. We find the realisations not in favour of model 2 (red points in the left plot) are generally associated with large χ^2_r – bad fitting. $\ln$ BF, on the other hand, is in favour of model 2 for $65/100$ realisations and in favour of model 2 for $35/100$ realisations.

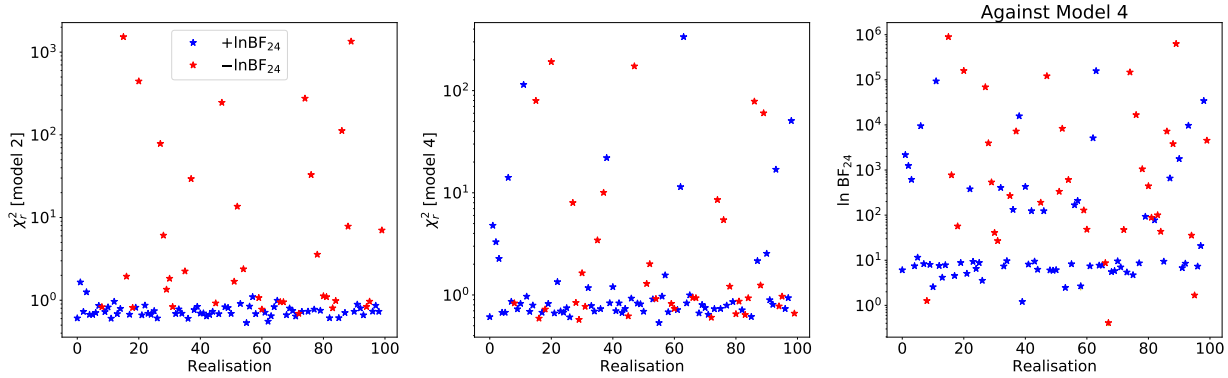

Figure 3.20: χ^2_r *and* $\ln$ *BF of model 2 and 4 fitted to two purely Faraday rotating patches*. Left plot: χ^2_r of model 2. Right plot: χ^2_r of model 4. Right plot: $\ln$ BF of model 2 and 4. Blue points: Positive $\ln$ BF in favour of model 2. Red points: Negative $\ln$ BF in favour of model 4. Both models fit the majority of the realisations with $\chi^2_r \sim 1$. Most of the realisation in favour of model 4 over model 2 have large χ^2_r (poor fit, red points in the left plot), with fewer exceptions. $\ln$ BF is in favour of model 2 for $65/100$ realisations (shown in blue) and in favour of model 2 for $35/100$ realisations.

Figure 3.21 shows the fitted parameter solutions for model 2 and 4. See figure caption for details. In general, solutions with large χ^2_r should be discarded – the estimated errors will be wrong, when the estimated separation is < 50 rad m^{-2} care must be taken in interpreting the results. Additionally, the values and errors in fitted parameters may provide an indication as to whether a term in a nested model is needed.

3.5 Summary

This chapter described Faraday rotation and showed that this could be a complicated phenomenon, particularly for real-life situations. We also presented the different analysis techniques, namely RM-Synthesis + RM-Clean, linear-fitting and QU-fitting. In this dissertation, we utilise RM-Synthesis and QU-fitting for analysing the data. These techniques are complementary: RM-Synthesis allows us to "visualise" the physical structure and emission strength in real space, while QU-fitting enables us to "model" the physical situation. We have demonstrated that the BF can discriminate between two models – for example, a single component from a double component model. We also showed cases where care must be taken in the interpretation of the results, for example, in a case where there are unresolved or weaker components, as well as when the fitted models are nested (see model 2 and 4 in section 3.4.3.3). In the latter situation, the estimated parameters tend to be associated with large fitting errors, which can then be used to determine whether a parameter is essential/exists or not. The χ^2_r is best used to determine whether a model describes the data or not – and should not be used to pick the best model. This is because a complicated model (with a large number of parameters) will fit the data well due to overfitting. On the other hand, the $\ln$ BF considers the model's complexity – it disadvantages a complicated model unless this model indeed describes the data better than the simple model.

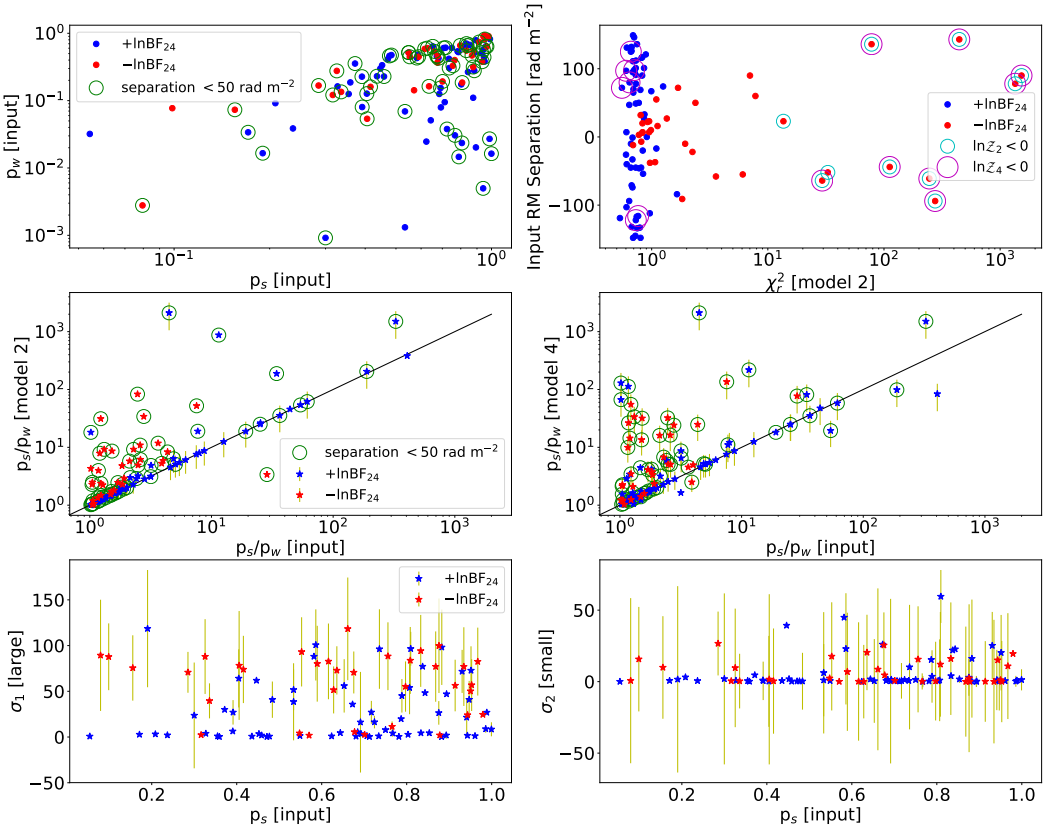

Figure 3.21: *Estimated parameters for model 2 and 4 fitted to two-uniform Faraday rotating screens.* Blue points: Realisations in favour of model 2. Red points: Realisations in favour of model 4. Open green circles: Component input separations < 50 rad m^{-2}. Empty cyan and magenta circles: Realisations with negative $\ln \mathcal{Z}$ for model 2 and 4, respectively. Top left plot: Input intrinsic fractional polarisation of the strong "s" and weak "w" component. Top right: χ^2_r of model 2 as a function of separation. Middle row: A ratio of the weak to strong component's intrinsic fractional polarisation of the input data vs model 2 (left), and model 4 (right). Bottom row: The derived σ_1 (larger) and σ_2 (smaller) from model 4. In general, we find that realisations favouring model 4 tend to have separation $\lesssim 50$ rad m^{-2}, or are associated with larger χ^2_r values. The derived p_0 ratios of the realisation favouring model 4 differ from the input ratios – indicating failed solutions. These results show the limitation of our technique towards small separations. The derived Faraday dispersions are close to 0 and those with large values are associated with large fitted errors. We find that for small σ_2, roughly 72% have errors $\gtrsim$ the estimated σ_2. This result reveals that σ is not important to the data (those close to 0), or the estimated values are unreliable (large errors).

CHAPTER 4

A Wideband Polarisation Study of Cygnus A

"I (God) have made the earth, and created man on it. I – My hands – stretched out the heavens, and all their host I have commanded."
Isaiah 45:12

4.1 Introduction

In this chapter, we present the results of our new wideband (2 – 18 GHz), full polarisation and high-spectral resolution observations of Cygnus A taken with the JVLA. The majority of the work presented here is also published in *The Astrophysical Journal*, titled "*A Wideband Polarisation Study of Cygnus A with the Jansky Very Large Array. I: The Observations and Data*" (Sebokolodi et al. 2020). The primary science goals of this study are to determine the spatial and frequency dependence of the depolarisation, identify the physical structures and conditions responsible for the depolarisation and to determine the structures in the magnetic fields of the source and the surrounding cluster. In this chapter, however, we mainly present the observations and primary data products and results from an analysis of the high-frequency data (6 - 18 GHz). The analyses of the full-band data are presented in Chapter 5.

In Section 4.2, we provide the background, research questions and objectives of our general study of Cygnus A radio galaxy. In Section 4.3, we present the details of our observations of Cygnus A, followed by the calibration and imaging of the data. Section 4.4 presents our polarisation data as a function of frequency and resolution. In Section 4.5, we present the results of high-frequency, high-resolution data modelling. In Section 4.6, we used the derived high-frequency, high-resolution maps to predict the low-frequency, low-resolution data. Section 4.7 compares the wideband data at two different resolutions, namely $0.75''$ and $1.50''$. Section 4.8 concludes with a summary and discussion.

4.2 Background: Cygnus A

4.2.1 The Radio Galaxy

Cygnus A (3C 405) is the prototypical FR type II radio galaxy (Fanaroff and Riley 1974). It is one of the best-known luminous radio galaxies and is exceptionally close ($z = 0.056$) compared to galaxies of

similar radio luminosity, see Figure 4.1 (Spinrad and Stauffer 1982). Adopting the ΛCDM cosmology with $H_0 = 69.3$ km s^{-1} Mpc^{-1}, $\Omega_m = 0.288$, and $\Omega_\Lambda = 0.712$ (Hinshaw et al. 2013), gives a distance of 227 Mpc and $1'' \approx 1.1$ kpc. Cygnus A's high flux density (~ 1000 Jy at 2 GHz), combined with its relatively small angular size (maximum projected extent of $\approx 120''$) means the source is unusually bright, making it an outstanding target for high-resolution radio polarimetric imaging with synthesis telescopes like the VLA.

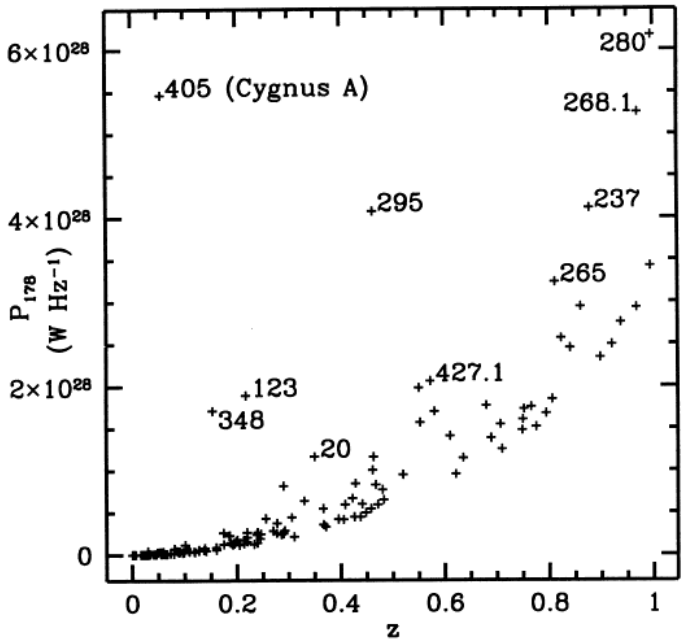

Figure 4.1: *Radio power as a function of redshift of 3CR galaxies.* Cygnus A is extraordinarily bright in comparison to radio galaxies at similar redshift. Image Credit: Stockton and Ridgway (1996).

4.2.2 The Ambient Intracluster Gas

Cygnus A is located at the centre of a dense CC X-ray emitting cluster (Giacconi et al. 1972; Fabbiano et al. 1979). The cluster has a core of radius ~ 18 kpc and density of $\sim 15 \times 10^{-26}$ g cm^{-3} (Smith et al. 2002; Halbesma et al. 2019). The gas temperature decreases from roughly 9 keV at 300 kpc radius to 3.5 keV within the core (Snios et al. 2018). Figure 4.2 shows the electron density, temperature and pressure of the cluster as a function of radius.

Cygnus A is surrounded by a weak cocoon-shock which extends 33 kpc north and 74 kpc west of the cluster centre (Carilli et al. 1994; Snios et al. 2018). The cocoon-shock is known to be driven by the expanding lobes into the ambient cluster gas. The Mach numbers across the shock ranges between $1.18 - 1.66$. Figure 4.3 shows the total intensity contours at 2 GHz with $1''$ resolution superimposed on the *Chandra* X-ray image in the energy interval $0.5 - 7$ keV. The well-known structures in the radio and X-ray are labelled, namely the central AGN, the lobes, the four hotspots and the radio jet, as well as filamentary structures across the lobes, a ring-like structure in the tail of the eastern lobe (Perley et al. 1984) and the X-ray "jet" (de Vries et al. 2018), cocoon-shock (Snios et al. 2018) and ribs (Duffy et al. 2018).

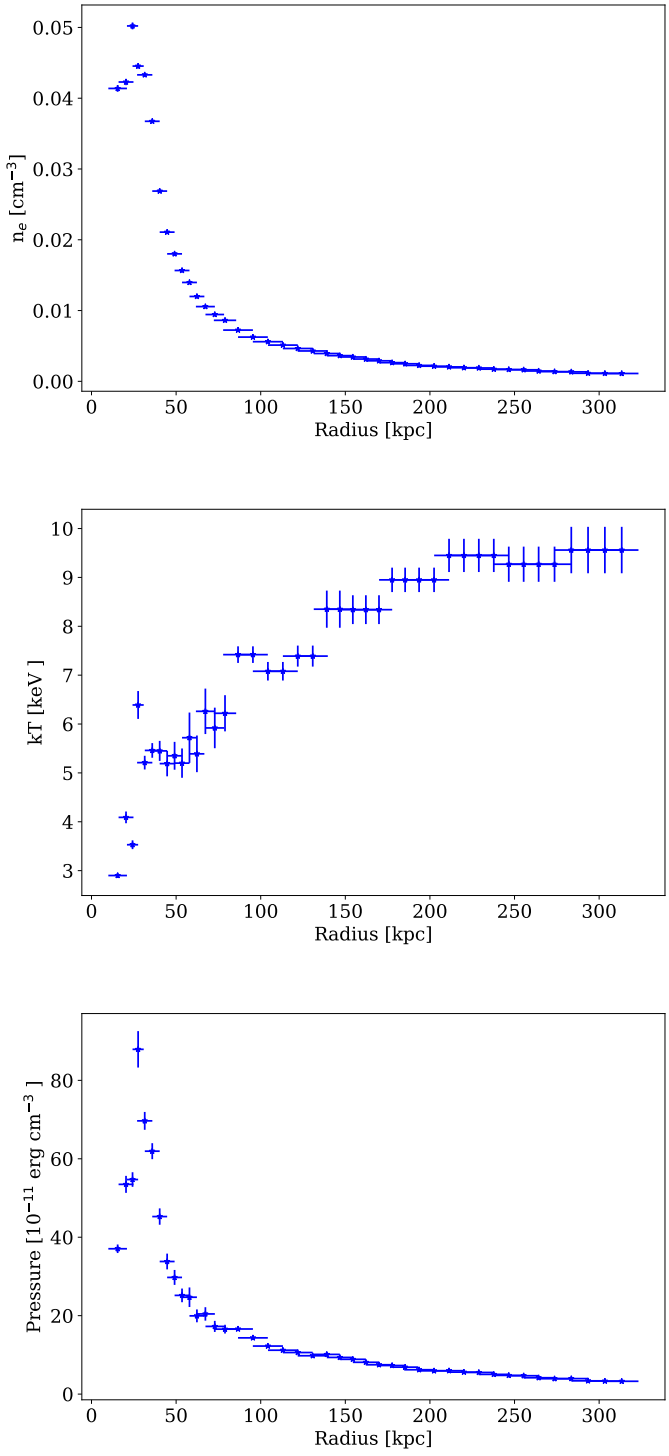

Figure 4.2: *X-ray properties of Cygnus A cluster gas.* Top: Electron density as a function of radius. Middle: Temperature radial profile. Bottom: Pressure radial profile. The cocoon-shock is visible at a radius of ~ 30 kpc. The plotted data are obtained from Snios et al. (2018) (See Figure 4 of the paper).

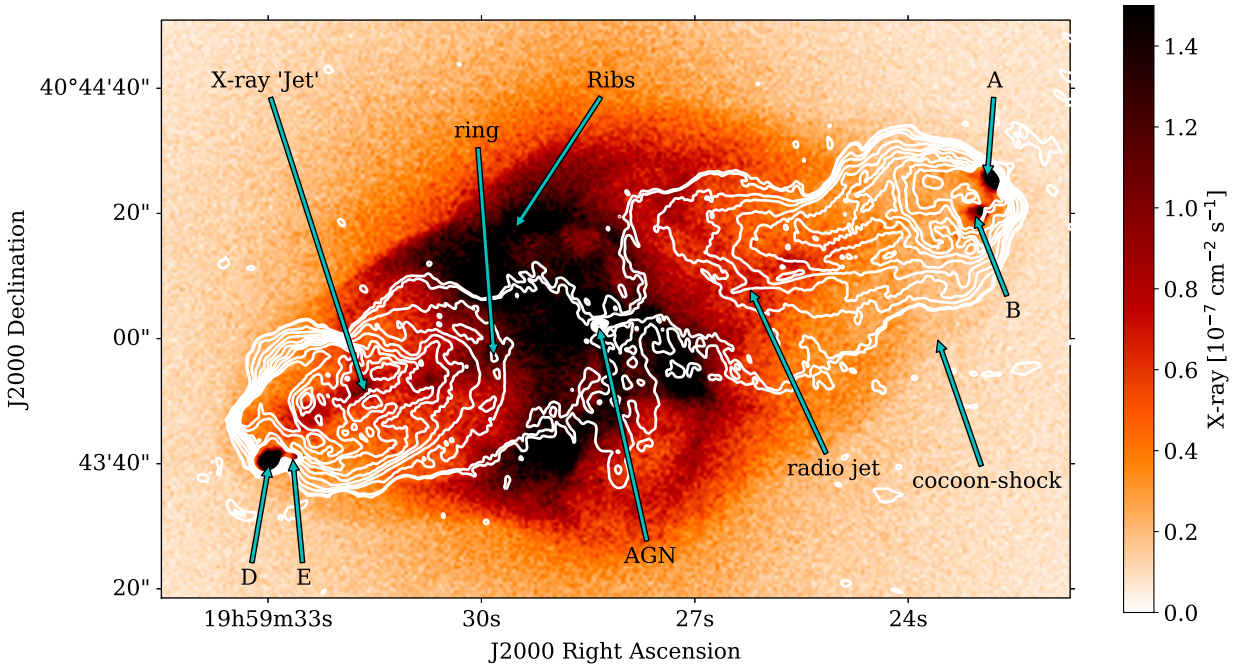

Figure 4.3: *Cygnus A total intensity contours (*2.4 *GHz and* $1''$*) superimposed on Chandra X-ray surface brightness emission (*$0.5 - 7$ *keV).* The contour levels are 0.005, 0.01, 0.05, 0.1, 0.2, 0.3, 0.4, 0.5, 0.6, 0.8, 1.0 Jy beam^{-1}. The radio features are shown; the hotspots A, B, D and E at the ends of the lobes, the ring-like feature at the tails of the eastern lobe, the radio jet in the western lobe, and the central AGN. Also shown are the X-ray features: the X-ray jet, cocoon-shock and the ribs (de Vries et al. 2018; Snios et al. 2018; Duffy et al. 2018). The off-source noise of the radio image is 1.7 mJy beam^{-1}.

4.2.3 Polarisation and Faraday Rotations

Cygnus A is significantly polarised with typical values of $\lesssim 40\%$ and as high as 70% in the lobes and hotspots at high-resolution (Carilli et al. 1989). Polarimetric observations of Cygnus A showed large Faraday rotations across its lobes, asymmetry in the polarisation properties of the lobes, as well as significant decreases in fractional polarisation with decreasing frequency at low resolutions (Slysh 1966; Mitton 1971; Dreher 1979; Alexander et al. 1984). The high-resolution study by Dreher et al. (1987) revealed typical RM ranging between -4000 rad m^{-2} and $+3000$ rad m^{-2} across the lobes, with gradients in the RM distribution of 300 rad m^{-2} arcsecond^{-1} in most parts of the lobes and with a few places having gradients up to 1000 rad m^{-2} arcsecond^{-1}. These large gradients are responsible for the low polarisation seen in the early low-resolution studies. The primary focus since then has been to understand the origin of the depolarisation and extraordinary Faraday rotations. The locations considered were our own galaxy, the X-ray cluster, the cocoon-shock or a mixed thermal/synchrotron gas region located at the boundary of the lobes, or within the lobes themselves.

4.2.4 Origin of Faraday Rotations and Depolarisation

Our own galaxy contributes no more than $RM \sim 300$ rad m^{-2} at Cygnus A's low galactic latitude of $b = 5.8^\circ$ (Simard-Normandin et al. 1981), and the Galactic RM gradients do not exceed 180 rad m^{-2} for components separated by $< 1^\circ$ (Clegg et al. 1992). Therefore, the origin of the large RM and large gradients must be local to the source (Dreher et al. 1987). Dreher et al. noting the high polarisation at 6 cm, the large total rotation of the electric vector (up to 600° at that wavelength) and the apparently perfect linearity of the observed electric field polarisation angle vs λ^2 between 6 and 2 cm wavelength, concluded that the great majority of the observed RM must be due to an external medium, and cannot originate from a mixed thermal-synchrotron region inside the lobes. If the origin of the RM is distributed throughout the cluster, the resulting magnetic fields were inferred to be ~ 5 μG. If the origin was confined to the cocoon-shock, the fields would be ~ 20 times higher.

However, a cluster origin for the majority of the RM does not exclude smaller contributions from the cocoon-shock. After discovering a region of enhanced RM in front of hotspot "D" of the western lobe, Carilli et al. (1988) suggested that both the cluster gas and the cocoon-shock contribute to the observed Faraday rotations. They estimated that the cocoon-shock is responsible for $|RM| \leq 1000$ rad m^{-2} ordered on scales < 5 kpc while the cluster is responsible for $|RM| > 1000$ rad m^{-2} ordered on scales > 20 kpc.

4.2.5 Why the New Observations

Dreher et al. (1987)'s results were based on only four wavelengths spanning λ 6 cm to 2 cm. Subtle depolarisation effects, such as those due to turbulence or to boundary layer effects, will not be visible with such sparse sampling. Since depolarisation effects due to Faraday rotation are manifested at lower frequencies, investigation of such mechanisms requires observations at frequencies below 5 GHz, with continuous frequency coverage. With the completion of the wideband JVLA (Perley et al. 2011), we have now the capability to observe Cygnus A at lower frequencies than those available to Dreher et al. (1987), – notably, use of

the new 2 – 4 GHz receiver – and with complete frequency coverage. This new observing capability should allow us to investigate these effects in detail.

4.3 Data Reductions

4.3.1 The Observations

The observations were taken under JVLA observing project 14B-336. The details of these observations are shown in Table 4.1. TOS is the time spent on source. This project utilised all array configurations (A, B, C and D) for four observing bands; 2 – 4 GHz ("S-band"), 4 – 8 GHz ("C-band"), 8 – 12 GHz ("X-band") and 12 – 18 GHz ("Ku-band"), providing complete frequency coverage from 2 to 18 GHz. The X-band observation in A-configuration on July 14 was repeated on August 11 because of a system failure in the control computers; none of the cross-hand (polarisation) data could be calibrated. All cross-hand data from this observation were flagged. The parallel-hand data were not affected and were retained.

Table 4.1: *Observing log*

Configuration	Date	Band	IAT Range [H:M]	TOS [min]	LST Range [H:M]
D	2015 Nov 15	S	20:09 - 01:96	20	16:40 - 22:20
	2015 Nov 15	X	20:09 - 01:96	60	16:40 - 22:20
	2015 Nov 15	Ku	20:09 - 01:96	95	16:40 - 22:20
C	2014 Nov 03	S	18:10 - 04:40	105	14:00 - 00:15
	2014 Nov 03	C	18:10 - 04:40	100	18:10 - 04:40
	2014 Nov 03	X	18:10 - 04:40	100	18:10 - 04:40
	2014 Nov 03	Ku	18:10 - 04:40	125	18:10 - 04:40
B	2015 Apr 05	S	09:15 - 16:50	130	15:10 - 22:30
	2015 Apr 12	C	10:00 - 17:35	130	16:25 - 23:30
	2015 Apr 12	X	10:00 - 17:35	180	16:25 - 23:30
	2015 Apr 05	Ku	09:15 - 16:50	185	15:10 - 22:30
A	2015 Aug 15	S	03:00 - 10:30	390	16:40 - 00:00
	2015 Jul 15	C	04:25 - 11:55	370	17:00 - 00:15
	2015 Jul 14	X	04:25 - 11:42	350	16:40 - 00:00
	2015 Aug 11	X	01:00 - 08:25	365	15:10 - 22:30
	2015 Jun 29	Ku	03:40 - 11:15	370	15:10 - 22:35

The correlator was configured to span the entire frequency range for each band. To facilitate data editing (primarily for radio frequency interference, RFI), the time averaging was set to 2 seconds and the channel width to 2 MHz for C, X and Ku bands and to 1 MHz at S band. Following editing and calibration, the data

were further time- and frequency-averaged, as described below.

A standard observing regimen was utilised – a nearby calibrator, J2007+4029 was observed periodically to monitor system health and to provide both complex gain and antenna cross-polarisation calibration. At S-band in D-configuration, the visibility from Cygnus A significantly perturbs observations of J2007+4029, so the more distant but weaker calibrator J2023+5427, was utilised for that band and configuration.

4.3.2 Calibration

All data reduction was done using the Astronomical Image Processing System (AIPS) software package. The procedures followed were standard and only a brief summary is given below:

1) To reduce spectral ringing due to RFI signals, the visibilities were Hanning smoothed.
2) Antennas that are shadowed at low observing elevations were identified and flagged.
3) Data corrupted by system failures or RFI were identified and removed.
4) Delay and bandpass calibration for each antenna was done using 3C286.
5) The flux densities of J2007+4029 or J2023+5427 were established by bootstrapping from 3C286.
6) The complex gains were computed from the calibrators and applied to all sources.
7) The cross-hand delays were found using 3C286 and applied to all sources.
8) Antenna cross-polarisation (D-terms) were computed using the calibrator observations and applied.
9) The cross-hand phase (to set the polarisation angle of the linearly polarised flux) was determined from observations of 3C286 and applied to all sources.

Following these procedures, the data were then averaged in time and frequency to generate the databases used in the imaging. The time and frequency averaging employed varied with the observing band as described below.

Time averaging reduces the visibility amplitude due to the phase rotation of a source, which is offset from the phase tracking centre. We adopted a criterion of a maximum loss of 10% on the longest baseline for a point source offset by $70''$ – the location of the western hotspot with respect to the AGN. The resulting condition is:

$$\delta t = \frac{\lambda}{4\, B_{\rm max}\, \omega\, \chi} \tag{4.1}$$

where $B_{\rm max}$ is the maximum baseline in metres, ω is the earth's rotation rate in radians s^{-1}, χ is the offset in rad and λ is the observing wavelength in metres. For Cygnus A and the 35-km maximum baseline, the integration time is 22, 11, 7.1 and 5 seconds, for the S, C, X and Ku-bands, respectively. We utilised 10 seconds for S and C, 8 seconds for X, and 6 seconds for Ku bands. Note that since the hotspots are well resolved, the actual loss of brightness due to this effect will be considerably less than the 10% condition utilised.

There are two conditions which set the maximum tolerable channel width – chromatic aberration (bandwidth smearing) and polarisation intensity reduction due to the RM. We discuss these in turn:

1) Frequency averaging radially stretches the emission from a source, with increasing offset from the phase tracking centre. We applied the same condition as for time averaging – that the longest baselines

suffer a maximum of 10% loss in amplitude for a point-source $70''$ from the AGN. This results in the following:

$$\delta\nu = \frac{c}{4\,B_{\rm max}\,\chi} \tag{4.2}$$

For the $70''$ offset of the western hotspot and the 35-km maximum baselines, the maximum channel width is 6.3 MHz. We adopted 8 MHz. We note again that as the hotspots are well resolved on the longest baselines, the actual intensity loss is much less than the 10% criterion.

2) A linearly polarised electromagnetic wave, propagating through a magnetised ionised medium has its plane of polarisation rotated by:

$$\Delta\chi = RM\lambda^2 \qquad \text{[radians]}. \tag{4.3}$$

Over a bandwidth $\delta\nu$, centred at frequency ν, the rotation of the plane of polarisation is given by:

$$\Delta\chi = 2\lambda^2 RM\frac{\delta\nu}{\nu} \tag{4.4}$$

where it has been assumed that $\delta\nu << \nu$. The absolute value of the maximum RM in Cygnus A is known to be ~ 5000 rad m^{-2} (Dreher et al. 1987). With this value and utilising the stringent condition of a maximum of 10 degrees rotation across a channel, the maximum channel width is 1.5 MHz at 2 GHz, 5.2 MHz at 3 GHz and 12.4 MHz at 4 GHz. Hence, only at S-band is the polarisation condition more stringent than the chromatic aberration condition. Thus, we adopted 2 MHz for the lower half of S-band (2 – 3 GHz), 4 MHz for the upper half of S-band (3 – 4 GHz) and 8 MHz for all other bands.

This data compression process resulted in a database for each spectral window (spanning 64 MHz at S-band and 128 MHz in all other bands) – hence 32 channels for the lower half of S-band and 16 channels for all other bands in each spectral window and each configuration – a total of 498 databases. These were then combined over configuration, resulting in 144 databases, each containing the data from all configurations for a single spectral window, from which the images were made.

Although Cygnus A has a nearby calibrator, standard phase calibration alone results in image dynamic range (ratio of the brightest component to the rms noise) of less than 1000 , far less than that needed for detailed imaging analysis. Fortunately, the high flux density of Cygnus A, combined with the "sharp" features of the AGN and hotspots, permits application of the technique of self-calibration (Cornwell and Wilkinson 1981). To accomplish this, total intensity images of Cygnus A were generated from each of these decimated databases for each spectral window, utilising a few central channels. These images were then used to self-calibrate the data to remove the residual phase and gain fluctuations inherent in the process of calibration with an external calibrator. During this process, care was taken to ensure the unresolved AGN was registered in the central (phase-tracking) cell and that the total flux density of Cygnus A (following correction for the primary beam) equalled the values published by Perley and Butler (2017). We believe the phase registration is accurate to 5% of the full resolution at all bands, and that the flux density matches the Perley and Butler (2017) scale to better than 2%. The resulting images showed imaging dynamic ranges up to $30,000$:1 – more than an order of magnitude better than the initial images.

4.3.3 Imaging

Figure 4.4 shows our best image of Cygnus A at S-band obtained using WSCLEAN imaging tool (Offringa et al. 2014). However, for creating image cubes we used IMAGR in AIPS as it was much faster. We used multiscale cleaning deconvolution algorithm for creating both Stokes Q, U and I image cubes (Greisen 2003; Cornwell 2008; Greisen et al. 2009).

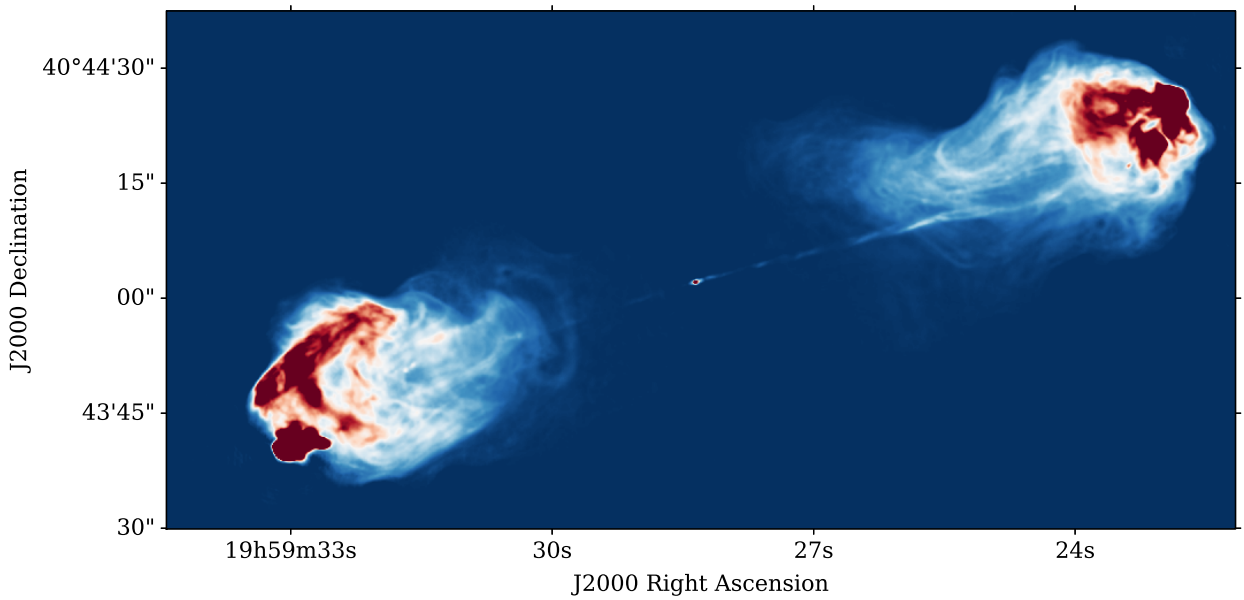

Figure 4.4: *Cygnus A total intensity map*. This map is at 3.5 GHz, bandwidth of 896 MHz and resolution of $0.38'' \times 0.42''$. Off-source image noise 3×10^{-5} Jy beam^{-1}. This image was obtained using the WSCLEAN imaging algorithm.

The number of frequency planes utilised to prevent depolarisation from the high RM of Cygnus A or from chromatic aberration for each frequency band is shown in Table 4.2. In total, 1184 frequency planes were used. The image cubes were made at two standard resolutions: i) $0.75''$ resolution – corresponding to the highest resolution available at 2 GHz (which thus includes all frequencies) and ii) $0.30''$ which corresponds to the highest resolution at 6 GHz. All the images were primary beam corrected using the AIPS task "PBCOR".

For demonstrative purposes, spectral index maps at S- and C-band are shown in Figure 4.5. The spectral index values of Cygnus A ranges between -0.5 and -1.5 at low-frequencies and steepens at relatively higher frequencies. The spectral index is steeper in the tails of the lobes towards the AGN, except within the jet. These spectral index distributions are consistent with the well-accepted model of FR II radio galaxies: that the electrons at the tails are relatively older than those closest to the hotspot due to radiative ageing. Detailed study of Cygnus A spectral index and spectral ageing is presented in Carilli et al. (1991).

We obtained both the amplitude of the polarised intensity P, and the polarisation angle using Equation 2.11 and Equation 2.12, respectively. Furthermore, we corrected the amplitude for Ricean bias using the

Table 4.2: *The number of frequency planes in each band utilised to avoid Faraday depolarisation*

Band	ν-interval [GHz]	$\Delta\nu$ [MHz]	No. of averaged channels	Total No. of channels
S_{lo}	2-3	2	1	512
S_{hi}	3-4	4	1	256
C_{lo}	4-6	8	1	256
C_{hi}	6-8	32	4	64
X_{lo}	8-10	64	8	32
X_{hi}–Ku	10-18	128	16	64

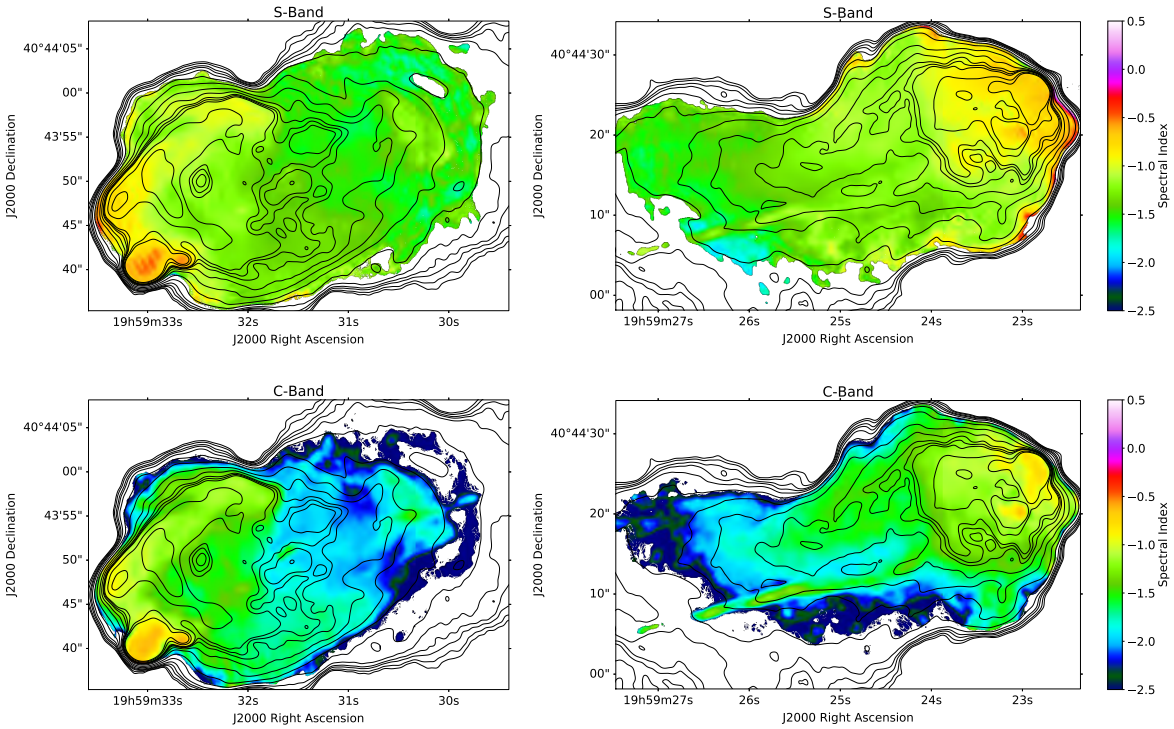

Figure 4.5: *Spectral index maps of Cygnus A radio galaxy at* $0.75''$. Left: Eastern lobe. Right: Western lobe. Top row maps were obtained using a 2 - 4 GHz frequency range and the bottom row using 4 - 6 GHz. We only show pixels with an error in spectral index less than 0.1. The spectral index is steeper towards the AGN and steepens at higher frequencies.

Maximum Likelihood approximation:

$$P_{\rm corr} \approx P - \frac{0.5\,\sigma_P^2}{P} \tag{4.5}$$

where σ_P is the error in P (Killeen et al. 1986). We derived fractional polarisation by taking the following ratio:

$$p = \frac{P_{\rm corr}}{I}. \tag{4.6}$$

Errors associated with these quantities were derived assuming standard propagation of error formulae with the noise in Q, U and I estimated in an off-source region of each map. At $0.30''$, the off-source noise ranges between 0.18 mJy beam^{-1} and 0.5 mJy beam^{-1} in Stokes Q and U and 0.3 mJy beam^{-1} and 1 mJy beam^{-1} in Stokes I. At $0.75''$ the off-source noise ranges between 0.6 mJy beam^{-1} and 1.6 mJy beam^{-1} for Stokes Q and U images, and 0.8 mJy beam^{-1} and 6 mJy beam^{-1} for Stokes I images.

We computed Faraday spectra using the RM-Synthesis and RM-Clean as described in Section 3.1.2. For our 2 - 18 GHz data we find the resolution in Faraday space 175 rad m^{-2}, and of 1700 rad m^{-2} for 6 - 18 GHz. Figure 4.6 shows the RMTF of our frequency data. Our λ^2 sampling is non-uniform – resampling the data on a uniform grid did not alter the results in any significant way. We used uniform weighting, $W = 1$, for all channels and defined λ_0^2 as a weighted mean of the observed λ^2.

The maximum Faraday depth we can observe without significant attenuation is 25000 rad m^{-2} at 2 GHz. For Cygnus A, the maximum derived RM is ~ 5000 rad m^{-2}, thus we do not expect any appreciable attenuation. The widest breadth in RM we can observe without much attenuation should have a width < 10000 rad m^{-2} for our minimum λ^2 of 3×10^{-4} m^2. We do not expect such extended structures in the case of Cygnus A.

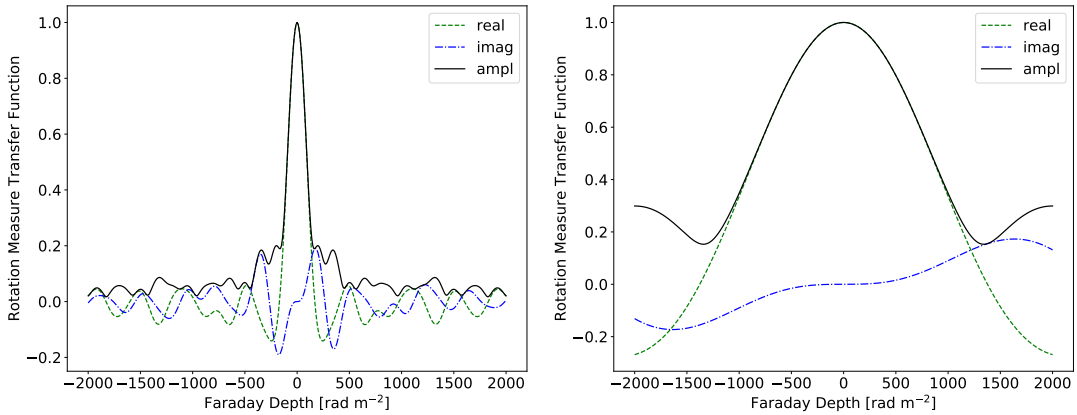

Figure 4.6: *RMTF of our data*. Left: Includes 2 - 18 GHz data. Right: Includes 6 - 18 GHz data. The RMTF resolution is ~ 175 rad m^{-2} for $2 - 18$ GHz and ~ 1700 rad m^{-2} for $6 - 18$ GHz.

4.4 Polarisation Imaging of Cygnus A

Polarised emission of a source undergoing Faraday rotation can be used to study the properties of the medium causing the rotation. Distinguishing between various depolarisation mechanisms can be difficult and requires high-resolution, low-frequency observations. In this section, we show the polarisation characteristics of Cygnus A as a function of resolution and frequency.

4.4.1 Polarisation as a Function of Frequency

4.4.1.1 Spatial Maps

Figure 4.7 shows the $0.75''$ resolution maps of the fractional polarisation across Cygnus A radio lobes at 10 GHz, 6 GHz, 4 GHz and 2 GHz. We show only those pixels with relative error in the fractional polarisation $(\sigma_p/p) \leq 0.5$. As seen in the figure, the fractional polarisation of the lobes decreases significantly with decreasing frequency. Note that the eastern lobe depolarises at higher frequencies than the western and for both lobes, the depolarisation is more rapid in the inner regions – those closer to the AGN. The spatial distribution of the fractional polarisation of the lobes is very uniform at high-frequencies, with typical values of 20%, with some regions as high as 70% and becomes clumpy on scales of ~ 1 kpc at low-frequencies (most notably at 2 GHz). The fractional polarisation at 2 GHz is less than 10% for virtually all lines-of-sight at this resolution. The emission from the bright hotspots and from the jet, depolarises in the same manner as that from the adjacent lobes. There is no correlation between the underlying source brightness or structure and the nature of the depolarisation.

The strong depolarisation and the very turbulent appearance of the low-frequency fractional polarisation images suggest that the depolarisation may be related to partially-resolved fluctuations in the Faraday depth of the surrounding medium. To investigate this, we determined the dependence of the polarisation as a function of frequency over our full bandwidth (2 - 18 GHz) at $0.75''$ resolution. This task is made challenging by the sheer quantity of information – over the solid angle subtended by the lobes, there are over ~ 3000 independent lines-of-sight. Thus, we can only show a few representative examples.

4.4.1.2 Lines-of-Sight View

In order to efficiently identify specific lines-of-sight, we have defined a relative coordinate system, centred on the galaxy AGN, with units of tens of milliarcseconds. Positive is to the west and north and negative to the east and south, for example, a line-of-sight with coordinates $(2444, -1024)$ is $24.44''$ west and $10.24''$ south of the AGN. We analyse only those locations with error in the fractional polarisation $< 10\%$ at 8 GHz. This resulted in a total of 2096 independent lines-of-sight.

Figure 4.8 shows these depolarisation functions for six representative lines-of-sight. Each row displays the fractional polarisation in the left column and the polarisation position angle in the middle column, all as functions of λ^2. The right colum shows the amplitude of the Faraday spectrum, superimposed in red is the Gaussian with width equal to that of the RMTF. The RMTF is shifted and scaled to match the location and

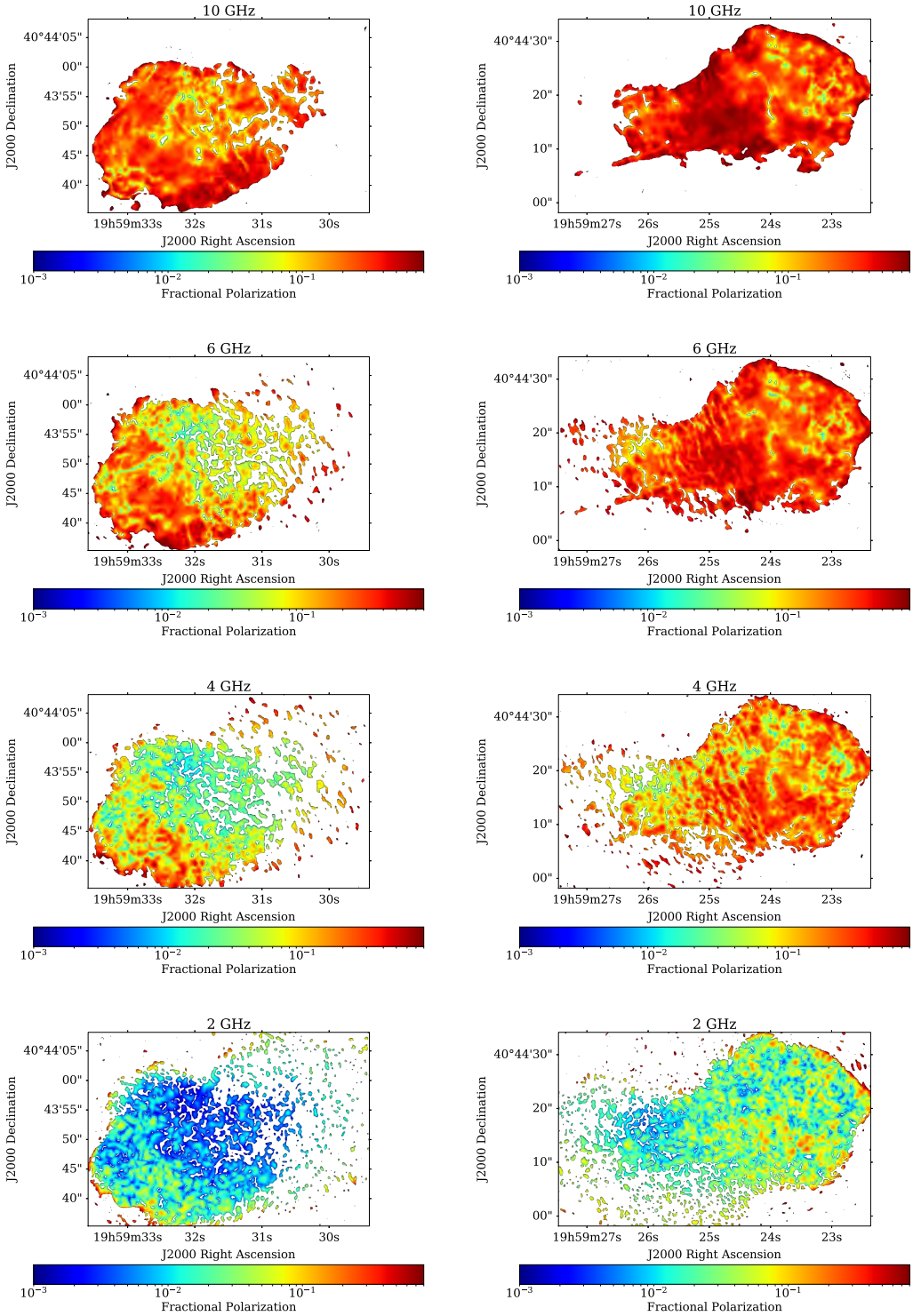

Figure 4.7: *Fractional polarisation maps of Cygnus A at* $0.75''$ *at different frequencies.* First row: 10 GHz. Second row: 6 GHz. Third row: 4 GHz. Bottom row: 2 GHz. The colour-bar ranges between 0.1% and 80%. Only pixels with $(\sigma_p/p) < 0.5$ are shown. There is a global decrease in fractional polarisation with decreasing frequency. The eastern lobe depolarises at higher frequency than the western. The inner regions (near the AGN) of the lobes depolarise more rapidly than the outer regions.

amplitude of the maximum amplitude of the Faraday spectrum. Each line-of-sight is labelled according to the coordinate offsets defined above.

The fractional polarisation of all lines-of-sight decreases significantly with increasing λ^2. For some lines-of-sight, the decrease is smooth, while for most, there is considerable structure in the depolarisation, ranging from sharp nulls and peaks as shown in the top two rows of the figure, to more complex behaviours, as shown in the bottom two rows. The polarisation angle as a function of λ^2 of the data (shown in black) is plotted together with the residual angle (shown in blue); obtained by removing $RM_{\text{peak}}\lambda^2$ of the peak of the Faraday spectrum. The residual polarisation angle, χ_{res}, shows significant deviations; we find that 38% of the lines-of-sight have $0 < \chi_{\text{res}} < \pi$, 22% have $\pi < \chi_{\text{res}} < 3\pi$, 13% have $3\pi < \chi_{\text{res}} < 6\pi$, 12% have $6\pi < \chi_{\text{res}}$, and the remaining 15% were noisy or the nπ-ambiguity couldn't be corrected. Lines-of-sight showing small deviations are usually associated with simple smooth decaying fractional polarisation with λ^2 or equivalently, with a single, nearly unresolved peak, similar to that shown on the third row of Figure 4.8. The nonlinearities are more prominent when the fractional polarisation vs λ^2 consists of oscillatory behaviour.

The Faraday spectra show interesting structures – some lines-of-sight show a simple single peak, some have multiple peaks and many lines-of-sight show a rather wide "base", indicating a wide range of Faraday depths within the resolving beam. As expected, the depolarisation curves with pronounced oscillations show multiple-peaked spectra, with the separation of the peaks typically $\lesssim 500$ rad m^{-2} and a maximum separation of ~ 1500 rad m^{-2} (approximated by eye).

4.4.1.3 Depolarisation Structure and Spatial Correlation

To investigate whether these different depolarisation functions have any spatial relationship, we generated a simple classification scheme based on the observed depolarisation behaviour. By viewing each fractional polarisation as a function of λ^2 (left column of Figure 4.8), we classified by eye the lines-of-sight into three categories as follows:

1) "Sinc-like" decay: the behaviour in the decreasing fractional polarisation as a function of increasing λ^2 is approximately that of a sinc function: $p \propto \sin(K\lambda^2)/K\lambda^2$. The minima are sharp and occur at nearly constant intervals, while the peaks decrease in amplitude towards large λ^2. Examples are shown in the top two rows in Figure 4.8.
2) Smooth decay: the fractional polarisation decreases smoothly with increasing λ^2 within measurement errors. Examples are shown in the third and fourth rows in Figure 4.8.
3) Complex decay: the depolarisation displays a combination of the above, or more complex behaviour in the fractional polarisation vs. λ^2. We further classified complex lines-of- sight into two sub-classes: "complex-oscillatory" and "complex non-oscillatory". The former resembles sinc-like pattern than smooth decay but the fractional polarisation doesn't approach 0 across λ^2 or the intervals are not periodic, or both and the latter resembles smooth decay more than sinc-like but the decay is not completely smooth. See the last two rows in Figure 4.8 for complex-oscillatory and non-oscillatory, respectively.

The fraction of lines-of-sight in each of these three classes are given in the second column of Table 4.3. Moreover, columns $3-7$ give a fraction of lines-of-sight with deviations in polarisation angle (the residual

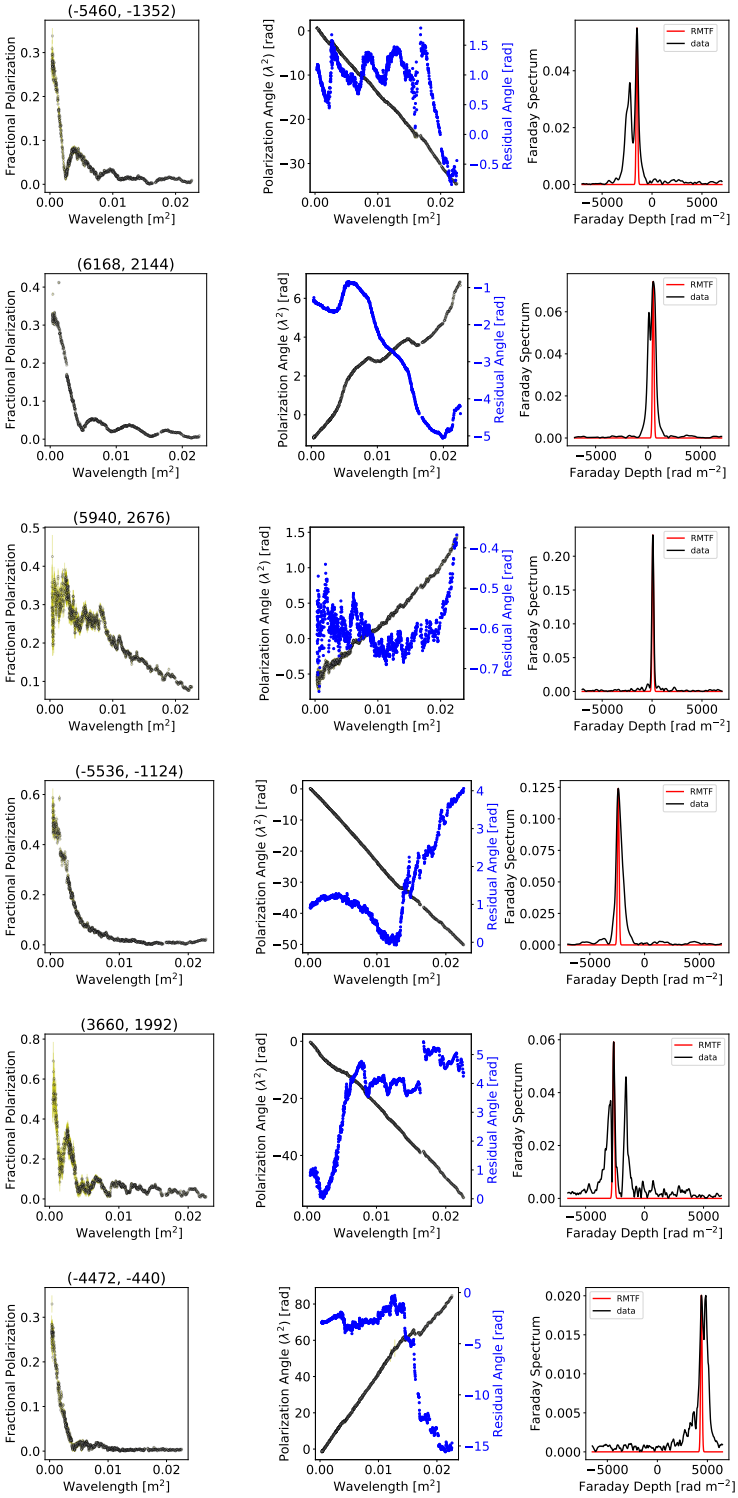

Figure 4.8: *Wideband ($2 - 18$ GHz) polarisation data at $0.75''$ resolution for six representative lines-of-sight.* Left column: Fractional polarisation vs λ^2. Middle column: Polarisationtion angle vs λ^2 (black) and the polarisation angle residual (blue). Right column: Amplitude of the Faraday spectrum (in black) superimposed by a Gaussian RMTF of width equal to that of the actual RMTF. The residuals were obtained by removing $RM\lambda^2$ of the dominant peak in the Faraday spectrum.

angle, $\chi_{\rm res}$) in each of the intervals: low ($0 < \chi_{\rm res} < \pi$), med ($\pi < \chi_{\rm res} < 3\pi$), high ($3\pi < \chi_{\rm res} < 6\pi$) and limit($6\pi < \chi_{\rm res}$), as well as a fraction of those that couldn't be classified (denoted as "N/A"). Most lines-of-sight are complex/intermediate – with the majority resembling smooth decays. In terms of the residual χ, we find that decaying behaviour without oscillations tends to have small deviations, while oscillatory structure results in slightly higher deviations.

Figure 4.9 shows a colour-coded display of the distribution of these classifications across the lobes: lines-of-sight with sinc-like behaviour are shown in red-orange (symbol x), smooth decay in green (o symbol) and complex decay in navy ($*$ symbol for oscillatory-like complex decay and "v" symbol for non-oscillatory). The figure shows there are no clear spatial relationships for these behaviours, yet they are not completely random as adjacent cells are more likely to show the same behaviour. These correlated "clumps" are typically of a few kpc scale. There is a tendency for more complex behaviour in the eastern lobes, and relatively fewer smooth decay and sinc-like behaviours. The distribution across the western lobe, on the other hand, consists mostly of smooth decay particularly at the extremes of the lobes and complex decay.

It should be noted that these classifications are only valid for this frequency span ($2 - 18$ GHz) and $0.75''$ resolution and that the classes are likely to change with a change in spectral coverage or resolution.

4.4.1.4 Frequency Depolarisation Ratio

Figure 4.10 shows the frequency depolarisation ratios (FDR): $\text{FDR}_1 = p_6/p_{10}$ and $\text{FDR}_2 = p_4/p_{10}$ where the subscripts are the frequencies in GHz. We show only pixels with errors in the FDR of less than 0.1. The quantity is a ratio of two ratios and it is thus prone to large errors. However, this error limit seemed to remove the majority of the pixels that look spurious.

The western lobe does not depolarise much between 6 GHz and 10 GHz, and the same is true for extreme regions in the eastern lobe. Both lobes depolarise significantly at 4 GHz. This depolarisation occurs globally across the lobes. There are, however, still regions in both lobes that still show a FDR of 0.8. In general, the inner regions of the lobes depolarise more rapidly than the extreme parts of the lobes reaching a ratio of < 0.2.

4.4.2 Polarisation as a Function of Spatial Resolution

The depolarisation behaviour shown in Section 4.4.1 can be explained by randomised fluctuations in the foreground Faraday screen on scales less than the $0.75''$ resolution. If this is the case, then the fractional polarisation will generally decrease as the resolution decreases at any given frequency.

4.4.2.1 Spatial Maps

Figure 4.11 shows the fractional polarisation at 4.0 GHz of Cygnus A at four resolutions – $0.45''$, $0.75''$, $1.50''$ and $3.00''$. The resolution $0.45''$ is the highest we can obtain at this frequency. We show only pixels with $(\sigma_p/p) < 50\%$. As expected, the fractional polarisation decreases as the resolution degrades, most notably in the inner regions of the eastern lobe. The figure shows the effects of wavelength-dependent beam

Table 4.3: *A fraction in % of lines-of-sight in different classes*

Class Name	Total	χ- deviations					p(λ^2) vs. θ			Predictions		
		Low	Med	High	Limit	N/A	class A	class B	class C	N/A	Good	Approx	N/A
sinc-like	11	30	42	17	7	4	36	16	46	2	8	73	19
smooth	25	70	14	8	4	4	35	22	40	3	13	72	15
complex osc	20	25	32	22	15	6	43	18	36	3	19	72	9
complex non-osc	30	40	24	14	13	9	38	20	40	2	17	70	13
All classifiable	86	41	28	15	10	6	38	19	40.5	2.5	14	72	14
Not class	14	-	-	-	-	-	-	-	-	-	-	-	-

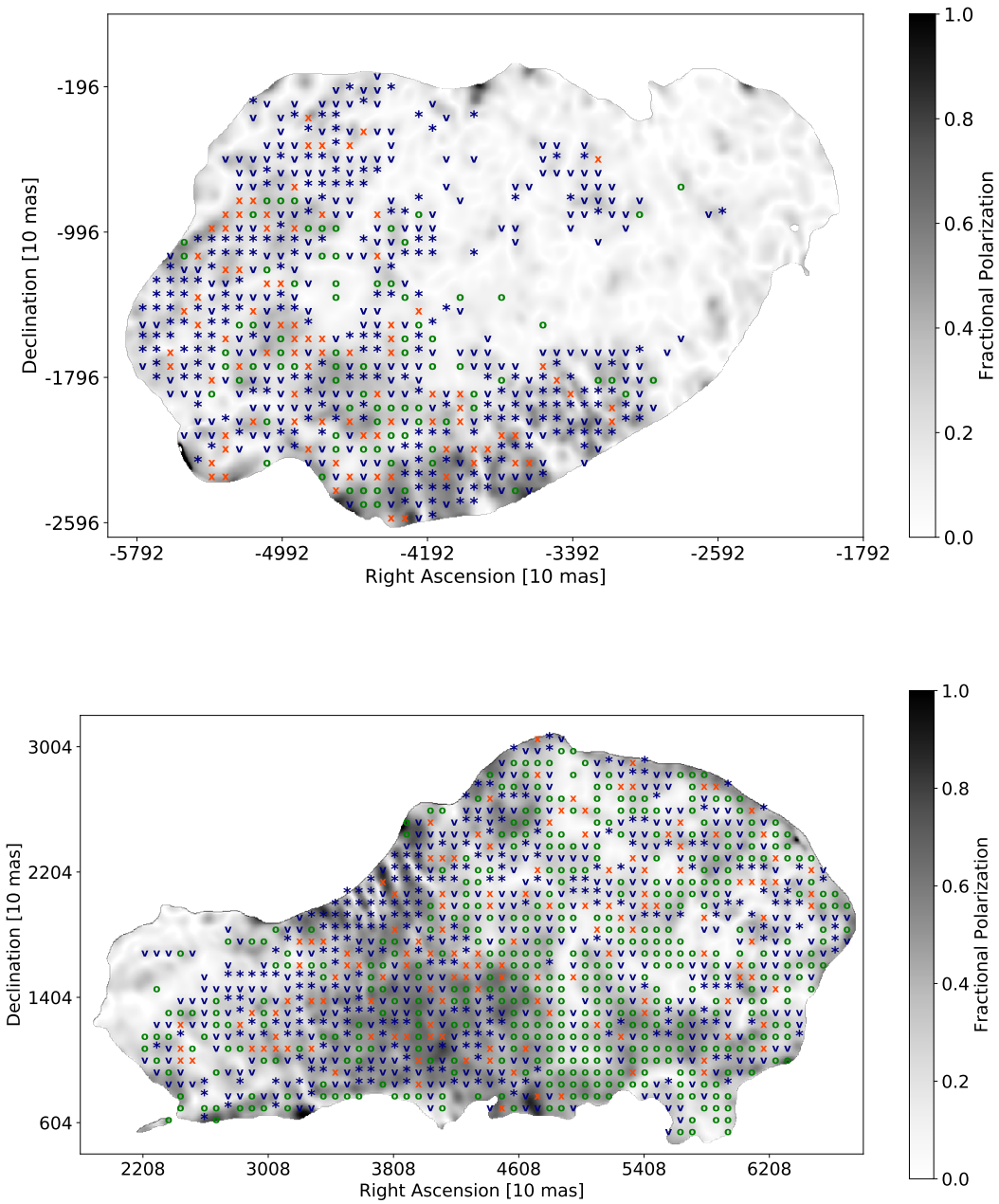

Figure 4.9: *Cygnus A lines-of-sight classified based on the behaviour of fractional polarisation vs* λ^2. Red x: Sinc-like behaviour. Green o: Smooth decay. Navy $*$: complex-oscillatory decay. Navy v: Complex non-oscillatory. The lines-of-sight are separated by the resolution beam of $0.75''$. These classes show no obvious large-scale spatial correlations. The majority (50%) of the lines-of-sight show complex behaviour, 25% show smooth decay, and show 11% sinc-like.

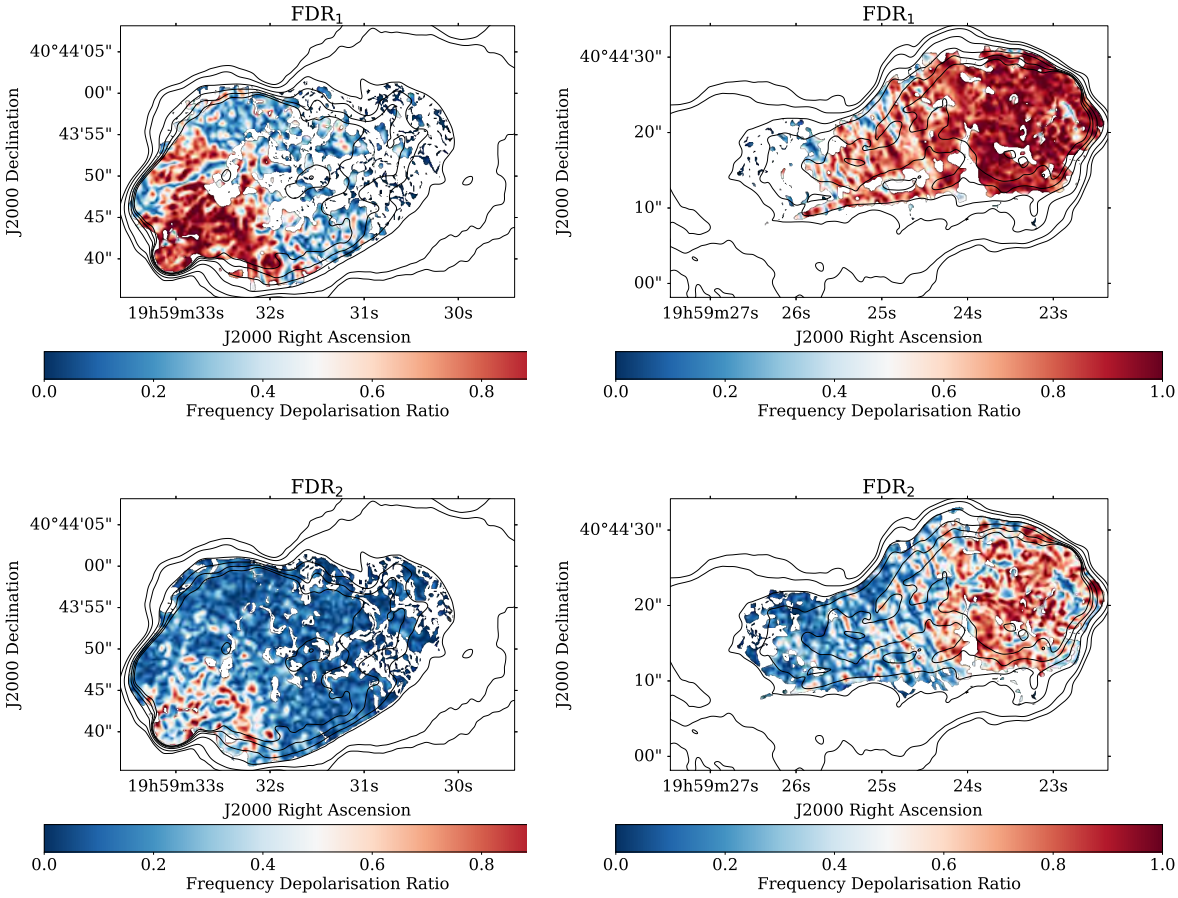

Figure 4.10: *Frequency depolarisation ratios (FDR) across the lobes.* FDR_1 is the ratio between 6 and 10 GHz; FDR_2 is the ratio between 4 and 10 GHz at $0.75''$. We show only pixels with $\sigma_{\mathrm{FDR}}/\mathrm{FDR} < 10\%$. The inner regions (close to the AGN) of the lobes are more depolarised than the extreme regions (around the hotspots). The lobes are most depolarised at 4 GHz.

depolarisation, as expected if the external medium is differentially rotating the polarised emission within the resolution element, as discussed below.

4.4.2.2 LoS View: Polarisation as a Function of Beam Resolution

If the depolarisation is due to transverse fluctuations in the foreground screen, then at a resolution corresponding to the smallest significant angular scale of the fluctuations, these structures will be resolved out, at which point the observed fractional polarisation will be that of the source itself. If this intrinsic value can be established, any fractional polarisation changes with frequency must then be due to intermixed thermal and synchrotron gas of the source itself, allowing an estimate of the thermal gas content. This is the only method known to us which can clearly discriminate between internal depolarisation (within the lobes or a mixed boundary layer) and external depolarisation (due to unresolved structures in the propagating medium).

Here, we describe our efforts to determine the intrinsic value of the polarisation by plotting the fractional polarisation as a function of resolution (θ) at five different frequencies, for 2096 lines-of-sight. Figure 4.12 shows a few examples of the typical behaviour. Each of the six plots shows the fractional polarisation at 2, 4, 6, 8 and 10 GHz as a function of resolution, from $3''$ to the highest permitted by the diffraction limit for given frequency, for different lines-of-sight through the lobes chosen to display the range of behaviour. The left side shows three lines-of-sight where the behaviour is close to the expected – a smooth rise in polarisation with a flattening at sub-arcsecond resolutions. Note, however, that only in the top two is there any evidence for asymptotic behaviour at the highest resolution. Even for these, the critical low-frequency polarisation needed to establish whether there is internal depolarisation that does not have sufficient resolution to determine what the asymptotic values are.

The right columns show much more complex behaviour, with structures in the depolarising behaviour which are likely due to the structure of the fields in the emitting medium (such as the lobes), or the external depolarising medium. We classified the lines-of-sight into three groups: i) those with fractional polarisation which increases monotonically at least across four frequencies (class A), ii) those with non-monotonic behaviour (class B) at four frequencies – this class also includes lines-of-sight with fractional polarisation which decreases at higher resolutions and iii) those whose fractional polarisation behaves differently at different frequencies as function of resolution (class C). For example, the left column of Figure 4.12 all fall into class A, the top two plots on the right column fall into class B and the bottom-right plot fall into class C. This classification was done by eye. Columns $7-11$ of Table 4.3 gives the fraction of lines-of-sight in each of the above classes for different decaying behaviour. We find that the same fraction (40%) of lines-of-sight are found in class A and C. Moreover, the classes do not seem to depend on whether the line-of-sight is sinc-like, smooth decaying, or complex.

It is clear that much higher resolutions – by at least an order of magnitude – are needed to be able to resolve out the beam depolarisation effects and permit an estimate of the true source polarisation at the critical lower frequencies where depolarisation phenomena are manifest. These plots emphasise that even with the VLA and its sub-kpc resolution, the responsible depolarising mechanisms and underlying structures cannot be uniquely identified. A much larger instrument will be needed to finally clarify the processes responsible.

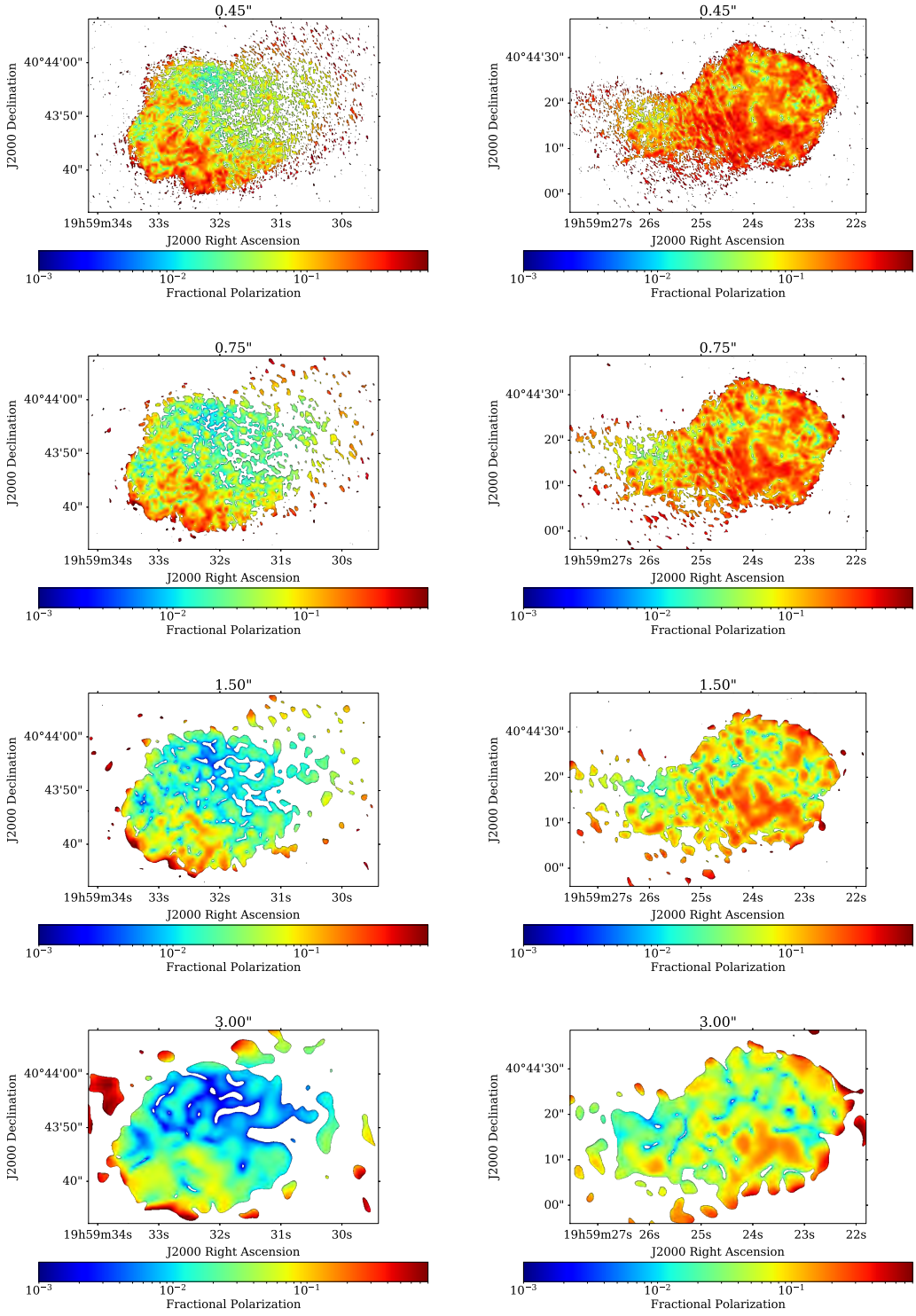

Figure 4.11: *Fractional polarisation maps at* 4.0 *GHz at different resolutions.* First row: $0.45''$. Second row: $0.75''$. Third row: $1.50''$. Bottom row: $3''$. The colour-bar ranges between 0.1% and 80%. Only pixels with $(\sigma_p/p) < 50\%$ are shown. The fractional polarisation decreases as the resolution degrades. This depolarisation is higher in the eastern lobe, especially in the region close to the galaxy.

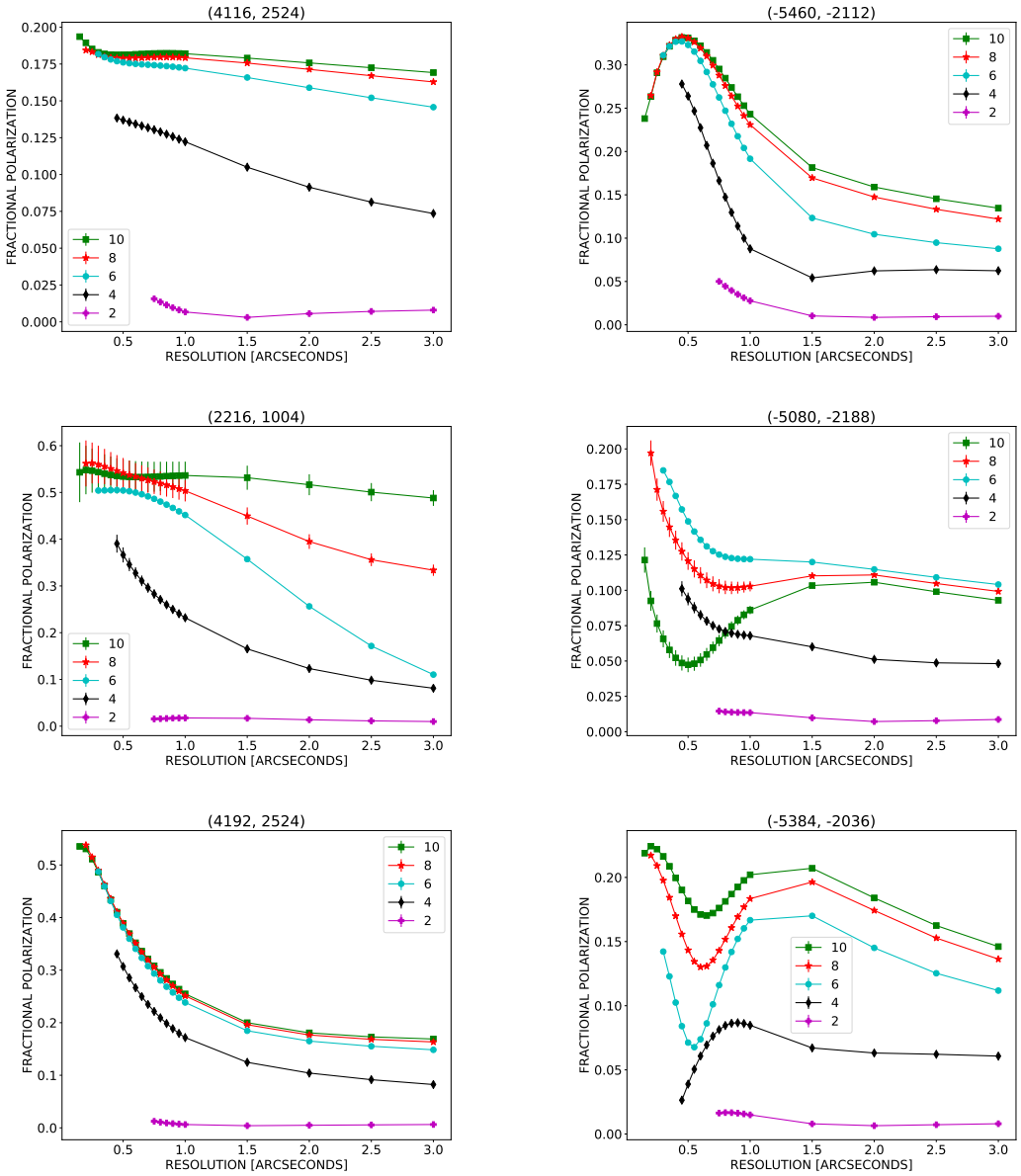

Figure 4.12: *Lines-of-sight fractional polarisation as a function of resolution.* Green: 10 GHz. Red: 8 GHz. Blue: 6 GHz. Black: 4 GHz. Purple: 2 GHz. The complex behaviour and the lack of a rise in the low-frequency plots demonstrates considerable beam-related depolarisation remains at the highest resolutions available.

4.5 Modelling the Rotation Measure Screen at $0.3''$

In the previous section, we showed the result that the depolarisation of the majority of the lines-of-sight are non-monotonic, showing fluctuating and in some cases oscillating, fractional depolarisation with increasing wavelength. For all lines of sight, there is strong overall depolarisation, resulting in almost complete depolarisation by a frequency of 2 GHz.

The higher frequency data provide a much higher resolution – at 6 GHz, the limiting resolution is $0.3''$. Noting that the oscillatory behaviour in the depolarisation is restricted to the lower frequencies – it is not seen above 6 GHz in all the 2000 independent lines-of-sight – we can determine the properties of the Faraday screen with the high-resolution, high-frequency data alone and use this to predict the lower-frequency, lower-resolution data which displays the complex depolarisation behaviour. A good match between such a prediction and the observations would be strong evidence that the unresolved fluctuations are primarily responsible for the majority of the depolarisation.

4.5.1 Fitting Procedure

We fitted simple models incorporating random unresolved fluctuations in a depolarising screen to our high-frequency, high-resolution data:

$$p = p_0 e^{2i\chi_0} e^{2iRM\lambda^2 - 2\sigma^2\lambda^4}, \tag{4.7}$$

where RM is the Faraday depth due to any large-scale magnetic field, p_0 and χ_0 are the intrinsic "zero wavelength" fractional polarisation and polarisation angles respectively and σ is the Faraday dispersion due small scale, random, Gaussian fluctuations in Faraday depths within clouds of fixed size (Burn 1966):

$$\sigma = 812 n_t \mathcal{B}_t d\sqrt{N} \qquad [\mathrm{rad\,m^{-2}}] \tag{4.8}$$

where $N = L/d$ is the number of turbulent cells of size d lying along the path length L, n_t is the electron density in the cell and $\mathcal{B}_t$ is the magnetic field of the cell.

Note however that the dispersion parameter can also describe the spread due a linear gradient across a Gaussian beam – the first-order term in a Taylor series expansion defined in Equation 2 of Laing et al. (2008a).

We used the LMFIT [1] software package to perform a nonlinear least-squares fitting. We performed fitting without weighting so that we do not disadvantage the high-frequency data since they are of low signal-to-noise ratios and are relatively less represented due to frequency averaging. We considered only pixels with an intensity in the 2 GHz image $5\times$ the off-source noise. Figure 4.13 shows a few examples of the fitting of this model to the data, indicating a reasonable fit to the data, as judged by eye.

The modelling returns values of the intrinsic (zero wavelength) fractional polarisation and polarisation polarisation angle, the Faraday depth (ϕ), (here equal to the RM, as there are no significant deviations from λ^2) and the Faraday dispersion, σ, which describes the overall decline in fractional polarisation between 18

[1] https://lmfit.github.io/lmfit-py/

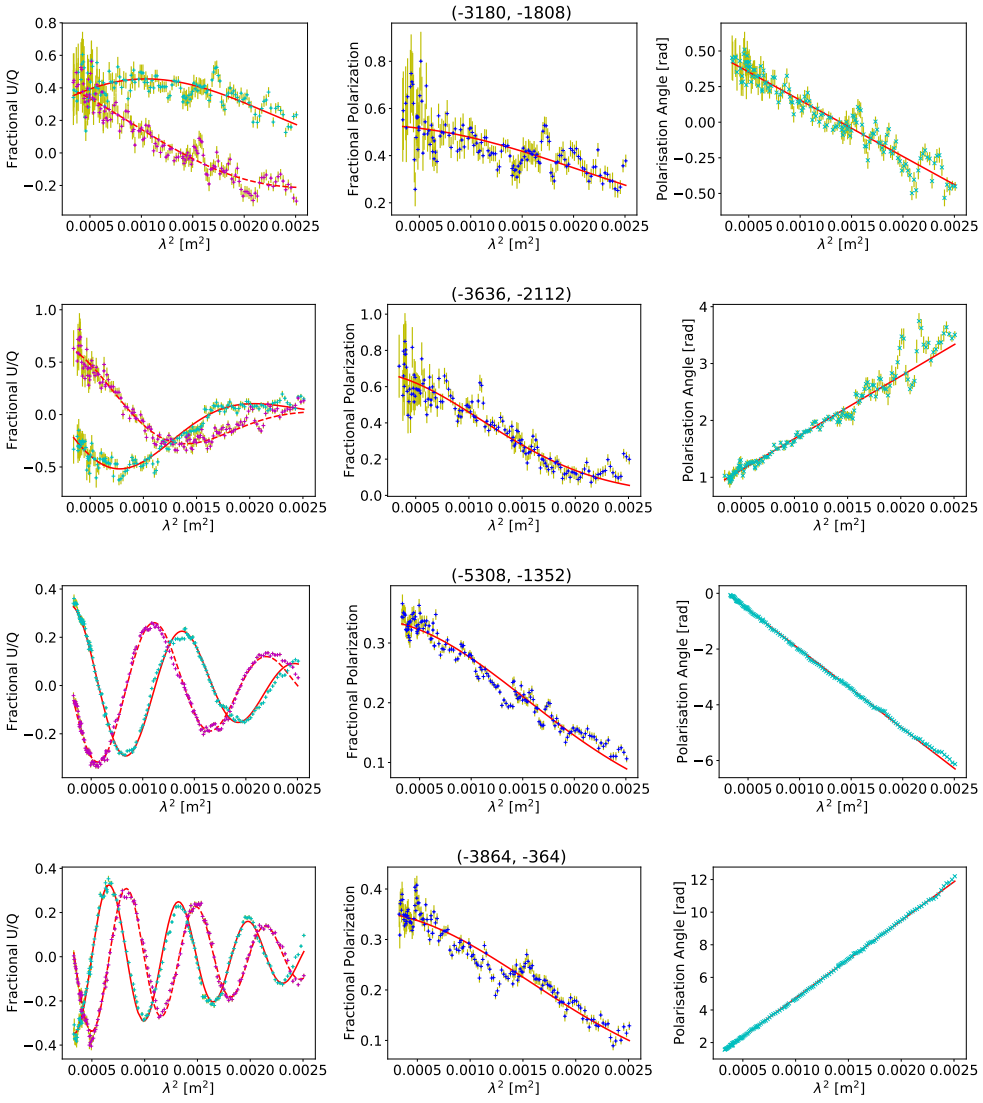

Figure 4.13: *Examples of a simple depolarisation screen fitted to the* 6 - 18 *GHz,* $0.3''$ *data of Cygnus A.* Left column: Fractional Q/I and U/I vs λ^2. Middle column: Fractional polarisation vs λ^2. Right column: Polarisation angle vs λ^2. The data are predicted very well by this simple depolarisation model.

and 6 GHz, at $0.3''$ resolution.

Figure 4.14 shows images of the intrinsic fractional polarisation across the two lobes (top row), the RM (middle row) and the Faraday dispersions (bottom row). These are discussed in the next section. The left columns show the eastern lobe, the right-hand columns show the western lobe. We consider only pixels with $\sigma_{RM}/RM < 0.2$ and $\sigma_{p_0}/p_0 < 0.2$, where σ_{RM} and σ_{p_0} are errors derived from the fits. This step ensures that we remove pixels which are less reliable.

4.5.2 Intrinsic Fractional Polarisation

The derived intrinsic fractional polarisation maps indicate that Cygnus A is highly polarised in nearly all areas, with typical values between 15% and 45% and some as high as 70%. Even the inner portions of the eastern lobe – which depolarises the most rapidly – show "zero wavelength" polarisation similar to all other parts of the source. These are consistent with the 10 GHz map shown in Figure 4.7. These results indicate that the low polarisation seen at intermediate wavelengths are not intrinsic to the source. The low fractional polarisation regions across the lobes seen at lower frequencies and resolutions are clearly largely a result of unresolved fluctuations.

4.5.3 Rotation Measure

The RM maps presented here are much more detailed than those derived by Dreher et al. (1987). These new results extend the RM mapping into the inner region of the eastern lobe and the tail of the western lobe. Both areas reveal extremely high RM, resulting in an increased maximum RM range: -4500 rad m^{-2} and $+6400$ rad m^{-2} in the eastern lobe and -5000 rad m^{-2} and $+3000$ rad m^{-2} in the western lobe. More striking is that the inner large RM have opposite signs suggesting field reversal in the surrounding material. In most regions, the RM gradients are typically a few 100 rad m^{-2} arcsec^{-1}, with a few regions having gradients as high as ~ 1000 rad m^{-2} arcsec^{-1}. The RM changes sign on 3–20 kpc scales, and this change in sign seems to occur along the source axis, particularly in the eastern lobe. The RM are relatively smooth across the western lobe and in general increase with decreasing radial distance from the AGN. These confirm the results, made with more limited data, given by Perley and Carilli (1996). The RM in the eastern lobe are relatively chaotic at this resolution, with the $|RM|$ showing no clear radial dependence but instead occurring in bands of large and small RM, similar to those seen in M84, 3C 353, 0206+35 and 3C 270 (Guidetti et al. 2011). Note that, with the exception of the enhanced RM arc surrounding hotspot B found by Carilli et al. (1988), there is no evident correlation between the RM values and the source brightness or with any of the evident structures in total intensity (the hotspot, jet, or filaments). This supports the interpretation that the observed RM structures originate outside the source of the emission.

4.5.4 Random Rotation Measure Dispersion

The bottom row of Figure 4.14 shows the dispersion images from the $0.3''$ modelling. This parameter essentially describes the rate of depolarisation between 18 and 6 GHz, also seen in Figure 4.13. The error in

these measurements is ≤ 10 rad m^{-2} for the brighter, outer regions in the lobe, rising to ≤ 50 rad m^{-2} at the tails of the lobe.

Typical dispersion values across the western lobe are $\lesssim 300$ rad m^{-2} with a few regions having dispersions of up to ~ 400 rad m^{-2}. Regions with very small dispersions close to zero may be a result of a lack of significant depolarisation, or due to repolarisation. The latter can be real or due to the noise – the form of Equation 4.7 does not account for this effect. The dispersion values in the eastern lobe are similar to those in the western lobe, with typical Faraday dispersions of $\lesssim 200$ rad m^{-2} in the extreme parts of the lobe close to the hotspots and regions closest to the AGN having dispersions of ~ 400 rad m^{-2}, with a few spatially narrow regions having a dispersion of ~ 800 rad m^{-2}. However, these latter regions are associated with very large errors – 100 – 300 rad m^{-2} and are mostly coincident with regions of large RM gradients and low polarisation, similar to 3C 31 (see Appendix C in Laing et al. 2008a). Note that the dispersions are rather chaotic in the innermost regions of the eastern lobe, likely indicating considerable structure remains on scales less than $0.3''$. The similarity in σ across both lobes is also suggestive of a common medium encompassing both lobes, with the more complex structures in the eastern lobe likely a result of the Laing-Garrington effect (Garrington et al. 1988; Garrington et al. 1991; Laing 1988) – with the eastern lobe further from us than the western lobe. However, it should be noted that this effect cannot explain the banded RM distribution across the lobes. Instead, the bands indicate the ordering of the large-scale magnetic field component, with a relatively large field ordering across the western lobe.

4.5.5 Intrinsic Magnetic Field Orientations

The fitting described above determines the intrinsic polarisation ("zero wavelength") angle values, from which we can directly determine the intrinsic projected magnetic field ($\chi_0 + \pi/2$) of the source. Figure 4.15 shows the magnetic field orientations superposed on a colour-coded image of the total intensity at 4 GHz. The fields follow the boundaries and filamentary structures of the lobe emission. This behaviour is quite common in radio galaxies, seen for example in 3C 465 (Eilek and Owen 2002), Hydra A (Taylor et al. 1990) and Pictor A (Perley et al. 1997) is generally understood as an effect resulting from shearing (compression at outer parts of the lobes) of the tangled lobe magnetic field at the lobe boundary, resulting in suppression of field components normal to the lobe boundaries (Laing 1980). The field vectors are generally smooth across the western lobe and brighter parts of the eastern lobe, while becoming slightly chaotic in the inner region of the eastern lobe. As with the other fitted parameters, this is likely due to significant structures on scales less than the $0.3''$ resolution utilised here.

4.5.6 Rotation Measure vs. Random Rotation Measure Fluctuations

One question that arises is whether the observed Faraday dispersions are correlated with the RM. This might occur if the major RM structures are associated with a mixing layer surrounding the source. The higher RM might then be associated with higher field values within the turbulent cells. Figure 4.16 shows the derived RM as a function of σ for lines-of-sight classified as described in Section 4.4.1. Shown are only those lines-of-sight with fractional errors in Faraday dispersions of less than 80%. There is no clear

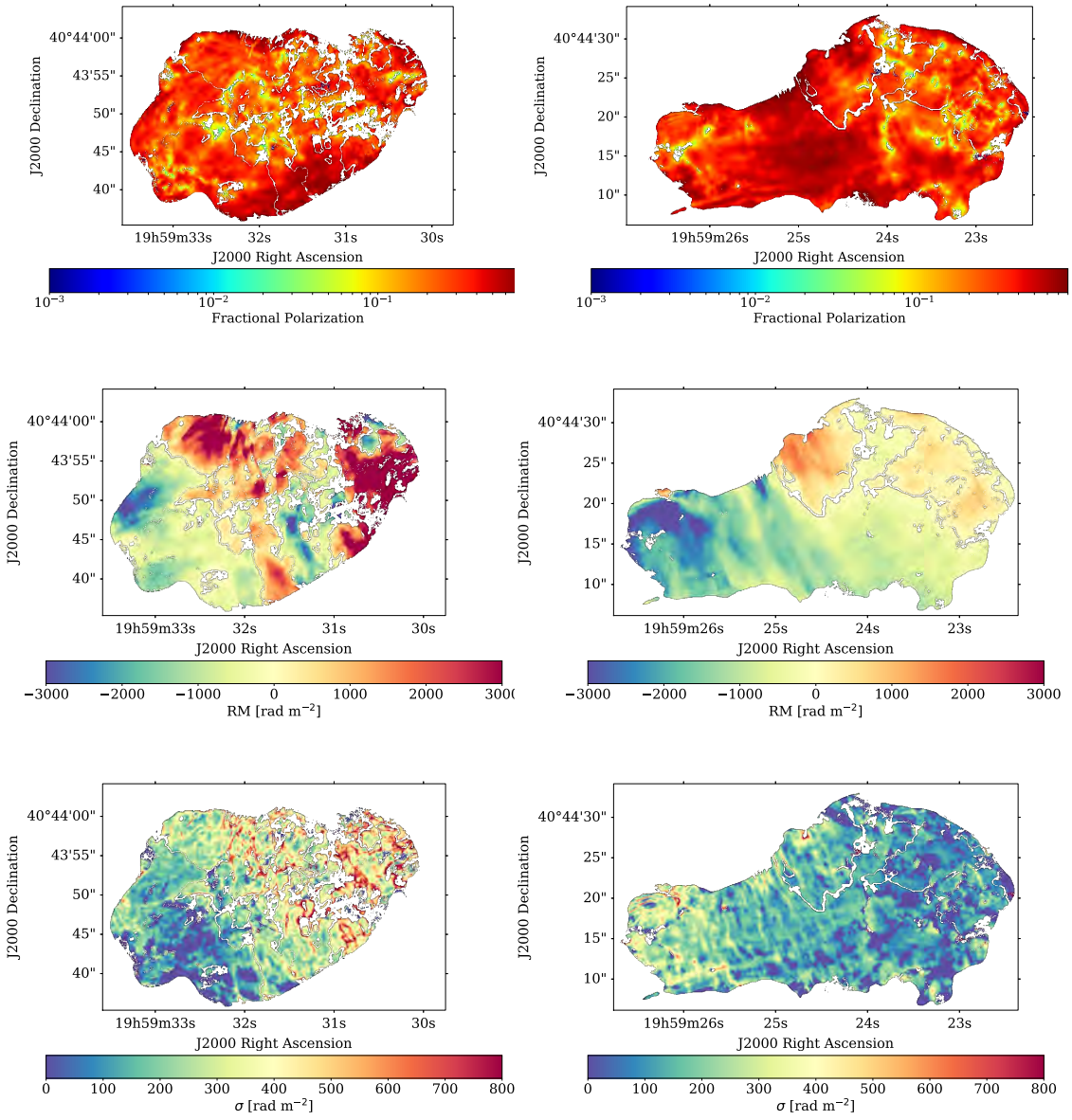

Figure 4.14: *Cygnus A high-Frequency, high-resolution QU-fitting estimated parameter maps.* Top row: Intrinsic fractional polarisation. Middle row: RM. Bottom row: Faraday dispersions. The intrinsic fractional polarisation is consistent with the maps at high-frequencies and high-resolution (see Figures 4.7 and 4.11). RM range between -4500 rad m^{-2} to $+6400$ rad m^{-2} in the eastern lobe and -5000 rad m^{-2} and $+3000$ rad m^{-2} in the western lobe. RM change signs on 3 - 20 kpc scales, with a banded structure orthogonal to the source axis particularly evident in the western lobe. The lobes depolarise much more rapidly in the inner regions towards the AGN as seen in the Faraday dispersion maps. Pixels shown have a fractional error in RM and p_0 of less than 0.2.

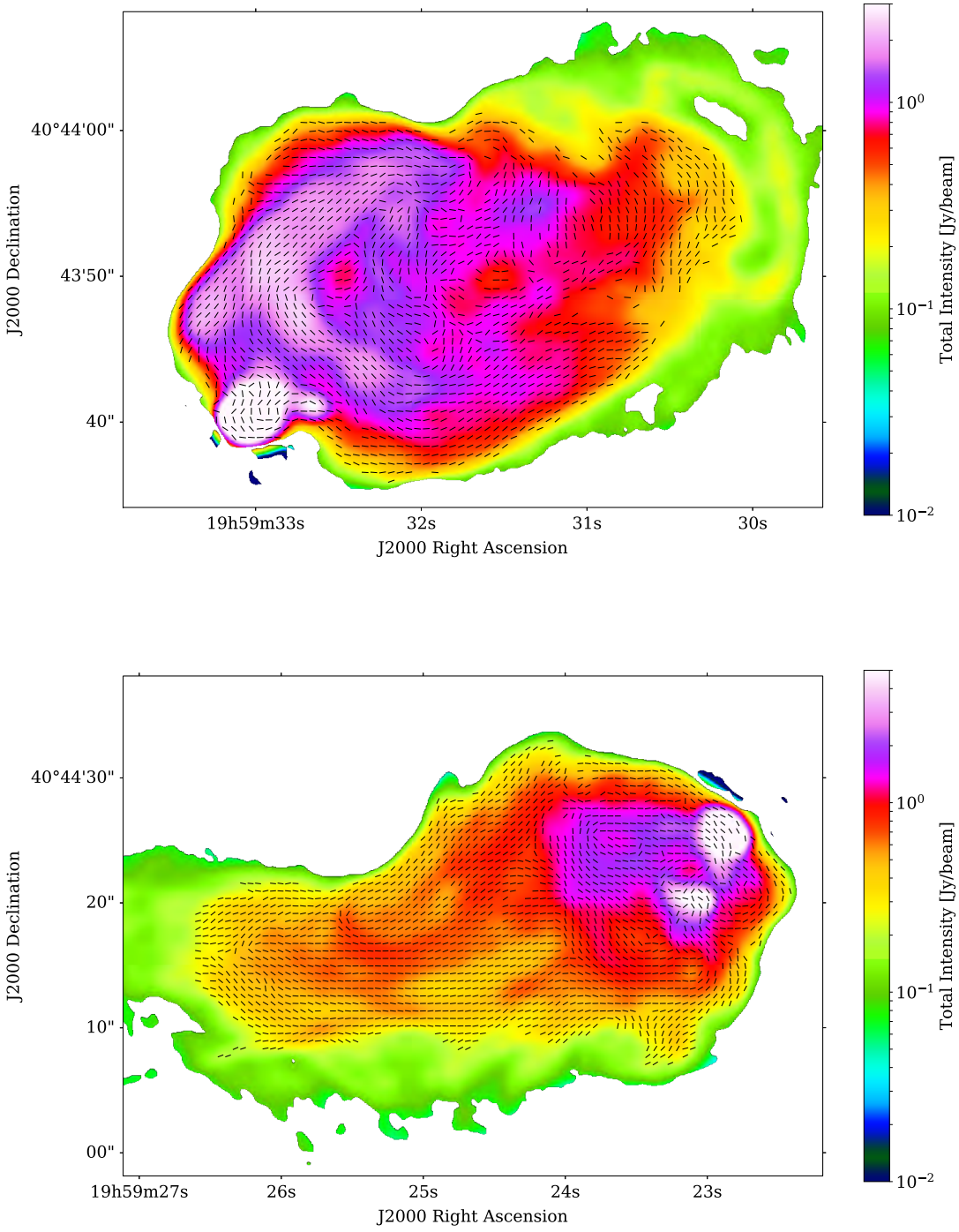

Figure 4.15: *Intrinsic magnetic field orientation across Cygnus A lobes at* $0.30''$. These are superimposed on a colour image of the total intensity at 3.979 GHz and $0.54'' \times 0.44''$ resolution. The field vectors follow the boundaries of the source as well as the filamentary structures.

correlation between these two quantities, from which we conclude that the Faraday dispersions are not a direct result of the observed RM, suggesting that the observed large-scale RM are not coming from a mixed region. However, there is a clear tendency for regions of very high RM to have high dispersions. A likely explanation is that a high RM gradient across the resolution beam will cause a larger apparent depolarisation, leading to an apparent increase in the dispersion. The regions with high gradients are the inner lobes, where the highest RM are accompanied by high dispersions.

4.5.7 Jet Rotation Measures and Magnetic Field Orientation

To obtain detailed solutions for the jets, we performed the above fitting separately for regions enclosing the jet emission. Figure 4.17 shows fractional polarisation, RM, Faraday dispersion and magnetic field orientation across the western jet. The pixels shown have $\sigma_{RM}/RM < 0.2$. No reliable solutions were found on or close to the counter jet – even with RM-Synthesis. The analysis of this region (and nearby structures such as the AGN and the ring structure in the eastern lobe) awaits more sensitive observations at higher frequencies.

The intrinsic field orientations lie parallel to the jet axis across most parts of the jet where the jet polarisation is visible. This polarisation behaviour along the jet is common in strong FR II sources (Bridle and Perley 1984). The RM of the jet are very similar to those of the lobe (see Figure 4.14) both in magnitude ~ -300 to -2000 rad m^{-2} and angular scale ~ 2 - 5 kpc, again supporting the argument that the origin of the RM is exterior to the source. The jet has similar Faraday dispersions as those of the lobe emission in the vicinity of the jet: $\sim$ a few 100 rad m^{-2} – with a slight (not conclusive) indication of larger dispersions towards the AGN. The jet is intrinsically highly polarised – with fractional polarisation $\sim 20\%$ to 50%.

The similarity of the jet RM to that of the lobes has been used to argue against mixing of external gas into the synchrotron-emitting regions – see Taylor and Perley (1993) for the case of Hydra A.

4.6 Predicting Low-Frequency Depolarisation

Section 4.4.2 showed that beam depolarisation – depolarisation from transverse fluctuations unresolved by the resolution beam – is an important factor in the depolarisation of Cygnus A. Can we state that the observed depolarisation is entirely explained by this effect? This is an important question, which can only be fully answered by observations with much higher resolution likely better than $0.20''$ at 2 GHz, which are not possible with current instruments. However, there is a hint in Figure 4.7 and 4.11, showing the polarisation as a function of resolution and frequency, that a significant fraction of the foreground depolarisation is resolved by a resolution of $0.45''$, which raises the question of whether the high-resolution, high-frequency foreground screen images shown in Figure 4.14 can be used to predict the lower-frequency, lower-resolution images where the depolarisation effects are very strong. An accurate prediction would be strong evidence for a screen origin of all, or nearly all, the observed depolarisation.

We assume that the fractional polarisation, p_0 and polarisation angles, χ_0, derived in Section 4.5 represent the intrinsic polarisation properties of the source. Further, we assume that the RM map is an accurate representation of the foreground Faraday rotating screen on a $0.3''$ scale – essentially assuming that this resolution

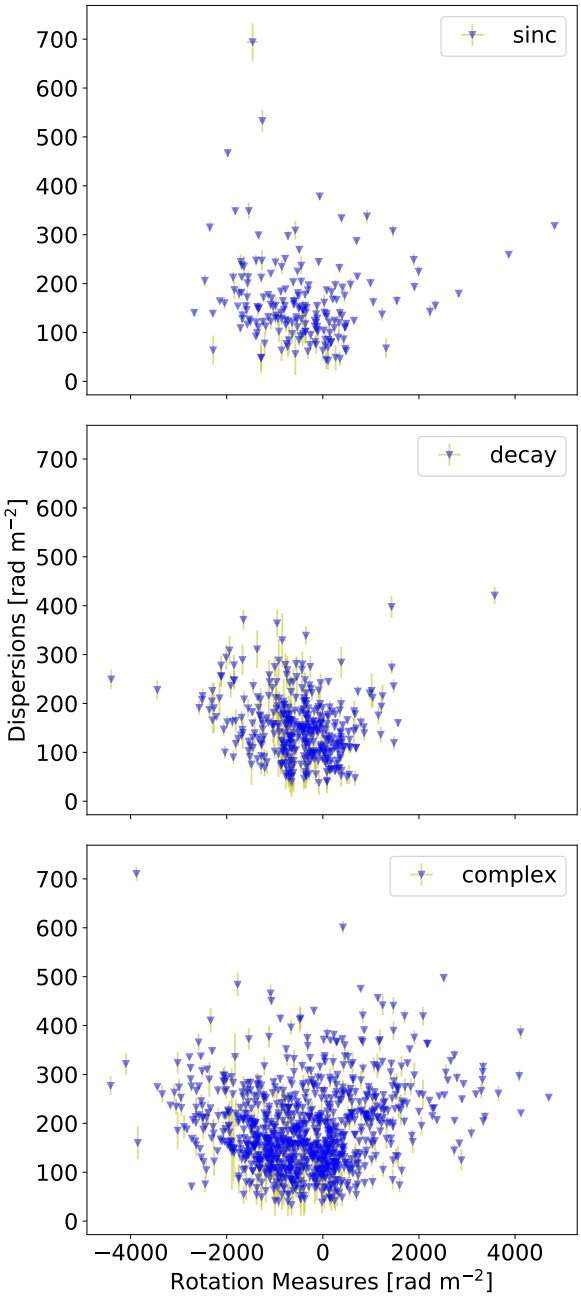

Figure 4.16: *Faraday dispersions as a function of* RM. These are separated based on their classes (see Section 4.4.1), namely sinc-like, smooth decay and complex decay. There is no clear correlation between the RM and σ. This suggests that the observed RM are not directly related to the observed depolarisation (decrease of fractional polarisation with increasing λ^2).

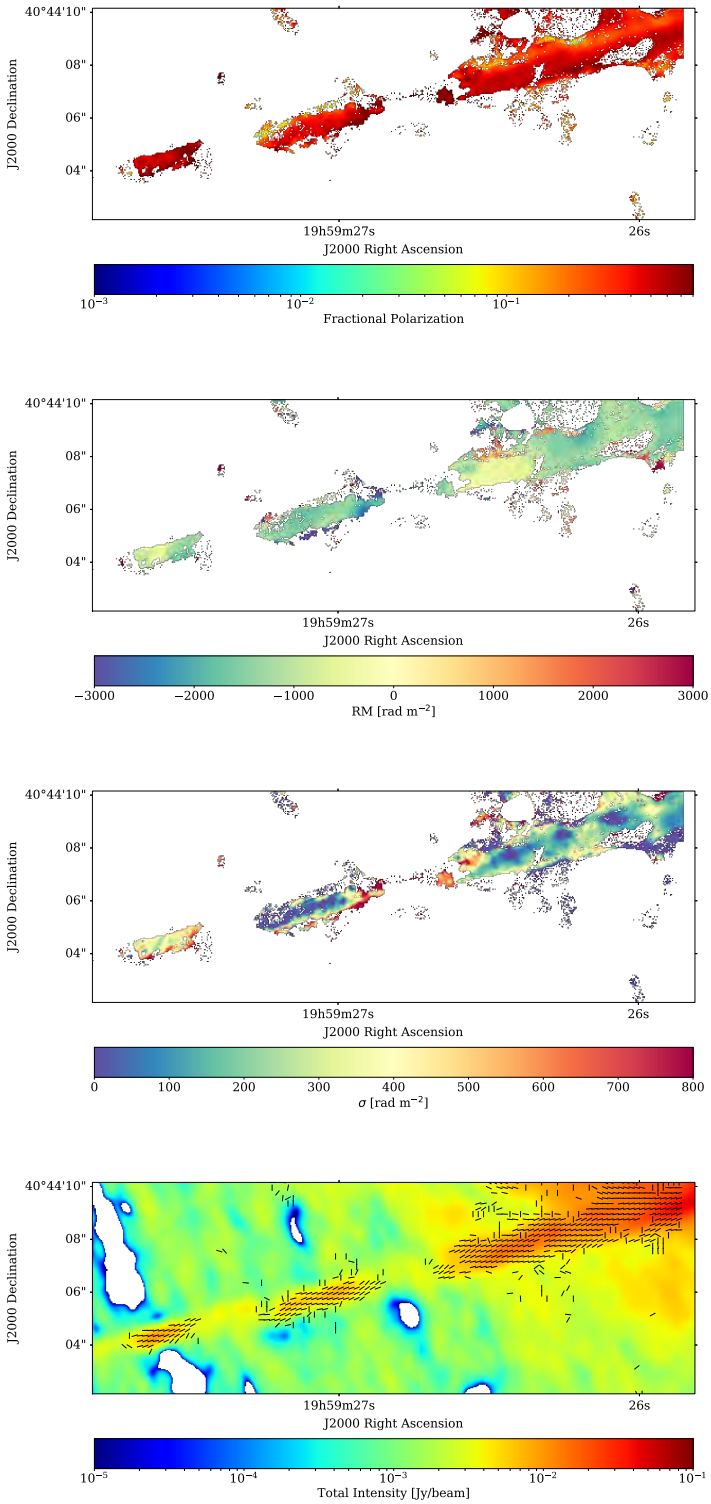

Figure 4.17: *QU-fitting parameters across Cygnus A western jet.* First row: Intrinsic fractional polarisation. Second row: RM. Third row: Faraday dispersion. Fourth row: Magnetic field vectors. The jet is intrinsically highly polarised $\sim 20\%$ - 50%. The RM and σ within the jet are similar to the RM of the adjacent lobe – indicating a similar origin for both. The field vectors lie parallel to the jet axis.

has fully resolved the RM screen. With these, we can calculate the low-frequency polarisation (< 6 GHz) at $0.3''$ resolution, by simply rotating the observed polarisation angle by $RM\lambda^2$ as follows:

$$P(\lambda^2) = p_0 I e^{2i\chi_0} e^{2iRM\lambda^2}. \tag{4.9}$$

We estimated I at $0.30''$ across 2 - 18 GHz first by determining the spectral index [2] at this resolution between 6 - 18 GHz, and then using this spectral index to extrapolate the total intensity at low-frequencies. We then convolved (using AIPS task "CONVL") the resulting estimates of the Q, U and I to the desired resolution ($0.75''$) providing the model images. These were then compared to the observed polarisation.

Figure 4.18 shows a few illustrative examples showing our original data at $0.75''$ (in black) and the model predictions (in red). The left column shows the fractional polarisation as a function of λ^2, the middle column shows the polaris ation angle as a function of λ^2 and the right column shows the amplitude of the Faraday depths.

Table 4.3 shows the result of the predictions. The top two rows show examples with smoothly decaying fractional polarisation as a function of λ^2. The top row shows an example where the predictions match the data very well – $\sim 13\%$ of the smooth decaying lines-of-sight fit as well as this. The second row shows an example in which the prediction underestimates the rate of depolarisation – denoted in Table 4.3 as "approx". About $\sim 72\%$ of the lines-of-sight fall within this category. The remaining lines-of-sight ($\sim 15\%$) are not accurately predicted by our simple model (denoted in Table 4.3 as "N/A").

The bottom four rows show examples of lines-of-sight with oscillatory behaviour. In general, the presence of an oscillatory depolarisation is well predicted by our model. This result suggests that although the dominant depolarisation mechanism is associated with unresolved fluctuations, larger-scale components responsible for the oscillatory depolarisation characteristics must be present in these cases, likely operating on scales only a little less than our standard $0.75''$ resolution.

The extraordinarily good fit shown in the third row is not common. Most often, the predicted nulls occur at longer λ^2 values than the data, so that the predicted peaks in the Faraday spectrum are too close together, as can be seen in the second column. See results of the predictions for sinc-like lines-of-sight in the first row, columns $12 - 14$. Results for complex lines-of-sight are given in rows $3 - 5$ and columns $12 - 14$.

Thus, on average (weighted by the total number of lines-of-sight in each class), we find that $\sim 14\%$ of the lines-of-sight are accurately predicted (within measurement errors) and $\sim 72\%$ have the correct functional form but with a scaling error, and $\sim 14\%$ of the predictions are incorrect.

What could be causing the shifting of the predicted nulls to higher λ^2 as well as underestimating the depolarisation? The simplest explanation for the latter is that the $0.3''$ resolution image from which these estimates are made is missing some smaller-scale structure. This is a reasonable conclusion given that we are still seeing depolarisation at $0.30''$, which we characterised using σ. The shifting of the nulls to higher λ^2, on the other hand, is caused by an underestimation of the RM difference between the "patches" of polarised emission as resolved on the $0.3''$ RM image. It is not clear to us why this small underestimation occurs.

[2] Using task SPIXR in AIPS.

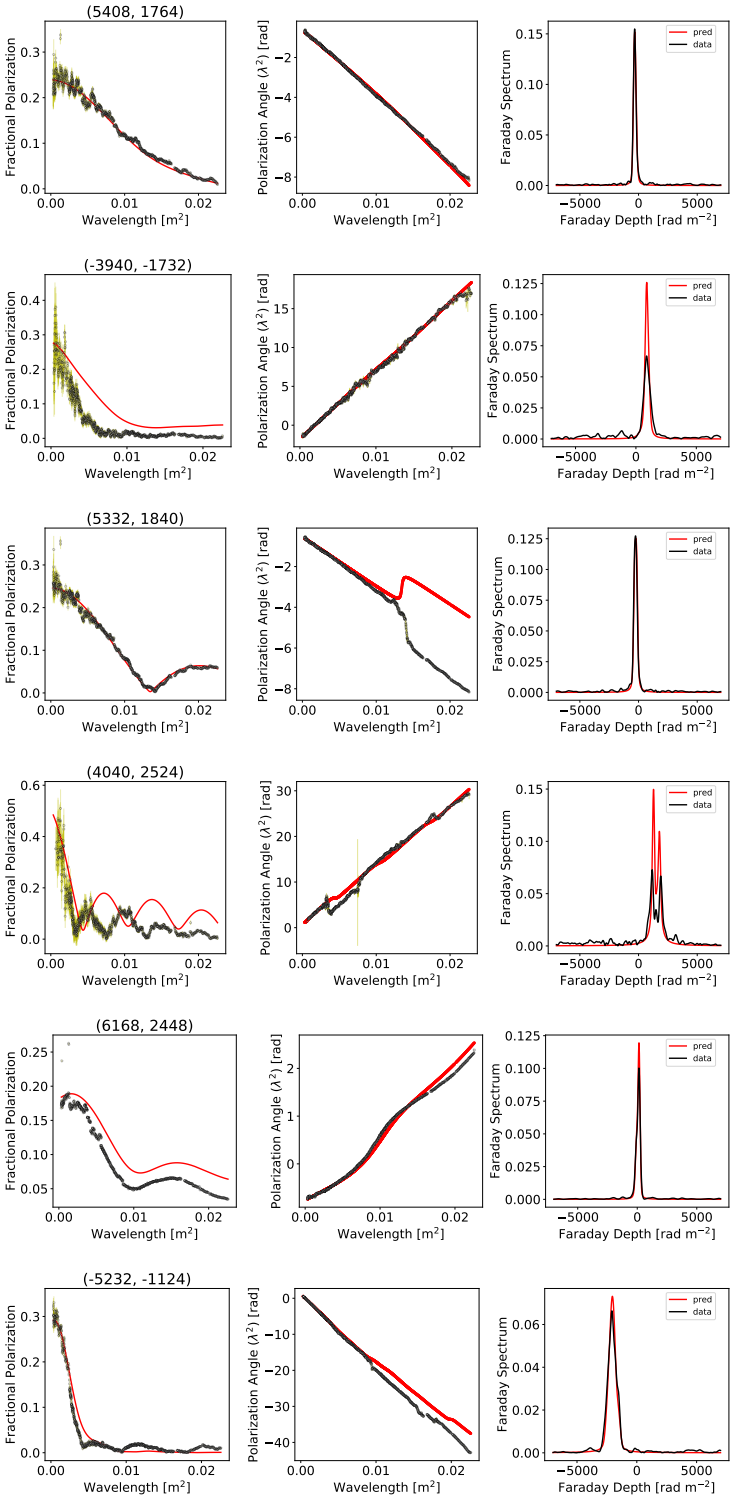

Figure 4.18: *Predictions of low-resolution ($0.75''$) data using the high-resolution ($0.3''$), high-frequency data.* Left column: Fractional polarisation vs λ^2. Middle column: Polarisation angle vs λ^2. Right column: Faraday spectra. Black: Original data. Red: Predicted data. The simple model fits the data remarkably well for about $2/3$ of the lines-of-sight.

4.7 Small-Scale Fluctuations

In the above section, we demonstrated how fluctuations in the RM map at 300 pc are able to explain the depolarisation and structures at 750 pc. This provides evidence of small-scale magnetic field fluctuations in or around Cygnus A. In this section, we demonstrate this even further, by showing the wideband data at two resolutions: $0.75''$ and $1.50''$. In this case, we convoled our original data at $0.75''$ to $1.50''$ using CONVL in AIPS. Figures 4.19 to 4.24 show examples of the results. We provided more lines-of-sight for the reader to appreciate the complexity in the data. Additionally, to demonstrate that our favoured hypothesis is supported by the data: the complexity in the data is due to multiple RM components within the synthesised beam – the higher the resolution, the simpler the Faraday spectra must become. This shows the presence of fluctuations even at larger (1500 pc) scales.

4.8 Summary

In this chapter, we presented the results from our wideband (2 - 18 GHz), high-spectral resolution polarimetry data on Cygnus A. We have shown how the fractional polarisation varies as a function of frequency and resolution. We also conducted a Faraday rotation analysis using high-frequency data, > 6 GHz at $0.30''$ resolution. In this Faraday rotation study, we derived maps of RM, intrinsic fractional polarisation (p_0), intrinsic polarisation angles (χ_0) and Faraday dispersions (σ), from which we predict the depolarisation behaviour at lower frequencies and resolutions with remarkable success. A complete analysis (physical interpretation) of our full band data will be presented in Chapter 5. A summary of our results shows:

1) All lines-of-sight through the lobes depolarise significantly with decreasing frequency. There is no relation between depolarisation behaviour and the various structural features (hot spots, filaments, jet). The eastern lobe, particularly those regions nearer the AGN, depolarise at higher frequencies than the western lobe.
2) The distribution of the fractional polarisation across the lobes is smooth at high-frequencies but becomes increasingly clumpy on ~ 1 kpc scales, at low-frequencies.
3) The fractional polarisation as a function of λ^2 for the different lines-of-sight reveal complex depolarisation behaviours: some lines-of-sight smoothly depolarise, while others show oscillations, which in extreme cases have "sinc-like" behaviour. By classifying these polarisation behaviours into three simple categories: i) smooth decaying, i) sinc-like and iii) complex, we find that 25% fall into the first class, 11% the second and 50% are complex, and the remaining 14% could not be classified. There is a tendency for more complex decay in the eastern lobes, with relatively fewer smooth decay and sinc-like behaviours. The distribution across the western lobe, on the other hand, consists mostly of smooth decay, particularly at the extremes of the lobes and complex behaviour. There is no clear spatial correlation between these decay patterns across the lobes, except that they are not random but are clumped on few-kpc scales.
4) Lines-of-sight with oscillations in their depolarisation behaviour also show strong deviations of the polarisation angle from linearity.

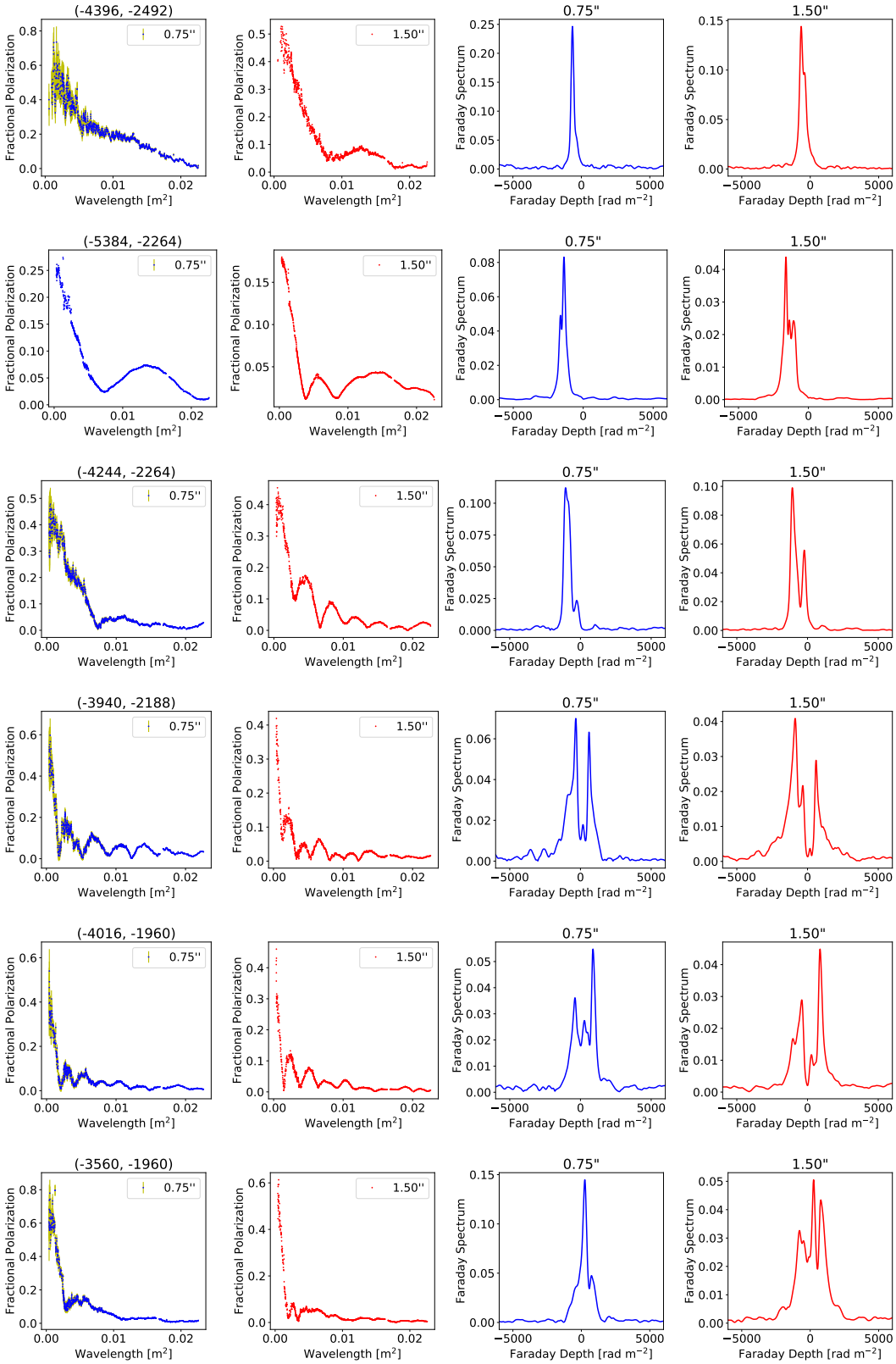

Figure 4.19: *Wideband polarisation behaviour at* $0.75''$ *compared to* $1.50''$. Two left columns: Fractional polarisation vs λ^2. Last two columns: Faraday spectra. Blue: $0.75''$. Red: $1.50''$. There is significant structure at poor resolution.

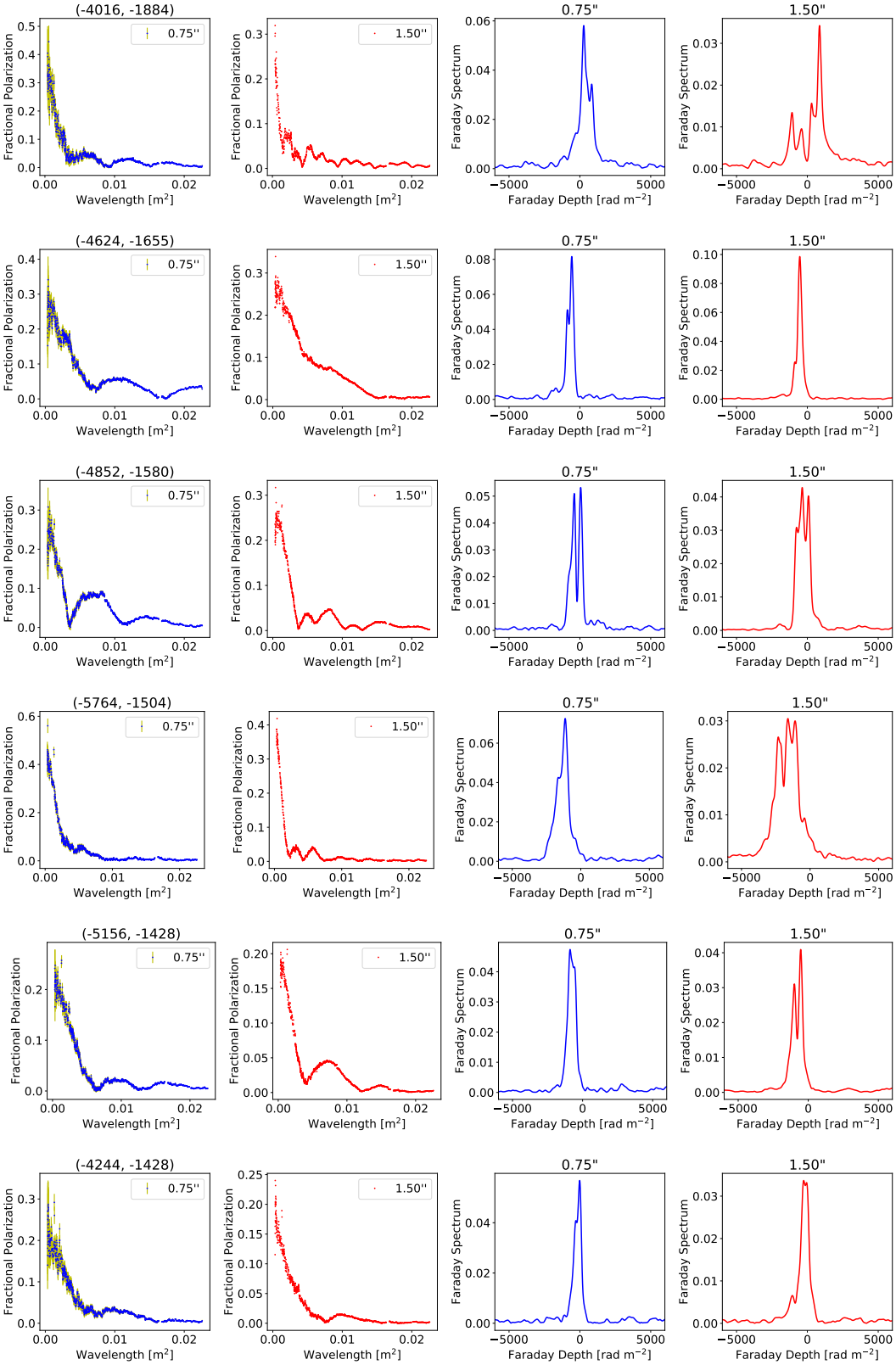

Figure 4.20: *Continuation of Figure 4.19.*

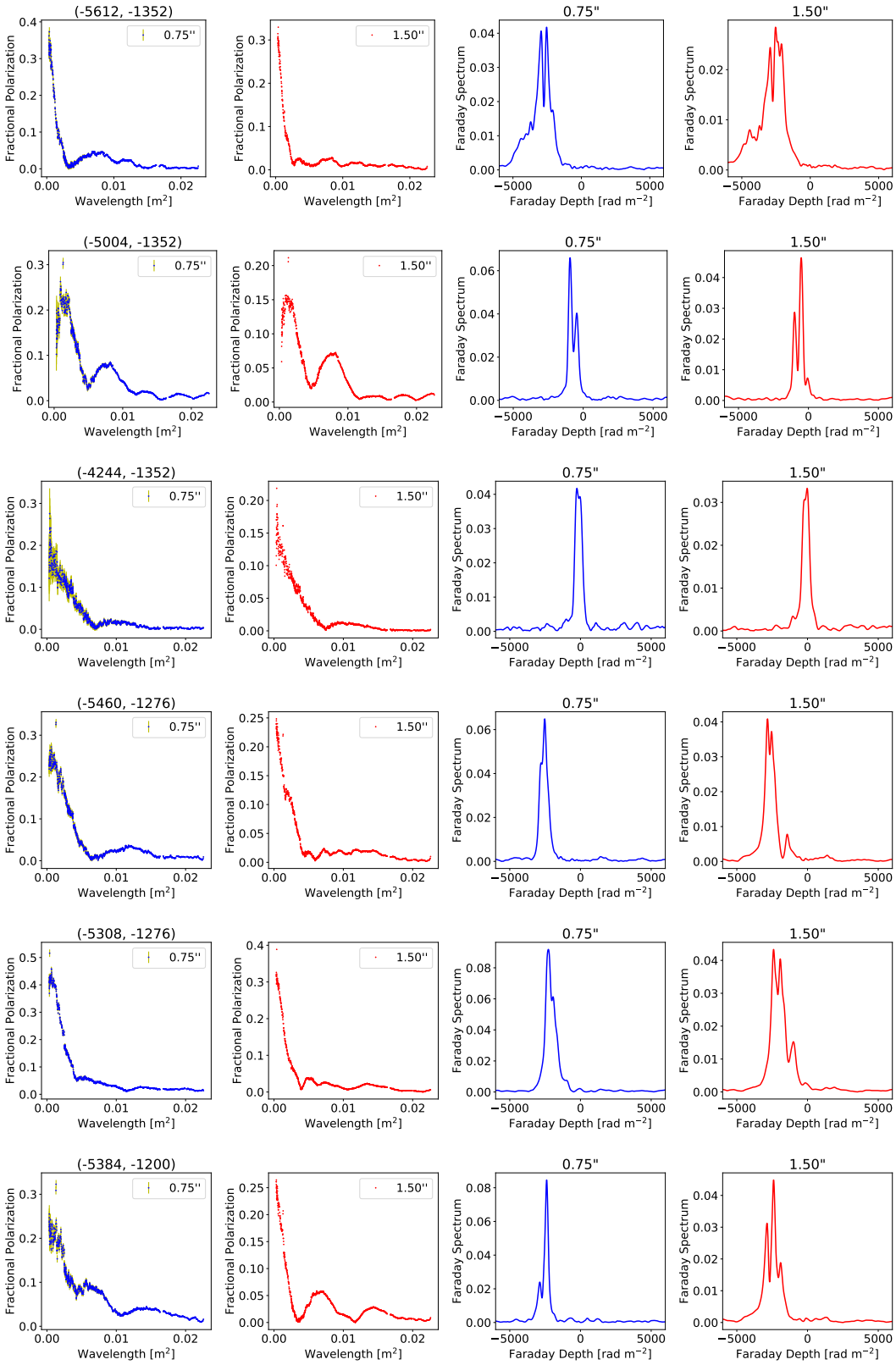

Figure 4.21: *Continuation of Figure 4.19.*

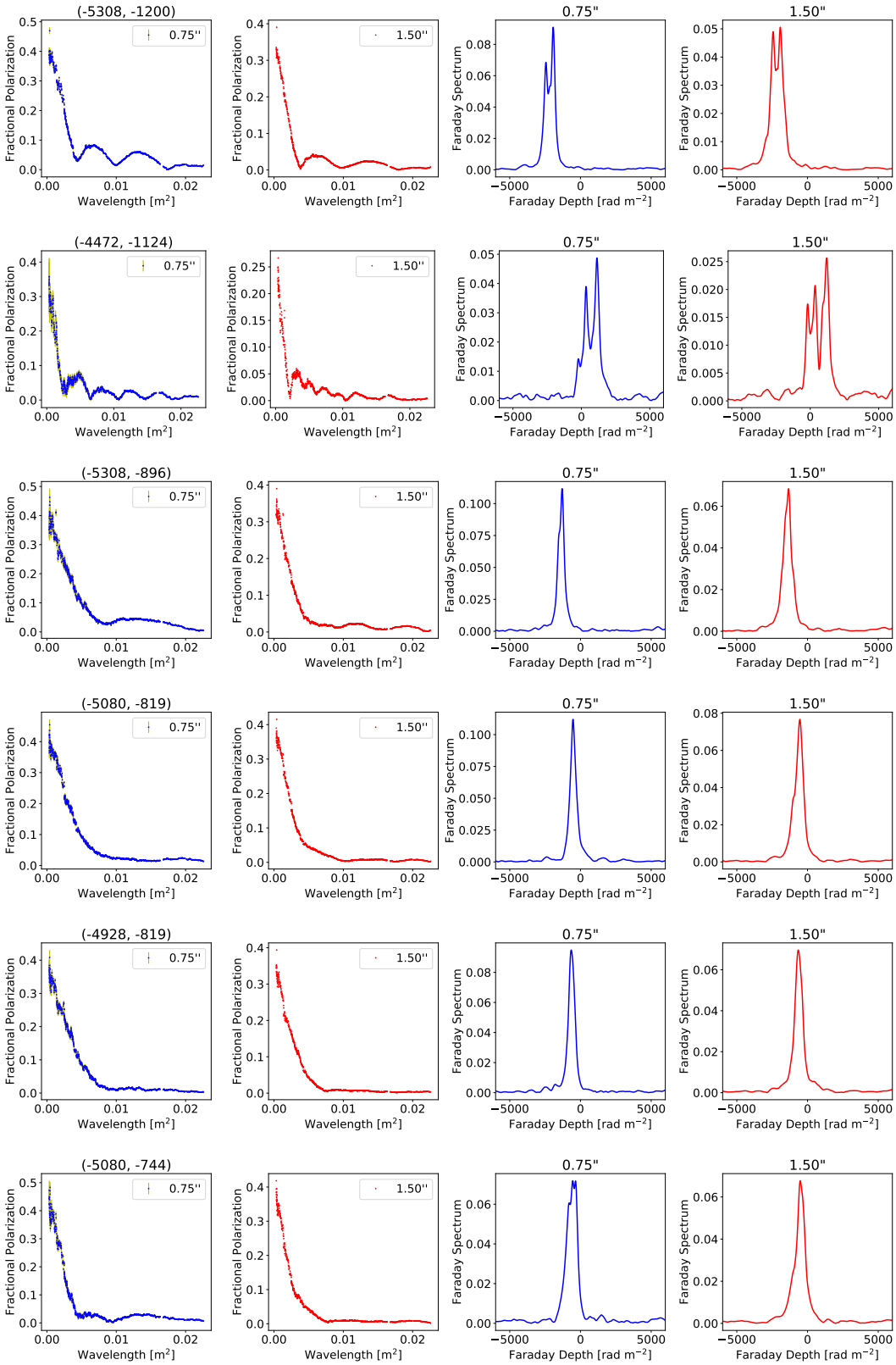

Figure 4.22: *Continuation of Figure 4.19.*

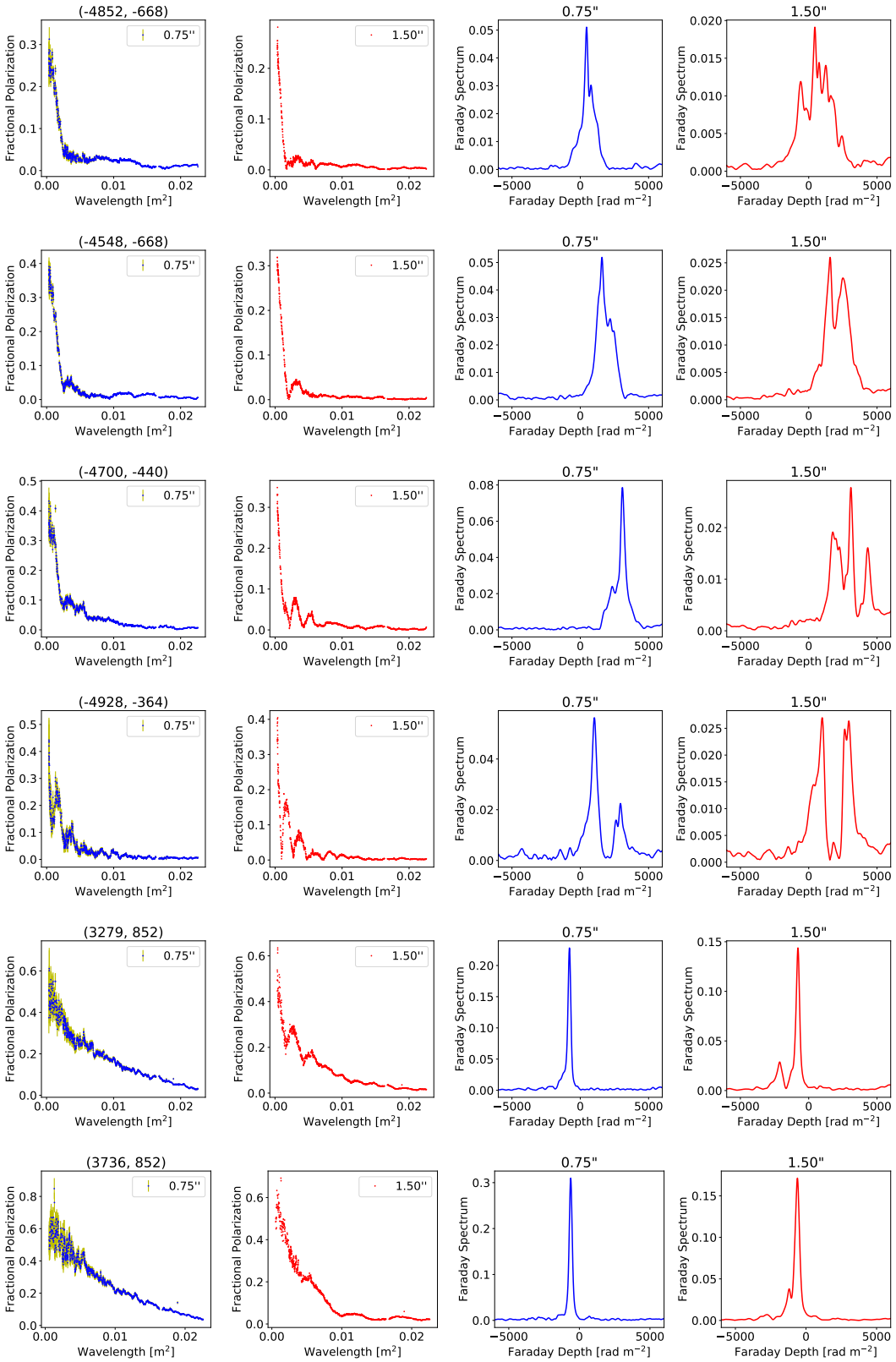

Figure 4.23: *Continuation of Figure 4.19.*

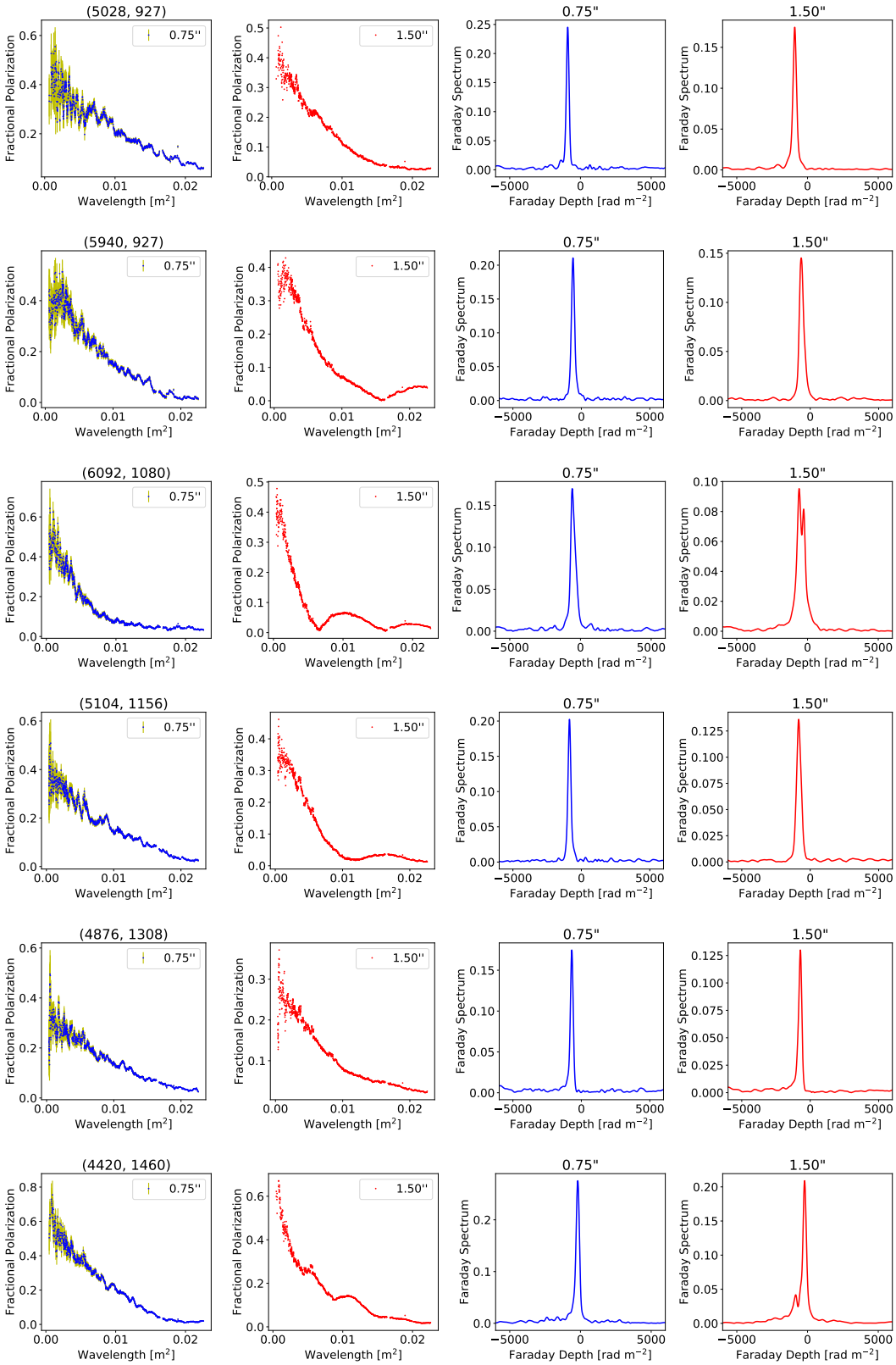

Figure 4.24: *Continuation of Figure 4.19.*

5) The lobe emission also depolarises significantly with decreasing resolution. The inner region of the eastern lobe (closest to the AGN), depolarises more rapidly than other regions of this lobe.
6) Plots of fractional polarisation as a function of resolution and frequency for different lines-of-sight reveal that the beam-related effects are complicated and that our observations do not have sufficient resolution to completely resolve the depolarising structures present in or around Cygnus at frequencies below 6 GHz.
7) The RM values derived are consistent with those found by Dreher et al. (1987) and Perley and Carilli (1996) and extend those results to the weaker emission nearer the AGN. Our new observations reveal very high RM values at the tails of the lobes – ranging between -4500 rad m^{-2} and $+6400$ rad m^{-2} in the eastern lobe and -5000 rad m^{-2} and $+3000$ rad m^{-2} in the western lobe. We find that the RM values in the eastern lobe occur in bands of low and high RM along the source-axis. The RM values are ordered on 3 - 20 kpc scales. There is no relation between the RM values and the presence of structural features in the total intensity (hotspots, jet, filaments).
8) The intrinsic magnetic fields follow the boundary and filamentary structures of the lobes – consistent with other radio galaxies. The only exception is the inner region of the eastern lobe where the fields appear to be slightly chaotic.
9) The derived intrinsic fractional polarisation of the source found from analysis of the high-frequency data alone at $0.3''$ resolution shows that Cygnus A is intrinsically highly polarised, with typical fractional polarisation between 15% to 45% and some regions as high as 70%. The intrinsic fractional polarisation of the inner region of the eastern lobe is very similar to that of the rest of the lobe, indicating that this region is not unique and that the observed depolarisation as well as the rapid depolarisation have an external origin.
10) We find that the Faraday dispersions across both lobes decrease with increasing distance from the AGN. The outermost regions in both lobes have small Faraday dispersions $\sim$ 0 rad m^{-2}. These increase towards the AGN to typical values of $\sim$ 200 rad m^{-2} to 400 rad m^{-2}. The innermost regions of the eastern lobe show the highest dispersions – up to $\sim$ 800 rad m^{-2}. The Faraday dispersions are weakly correlated with the observed RM, again suggesting that the RM are external to the lobes.
11) Assuming that the derived p_0, χ_0 and RM generated from the high-frequency, high-resolution data represent the intrinsic polarisation properties of the source and that there is no synchrotron emission in the external medium, we generated predictions of the low-frequency polarisation emission at $0.3''$ resolution, which were then convolved to our resolution of $0.75''$. Comparison of the predictions with the observations shows remarkable agreement, with about 14% of the lines-of-sight predicted accurately and a further 72% with the correct shape but with small scale errors. This result supports the interpretation that the majority of the observed depolarisation is due to unresolved fluctuations on scales of $0.3''$ – $0.7''$ in the external medium.
12) **Fractional polarisation data as a function of λ^2 and Faraday spectra data are made available via an online tool http://cygnus.ratt-ru.org/cygnus/. This tool was developed by Lexy Andati, a PhD student at Rhodes University, South Africa.**

CHAPTER 5

Cygnus A: Wideband Data Modelling and Characterisation

"He who made the Pleiades and Orion and turns deep darkness into morning and darkens the day into night, who calls for the waters of the sea and pours them out on the surface of the earth, the Lord is His name."
Amos 5:8

5.1 Introduction

In the previous chapter, we presented the data of the wideband observations of Cygnus A and showed that the data reveal significant complexities, namely the large depolarisation, depolarisation structures and single-, double- and multiple-peaked Faraday spectra. Using high-frequency (6 - 18 GHz), high-resolution ($0.30''$) data, we have demonstrated that the depolarisation structures are predominantly a result of unresolved fluctuations. In this chapter, we analyse our full-band (2 - 18 GHz) data at $0.75''$ with the intention of describing the nature (such as the structure) of the magnetic fields within or surrounding Cygnus A.

In Section 5.2, we classify and describe the data as seen in Faraday space (using Faraday spectrum). In Section 5.3, we characterise the Faraday spectra by fitting a simple 1D Gaussian function to the amplitude of the spectra. The Faraday spectra classes are combined with the depolarisation classifications (from Section 4.4.1.3) to choose the form of analytical models to fit to the data. From Section 5.4 to 5.9, we present our wideband data modelling results. Section 5.10 summarises the results of the model selection and determines the best model for the $0.75''$ data. Section 5.11 summarises the derived parameters of the best model(s) and compares these parameters with those derived from high-frequency, high-resolution modelling as well as those from Faraday spectra characterisation section. Section 5.12 provides the overall physical picture of the magnetic fields within and around Cygnus A, as depicted by the wideband modelling.

5.2 Faraday Spectra Classification

In Section 4.4.1.2, we classified the various (~ 2000) lines-of-sight across Cygnus A based on the structure in the depolarisation as a function of λ^2. In this section, we provide a further classification based on the structure in the Faraday spectrum, specifically based on the number of resolved and unresolved peaks. We were able to categorise the different Faraday spectra into six classes, as defined below.

- **Single-peaked**: the Faraday spectrum is dominated by one strong peak. We find that the width of the peak in the spectra is most often larger than the width of the RMTF.
- **Single-peaked with smaller peaks**: the spectrum is dominated by one strong Faraday component with additional weaker components, which are usually blended with the strong component but occasionally separate.
- **Blended double-peaked**: the spectrum is dominated by two strong Faraday components which are blended together – their separation is less than their width.
- **Resolved double-peaked**: the spectrum is dominated by two strong Faraday components that are partially or almost fully resolved. Weaker components are often seen.
- **Blended multiple-peaked**: the spectrum is dominated by three or more Faraday components that are closely blended together and sometimes partially separated.
- **Resolved multiple-peaked**: several Faraday components are apparent, with some well separated peaks (by more than their width). There is no significant distinction between these with the blended multiple-peaked spectra. However, we separated these two classes to bring attention the existence of some Faraday spectra with well-resolved multiple-peak components.

We find that roughly 40% of the lines-of-sight have single-peaked Faraday spectra, 14.5% have single-peaked with smaller peaks, 19.6% have blended double-peaked spectra, 7% resolved double-peaked spectra, 14.5% blended multiple-peaked spectra and 4.4% resolved multiple-peaked spectra. Table 5.1 shows how this classification in Faraday depth space compares with the classification made in λ^2-space (see Chapter 4 for the details on the classification). We find that the majority of the single-peaked spectra are associated with smooth and non-oscillatory decaying fractional polarisation as a function of λ^2, while more complicated spectra are associated with lines-of-sight having structure in their depolarisation. No smooth-decaying line-of-sight has a resolved double- and multiple-peaked Faraday spectrum.

Table 5.1: *Faraday Spectra Classification*

Faraday Spectra Class	Depolarisation Class				Classifiable
	sinc-like	smooth	complex oscillatory	complex non-oscillatory	
Single-peaked	24	440	26	206	696
Single-peaked with smaller peaks	11	47	47	148	253
Blended double-peaked	111	19	104	109	343
Resolved double-peaked	39	0	68	13	120
Resolved multiple-peaked	10	0	52	15	77
Blended multiple-peaked	23	8	124	99	254

Figure 5.1 shows example lines-of-sight with single-peaked Faraday spectra. For each line-of-sight, we show the amplitude of the fractional polarisation as a function of λ^2 and the RM-Cleaned Faraday spectrum. The Faraday spectra are superimposed on a Gaussian of width equal to that of the RMTF (~ 180 rad m^{-2}). In almost all cases, the width of the Faraday spectra is larger than the width of the RMTF. The top row

shows examples with smooth decaying depolarising lines-of-sight, the second with sinc-like decay, third with complex oscillatory decay and last row with complex non-oscillatory decay. These plots demonstrate the importance of evaluating both the Faraday-space and λ^2-space to obtain a better picture of the polarisation behaviour, as noted in Section 3.4. In the case of the single-peaked spectra, we find that the Faraday space reveals very little structure, while the data in λ^2-space show depolarisation structure.

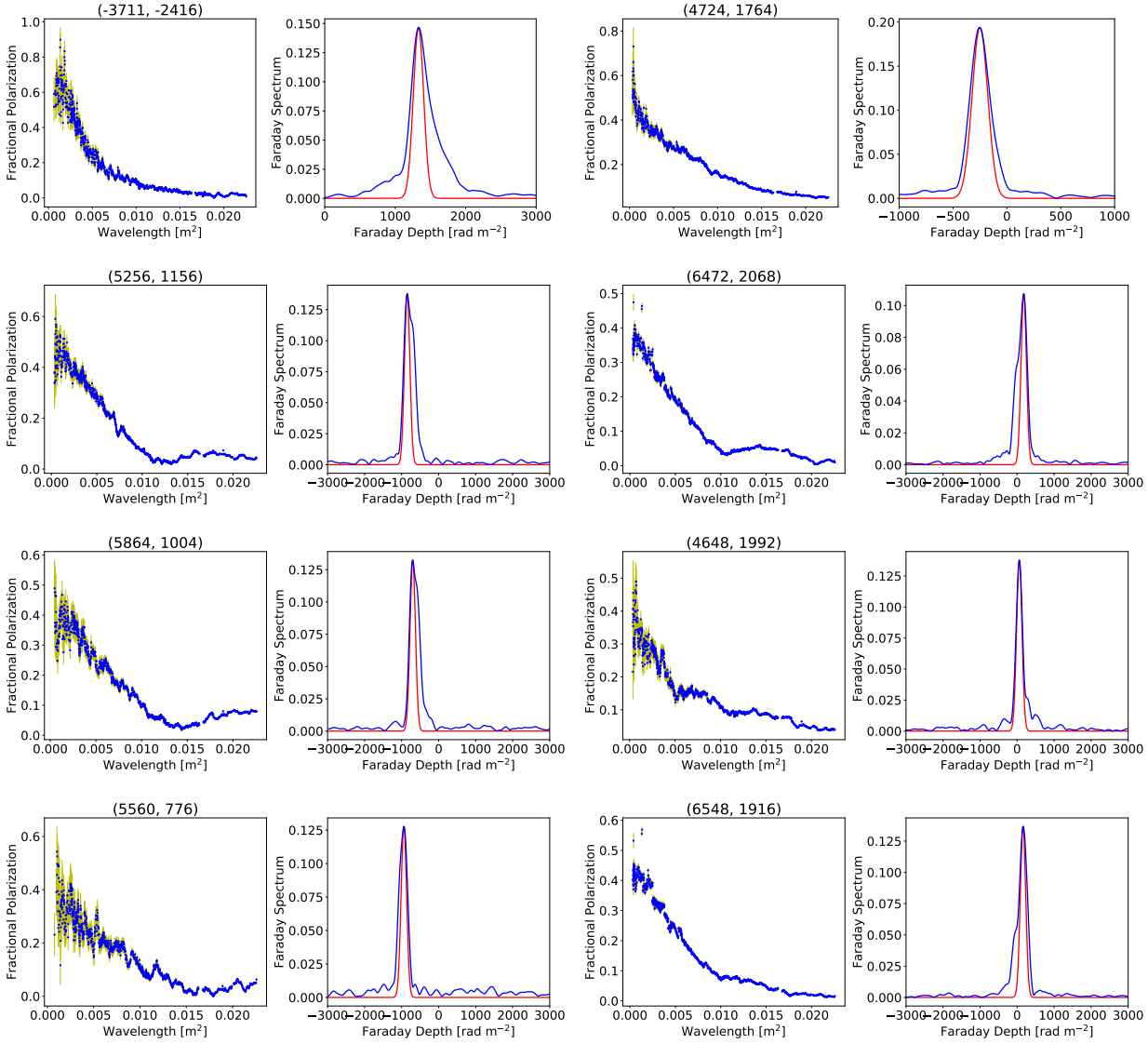

Figure 5.1: *Cygnus A example lines-of-sight with single-peaked Faraday spectra*. Left plot: Fractional polarisation as a function of λ^2. Right plot: RM-Cleaned Faraday spectrum amplitude (blue) superimposed by a Gaussian RMTF of width equal to that of the actual RMTF. Top row: Smooth decaying lines-of-sight. Second row: Sinc-like decay. Third row: Complex-oscillatory. Fourth row: Complex non-oscillatory.

Figure 5.2 shows another set of examples, however for lines-of-sight with single-peaked Faraday spectra with smaller peaks. There is no case where the smaller peaks are completely resolved – they are always situated next to the stronger component.

Figure 5.3 shows example lines-of-sight with blended double-peaked Faraday spectra. In this case, the

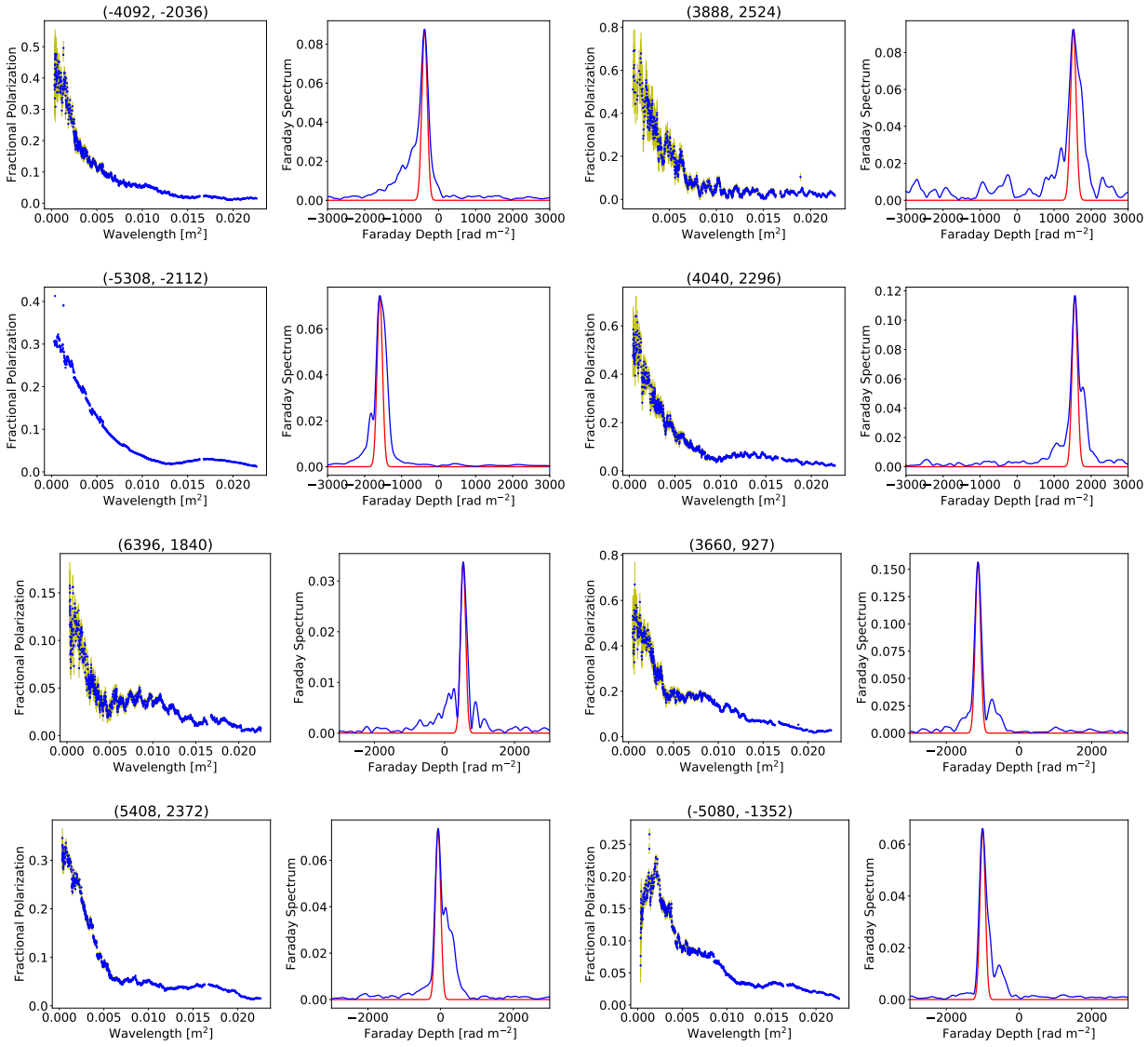

Figure 5.2: *Cygnus A example lines-of-sight with single-peaked spectra with smaller unresolved (or partially resolved) peaks*. Similar to Figure 5.1 (from top to bottom): smooth decaying, sinc-like, complex oscillatory and complex non-oscillatory depolarisation, respectively.

two peaks have relatively similar strengths. The pronounced nulls are immediately noticeable for the sinc-like depolarisation with blended double-peaked Faraday spectra. This behaviour is different from those associated with single-peaked spectra (see Figures 5.1 and 5.2). Moreover, sinc-like depolarisation patterns are largely associated with the blended double-peaked Faraday spectrum (roughly 50%).

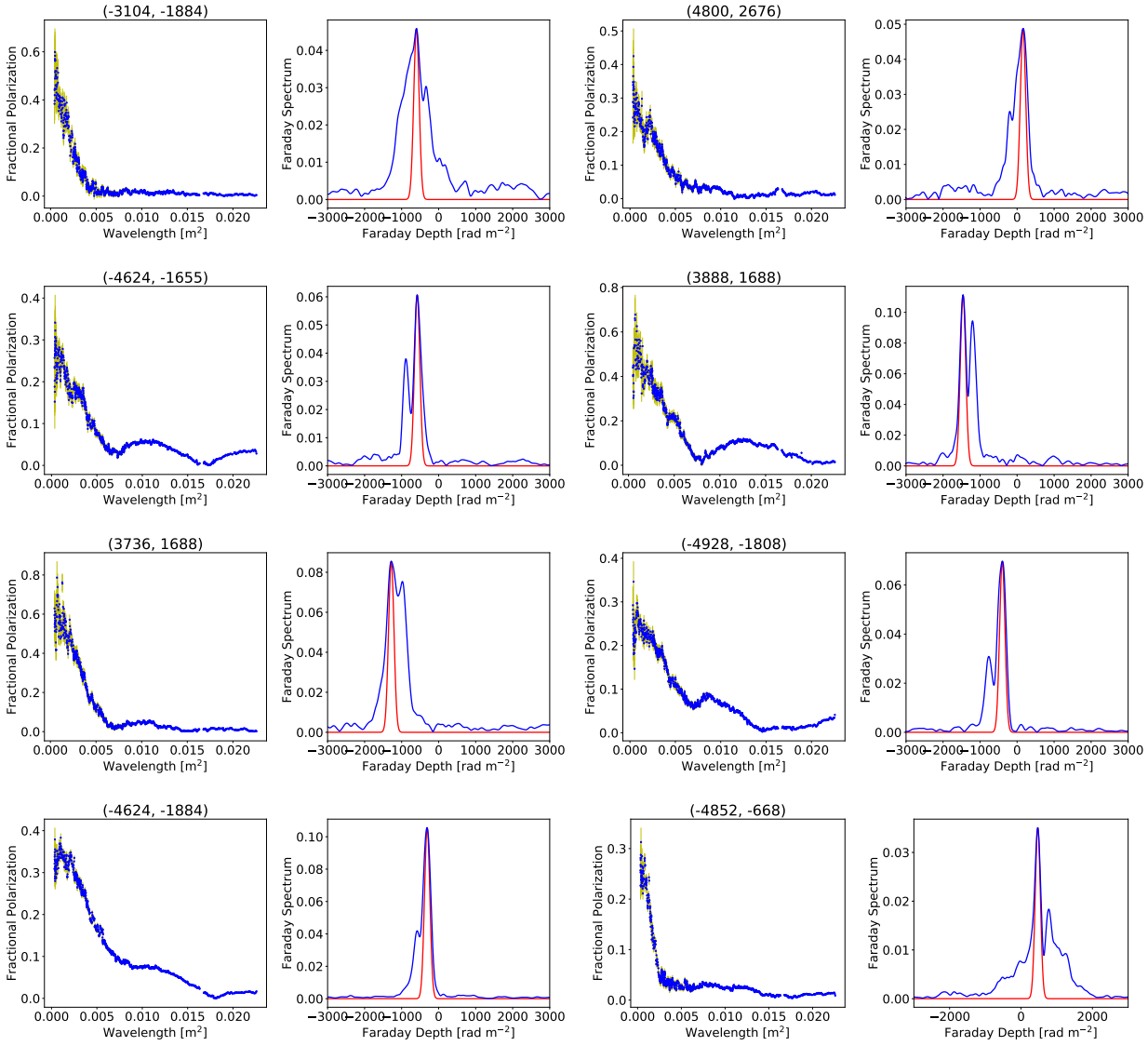

Figure 5.3: *Cygnus A example lines-of-sight with unresolved blended double-peaked Faraday spectra*. From top to bottom: smooth decaying, sinc-like, complex oscillatory, and complex non-oscillatory depolarisation, respectively.

Figure 5.4 shows six examples with resolved double-peaked spectra. None of the lines-of-sight with smooth-decaying depolarisation has a spectrum of this type. The width of each component is usually relatively wider than the RMTF – suggesting that each Faraday component is extended in Faraday space and not a simple delta function. Additionally, although the peaks are resolved, they are still connected at their base. This could suggest the presence of weak unresolved Faraday components that connect the two strong peaks, or a continuum distribution of Faraday depths with weaker strength. For example, a plot on the top

left is suggestive of the former; a case where a “connecting” weaker, partially resolved Faraday component is situated in between the two strong components, while the left plot in the middle row is somewhat suggestive of a continuum distribution. There are a few cases wherein two peaks appear – there is usually much weaker partially resolved Faraday peaks in between or at the extreme of the two strong peaks.

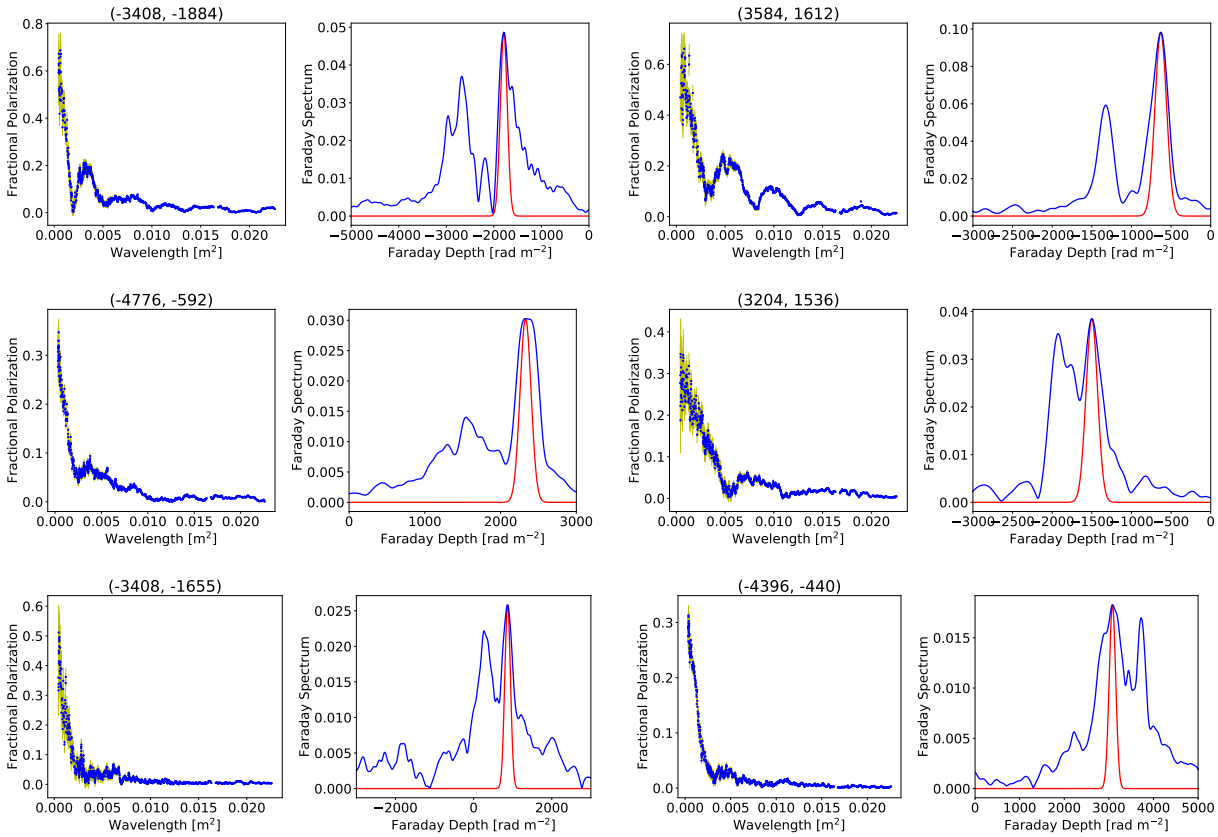

Figure 5.4: *Cygnus A example lines-of-sight with resolved double-peaked Faraday spectra.* From top to bottom: sinc-like, complex oscillatory and complex non-oscillatory depolarisation, respectively.

Figures 5.5 and 5.6 show another set of interesting lines-of-sight with complex multiple-peaked Faraday spectra. Figure 5.5 show examples where the multiple peaks are not resolved or are partially resolved. Figure 5.6, on the other hand, shows examples where the peaks are resolved. We find that none of the resolved multiple spectra have a smooth decaying depolarisation pattern.

Figure 5.7 shows the distribution of the different Faraday spectrum classes across the lobes. The single-peaked spectra occur predominantly across the western lobe and tend to occur at the extreme regions of the lobes – further from the AGN. The lines-of-sight with multiple peaked spectra are situated mostly at the tails of the western lobe, and everywhere across the eastern lobe.

Why are simple spectra predominantly within the western lobe and at the extreme regions of the lobes? First, these extreme regions have relatively small rotation measures (see Figure 4.14) and depolarisation (see Figure 4.10). Secondly, Snios et al. (2018) shows that the cocoon-shock is more prominent in this region (see their Figure 7 also shown in the right plot of Figure 1.2). Thirdly, they are far from cluster centre – were the gas is most dense and largely structural (for example, the ribs). Using MHD simulations for cluster formation

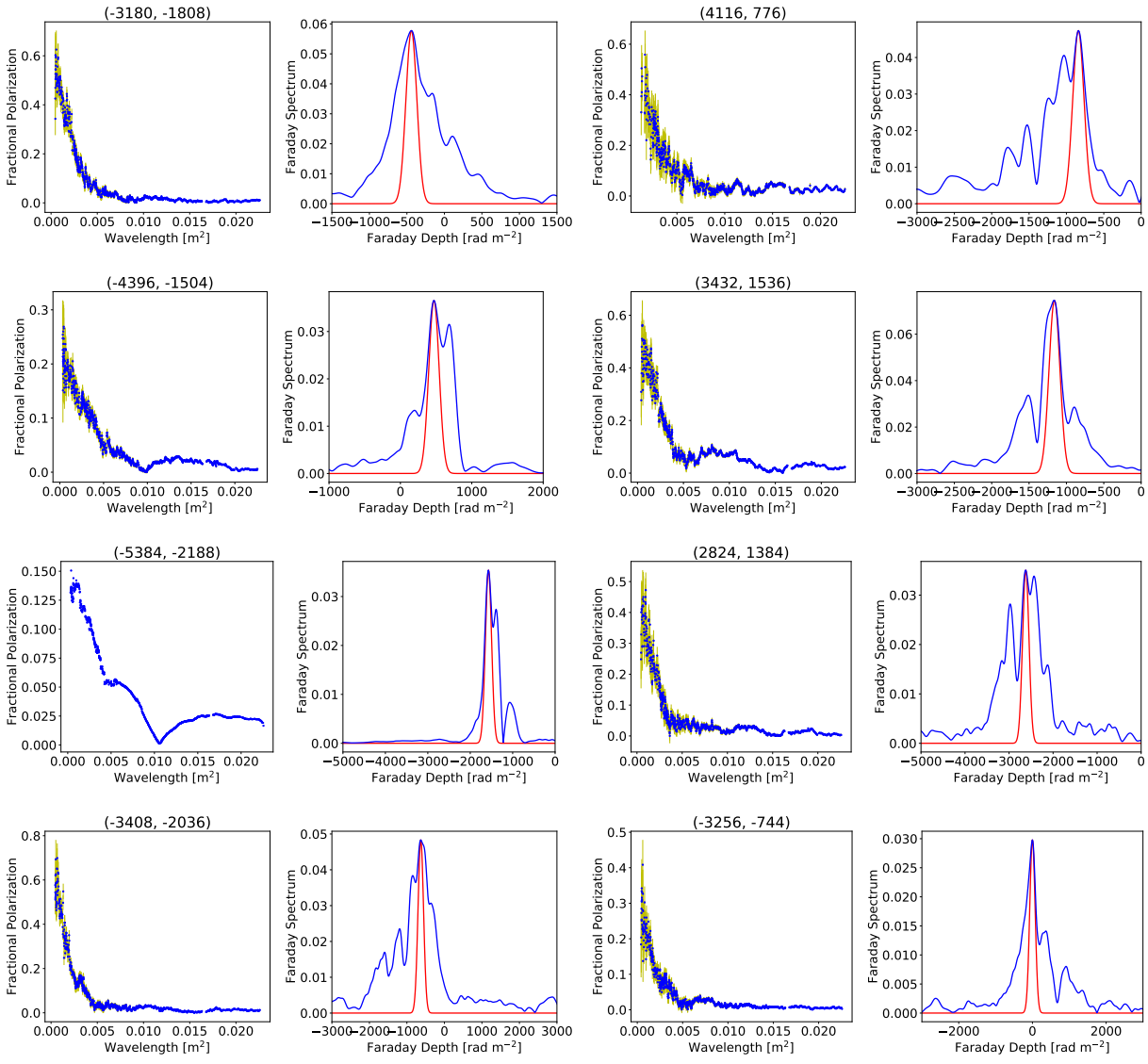

Figure 5.5: *Cygnus A example lines-of-sight with blended multiple-peaked Faraday spectra.* From top to bottom: Smooth decaying, sinc-like, complex oscillatory and complex non-oscillatory depolarisation, respectively.

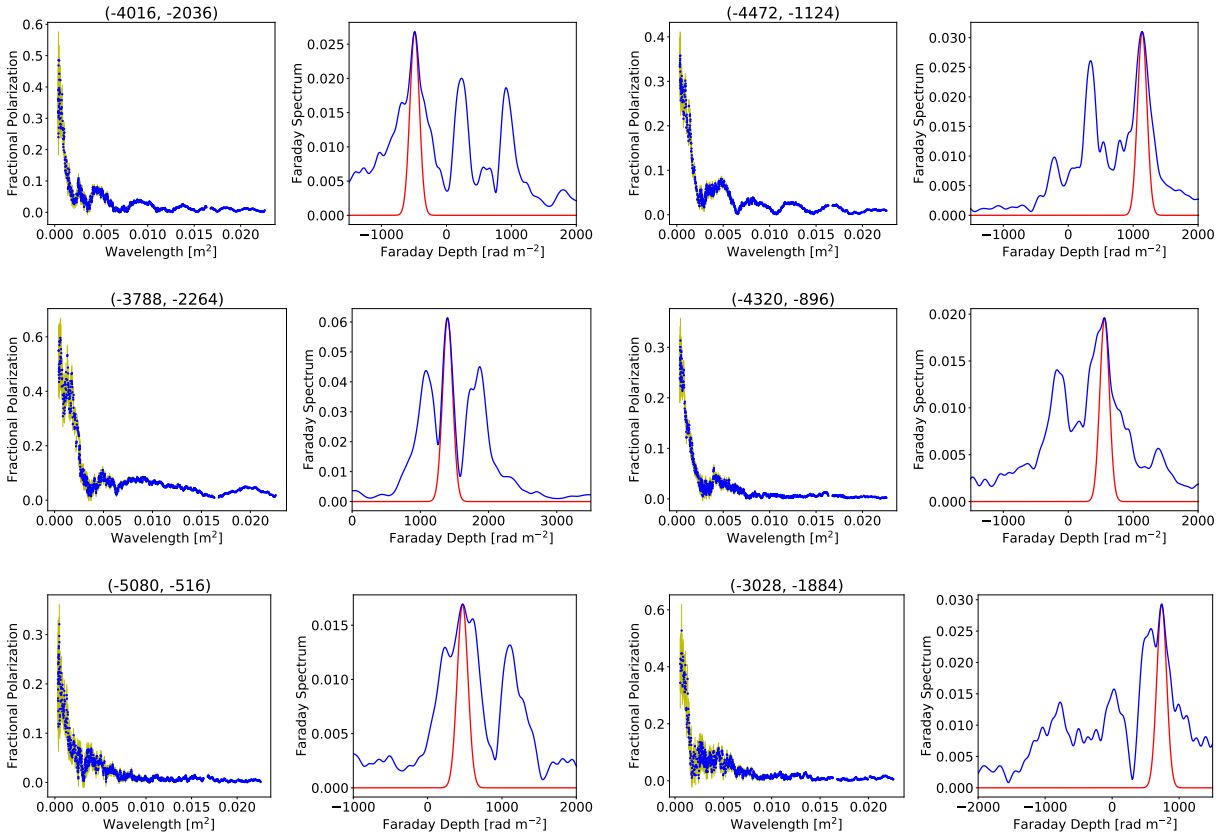

Figure 5.6: *Cygnus A example lines-of-sight with resolved multiple-peaked Faraday spectra.* From top to bottom: Sinc-like, complex oscillatory, and complex non-oscillatory depolarisation, respectively.

and evolution, Dolag et al. (1999) showed that the magnetic fields are more turbulent in the cluster centre (see their figure 3). So the relatively simpler polarisation structure (singe-peaked) at the extreme regions could be a result of less turbulence.

It is not clear why the Faraday spectra class' distribution and dominance across the two lobes significantly differ. The western lobe is associated with relatively simpler (single-peaked) spectra than the eastern lobe. The difference between the nature of these two lobes remains a mystery. Could it be that the eastern lobe is intrinsically different from the western lobe? Given the similarity with the tail of the western lobe, the eastern lobe is likely to be submerged into a relatively denser local environment or is farther from us. As such, the increased complexity in these regions can be attributed to the Laing-Garrington effect.

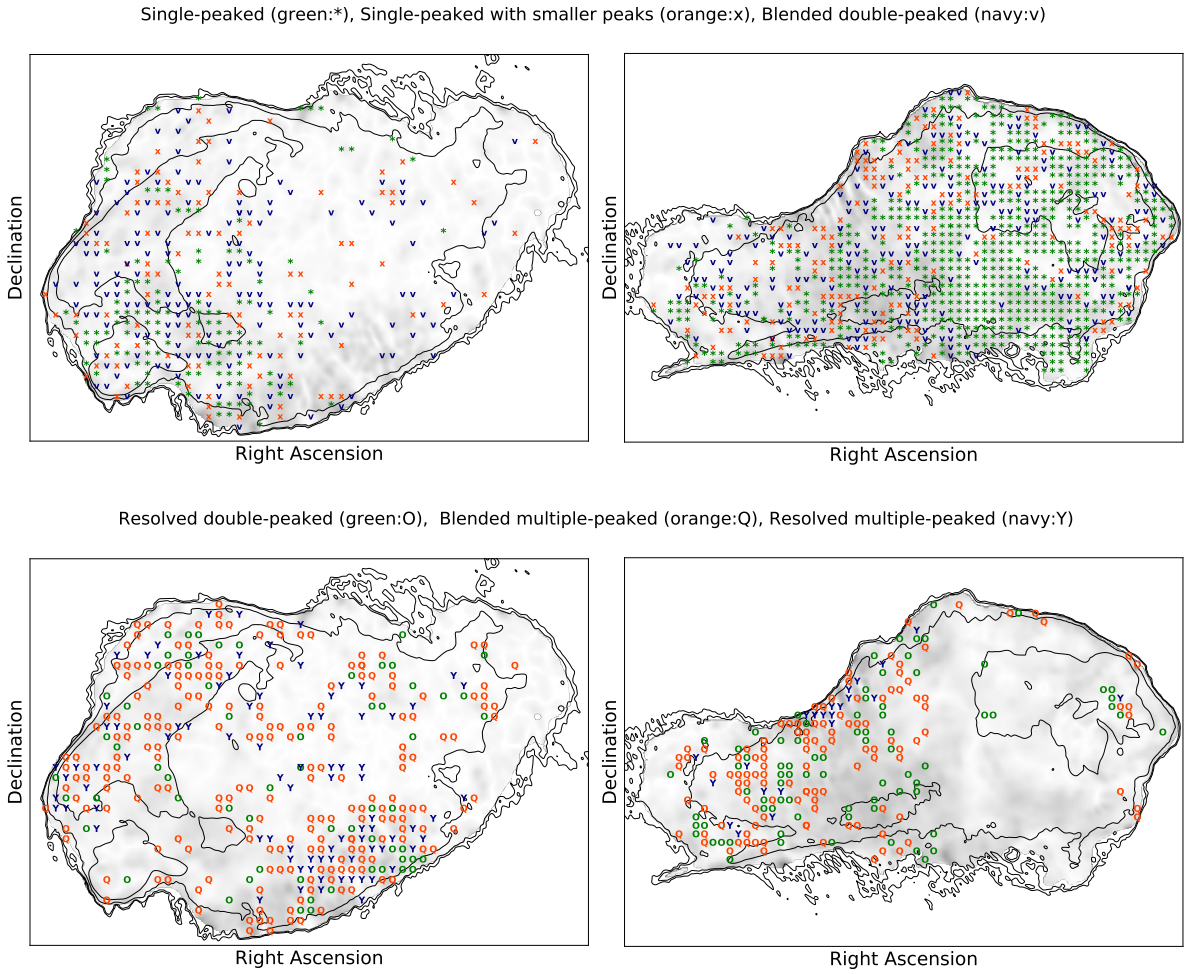

Figure 5.7: *Spatial distribution of the Faraday spectrum classes across Cygnus A.* Green *: Single-peaked spectra. Orange x: Single-peaked with smaller peaks. Navy v: Blended double-peaked. Green O: Resolved double-peaked. Orange Q: Blended multiple-peaked. Navy Y: Resolved multiple-peaked. The single-peaked Faraday spectra are largely found across the western lobe and are situated at the extreme regions (further from the AGN) of both lobes. The multiple-peaked Faraday spectra lines-of-sight, on the other hand, are situated at the tails of the western lobe. In general, the eastern lobe is associated with multiple-peaked spectra.

5.3 Faraday Spectra Properties

To characterise the Faraday spectra, we decided to fit the following single 1D Gaussian function to the amplitude of the spectrum for each line-of-sight:

$$f = f_0 e^{-\frac{1}{2}\left(\frac{\phi-\phi_{\text{mean}}}{\sigma_{\text{stdev}}}\right)^2}, \tag{5.1}$$

where ϕ_{mean} is the mean, σ_{stdev} is the width of the distribution and f_0 is the amplitude.

The goal is to characterise the width, amplitude and mean Faraday depth of each spectrum. This spectra fitting procedure is a straightforward task which we accomplish using a simple χ^2_r minimisation via LMFIT. Moreover, we are not interested in characterising the individuals peaks in the spectra – these will require sophisticated modelling.

Figure 5.8 shows examples of the Gaussian fitting to the different spectra. The derived amplitudes for spectra with large Faraday spread are underestimated. Therefore, from the fitting results, we only consider the mean, ϕ_{mean} and the width, σ_{stdev}. We derive the amplitudes by taking the maximum peak of the each spectrum. We evaluate the goodness-of-fit by eye. We find that the 1D Gaussian function provides a good approximation of the mean and width for most lines-of-sight. A few exceptions are with single-peaked spectra with smaller peaks, in which the Gaussian function tends to exclude the smaller peaks (see Figure 5.8 top right). A reason may be that the smaller peaks (weaker) are erroneously considered as part of the noise.

Figure 5.9 shows the maximum peak of the Faraday spectra as a function of fractional polarisation at 8 GHz for the 2000 lines-of-sight. The different Faraday classes are shown in different colours. Lines-of-sight with low fractional polarisation in λ^2 have a low peak in Faraday space. The different Faraday classes occur uniformly across λ^2-space – the classes are not clustered at any fractional polarisation values. However, in Faraday space, the single-peaked Faraday spectra tend to have relatively higher peak values, followed by single-peaked spectra with smaller peaks and blended double-peaked spectra. The separation between the resolved double-peaked spectra, blended and resolved multiple-peaked spectra is obscured.

Figure 5.10 shows the derived Gaussian σ_{stdev} as a function of ϕ_{mean}. The different Faraday classes are shown in different colours. Due to resolution limitation in Faraday space, the smallest Gaussian σ_{stdev} we can derive is $\sim$ 77 rad m^{-2} (FWHM$/2.35$, where FWHM $\sim$ 180 rad m^{-2}). The Gaussian σ_{stdev} goes as high as 1600 rad m^{-2}, that is roughly a factor of 20 larger than our RMTF resolution. The single-peaked spectra have smaller widths and lower mean Faraday depths. This may be because most the single-peaked spectra are situated at the extremes of the western lobe, where the lower RM are found and there is less turbulence due to the emission being closer to the edge of the cluster gas. Multiple-peaked Faraday spectra (including resolved double-peaked spectra) are associated with large Faraday spectra width of up to 1600 rad m^{-2}. There is a weak correlation between the mean Faraday depth with the Faraday spectra width. Large mean depths are associated with large σ_{stdev}. This implies that for the most part, the width is independent of the mean Faraday depths. A similar pattern is seen in a plot of RM as a function of Faraday dispersions (see Figure 4.16).

Figure 5.11 compares the RM and Faraday dispersions derived from fitting the random-depolarising

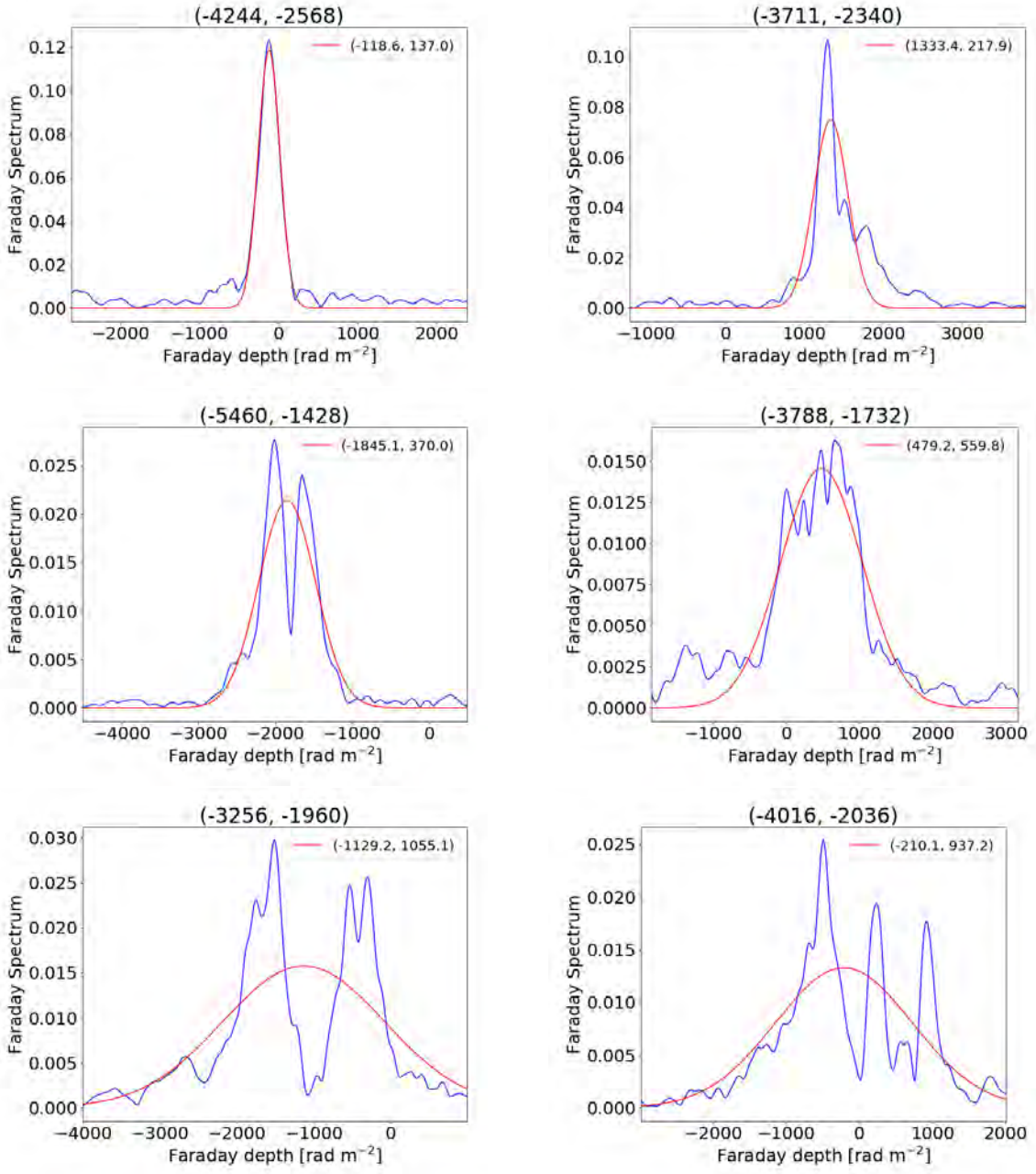

Figure 5.8: *Fitting examples of 1D Gaussian function to Faraday spectrum amplitudes*. Title: Line-of-sight position in milli-arcsecond. Legend in parenthesis: The mean, ϕ_{mean} and spectra width, σ_{stdev} of the fitted Gaussian function. Top row: Single peaked spectra class (left) and single peaked spectra with smaller peaks (right). Second row: Blended double-peaked spectrum (left), and blended multiple-peaked spectrum (right). Bottom row: Resolved double-peaked (left), and resolved multiple-peaked spectrum (right).

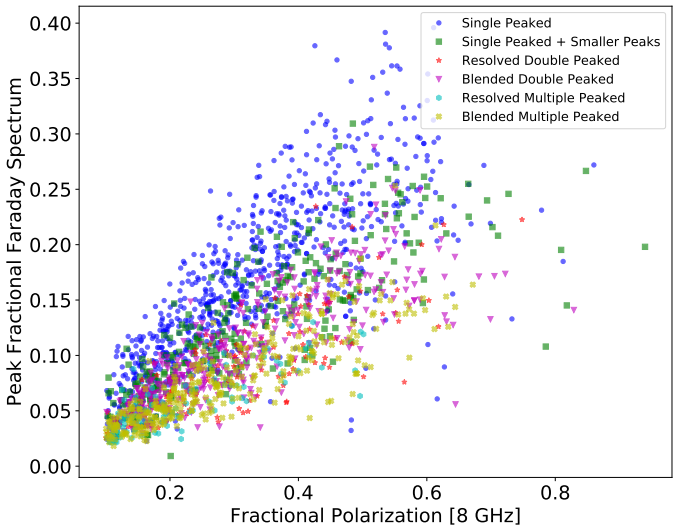

Figure 5.9: *Fraction polarisation at* 8 *GHz as a function of the maximum peak of the Faraday spectrum amplitude*. The different Faraday spectrum classes are shown in different colours. Lines-of-sight with single-peaked and single-peaked with smaller peaks tend to have higher Faraday amplitude, while many multiple-peaked spectra have low peak values. The different spectra classes cannot be discerned based on fractional polarisation in λ^2-space.

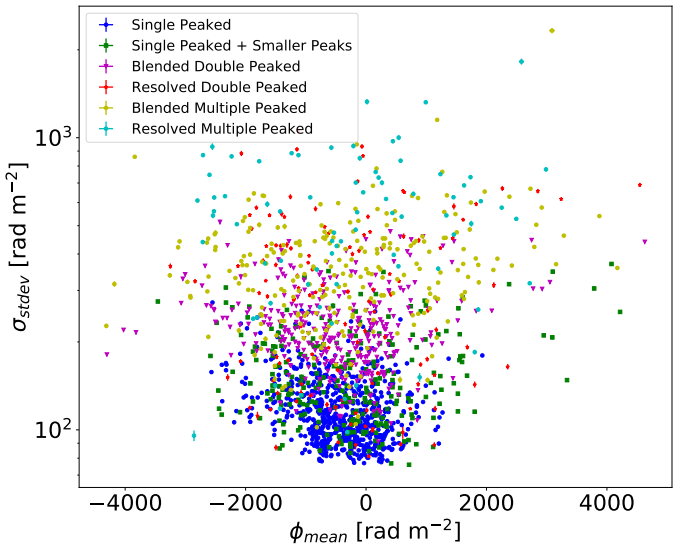

Figure 5.10: *The derived mean and width of 1D Gaussian function fitted to Cygnus A Faraday spectra*. The different Faraday classes are shown in different colours. The lines-of-sight with multiple-peaked spectra have larger width $\sigma_{\rm stdev}$ $\lesssim$ 1600 rad m^{-2}. There is a weak correlation between $\sigma_{\rm stdev}$ and $\phi_{\rm mean}$, particularly for large $\phi_{\rm mean}$ which tends to be associated with large $\sigma_{\rm stdev}$.

model to $6 - 18$ GHz data at $0.30''$ (see Section 4.5) to $\phi_{\rm mean}$ and $\sigma_{\rm stdev}$ at $0.75''$. RM values at $0.30''$ are consistent with $\phi_{\rm mean}$. This comparison is important as it demonstrates that the 1D Gaussian fits are consistent with the simpler fits performed in Section 4.5. A reason for the similarity is that high-frequency Faraday spectra are a smoothed version (by a large RMTF) of the low-frequency spectra.

The σ at $0.3''$ and $\sigma_{\rm stdev}$, although plotted together, represent different things. The σ describes the decay rate of fractional polarisation with increasing λ^2, while $\sigma_{\rm stdev}$ represents the maximum separation of the Faraday components in the spectrum. The σ seems independent of the Faraday spectra class. The single-peaked spectra depolarise at a similar rate as double-peaked and multiple-peaked spectra. However, there seems to be a tendency for the multi-component spectra to have relatively large Faraday dispersions. The $\sigma_{\rm stdev}$, on the other hand, is larger for resolved double-peaked and multiple-peaked spectra.

In a simple case of a single random depolarising screen, σ and $\sigma_{\rm stdev}$ should be relatively similar – assuming that we have a sufficient resolution in Faraday space. These results imply that all the spectra lines-of-sight have a common σ ranging between $50-400$ rad m^{-2}. It could be that the individual components in the double- and multiple-peaked spectra are all affected by the same depolarising screen. Another possibility is that the components have intrinsic width in Faraday space; that is, they are depolarising in themselves in a similar manner.

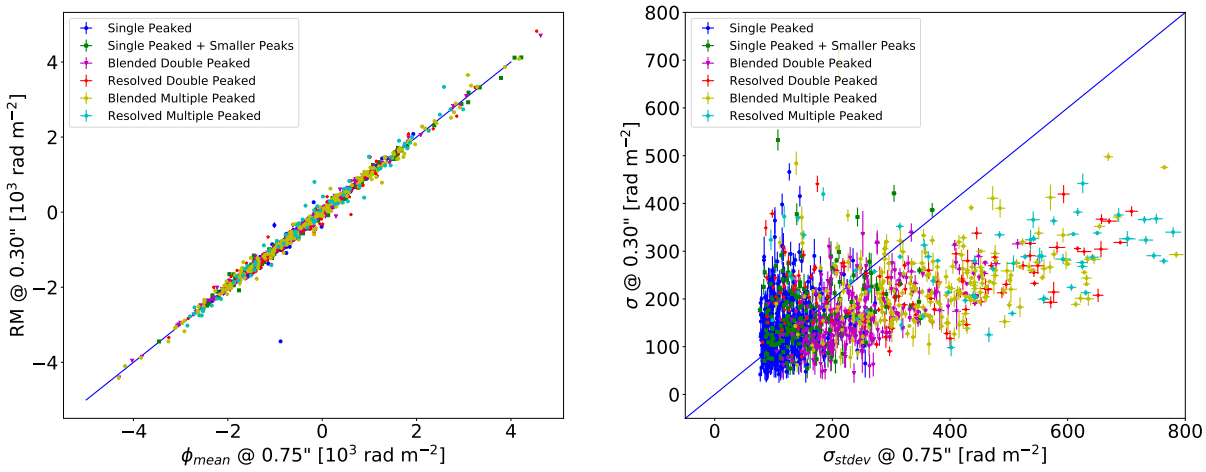

Figure 5.11: *A comparison of the derived parameters from high-frequency, high-resolution modelling with solutions from 1D Gaussian fitting.* Left plot: Compares the high-frequency RM (see Section 4.5) with $\phi_{\rm mean}$. Right plot: Compares the Faraday dispersions at $0.30''$ (see Figure 4.14) with $\sigma_{\rm stdev}$. The Faraday dispersions shown have fractional errors of less than 0.5. The RM at $0.30''$ are consistent with $\phi_{\rm mean}$. Faraday dispersions are independent of the Faraday class, with a weak tendency for large σ to be associated with large $\sigma_{\rm stdev}$.

5.4 Modelling of Wideband Data

This section uses the QU-fitting technique described in Section 3.4 to model our wideband (2 - 18 GHz) data of Cygnus A. We fit mainly to the lines-of-sight with single-peaked Faraday spectra, single-peaked spec-

tra with smaller peaks, blended double-peaked spectra, and resolved double-peaked spectra. The blended multiple-peaked and resolved multiple-peaked spectra will require much more advanced models that are currently not available or models with a combination of multiple components that are computationally expensive and difficult to interpret. The models we fit are defined in previous chapters, however we will repeat them in this chapter; we will also make mention of their location within the dissertation.

The data revealed that all the lines-of-sight across Cygnus A depolarise and have non-zero RM. Therefore, each model must consist of a RM and the depolarisation term. We fit the following models/hypothesis to the data: (**note that we shorten the names of each model: to represent a foreground screen we use a symbol "F", internal mixing a symbol "I", random magnetic fields with "R", unresolved uniform RM-difference "U" and a depolarisation screen with "D". Preceding these symbols is a number indicating the number of components/screens – this number is only written if the number of screens is greater than** 1).

1) The first model is the random foreground depolarising Faraday rotating screen, hereafter referred to as RFD, first defined in Equation 3.29:

$$p(\lambda^2) = p_0 e^{2i\chi_0 + 2i\phi\lambda^2} e^{-2\sigma^2\lambda^4}, \tag{5.2}$$

where σ describes the Faraday dispersion due to random magnetic fields, ϕ is the Faraday depth of the screen and p_0 and χ_0 are the intrinsic fractional polarisation and polarisation angle of the background radio galaxy (Cygnus A). This model assumes that the depolarisation around Cygnus A results from a turbulent magnetic field in the foreground cluster gas or cocoon-shock (the compressed cluster gas at the contact layer between the lobes and the cluster).

2) The second model is a single uniform foreground depolarising screen, first defined in Equation 3.26 (hereinafter UFD):

$$p(\lambda^2) = p_0 e^{2i\chi_0 + 2i\phi\lambda^2} \frac{\sin(\Delta\phi\lambda^2)}{\Delta\phi\lambda^2}, \tag{5.3}$$

where $\Delta\phi$ is the uniform RM-difference across the beam. This model assumes that the depolarisation is due to unresolved uniform RM-differences across the beam. It can also represent uniform mixing within the lobes or sheath with $\phi = \phi_{\rm ICM} + \frac{1}{2}\,\phi_{\rm LOBE}$ and $\Delta\phi = \phi_{\rm LOBE}$.

3) The third model is a single random, uniform foreground depolarising screen (hereinafter RUFD):

$$p(\lambda^2) = p_0 e^{2i\chi_0 + 2i\phi\lambda^2} e^{-2\sigma^2\lambda^4} \frac{\sin(\Delta\phi\lambda^2)}{\Delta\phi\lambda^2}. \tag{5.4}$$

This model is similar to UFD except for the fact that we also incorporate random fluctuations. The physical picture supposes that the random and uniform magnetic fields are superimposed.

4) The fourth model is a random, uniform internal depolarising gas defined in Equation 3.19 (hereinafter RUID):

$$p(\lambda^2) = p_0 e^{2i\chi_0} \left(\frac{1 - e^{-\eta}}{\eta} \right), \tag{5.5}$$

where $\eta = 2\sigma_0^2\lambda^4 - 2i\phi_0\lambda^2$. This model assumes that the observed RM and depolarisation across Cygnus A come from an intermixed gas along the line-of-sight. This model is generally ruled out for the case of Cygnus A for two main reasons. The first reason is that the observed RM do not correlate with the observed depolarisation (see Figure 4.16). Secondly, the large rotation $> 600^\circ$ will lead to a large depolarisation not seen in the data (when using 15 GHz and 5 GHz maps). However, the hypothesis of ruling out this possibility has never been tested using analytical models over a wider bandwidth ($2-18$ GHz) and at frequencies below < 5 GHz.

5) The fifth model is a random, uniform internal depolarising gas behind a single Faraday rotating screen (hereinafter RUID+F):

$$p(\lambda^2) = p_0 e^{2i\chi_0}\left(\frac{1-e^{-\eta}}{\eta}\right)e^{2iRM\lambda^2}. \tag{5.6}$$

This model is similar to RUID except that in addition to a mixed gas, we also have a purely foreground Faraday rotating screen.

6) The sixth model is a two randomly depolarising Faraday foreground screens (or "patches" in the case of unresolved fluctuations) (hereafter 2RFD):

$$p(\lambda^2) = p_1 e^{2i\chi_1+2i\phi_1\lambda^2}e^{-2\sigma_1^2\lambda^4} + p_2 e^{2i\chi_2+2i\phi_2\lambda^2}e^{-2\sigma_2^2\lambda^4}, \tag{5.7}$$

where $p_1 = P_1/I_{\text{tot}}$ and $p_2 = P_2/I_{\text{tot}}$ are the fractional polarisation of the two patches/screens, respectively, P_1 and P_2 are the polarisation intensity for patch "1" and "2" respectively and I_{tot} is the total intensity $I_1 + I_2$.

This model can represent a line-of-sight effect where there are two emission regions along the line-of-sight passing through two intervening randomly depolarising screens. It could also represent beam-related effects, whereby the two depolarising patches and two emission components occur within the same beam resolution. We will later discuss which of the two is likely to occur across Cygnus A.

7) The seventh model is a two random, uniform foreground depolarising screens (hereafter 2RUFD):

$$p(\lambda^2) = p_1 e^{2i\chi_1+2i\phi_1\lambda^2}e^{-2\sigma_1^2\lambda^4}\frac{\sin(\Delta\phi_1\lambda^2)}{\Delta\phi_1\lambda^2} + p_2 e^{2i\chi_2+2i\phi_2\lambda^2}e^{-2\sigma_2^2\lambda^4}\frac{\sin(\Delta\phi_2\lambda^2)}{\Delta\phi_2\lambda^2}. \tag{5.8}$$

8) The eighth model is a three random foreground depolarising screens (hereafter 3RFD):

$$p(\lambda^2) = p_1 e^{2i\chi_1+2i\phi_1\lambda^2}e^{-2\sigma_1^2\lambda^4} + p_2 e^{2i\chi_2+2i\phi_2\lambda^2}e^{-2\sigma_2^2\lambda^4} + p_3 e^{2i\chi_3+2i\phi_3\lambda^2}e^{-2\sigma_3^2\lambda^4}, \tag{5.9}$$

where p_1 is P_1/I_{tot} is the intrinsic fractional polarisation of patch "1", and $p_2 = P_2/I_{\text{tot}}$ and $p_3 = P_3/I_{\text{tot}}$, and $I_{\text{tot}} = I_1 + I_2 + I_3$.

The fractional polarisation of each component is its respective polarised intensity normalised by the sum of the total intensities of the components within a patch.

Table 5.2 summarises these models.

Table 5.2: *Models used for QU-fitting to Cygnus A lines-of-sight*

Acronym	Full name	Reference Equation no.
RFD	Single random foreground depolarising screen	Equations 3.29 and 5.2
UFD	Single RM-difference foreground depolarising screen	Equation 5.7
RUFD	Single random + uniform depolarising screen	Equations 3.26 and 5.3
RUID	Single random + uniform internal mixing depolarising gas	Equation 5.4
RUID+F	RUID behind a non-depolarising Faraday rotating screen	Equations 3.19 and 5.5
2RFD	Two random foreground depolarising screens	Equation 5.6
2RUFD	Two random foreground depolarising screens	Equation 5.8
3RFD	Three random + uniform foreground depolarising screens	Equation 5.9

5.5 Fitting and Analysis Procedure

We use the $\ln$ BF to select a best fitting model between two models. As explained in Section 3.4, the $\ln$ BF is reliable for choosing a best fitting model as it takes into account the complexity (increasing number of free parameters) of the models. This quantity prevents erroneous selection of a relatively complex model due to overfitting. The $\ln$ BF is the difference of the models' Log-evidences: $\ln \text{BF} = \ln \mathcal{Z}_1 - \ln \mathcal{Z}_2$, where $\mathcal{Z}_1$ and $\mathcal{Z}_2$ is the evidence of model 1 and model 2, respectively. The definition and description of the evidence is presented in Section 3.4.1.3. A model with the largest evidence, $\ln \mathcal{Z}$, is favoured. If $\mathcal{Z}_1 > \mathcal{Z}_2$, then $\ln$ BF is > 0 and model 1 is favoured over 2 and if $\mathcal{Z}_2 > \mathcal{Z}_1$, then $\ln \text{BF} < 0$, model 2 is favoured over model 1. The magnitude of the $\ln$ BF, on the other hand, provides the degree by which one model is preferred over the other. For example, if the magnitude of $\ln$ BF is ~ 10 between model 1 and 2, and 100 for model 1 and 3, then model 1 is strongly favoured over model 3, than model 2. Table 3.1 provides the selection criteria. A value of $\ln$ BF greater than 3 indicates model 1 is strongly favoured over model 2. The $\ln$ BF is a relative quantity – it only tells us a model that is most preferred between two models. It is does not tell us whether a model is true or false, nor does it tell us whether a model fits the data well or not. As a result, a model selected as "best" may not necessarily be a true representation of the data, but rather, the most preferred of the two.

We use the reduced chi-square, χ^2_r, to determine whether a model describes the data. A value of $\chi^2_r \approx 1$ indicates a good fit, $\chi^2_r < 1$ an overfit and $\chi^2_r \gg 1$ a bad fit. We do not use χ^2_r to select a best-fitting model since this quantity takes no account of a model's complexity. Thus, a more complex model is most likely to have small χ^2_r due to overfitting. For this reason, we use the χ^2_r, mainly to determine whether a best fitting model describes the data. There are factors that can affect the value of χ^2_r: i) nonlinear problems, ii) the noise (Andrae et al. 2010), iii) and high signal-to-noise data tends to have $\chi^2_r \gg 1$ than low signal-to-noise data. This latter bias was also noted by Schnitzeler et al. (2019). We do not have an immediate solution. We consider χ^2_r value of 5 as a median threshold – with lines-of-sight with $\chi^2_r \ll 5$ most reliable and than those with $\chi^2_r \approx 5$. However, bearing in mind that due to the third limiting factor, a line-of-sight may have $\chi^2_r < 5$ because it is relatively noisy and another may have $\chi^2_r > 5$ because of high SNR. We also evaluate the fits

by eye to check if they are good or bad.

We compare a pair of models at a time, and eliminate models sequentially – the $\ln$ BF can only compare two models at a time. For example, we compare RFD with UFD, RUID with RUID+F and so forth. We assume a uniform distribution for all our prior probabilities. The intrinsic fractional polarisation is set to range between 0 and 1, polarisation angle between $\pm\pi/2$ radians, RM/Faraday depth between ± 7000 rad m^{-2}, Faraday dispersion and uniform gradient between $0 - 1500$ rad m^{-2}.

In this study, we focus on a model that is preferred for the majority of the lines-of-sight and a model that best describes most of the lines-of-sight, rather than checking a success of each model per line-of-sight. A detailed modelling of the individual lines-of-sight is beyond the scope of this dissertation.

5.6 Single-Peaked Faraday Spectra

We start by modelling the lines-of-sight with single-peaked Faraday spectra. For Cygnus A, these lines-of-sight represent a significant fraction of the lines-of-sight – 40%. We fit all the eight models described in Section 5.4 to the single-peaked lines-of-sight, namely RFD, RUFD, UFD, RUID, RUID+F, 2RFD, 2RUFD and 3RFD.

The single-peaked spectra may appear single-peaked because they consist of a single Faraday component or it could be that there are multiple unresolved Faraday components (separated by < 180 rad m^{-2}). We hope to determine whether the single-peaked spectra data are best described by single or multiple components models.

5.6.1 Best-Fitting Model

Figure 5.12 shows the $\ln$ BF for model RFD, UFD and RUFD. The left plot compares RFD and UFD, middle plot compares RFD and RUFD and right plot compares RUFD and UFD. The blue points show positive $\ln$ BF in favour of RFD (left and middle) and RUFD (right). The red points correspond to the negative $\ln$ BF in favour of UFD (left and right) and RFD (middle). RFD is favoured against UFD for 83% of the lines-of-sight and against RUFD for 66% of the lines-of-sight. However, data points against RUFD (middle plot) consist of small values of $\ln$ BF, with values concentrated between 4 ± 1. These small values suggest a weak evidence against RUFD. RUFD, on the other hand, is favoured over UFD for 94% of the lines-of-sight. These results suggest that random fluctuations are important for the majority of the lines-of-sight, while the unresolved uniform RM-difference are important for only $1/3$ of the lines-of-sight. RUFD is the most preferred model of the three.

We now compare our most preferred model from the above step to RUID and RUID+F models. Figure 5.13 shows the $\ln$ BF of model RUFD, RUID, and RUID+F. The blue points show lines-of-sight in favour of RUFD (left and middle) and RUID+F (right). The red points show those in favour of RUID (left and right) and RUFD (middle). RUID is highly disfavoured for 97% of the lines-of-sight. RUID+F, on the other hand, is favoured against RUFD for $2/3$ of the lines-of-sight. The large degree of disfavour for RUID implies that the data cannot be explained by a completely mixed gas. Rather, the data require that there

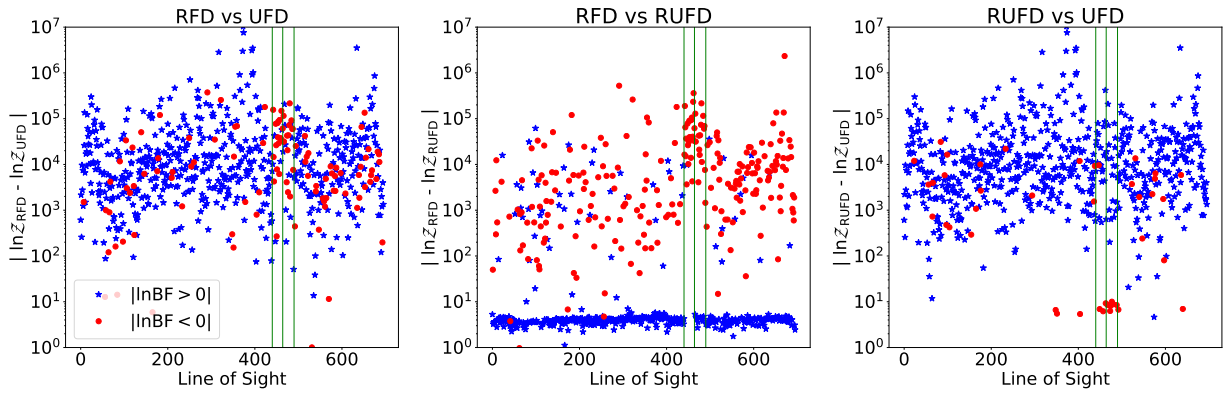

Figure 5.12: $\ln$ *BF solutions of model RFD, RUFD and UFD fitted to single-peaked spectra lines-of-sight.* Blue points: In favour of RFD (left and middle) and RUFD (right). Red points: In favour of UFD (left and right) and RUFD (middle). Vertical lines (from left to right) separate the smooth, sinc-like, complex oscillatory and complex non-oscillatory lines-of-sight. RFD is favoured over UFD for 83% of the fitted lines-of-sight and over RUFD for 66%. The data points against RUFD (middle) have small values clustered between 4 ± 1 – indicating a weak evidence against this model. RUFD is favoured over UFD for 94% of the fitted lines-of-sight. These results suggest that random fluctuations are the most important to the data, while the uniform RM-differences are important for only $1/3$ of single-peaked lines-of-sight. RUFD is the most preferred model of the three.

exist a foreground Faraday rotating screen to account for the large RM. This result is consistent with the conclusion reached by Dreher et al. (1987) – who argued that the observed depolarisation is too small to result from the observed Faraday rotations ($> 600°$). Our wideband data show that even upon incorporating the new information (the low-frequency and the high-spectral resolution), a mixed gas alone cannot explain the situation in/around Cygnus A. Of the three models, RUID+F leads. Noting that RUFD and RUID+F are similar, the only difference is that the latter is able to account for any asymmetry in the emission distribution, while the former cannot. Thus, a favour towards RUID+F suggests some form of asymmetries in the emission gas region – consistent with what can be expected in real life.

Figure 5.14 shows $\ln$ BF of model RUID+F and 2RFD. In this situation, we want to determine whether the single component models are sufficient to explain the data or whether the data require multiple components. 2RFD is favoured over RUID+F for 89% of the lines-of-sight. Thus, the single-peaked Faraday spectra data are best described by a two-component model. This implies that there may be two emission regions along the line-of-sight or unresolved patches (separated by < 180 rad m^{-2}) across the beam.

Figure 5.15 compares the multi-component models, namely 2RFD, 2RUFD and 3RFD. The blue points show lines-of-sight in favour of 2RUFD (left) and 3RFD (middle and right). The red data points show the lines-of-sight in favour of 2RFD (left and middle) and 2RUFD (right). 2RFD is highly disfavoured when compared to the other two models, with only 2% of the lines-of-sight in favour of 2RFD over 3RFD and 15% in favour of 2RFD against 2RUFD. We find that roughly 69% lines-of-sight favour 3RFD over 2RUFD.

5.6.2 Goodness-of-Fit of Competing Models

Figure 5.16 shows the χ^2_r for model 2RUFD (left), 3RFD (middle) and the right plot shows the difference in the χ^2_r of the two models. Both models describe most of the lines-of-sight relatively well, with 78%

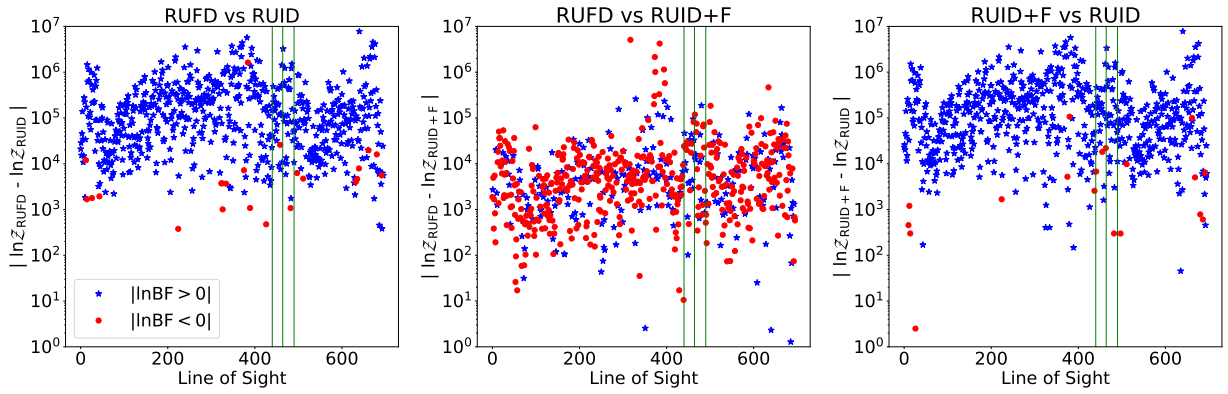

Figure 5.13: ln *BF solutions of model RUFD, RUID and RUID+F fitted to single-peaked spectra lines-of-sight.* Vertical lines are the same as in Figure 5.12. Blue points: In favour of RUFD (left and middle) and RUID+F (right). Red points: In favour of RUID (left and right) and RUFD (middle). RUID is highly disfavoured for 97% of the fitted lines-of-sight, RUID+F is favoured over RUFD for 66% fitted lines-of-sight. A completely internal mixed region (described by RUID) cannot explain the data, instead, the data require the presence of a Faraday rotating foreground screen to explain the large RM – consistent with the conclusion reached by Dreher et al. (1987).

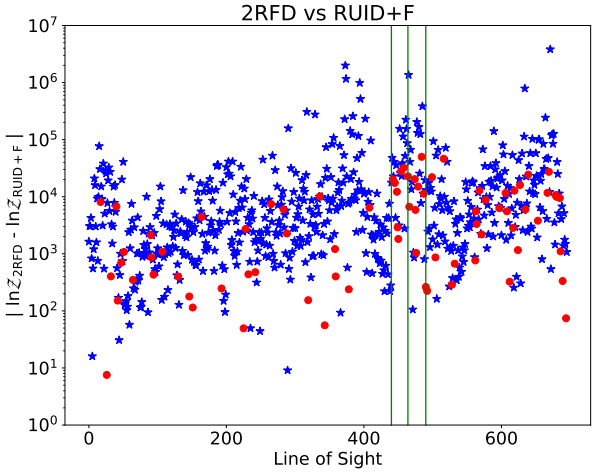

Figure 5.14: ln *BF solutions of model RUID+F and 2RFD fitted to single-peaked spectra lines-of-sight.* Vertical lines are the same as in Figures 5.12 and 5.13. Blue points: In favour of 2RFD. Red points: In favour of RUID+F. 2RFD is favoured over RUID+F for 89% of the fitted lines-of-sight. The data are best described by a two-component model.

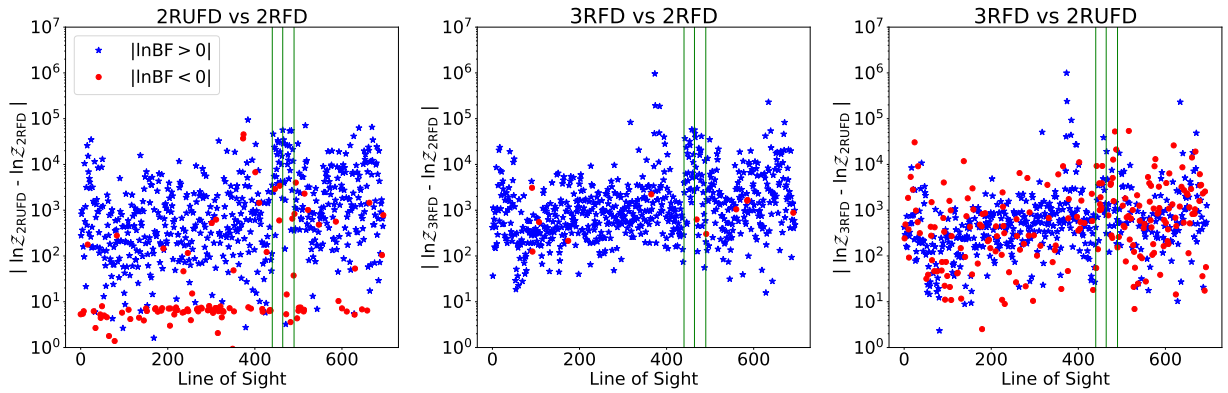

Figure 5.15: $\ln$ *BF solutions of model 2RFD, 2RUFD and 3RFD fitted to single-peaked spectra lines-of-sight.* Vertical lines are the same as in Figure 5.12. Blue points: In favour of 2RUFD (left) and 3RFD (middle and right). Red points: In favour of 2RFD (left and middle) and 2RUFD (right). 2RUFD is favoured over 2RFD for 85% of the fitted lines-of-sight, with those in favour of model 2RFD clustered around small values of $\ln \text{BF} \sim 7 \pm 2$. 3RFD is favoured over 2RFD for 98% of the fitted lines-of-sight (middle) and over 2RUFD for 69% (right). 3RFD model is the most favoured of all the three models, followed by 2RUFD. These results suggest that 69% of the single-peaked spectra are best described by a three-component model, while 31% are best described by a two-component model with random fluctuations superimposed on unresolved uniform RM-difference.

having $\chi^2_r \leq 5$. However, the difference in the χ^2_r indicates that 3RFD describes the majority $\sim 69\%$ of the lines-of-sight much better than 2RUFD. These results are consistent with those of the $\ln$ BF. We cannot immediately rule out 2RUFD since our results show that this model does well for at least 31% of the lines-of-sight. We conclude that both models are relevant to the data and require consideration. This result suggests that some line-of-sight are best represented by a three randomly-depolarising model, while others require two components with random fluctuations superimposed on unresolved uniform RM-difference.

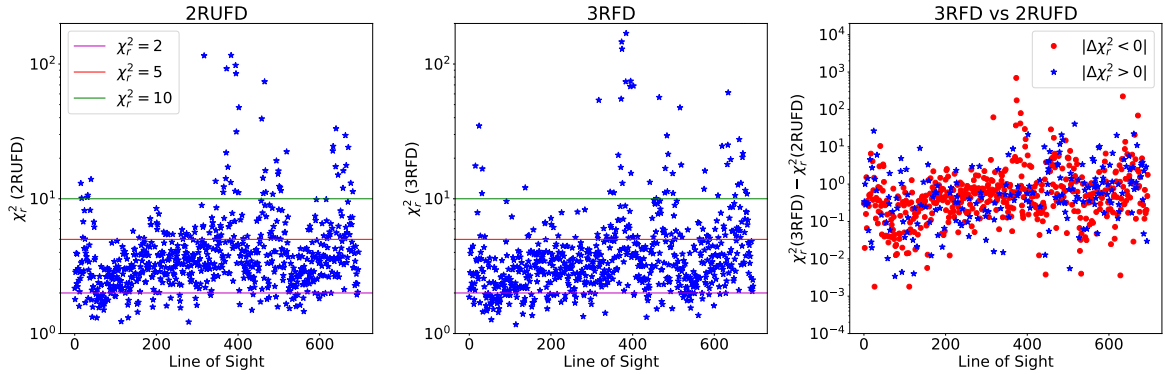

Figure 5.16: χ^2_r *of model 2RUFD and 3RFD fitted to single-peaked spectra lines-of-sight.* Left plot: χ^2_r of 2RUFD. Middle plot: χ^2_r of 3RFD. Right plot: The difference in χ^2_r of 3RFD and 2RUFD. For 2RUFD, $\sim 77\%$ of the fitted lines-of-sight have $\chi^2_r \leq 5$ and $\sim 79\%$ for 3RFD. Right plot: Blue points show lines-of-sight (31%) where model 2RUFD describes the data better than 3RFD and red points show the opposite. Most of the single-peaked spectra lines-of-sight are best described by 3RFD.

5.6.3 Fitting Examples

Figure 5.17 shows fitting examples to single-peaked spectra lines-of-sight in favour of model 2RUFD over 3RFD. In most cases, both models appear to the eye to fit the data relatively similar.

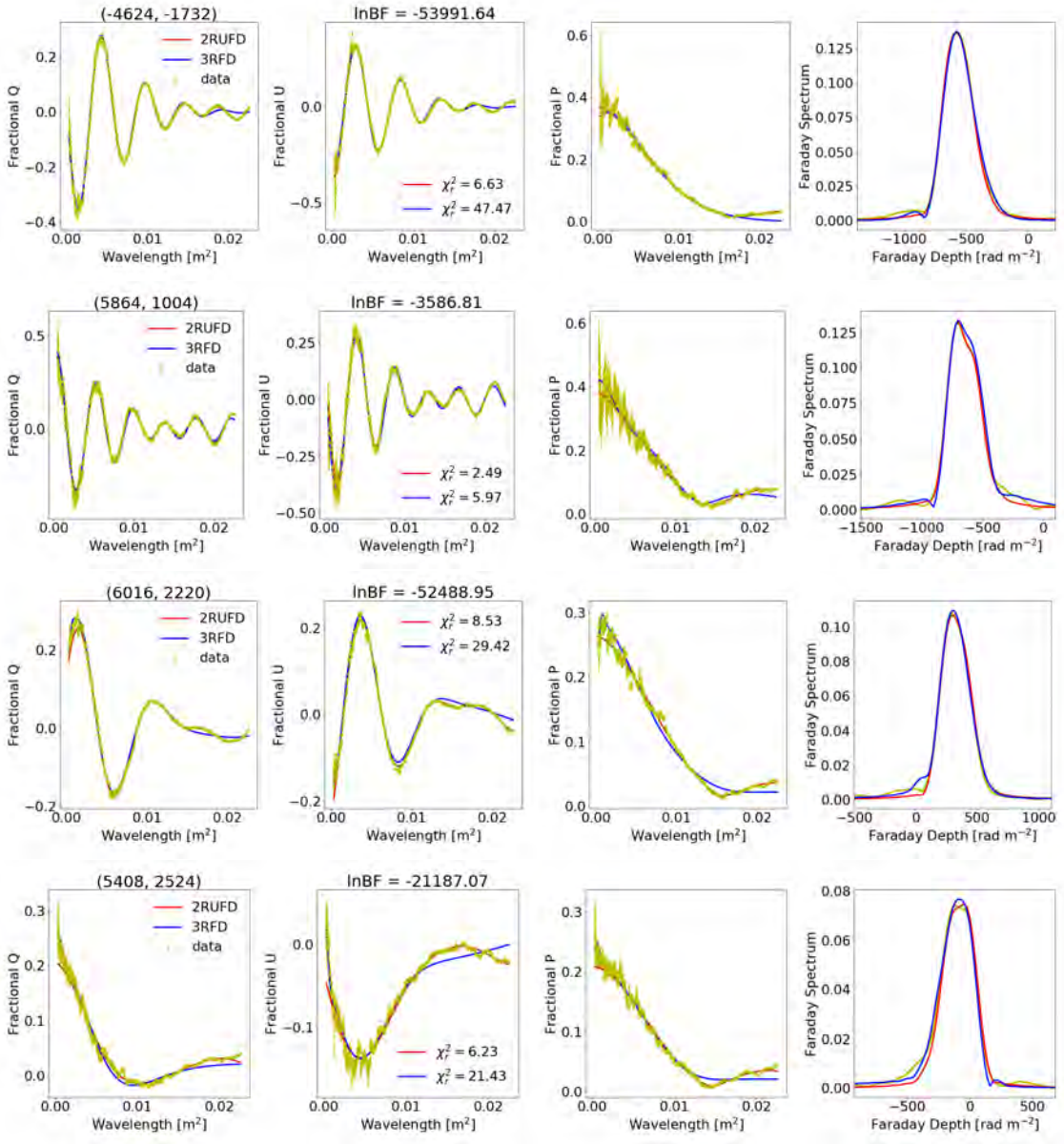

Figure 5.17: *Fitting examples in favour of 2RUFD over 3RFD for lines-of-sight with single-peaked Faraday spectra*. First column: Fractional Q vs λ^2. Second: Fractional U vs λ^2. Third: Fractional P vs λ^2. Left title: Lines-of-sight location. Middle title: The $\ln$ BF. These represent 31% of the fitted lines-of-sight. In particular, we show examples where 2RUFD is highly favoured (large negative $\ln$ BF).

Figure 5.18 shows fitting examples where model 3RFD is favoured over 2RUFD.

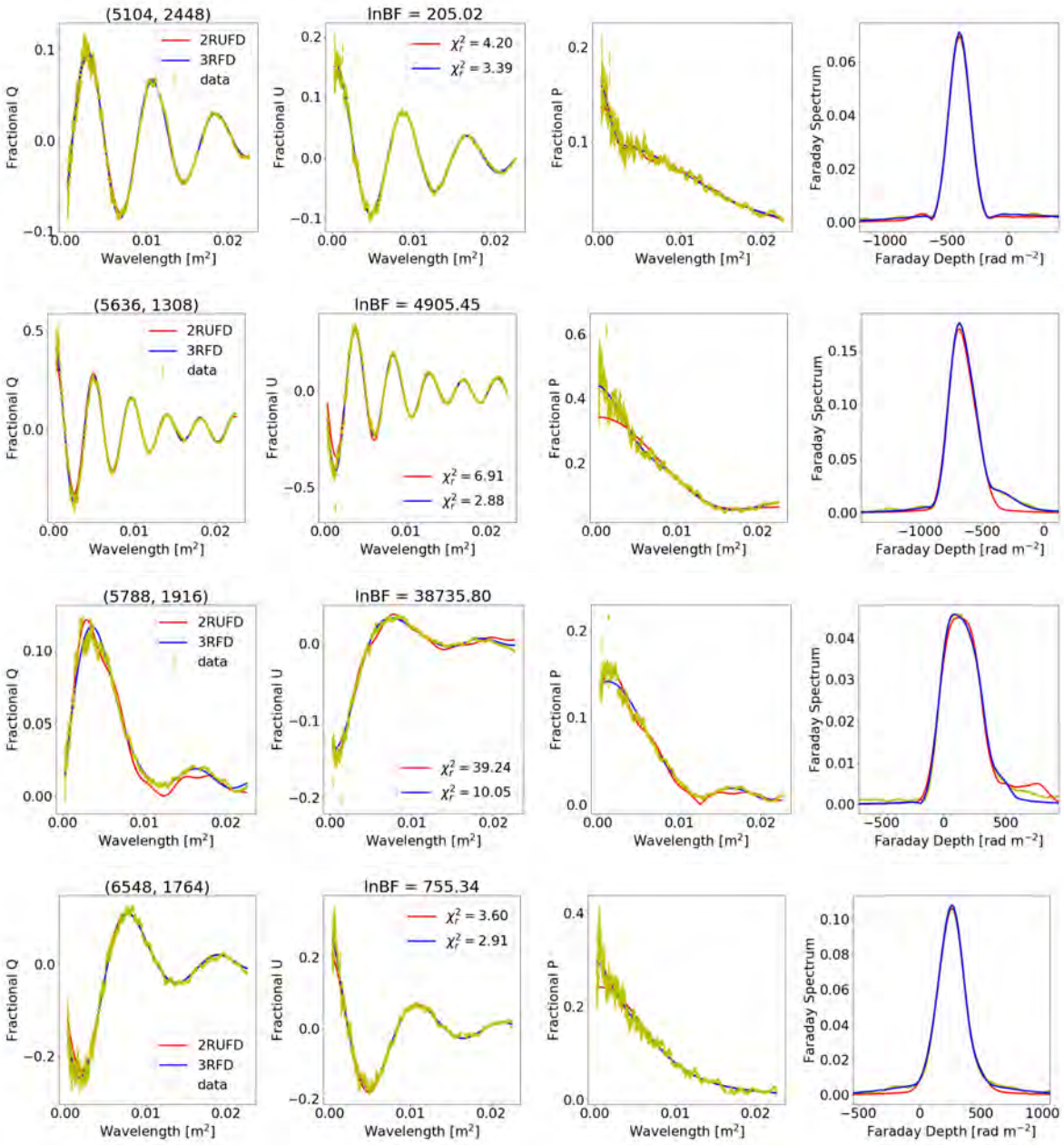

Figure 5.18: *Fitting examples in favour of 3RFD over 2RUFD for lines-of-sight with single-peaked Faraday spectra*. First column: Fractional Q vs λ^2. Second: Fractional U vs λ^2. Third: Fractional P vs λ^2. Left title: Lines-of-sight location. Middle title: The $\ln$ BF. These represent 69% of the fitted lines-of-sight. Top row: Both models seem to fit the data well ($\sim 50\%$). Second row: 3RFD obviously outperforms 2RUFD ($\sim 42\%$). Third and fourth row: Large χ^2_r ($\sim 4\%$). The latter mostly correspond to lines-of-sight with high SNR.

5.6.4 The Estimated Parameters for the Leading Models: 2RUFD and 3RFD

In the above sections, we have demonstrated that our 3RFD is the leading model, followed by 2RUFD. 3RFD explains 69% of the lines-of-sight better than 2RUFD. However, we also find that 2RUFD explains the remaining lines-of-sight, 31%, significantly better than 3RFD. Since 31% still forms a significant part of the data, we present both models' estimated parameters. We only show estimated parameters for the lines-of-sight with $\chi^2_r \leq 5$ and fractional errors ≤ 0.1. In each plot's title, we provide the percentage number of the lines-of-sight that satisfy these two conditions.

5.6.4.1 Three-Random Depolarising Screens

Figure 5.19 shows the estimated intrinsic fractional polarisation of the three components in model 3RFD (top) and ratios (bottom). The estimated values suggest the presence of a strong, intermediate and weak component. The strong component is generally about a factor of $\lesssim 5$ stronger than the intermediate component and a factor of $2 - 60$ highly polarised than the weaker component.

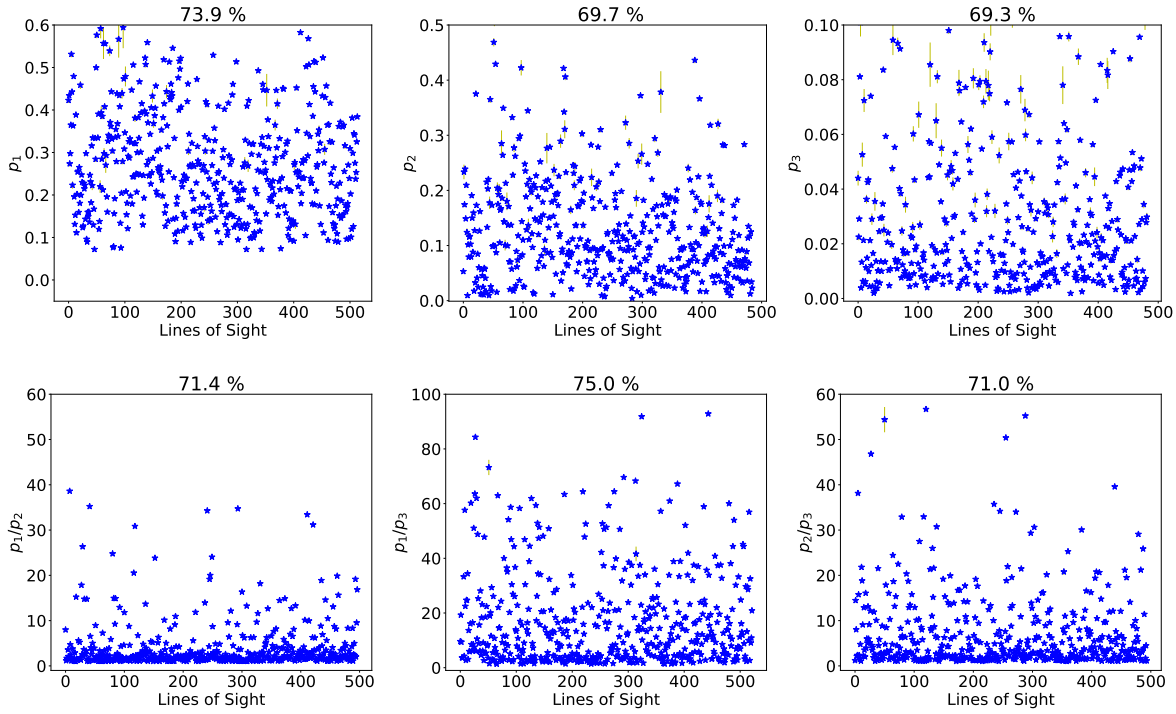

Figure 5.19: *Estimated intrinsic fractional polarisation of model 3RFD fitted to lines-of-sight with single-peaked Faraday spectra*. Top row: Intrinsic fractional polarisation. Bottom row: Ratio of the intrinsic fractional polarisation. The lines-of-sight shown have $\chi^2_r \leq 5$ and fractional errors ≤ 0.1. Title: A percentage of fitted lines-of-sight that satisfy both conditions. The estimated fractional polarisation suggest the presence of a strong, intermediate and weak component. The intermediate component is generally a factor of 2 to 5 smaller than the strong component, while the weaker component is a factor of 2 to 60 less polarised than the strong component.

Figure 5.20 shows the separation of the components in the Faraday space. The strong and the intermediate components are separated by no more than ± 250 rad m^{-2}. The weaker component is separated from both

the strong and intermediate by up to ± 500 rad m^{-2} and never less than ~ 50 rad m^{-2} from the intermediate component (rightmost plot).

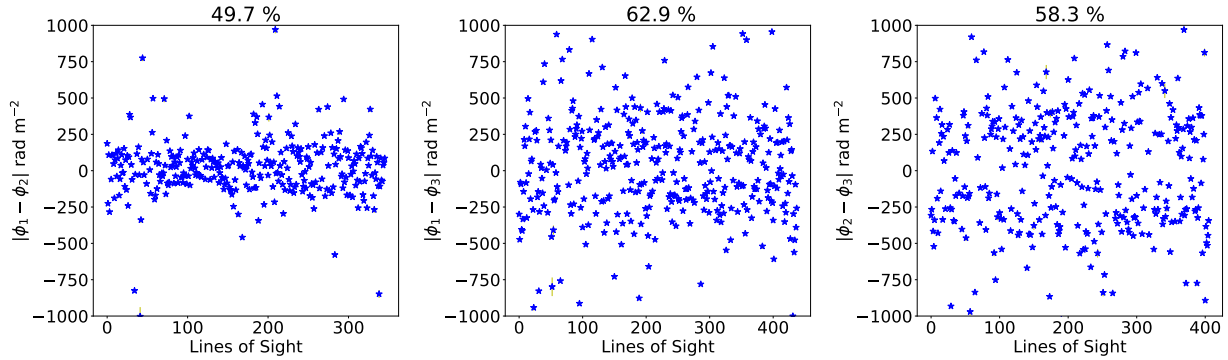

Figure 5.20: *The estimated components' separation in Faraday space of model 3RFD fitted to line-of-sight with single-peaked Faraday spectra.* The strong and intermediate (left) components are separated by $\leq \pm 250$ rad m^{-2}, while the weaker component is separated from the other two components by up to 500 rad m^{-2} (with fewer larger separations). The right plot also suggests a minimum separation of ~ 50 rad m^{-2} between the intermediate and weak component.

Figure 5.21 shows the Faraday dispersions of the three components in model 3RFD for the lines-of-sight with single-peaked Faraday spectra. The dispersions of the three components range between $0 - 300$ rad m^{-2}, with few lines-of-sight having larger dispersions going up to ~ 600 rad m^{-2}. The dispersions of the strong and the intermediate component are concentrated within $0 - 150$ rad m^{-2} and between $0 - 100$ rad m^{-2} for the weak component.

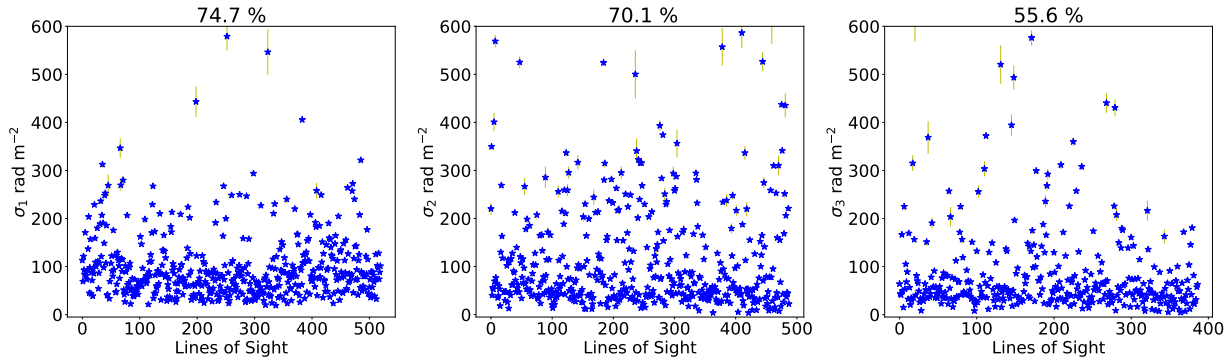

Figure 5.21: *The estimated Faraday dispersions of model 3RFD fitted to lines-of-sight with single-peaked Faraday spectra.* The dispersions of the components range between $0 - 300$ rad m^{-2}, with a few lines-of-sight having larger dispersions of up to $\lesssim 600$ rad m^{-2}. The dispersions of a strong and the intermediate component are clustered between $0 - 150$ rad m^{-2}, while the dispersions for the weaker component are clustered between $0 - 100$ rad m^{-2} .

5.6.4.2 Two Random-Uniform Depolarising Screens

Figure 5.22 shows the derived intrinsic fractional polarisation of the first component (left, the strong component), the second component (middle, the weak component) and the ratio of the two-component (right). The lines-of-sight shown have $\chi^2_r \leq 5$ and fractional polarisation ≤ 0.1. The strong component's fractional

polarisation ranges between $0.1 - 0.6$, and the weak component between $\sim 0.01 - 0.3$. The intrinsic polarisation of the weaker component is a factor of $1 - 10$ less polarised than the strong component. The majority of the ratios are clustered ≤ 4.

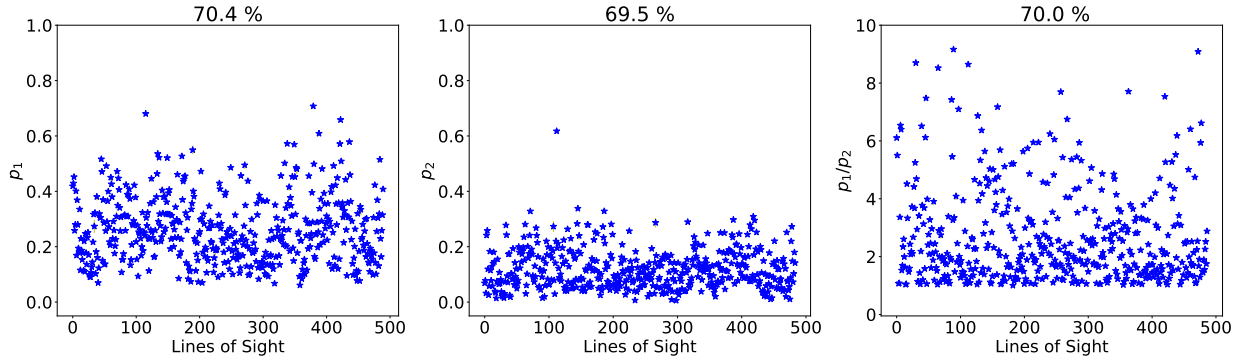

Figure 5.22: *The estimated intrinsic fractional polarisation of model 2RUFD fitted to lines-of-sight with single-peaked Faraday spectra*. Left and middle plot: Intrinsic fractional polarisation. Right plot: Ratios of the intrinsic fractional polarisation. Lines-of-sight shown have $\chi^2_r \leq 5$ and fractional errors ≤ 0.1. Component 1, "the strong component", is about a factor of $1 - 10$ more polarised than component 2, "the weak component".

Figure 5.23 shows the Faraday dispersions of the two components in model 2RUFD (left and middle plot) and the separation of the components in Faraday space (right). The dispersions of the strong component range between $0 - 150$ rad m^{-2} and the weak component between $0 - 50$ rad m^{-2}. The components are separated by $\leq \pm 250$ rad m^{-2}.

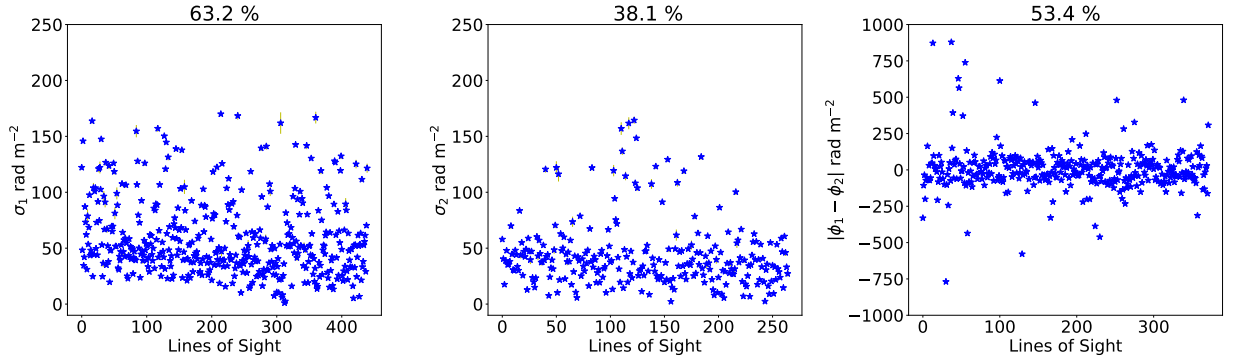

Figure 5.23: *The estimated Faraday dispersion and the components separation of model 2RUFD fitted to lines-of-sight with single-peaked spectra*. Left and middle plot: Faraday dispersions. Right plot: Component separation in Faraday space. Faraday dispersions of the strong component range between $0-150$ rad m^{-2} and the weaker component between $0 - 50$ rad m^{-2}. The two components are separated by no more than ± 250 rad m^{-2}.

Figure 5.24 shows the unresolved uniform RM-difference of the two-components in 2RUFD. The RM-difference range between $0-500$ rad m^{-2} for a strong component, and $0-800$ rad m^{-2} for a weak component.

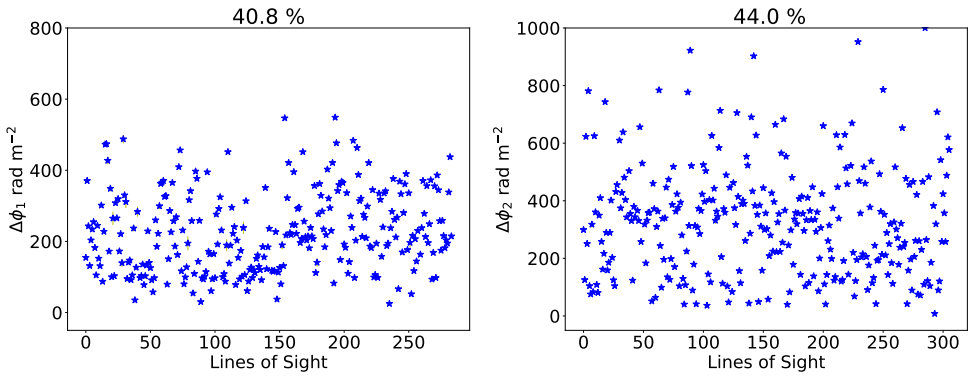

Figure 5.24: *The estimated RM-difference of model 2RUFD fitted to lines-of-sight with single-peaked spectra.* The lines-of-sight shown have solutions with $\chi^2_r \leq 5$ and fractional errors ≤ 0.1. RM-difference associated with the strong component range between 0 and 500 rad m^{-2} and the weak component between 0 and 800 rad m^{-2}.

5.7 Single-Peaked Spectra with Smaller Peaks

The lines-of-sight with single-peaked spectra with smaller peaks represent 15% of the lines-of-sight. Since the Faraday spectrum of the lines-of-sight shows two or more peaks, the single screen/component models need not be fitted to the data. For these lines-of-sight, it is no longer a question of whether there are multiple components or not, but rather, our interest is in determining a model that best describes the data. We consider the multi-component models, namely 2RFD, 3RFD and 2RUFD.

5.7.1 Best-Fitting Model

Figure 5.25 shows the results of the $\ln$ BF for the three models. 3RFD and 2RFD are compared in the left plot, 2RUFD and 2RFD in the middle plot, and 2RUFD and 3RFD in the right plot. The blue points are in favour of 3RFD (left and right) and 2RUFD (middle), and the red points are in favour of 2RFD (left and middle), and 2RUFD (right). 3RFD is most favoured for 99% of the lines-of-sight against 2RFD and 78% lines-of-sight against 2RUFD. 2RUFD, on the other hand, is preferred over 2RFD for 83% lines-of-sight. 3RFD outperforms 2RUFD and 2RFD for the majority of the lines-of-sight. This implies that the single-peaked spectra with smaller peaks lines-of-sight are best described by a model with at least three components.

5.7.2 Goodness-of-Fit of Competing Models

In Section 5.7.1, we have shown that model 3RFD is the most preferred of the three models. We consider the $\chi^2_r < 5$ to indicate whether a model describes the data or not. Figure 5.26 shows χ^2_r for the three models: 2RFD, 2RUFD and 3RFD. 3RFD also describes 80% of the single-peaked spectra with smaller peaks data, while 2RUFD describes 70% and 2RFD describes 55%. Model 3RFD describes the majority of the lines-of-sight.

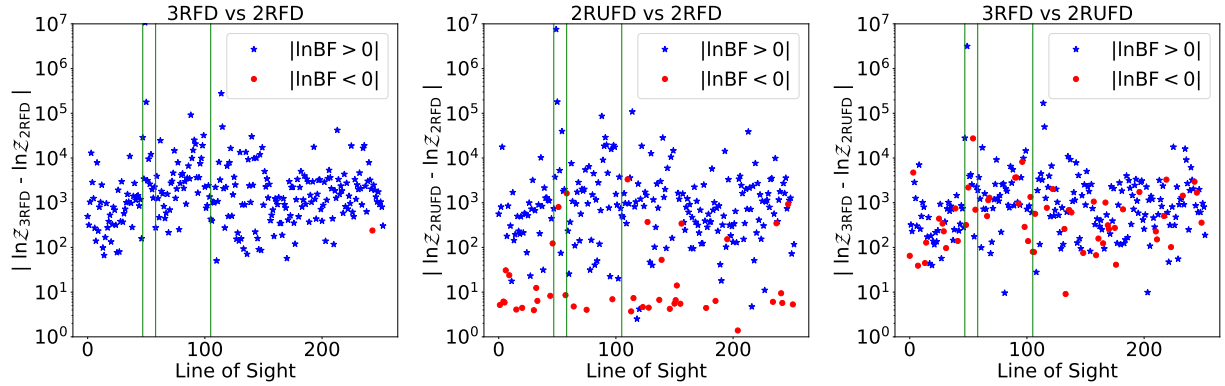

Figure 5.25: $\ln$ *BF solutions of model 2RFD, 3RFD and 2RUFD fitted to lines-of-sight with single-peaked spectra with smaller peaks.* Blue points: In favour of 3RFD (left and right) and 2RUFD (middle). Red points: In favour of 2RFD (left and middle) and 2RUFD (right). Vertical lines (from left to right) separates lines-of-sight with smooth decaying, sinc-like, complex oscillatory, and complex non-oscillatory depolarisation. 3RFD is favoured over 2RFD for 99% of the fitted lines-of-sight and over 2RUFD for 78%. 2RUFD is favoured over 2RFD for 83%. The red points in favour of 2RFD (middle) are associated with small $\ln$ BF, with $\sim 2/3$ having $\ln \mathrm{BF} < 10$ – indicating a weaker preference towards 2RFD. 3RFD is the most favoured model of the three models for the majority of the lines-of-sight.

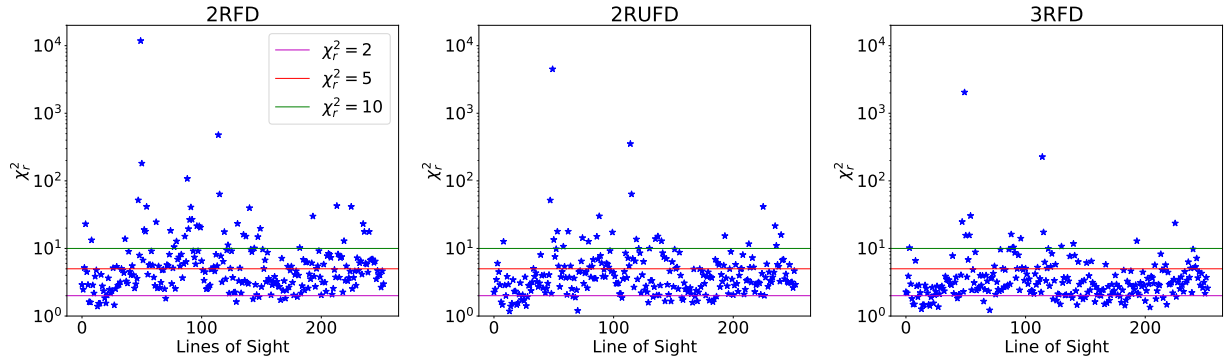

Figure 5.26: χ_r^2 *of model 2RFD, 2RUFD and 3RFD fitted to lines-of-sight with single-peaked Faraday spectra with smaller peaks.* Left: χ_r^2 of 2RFD. Middle: χ_r^2 of 2RUFD. Right: χ_r^2 of 3RFD. The horizontal lines correspond to $\chi_r^2 = 2$ (magenta), $\chi_r^2 = 5$ (red), and $\chi_r^2 = 10$ (green). For all the models, the majority of the lines-of-sight have $\chi_r^2 \lesssim 5$. For 2RFD, we find $\sim 55\%$ of the fitted lines-of-sight have $\chi_r^2 \leq 5$, $\sim 70\%$ for 2RUFD and $\sim 80\%$ for 3RFD.

Figure 5.27 shows the difference in the χ^2_r of 2RFD and 3RFD (left), 2RFD and 2RUFD (middle) and 2RUFD and 3RFD (right). The blue points are in favour of 3RFD (left and right plot) and 2RUFD (middle plot). The red points in favour of 2RFD (left and middle plot) and 2RUFD (right). 2RFD describes the data poorly, while 2RUFD and 3RFD are able to describe a significant fraction of the data. However, 3RFD outperforms 2RUFD by describing 75% of the lines-of-sight better. We can confidently discard 2RFD.

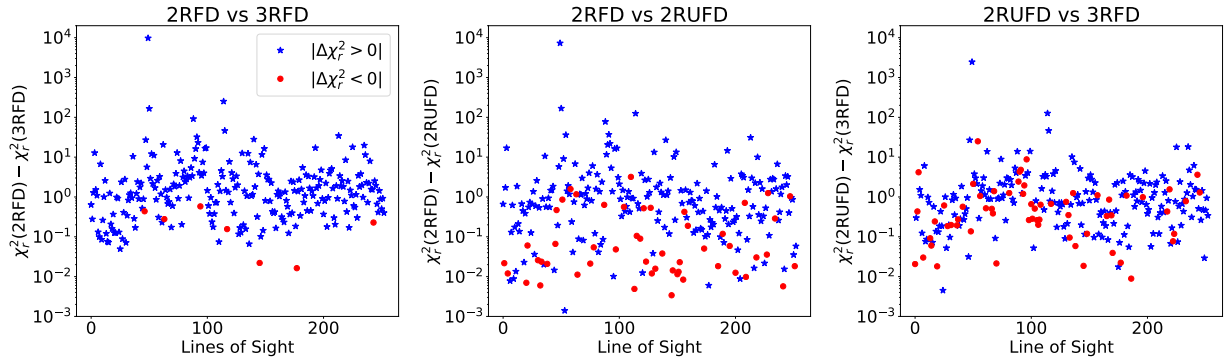

Figure 5.27: *The difference in χ^2_r of models 2RFD, 3RFD and 2RUFD fitted to lines-of-sight with single-peaked with smaller peaks.* Blue points: In favour of 3RFD (left and right) and 2RUFD (middle). Red points: In favour of 2RFD (left and middle) and 2RUFD (right). 3RFD outperforms 2RFD for 97% of the fitted lines-of-sight and outperforms 2RUFD for 75%.

5.7.3 Fitting Examples

In the above sections, we were able to demonstrate that 3RFD outperforms 2RFD and 2RUFD. Although 3RFD significantly outperforms 2RFD, the same is not always true for 2RUFD (see right plot of Figures 5.25 and 5.27). We find that 2RUFD is significantly favoured for 18% of the lines-of-sight over 3RFD.

In Figure 5.28, we show six examples whereby model 2RUFD is favoured over 3RFD (red points in Figure 5.25). The top row shows an example where both models seem to fit the data reasonably well, as such, model 3RFD is disfavoured mainly because of its relatively high complexity. We find that roughly $\sim 56\%$ of the lines-of-sight in favour of 2RUFD are fitted well by both models. Second row shows an example where 3RFD fails to fit the data at lower-frequencies. We find that 24% of the fitted lines-of-sight in favour of 2RUFD are of this kind. The third row is one of the three (5%) situations where 3RFD fails at higher-frequencies. The fourth is an example where 3RFD is unable to reproduce the oscillatory behaviour – only five (9%) cases were found.

Figure 5.29 shows situations where 3RFD is favoured over 2RUFD (blue points in Figure 5.25).

5.7.4 The Estimated Parameters for the Leading Models

5.7.4.1 Three-Random Depolarising Screens

Figures 5.30 shows the estimated intrinsic fractional polarisation and ratios for model 3RFD. We only show fitting solutions with fractional errors less than 10% and $\chi^2_r \leq 5$. In each plot, we indicate a frac-

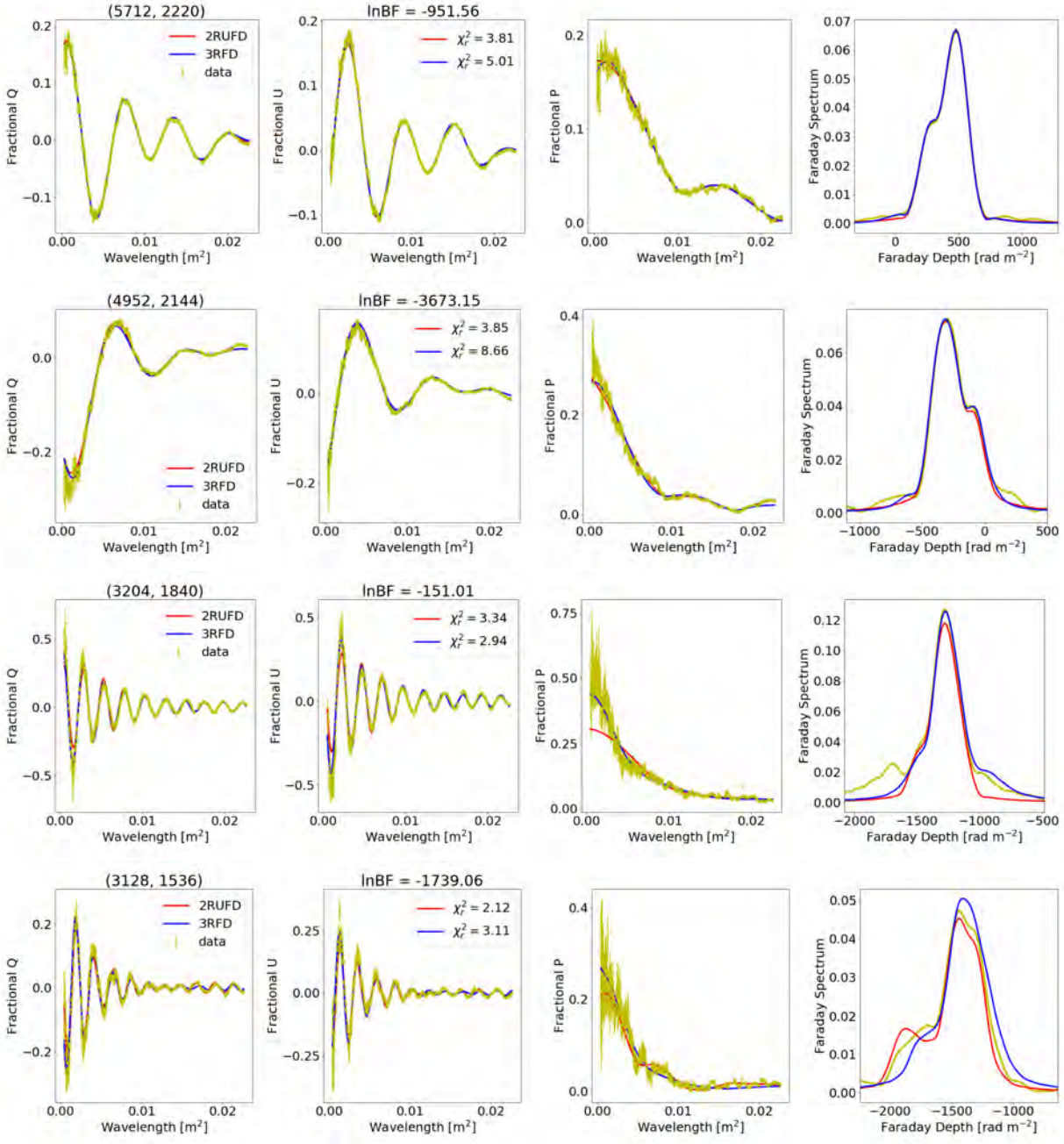

Figure 5.28: *Fitting examples in favour of model 2RUFD over 3RFD for lines-of-sight with single-peaked spectra with smaller peaks*. Red: 2RUFD. Blue: 3RFD. First column: Fractional Q vs λ^2. Second: Fractional U vs λ^2. Third: Fractional P vs λ^2. Right column: Amplitude of the Faraday spectrum. Left title: Lines-of-sight location. Middle title: The ln BF. See Section 5.7.3 for details.

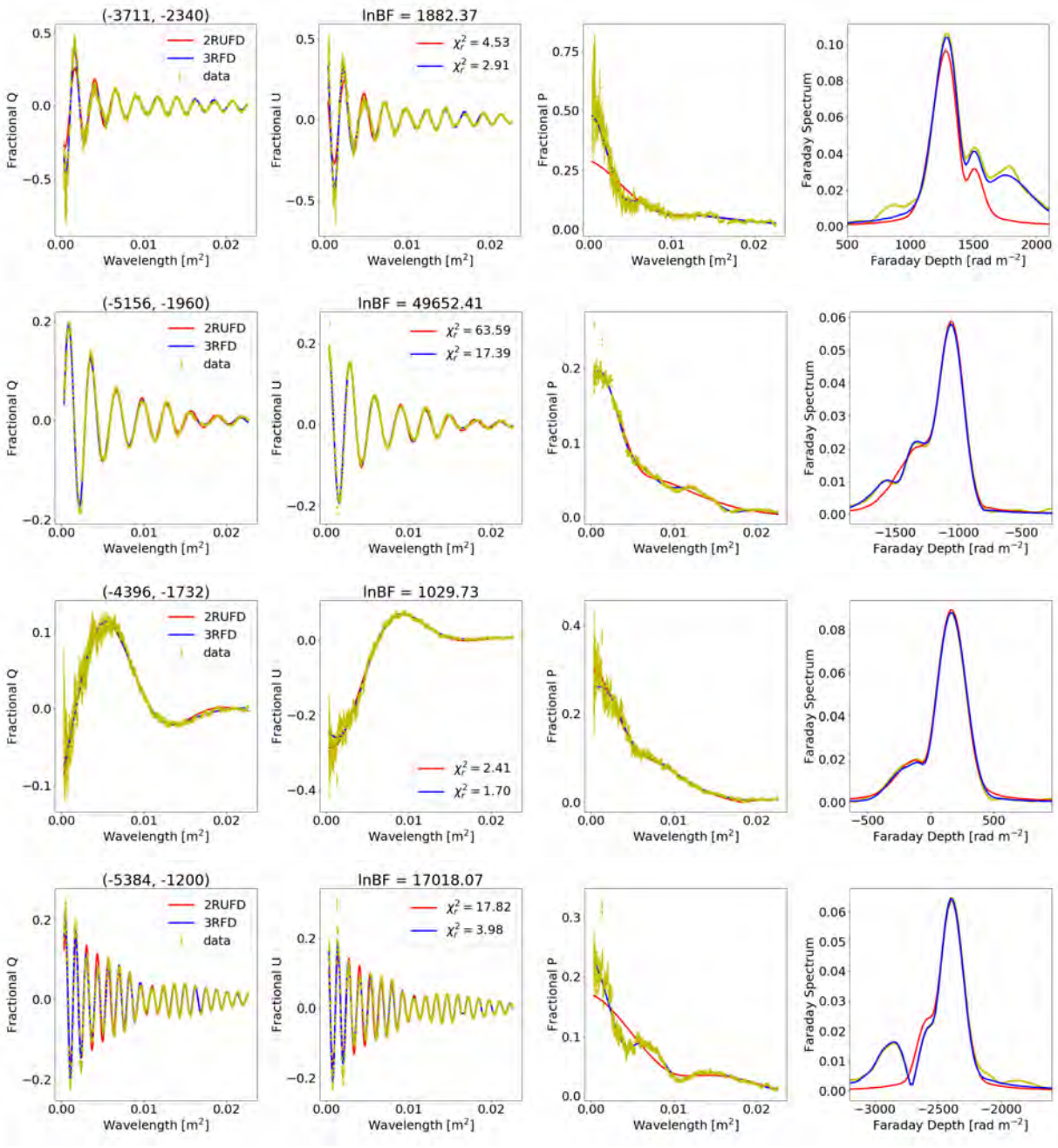

Figure 5.29: *Fitting examples in favour of model 3RFD over 2RUFD for lines-of-sight with single-peaked with smaller peaks*. Red: 2RUFD. Blue: 3RFD. First column: Fractional Q vs λ^2. Second: Fractional U vs λ^2. Third: Fractional P vs λ^2. Fourth: Amplitude of the Faraday spectrum. Left title: Lines-of-sight location. Middle title: The $\ln$ BF.

tion of lines-of-sight satisfy these two conditions. There seem to be at least three components with different strengths, namely the strong, intermediate, and weak component. The strong component is a factor of $0-10$ more polarised than the intermediate component and a factor of $0-30$ more polarised than the weaker component. The components are associated with small fitting errors in the derived intrinsic fractional polarisation, which suggests that the components are important and may very well be real.

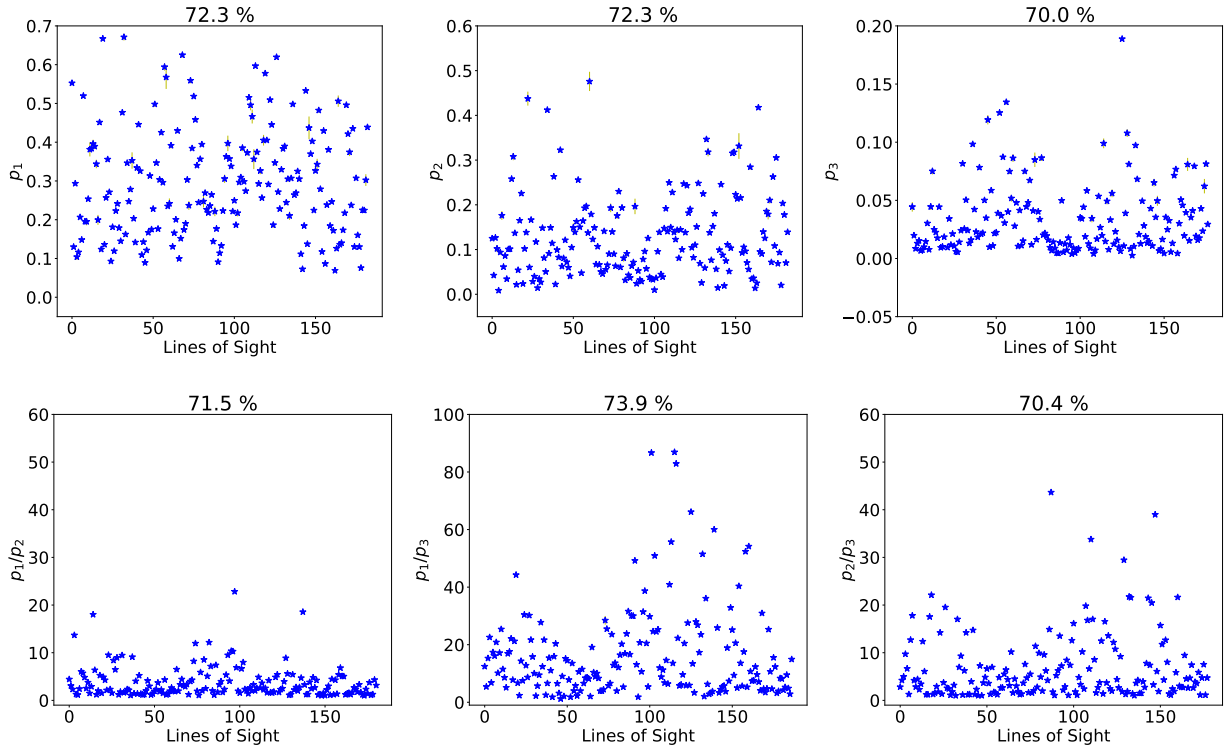

Figure 5.30: *The estimated intrinsic fractional polarisation of model 3RFD fitted to lines-of-sight with single-peaked spectra with smaller peaks.* Top row: Intrinsic fractional polarisation. Bottom row: Ratios of the intrinsic fractional polarisation. Lines-of-sight shown have fractional errors ≤ 0.1 and $\chi^2_r \leq 5$. Title: A fraction of lines-of-sight that satisfies these two conditions. The derived polarisation suggests three components of differing strengths, namely a strong (more polarised), intermediate and weak component (less polarised). The strong component is a factor of $1-10$ more polarised than the intermediate component and a factor of $1-30$ more polarised than the weak component.

Figure 5.31 shows the estimated components' separation in Faraday space. The lines-of-sight shown have fractional errors in the estimated separations less than 0.1 and $\chi^2_r \leq 5$. The strong and intermediate components are relatively close in Faraday space, with separations not exceeding 300 rad m^{-2} – about $\lesssim 1.6\times$ the width of the RMTF. The weaker component is separated from the strong component not more than 500 rad m^{-2} for most of the lines-of-sight. The weak and intermediate components are much further from each other in Faraday space – with separations not less than ± 200 rad m^{-2} and of up to ± 700 rad m^{-2}.

Figure 5.32 shows the estimated Faraday dispersions. Lines-of-sight shown have fractional errors in the estimated dispersions of ≤ 0.1 and $\chi^2_r \leq 5$. The Faraday dispersions range between $0-400$ rad m^{-2} for the strong component and $0-100$ rad m^{-2} for both the intermediate and weak component. This result implies that the strong component depolarises much more rapidly than the two relatively weaker components.

However, an issue that arises is whether can we trust the dispersions smaller than our resolution (~ 180 rad

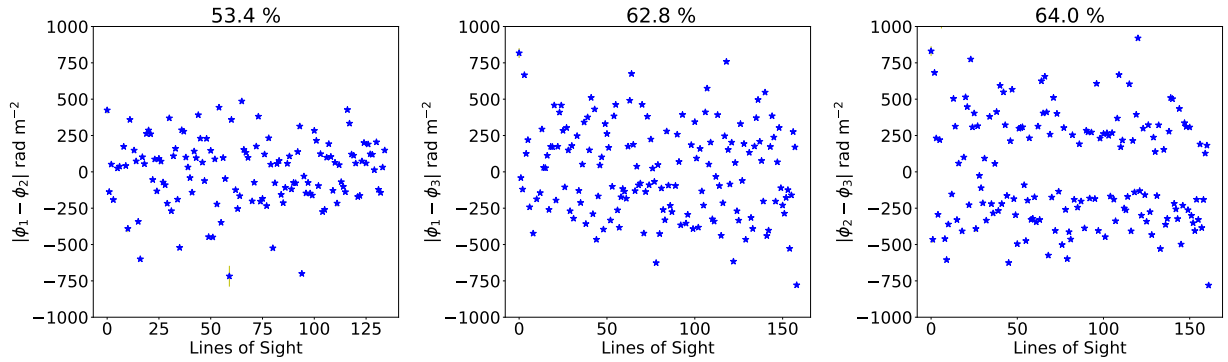

Figure 5.31: *The estimated components' separation of model 3RFD fitted to lines-of-sight with single-peaked spectra with smaller peaks.* Lines-of-sight shown have fractional errors ≤ 0.1 and $\chi^2_r \leq 5$. The title shows a fraction of lines-of-sight that satisfies these two conditions. The strong and intermediate components are relatively close in Faraday space with separation for most lines-of-sight not larger than ± 300 rad m^{-2} – about a factor 1.6 wider than our RMTF. The weaker component is separated from the strong component by no more than ± 500 rad m^{-2} (middle). The weak and intermediate components are largely separated $> \pm 200$ and $< \pm 700$ rad m^{-2} (right).

m^{-2}) and separations less than the width of the RMTF? There is no straightforward answer to this question. However, we do know that the Faraday components need to have a width in Faraday space to produce the global decaying fractional polarisation as a function of λ^2. A delta function (a purely Faraday rotating gas without depolarisation) cannot produce this observed global decline. The only way a purely Faraday rotating screen can produce a decline is if there is an infinite number of screens across the resolution beam, as such, their average ultimately converge to a continuous distribution.

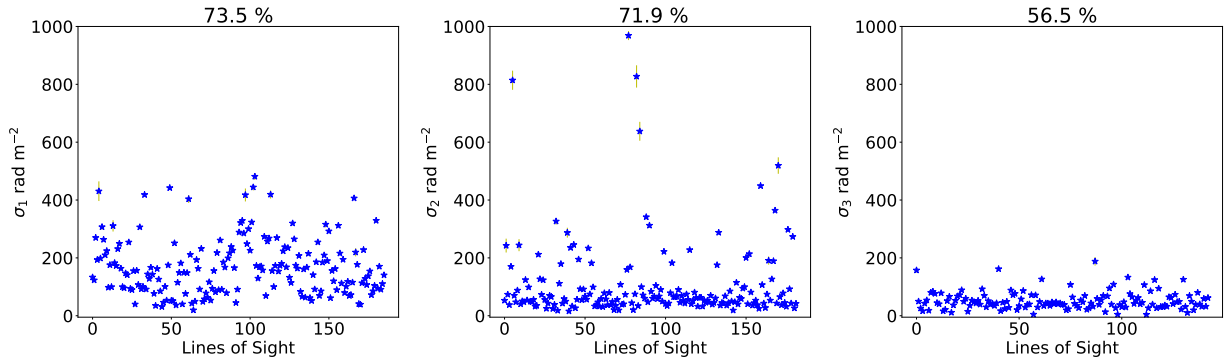

Figure 5.32: *The estimated Faraday dispersions of model 3RFD fitted to lines-of-sight with single-peaked spectra with smaller peaks.* Lines-of-sight shown have fractional errors less than 0.1. The title shows a fraction of lines-of-sight that satisfies these two conditions. The strong component depolarises more rapidly with dispersions ranging between $0 - 400$ rad m^{-2}, while the other components depolarise less rapidly with typical values ranging between $0 - 100$ rad m^{-2}.

5.7.4.2 Two Random-Uniform Depolarising Screens

Figures 5.33, 5.34 and 5.35 show the estimated fitting parameters for model 2RUFD fitted to lines-of-sight with single-peaked with smaller peaks Faraday spectra. The lines-of-sight shown have $\chi^2_r \leq 5$ and

fractional errors ≤ 0.1 in the estimated parameters. Figure 5.33 shows the intrinsic fractional polarisation of the two-components (left and middle) and the ratios (right). A strong component is a factor of $1-10$ more polarised than the weak component.

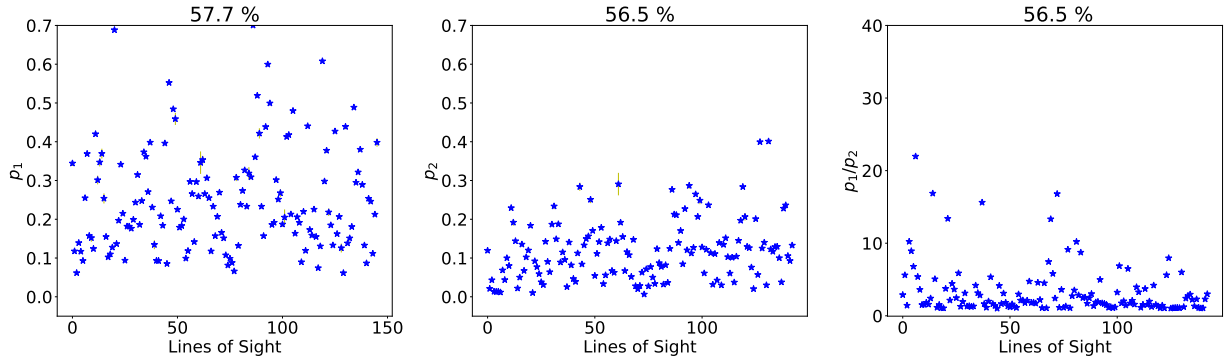

Figure 5.33: *The estimated intrinsic fractional polarisation of model 2RUFD fitted to lines-of-sight with single-peaked with smaller peaks Faraday spectra.* Lines-of-sight shown have solutions $\chi^2_r \leq 5$ and fractional errors ≤ 0.1. The title shows a fraction of the fitted lines-of-sight that satisfy these two conditions. The strong component is a factor of $1-10$ more polarised than the weak component.

Figure 5.34 shows the Faraday dispersions of the components (left and middle) and their separation in Faraday space (right). The Faraday dispersions of the strong component range between $10-300$ rad m^{-2} and of the weak component ranges between $\sim 1-60$ rad m^{-2}. The components are separated by no more than ± 250 rad m^{-2}.

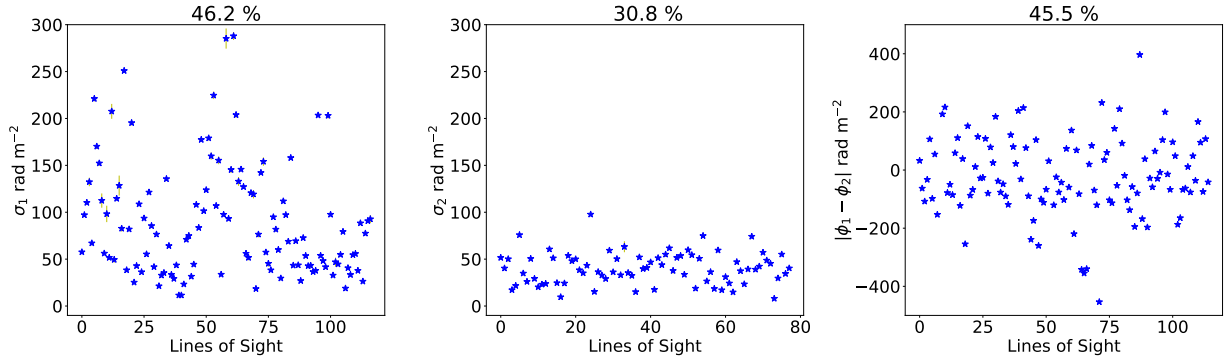

Figure 5.34: *The estimated Faraday dispersions and components separation in Faraday space of model 2RUFD fitted to lines-of-sight with single-peaked spectra and smaller peaks.* Left and middle plot: Faraday dispersions. Right plot: Separations in Faraday space. Lines-of-sight shown have $\chi^2_r \leq 5$ and fractional errors of ≤ 0.1. The titles show a fraction of fitted lines-of-sight that satisfy these two conditions. The dispersions of the strong component range between $10-300$ rad m^{-2} and weak component between $\sim 1-60$ rad m^{-2}. The components are separated by no more than ± 250 rad m^{-2}.

Figure 5.35 shows the derived unresolved uniform RM-difference. For both components, the RM-differences range between $\sim 10-800$ rad m^{-2}.

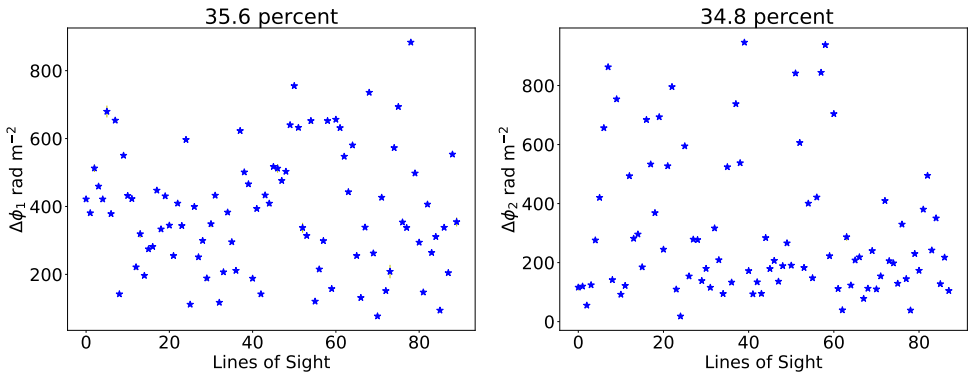

Figure 5.35: *The estimated RM-difference of model 2RUFD fitted to lines-of-sight with single-peaked Faraday spectra and smaller peaks.* Lines-of-sight shown have $\chi^2_r \leq 5$ and fractional errors of ≤ 0.1. The titles show a fraction of the fitted lines-of-sight that satisfy these two conditions. The estimated RM-difference for both components range between $\sim 10 - 800$ rad m^{-2}.

5.8 Blended Double-Peaked Spectra

The blended double-peaked spectra represent 20% of the lines-of-sight. We fit 2RUFD, 2RFD, and 3RFD models to these lines-of-sight, similar to single-peaked spectra with smaller peaks.

5.8.1 Best-Fitting Model

Figure 5.36 shows the results of the $\ln$ BF for 2RFD, 2RUFD and 3RFD models. The $\ln$ BF of 3RFD and 2RFD is shown in the left plot, of 2RUFD and 2RFD in the middle plot, and 2RUFD and 3RFD in the right plot. The blue points are in favour of 3RFD (left and right) and 2RUFD (middle) and the red points are in favour of 2RFD (left and middle), and 2RUFD (right). 3RFD is favoured for 98% of the fitted lines-of-sight over 2RFD and 73% lines-of-sight over 2RUFD. 2RUFD, on the other hand, is favoured over 2RFD for 80% of the fitted lines-of-sight. In general, 3RFD is the favoured for the majority of the lines-of-sight.

5.8.2 Goodness-of-Fit of Competing Models

Figure 5.37 shows χ^2_r for the 2RUFD (left), 3RFD (middle) and the difference in their χ^2_r (right). There are 67% lines-of-sight with $\chi^2_r \leq 5$ for 2RUFD, and 76% for 3RFD. 3RFD describes the majority of the lines-of-sight better than 2RUFD.

5.8.3 Fitting Examples

We present a couple of examples showing fitting to blended double-peaked Faraday spectra by 2RUFD and 3RFD. Figures 5.38 and 5.39 show examples where 2RUFD is favoured over 3RFD, and Figures 5.40 and 5.41 shows those where 3RFD is favoured over 2RUFD.

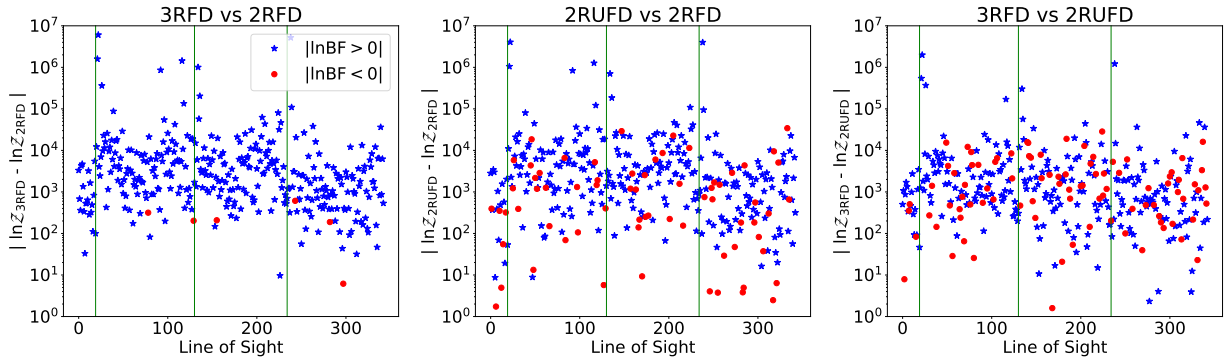

Figure 5.36: $\ln$ *BF solutions of model 2RFD, 3RFD and 2RUFD fitted to lines-of-sight with blended double-peaked Faraday spectra*. Blue points: In favour of 3RFD (left and right) and 2RUFD (middle). Red points: In favour of 2RFD (left and middle) and 2RUFD (right). Vertical line (from left to right) separates lines-of-sight with smooth, sinc-like, complex oscillatory, and complex non-oscillatory decaying depolarisation. Model 3RFD is favoured over 2RFD for 98% of the fitted lines-of-sight and over 2RUFD for 73%. 2RUFD is favoured over 2RFD for 80% of the fitted lines-of-sight. 3RFD is the most favoured model.

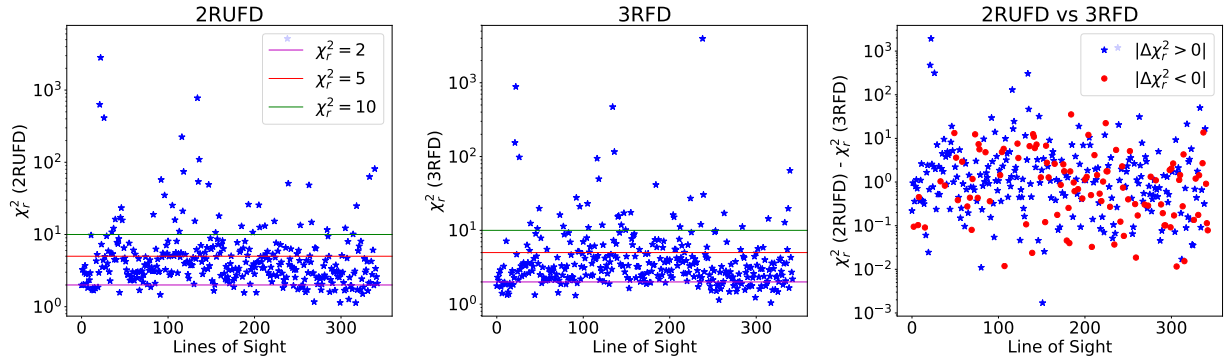

Figure 5.37: χ^2_r *of model 2RUFD and 3RFD fitted to lines-of-sight with blended double-peaked spectra*. Left: χ^2_r of 2RUFD. Middle: χ^2_r of 3RFD. Right: Difference in χ^2_r of 2RUFD and 3RFD. Horizontal lines correspond to $\chi^2_r = 2$ (magenta), 5 (red) and 10 (green). Blue points (right plot): In favour of 3RFD. Red points: In favour of 2RUFD. We find that for both models, most of the lines-of-sight χ^2_r are concentrated between $0 - 5$ – roughly 67% of the fitted lines-of-sight for 2RUFD and 76% for model 3RFD. Model 3RFD is favoured for the majority of the lines-of-sight.

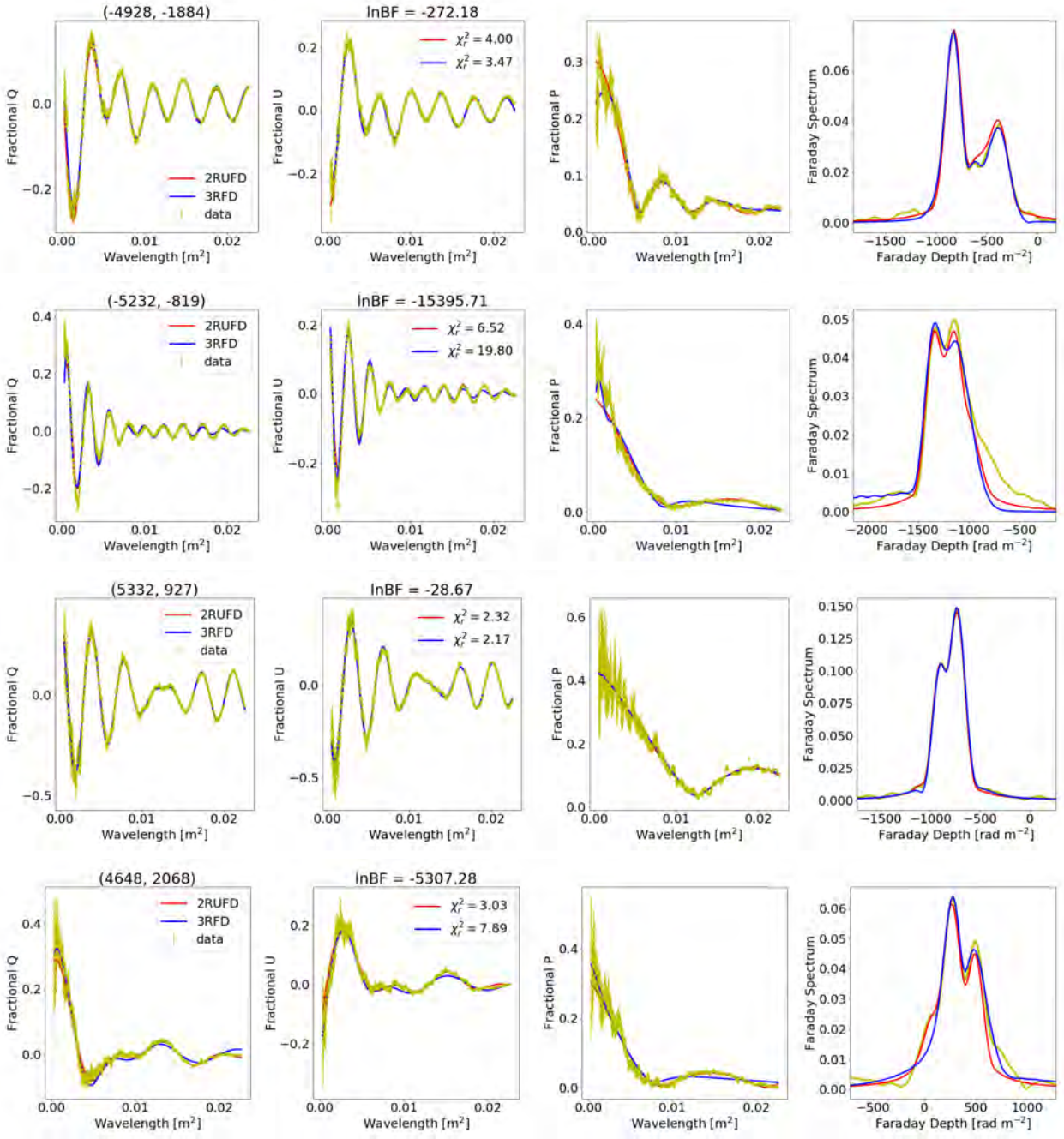

Figure 5.38: *Fitting examples in favour of model 2RUFD over 3RFD for blended double-peaked spectra lines-of-sight with sinc-like decay*. First column: Fractional Q vs λ^2. Second: Fractional U vs λ^2. Third: Fractional P vs λ^2. Fourth: Amplitude of the Faraday spectrum. Left title: Lines-of-sight location. Middle title: The $\ln$ BF.

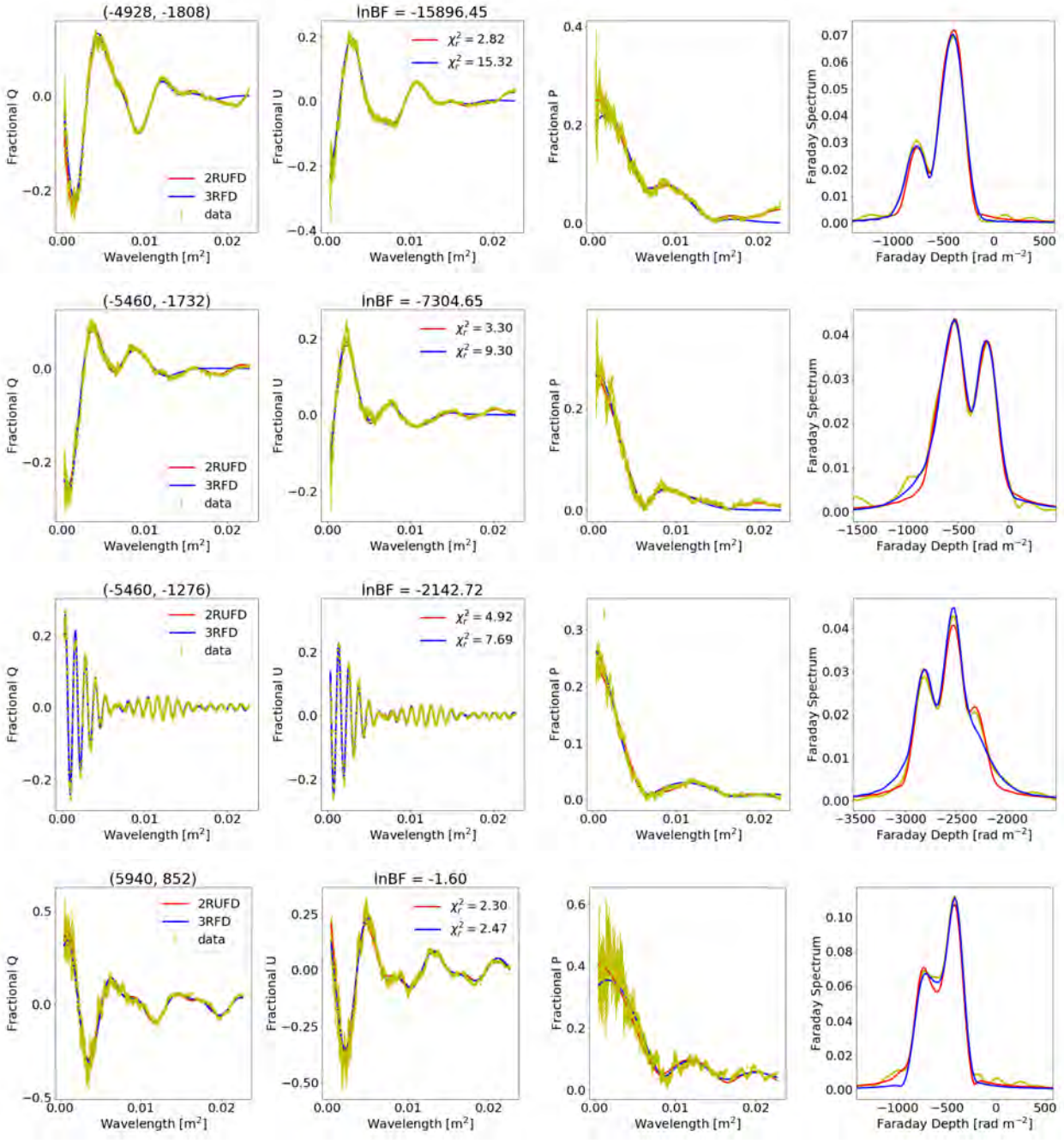

Figure 5.39: *Fitting examples in favour of model 2RUFD over 3RFD for blended double-peaked spectra lines-of-sight with complex oscillatory decay.* First column: Fractional Q vs λ^2. Second: Fractional U vs λ^2. Third: Fractional P vs λ^2. Fourth: Amplitude of the Faraday spectrum. Left title: Lines-of-sight location. Middle title: The $\ln$ BF.

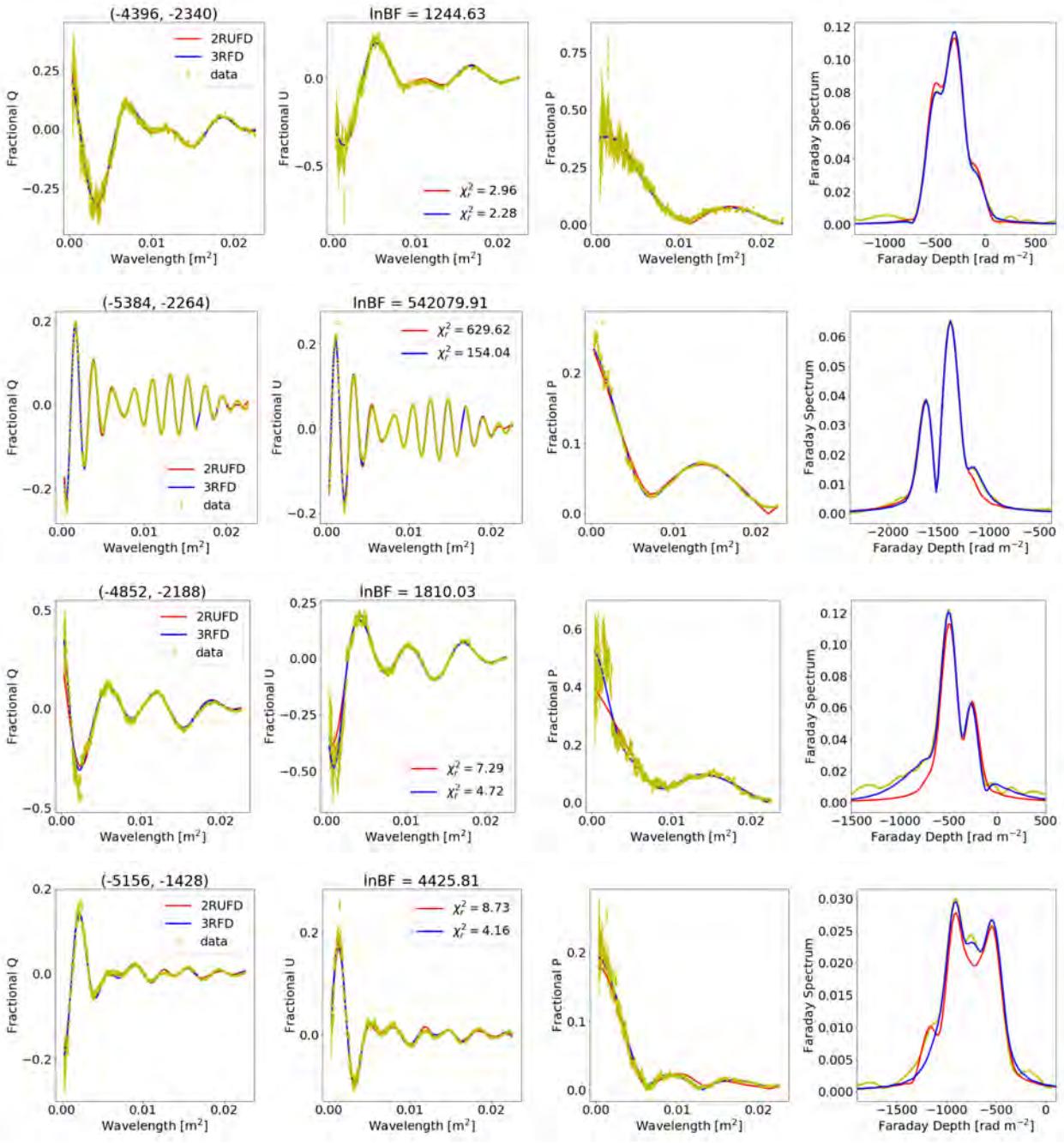

Figure 5.40: *Fitting examples in favour of model 3RFD over 2RUFD for blended double-peaked spectra lines-of-sight with sinc-like decay*. First column: Fractional Q vs λ^2. Second: Fractional U vs λ^2. Third: Fractional P vs λ^2. Fourth: Amplitude of the Faraday spectrum. Left title: Lines-of-sight location. Middle title: The $\ln$ BF.

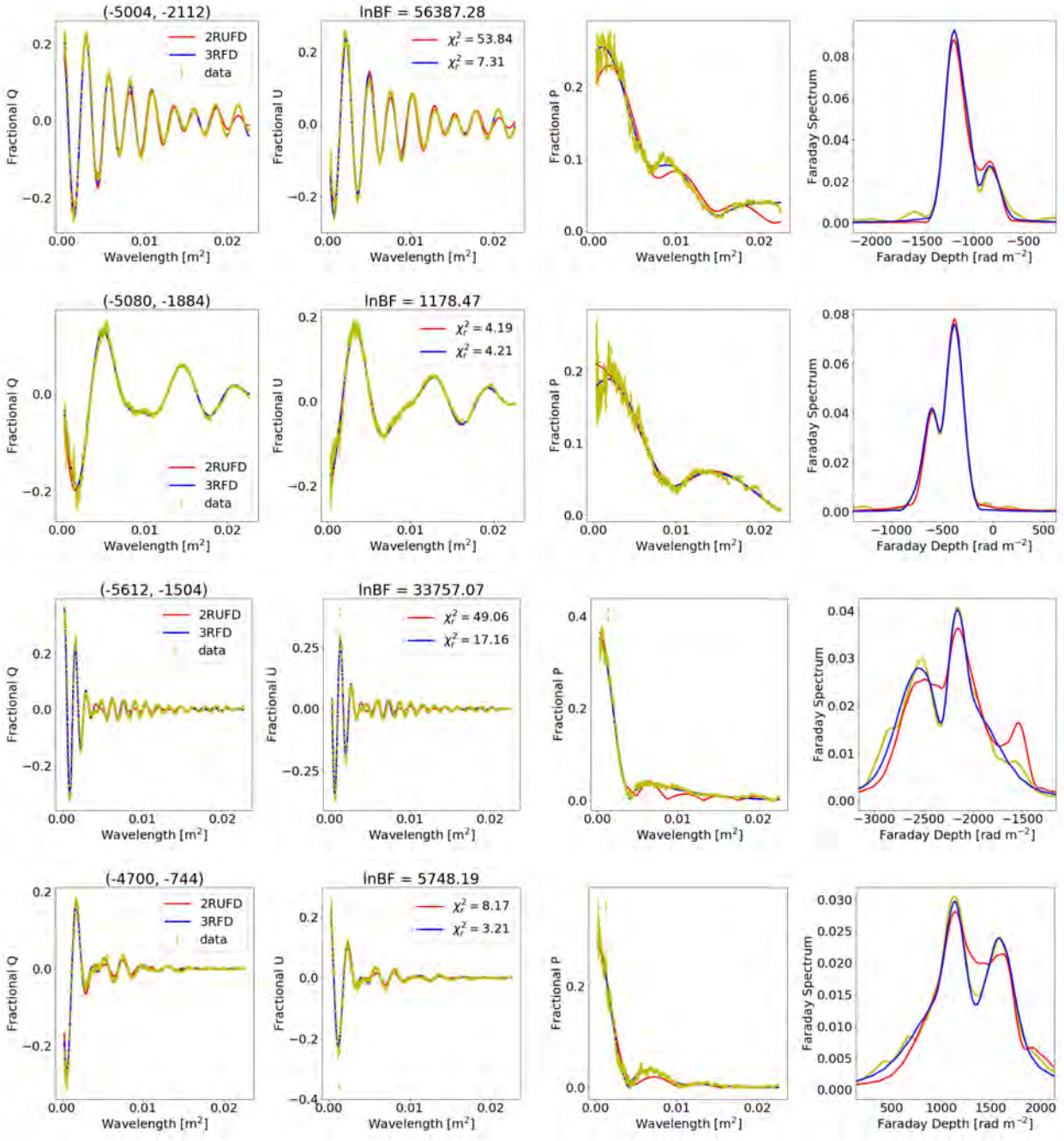

Figure 5.41: *Fitting examples in favour of model 3RFD over 2RUFD for blended double-peaked spectra lines-of-sight with complex oscillatory decay.* First column: Fractional Q vs λ^2. Second: Fractional U vs λ^2. Third: Fractional P vs λ^2. Fourth: Amplitude of the Faraday spectrum. Left title: Lines-of-sight location. Middle title: The $\ln$ BF.

5.8.4 The Estimated Parameters for the Leading Models

5.8.4.1 Three-Random Depolarising Screens

Figure 5.42 shows the derived intrinsic fractional polarisation of 3RFD fitted to lines-of-sight with blended double-peaked Faraday spectra. The ratios of the intrinsic fractional polarisation are shown in the bottom row. The lines-of-sight shown have fitting fractional errors ≤ 0.1 and $\chi^2_r \leq 5$. The number of lines-of-sight that satisfy these two conditions are given at the top of each plot. We find that the predicted components have different strengths, namely a strongly polarised component, intermediate and weak component. The strong component is generally a factor of 5 more polarised than the intermediate component and a factor $1 - 80$ more polarised than the weak component.

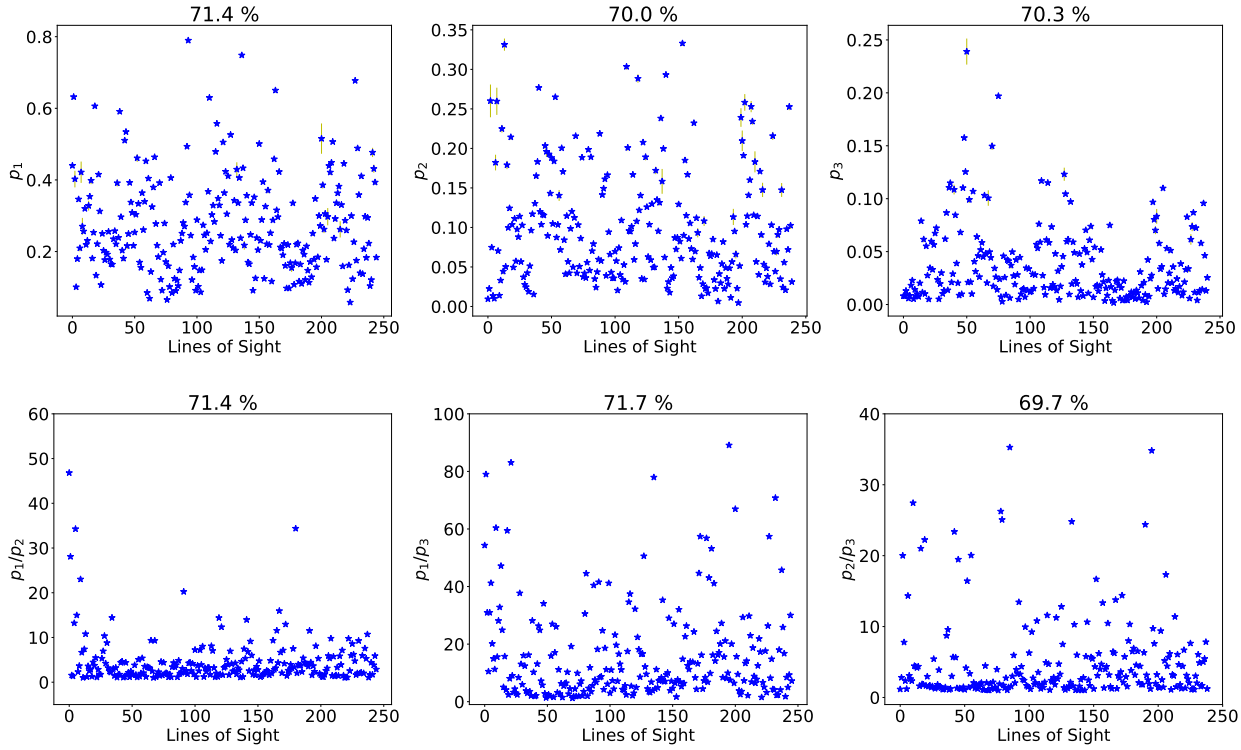

Figure 5.42: *The estimated intrinsic fractional polarisation of model 3RFD fitted to lines-of-sight with blended double-peaked Faraday spectra*. Top row: Fractional polarisation. Bottom row: Ratios of the fractional polarisation. Lines-of-sight shown have $\chi^2_r \leq 5$ and fractional errors ≤ 0.1. Title: A fraction of lines-of-sight that satisfies these two conditions. The fitting predicts components of different strengths, namely a strong, intermediate and weak component. The strong component is a factor of 5 more polarised than the intermediate component and a factor of $20 - 80$ more polarised than weak component.

Figure 5.43 shows the components' separation in Faraday space. The strong component is separated from the intermediate component by ± 250 rad m^{-2}, with a few lines-of-sight showing small separations close to ~ 0 rad m^{-2}. The strong and the weak component, as well as the intermediate and the weak component are separated by no more than ± 500 rad m^{-2}. The minimum separation between the intermediate and weak components is roughly ± 200 rad m^{-2}.

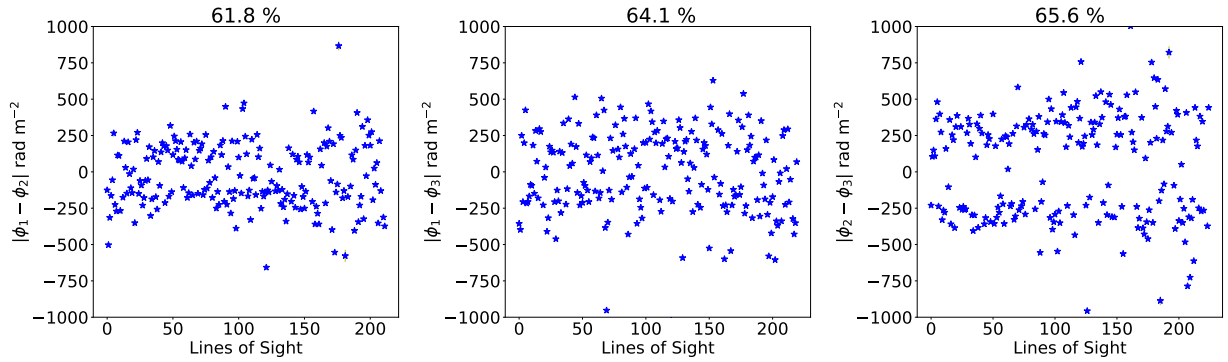

Figure 5.43: *The estimated components separation in Faraday space of model 3RFD fitted to lines-of-sight with blended double-peaked Faraday spectra*. Lines-of-sight shown have $\chi^2_r \leq 5$ and fractional errors ≤ 0.1. The strong and intermediate components are separated by no more than ± 250 rad m^{-2}, the strong and weak components, and the intermediate and weak by no more than ± 500 rad m^{-2}. The intermediate and weak component largely apart from each other, with minimum separation of $\sim \pm 200$ rad m^{-2}.

Figure 5.44 shows the derived Faraday dispersions of model 3RFD fitted to lines-of-sight with blended double-peaked Faraday spectra. The dispersions of the strong component range between $0 - 300$ rad m^{-2}, of the intermediate and weak component between $0 - 100$ rad m^{-2}.

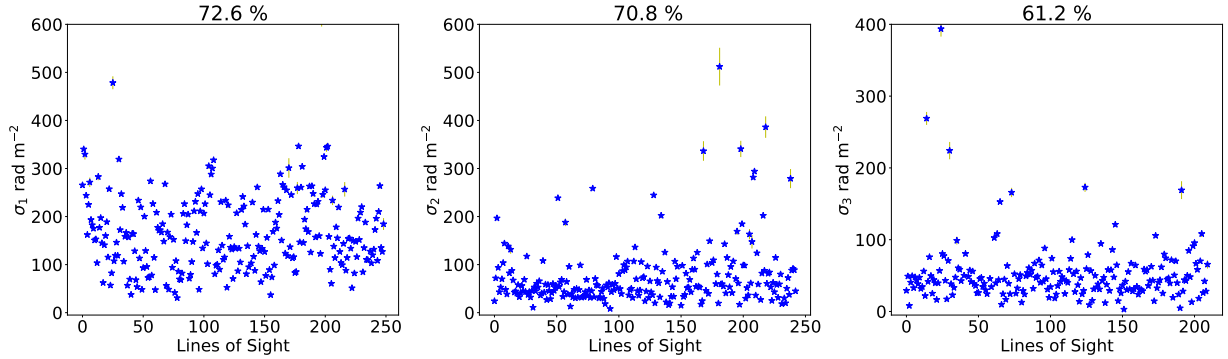

Figure 5.44: *The estimated Faraday dispersions of model 3RFD fitted to lines-of-sight with blended double-peaked Faraday spectra*. Lines-of-sight shown have $\chi^2_r \leq 5$ and fractional errors of ≤ 0.1. The dispersions of the strong component range between $\sim 0 - 300$ rad m^{-2} and of the weak and intermediate between $0 - 100$ rad m^{-2}.

5.8.4.2 Two Random-Uniform Depolarising Screens

Figures 5.45, 5.46 and 5.47 show the estimated parameters for model 2RUFD fitted to lines-of-sight with blended double-peaked Spectra. The lines-of-sight shown have $\chi^2_r \leq 5$ and fractional error of ≤ 0.1 in the estimated parameters. Figure 5.45 shows the intrinsic fractional polarisation of the two components (left and middle) and their ratios (right). The weak component is a factor of ≤ 10 less polarised than the strong component.

Figure 5.46 shows the derived Faraday dispersions of the two components (left and middle plot), and the separation of the components in Faraday space. The strong component has dispersions ranging between

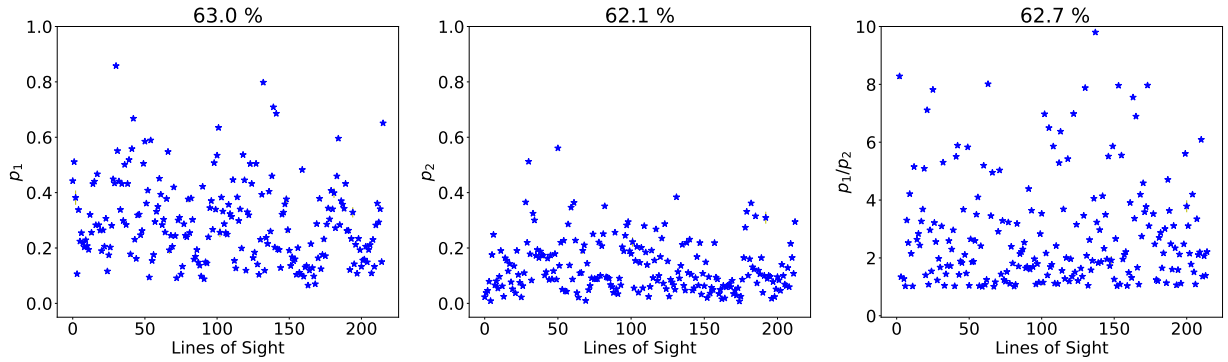

Figure 5.45: *The estimated intrinsic polarisation of model 2RUFD fitted to lines-of-sight with blended double-peaked Faraday spectra.* Lines-of-sight shown have $\chi^2_r \leq 5$ and fractional errors ≤ 0.1. The weak component is within a factor of 10 less polarised than the strong component.

$0 - 100$ rad m^{-2}, while the dispersions of the weak component range between $0 - 60$ rad m^{-2}, with a few lines-of-sight having larger dispersions. The strong and weak components are separated by no more than ± 200 rad m^{-2}.

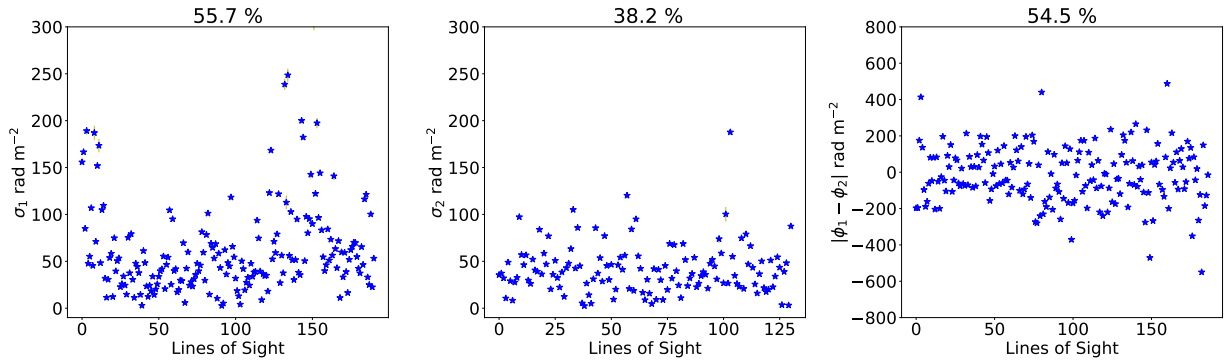

Figure 5.46: *The estimated Faraday dispersions and components separation in Faraday space of model 2RUFD fitted lines-of-sight with blended double-peaked Faraday spectra.* Left and middle: Faraday dispersions. Right: Separation. The dispersions of the strong component range between $\sim 1 - 100$ rad m^{-2} and of the weak component between $\sim 1 - 60$ rad m^{-2}. The components are separated by no more than ± 200 rad m^{-2}.

Figure 5.47 shows the unresolved uniform RM-difference of the two components in 2RUFD model. The RM-difference of the strong component are clustered between $200 - 400$ rad m^{-2}, with fewer points going up to ~ 1000 rad m^{-2}. For the weak component, the RM-difference are clustered between $100 - 400$ rad m^{-2}.

5.9 Resolved Double-Peaked Spectra

We now fit to the lines-of-sight with resolved double-peaked Faraday spectra, our final spectra data. The resolved double-peaked data represent only 7% of the lines-of-sight across Cygnus A at $0.75''$ beam resolution. We fit these data to similar models, namely 2RFD, 2RUFD, and 3RFD. Although we have already

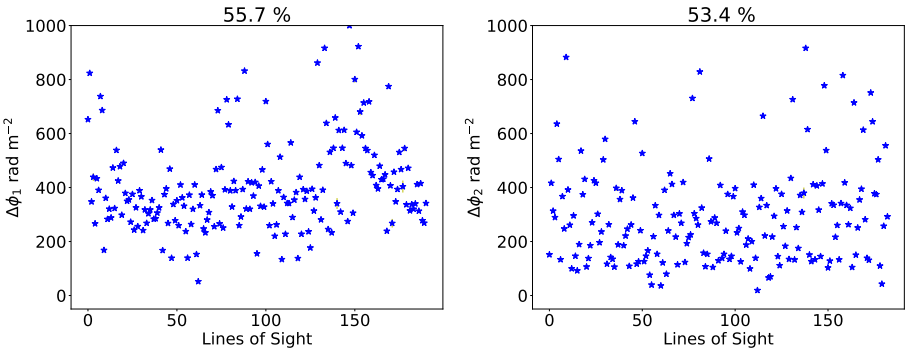

Figure 5.47: *The estimated RM-difference of model 2RUFD fitted to lines-of-sight with blended double-peaked Faraday spectra.* The RM-difference of the strong component are clustered between $200 - 400$ rad m^{-2} and of the weak component between $\sim 100 - 400$ rad m^{-2}, with fewer lines-of-sight having larger values.

demonstrated that 2RFD is not worth fitting to these data, we include the results for consistency.

5.9.1 Best-Fitting Model

Figure 5.48 shows the ln BF of 2RFD, 2RUFD and 3RFD models. Vertical lines separate from left to right the lines-of-sight with sinc-like, complex-oscillatory and complex non-oscillatory decaying depolarisation, respectively. The blue points are in favour of 3RFD (left and middle plot) and 2RUFD (middle), and the red points are in favour of 2RFD (left and middle) and 2RUFD (right). 3RFD is favoured for 99% of the lines-of-sight over 2RFD, and for 76% of the lines-of-sight over 2RUFD. 2RUFD, on the other hand, is favoured over 2RFD for 86% of the lines-of-sight.

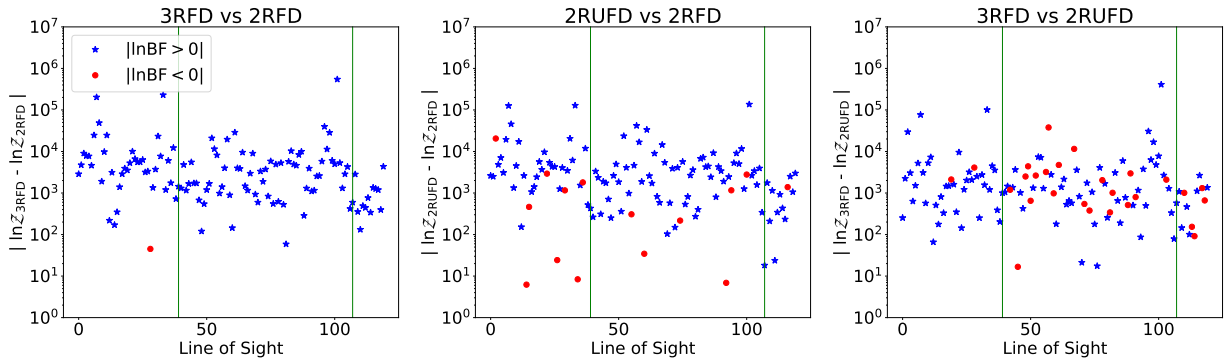

Figure 5.48: ln *BF solutions of model 2RFD, 2RUFD and 3RFD fitted to lines-of-sight with resolved double-peaked Faraday spectra.* Vertical lines (from left to right) separates lines-of-sight with sinc-like, complex oscillatory and complex non-oscillatory depolarisation. Blue points: In favour of 3RFD (left and right) and 2RUFD (middle). Red points: In favour of 2RFD (left and middle) and 2RUFD (right). 3RFD is favoured over 2RFD for 99% fitted lines-of-sight and over 2RUFD for 76%. 2RUFD is favoured over 2RFD for 86% lines-of-sight. Model 3RFD remains the most favoured of the models.

5.9.2 Goodness-of-Fit of Competing Models

Figure 5.49 shows the χ^2_r of 2RUFD and 3RFD for lines-of-sight with resolved double-peaked spectra. 3RFD fits 78% of the resolved double-peaked spectra relatively better than 2RUFD. The remaining 12% of the lines-of-sight are best described by 2RUFD.

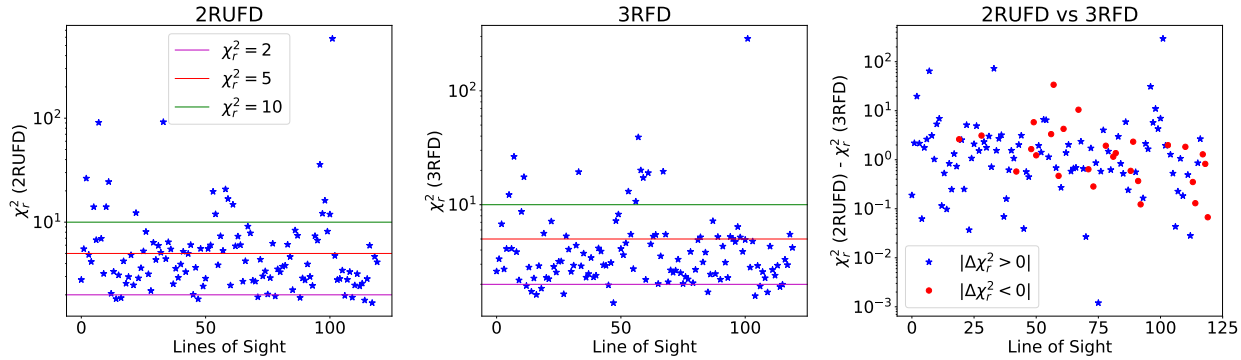

Figure 5.49: *χ^2_r of model 2RUFD and 3RFD fitted to lines-of-sight with resolved double-peaked spectra data.* Left: χ^2_r of 2RUFD. Middle: χ^2_r of 3RFD. Right: Difference in the χ^2_r of 2RUFD and 3RFD. Model 3RFD is favoured over 2RUFD for 78% of the fitted lines-of-sight.

5.9.3 Fitting Examples

Figure 5.50 shows example lines-of-sight with resolved double-peaked spectra in favour of 2RUFD over 3RFD. Figures 5.51 - 5.56 show example lines-of-sight in favour of 3RFD over 3RUFD. We show more examples to allow the reader to appreciate the complicated structures that these models can reproduce.

5.9.4 The Estimated Parameters for the Leading Model

In this section, we present the estimated model fitting parameters for 2RUFD and 3RFD models fitted to the resolved double-peaked lines-of-sight. The parameters presented have $\chi^2_r \leq 5$ and fractional errors of ≤ 0.1. A fraction of lines-of-sight that satisfy these two conditions are specified in the title of each plot.

5.9.4.1 Three-Random Depolarising Screens

Figure 5.57 shows the derived intrinsic fractional polarisation (top row) and ratios (bottom row) of 3RFD for lines-of-sight with resolved double-peaked Faraday spectra. The strong component is $10\% - 70\%$ polarised and the intermediate and weak components are similarly polarised up to 20%. The intermediate and weak components are about a factor of $1 - 15$ less polarised than the strong component.

Figure 5.58 shows the estimated components' separation in Faraday space of model 3RFD. The lines-of-sight in question are those with resolved double-peaked spectra. The intermediate and weak components are separated from the strong component by no more than ± 500 rad m^{-2} but from each other by up to ~ 1200 rad m^{-2} with a minimum separation of ± 200 rad m^{-2}.

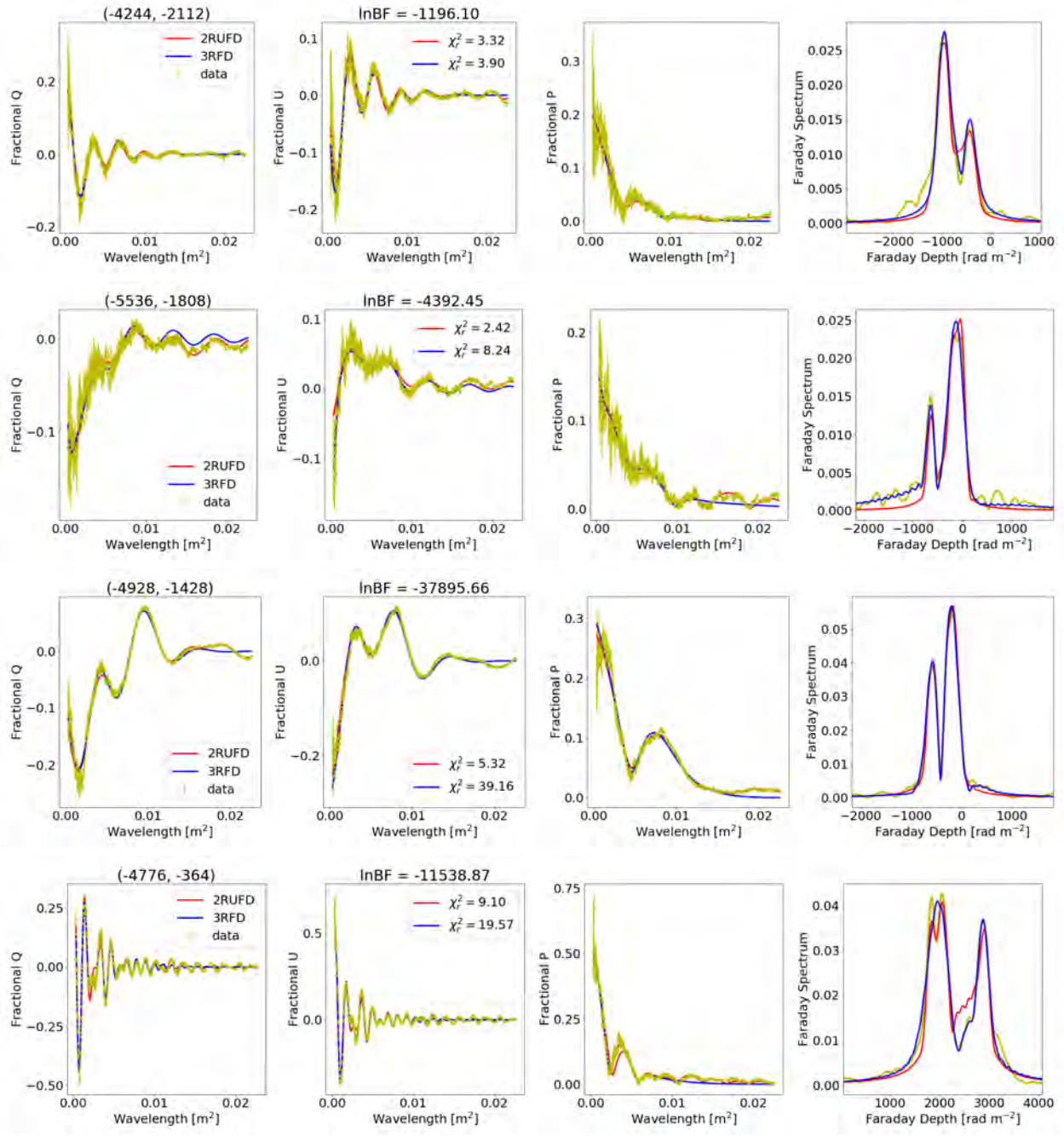

Figure 5.50: *Fitting examples in favour of model 2RUFD over 3RFD for lines-of-sight with resolved double-peaked spectra*. First column: Fractional Q vs λ^2. Second: Fractional U vs λ^2. Third: Fractional P vs λ^2. Fourth: Amplitude of the Faraday spectrum. Left title: Lines-of-sight location. Middle title: The ln BF.

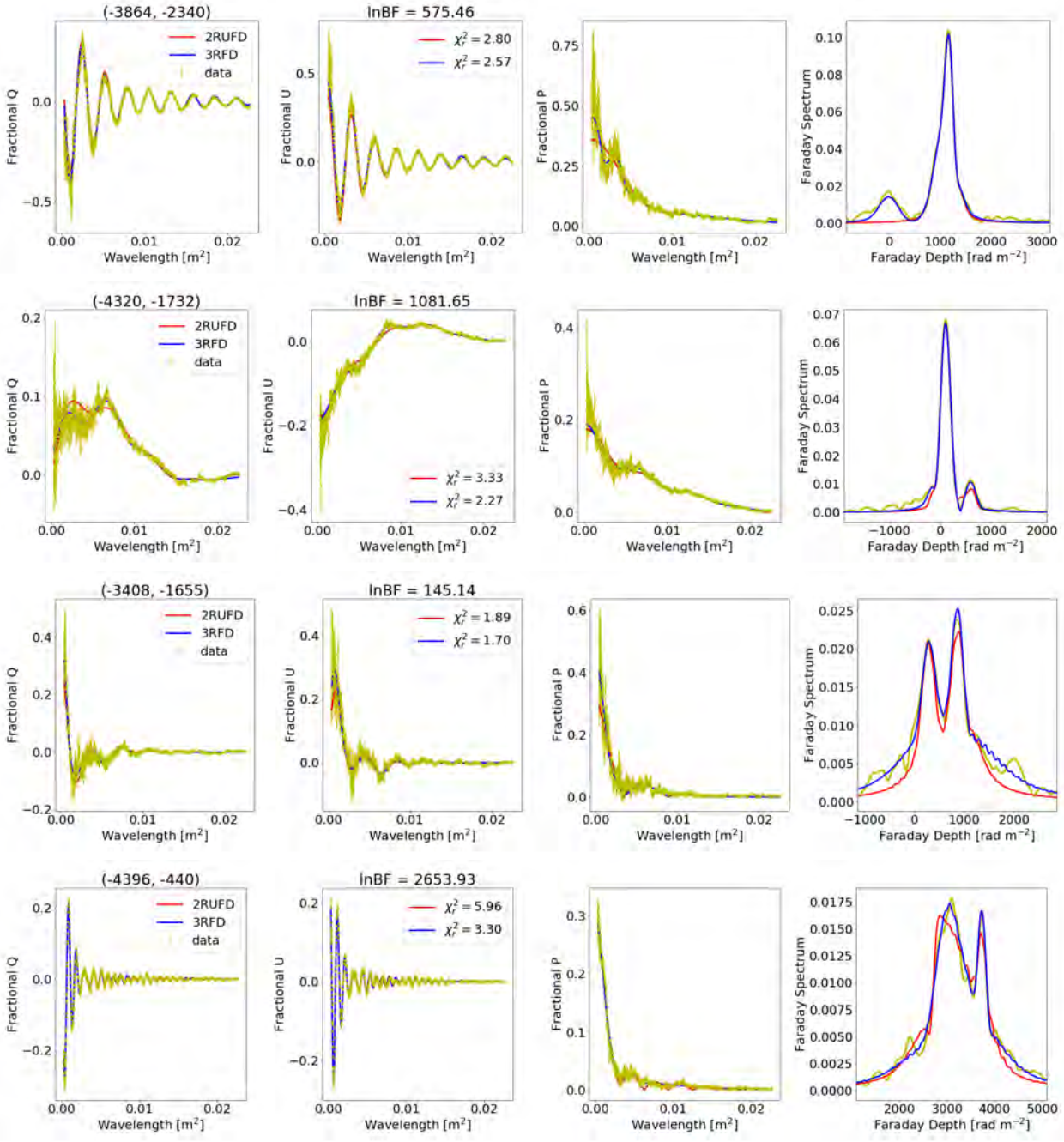

Figure 5.51: *Fitting examples in favour of model 3RFD over 2RUFD for resolved double-peaked spectra lines-of-sight with complex non-oscillatory decay*. First column: Fractional Q vs λ^2. Second: Fractional U vs λ^2. Third: Fractional P vs λ^2. Fourth: Amplitude of the Faraday spectrum. Left title: Lines-of-sight location. Middle title: The $\ln$ BF.

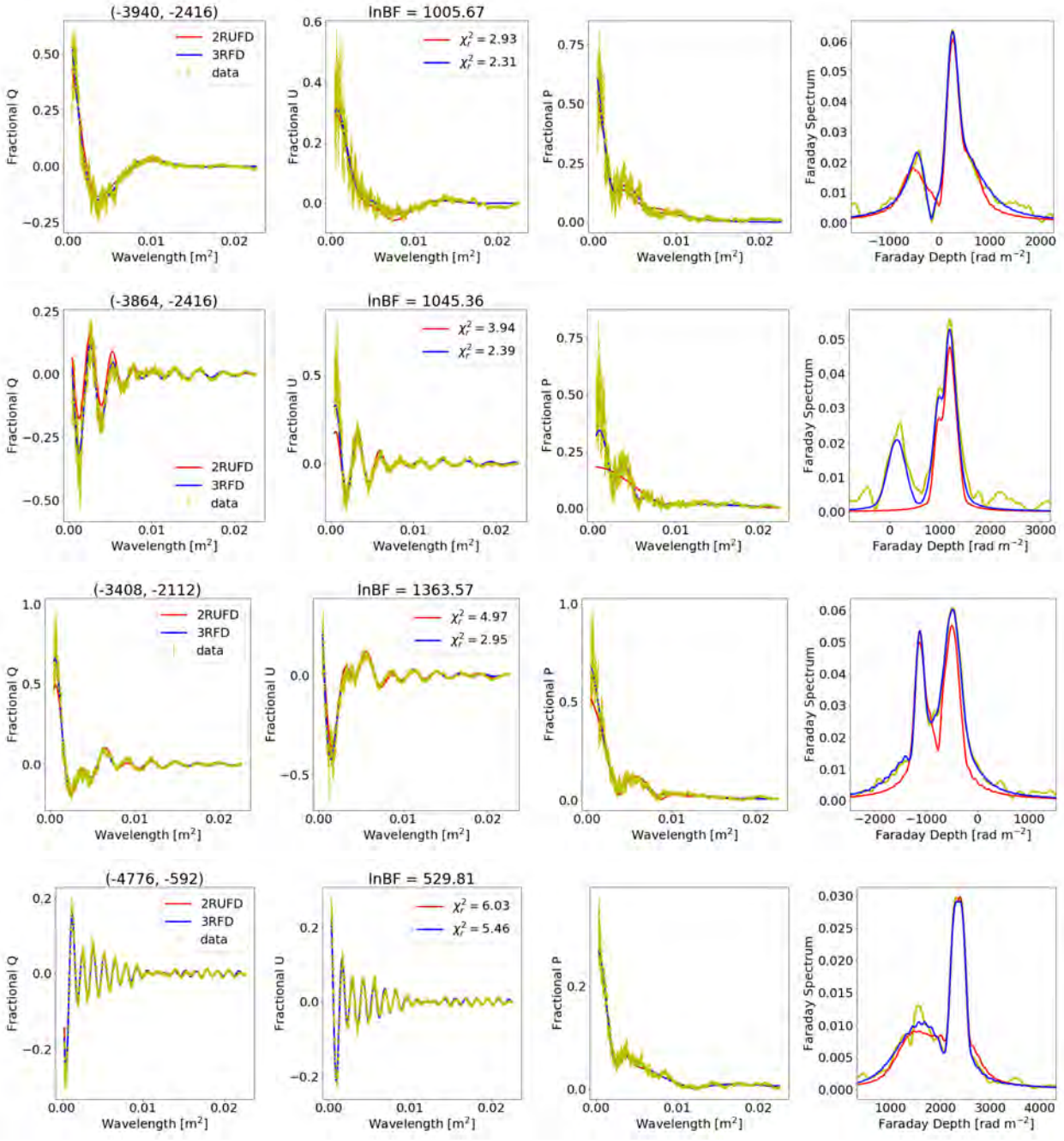

Figure 5.52: *Fitting examples in favour of model 3RFD over 2RUFD for resolved double-peaked spectra lines-of-sight with complex oscillatory decay.* First column: Fractional Q vs λ^2. Second: Fractional U vs λ^2. Third: Fractional P vs λ^2. Fourth: Amplitude of the Faraday spectrum. Left title: Lines-of-sight location. Middle title: The $\ln$ BF.

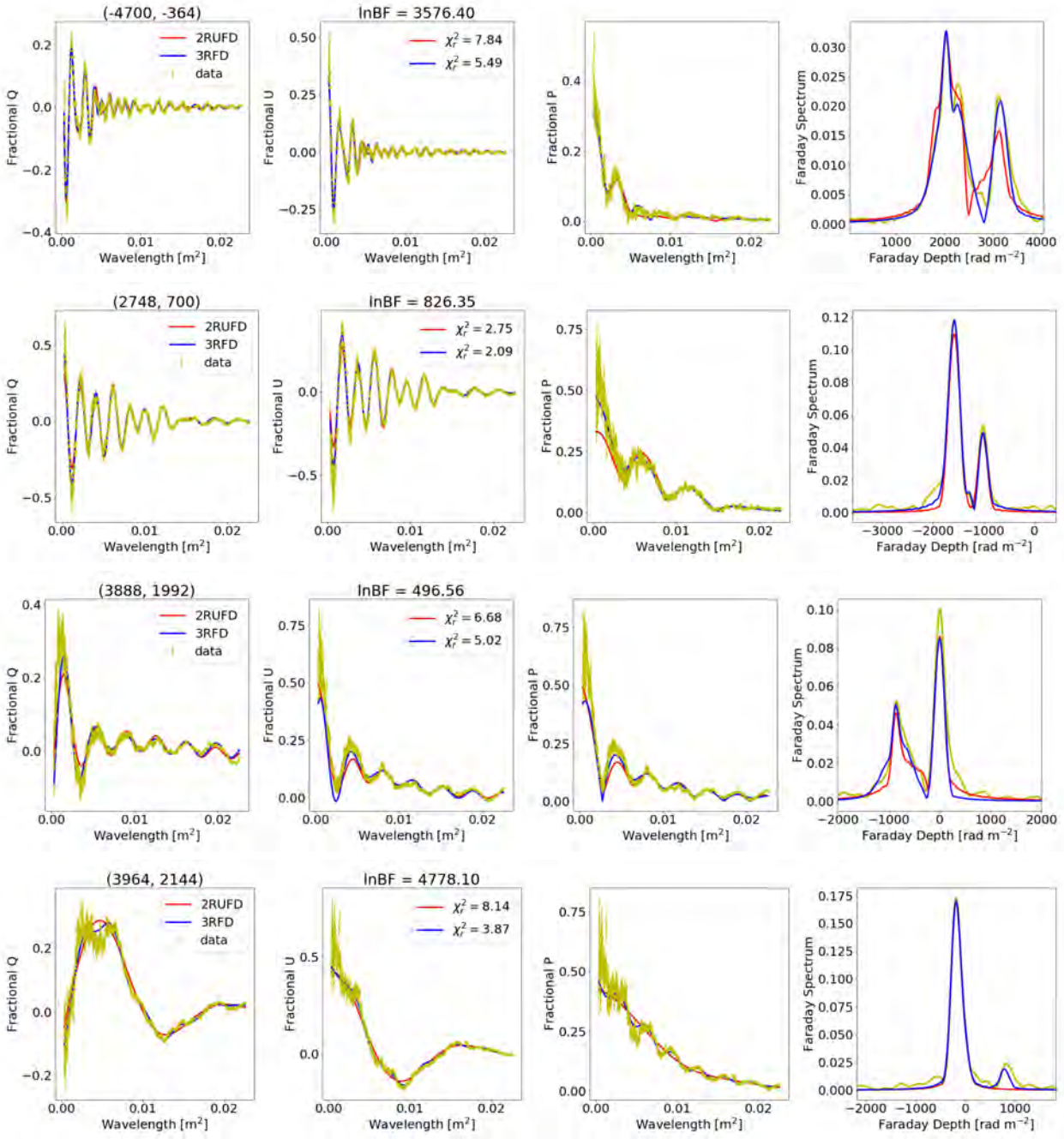

Figure 5.53: *Similar to Figure 5.52.* First column: Fractional Q vs λ^2. Second: Fractional U vs λ^2. Third: Fractional P vs λ^2. Fourth: Amplitude of the Faraday spectrum. Left title: Lines-of-sight location. Middle title: The $\ln$ BF.

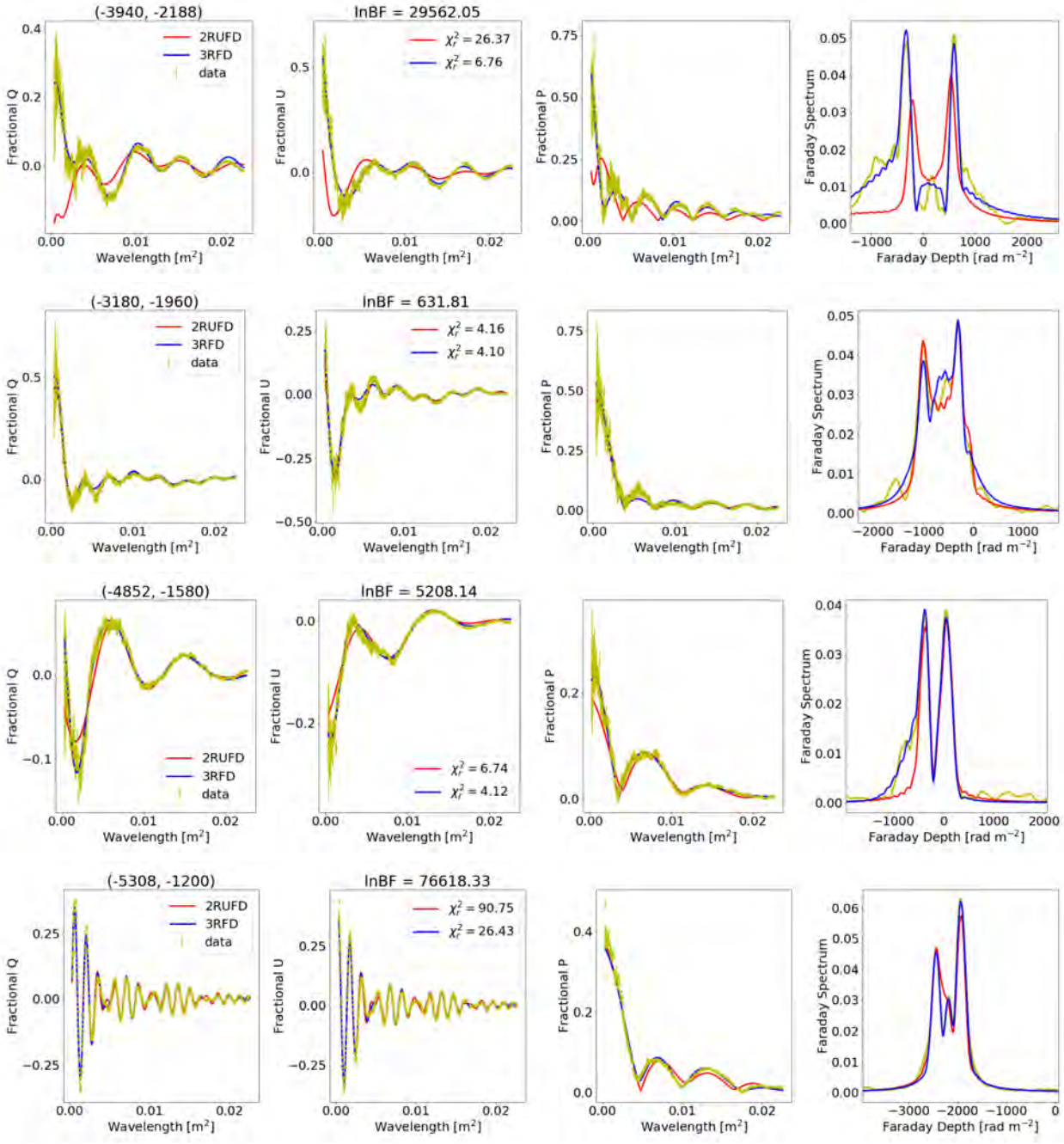

Figure 5.54: *Fitting examples in favour of model 3RFD over 2RUFD for resolved double-peaked spectra lines-of-sight with sinc-like decay*. First column: Fractional Q vs λ^2. Second: Fractional U vs λ^2. Third: Fractional P vs λ^2. Fourth: Amplitude of the Faraday spectrum. Left title: Lines-of-sight location. Middle title: The $\ln$ BF.

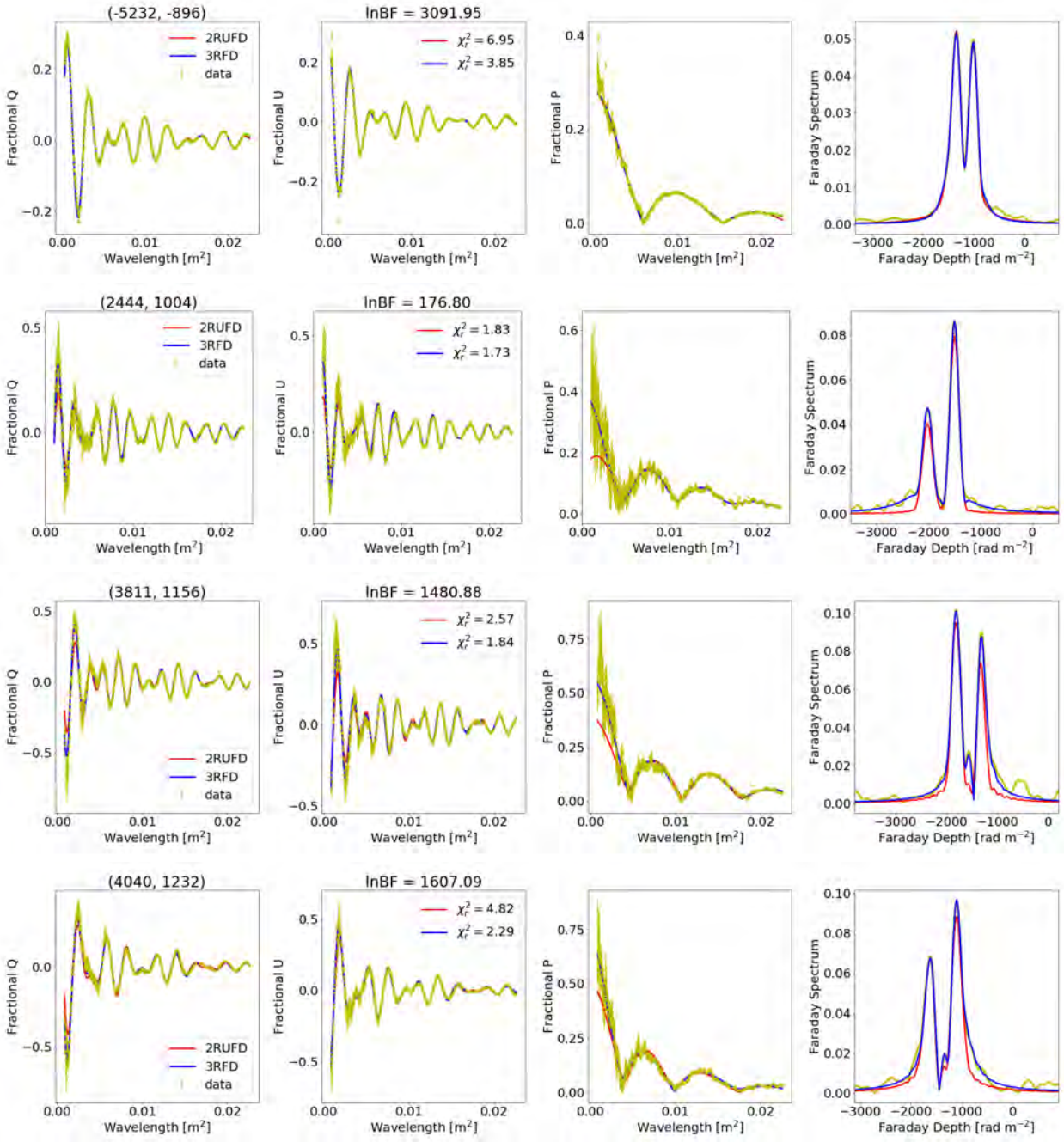

Figure 5.55: *Similar to Figure 5.54.* First column: Fractional Q vs λ^2. Second: Fractional U vs λ^2. Third: Fractional P vs λ^2. Fourth: Amplitude of the Faraday spectrum. Left title: Lines-of-sight location. Middle title: The $\ln$ BF.

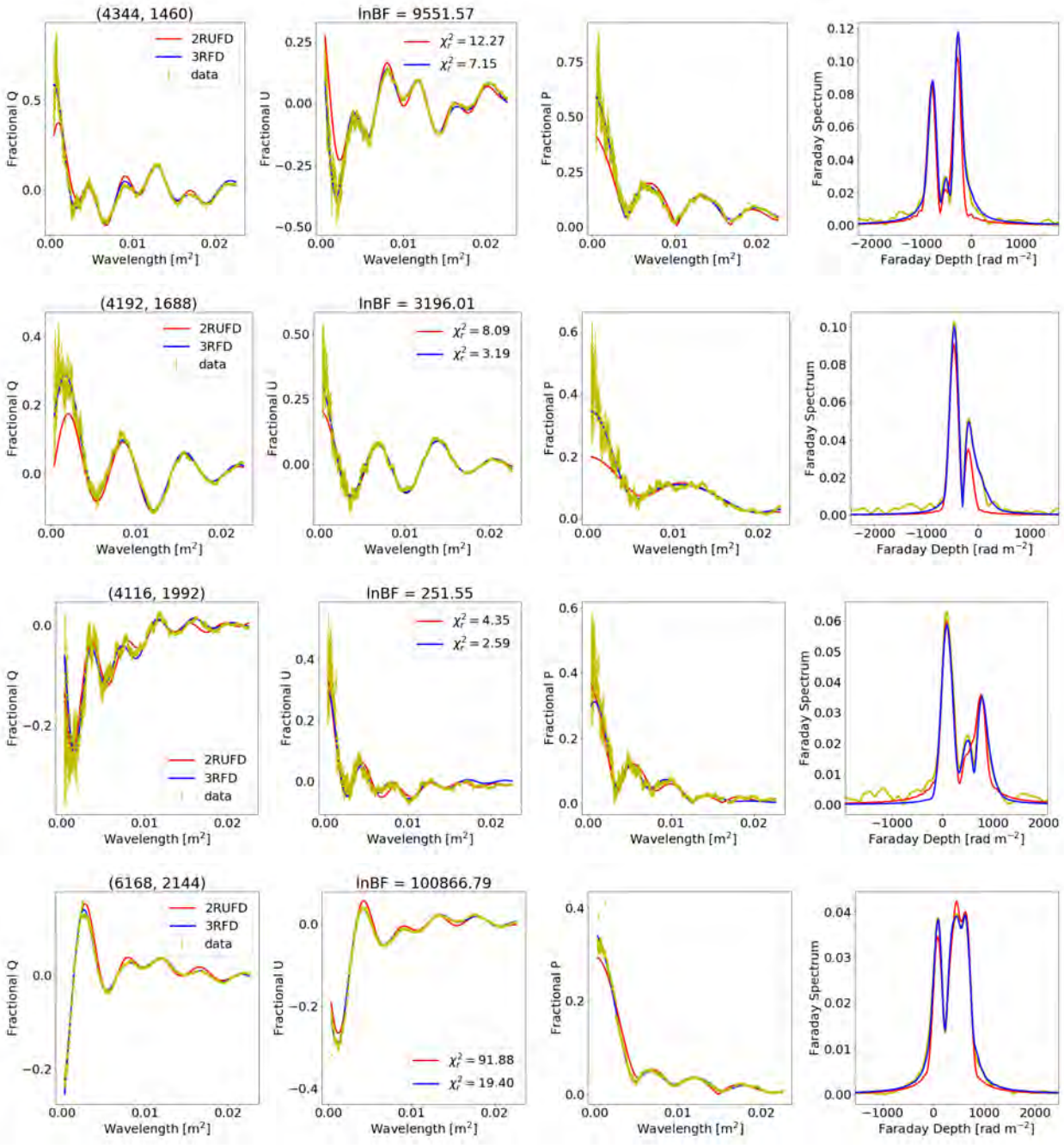

Figure 5.56: *Similar to Figures 5.54 and 5.55.* First column: Fractional Q vs λ^2. Second: Fractional U vs λ^2. Third: Fractional P vs λ^2. Fourth: Amplitude of the Faraday spectrum. Left title: Lines-of-sight location. Middle title: The ln BF.

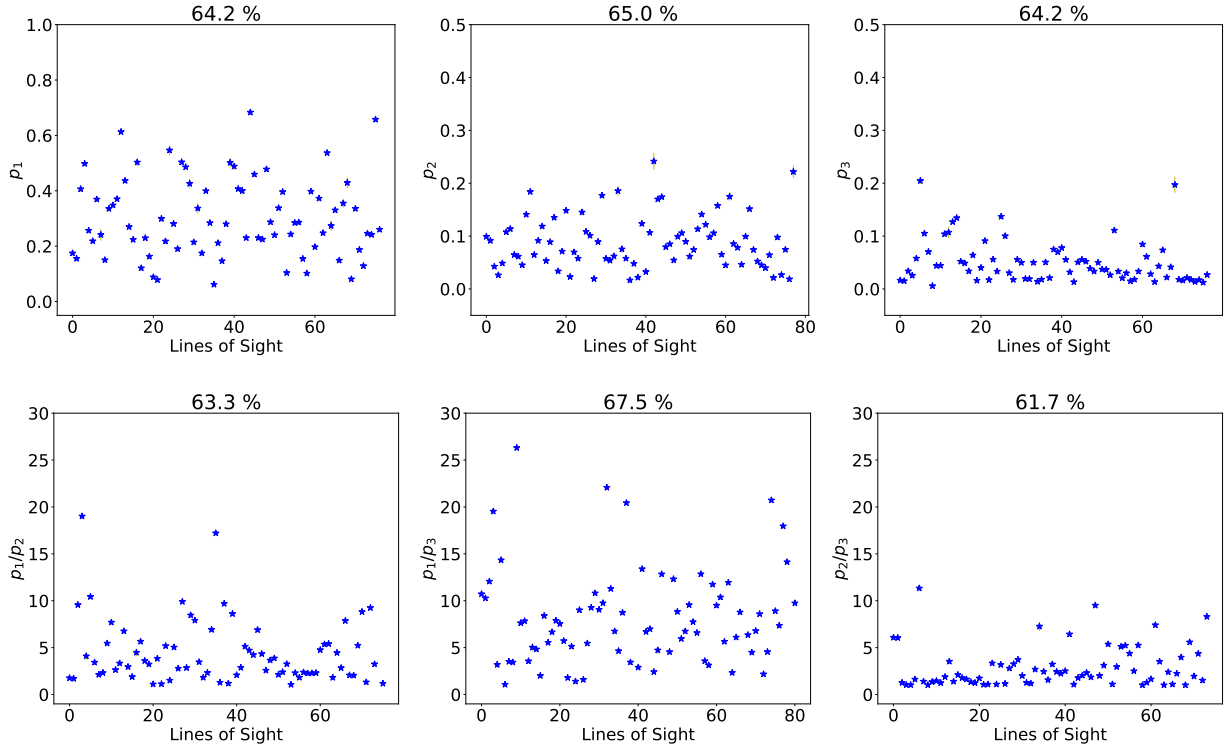

Figure 5.57: *The estimated intrinsic fractional polarisation of model 3RFD fitted to lines-of-sight with resolved double-peaked Faraday spectra line-of-sight.* The lines-of-sight shown have fractional errors ≤ 0.1 and $\chi^2_r \leq 5$. Title: A fraction of lines-of-sight that satisfy these two conditions. The modelling predicts three components with different fractional polarisation, namely the strong, intermediate and weak. The intermediate and weak components are comparable in strength (both having polarisation of up to 20%) and are a factor of $1 - 10$ less polarised than the strong component.

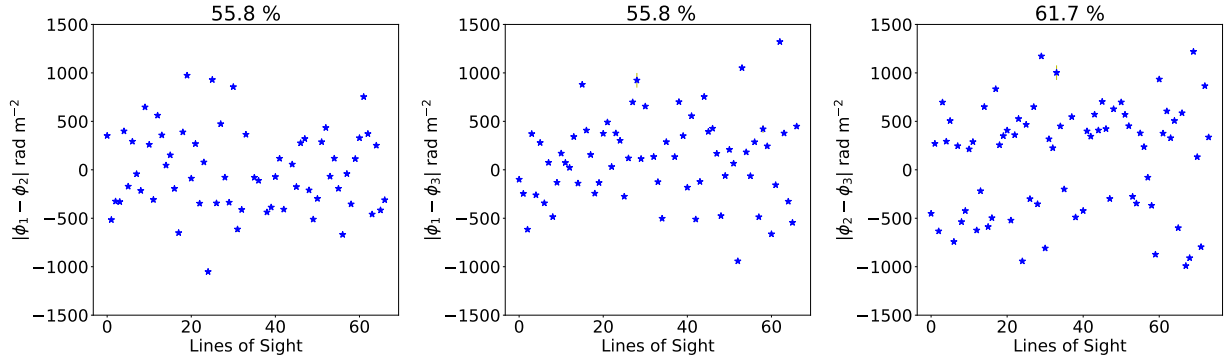

Figure 5.58: *The estimated components separation in Faraday space of model 3RFD fitted to lines-of-sight with resolved double-peaked spectra.* Lines-of-sight shown have $\chi^2_r \leq 5$ and fractional errors ≤ 0.1. The intermediate and weak components are separated from the strong component by no more than ± 500 rad m^{-2} and from each other by $\sim 200 - 1200$ rad m^{-2}.

Figure 5.59 shows the derived Faraday dispersions of model 3RFD fitted to lines-of-sight with resolved double-peaked Faraday spectra. The strong component has dispersions going up to 600 rad m^{-2}, and the dispersions of the intermediate and weak components range between $\sim 1 - 100$ rad m^{-2}.

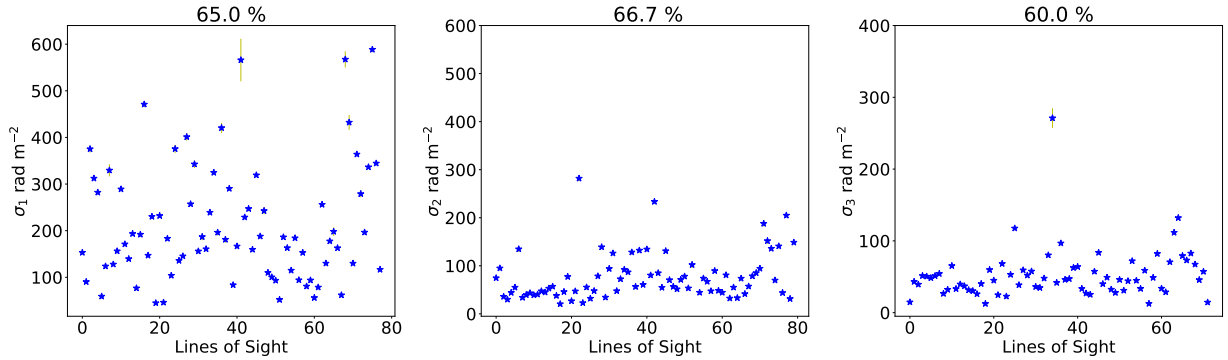

Figure 5.59: *The estimated Faraday dispersions of model 3RFD fitted to lines-of-sight with resolved double-peaked Faraday spectra*. Lines-of-sight shown have $\chi^2_r \leq 5$ and fractional errors ≤ 0.1. The dispersions of the strong component range between $10 - 600$ rad m^{-2} and the intermediate and weak components have dispersions $1 - 100$ rad m^{-2}.

5.9.4.2 Two Random-Uniform Depolarising Screens

Figure 5.60 shows the derived intrinsic fractional polarisation (left and middle plot) and ratios (right plot) of model 2RUFD fitted to the resolved double-peaked spectra data. The strong component is polarised to about $10\% - 60\%$, with a few lines-of-sight having $> 60\%$ polarisation, and is a factor of $2 - 4$ more polarised than the weak component.

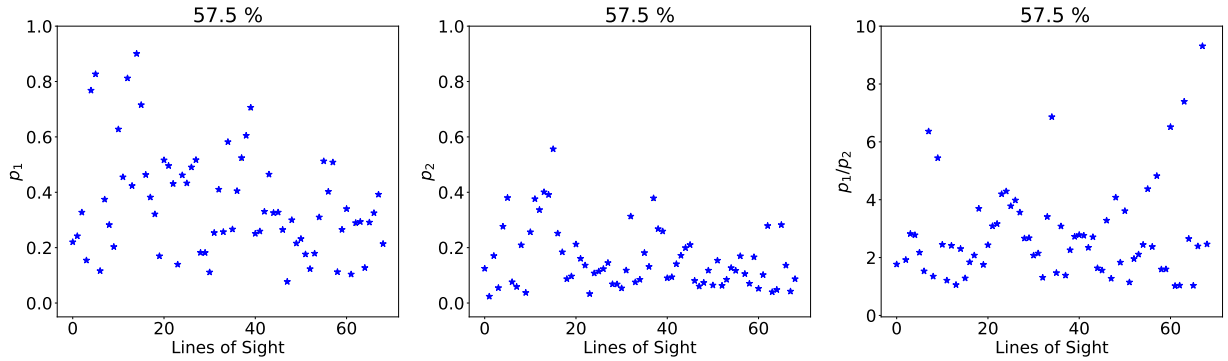

Figure 5.60: *The estimated intrinsic fractional polarisation of model 2RUFD fitted to lines-of-sight with resolved double-peaked Faraday spectra*. Lines-of-sight shown have $\chi^2_r \leq 5$ and fractional errors ≤ 0.1. The strong component is $10\% - 60\%$ polarised, with a few lines-of-sight having $> 60\%$ polarisation, and a factor of $2 - 4$ more polarised than the weak component.

Figure 5.61 shows the Faraday dispersions of model 2RUFD (left and middle plot) and the component's separation in Faraday space (right). The dispersions of both components range between $1 - 100$ rad m^{-2},

with the majority of the solutions concentrated below 50 rad m^{-2}. The components are separated in Faraday space by no more than ± 600 rad m^{-2}.

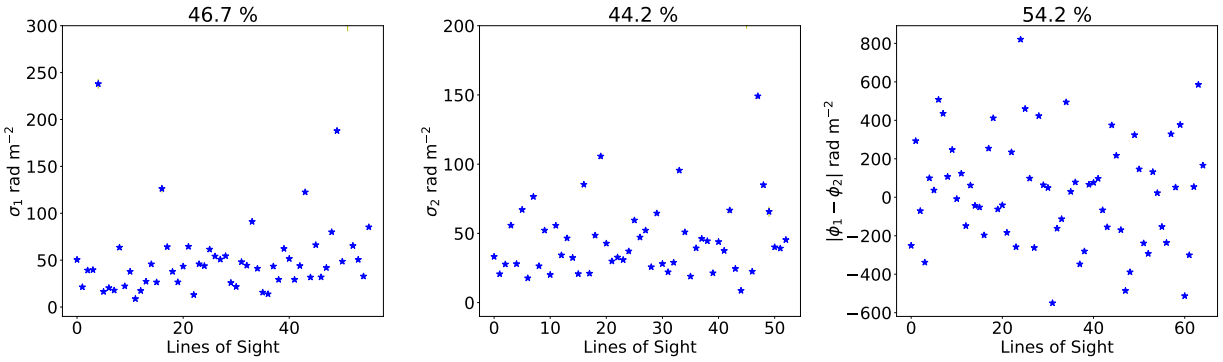

Figure 5.61: *The estimated Faraday dispersions and components separation of model 2RUFD fitted to lines-of-sight with resolved double-peaked spectra*. Left and middle plot: Faraday dispersions. Right plot: Components separation. Lines-of-sight shown have $\chi^2_r \leq 5$ and fractional errors ≤ 0.1. Title: A fraction of lines-of-sight that satisfy these two conditions. The dispersions of both components range between $1- \leq 100$ rad m^{-2}, with most dispersions concentrated below 50 rad m^{-2}. The components are separated by no more than ± 600 rad m^{-2}.

Figure 5.62 shows the unresolved uniform RM-difference of model 2RUFD across the $0.75''$ resolution beam for lines-of-sight with resolved double-peaked spectra. The RM-difference associated with the strong component range between $200 - 1300$ rad m^{-2}, with the majority clustered between $200 - 800$ rad m^{-2}. The unresolved uniform RM-differences of the weak component range between $50 - 1000$ rad m^{-2}, with the majority concentrated below 400 rad m^{-2}.

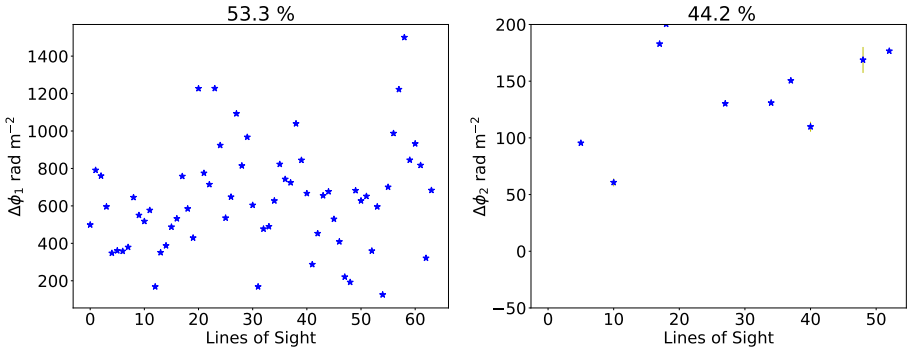

Figure 5.62: *The estimated RM-difference of model 2RUFD fitted to lines-of-sight with resolved double-peaked Faraday spectra*. Lines-of-sight shown have $\chi^2_r \leq 5$ and fractional errors ≤ 0.1. Title: A fraction of lines-of-sight that satisfy these two conditions. The RM-difference associated with a strong component range between $200 - 1300$ rad m^{-2}, with the majority concentrated between $200 - 800$ rad m^{-2}. The RM-differences of the weak component range between $50 - 1000$ rad m^{-2}, with the majority of the RM-difference clustered below 400 rad m^{-2}.

5.10 Summary: Model Fitting

Table 5.3 presents a fraction of lines-of-sight in favour of 2RUFD over 2RFD (second column), 3RFD over 2RFD (third column) and 3RFD and 2RUFD (fourth column) as determined using the $\ln$ BF. 3RFD is favoured for almost 100% of the lines-of-sight over 2RFD and for $\sim 75\%$ of the lines-of-sight over 2RUFD. 2RUFD is favoured over 2RFD for $\sim 85\%$. These results suggest that the data are best described by multiple random depolarising components, both with and without unresolved uniform RM-differences.

Table 5.3: *A fraction of lines-of-sight favouring by one model over the other based on the* $\ln$ *BF*

Faraday Class	2RUFD over 2RFD [%]	3RFD over 2RFD [%]	3RFD over 2RUFD [%]
Single-peaked	85	98	69
Single-peaked + small peaks	83	99	78
blended double-peaked	80	98	73
resolved double-peaked	86	99	76

Table 5.4 presents a fraction of lines-of-sight with solutions having $\chi^2_r \leq 5$ for the 2RUFD, 2RFD and 3RFD models. On average, 2RFD only fits 50% of the lines-of-sight well, 2RUFD fits about 69% and 3RFD about 77%. The performance of each model decreases towards complex spectra. Ideally, we would prefer $\chi^2_r \approx 1$. However, the value of the χ^2_r is affected by several issues (see Section 5.5). We would like to point out that the components need not be three, it is possible that as we increase the number of components, the fits improve and the $\ln$ BF also favours these models. However, we ended with three components due to time constraints. In the near future, it will be important to incorporate more components to check what N-number of components is needed. The current fits provide an important insight: the presence of multiple Faraday components.

Table 5.4: *A fraction of fitted lines-of-sight with* $\chi^2_r \leq 5$

Faraday Class	2RFD [%]	2RUFD [%]	3RFD [%]
Single-peaked	60	78	78
Single-peaked + small peaks	56	70	80
Blended double-peaked	45	67	76
Resolved double-peaked	38	61	74

Table 5.5 shows a fraction of lines-of-sight with the difference in the models' χ^2_r greater than zero. The second row shows those in favour of 2RUFD and the third and fourth columns show those in favour of 3RFD. 2RUFD best describes the data than 2RFD, for 81% of the lines-of-sight. 3RFD best describes the data than 2RFD for 97% of the lines-of-sight and 2RUFD for 73% of the lines-of-sight. Thus, unresolved uniform RM-differences are important for 27% of the lines-of-sight over an additional depolarising component (3RFD).

Table 5.5: *A fraction of fitted lines-of-sight with the difference in χ^2_r greater than zero*

Faraday Class	2RUFD over 2RFD [%]	3RFD over 2RFD [%]	3RFD over 2RUFD [%]
Single-peaked	79	95	69
Single-peaked + small peaks	80	97	75
Blended double-peaked	78	98	69
Resolved double-peaked	86	99	78

Figure 5.63 shows the spatial distribution of the lines-of-sight favouring 3RFD (blue) and 2RUFD (red) for the four Faraday classes, namely the single-peaked spectra, single-peaked with smaller peaks, blended double-peaked and resolved double-peaked spectra. The distribution is not random and yet also not largely clustered except for a few nearby lines-of-sight.

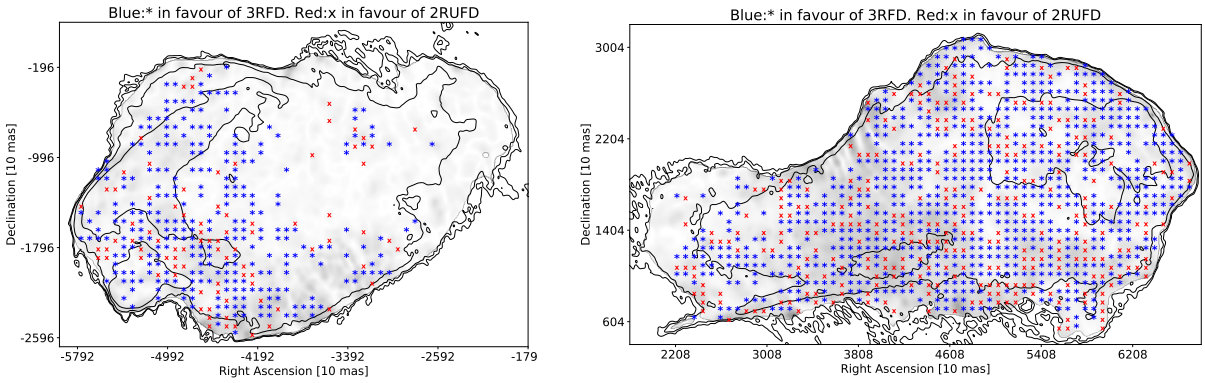

Figure 5.63: *Spatial distribution of the fitted lines-of-sight in favour of model 3RFD and 2RUFD across Cygnus A.* Blue "*": In favour of 3RFD. Red "x": In favour of 2RUFD.

5.11 Reconciling the Estimated Parameters

Tables 5.6 and 5.7 give a summary of the range of the estimated parameters for 3RFD and 2RUFD, respectively. This range excludes outliers. In both models, the intrinsic fractional polarisation of the strongest component ranges between $10\% - 60\%$. The weaker component of 2RUFD is consistent with the intermediate component of model 3RFD. With the exception that 2RUFD estimates a relatively more polarised component ranging between $2\% - 40\%$, while 3RFD estimates a range between $1\% - 30\%$.

The two components in 2RUFD have similar Faraday dispersions ranging between $10 - 200$ rad m^{-2}. These dispersions are consistent with the intermediate and weaker components of 3RFD. 3RFD estimates larger dispersions for the strong component ranging between $20 - 400$ rad m^{-2}.

2RUFD estimates components that are separated by $10 - 200$ rad m^{-2}; going up to 600 rad m^{-2} for the resolved double-peaked spectra data. 3RFD, on the other hand, estimates larger separations ranging between

$10-400$ rad m^{-2} for the strong component and $10-500$ rad m^{-2} for the intermediate and weak components, going up to 750 rad m^{-2} for the resolved double-peaked spectra.

The estimated unresolved uniform RM-differences for model 2RUFD range between $40-800$ rad m^{-2}; with fewer lines-of-sight with resolved double-peaked spectra having RM-difference up to 1000 rad m^{-2}.

Table 5.6: *Estimated Parameter Ranges of Model 3RFD*

Parameter	Single-peaked	Single-peaked + small peaks	Blended double-peaked	Resolved double-peaked
p_1	$0.1-0.6$	$0.1-0.6$	$0.1-0.5$	$0.1-0.6$
p_2	$0.01-0.3$	$0.02-0.3$	$0.02-0.25$	$0.02-0.2$
p_3	$0.005-0.1$	$0.005-0.1$	$0.004-0.125$	$0.0125-0.15$
σ_1	$20-150$	$40-350$	$40-350$	$40-400$
σ_2	$10-100$	$20-120$	$15-150$	$20-150$
σ_3	$10-80$	$20-100$	$10-80$	$15-80$
$\lvert\phi_1-\phi_2\rvert$	$10-200$	$50-400$	$25-300$	$50-750$
$\lvert\phi_1-\phi_3\rvert$	$10-500$	$50-500$	$25-400$	$50-750$
$\lvert\phi_2-\phi_3\rvert$	$50-500$	$100-500$	$150-600$	$200-750$

Note: σ and RM separation are in units of rad m^{-2}.

Table 5.7: *Estimated Parameter Range of model 2RUFD*

Parameter	Single-peaked	Single-peaked + small peaks	Blended double-peaked	Resolved double-peaked
p_1	$0.1-0.6$	$0.1-0.6$	$0.1-0.6$	$0.1-0.6$
p_2	$0.02-0.2$	$0.02-0.2$	$0.02-0.4$	$0.04-0.4$
σ_1	$20-150$	$20-200$	$10-120$	$15-75$
σ_2	$20-80$	$10-60$	$10-100$	$20-80$
$\lvert\phi_1-\phi_2\rvert$	$10-100$	$20-200$	$25-200$	$25-600$
$\Delta\phi_1$	$40-500$	$100-700$	$250-600$	$150-1000$
$\Delta\phi_2$	$40-800$	$100-800$	$100-400$	$100-800$

Note: σ, RM separation and $\Delta\phi$ are in units of rad m^{-2}.

Figure 5.64 compares the mean of the 1D Gaussian fitted to Faraday spectra data with the average of the Faraday depths of the components weighted by their respective intrinsic fractional polarisation. The left plot shows 3RFD and the right plot shows 2RUFD. The derived weighted RM are consistent with the mean of the Gaussian fits. A few data points deviate from the straight line, however these are generally associated with large fitting errors. Figure 5.11 have already demonstrated that the mean RM of the 1D Gaussian is consistent with RM at $0.30''$. Thus, we expect the same consistency between weighted RM at $0.75''$ with RM at $0.30''$.

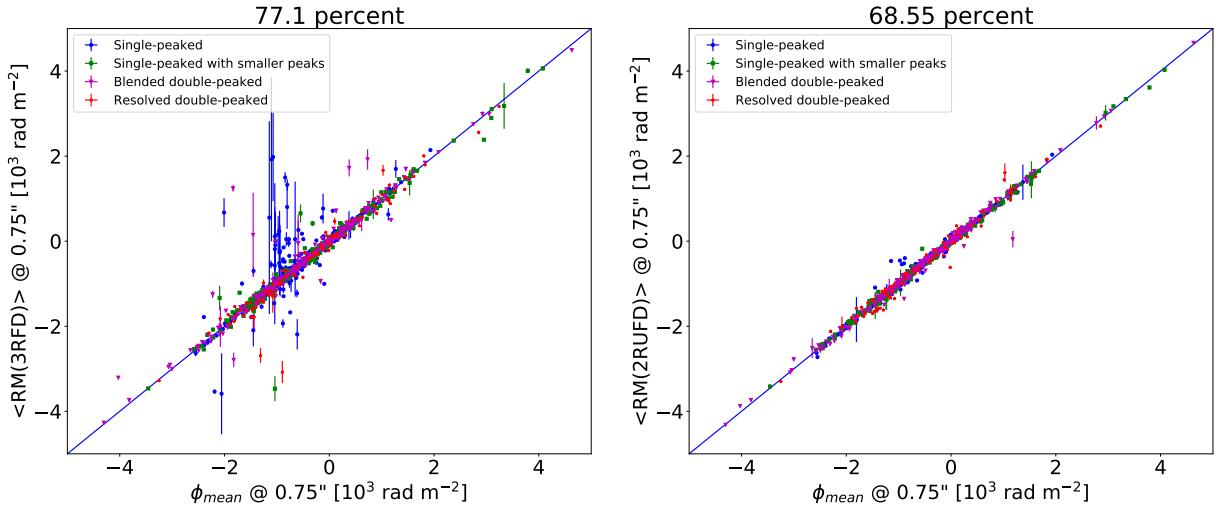

Figure 5.64: *A comparison of RM derived from wideband modelling with those derived from fitting 1D Gaussian function.* Lines-of-sight shown have $\chi^2_r \leq 5$ from wideband modelling solutions. The RM are consistent, with a few deviations. However, the points that deviate are associated with large fitting errors.

Figure 5.65 compares the intrinsic fractional polarisation derived from model fitting to $2-18$ GHz data at $0.75''$ and those derived from fitting to $6-18$ GHz data at $0.30''$. The intrinsic fractional polarisation at higher resolutions are relatively larger than at lower resolutions. We, therefore, attribute the deviation from a straight line to beam-related depolarisation.

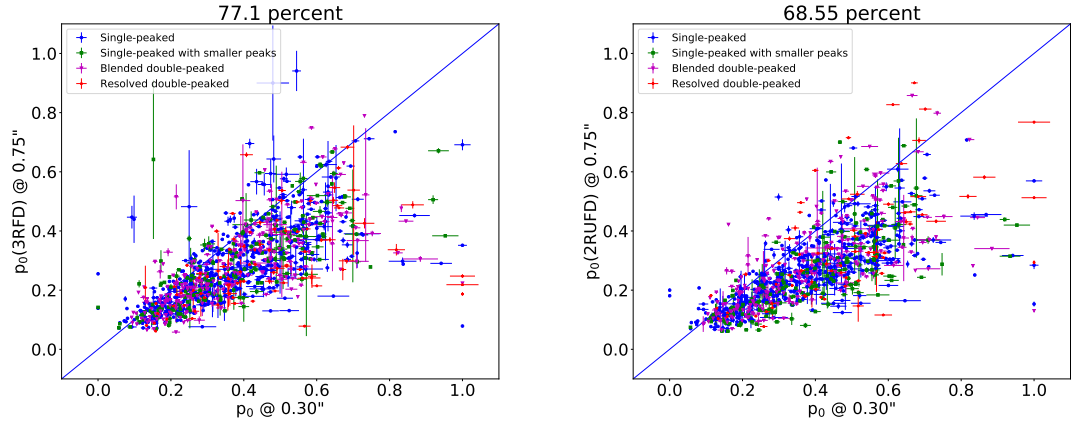

Figure 5.65: *A comparison of p_0 from wideband modelling with those derived from high-frequency, high-resolution modelling.* We compare p_0 of the strongest component. We show results with $\chi^2_r \leq 5$ from our wideband modelling. The p_0 predicted from high-frequency modelling is relatively higher than from wideband modelling. We attribute the decline in polarisation to beam-depolarisation.

Figure 5.66 compares the derived Faraday dispersions of 2RUFD and 3RFD to the dispersions derived from the high-resolution, high-frequency fits. We only compare the dispersions of the strongest components from both models. The dispersions for model 2RUFD at $0.75''$ are smaller than those at $0.30''$. This may

be because of the unresolved uniform RM-differences in the model, which also account for some of the depolarisation. The dispersions of the strong component in 3RFD are larger for the double-peaked spectra and smaller for the single-peaked spectra. However, the dispersions at $0.30''$, which describe the decay rate of high-frequency fractional polarisation as a function of λ^2, indicate that the decay is independent of the spectra class. As such, the single-peaked spectra decay at the same rate as the double-peaked spectra.

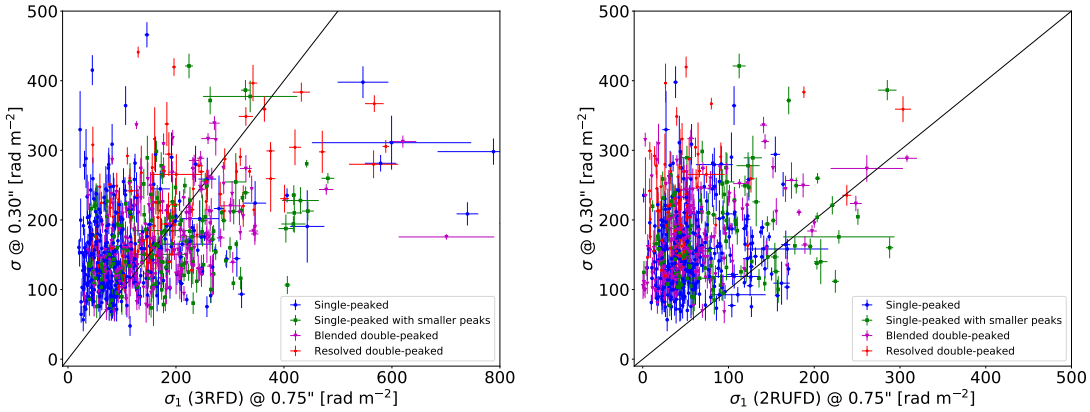

Figure 5.66: A comparison of the derived Faraday dispersions from wideband modelling with those derived from high-frequency, high-resolution modelling. We compare the dispersions of the strong components. We show results with $\chi^2_r \leq 5$ from wideband modelling and fractional errors $< 30\%$. The high-frequency dispersions are generally larger than those from wideband modelling, particularly for 2RUFD. The high-frequency dispersions and those of 2RUFD seem to be independent of the Faraday class. For 3RFD, the double-peaked spectra are associated with larger dispersions than the single-peaked spectra.

Figure 5.67 compares the separation in Faraday space of the two strongest components with the width, $\sigma_{\rm stdev}$, of the 1D Gaussian fitted to Faraday spectra data. These two quantities represent the same property except that one is the width of a Gaussian function, while the other is top-hat like, with width determined by the actual component separation. The $\sigma_{\rm stdev}$ are relatively larger than the separation between the two strong components.

5.12 The Overall Physical Picture

5.12.1 Large-Scale Magnetic Fields

Using our wideband modelling, we find that RUID significantly fails to describe the data. This indicates that the observed large RM cannot originate entirely from a mixed region. We find that a foreground Faraday rotating screen is required to describe the data. This is consistent with the conclusion reached by Dreher et al. (1987), that the observed rotations of up 600° will cause significant depolarisation not seen in the data (at 5 GHz). We can confidently rule out the possibility of internally mixed gas, particularly for RM larger than $\sim$ 1000 rad m^{-2}. Therefore, the large-scale magnetic field is external to the radio lobes, either within the large-scale cluster or cocoon-shock.

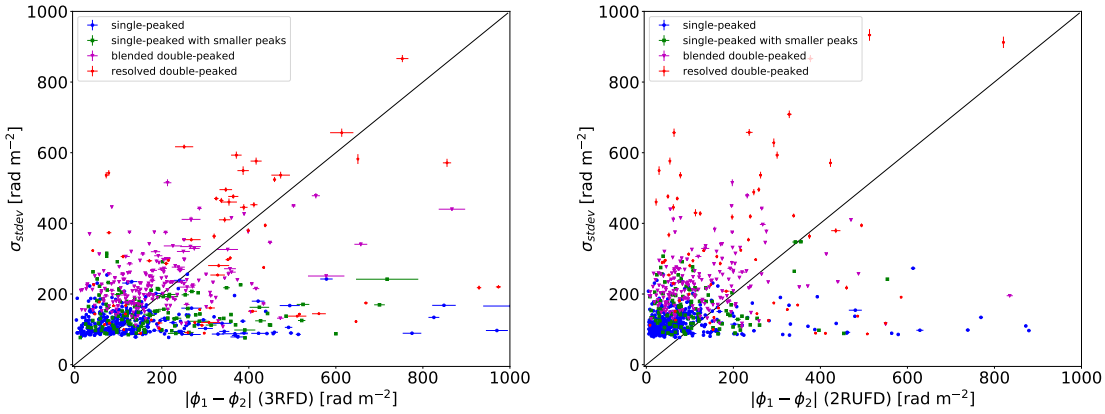

Figure 5.67: *A comparison of the derived σ_{stdev} with the Faraday separation of the two strongest components.* We show results with $\chi^2_r \leq 5$ and fractional errors in the separation $\leq 10\%$. The estimated $\sigma_{\rm stdev}$ is generally larger than the components' separation.

Given the similarity in the mean RM values across both lobes, the gas responsible for the observed Faraday rotations should encompass the whole source suggesting field scales $\gtrsim 120$ kpc. The distribution of RM, on the other hand, show field reversals on scales in the order of $\sim 3-20$ kpc, indicating multiscale fields. We are also aware that there exists field scales ~ 300 pc. We can, therefore, compute the magnetic field strengths associated with each scale using $RM = 812\, n_0\, \mathcal{B}_0\, d$, where n_0 is the electron density, $\mathcal{B}_0$ is magnetic field strength and d is a scale-size. We take Cygnus A's cluster-core electron density to be $n_e = 0.045$ cm^{-3}, cluster-core average temperature to be 4.5 keV (7.2×10^{-9} dyn cm, see Figure 4.2 and Section 4.2.2), and thermal gas pressure ($\mathcal{P}_T$, obtained using Equation 2.2 and $n = 1.93 n_e$) to be $\approx 6.3 \times 10^{-10}$ dyn cm^{-2}.

Figure 5.68 shows the estimated field strength as a function of scale (left) and the corresponding β-parameter (the ratio of magnetic to thermal gas pressure, see Equation 2.3). The scales range between $0.30 - 130$ kpc. The cyan colour encompasses a region corresponding to the minimum energy magnetic field strengths and the β-parameter corresponding to these fields ($45 - 65$ μG, Carilli and Barthel 1996). The magnetic fields are important at small-scales $\ll 25$ kpc and large $RM > 1000$ rad m^{-2}. For example, to find dynamically important fields, say $\beta = 0.1$, we need field strengths ≥ 40 μG. This requires RM of 4300 rad m^{-2} at 3 kpc, and ~ 30000 rad m^{-2} at 20 kpc. The former value is consistent with those across Cygnus A, while the latter is not. Since the RM across the eastern lobe of Cygnus A are mostly ordered on small-scales of ~ 3 kpc and are as large as $\gtrsim 4000$ rad m^{-2}, the magnetic fields across this lobe may be dynamically important. The magnetic fields across the western lobe, on the other hand, are likely to be dynamically unimportant, given that the RM across this lobe are largely ordered on scales > 5 kpc and have magnitudes $\gtrsim 2000$ rad m^{-2}.

5.12.1.1 Radial Dependence of the Magnetic Fields

The approach we used in the above paragraph assumes that the electron density and magnetic field strengths are independent of the location across the lobes, thus, constant across a given pathlength. However,

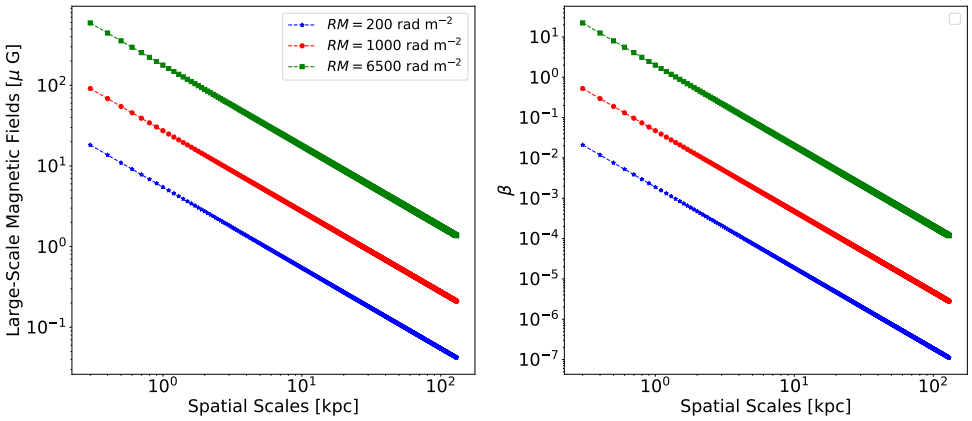

Figure 5.68: *Magnetic field strengths (left) and the corresponding β-parameter (the ratio of magnetic to thermal gas pressure, right) as a function of spatial scale*. Cyan: The range of field strength and β-parameter corresponding to the minimum energy magnetic fields in the lobes. The different coloured curves correspond to different RM values. We used the electron density of the cluster of 0.045 cm^{-3}, temperature of 4.5 keV and spatial scales ranging between $0.30 - 130$ kpc. The field strengths at $RM \sim 200$ rad m^{-2} are dynamically unimportant at all scales, while for $RM > 1000$ rad m^{-2} the fields become important at scales < 1 kpc.

that is an ideal situation since we would expect these quantities to vary with the cluster radius. X-ray measurements show that the electron density decreases with increasing radius from the cluster centre (see Figure 5.69). To characterise this profile, we fit to it the electron density profile defined in Equation 5.10.

$$n_e = n_0 \Big(\frac{r}{r_0}\Big)^{\varsigma}. \tag{5.10}$$

We find $r_0 \approx 8$ kpc, $\varsigma \approx -1.5$ and $n_0 \approx 0.3$ cm^{-3}. These solutions are only valid for data $r > 45$ kpc (right side of the blue solid line in Figure 5.69).

The way in which magnetic fields vary with radial distance is unknown. There are a few basic assumptions used in the literature but their practice is generally criticised (see Section 2.2.7). For the case of flux conservation, magnetic fields vary as $\propto n_e^{2/3} = r^{-1}$. For magnetic energy density that scales with thermal energy density, the magnetic fields vary as $\propto n_e^{1/2} = r^{-0.75}$. The RM can then be evaluated as follows:

$$RM = 812 \int_0^{45} n_e \, \mathcal{B} dL + 812 \int_{45}^{10^3} n_0 \Big(\frac{r}{r_0}\Big)^{-1.5} \mathcal{B}_0 \Big(\frac{r}{r_0}\Big)^{-1} dL, \tag{5.11}$$

where $r^2 = (L^2 + x^2)$, x is the distance from the centre to the any location within the lobes and L is the line-of-sight pathlength. The first term represents the core region of the cluster. The electron density in the core region does not change significantly with radius, so we assume that $n_e = n_0 = 0.045$ cm^{-3}. We can further assume that the magnetic field also remains constant with radius in the cluster-core but still varies as $B_0 (n_e/n_0)^{2/3}$. The second term, on the other hand, integrates up to the cluster radius of 1 Mpc. To simplify the integral, we consider the AGN, such that $r = l$ and $x = 0$, thus $dl = dr$. Equation 5.11 becomes:

$$RM = 812 \, n_0 \, \mathcal{B}_0 \, L + 812 \, n_0 \, \mathcal{B}_0 \int_{45}^{10^3} \Big(\frac{r}{r_0}\Big)^{-2.5} dr. \tag{5.12}$$

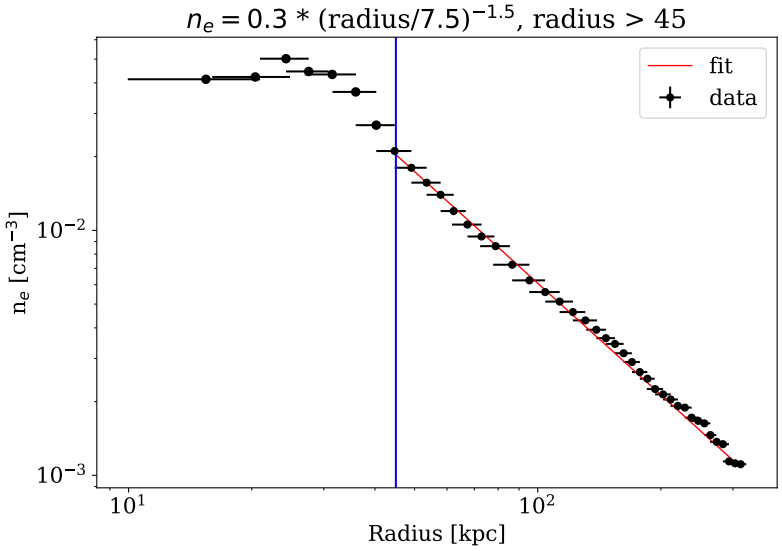

Figure 5.69: *Model fitting to Cygnus A cluster electron density radial profile.* Data points: X-ray data. Red line: A fitting of a model defined in Equation 5.10. We only fit to the data on the right of the solid blue line. X-ray data credit: Snios et al. (2018).

The integral term integrates to ~ 0.06 kpc, causing the second term to contribute a little to the overall RM across the lobes. Therefore, the above estimated magnetic field strengths using constant densities remain good approximations of the large-scale field strengths.

5.12.2 Random Magnetic Fields

Modelling of the wideband data using simple analytical models predicted the existence of multiple Faraday components within our $0.75''$ ($\sim$ 750 pc). Single component models cannot sufficiently describe the data. The preference towards multiple Faraday components in model selection is consistent with the spectra consisting of a single-peaked with smaller peaks, double-peaked and multiple-peaked lines-of-sight. Additionally, our wideband data modelling also suggests that even the single-peaked spectra consist of more than one Faraday component.

Multiple Faraday structures may occur along the line-of-sight or across the resolution beam (due to unresolved fluctuations). However, in the case of along the line-of-sight, the multiple Faraday structures only work if there is an intervening emission. Consecutive Faraday screens, without intervening emission, occur concurrently; there is simply no way to separate them. Our prediction analysis in Section 4.6, and the convolution of $0.75''$ data to $1.5''$ data in Section 4.7, have demonstrated that small-scale fluctuations are present in the vicinity of Cygnus A. Combining these results, we can safely conclude that the magnetic fields around Cygnus A are mostly turbulent. So instead of using the term turbulent "screens", we will use "patches" – to differentiate between a line-of-sight effect from beam-related effect. These unresolved patches are responsible for the observed depolarisation. We were able to rule out internal mixing, particularly for $RM > 1000$ rad m^{-2}. However, our analysis supports unresolved fluctuations as a primary cause for the observed depo-

larisation. It will only be possible to investigate internal mixing in regions with $RM \lesssim 1000$ rad m^{-2} once we are able to resolve the patches (or fluctuations). We estimate the upper limit for the fluctuations to be $0.30''$, our highest resolution at 6 GHz. Obtaining a better resolution than $0.30''$ at 2 GHz, will require an instrument with a maximum baseline of at least 100 km.

In Section 2.2.7.2 and 3.2, we made mention that the Gaussian random fields, quantified by σ, are not the best representation of real-life turbulent magnetic fields. However, we do not know of other analytical models that incorporate non-Gaussian and spatial correlations. Our understanding and parameterisation of magnetic fields is still poor. Thus, our estimate of random magnetic fields from the derived dispersions should be taken as approximations of the real "non-Gaussian" random fields.

The derived dispersions for 3RFD range between $10 - 400$ rad m^{-2} for the patches. We use Equation 3.20 to estimate the strength of the random magnetic fields. The random fields are situated either within the cluster-core or the cocoon-shock. We assume the cluster-core of pathlength, $L \approx 70$ kpc, cluster-core electron density, $n_0 \approx 0.045$ cm^{-3} (see Figure 4.2) and unresolved patch sizes that range between $\approx 0.3 - 1.5$ kpc.

Figure 5.70 shows the strength of the random magnetic fields and the corresponding β-parameter as a function of spatial scale. The spatial scale range between $0.05 - 1.5$ kpc. The fields are important at scales < 0.1 and dispersions > 100 rad m^{-2}

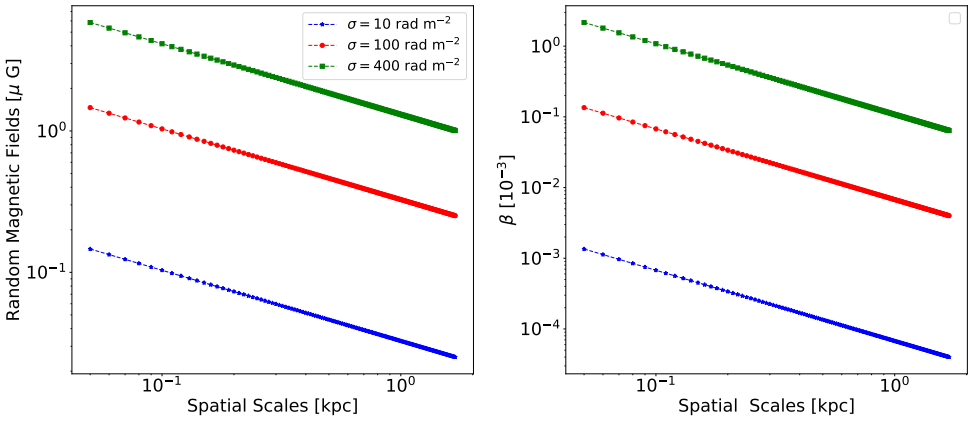

Figure 5.70: *Estimated random magnetic field strengths using Equation 3.20 (left) and the corresponding β-parameter (right) as a function of spatial scale across Cygnus A.* The spatial scales are set to range between 0.05 kpc and 1.5 kpc. The different coloured curves correspond to different dispersion values. We used the electron density value of the cluster-core of 0.045 cm^{-3} and temperature of 4.5 keV across. The random magnetic fields are important at scales < 0.1 kpc for dispersions > 100 rad m^{-2}.

5.12.3 Magnetic Fields due to Unresolved Uniform RM-difference

Our wideband data modelling also demonstrates that model 2RUFD fits at least 30% of the data better than the three-component random depolarising model. It is thus important to consider the magnetic fields implied by the presence of unresolved uniform RM-difference. These RM-differences can be thought of as unresolved uniform patches. We use Equation 2.23 to estimate the field strength of each patch. The derived

unresolved uniform RM-differences range between $40 - 1000$ rad m^{-2}. The resulting field strengths are consistent with those in Figure 5.68 for $RM \leq 1000$ rad m^{-2} and patch-size ranges between $0.05 - 1.5$ kpc (the red and blue curves). The magnetic fields are dynamically unimportant at small values of RM-difference (blue curve) and dynamically important at larger values of RM-difference (red curve), particularly at spatial scales < 1 kpc. The field strengths at large RM-difference are comparable to those in the lobes: the minimum energy magnetic field (Carilli and Barthel 1996).

5.12.4 Mixed Gas

Unresolved uniform RM-difference in model 2RUFD can also represent internal mixing in the presence of uniform magnetic fields (see Equation 3.18). This implies that internal mixing is feasible for Faraday depths not exceeding 1000 rad m^{-2}, the upper limit of the unresolved uniform RM-difference. Taking the magnetic field in the mixed gas to be $\mathcal{B}_0 = 65$ µG (Carilli and Barthel 1996) the mixed gas region to be $L = 25$ kpc in width (lobe width) and the mean Faraday depths to range between $\phi_0 = 40 - 1000$ rad m^{-2}. Figure 5.71 shows the electron density limit for a wide range of lobe filling factors, f (note that $\phi_0 = 812\, f\, n_0\, B_0\, L$). It is only at the lobe filling factor of $\leq 2\%$ that the electron density in the lobes approaches that of the external cluster gas. The estimated electron density values at 100% filling factor are consistent with those derived by Dreher et al. (1987) (assuming a uniform Burn slab).

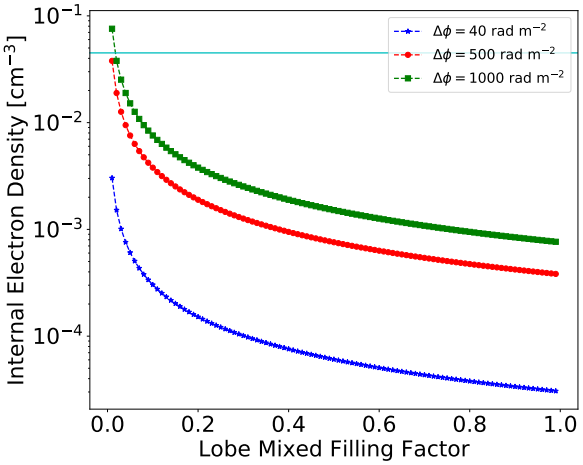

Figure 5.71: *Estimated internal electron density as a function of lobe filling factor*. The different coloured curves correspond to different internal RM. The horizontal cyan line indicates the electron density of the cluster gas (0.045 cm^{-3}). The electron density at 100% filling factor is consistent with those derived by Dreher et al. (1987). At filling factor $\lesssim 2\%$, the estimated internal electron density approaches that of the ambient cluster gas.

5.12.5 RM-Components

Our modelling results give consistent estimates of the RM, regardless of the modelling technique or the spatial resolution. This means that there is a mean RM that is unaffected by the difference in resolution, width in Faraday space, nor frequency coverage. As a result, there must exist a large-scale, ordered, foreground

magnetic field that affects all lines-of-sight across the lobes. Moreover, we find that the Faraday dispersions and separations of the individual components are smaller than the width of the Faraday spectra, the σ_{stdev}. This is particularly true for double- and multiple-peaked spectra. This further suggests that the components may be experiencing an additional Faraday rotation before they pass through the turbulent broadening screen, which broadens each component to the same width. The individual components themselves do not contribute significantly to the RM, as their separation needs to be no more than 800 rad m^{-2}. The RM of the component should also consist of both negative and positive values, so that the components are distributed about the observed mean component.

We are surprised to find these multiple RM components, and we do not have a good understanding of what they are. These components may be physically separate structures within the observing beam, or may be polarisation structures coming from the complicated, non-Gaussian MHD turbulence (see Section 3.2).

5.12.6 Possible Locations of the Magnetic Fields

Our data are consistent with the presence of turbulent gas, consisting of a wide range of spatial scales. This purely turbulent gas may be located in the ambient cluster or the cocoon-shock. Our data cannot rule between these two locations as both can equally account for the observed structures and Faraday rotation. However, given the presence of scales larger than ~ 6 kpc (the physical size of the cocoon-shock), the large-scale cluster-core is the most favourable location. However, making a conclusion is difficult as it has broader implications; specifically, is it possible that Cygnus A (and Hydra A) are unique? This question necessitates further wideband observations of other clusters.

CHAPTER 6

A New Wideband Polarisation Study of Hydra A

"Who commands the sun and it does not shine; Who seals up the stars from view; Who alone stretches out the heavens and tramples the waves of the sea; Who made the constellations the Bear, Orion and the Pleiades and the vast starry spaces of the south; Who does great things beyond understanding, unfathomable and marvellous and wondrous things beyond number?"
Job 9:7-10

6.1 Introduction

This chapter presents the results of our new wideband ($2 - 12$ GHz), full-polarisation, high-spectral resolution observations of Hydra A radio galaxy. We observed Hydra A using the JVLA from December 2013 to October 2014.

In Section 6.2, we present the background information relevant to this study, followed by the observations and calibration of the data in Section 6.3 and imaging of the data in Section 6.4. Section 6.5 presents the polarisation results as a function of frequency and resolution. Section 6.6 presents the result of our high-frequency, high-resolution Faraday rotation study and Section 6.7 presents low-frequency, low-resolution data predictions using maps from the high-frequency, high-resolution Faraday rotation study. In Section 6.8, we present our wideband data at two different resolutions, namely, $1.50''$ and $3.0''$. Section 6.9 presents a classification of the data in Faraday space (the Faraday spectra). Section 6.10 gives summary of the data and Section 6.11 presents a wideband data modelling and provides our proposed physical picture around and within Hydra A as revealed by our study.

6.2 Background

6.2.1 Hydra A Radio Galaxy

Hydra A (3C 218) is a wide-tailed FR I radio galaxy. It is one of the most luminous FR I galaxy ($P_{178\,\mathrm{MHz}} = 3 \times 10^{26}$ W) – roughly a factor of 10 above the FR I - FR II break (Taylor et al. 1990). The parent galaxy of Hydra A is a cD elliptical galaxy with redshift of 0.054 (Dwarakanath et al. 1995; Owen et al. 1995; Taylor 1996). Assuming $\mathrm{H}_0 = 70$ km s^{-1} Mpc^{-1}, $\Omega_M = 0.3$ and $\Omega_\Lambda = 0.7$, the projected

linear scale of the Hydra A is 1.05 kpc arcsec^{-1}. The parent galaxy is the dominant member of the relatively poor Abell cluster A780 (Abell 1958). The low-frequency radio emission structure of Hydra A shows tails extending ~ 530 kpc in the north-south direction and ~ 265 kpc in the east-west direction (Taylor et al. 1990; Lane et al. 2004). The radio emission from the jets to the tails display a "S" symmetry about the core. The southern tail shows a hotspot a few kpc from the AGN, while the northern tail has no hotspot (Taylor et al. 1990).

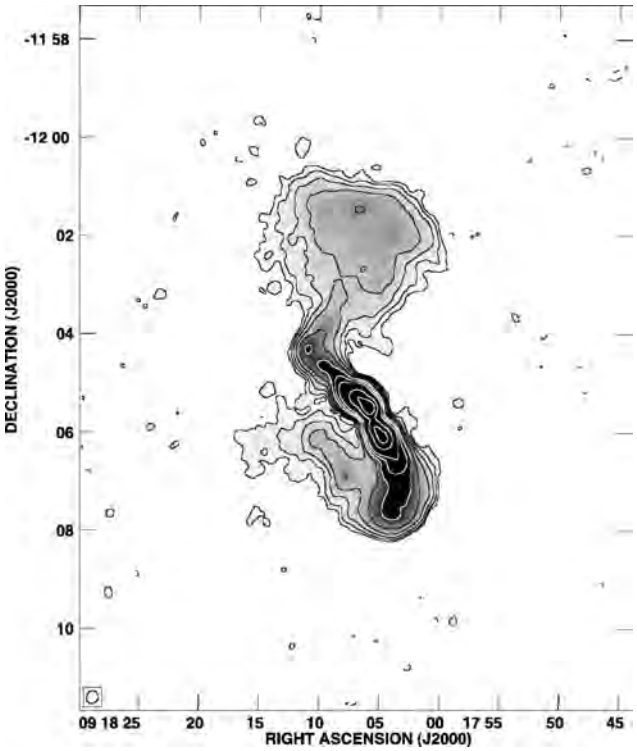

Figure 6.1: *Contour image of Hydra A radio emission at* 330 *MHz.* Data: A, B and C VLA configurations. Image resolution: $15.7'' \times 13.9''$. Contour levels are in multiples of $3\times$ image noise, $0.01605 \times (-1, 1, 2, 4, 8, 16, \dots)$. Image Credit: Lane et al. (2004).

6.2.2 Hydra A Intracluster Gas

Hydra A is embedded in a CC X-ray cluster gas of luminosity of $L = 4 \times 10^{44}$ ergs s^{-1} between 0.5 and 4.5 keV (David et al. 1990). The cluster gas temperature decreases from ~ 4 keV at 200 kpc radius to 3 keV at 10 kpc (McNamara et al. 2000; David et al. 2001). The electron density, n_e, within 10 kpc is 0.06 cm^{-3} and decreases with radius as $r^{-0.4}$ out to 30 kpc and as $r^{-1.6}$ out to 100 kpc (McNamara et al. 2000; David et al. 2001). Figure 6.2 shows the electron density and temperature profiles of Hydra A X-ray cluster (Nulsen et al. 2005b). X-ray deficit regions (cavities) are also found coincident with the radio tails (McNamara et al. 2000; David et al. 2001; Nulsen et al. 2002). These cavities are most obvious in a X-ray map superimposed on a radio intensity at 330 MHz (see Fig 1 and 2 of Simionescu et al. (2009) and Figure 2 of Nulsen et al. (2005b)). Such cavities are common in clusters of galaxies (for example, Boehringer et al. 1993; Carilli et al. 1994; Fabian et al. 2000; Blanton et al. 2001; Heinz et al. 2002), and are believed to result from an exclusion

of the thermal cluster gas by the expanding bubble of synchrotron-emitting relativistic gas originating from the AGN. Surrounding the cavities in the cluster gas is a region of enhanced X-ray surface brightness gas and pressure (Nulsen et al. 2005b; Simionescu et al. 2009). This enhanced region extends $6'$ north of the AGN and $4.3'$ east of the AGN ($200 - 300$ kpc from the AGN) (Nulsen et al. 2005b). This region is interpreted as weak shocks of mach number ~ 1.3 due to expansion (buoyantly rising) of the tails into the cluster gas. Similar weak shocks are also observed in the Perseus cluster (Fabian et al. 2003), M87 (Young et al. 2002) and Cygnus A (Snios et al. 2018).

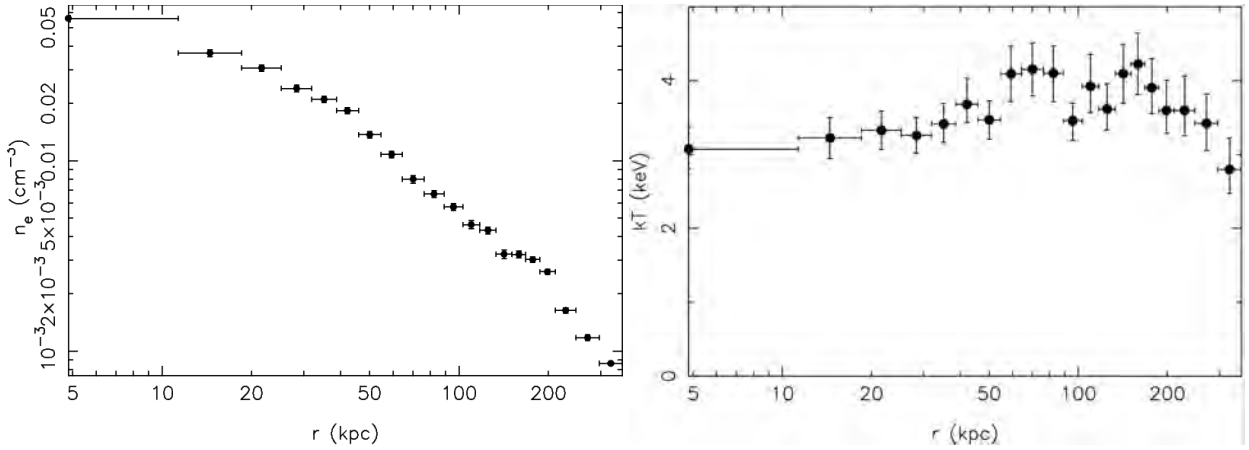

Figure 6.2: *Electron density (left) and temperature (right) profiles of western shock (along the position angle* $240° - 300°$*) in Hydra A X-ray cluster*. The weak shock is seen at radius 211 kpc. Image Credit: Nulsen et al. (2005b)

6.2.3 Previous Faraday Rotation Study

The radio emission from Hydra A displays extremely large RM, with the northern tail showing RMs ranging from -1000 and $+3300$ rad m^{-2} and southern tail showing RM ranging between a few $+1000$ rad m^{-2} and up to -12000 rad m^{-2} (Taylor et al. 1990; Taylor and Perley 1993). The RM are predominantly positive in the northern tail and predominantly negative and very patchy in the southern tail (Taylor and Perley 1993). Large rotation measure gradients are observed in both tails, with gradients of up to ~ 1000 rad m^{-2} arcsec^{-1} in the northern tail and much larger values in the southern tail (Taylor and Perley 1993). Furthermore, the southern tail is less polarised compared to the northern tail and depolarises much rapidly with frequency between $15 - 5$ GHz (Taylor and Perley 1993).

6.2.4 Origin of Faraday Rotations

Our Galaxy contributes < 100 rad m^{-2} at the Galactic latitude of Hydra A. Therefore, our Galaxy cannot explain the observed RM across Hydra A (Simard-Normandin et al. 1981). The IGM contributes no more than 2 rad m^{-2} (Vallee 1990). The observed optical gas only extends to a radius of $15''$ from the AGN; thus, it cannot account for the overall RM across Hydra A (Baum et al. 1988). Given these reasons, Taylor and Perley (1993) attributed the observed large RM to a gas at the radio galaxy; either in the ICM, cocoon-shock and

mixed gas in the tails or the boundary layer. The latter two regions are expected to result in depolarisation and non-linearities in the polarisation angle as a function of λ^2. The observation data used by Taylor and Perley (1993) only consisted of five sparsely sampled frequency channels between $5 - 15$ GHz. At such sparsity, it was not possible to see deviations and peculiarities in the data. For these reasons, the authors were inclined to the ICM being responsible for the observed RM. However, our new wideband data show that the situation is much more complicated and interesting. Therefore, we revisit the question of the origin and location of the large RM, RM gradients, RM asymmetries and depolarisation.

6.2.5 Why the New Observations?

Previous work by Taylor and Perley (1993) consists of only five wavelengths spanning λ 3.6 cm to 2 cm. With such sparse sampling, subtle depolarisation effects such as those due to random small-scale magnetic fields or due to boundary layer effects will not be visible. Additionally, the depolarisation effects do not manifest at short wavelengths. With the completion of the wideband JVLA (Perley et al. 2011), we have now the capability to observe Hydra A at lower frequencies than those available to Taylor et al. (1990) and Taylor and Perley (1993). Notably, we could make use of the $2 - 4$ GHz system – and with complete frequency coverage.

6.3 Observations and Calibration

Hydra A was observed in all four JVLA configurations under project code 13B-088 at L (1 - 2 GHz), S (2 - 4 GHz), C (4 - 8 GHz) and X (8 - 12 GHz) band resulting in a total frequency coverage of 1 - 12 GHz. The original PI for the observations is Mike Bell. The observing dates, durations and configurations are shown in Table 6.1.

Table 6.1: *Observing log*

Configuration	Date [dd:mm:yy]	Duration [hr]
D	27: 06: 2014	4.0
D	08/09: 09: 2014	3.5
DnC	16: 09: 2014	2.7
C	19: 10: 2014	4.0
C	23: 10: 2014	2.7
B	14: 12: 2013	6.0
A	27: 02: 2014	5.0
A	07: 03: 2014	5.0

The data were taken with a time-resolution of 2 seconds at A-configuration and 3 seconds at other configurations. The frequency channelisation varied with band and configuration: 2 MHz for S-, C- and X-bands

in B, C and D configuration, 1 MHz for L-band in those same configurations. For A configuration, 2 MHz was used for X-band, 1 MHz for C-band, 0.5 MHz for S-band and 0.25 MHz for L-band. These data were subsequently resampled to the same spectral resolution as in the B, C and D configurations using the AIPS program SPEC. This resulted in a spectral resolution of 1 MHz in L-band and 2 MHz in the other bands. These values were chosen so as to minimise both the bandwidth smearing and bandwidth depolarisation.

The editing and calibration procedures are the same as those for Cygnus A (see Section 6.3 of Chapter 4, for the details). After calibration, the data were averaged in frequency and time to: 1 MHz/12 seconds for L-band, 2 MHz/12 seconds for S-Low (2 - 3 GHz), 4 MHz/12 seconds for S-Hi (3 - 4 GHz), 8 MHz/12 seconds for C- and X-band.

The original, external phase and amplitude calibration does not enable high-fidelity imaging, self-calibration of the Hydra A data was performed in the same way as in Cygnus A. The self-calibration process can introduce small temporal gain drifts between the individual spectral windows. To eliminate these, we utilised the emission from the bright, unresolved AGN to put all the data on a common flux density scale and also to spatially correct the images.

6.4 Imaging

Following the self-calibration, we made cube images of Stokes Q, U, and I using a single scale cleaning algorithm. We generated 4096×4096 images sampled in pixel sizes of $0.05''$. The cubes were made at two standard resolutions, namely $1.50'' \times 1.0''$ and $0.50'' \times 0.35''$, hereinafter $1.50''$ and $0.50''$, respectively. The lower resolution includes data between 2 - 12 GHz and the higher resolution includes data between 6 - 12 GHz. The L-band data, being at lower resolution and frequency, are completely depolarised and not useful in the analysis. As a result, the L-band data were excluded from our analysis. Figure 6.3 shows an image of Hydra A at 10 GHz and $0.35''$.

In terms of channelising each band, we took note of the maximum number of channels we can combine while avoiding bandwidth depolarisation. Equation 4.4 is used to the determine the number of channels, $N_{\rm avg}$, to average together at frequency ν, bandwidth $\Delta\nu$ and maximum RM. We chose $N_{\rm avg}$ such that the rotation of the plane of polarised emission between channels due to the maximum RM of 12000 rad m^{-2} is less than 10 degrees. Table 6.2 shows the channelisation utilised for the different bands.

We used single-scale CLEAN because of its speed and simplicity. The accuracy of single-scale deconvolution by CLEAN degrades at high frequencies and high resolutions, particularly for extended structures such as those of Hydra A. The problem is particularly severe in Stokes I, where the brightness of the extended regions is broken into synthesised beam-sized "islands" of emission. To reduce these effects, we first fitted a smooth brightness profile across frequency to all image pixels. We then used the spectral index value derived from the profile fitting to generate the Stokes I emission at all frequencies. We carried out this procedure separately for 2 - 6 GHz and 6 - 12 GHz cubes. The polarised emission is not affected by this problem. Figure 6.4 shows the spectral index maps used for deriving the model I images.

Following the same procedure as in Section 4.3.3, we derived maps of the polarised intensity P (with corrected Ricean bias), fractional polarisation and polarisation angles. Errors are derived using the propa-

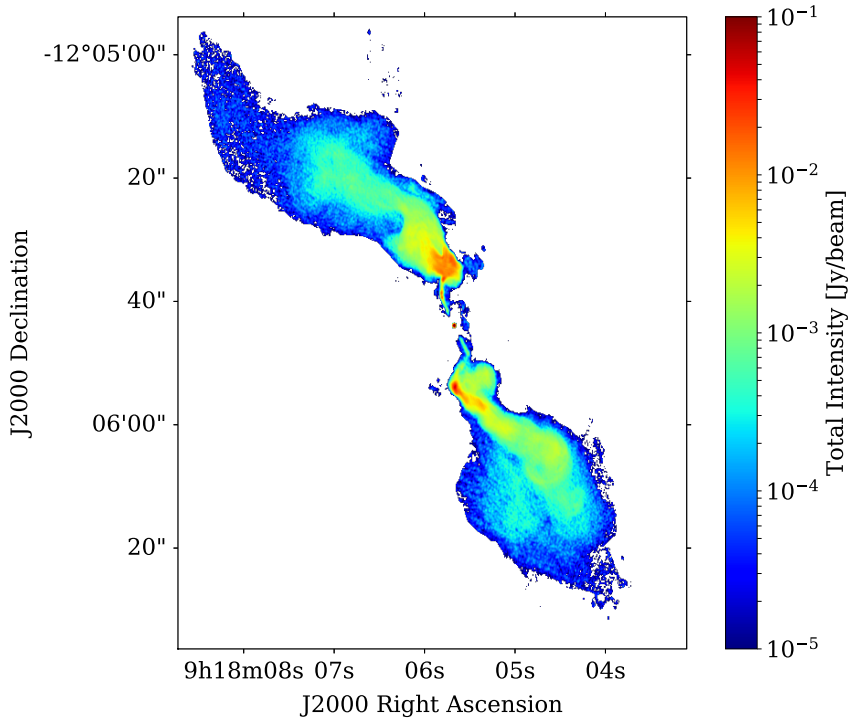

Figure 6.3: *Stokes I image of Hydra A at* 10 *GHz and* $0.35''$ *resolution.* Pixels shown have intensities $3 \times \sigma_{\rm noise}$, where $\sigma_{\rm noise} = 0.2$ mJy beam^{-1}.

Table 6.2: *A number of averaged frequency planes utilised to avoid Faraday depolarisation for each band*

Band	ν - interval [GHz]	$\Delta\nu$ [MHz]	$N_{\rm avg}$	$N_{\rm planes}$
L	1 - 2	1	1	1024
$S_{\rm lo}$	2 - 3	2	1	512
$S_{\rm hi}$	3 - 4	4	1	256
$C_{\rm lo}$	4 - 6	8	1	256
$C_{\rm hi}$	6 - 8	16	2	128
$X_{\rm lo}$	8 - 10	32	4	64
$X_{\rm hi}$	10 - 12	64	8	32

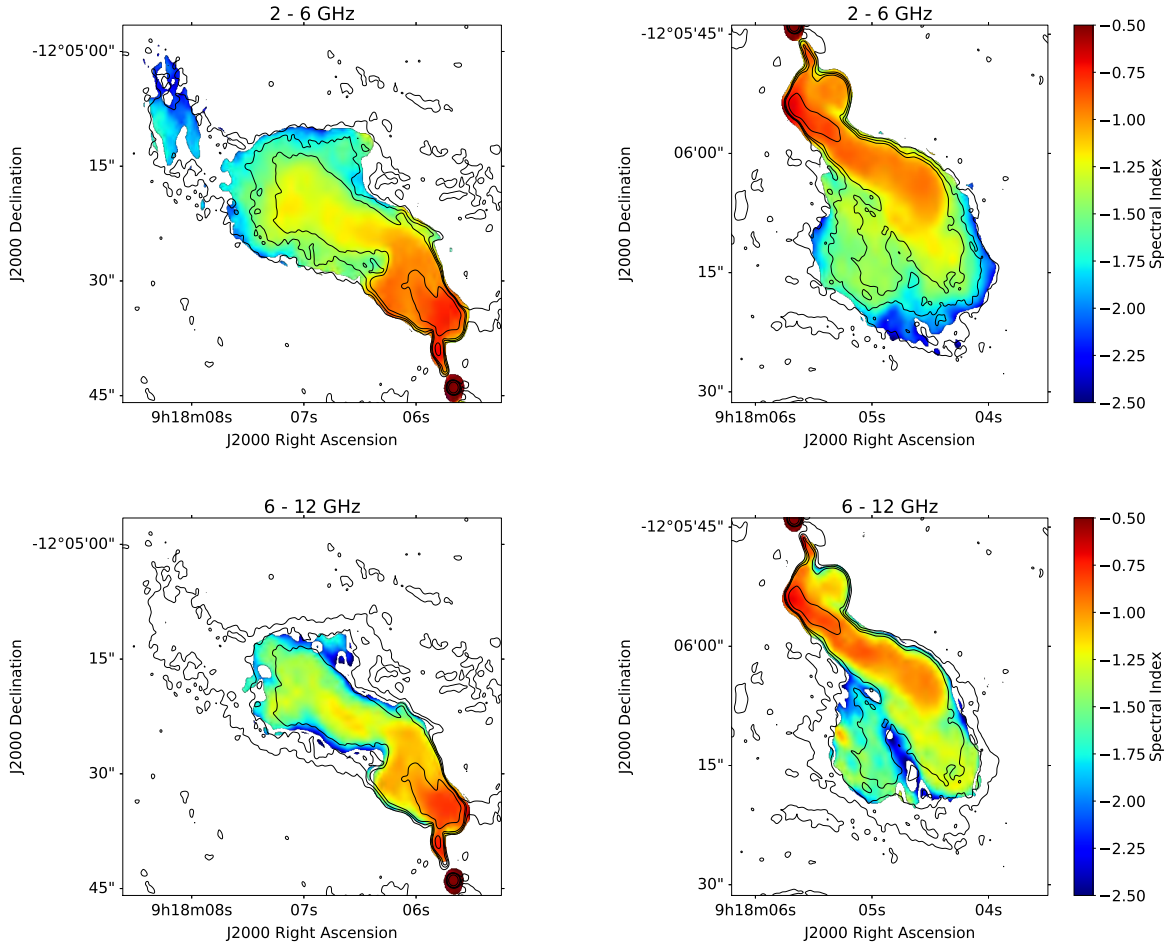

Figure 6.4: *Hydra A spectral index maps at* $1.50''$. Top row: $2-6$ GHz. Bottom row: $6-12$ GHz. We show pixels with fitting error in spectral index < 0.1 and $> 3\times$ off-source image noise in Stokes I at 1.5 GHz.

gation of error method, with the noise in each map estimated in a region far from the source emission. At $0.50''$, the off-source noise ranges between 0.03 mJy beam^{-1} and 0.07 mJy beam^{-1} in Stokes Q and U and ranges between 0.04 m Jy beam^{-1} and 0.05 mJy beam^{-1} in Stokes I. At $1.50''$, the off-source noise ranges between 0.06 mJy beam^{-1} and 1.1 mJy beam^{-1} in Stokes Q and U and ranges between 0.1 mJy beam^{-1} and 5 mJy beam^{-1} in Stokes I.

We also derived Faraday spectra using RM-Synthesis and RM-Clean. The resulting RMTF is similar to Figure 4.6 of Cygnus A. The resolution in the Faraday space is ~ 175 rad m^{-2} for 2 - 12 GHz and ~ 2030 rad m^{-2} for 6 - 12 GHz. We used uniform weighting ($W = 1$, see Section 3.1.2) for all channels and defined λ_0^2 to be a weighted mean of all λ^2 for a particular frequency-range. The maximum Faraday depth we can observe is 25000 rad m^{-2}, well beyond those of Hydra A (~ 12500 rad m^{-2}). The largest extended Faraday structure we are sensitive to without significant attenuation is 5000 rad m^{-2}, far wider than those expected in Hydra A (see Section 6.9 and right plot of Figure 6.26).

6.5 Polarisation Data

In this section, we look at the polarisation data of Hydra A in detail. In particular, we look at how the polarisation changes with frequency, as well as with resolution. This is essential since the depolarisation can occur due to differential rotation along the lines-of-sight, or within our synthesised beam. Thus, we need to have a clear understanding of both phenomena if we are to fully understand the underlying physics associated with this radio galaxy.

6.5.1 Polarisation as a Function of Frequency

Figure 6.5 shows the fractional polarisation maps across the inner tails of Hydra A. The northern tail is more highly polarised than the southern tail at all the four frequencies. In general, the fractional polarisation of both tails decreases with decreasing frequency. The inner regions of the tails close to the AGN depolarise more rapidly than the outer regions further from the AGN. Similar to Cygnus A (Sebokolodi et al. 2020), the structural features such as the hotspot (the high surface brightness spots) and jets are not discernible in the fractional polarisation maps. The fractional polarisation is relatively smooth across the northern tail and patchier across the southern tail. The fractional polarisation of both tails becomes clumpier towards low frequencies.

To properly determine the degree by which the tails depolarise, we computed the depolarisation ratio, by dividing the fractional polarisation map at 2 GHz with a map at 10 GHz and 6 GHz with 10 GHz. Figure 6.6 shows the FDR maps. Note that the FDR is prone to large errors since it is a ratio of ratios. To remove spurious emission in the images shown, we exclude all pixels with fractional errors greater than 60%. The FDR$_1$ are commonly larger than 0.01 but less than 0.1, implying that the tails depolarise by more than $\sim 90\%$ between 10 GHz and 2 GHz at ~ 1 arcsecond resolution. The northern tail is dominated by ratios < 0.075, while the southern tail is dominated by ratios < 0.075 at regions closer to the AGN and $> 0.075 - 0.2$ at the extreme regions (away from the AGN). However, we cannot tell if the high FDR$_1$ in the southern tail are real or not, especially given that this tail is associated with low-SNR – particularly in the extreme regions.

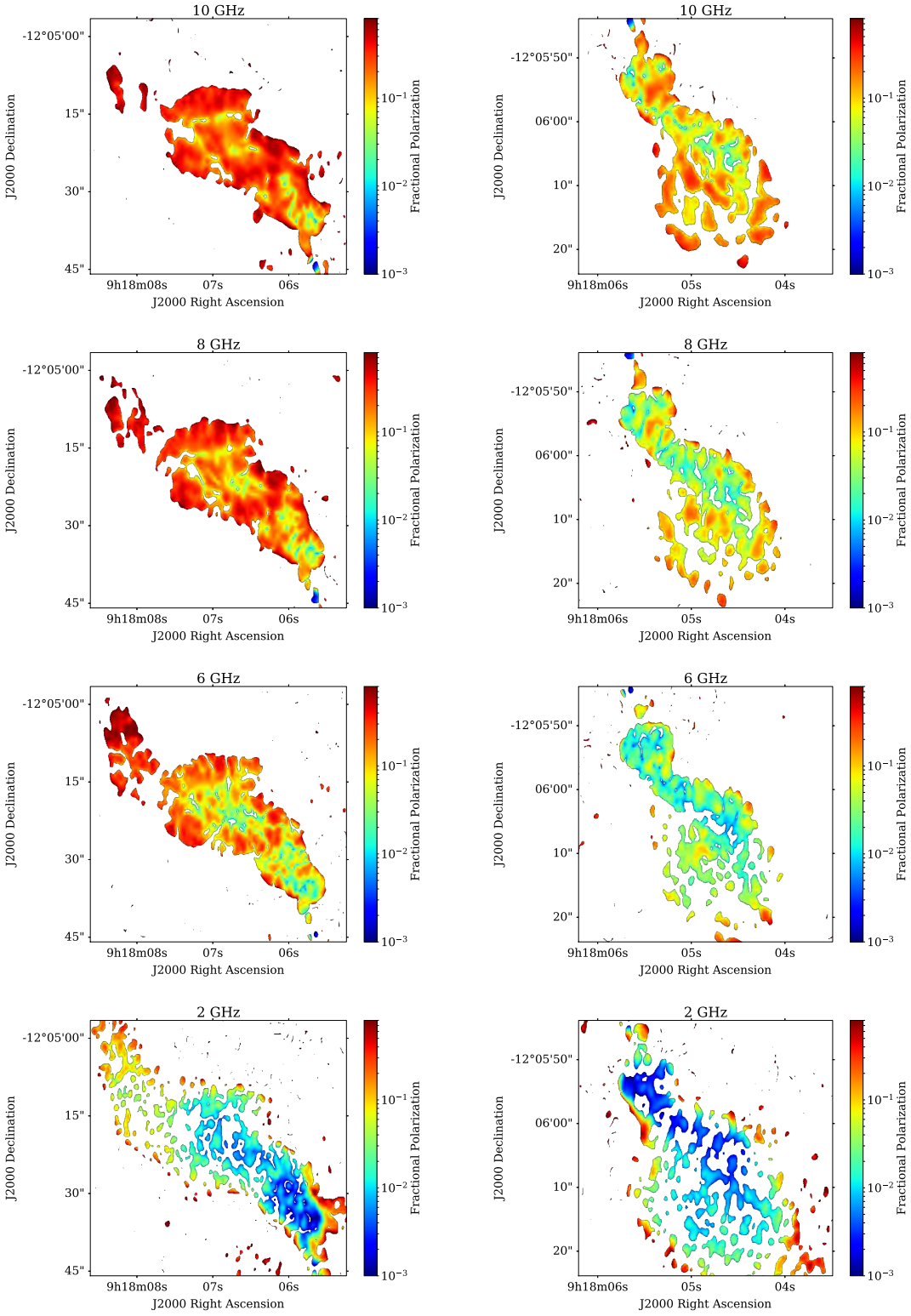

Figure 6.5: *Hydra A fractional polarisation maps at* $1.5''$ *as a function of frequency*. Left: Northern tail. Right: Southern tail. Pixels shown have fractional errors $\sigma_p/p < 60\%$. Both tails depolarise significantly with decreasing frequency. In general, the northern tail is less depolarised than the southern tail.

Increasing the pixel selection criteria (increasing the fractional errors in fractional polarisation) to remove the high ratio regions only compromises the signal across the rest of the tails. The FDR_2, on the other hand, show relatively little depolarisation between 6 and 10 GHz. FDR_2 range between a few 1% to 80%. There are regions of large and small FDR_2 throughout the tails.

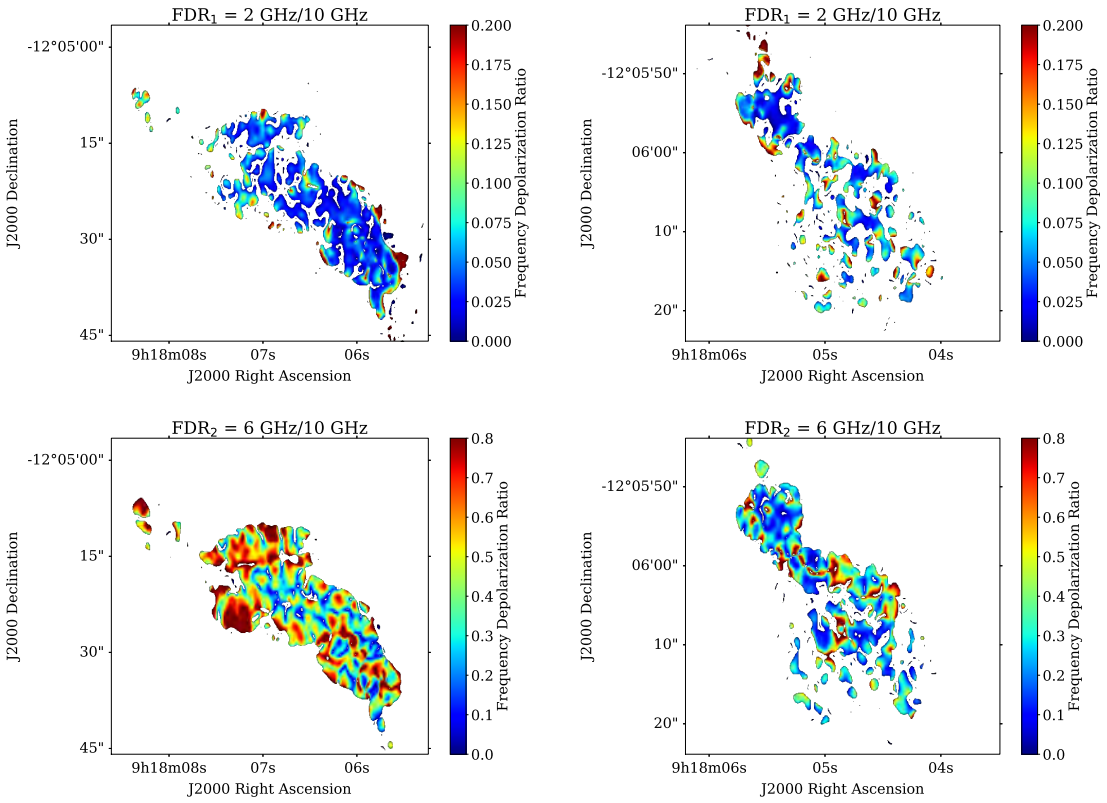

Figure 6.6: *FDR maps at* $1.50''$ *of Hydra A radio tails.* Pixels shown have $\sigma_{\mathrm{FDR}}/\mathrm{FDR} < 60\%$. Top row: $2\,\mathrm{GHz}/10\,\mathrm{GHz}$. Bottom row: $6\,\mathrm{GHz}/10\,\mathrm{GHz}$. FDR_1 of both tails range between $0.01 - 0.1$, with the majority of the pixels across the northern tail and the inner southern tail having ratios < 0.075 and the extreme regions of the southern tail having ratios $> 0.075 - 0.2$. FDR_2 range between $1\% - 80\%$. FDR shows narrow regions of large and small depolarisation values across the tails. The areas of large FDR may or may not be real but we think they are most likely unreal especially given they are associated with low-SNR. In general, the tails depolarise by up to $\sim 90\%$ between $10 - 2$ GHz.

We have so far studied how the polarisation behaves globally across the tails in all regions. We found that the tails are depolarising with decreasing frequency. Next, we look at the polarisation behaviour of the different lines-of-sight across the tails as a function of frequency (high-spectral resolution). These will provide a more detailed probing of the nature of the depolarisation. However, this approach is made difficult by the large number of lines-of-sight available. Therefore, for the purpose of this dissertation, we will show a few representative examples.

We use the same coordinate system used for Cygnus A study. To select the lines-of-sight, we considered pixels separated by $0.7''$ with fractional polarisation above 0.1 at 8 GHz. This resulted in 696 lines-of-sight. We looked through the individual lines-of-sight and found that $562/696$ are usable, while the remaining are extremely noisy. The majority of the excluded lines-of-sight are from the southern tail with a few in the

outskirts of both tails (further from the centre).

Figure 6.7 shows six polarisation functions for six representative lines-of-sight. For each line-of-sight (each row), we display fractional polarisation as a function of λ^2 (left), polarisation angle as a function of λ^2 (middle) and the amplitude of the deconvolved Faraday spectrum (right, in blue) superimposed on a Gaussian of width equal to that of the RMTF (in red). To match the Gaussian function to the data, we shifted and scaled its amplitude to the location and amplitude of the peak in the Faraday spectrum. Each line-of-sight is labelled using the derived coordinate system.

The fractional polarisation of all the lines-of-sight decreases significantly with increasing λ^2. Similar to Cygnus A, the decline in the fractional polarisation with increasing λ^2 is non-monotonic. The fractional polarisation of some lines-of-sight decreases relatively smooth (first two rows), some consists of well-defined oscillations (third and fourth row) and others show intermediate and less defined decaying behaviour (last two rows). Hereafter, we refer to these decaying behaviours as "smooth decay", "oscillatory decay" and "complex decay", respectively.

The middle column shows the polarisation angle as a function of λ^2 in black and the residual polarisation angle in blue. The residual angles are obtained by removing $RM\lambda^2$ of the peak component in the Faraday spectrum (right column) from the observed polarisation angles. The polarisation angles reveal significant deviations from linearity with λ^2 for most of the lines-of-sight. These deviations are concentrated at low frequencies, as expected since the Faraday rotation effects are most dominant in this frequency-regime. As a result, the earlier observations would not have allowed us to notice the deviations in the polarisation angles, due to the fact that these observations were at high-frequencies (> 5 GHz) and had a few, sparsely sampled frequency channels.

The observed Faraday spectra reveal very interesting structures (right column of Figure 6.7). In general, the Faraday spectra of the smooth-decaying lines-of-sight consist of a single dominant peak and in some cases, a broadened Faraday spectrum whose width is larger than that of the RMTF (~ 180 rad m^{-2}). The oscillatory decaying and complex decaying lines-of-sight, on the other hand, are associated with resolved multiple-peaked Faraday spectra. Evaluating the peak separations and spectra widths by eye, we estimate that the separations and widths range between $\sim 500-5000$ rad m^{-2}, with the majority having separations/widths between $1000 - 3000$ rad m^{-2}. The Faraday spectra give a good impression of the number and strengths of the individual Faraday patches/components within the resolution beam or along the lines-of-sight.

We classified the different lines-of-sight into one of three categories: smooth, oscillatory or complex based on the decay in fractional polarisation with increasing λ^2. We find that roughly 22% are smooth decays, 11% are oscillatory decays and 67% are complex decays. Figure 6.8 shows the spatial distribution of the three classes across the tails. It should be noted that these classes are only valid for this frequency range (2 - 12 GHz) and resolution ($1.5''$). The polarisation behaviour may completely change by adjusting the resolution and frequency range span (most notably, the lower frequency bound). We find that the majority of the complex decays resemble the bottom row of Figure 6.7 rather than fifth row – the fractional polarisation rapidly drops to near zero, with no subsequent structures visible at lower frequencies.

The northern tail consists of all the decaying classes, while the decays across the southern tail are mostly complex and smooth with no oscillations. Most of the smooth decays are situated at the ends of the tails

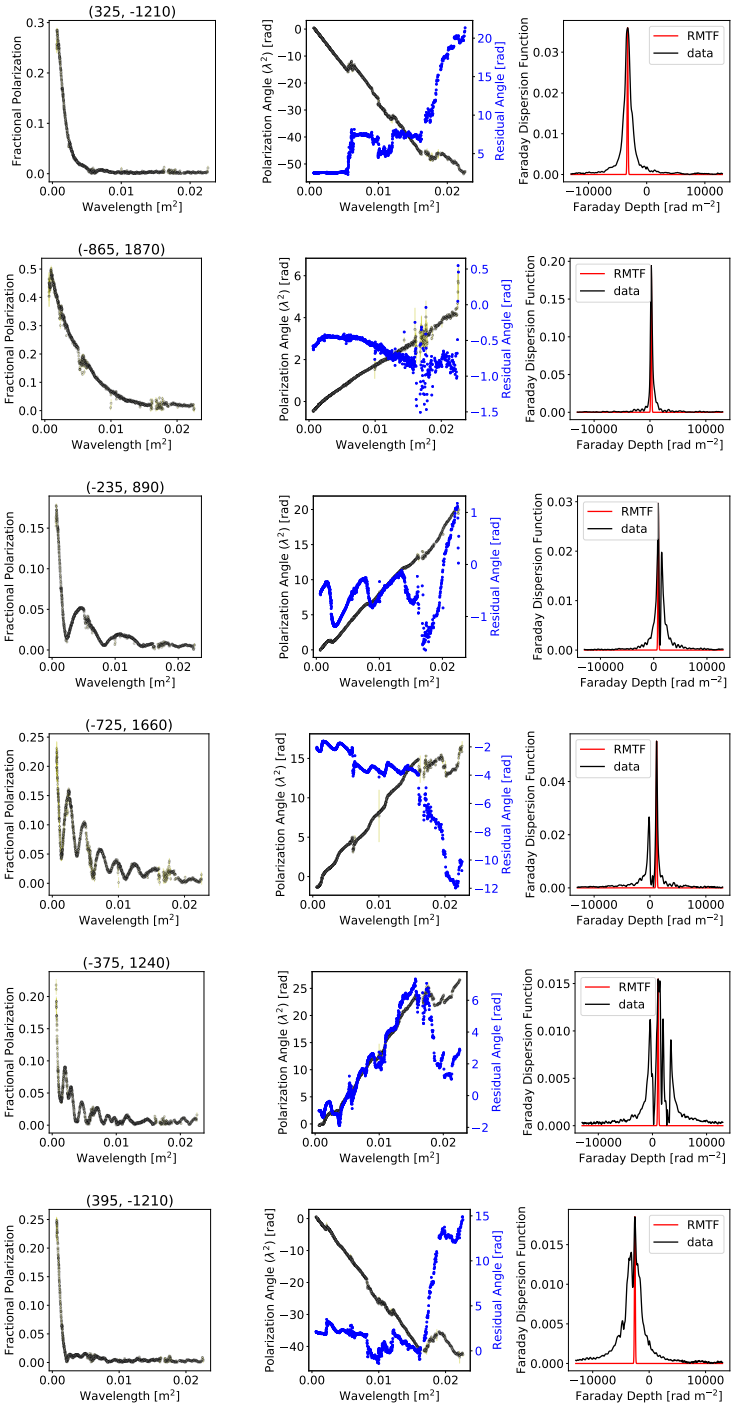

Figure 6.7: *Hydra A wideband ($2 - 12$ GHz) polarisation data at $1.50''$ for six representative lines-of-sight.* Left column: Fractional polarisation vs λ^2. Middle column: Polarisation angles vs λ^2 (black) and the residual polarisation angles (blue). Right column: Faraday spectra (blue) superimposed on a real-valued Gaussian RMTF (red). The residual polarisation angles were obtained by subtracting $RM\lambda^2$ the dominant peak in the Faraday spectrum from the observed polarisation angles. First two rows: Smooth decaying. Middle two rows: Oscillatory decay. Last two rows: Complex decay.

(further from the AGN), and the complex decays are near the AGN. It makes sense that there is a few occurrence of oscillatory decays, since this decaying behaviour results from a special physical setup of two or more polarised patches "patches" with different RMs within the resolution element.

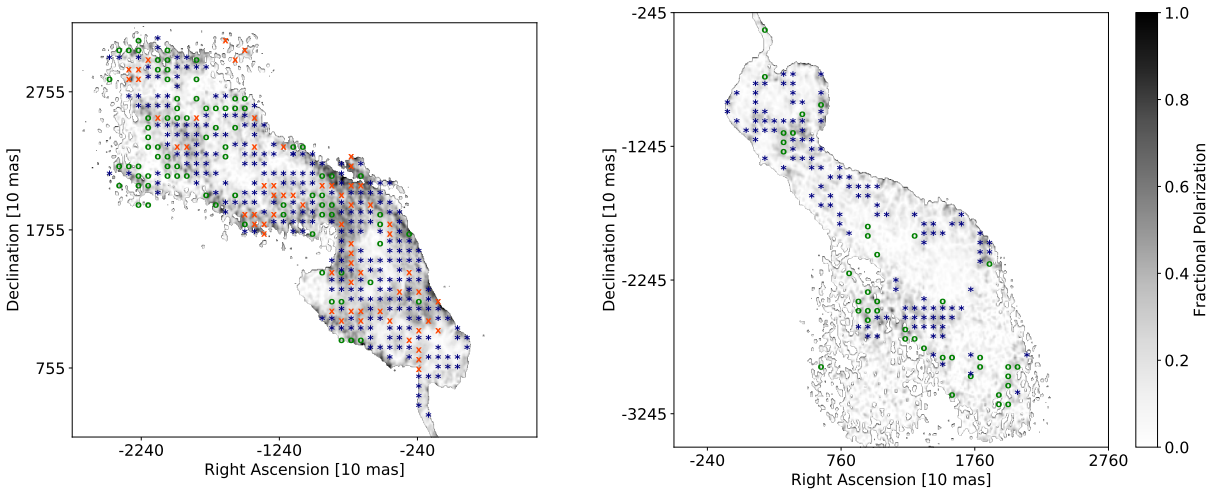

Figure 6.8: *Classifications of the lines-of-sight frequency depolarisation across Hydra A tails.* Red x: Oscillatory decays. Green o: Smooth decays. Navy blue *: Complex decays. The oscillatory constitutes 11% of the lines-of-sight, smooth decay about 22% and complex decay about 67%.

6.5.2 Polarisation as a Function of Spatial Resolution

The observed depolarisation can be a result of differential rotation along the line-of-sight or across the synthesised beam. These two have completely different physical implications: the first implies a mixing of gases and the second implies the presence of turbulent magnetic fields. It is thus important that we distinguish these two physical situations. However, the only definitive way to distinguish the two is to eliminate beam-depolarisation by increasing our resolution until all transverse variations are resolved. Any remaining depolarisation can then be attributed to the line-of-sight effect. In this section, we investigate whether our data are limited by the observation's resolution or not.

Figure 6.9 shows a 6 GHz fractional polarisation map at different resolutions, from $3''$ to the highest possible resolution of $0.5''$. It is evident that the tails depolarise with decreasing resolution, with the largest depolarisation occurring in the inner regions of the tails, close to the centre.

To see the degree by which the tails depolarise with resolution, we compute a depolarisation ratio map by dividing a 10 GHz fractional polarisation map at $3''$ with a map of the same frequency at $0.3''$, and 6 GHz maps at $3''$ with $0.5''$. Figure 6.10 shows the resolution depolarisation ratio (RDR) maps. Similarly, we consider pixels with fractional errors of less than 60%. The RDR at 10 GHz across the northern tail is small, particularly in the outer regions of tail (further from the centre), while the southern tail is significantly depolarised in most of the regions (except in region near the hotspot). The tails are most depolarised at a low-frequency even though the difference in the minimum and maximum resolutions is less than at 10

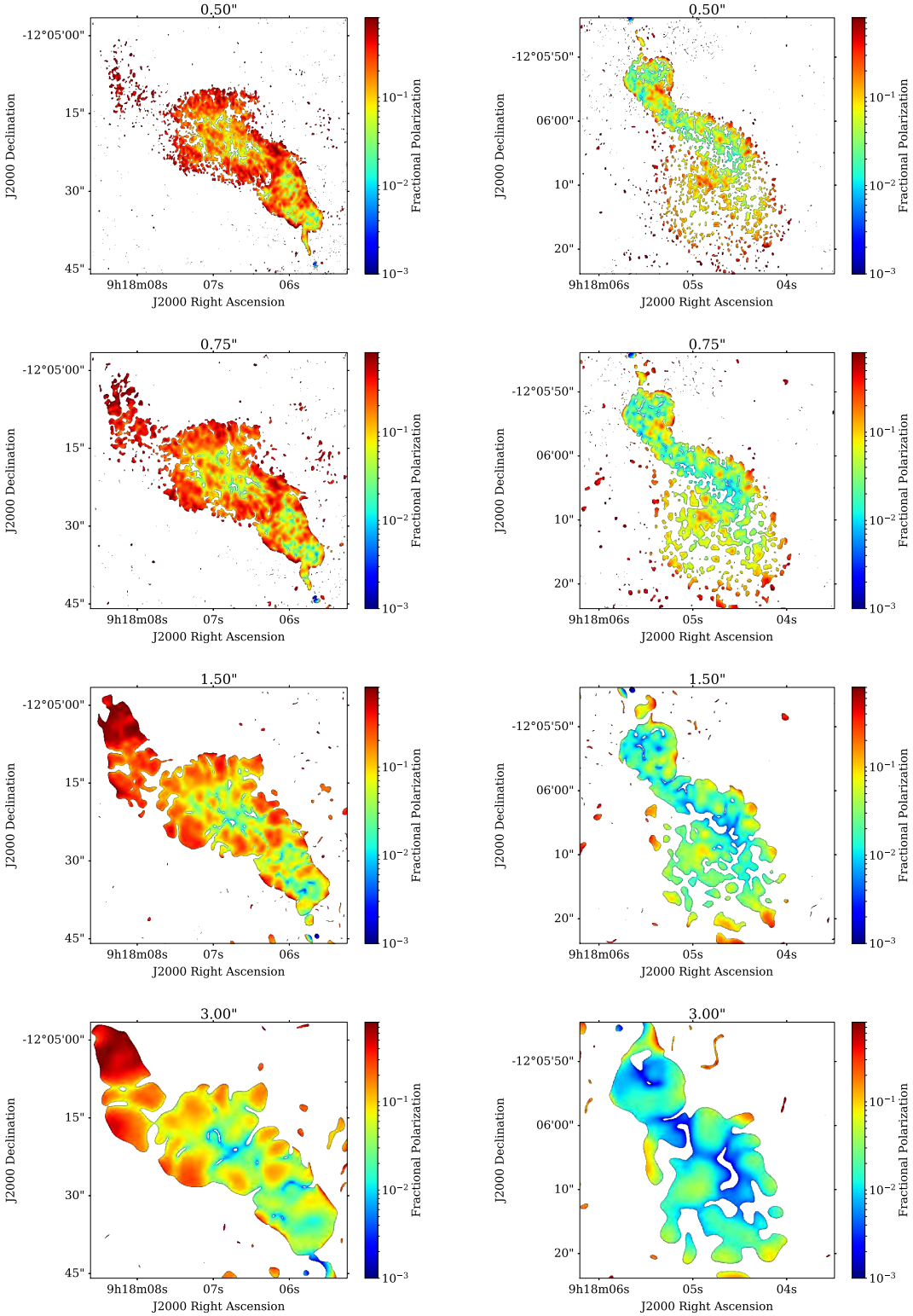

Figure 6.9: *Hydra A fractional polarisation maps at* 6 *GHz as a function of resolution.* We only show pixels with $\sigma_p/p < 60\%$. The tails depolarise with decreasing resolution.

GHz, indicating a wavelength-dependent beam-depolarisation. Beam-depolarisation accounts for more than 70% depolarisation (bluer regions) at 6 GHz, with a few regions showing slight depolarisation of about 20% (redder regions).

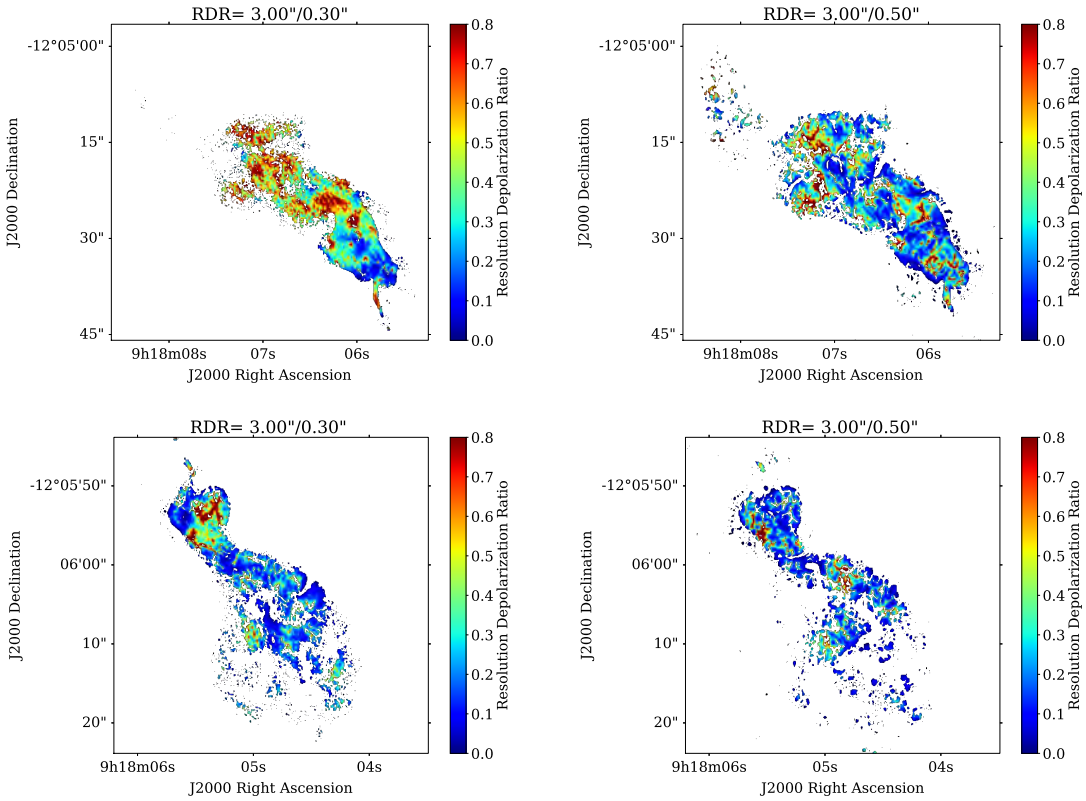

Figure 6.10: *Resolution depolarisation ratio (RDR) across Hydra A tails.* Left column: RDR$= 3''/0.30''$ at 10 GHz. Right column: RDR$= 3''/0.50''$ at 6 GHz. Pixels shown have $\sigma_{\rm RDR}/{\rm RDR} < 60\%$. The 10 GHz RDR indicate small beam-related depolarisation at the extreme regions of the northern tail. The depolarisation is strong at low-frequency, suggesting wavelength-dependent beam-depolarisation.

Figure 6.11 shows plots of fractional polarisation as a function of resolution for a few selected lines-of-sight. We classify the lines-of-sight into Class A, Class B and Class C using the classification scheme developed in Section 4.4.2.2 for Cygnus A data. The first row shows examples from class A, which constitutes about 59% of the lines-of-sight. The second row shows examples from Class B, which constitutes $\sim 12\%$ of the total lines-of-sight. The bottom row shows examples from Class C, which constitutes about $\sim 29\%$ lines-of-sight. In the case of Cygnus A, we find 40% of the lines-of-sight belong to Class A and C, and 20% to class B.

The general expectation is that in the presence of small-scale transverse fluctuations, the observed fractional polarisation should increase (usually) monotonically with increasing resolution, until it reaches a resolution which resolves the foreground fluctuations in the depolarising screen. At this resolution, the observed fractional polarisation will be that of the source itself. However, the way in which fractional polarisation varies with resolution in Hydra A is complex; there are instances where the fractional polarisation begins to decrease at higher resolutions, or decrease/increase at mid-resolutions. Furthermore, the form of variation

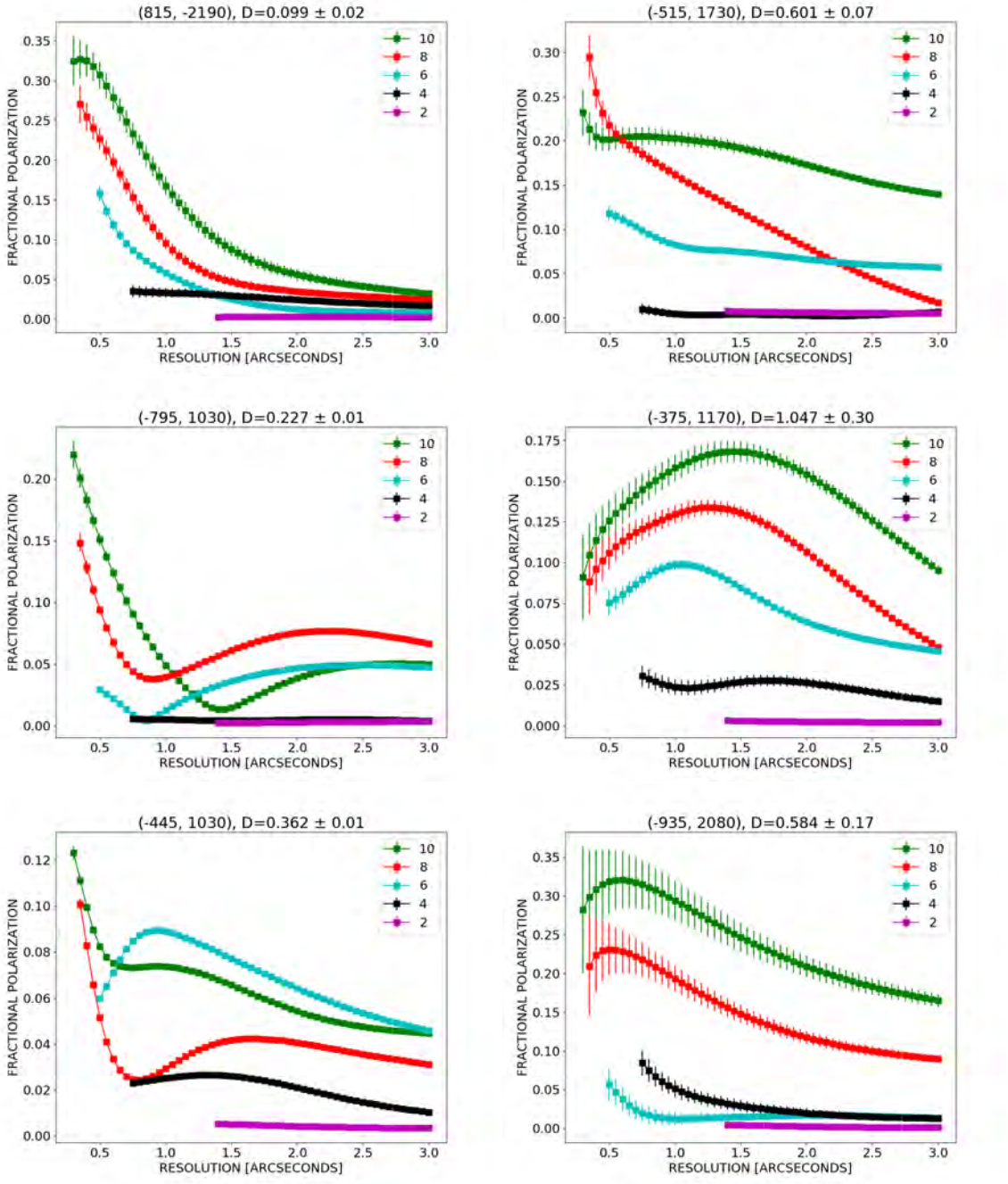

Figure 6.11: *Lines-of-sight fractional polarisation as a function of resolution*. Green: 10 GHz. Red: 8 GHz. Cyan: 6 GHz. Black: 4 GHz. Magenta: 2 GHz. Plot titles: Lines-of-sight position coordinates and the RDR value at $3''/0.3''$ (10 GHz). Top row: Class A. Second row: Class B. Third row: Class C. We find that 59% of the lines-of-sight fall in Class A, 12% in Class B and 29% in Class C.

of the fractional polarisation with resolution of some lines-of-sight differs for different frequencies; which indicates significant wavelength-dependent effects.

6.6 High-Frequency, High-Resolution Faraday Rotation Study

In the previous section, we showed that Hydra A is experiencing significant depolarisation with decreasing frequency at the resolution of our data. The data also strongly suggest that the depolarisation is mostly beam-related and wavelength-dependent. These results, therefore, imply the presence of a turbulent magneto-ionic medium dominant on scales less than 1.5 kpc lying between us and the source of emission.

At higher frequencies, we can achieve even higher resolutions, minimising beam-related depolarisation effects. Additionally, wavelength-dependent depolarisation structures (such as oscillatory and complex decays) are mostly concentrated at longer wavelengths. Utilising the high-frequency data will allow us to derive the "true" emission properties of the polarised source and the ambient Faraday rotating gas, without the complications introduced by the turbulent propagation gas exterior to the source. We intend to use these estimations of the "true" emission properties of the tails and ambient cluster gas to predict polarisation data at lower-frequencies and lower-resolution. A good match between such predictions with the observed data would provide strong evidence that the foreground Faraday rotating gas alone is primarily responsible for the majority of the depolarisation through beam-related effects.

Thus, we utilised the 6 - 12 GHz frequency data at the highest resolution of $0.5'' \times 0.35''$. By looking through the 567 lines-of-sight, we find that the structures in the depolarisation functions are negligible within this frequency range. We fit the fractional Q and U of our images to the real and imaginary parts of the following model, respectively:

$$p = p_0 e^{2i\chi_0} e^{2i\phi\lambda^2 - 2\sigma^2\lambda^4}, \tag{6.1}$$

where p_0 and χ_0 are the zero wavelength fractional polarisation and polarisation angle of the source, respectively, RM is the rotation measure of the ambient gas and σ represents the dispersion of the Faraday depths' distribution due to unresolved fluctuations:

$$\sigma = 812 n_t B_t d\sqrt{N} \quad \text{rad m}^{-2}, \tag{6.2}$$

where $N = L/d$ is the number of turbulent cells of size d along the total pathlength L, n_t is the electron density in the cell and B_t is the magnetic field strength of the cell (Burn 1966; Sokoloff et al. 1998).

We use a simple non-linear least squares fitting algorithm for fitting our model to the data. This was done using minimisation tools provided through the LMFIT software. The parameter search space was confined to $[0.0001, 1]$ for p_0, $\pm\pi/2$ for χ_0, ± 12500 rad m^{-2} for RM and $[0, 2500]$ rad m^{-2} for σ. We only considered pixels with flux density five times above the off-source noise in Stokes I at 1 GHz. This is so that we avoid evaluating spurious/noisy pixels and also to reduce computational time. Figure 6.12 shows the example fits, indicating that the model fits the data well (checked by eye).

Figure 6.13 shows maps of the derived zero wavelength fractional polarisation (top row), RM (middle column) and Faraday dispersions (bottom column). The left column shows the northern tail and the right

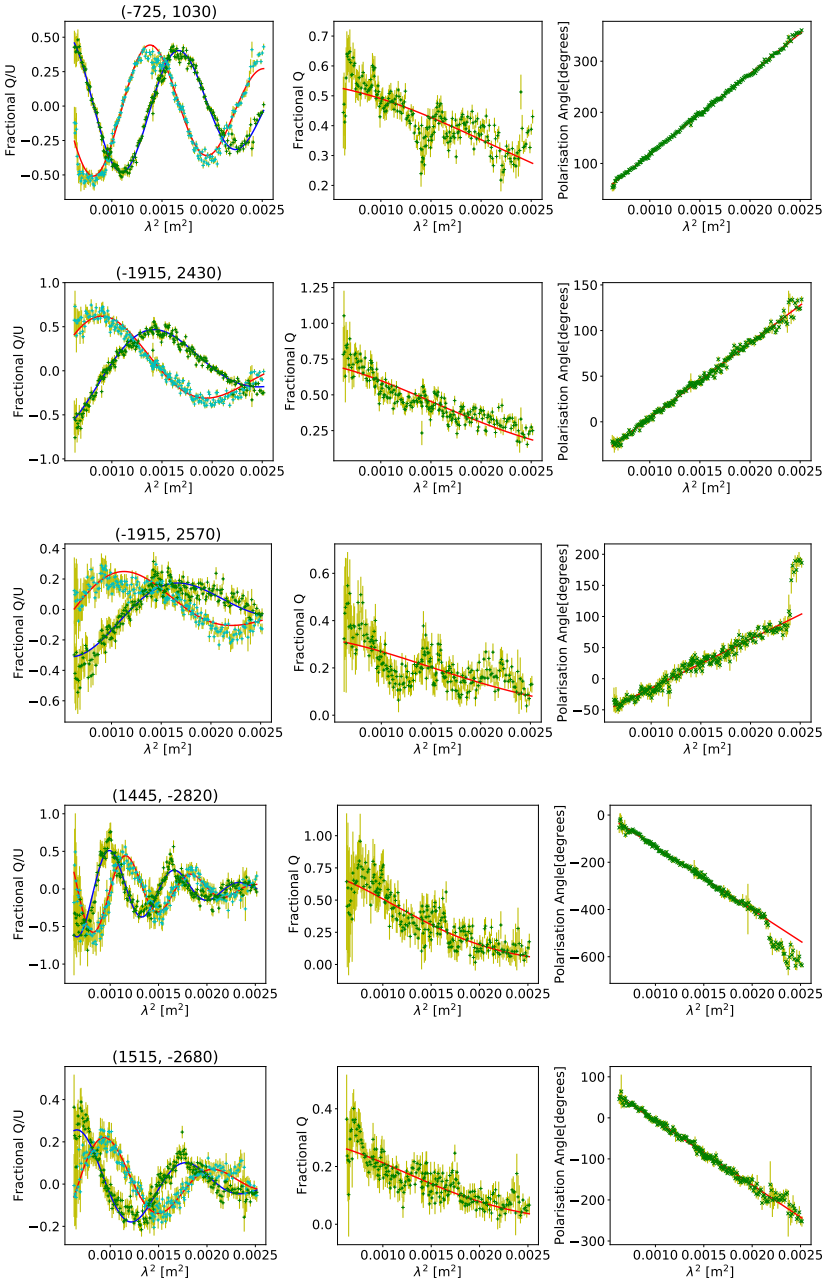

Figure 6.12: *[Lines-of-sight examples showing a model fitting of a single random depolarising screen (see Equation 6.1) to* 6 - 12 *GHz Hydra A data at* $0.50''$*..* Left column: Fractional Q and U as a function of λ^2. Middle column: Fractional p as a function of λ^2. Right column: Polarisation angle as a function of λ^2. The jumps in the polarisation angle on the right side are due to the null in the fractional polarisation, which marks the beginning of the importance of the patchy nature of the Faraday rotating gas. The simple random depolarising model is able to characterise these high-frequency, high-resolution data.

column shows the southern tail. We display pixels with fractional errors of RM and p_0 less than 0.5. The projected magnetic fields ($\chi_0 + \pi/2$) across the tails are shown in Figure 6.14. These images are discussed in the following sections.

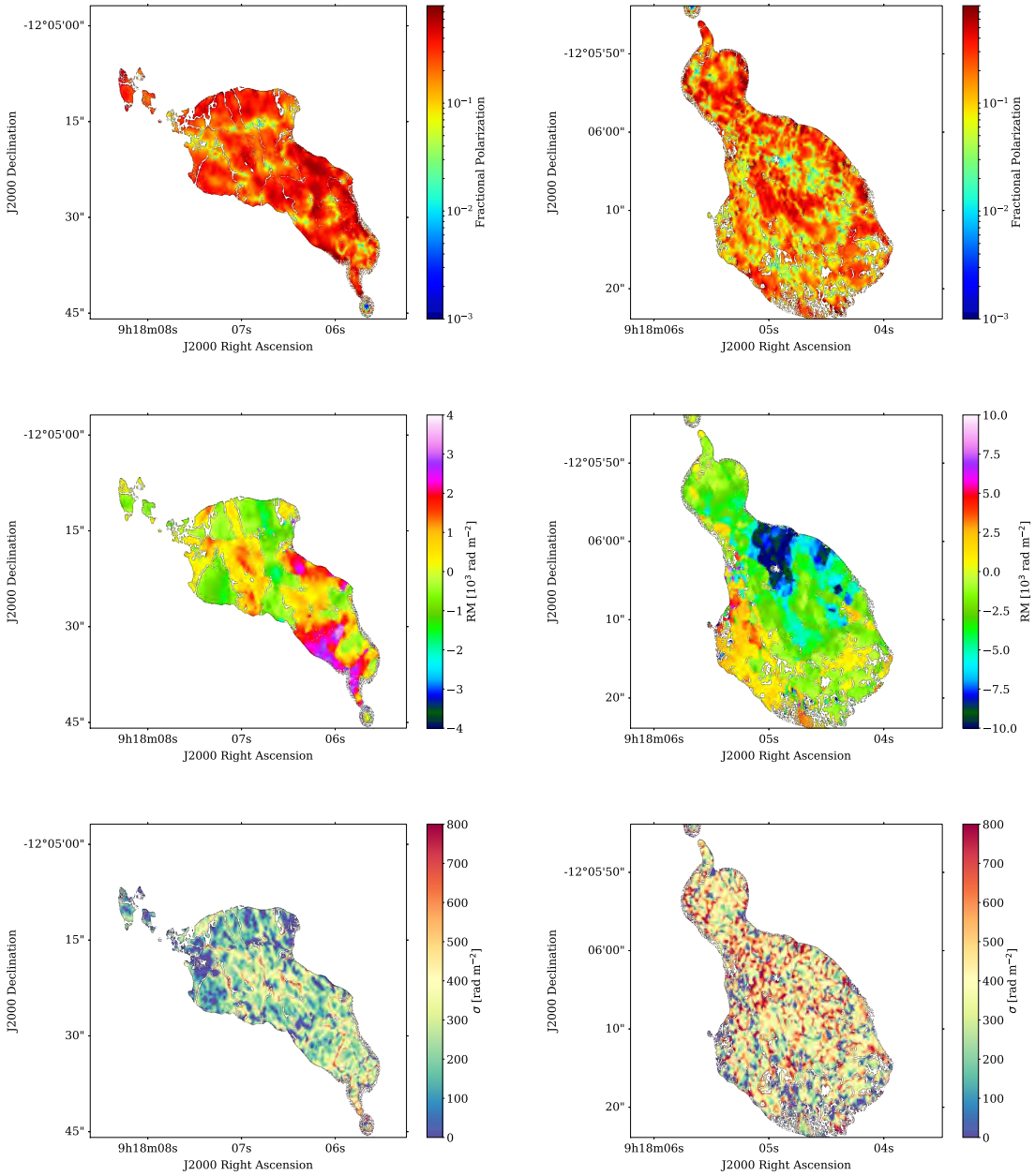

Figure 6.13: *Maps of the estimated parameters obtained by fitting a randomly depolarising model to* $6 - 12$ *GHz* $0.50 \times 0.35''''$ *Hydra A data*. Left column: Northern tail. Right column: Southern tail. First row: Intrinsic fractional polarisation (extrapolated to zero λ^2). Second row: RM. Third row: Faraday dispersions. We show pixels with fractional fitting errors in RM and p_0 less than 0.5.

6.6.1 Intrinsic Fractional Polarisation

The derived zero wavelength fractional polarisation indicate that Hydra A is intrinsically highly linearly polarised, with typical values between 20% and 55% in the northern tail and up to 65% towards the edges of the tail. The southern tail is less polarised and is extremely patchy, with typical polarisation values as low as 0.5% and as high as 50%. The patchiness in the fractional polarisation of this tail could indicate that our resolution is not sufficient to allow probing of the source properties, or that there is an interesting phenomenon occurring inside the tail. We think that the former is probably what is taking place in this tail, especially because in Section 6.5, we showed that the depolarisation structure across this tail is mostly complex with smooth- and complex-decays, which indicate the presence of small-scale magnetic fields. It should be noted that this does not rule out the possibility that this tail may be intrinsically different but at this point, there is no substantial evidence to support this claim.

6.6.2 Rotation Measures

The RM maps presented in this paper are much more detailed than those available in the literature (for example, Taylor and Perley 1993; Laing et al. 2008a). RM range between -2000 rad m^{-2} and 3300 rad m^{-2} across the northern tail and -2000 rad m^{-2} and 11900 rad m^{-2} across the southern tail. The RM across the southern tail are mostly negative, with a small region situated in the south-eastern parts of the tail with positive RM. The RM associated with this tail are remarkably patchy on small-scales of ~ 1 kpc. A region of extremely high RM does not seem to be associated with any obvious tail features: neither in total intensity, fractional polarisation, or dispersions. The RM across the northern tail, on the other hand, are both negative and positive and are relatively more ordered on small-scales of ~ 2 to 6 kpc. They also seem to occur in alternating bands of positive and negative values. The rotation measures at the tail of the source (further from the AGN) are similar to that of the body of the tail. Alternating bands in RM are very common in radio sources; they were observed in Cygnus A (Sebokolodi et al. 2020), as well as in M84, 3C 353, 0206+35 and 3C 270 (Guidetti et al. 2011). Similar to the results of Taylor and Perley (1993), the RM across the jets are consistent with those of the nearby tail, suggesting a common origin.

6.6.3 Faraday Dispersions

The Faraday dispersions characterise the rate of depolarisation between 12 GHz and 6 GHz. The dispersions in the northern tail range between 150 rad m^{-2} and 450 rad m^{-2} and a few narrow regions with dispersions going up to 850 rad m^{-2}. Errors associated with these dispersions range from typical values of $\lesssim 10-30$ rad m^{-2}. There are regions which display very small dispersions close to zero. These regions can be a result of no significant depolarisation, or re-polarisation due to a noisy signal. The dispersions across the southern tail range between $300-950$ rad m^{-2}. The small dispersions are generally associated with small fitting errors of no more than 10 rad m^{-2}, and higher dispersions with errors of up to 100 rad m^{-2}. The dispersions across this tail are extremely chaotic. However, it is not surprising given the large RM gradients associated with this tail. Looking through the narrow regions in the northern tail, we find that these narrow

high dispersion features are indeed associated with large RM jumps. Similar features can be seen across 3C 31 (Laing et al. 2008a). There is no dependence of the dispersions on radial distance. The dispersions are similar across both the tails and in the jets.

6.6.4 Intrinsic Projected Magnetic Field Orientation

Figure 6.14 shows the intrinsic magnetic field orientation across the tails obtained by adding $\pi/2$ to the derived intrinsic polarisation angle, χ_0. The fields follow the boundaries and filamentary structures of the tail emission. This behaviour is quite common in radio galaxies, for example 3C 465 (Eilek and Owen 2002), Cygnus A (Dreher et al. 1987; Sebokolodi et al. 2020) and Pictor A (Perley et al. 1997); it is generally understood as an effect resulting from shearing (and compression) of the tangled tail magnetic fields at the tail boundary, resulting in suppression of field components normal to the boundaries of the tails (Laing 1980). The field vectors are generally smooth across the northern tail, while slightly chaotic across the southern tail. As with the other fitted parameters, this is likely due to significant structures on scales less than the $0.5''$ resolution.

6.6.5 Faraday Dispersions vs Rotation Measures Across Hydra A at $0.5''$

Figure 6.15 shows the RM as a function of Faraday dispersions for lines-of-sight with fitting error in RM and σ less than 20 rad m^{-2}. There is a tendency for larger dispersions to be associated with larger Faraday RM. The general correlation is very weak. The observed Faraday dispersions are likely a result of larger gradients which are associated with large RM.

6.6.6 V-shaped Structure in Northern Tail

An examination of the highest resolution intensity image from the inner part of the northern tail shows a distinct V-shaped feature. It sits $\sim$ 12 kpc north of the galactic core and is oriented roughly along the local direction of the tail. It is apparent in total intensity and is also traced by projected magnetic field lines. However, there is only a small effect in the fractional polarisation on the V-shape. A close-up image is shown in Figure 6.16. The apex of the "V" points toward the galaxy, which is also the "upstream" direction relative to the systematic outflow likely to be moving through the northern bright spot.

We do not know the cause of this structure, however, its shape suggests a bow shock or magnetic draping around an object within the tail. If it is a bow shock, its opening angle requires a Mach number of $\sim 3-4$. Although large-scale tails in FR I sources are thought to be subsonic, the jets close to the AGN are likely supersonic. If this is the case, the supersonic flow may continue through the growth of the instability which causes the bright spot and changes the narrow inner jet to a broad tail. Alternatively, a slower flow can 'drape' a weak magnetic field around an object in the flow (for example, Lyutikov 2006; Dursi and Pfrommer 2008) and can also explain the ordered magnetic fields along the sides of the structure. A third possibility suggested by the V-shape could be a wake behind some object in the flow. However, the ordered magnetic field along the sides of the 'V' seem inconsistent with the turbulence characteristic of subsonic wakes.

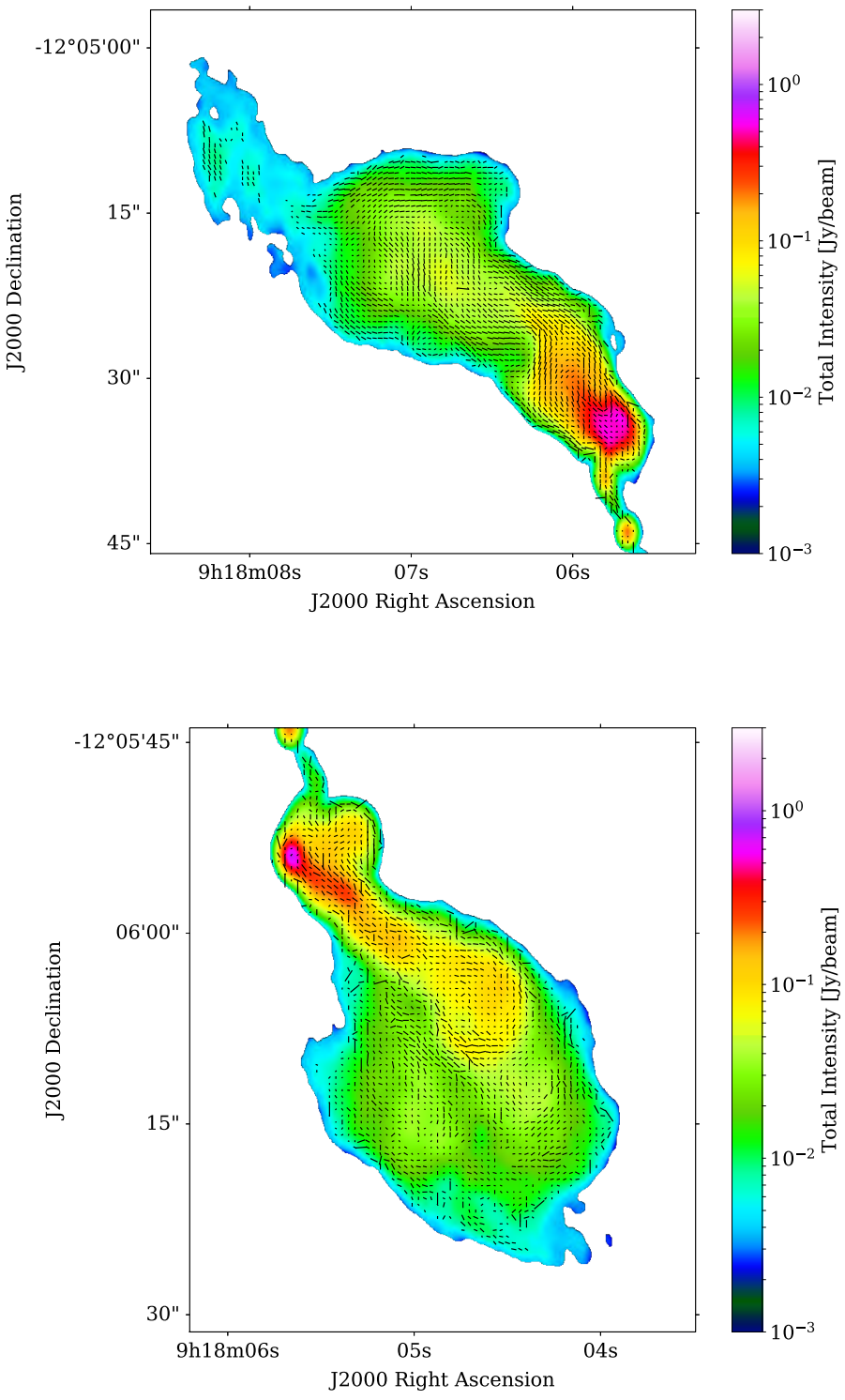

Figure 6.14: *Magnetic field orientation across Hydra A tails at* $0.5''$*, superimposed on a* 2 *GHz total intensity map.* The vector lengths represent the fractional polarisation scaled by a factor of 10 (for magnification).

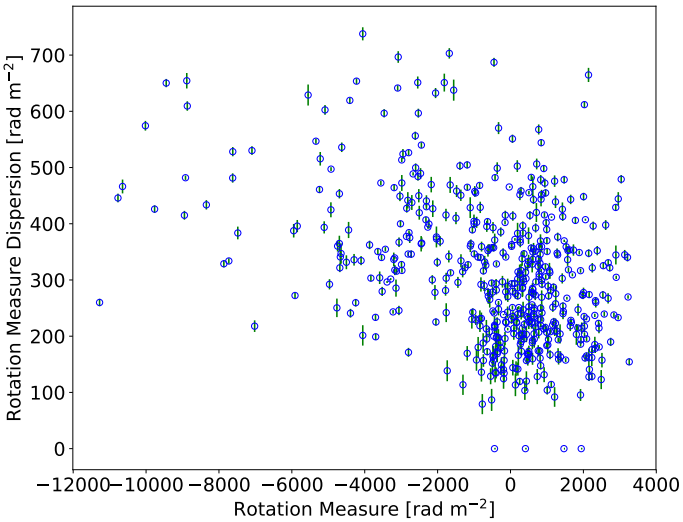

Figure 6.15: *RM as a function of Faraday dispersions*. The data points shown correspond to the lines-of-sight shown in Figure 6.8 with fitting error in RM and σ less than 20 rad m^{-2}.

Each of these possibilities depend on the existence of a heavy object – say a cold gas cloud – within the flow. The inner regions of many galaxies in CC clusters contain filaments and clouds of thermal and molecular gas (Olivares et al. 2019). Similar objects might exist in the Hydra A galaxy, however they have not yet been detected. The Hydra A galaxy contains a 5 kpc cool gas disk, rotating around the core of the central galaxy (Rose et al. 2019) but no $H\alpha$ or molecular emission has been detected yet outside of this disk.

6.7 Predictions of Low-Frequency, Low-Resolution Data

In Section 6.5, we showed that the interpretation of the depolarisation in Hydra A data is limited by spatial resolution – our observations do not provide enough resolution to properly resolve the variations occurring across the tails. Though it is clear that the beam-related effects are important, it is still uncertain as to how much of the effects are beam-related. This can only be fully answered with higher-resolution observations, particularly at low-frequencies. Based on the left column of Figure 6.10, we would need resolutions much better than $0.30''$ (perhaps 10 times better), at frequencies down to 2 GHz. Instruments with such observing capability are currently not available. Thus, we have developed a method of using the high-frequency, high-resolution images of the derived RM and polarised emission to predict the lower-resolution, lower-frequency emission properties. Comparison of the observed with the predicted emission will then allow a judgement on whether the assumptions inherent in the prediction are correct. The basic assumption here is that these high-resolution maps approximate that of the true emission of the tails and rotating gas. A close prediction will be a strong indication for a foreground Faraday rotating screen with small-scale magnetic fluctuations which cause the depolarisation. A mismatch, on the other hand, will be an indication of either the presence of much smaller scales $< 0.35''$, which were not accurately modelled, or that the beam-related effects are not

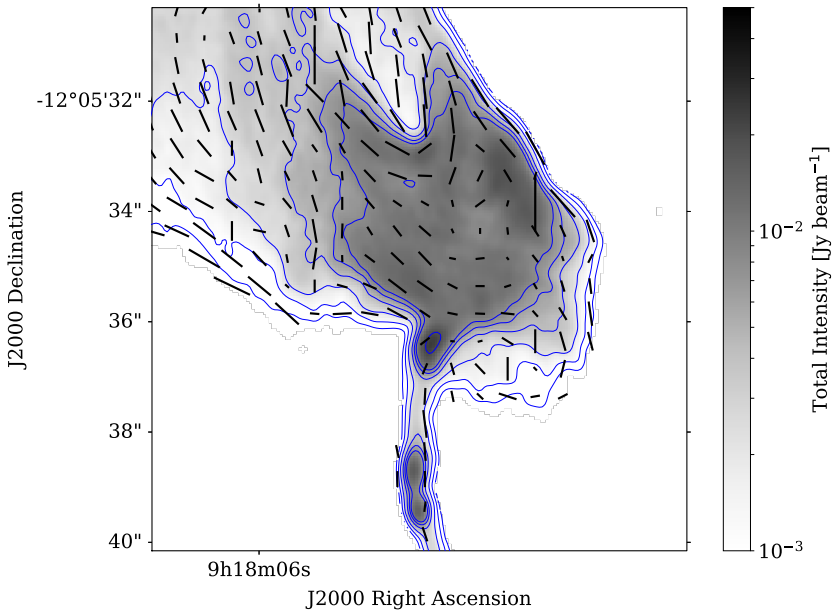

Figure 6.16: *The "V"-shape like structure in the northern tail of Hydra A.* The orientation vectors correspond to the magnetic field orientation and the lengths give the fractional polarisation, scaled by a factor of 10 for visibility. The magnetic field orientation traces the "V", while the fractional polarisation has a minimal effect.

a dominant effect and the depolarisation is due to a different physical origin. Both of these have an important physical implication but this is beyond the scope of this work.

Given the derived p_0, χ_0 and RM, we determine the model polarised flux as:

$$P = p_0 I e^{2i\chi_0} e^{2iRM\lambda^2}. \tag{6.3}$$

We obtain I by first determining the spectral index at $0.50'' \times 0.35''$ (using 6 - 12 GHz data) and using this index map to predict total intensities across 2 - 12 GHz. The polarised flux in Equation 6.3 are computed for λ^2 between 2 - 12 GHz – the resulting polarised cubes will be at the resolution of the input maps ($0.50'' \times 0.35''$). We then obtain Stokes Q and U by taking the real and imaginary part of Equation 6.3, then convolve these Stokes maps, including Stokes I to $1.50'' \times 1.0''$. The convolution is done using AIPS task CONVL, with factor input as 0. This is the same procedure which was used for Cygnus A (see Section 4.6, Sebokolodi et al. 2020).

Figure 6.17 shows the predictions in red and the actual data in black. The plots show fractional polarisation as a function of λ^2 in the left column, polarisation angle as a function of λ^2 in the middle column, and the Faraday spectra in the right column. The two top rows in Figure 6.17 show example lines-of-sight whose data are predicted well within measurement errors. We find that roughly 4% of the lines-of-sight are reproduced well. The last three rows show example lines-of-sight whose general depolarisation pattern/structure is well reproduced but with underestimated depolarisation (nearly all) or shifted nulls of the oscillations. We find that roughly 71% of the lines-of-sight are partially reproduced. The remaining 25% are poorly predicted, or

are too noisy to make any accurate judgment. We used fractional polarisation (the left columns) to decide whether a prediction is good or not. This judgment was done by eye.

Although this approach is simple and naive, we find that the depolarisation structures that are seen in the data are reproduced remarkably well. This has an important implication, namely that the structures in the RM map are responsible for the observed depolarisation. Thus, beam-related effects are indeed the main contributor to the depolarisation. This is perhaps more obvious when looking at the Faraday spectra; the different peaks in the data come from different RM components across the resolution beam. The shift in the nulls of the oscillation occur very rarely, while the underestimation of the depolarisation is common. These underestimations are likely due to the presence of smaller field scales not mapped by our $0.50'' \times 0.35''$ resolution. If this is the case, we would expect broadening of the components in the Faraday spectra, which is not seen. However, it could simply be because the resolution in Faraday space is too poor to notice this effect. This will imply scales of $\lesssim 0.35$ kpc and changes in $RM \lesssim 180$ rad m^{-2}. Another possible cause for the underestimations is systematic errors, or lines-of-sight effects. Thus, we emphasise that these predictions should be treated as approximations, not as proof but still indicative of the main effect for the depolarisation.

The oscillatory structures are remarkably reproduced, indicating well-resolved field scales on the order of our resolution beam $\gtrsim 0.5$ kpc. This work provides further evidence for a very complex magnetic field structures around this radio galaxy. Moreover, to definitively probe the line-of-sight effects (mixing of tail emission and the ambient cluster gas), we are going to need high-sensitivity instruments with exceptionally high-resolution. To obtain a $0.1''$ resolution across the 2 - 12 GHz, will require an instrument with a maximum baseline ~ 10 times larger than that the current maximum baseline of JVLA at A-configuration. Such baselines are proposed for future instruments. For example, the SKA phase 1 mid-frequency in South Africa will have a baseline of up to 150 km (allowing a resolution of $\sim 0.3''$ at 1.4 GHz) and six times more sensitivity than the JVLA. The SKA phase 2, on the other hand, is planned to have fifty times better sensitivity and ten times better spatial resolution (at 1.4 GHz) than the JVLA. The New Generation of VLA (ngVLA) in the United States is planned to have ten times better sensitivity than the JVLA and baselines thirty times longer than the current VLA, allowing sub-arcseconds to a few milli-arcseconds resolutions (McKinnon and Selina 2018; Selina et al. 2018; Dunbar et al. 2019; Murphy and ngVLA Science Advisory Council 2021)

6.8 Small-Scale Fluctuations

In the above section, we demonstrated how fluctuations in the RM map at ~ 500 pc are able to explain the depolarisation and structures at ~ 1500 pc. This provides evidence of small-scale magnetic field fluctuations in or around Hydra A. In this section, we demonstrate this even further, by looking at the wideband data at two resolutions: $1.5''$ and $3''$. In this case, we convolved our original data at $1.5''$ to $3''$ using CONVL in AIPS. Figures 6.18 to 6.20 show examples of the results. We provided more lines-of-sight so that the reader might further appreciate the complexity in these data. Once again, the importance of spatial variations across the tails of the source is evident. The Faraday spectra become simpler at higher resolutions, further suggesting the presence of unresolved fluctuations on scales $\lesssim 3$ kpc.

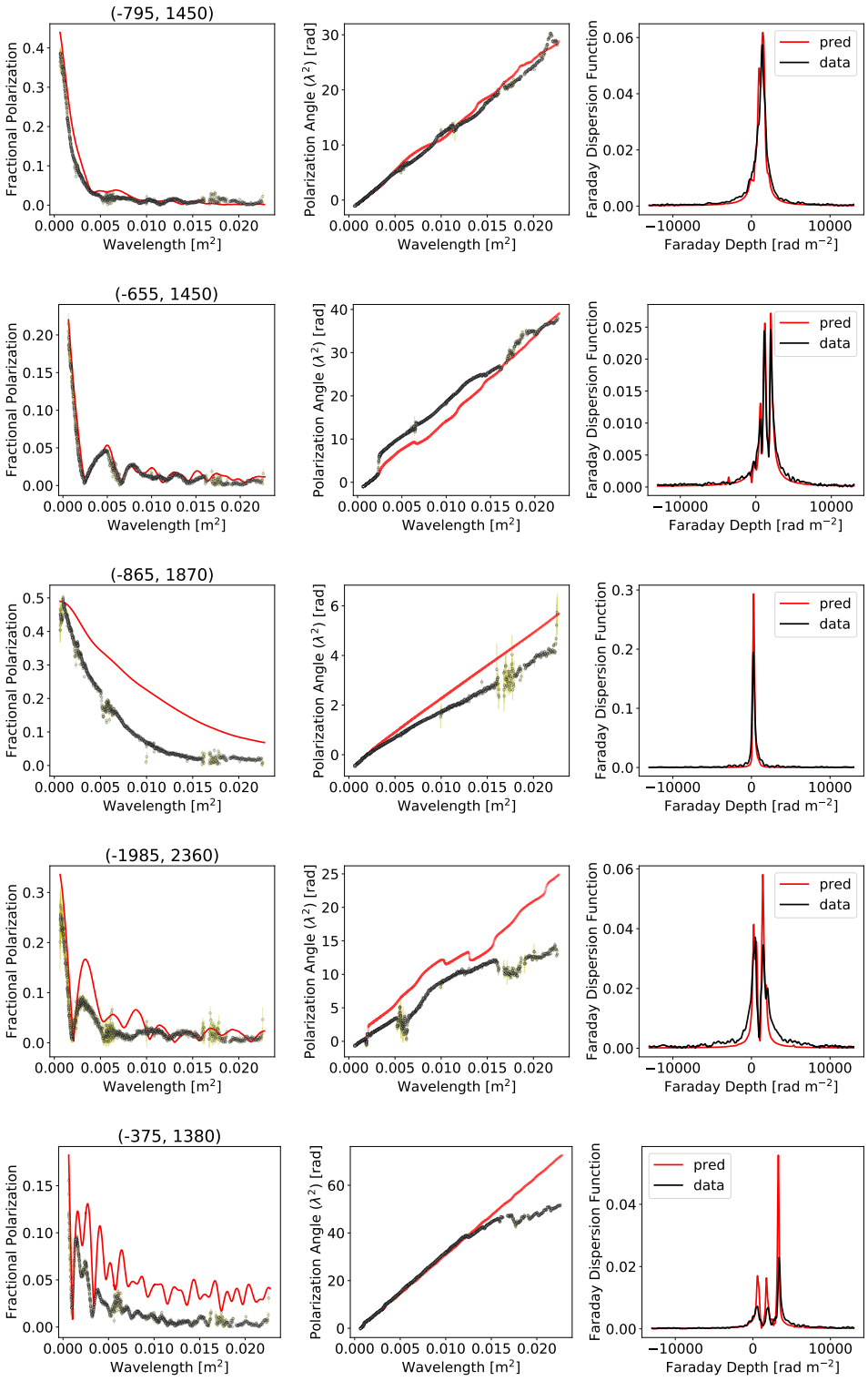

Figure 6.17: *Predictions of low-frequency, low-resolution data using high-resolution polarisation and RM maps.* Left column: Fractional polarisation vs λ^2. Middle column: Polarisation angle vs λ^2. Right column: Faraday spectra. Black: Observed data. Red: Predictions. Two top rows: Good predictions (roughly 4% of the lines-of-sight). Last three rows: Partially reproduced ($\sim 71\%$).

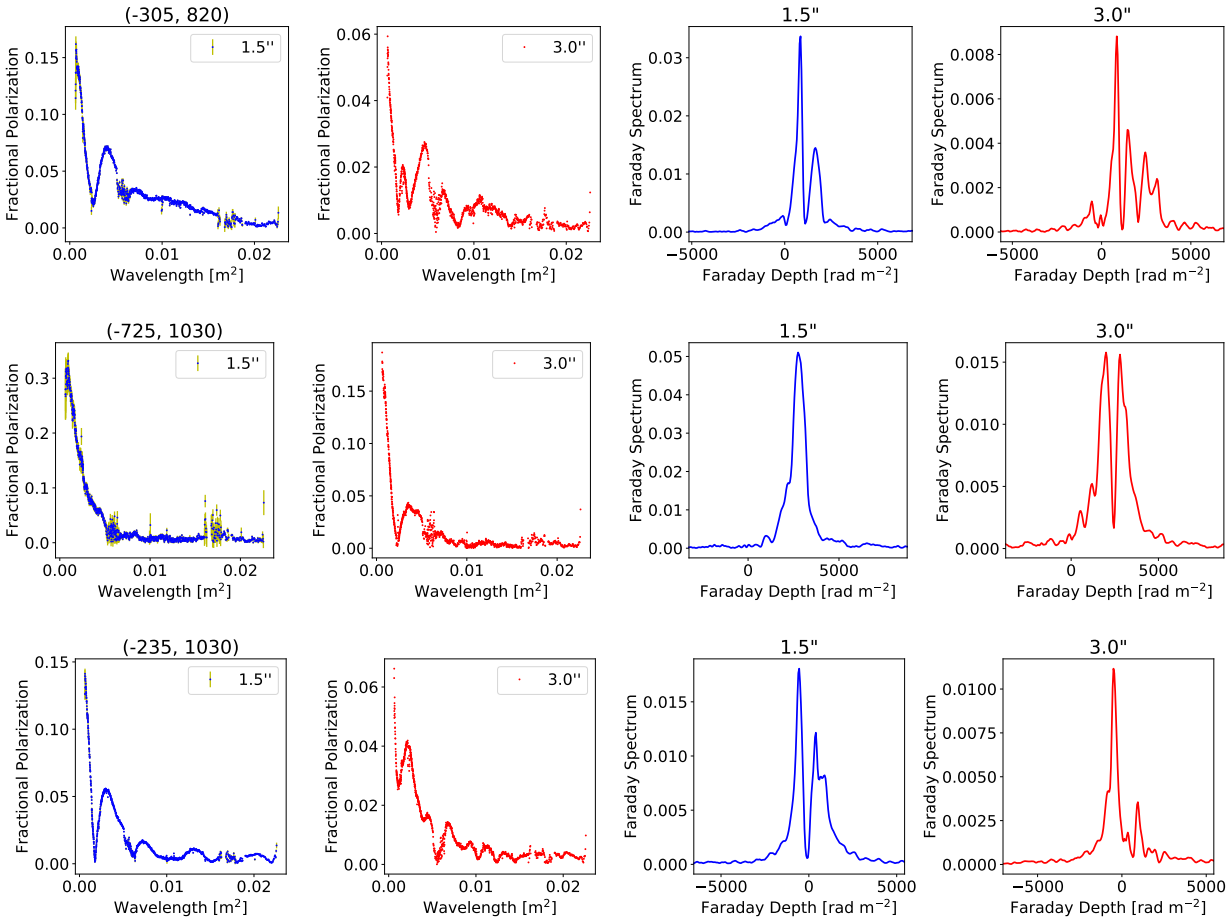

Figure 6.18: *Lines-of-sight polarisation behaviour at* $1.5''$ *(blue) and* $3''$ *(red).* Two left columns: Fractional polarisation vs λ^2. Two last columns: Faraday spectra of 2 - 12 GHz data. The polarisation structure is simpler at a higher-resolution, indicating the presence of unresolved fluctuations.

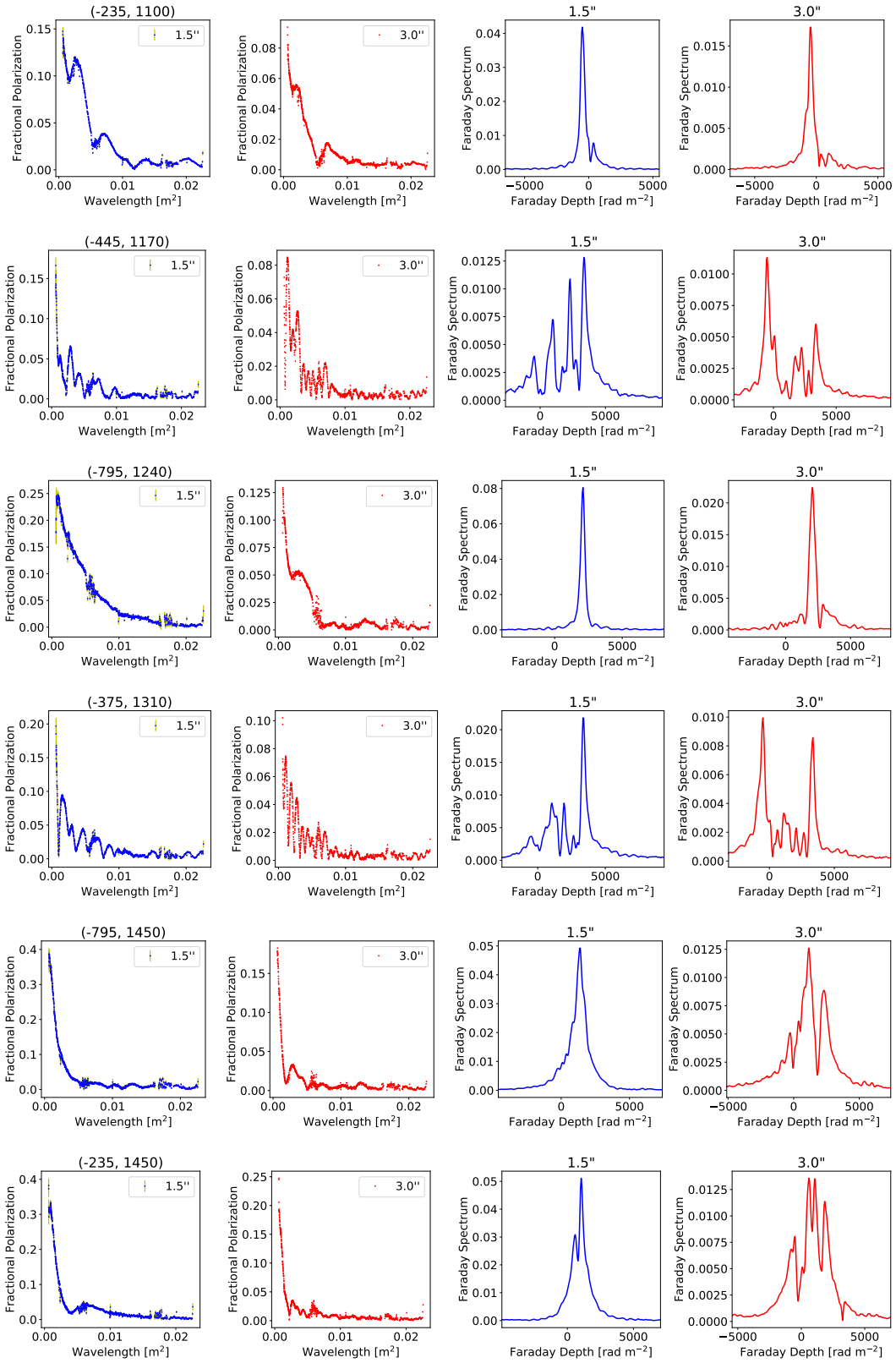

Figure 6.19: *Lines-of-sight polarisation behaviour at* $1.5''$ *and* $3''$. Similar to Figure 6.18.

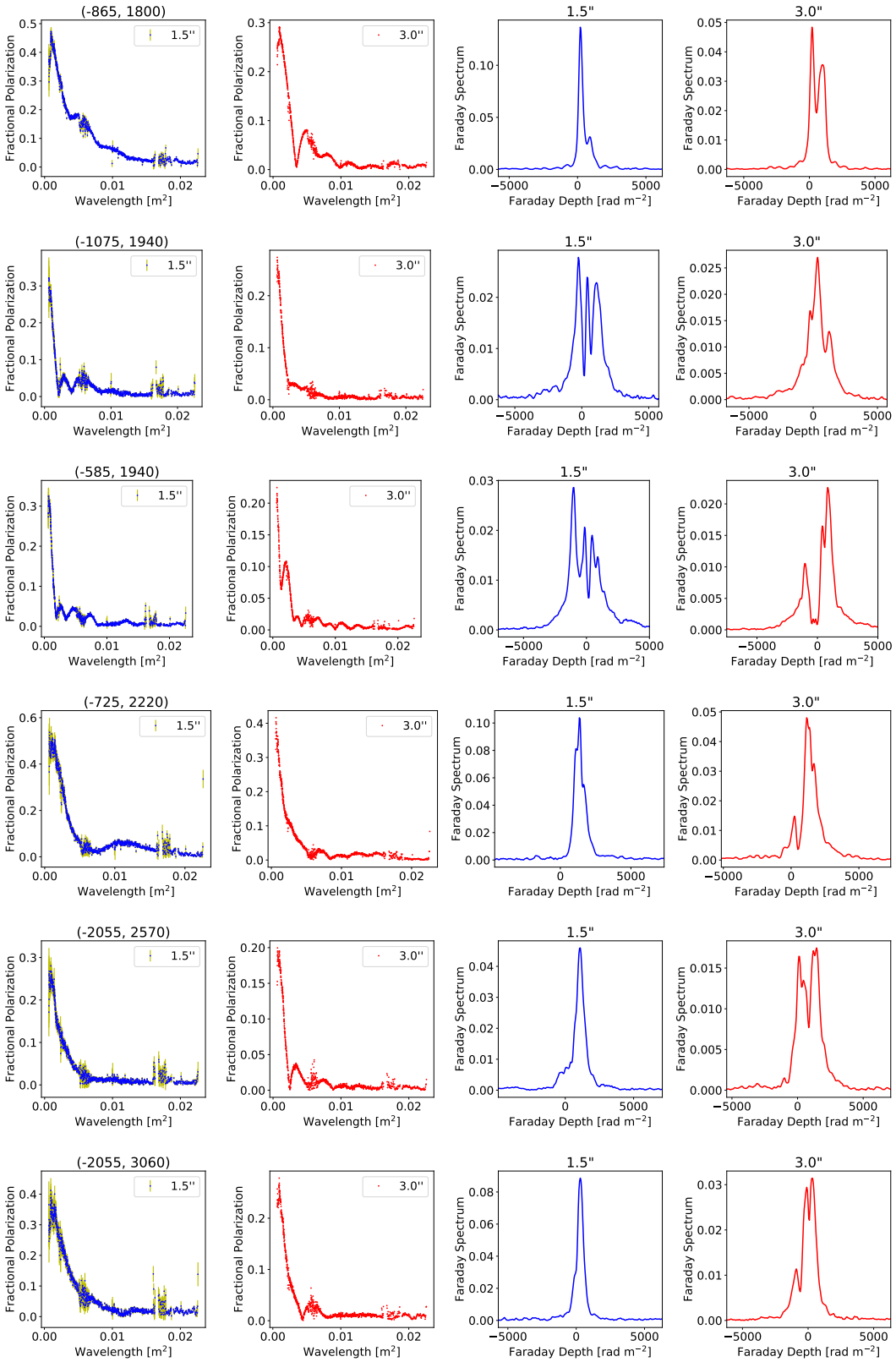

Figure 6.20: *Lines-of-sight polarisation behaviour at* $1.5''$ *and* $3''$. Similar to Figure 6.18 and 6.19.

6.9 Classification and Characterisation of the Faraday Spectra

We classified the different lines-of-sight based on their Faraday spectra as in Section 5.2. There are six categories, namely the single-peaked spectra, single-peaked with smaller peaks spectra, blended double-peaked spectra, resolved double-peaked spectra, blended multiple-peaked and resolved multiple-peaked spectra. Table 6.3 summarises the results. Figure 6.21 shows a few examples of these classes for smooth decaying depolarising lines-of-sight, Figure 6.22 show similar examples but for lines-of-sight with oscillatory depolarisation structures and Figure 6.23 shows example lines-of-sight with complex decaying depolarisation. The majority of the Faraday spectra across Hydra A spectra are multiple-peaked, with a few (about 10%) showing single peaks. This is unlike the case of Cygnus A, where there are 40% of the lines-of-sight that are single-peaked. The differences between the polarisation behaviour in Hydra A and Cygnus A may be attributed to the difference in resolution: the data of Cygnus A are at resolution ~ 0.75 kpc, while the data of Hydra A data are at resolution ~ 1.5 kpc. In Figure 4.19 to 4.24, we showed that Cygnus A data tends to show complexity (such as multiple structure) in the Faraday spectra at poorer resolution. However, some single-peaked lines-of-sight are not affected by the change in resolution, thus we doubt that the difference in resolution is the only factor contributing to the difference in Faraday structure. The second contributing factor may be the presence of more turbulence in the Hydra A's ambient cluster gas magnetic fields.

Table 6.3: *Faraday Spectra Classification*

Definition	Depolarisation Class			Classifiable
	smooth	oscillatory	complex	
Single-peaked	43	0	12	55
Single-peaked with smaller peaks	15	1	57	73
Blended double-peaked	13	8	51	72
Resolved double-peaked	0	8	12	20
Blended multiple-peaked	46	20	109	175
Resolved multiple-peaked	7	23	128	158

Figure 6.24 shows the distribution of the six Faraday classes across the tails. The southern tail is dominated by blended and resolved spectra and the northern tail consists of all the Faraday classes. The distribution of the spectra does not show any spatial correlation, suggesting some level of randomness.

Further, we characterise the width and mean of Faraday spectra by fitting a 1D Gaussian function. We did the same fitting for Cygnus A data (see Section 5.3). Figure 6.25 shows fitting examples to the different Faraday spectra across the tails. The location of each line-of-sight is indicated at the top of each plot. The derived mean ϕ_{mean} and the width σ_{stdev}, are shown inside the parenthesis, respectively. The mean and width are presented in rad m^{-2}.

Figure 6.26 shows fractional polarisation in λ^2-space at 8 GHz as a function of peak of the fractional Faraday spectrum (left). On the right, the derived ϕ_{mean} and σ_{stdev} of the 1D Gaussian fitted to the Faraday spectra. The multiple-peaked spectra tend to have a low peak Faraday amplitude. The fractional polarisation

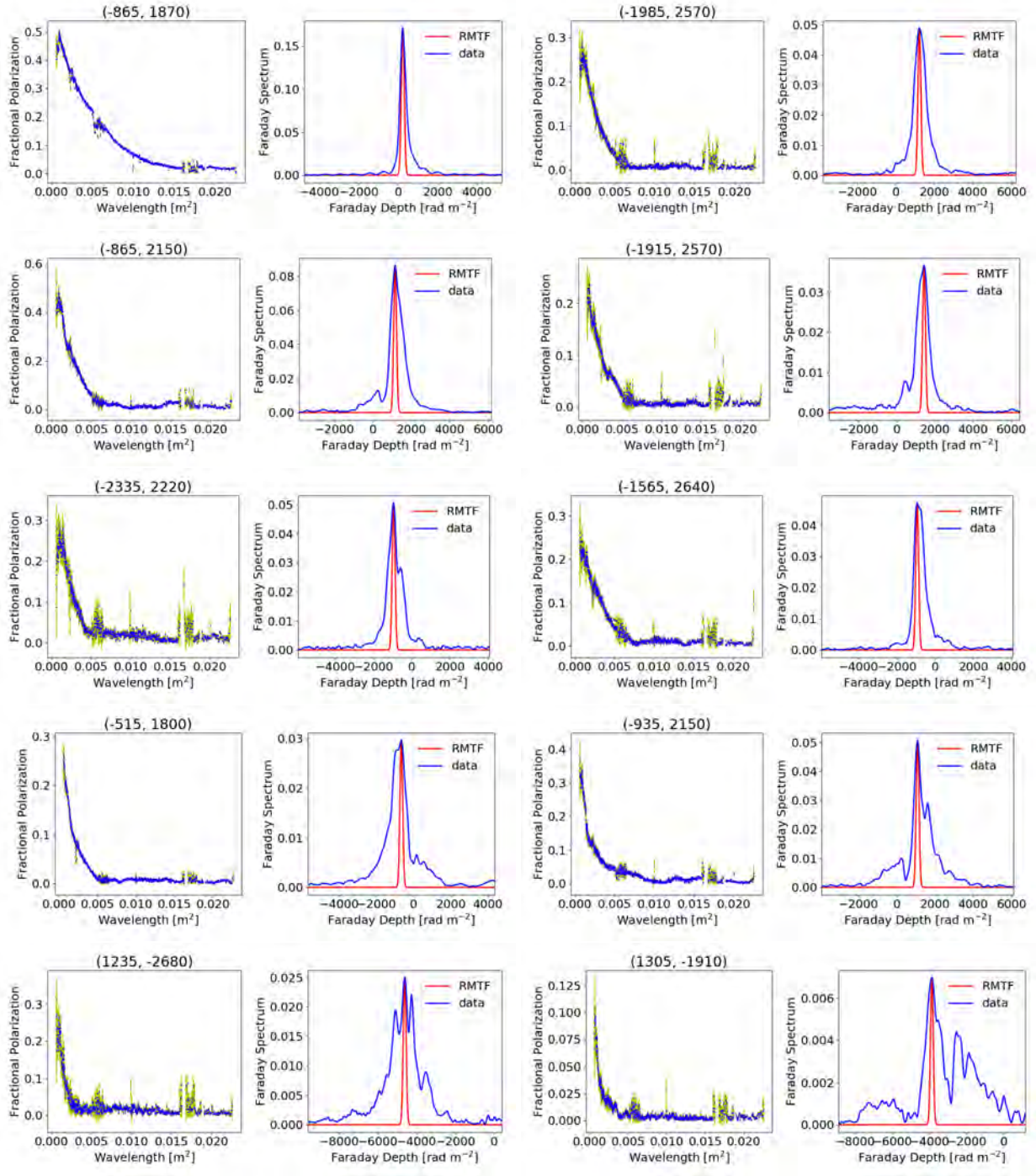

Figure 6.21: *Faraday spectrum classes for lines-of-sight with smooth decays*. Top row: Single-peaked spectrum. Second row: Single-peaked with smaller peaks. Third row: Blended double-peaked. Fourth row: Blended multiple-peaked. Fifth row: Resolved multiple-peaked.

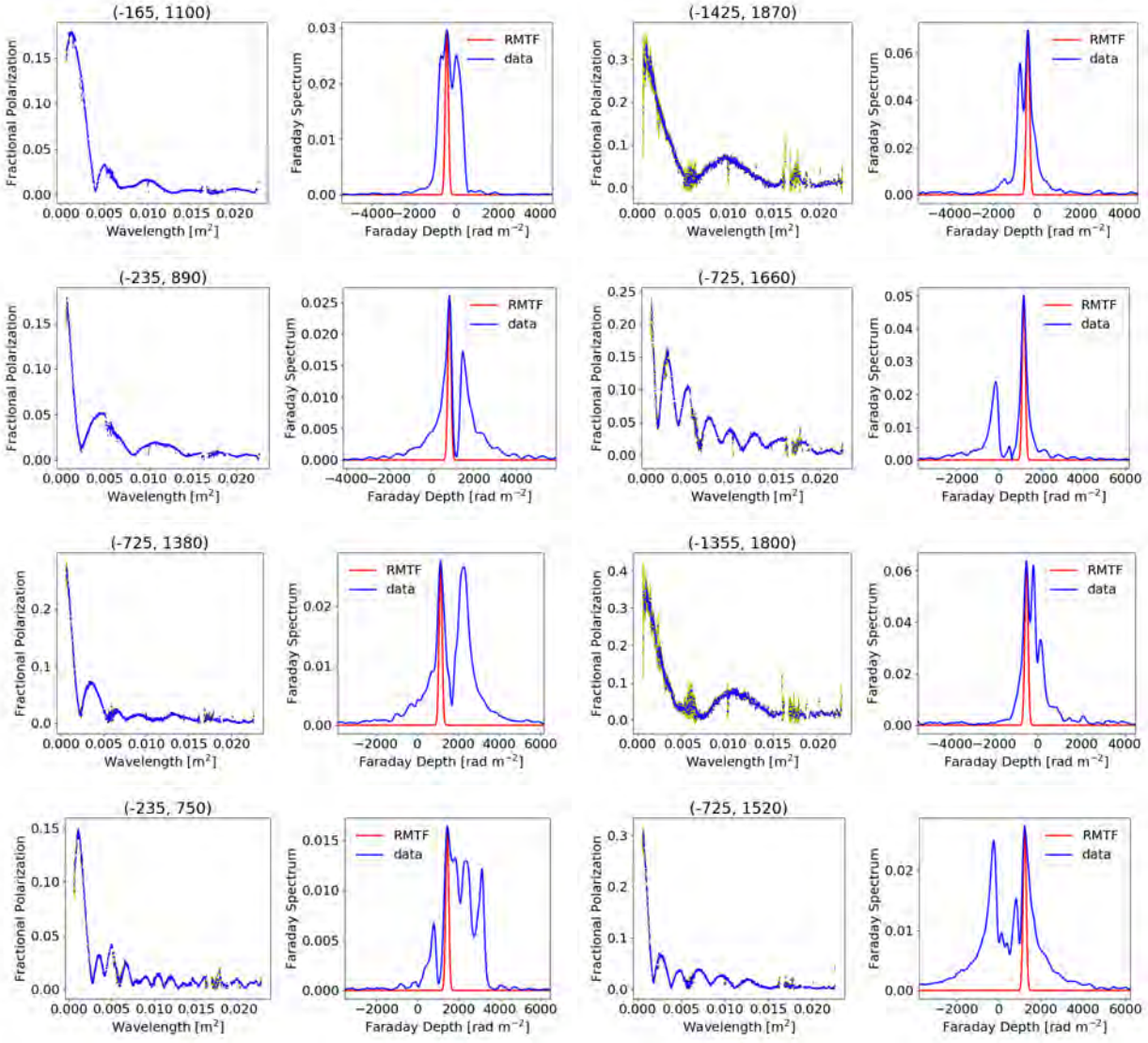

Figure 6.22: *Faraday spectrum classes for lines-of-sight with oscillatory decays.* Top row: Blended double-peaked spectra. Second row: Resolved double-peaked. Third row: Blended multiple-peaked. Fourth row: Resolved multiple-peaked spectra.

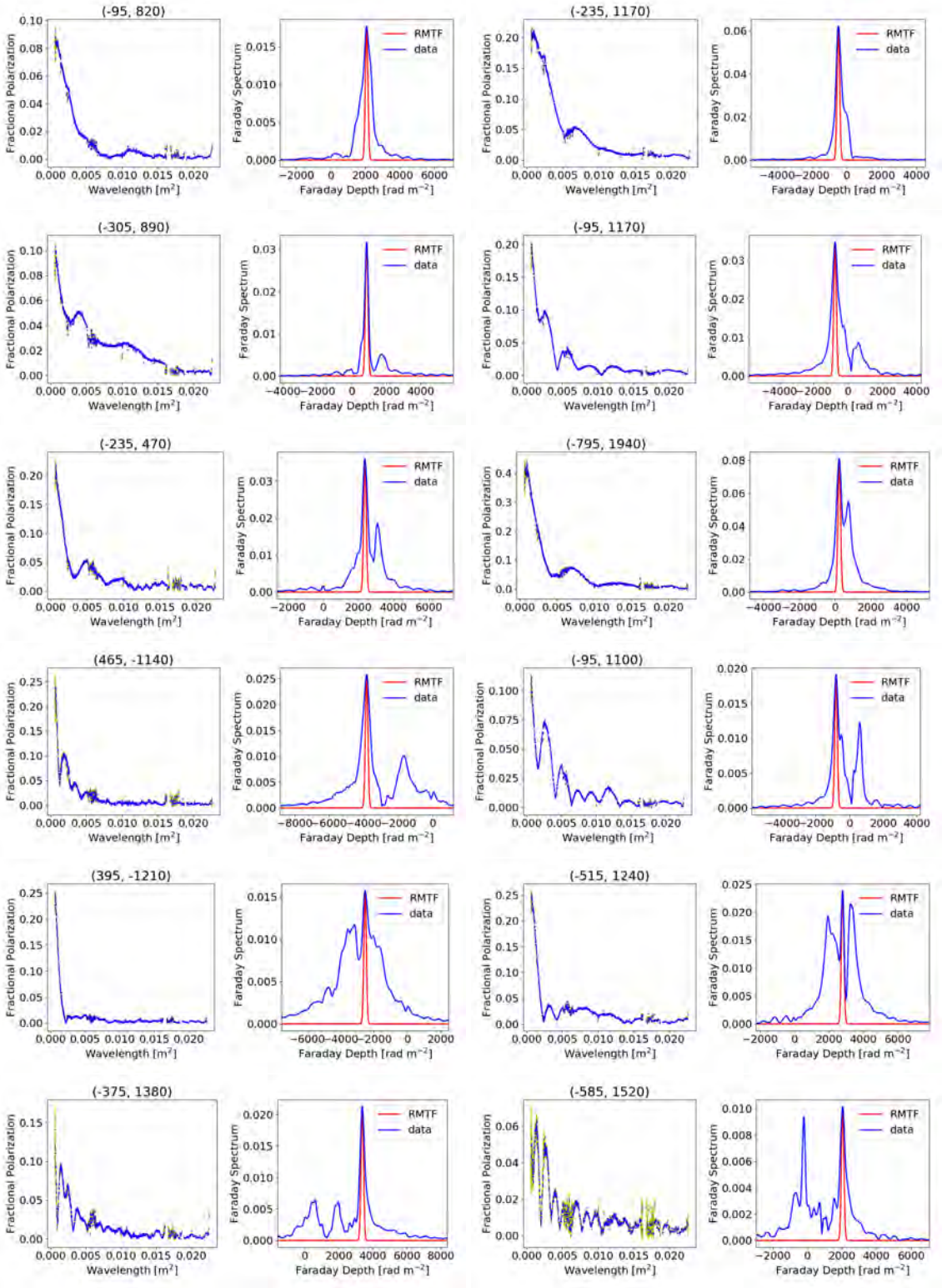

Figure 6.23: *Faraday spectrum classes for lines-of-sight with complex decays*. Top row: Single-peaked spectra. Second row: Single-peaked with smaller peaks. Third row: Blended double-peaked. Fourth row: Resolved double-peaked. Fifth row: Blended multiple-peaked. Sixth row: Resolved multiple-peaked.

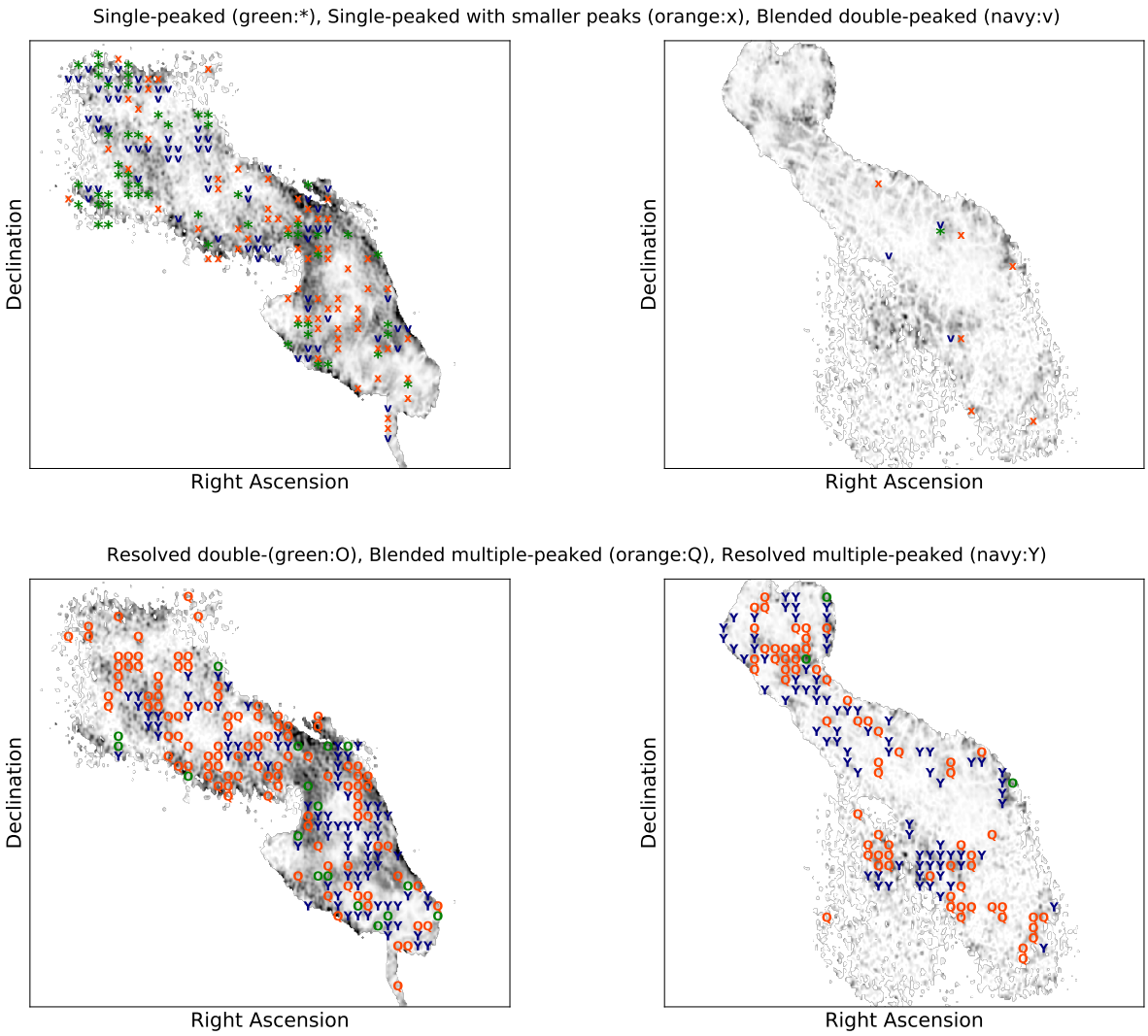

Figure 6.24: *Spatial distribution of the different Faraday spectrum classes across the tails of Hydra A.* Green *: Single-peaked. Orange x: Single-peaked with smaller peaks. Navy v: Blended double-peaked. Green O: Resolved double-peaked. Orange Q: Blended multiple-peaked. Navy Y: Resolved multiple-peaked. The tails of Hydra A are dominated by lines-of-sight with multiple-peaked Faraday spectra, most of which are blended.

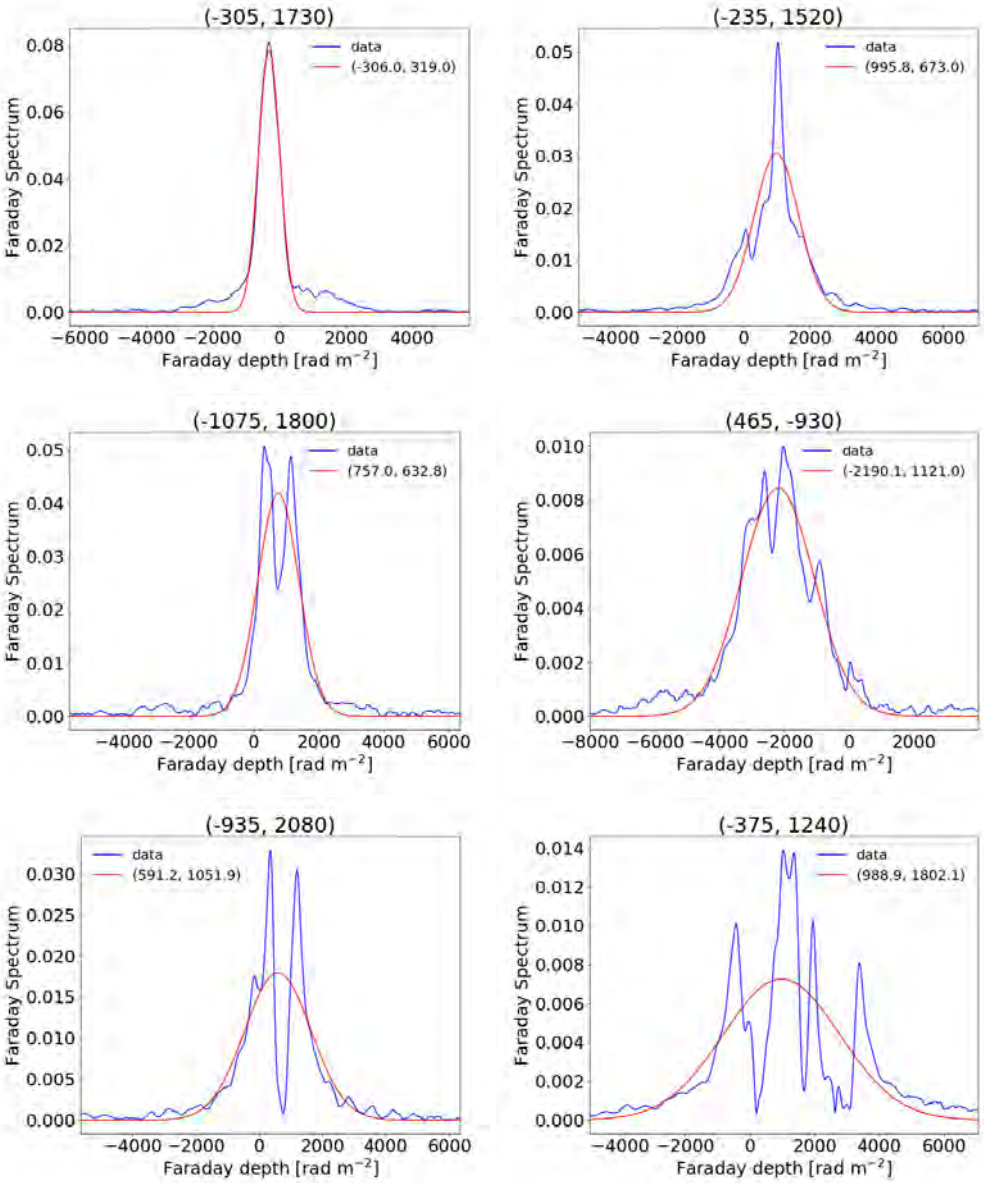

Figure 6.25: *Fitting examples of 1D Gaussian function to Faraday spectrum amplitudes*. Blue: Data. Red: A fitted Gaussian function. Plot titles: Lines-of-sight location. Legend in parenthesis: Mean and width of the Gaussian function in rad m^{-2}. Top left: Single-peaked Faraday spectra. Top right: Single-peaked with smaller peaks. Middle left: Blended double-peaked. Middle right: Blended multiple-peaked. Bottom left: Resolved double-peaked. Bottom right: Resolved multiple-peaked.

in λ^2-space, on the other hand, does not seem to depend on the Faraday class. The $\sigma_{\rm stdev}$ ranges between $\gtrsim 100 - 3000$ rad m^{-2}. The spread of the Faraday depths in Hydra A are a factor of $\lesssim 2$ larger than those in Cygnus A (the $\sigma_{\rm stdev}$ of Cygnus A only goes up to ~ 1600 rad m^{-2}).

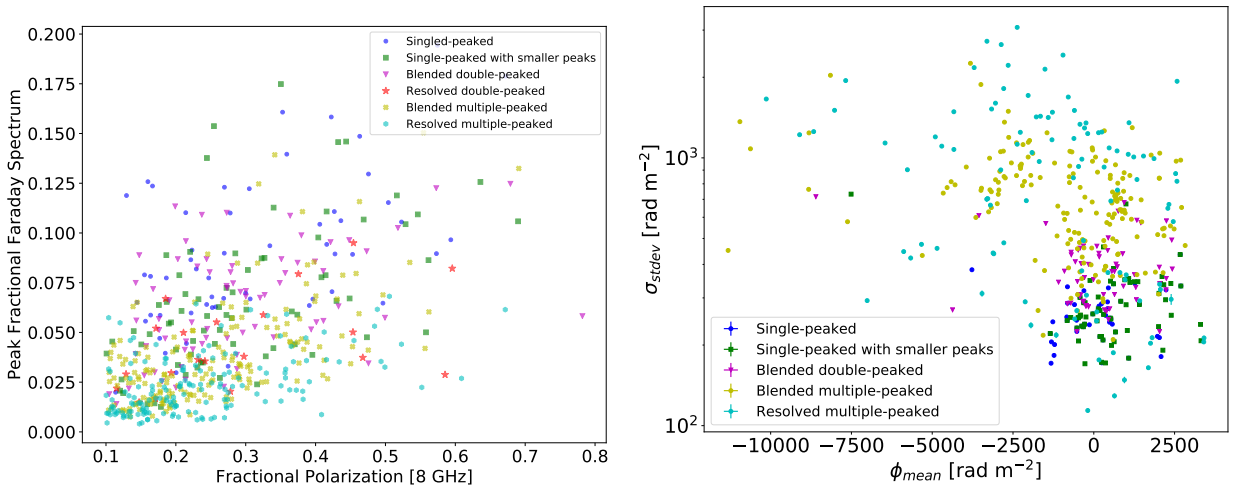

Figure 6.26: *Fractional polarisation at 8 GHz vs Faraday spectrum peak amplitude (left) and derived ϕ_{mean} vs σ_{stdev} (right).* Multiple-peaked spectra are associated with a low peak Faraday amplitude. Fractional polarisation in λ^2-space is independent of the Faraday spectra class. The spectra of Hydra A have $\sigma_{\rm stdev}$ ranging between $\gtrsim 100 - 3000$ rad m^{-2} – about a factor of $\lesssim 2$ larger than those of Cygnus A.

Figure 6.27 compares the RM and Faraday dispersions derived by fitting a random depolarisation screen to high-frequency ($6 - 12$ GHz), high-resolution ($0.50''$) data with the $\phi_{\rm mean}$ and $\sigma_{\rm stdev}$ derived by fitting a 1D Gaussian to the Faraday spectra. We find that the RM derived at high frequencies are consistent with $\phi_{\rm mean}$ of the Faraday spectra. A plot on the right, on the other hand, indicates an independence of the rate of depolarisation at high frequencies on the spread of Faraday thickness in Faraday spectra. We found a similar behaviour in the case of Cygnus A.

6.10 Summary of the Data

In the above sections, we presented the results from our wideband (2 - 12 GHz), high-spectral resolution polarimetry data on Hydra A. We looked at how the source polarisation emission changes across both frequency and resolution. We have also derived high-resolution maps of the intrinsic polarised emission of the tails, the rotation measure and Faraday dispersion of a foreground cluster gas. Further, we used these high-resolution maps to predict the data at low-frequencies and low-resolution. The results are summarised as follows:

1) The tails as well as the jets depolarise globally with decreasing frequency. The regions closest to the AGN depolarise more rapidly than those further away.

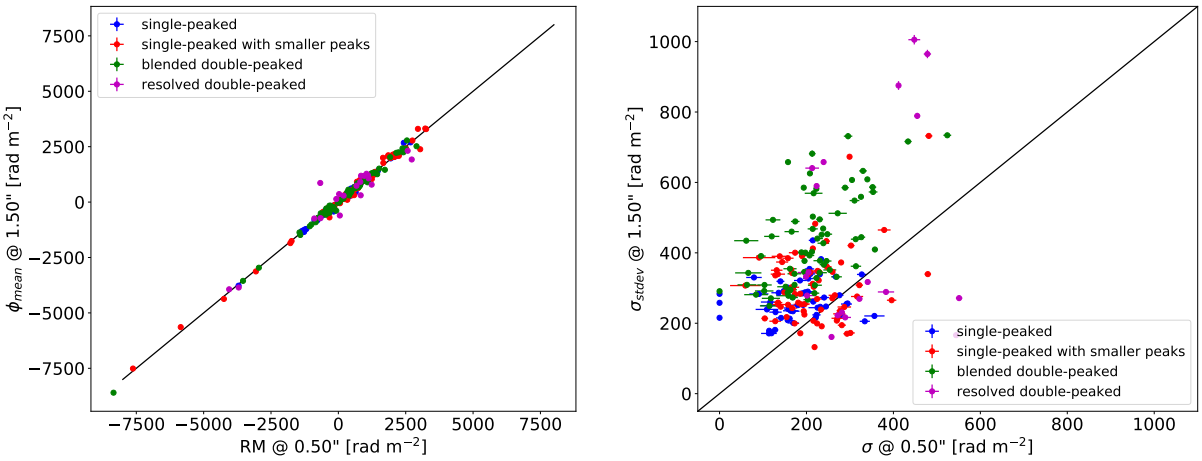

Figure 6.27: *A comparison of parameters derived from 1D Gaussian fitting with those from high-frequency, high-resolution modelling*. Left plot: Compares RM at $0.50''$ with ϕ_{mean} at $1.50''$. Right plot: Compares Faraday dispersions at $0.50''$ with σ_{stdev}. The derived RM are consistent. The rate of decay at high frequencies is independent of the spread of Faraday depths in Faraday space.

2) The fractional polarisation across the northern tail is smooth at higher-frequencies while the southern tail is patchier. However, both the tails become clumpier towards lower-frequencies.
3) We find that the tails depolarise by more than 90% between 10 GHz and 2 GHz.
4) Fractional polarisation as a function of λ^2 of the different lines-of-sight across the tails reveal very complex depolarisation behaviour, with some lines-of-sight showing smooth decaying fractional polarisation (roughly 22% of the lines-of-sight), some show oscillations (11%) and others show complex/intermediate decaying structure (67%). The depolarisation across the southern tail is mostly complex, with a few lines-of-sight decaying smoothly. There are no oscillatory decaying lines-of-sight across the southern tail. The northern tail, on the other hand, consists of all three depolarisation structures, with the smooth decaying lines-of-sight concentrated at extreme regions of the tail (further from the AGN) and the complex decays situated close to the AGN.
5) We derived Faraday spectra of the lines-of-sight using RM-Synthesis and we find interesting structures in the spectra. In general, the spectra for smooth decaying lines-of-sight consist of a single peak (or a few closely-separated peaks), while the spectra of oscillatory and complex decays show multiple peaks and large broadening of the spectra. The peak separations range between $\sim 500 - 5000$ rad m^{-2}. Most of the large separations are between $1000 - 3000$ rad m^{-2}.
6) Polarisation angles as functions of λ^2 show significant deviations from linearity. The deviations are > 1 rad. Most deviations are associated with multiple-peaked Faraday spectra.
7) We also find that the tails depolarise with decreasing resolution.
8) The fractional polarisation of the different lines-of-sight across the tails decreases with decreasing resolution. The fractional polarisation of roughly 59% of the lines-of-sight fall within Class A, while $\sim 12\%$ fall within Class B, and 29% within Class C. These results indicate that beam-related effects are complicated.

9) Convolving the wideband data at $1.5''$ to $3''$ resolution, reveal the increase in the complexity of the data at poor resolution, indicating the presence of an unresolved foreground Faraday rotating gas.
10) We classified the Faraday spectra data of Hydra A. We find that $\sim 60\%$ of the lines-of-sight consist of multiple-peaked spectra, $\sim 17\%$ are double-peaked and $\sim 23\%$ are single-peaked.
11) The high-resolution ($0.5''$) RM map across the northern tail range between -2000 rad m^{-2} and 3300 rad m^{-2} and between -2000 rad m^{-2} and ~ 11900 rad m^{-2} across the southern tail. The RM are ordered on scales $2-6$ kpc across the northern tail and ~ 1 kpc across the southern tail. RM across the northern tail occur in bands of alternating positive and negative values. Those of the southern tail are mostly negative, with a small region of positive values situated in the outskirts of the tail (south-east).
12) The derived intrinsic fractional polarisation at $0.5''$ shows values ranging between $20\% - 50\%$ across the northern tail and $0.5\% - 50\%$ across the southern tail. There is also a highly polarised region with fractional polarisation of up to 65% at the edge of the northern tail (the west side) and narrow regions of up to 70% polarisation across the southern tail. In general, the southern tail is relatively less polarised and is patchier. The southern tail is either intrinsically different or is behind the more turbulent cluster gas. The turbulent cluster gas is likely the major contributing factor to the observed polarisation behaviour. However, our data cannot disprove any intrinsic effects.
13) The magnetic field orientation follows the boundary and filamentary structures in the tails, consistent with other radio galaxies. The orientations are slightly chaotic in the southern tail.
14) The Faraday dispersions range between 150 rad m^{-2} and 350 rad m^{-2} across the northern tail and 300 rad m^{-2} and 950 rad m^{-2} across the southern tail. The dispersions show no radial dependence. The dispersions are extremely chaotic across the southern tail. The southern tail also consists of narrow regions of higher dispersions, that are coincident with large gradients.
15) We used the derived intrinsic fractional polarisation and RM at high-resolutions ($0.5'' \times 0.35''$) to predict low-frequency, low-resolution data ($1.50'' \times 1.0''$). The assumption is that these high-resolution maps present a close representation of the "true" source properties and foreground Faraday rotating gas. We find that the depolarisation structure in the data are reproduced, with 4% lines-of-sight closely reproduced and 71% partially reproduced. For the latter, the depolarisation are mostly underestimated and in some rare cases the nulls in the oscillatory decay are shifted to lower frequencies. These results suggest that the depolarisation is mostly a result of small-scale fluctuations across a foreground Faraday rotating medium. This depolarising medium must consist of multiscale magnetic fields ordered 0.30 - 1.5 kpc.

6.11 Preliminary Modelling of the Wideband Data

In this section, we model the wideband data of Hydra A radio galaxy following the same procedure we used for Cygnus A in Section 5.4. We assume a uniform distribution for all priors. The intrinsic fractional polarisation ranges between 0 and 1, polarisation angle between $\pm\pi/2$ radians, RM/Faraday depth between ± 15000 rad m^{-2}, Faraday dispersions and unresolved uniform RM-differences between 0 and 5000 rad m^{-2}.

6.11.1 Best Fitting Model

We fit to the data of Hydra A the eight analytical models described in Section 5.4 and summarised in Table 5.2. The models are RFD, UFD, RUFD, RUID, RUID+F, 2RFD, 2RUFD and 3RFD, where "R" stands for random magnetic fields, "U" stands for unresolved uniform RM-difference, "F" stands for foreground, "I" stands for internal mixing, "D" is the depolarising gas and the preceding number indicate the number of media in question. We fit these eight models to the single-peaked spectra, single-peaked with smaller peaks spectra, blended and resolved double-peaked spectra. These spectra data account for $220/553$ (40%) of the lines-of-sight across Hydra A.

Figure 6.28 shows the $\ln$ BF solutions of RUFD, RFD and UFD models. Positive $\ln$ BF is shown in blue and negative $\ln$ BF in red. The blue points are in favour of RUFD (left and middle plot) and RFD (right) and the red data points are in favour of RFD (left) and UFD (middle and right plot). The vertical lines separate the different Faraday spectra classes. The single-peaked spectra are in the far left, followed by the single-peaked with smaller peaks, blended double-peaked and resolved double-peaked spectra. RUFD is favoured over RFD for 60% of the fitted lines-of-sight and over UFD for 94% of the fitted lines-of-sight. Additionally, we find small values of $\ln$ BF (red points in the left plot) are in favour of RFD against 2RUFD – suggesting a weak evidence against RUFD. Our overall results suggest that random fluctuations are particularly important to these data, while unresolved uniform RM-differences are weakly important to $\sim 40\%$ of the fitted lines-of-sight.

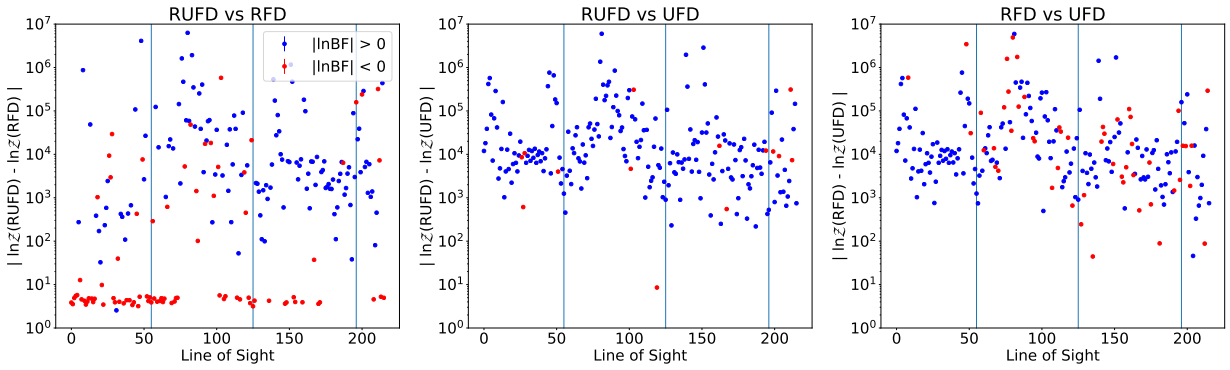

Figure 6.28: $\ln$ *BF of model RUFD, RFD and UFD fitted to the lines-of-sight across Hydra A.* Blue points: In favour of RUFD (left and middle plot) and RFD (right plot). Red points: In favour of RFD (left) and UFD (middle and right). Vertical lines (from left to right) separate lines-of-sight with single-peaked, single-peaked with smaller peaks, blended double-peaked and resolved double-peaked. RUFD is favoured over RFD for 60% of the fitted lines-of-sight and over UFD for 94%. RFD is preferred over UFD for 76% of the fitted lines-of-sight. $2/3$ of the fitted lines-of-sight have $\ln \text{BF} < 10$ in favour RFD over RUFD. These small values suggest a weaker evidence against RUFD over RFD. The random fluctuations are particularly important to these data, while the unresolved uniform RM-differences are weakly important $\sim 40\%$ of the fitted lines-of-sight.

Figure 6.29 shows the $\ln$ BF of RUFD, RUID and RUID+F models. The blue data points are in favour of RUID+F (left and middle) and RUFD (right) and the red data points are in favour RUFD (left) and RUID (middle and right). RUID is disfavoured for 99% of the fitted lines-of-sight over RUID+F and RUFD. These results rule out a completely mixed region as a location for the observed RM but necessitates the presence

of a foreground Faraday rotating screen. These results are consistent with the previous claim by Taylor et al. (1990) and Taylor and Perley (1993). We reached the same conclusion, even for the Cygnus A radio galaxy.

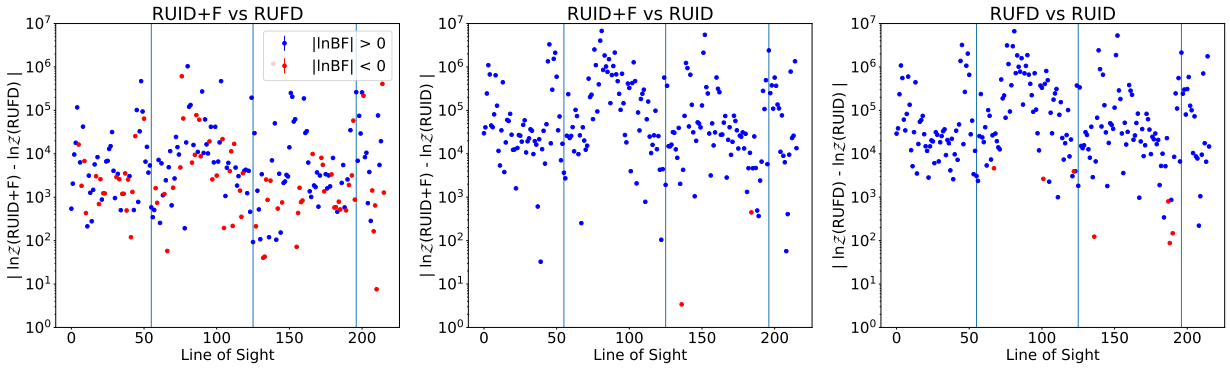

Figure 6.29: ln *BF of model RUID+F, RUID and RUFD fitted to lines-of-sight across Hydra A.* Blue points: In favour of RUID+F (left and middle) and RUFD. Red points: In favour of RUFD (left) and RUID (middle and right). RUID+F is favoured over RUFD for 63% of the fitted lines-of-sight and over RUID for 99%. A completely mixed gas cannot explain the data, instead, a foreground screen is required to account for the observed RM.

Figure 6.30 shows the ln BF of the 2RFD, RFD and RUID+F. The blue data points are in favour of 2RFD and the red data points are in favour of RUFD (left) and RUID+F (right). 2RFD is favoured over RUFD for 77% of the fitted lines-of-sight and against RUID+F for 67% of the fitted lines-of-sight. There also seems to be a tendency for these two single-component (RUFD and RUID+F) to fit the blended doubled-peaked spectra well. This could be due to two reasons: i) a second component is not needed for the majority of the blended double-peaked lines-of-sight, ii) or the lines-of-sight in question require unresolved uniform RM-difference to be incorporated in the models. In general, these results suggest that the majority ($\sim 70\%$) of the data require multiple Faraday components.

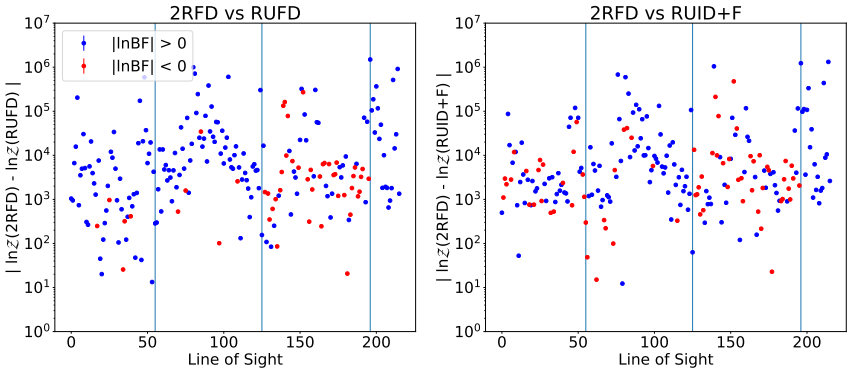

Figure 6.30: ln *BF of model 2RFD, RUID+F and RUFD fitted to lines-of-sight across Hydra A.* Blue points: In favour of 2RFD (left and right). Red points: In favour of RUFD (left) and RUID+F (right). 2RFD is favoured over RUFD for 77% of the fitted lines-of-sight and over RUID+F for 67%.

Figure 6.31 shows the ln BF for 2RUFD, 2RFD and 3RFD fitted to the Hydra A data. The blue data points are in favour of 2RUFD (left and middle) and 3RFD (right) and the red data points are in favour of 2RFD (left and right) and 2RUFD (middle). 2RFD is the most disfavoured of the three models. On

average, 2RFD is favoured for $\sim 16\%$ of the fitted lines-of-sight. 2RUFD is favoured over 3RFD for 58% of the fitted lines-of-sight. These results indicate the importance of unresolved uniform RM-differences over an additional purely random depolarising component. The results are quite the opposite of Cygnus A, where 3RFD was strongly favoured ($\gtrsim 70\%$ of the lines-of-sight) over 2RUFD. The difference in the model preferences possibly indicates the difference in the dominant structures in the magnetic fields in and around these radio galaxies. However, we also note that the model preference between 2RUFD and 3RFD remains small, particularly for Hydra A. As a result, we consider these as competing models.

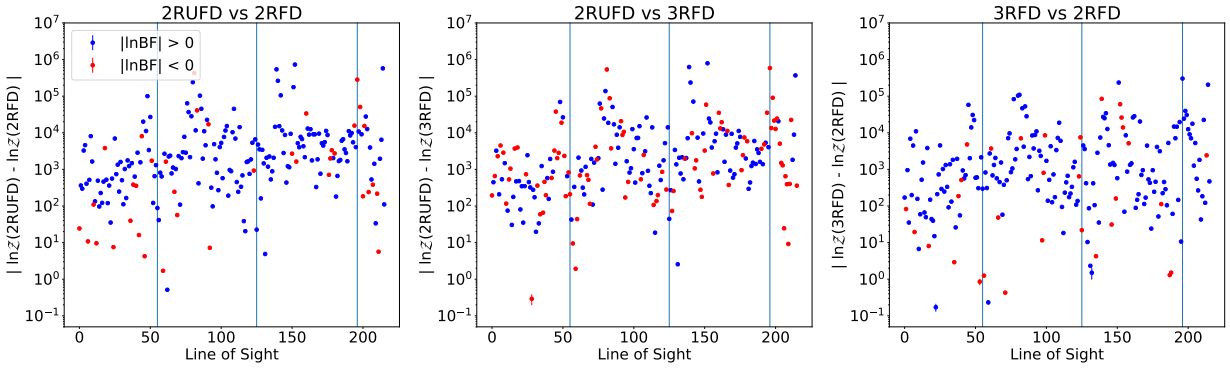

Figure 6.31: $\ln$ *BF of model 2RUFD, 3RFD and 2RFD fitted to lines-of-sight across Hydra A.* Blue points: In favour of 2RUFD (left and middle) and 3RFD (right). Red points: In favour of 2RFD (left and right) and 3RFD (middle). 2RUFD is favoured over 2RFD for 82% of the fitted lines-of-sight and over 3RFD for 58%. 3RFD is favoured over 2RFD for 86% lines-of-sight. 2RUFD and 3RFD compete but the former is the most favoured of the two.

Figure 6.32 shows the spatial distribution of model selection results. In blue, we show lines-of-sight in favour of 3RFD and in red, those in favour of 2RUFD. Similar to Cygnus A, the model preference does not depend on the location of a line-of-sight across the tails of the radio galaxy. Given the few fitted lines-of-sight across the southern tail, the analysis best represents the physics in the northern tail and very little about the southern tail. Analysis of the southern tail requires including the remaining spectra classes (the blended and resolved multiple-peaked), however, these are beyond the scope of this work.

6.11.2 Goodness-of-Fit of the Best-Fitting Models

Simply because a given model is favoured over another based on the $\ln$ BF does not mean the best model truly describes the data. We consider χ^2_r to evaluate whether a best-fitting model does indeed describe the data. However, the value of χ^2_r is subject to noise and is generally affected by the SNR of the lines-of-sight. The high-SNR lines-of-sight tend to have larger χ^2_r (suggesting a bad fit) and low-SNR lines-of-sight (those that resemble the noise) tend to have smaller χ^2_r, indicating a good fit. To derive the statistics, we consider lines-of-sight with $\chi^2_r \leq 5$ as "good fits", similar to what was done for Cygnus A modelling.

Figure 6.33 shows the χ^2_r of our three best-fitting models, namely 2RFUD, 3RFD and 2RFD. We find 38% of the fitted lines-of-sight with $\chi^2_r \leq 5$ in 2RFD, 46% in 3RFD and 50% in 2RUFD. Model 2RUFD describes the majority of the lines-of-sight better than 3RFD and 2RFD. However, 50% is still a small fraction of the fitted lines-of-sight. This indicates that Hydra A data require sophisticated modelling.

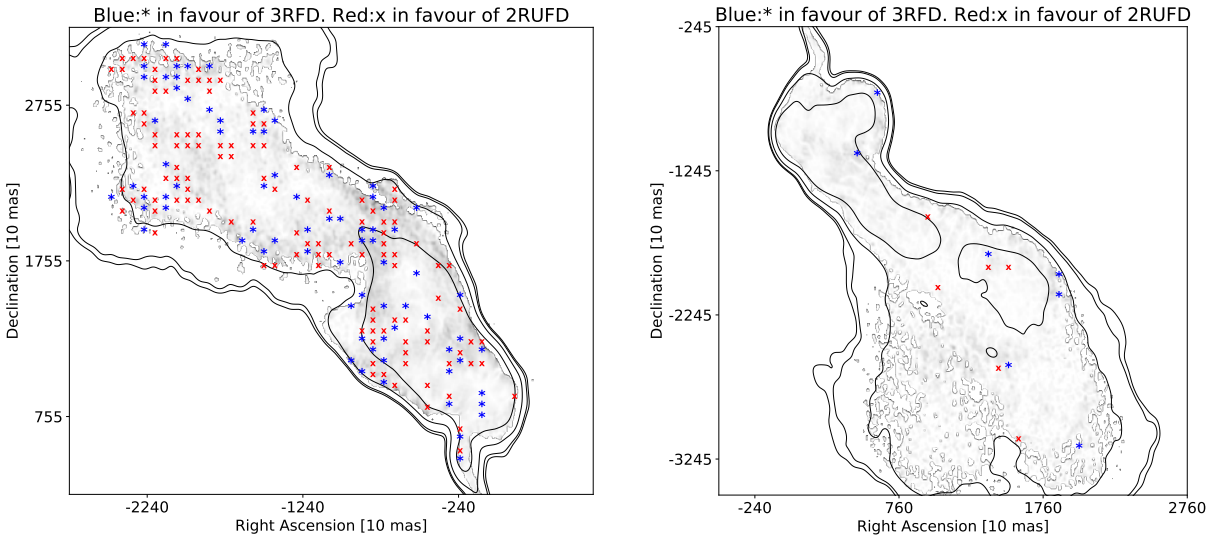

Figure 6.32: *Spatial distribution of model selection results between model 3RFD and 2RUFD.* Blue: In favour of 3RFD. Red: In favour of 2RUFD. There is no spatial preference. The majority of lines-of-sight are concentrated across the northern tail, as such, the analysis best represents the physics occurring in/near this tail than the southern tail.

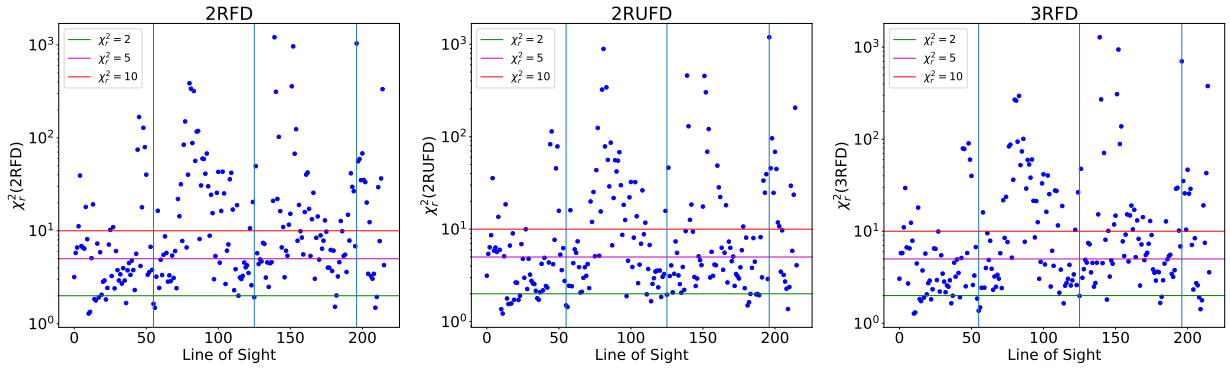

Figure 6.33: χ_r^2 *solutions of model 2RFD, 2RUFD and 3RFD fitted to lines-of-sight across Hydra A.* We find that 38% of the fitted lines-of-sight in 2RFD have $\chi_r^2 \leq 5$, 50% in 2RUFD and 46% in 3RFD.

Figure 6.34 shows the absolute difference in the χ^2_r of the three models; 2RFD, 3RFD and 2RUFD. The blue points are in favour of 2RUFD (left) and 3RFD (middle and right). The red points, are in favour of 2RFD (left and middle) and 2RUFD (right). We find that 2RFD is disfavoured for over $\sim 80\%$ of the fitted lines-of-sight against 2RUFD and 3RFD, and 2RUFD fits 57% of the lines-of-sight better than 3RFD.

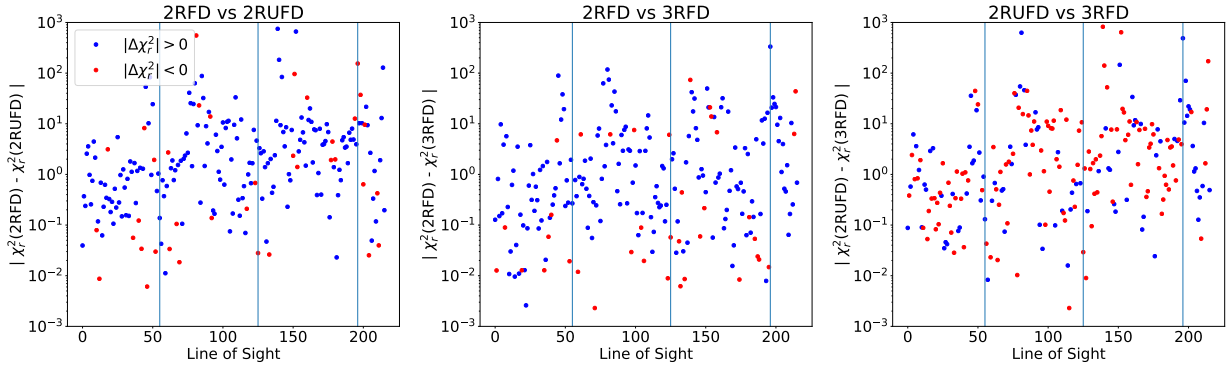

Figure 6.34: *The difference in the χ^2_r of model 2RUFD, 2RFD and 3RFD fitted to lines-of-sight across Hydra A.* Blue points: In favour of 2RUFD (left) and 3RFD (middle and right). Red points: In favour of 2RFD (left and middle) and 2RUFD (right). 2RUFD fits 83% of the fitted lines-of-sight much better than 2RFD and 57% of the fitted lines-of-sight better than 3RFD. 3RFD fits 82% of the lines-of-sight much better than 2RFD. 2RUFD describes the majority of the fitted lines-of-sight better than 2RFD and 3RFD.

Figure 6.35 shows fitted lines-of-sight examples where 3RFD is favoured over 2RUFD. We show one example from each of the four Faraday spectra classes.

Figure 6.36, on the other hand, shows example lines-of-sight whereby 2RUFD is favoured over 3RFD.

Figure 6.37 shows example lines-of-sight not well-produced by either model. We find that in the majority of failed cases, 2RUFD tends to reproduce the oscillatory nature of the depolarisation curves. However, the nulls are either offset or the depolarisation is overestimated. The models are insufficient, therefore, more added components (likely representing a more realistic screen) would likely fit better.

6.11.3 Estimated Fitting Parameters of the Best-Fitting Models

In this section, we present the parameter estimates of 2RUFD and 3RFD for the fitted lines-of-sight with $\chi^2_r \leq 5$ and fractional errors in each parameter of ≤ 0.1. We indicate the fraction of the fitted lines-of-sight satisfying these two conditions at the top of each plot.

6.11.3.1 Two Random-Uniform Depolarising Screens

Figure 6.38 shows the derived intrinsic fractional polarisation (left and middle plot) and their ratios (right) for model 2RUFD. The "strong" component is polarised at $5\% - 45\%$ (left plot); the weaker at $1\% - 30\%$ (middle plot). The two components have relatively similar strength, with ratios in the intrinsic fractional polarisation ranging between $1 - 8$ and the majority of ratios concentrated below 4.

Figure 6.39 shows the separation of the two components in Faraday space and the derived Faraday dispersions of 2RUFD. The components are separated by no more than ± 750 rad m^{-2}, with the majority con-

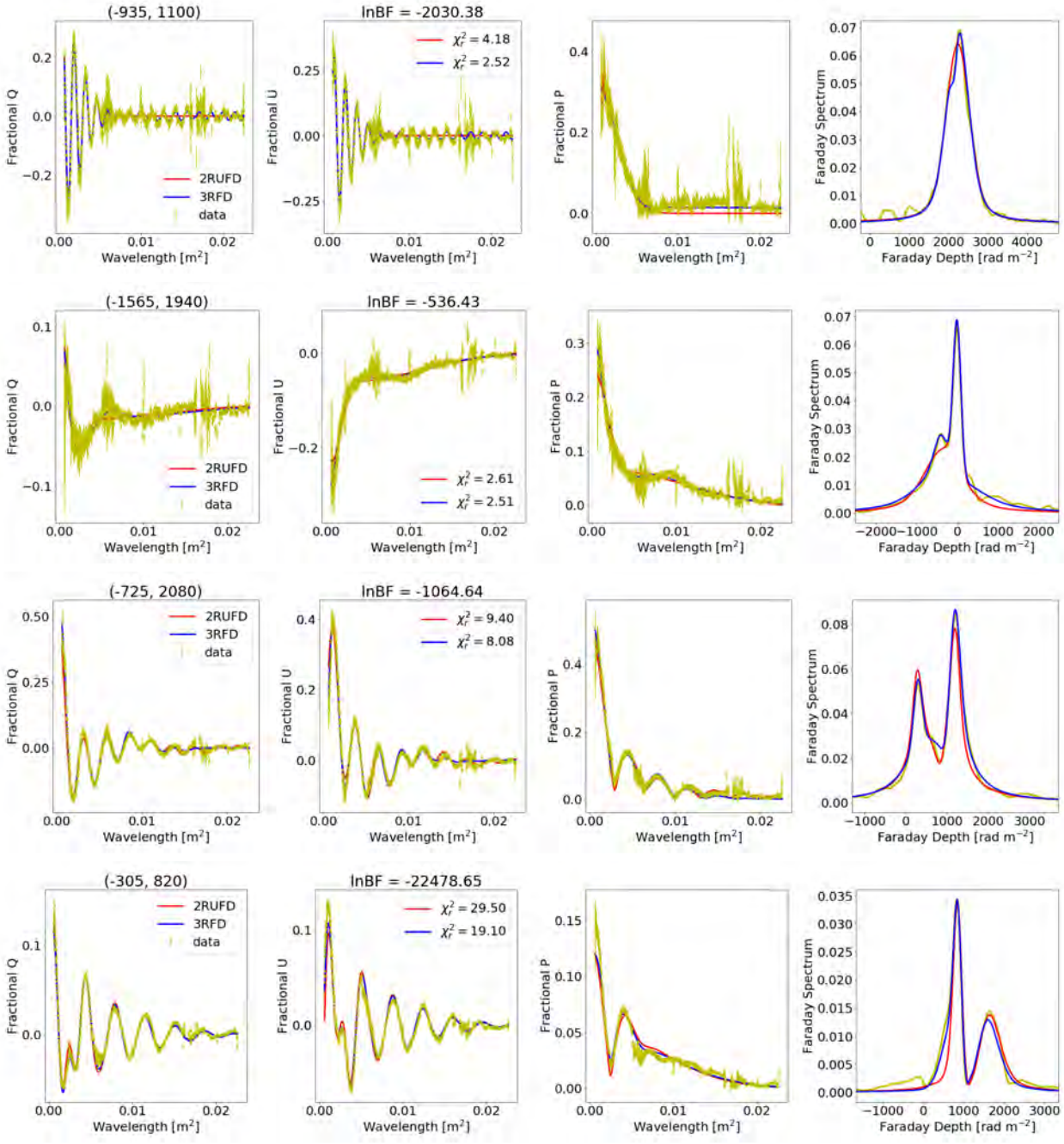

Figure 6.35: *Example lines-of-sight in favour of model 3RFD over 2RUFD.* Title (left column): Lines-of-sight location. Title (second column): ln BF. Top row: Single-peaked spectrum. Second row: Single-peaked with smaller peaks. Third row: Blended double-peaked spectrum. Last row: Resolved double-peaked spectrum.

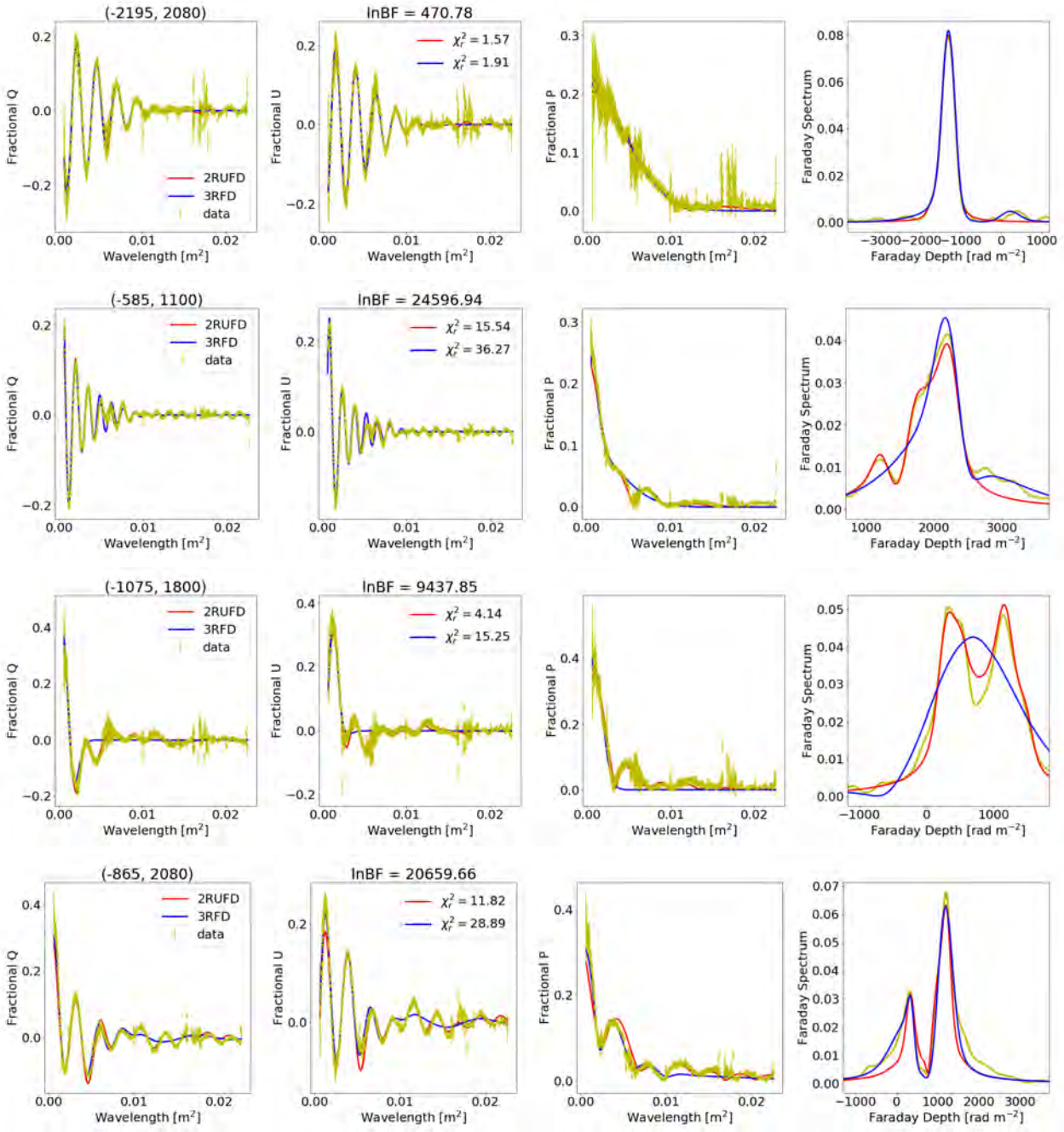

Figure 6.36: *Fitted example lines-of-sight with single-peaked spectra in favour of model 2RUFD over 3RFD.* Title (left column): Line-of-sight location. Title (second column): ln BF. Top row: Single-peaked spectrum. Second row: Single-peaked with smaller peaks. Third row: Blended double-peaked spectrum. Last row: Resolved double-peaked spectrum.

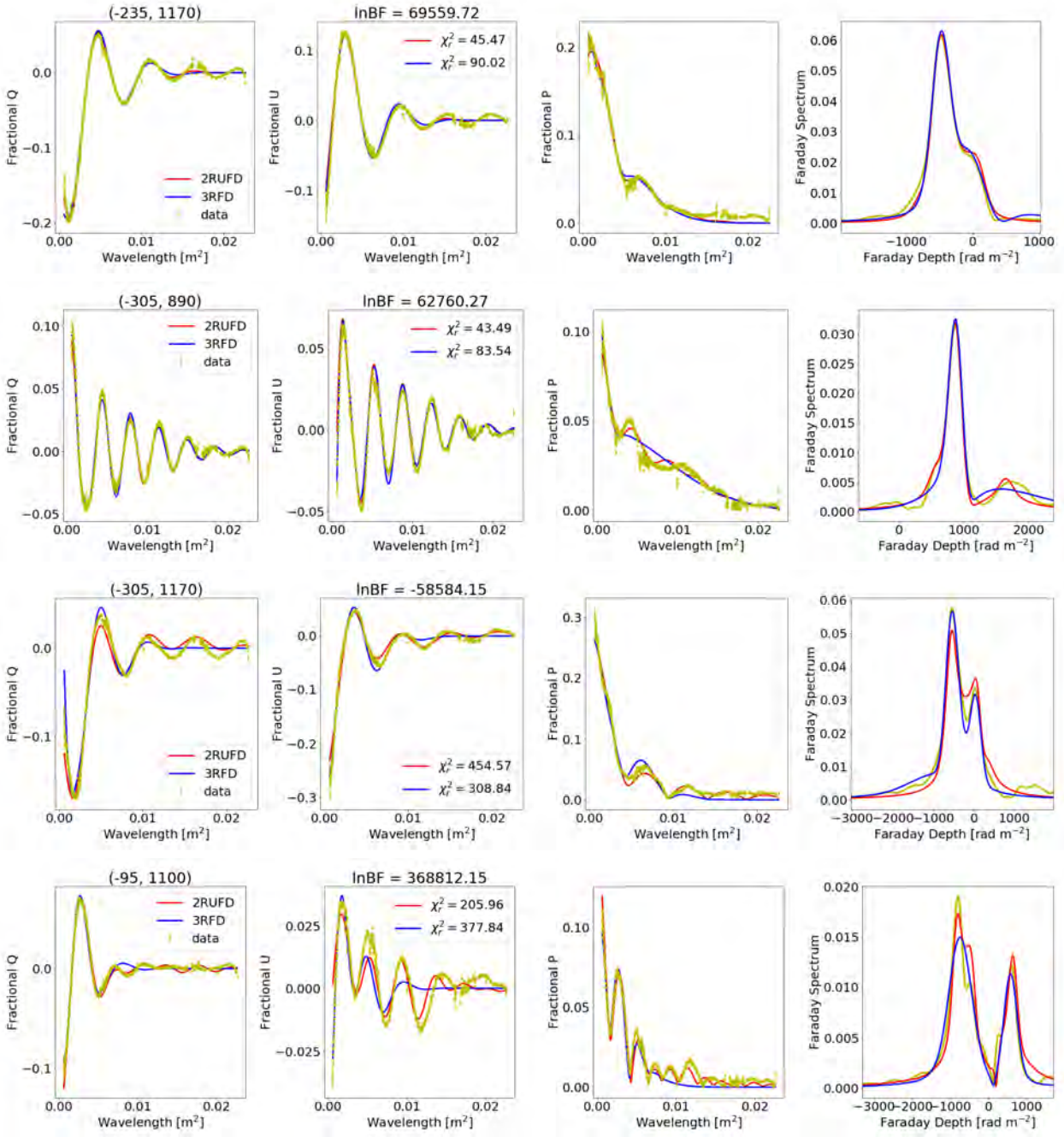

Figure 6.37: *Example lines-of-sight with failed fits.* Title (left column): Line-of-sight location. Title (second column): ln BF. Top row: Single-peaked spectrum. Second row: Single-peaked with smaller peaks. Third row: Blended double-peaked spectrum. Last row: Resolved double-peaked spectrum. 2RUFD model is good at reproducing the oscillatory nature of the depolarisation.

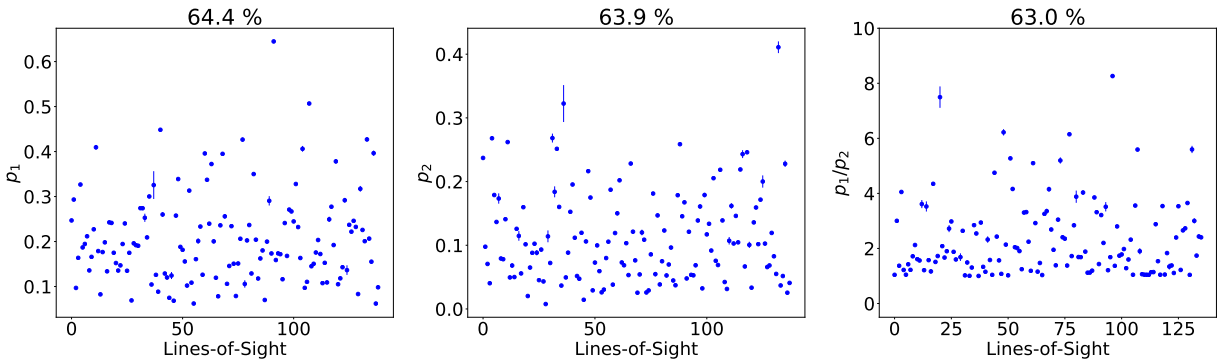

Figure 6.38: *The derived intrinsic fractional polarisation of model 2RUFD fitted to Hydra A wideband data.* Left and middle: Intrinsic fractional polarisation. Right: Ratios of the intrinsic fractional polarisation. The strong component is $5\% - 45\%$ polarised while the weaker component is $1\% - 30\%$ polarised. The ratios suggest that the components have similar strength, with the majority of the ratios concentrated below 4 and a few cases with larger ratios going up to 8.

centrated between ± 500 rad m^{-2}. The Faraday dispersions of a strong component go up to ~ 400 rad m^{-2} and of a weak component go up to ~ 150 rad m^{-2}.

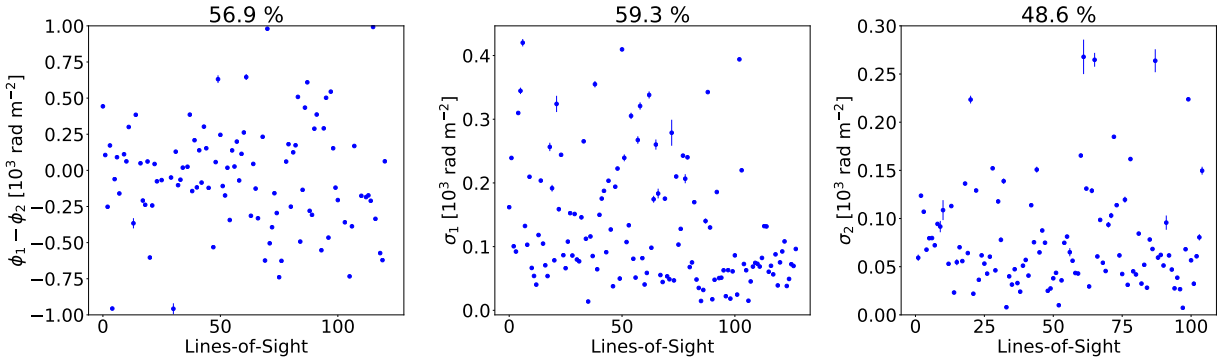

Figure 6.39: *The derived components separation (left) and Faraday dispersion (middle and right) of model 2RUFD fitted to Hydra A wideband data.* The components are separated by no more than ± 750 rad m^{-2} and the dispersions up to 400 rad m^{-2} for the strong component and 150 rad m^{-2} of the weaker component.

Figure 6.40 shows the derived unresolved uniform RM-difference of 2RUFD as fitted to Hydra A wideband data. The majority of the unresolved uniform RM-difference ranges between $\sim 200 - 2000$ rad m^{-2}, with a few fitted lines-of-sight having a larger RM-difference of up to $\lesssim 4500$ rad m^{-2}.

6.11.3.2 Three-Random Depolarising Screens

Figure 6.41 shows the derived intrinsic fractional polarisation of the three components in 3RFD (top row) and the ratio of the intrinsic fractional polarisation (bottom row). We show fitted lines-of-sight with fractional errors less than 0.1 and $\chi^2_r \leq 5$. The fraction of the fitted lines-of-sight that meet these two conditions are indicated at the top of each plot. The intrinsic fractional polarisation of the strong component is mostly $\lesssim 40\%$ polarised, the intermediate component is $\lesssim 30\%$ polarised and the weaker component is $\lesssim 20\%$. The

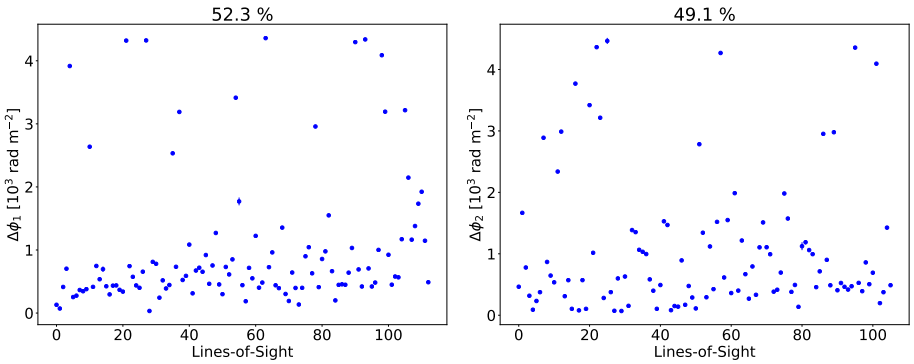

Figure 6.40: *The derived RM-differences of model 2RUFD fitted to Hydra A lines-of-sight.* The majority of the unresolved RM-differences for both components range between $\sim$ 200 $-$ 2000 rad m^{-2}, with a few lines-of-sight having larger RM-difference of up to $\lesssim$ 4500 rad m^{-2}.

strong component is a factor of $1-3$ more polarised than the intermediate component and about a factor of <20 more polarised than the weak component for most of the fitted lines-of-sight.

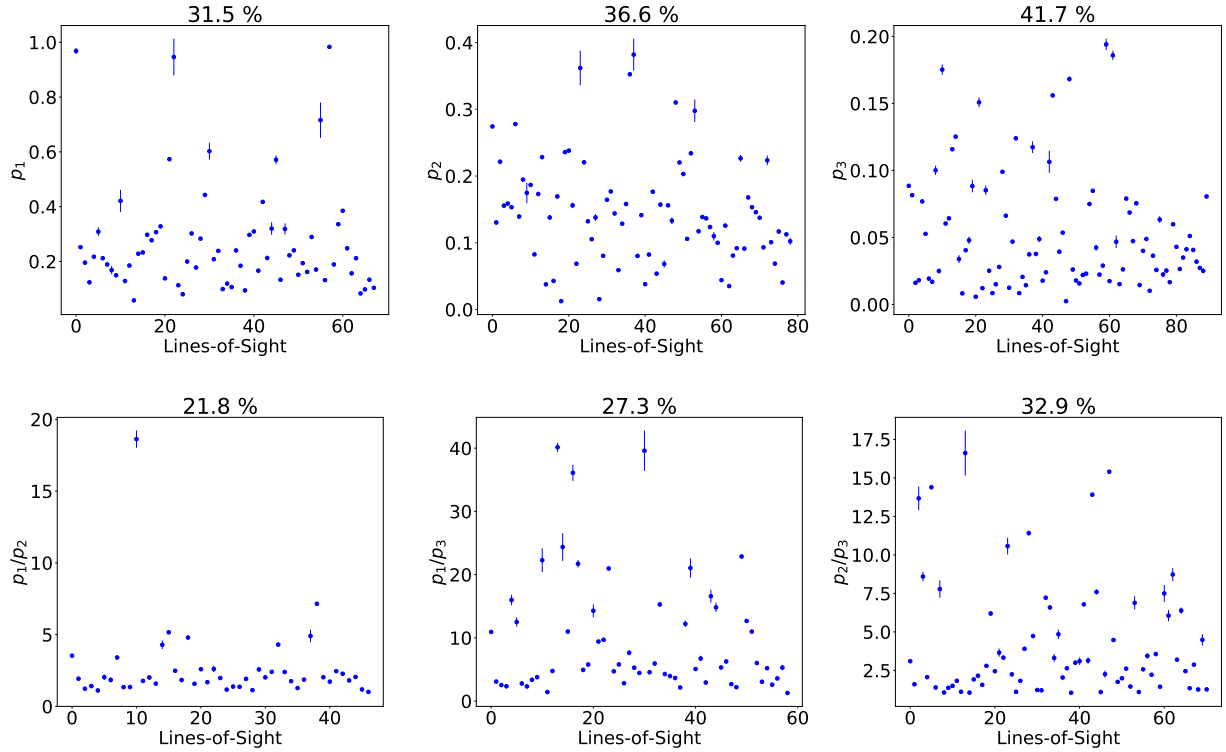

Figure 6.41: *The derived intrinsic fractional polarisation (top) and ratios (bottom) of model 3RFD fitted to Hydra A wideband data.* The strong component is $\lesssim 40\%$ polarised, the intermediate component about $\lesssim 30\%$ polarised and the weak component about $\lesssim 20\%$ polarised. The strong component is a factor of $1-3$ more polarised than the intermediate and <20 than the weak component for the majority of the fitted lines-of-sight.

Figure 6.42 shows the separation of the three components in Faraday space. The strong and intermediate component are separated by no more than ± 1000 rad m^{-2} for most of the fitted lines-of-sight. The strong

and the weak component, as well as the intermediate and the weak component are separated by not more than ± 2500 rad m^{-2}.

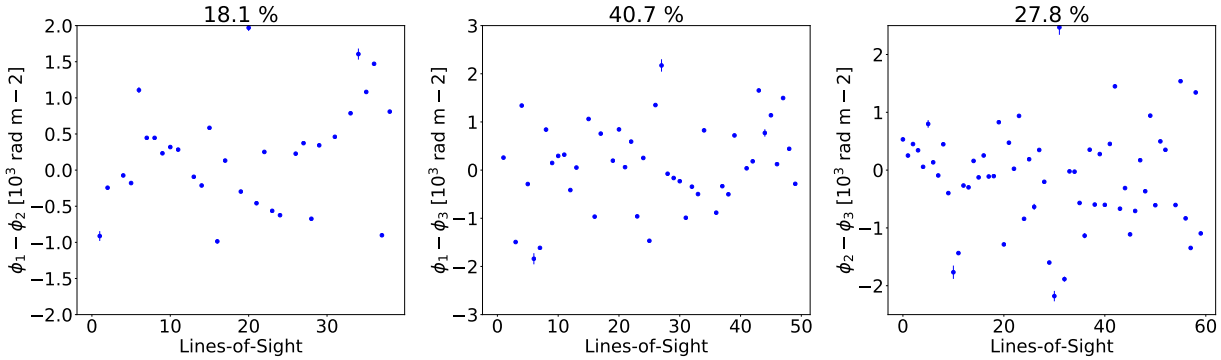

Figure 6.42: *The derived components separation of model 3RFD fitted to Hydra A wideband data*. The strong and the intermediate component are separated by no more than ± 1000 rad m^{-2}, both the strong and weak, as well as the intermediate and weak are separated by no more than ± 2500 rad m^{-2}.

Figure 6.43 shows the derived Faraday dispersions of 3RFD fitted to Hydra A lines-of-sight. The dispersions of the strong component (left plot) are mostly $\lesssim 500$ rad m^{-2} with a few going up to 5000 rad m^{-2}. The dispersions of the intermediate component are mostly $\lesssim 750$ rad m^{-2} and dispersions of the weak component are mostly $\lesssim 300$ rad m^{-2}. Large dispersions are associated with relatively large fitting errors.

In general, 3RFD is associated with large fitting errors and $\chi^2_r > 5$ compared to 2RUFD. This is evident on the resulting fraction of fitted lines-of-sight at the top of each plot. 2RUFD describes $\sim 50\%$ of the fitted lines-of-sight while 3RFD shows less than 50%.

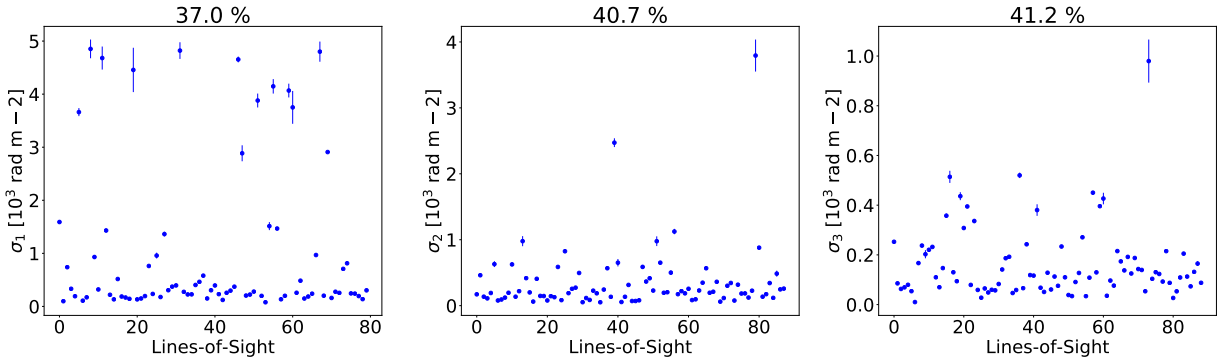

Figure 6.43: *The derived Faraday dispersions of model 3RFD fitted to Hydra A wideband data*. Typical dispersions for the strong component (left) are $\lesssim 500$ rad m^{-2} and for the intermediate component of $\lesssim 1000$ rad m^{-2} (middle) and weak component of $\lesssim 300$ (right). However, there are a few large dispersions going up to ~ 5000 rad m^{-2} but these are generally associated with large fitting errors.

6.11.4 Model Fitting in Summary

In this section, we summarise the results of our fitting. Table 6.4 shows the $\ln$ BF of our two best-fitting models. The results are given in terms of the fraction of lines-of-sight that are best described by a particular model over the other. As already mentioned, 2RFD is the most disfavoured, while 2RUFD is most favoured (except for lines-of-sight with resolved double-peaked spectra).

Table 6.4: *A fraction of lines-of-sight favouring by one model over the other based on the* $\ln$ *BF*

Faraday Class	2RUFD over 2RFD [%]	3RFD over 2RFD [%]	3RFD over 2RUFD [%]
Single-peaked	76	85	47
Single-peaked + small peaks	87	86	37
blended double-peaked	89	83	32
resolved double-peaked	60	95	80

Table 6.5 shows the fraction of lines-of-sight with solutions having $\chi^2_r \leq 5$.

Table 6.5: *A fraction of lines-of-sight with solutions* $\chi^2_r \leq 5$

Faraday Class	2RFD [%]	2RUFD [%]	3RFD [%]
Single-peaked	54	58	60
Single-peaked + small peaks	36	43	41
blended double-peaked	28	54	43
resolved double-peaked	35	35	35

Table 6.6 shows the difference in the χ^2_r for the three models. We find that although the models describe a similar fraction of lines-of-sight according to $\chi^2_r \leq 5$, 2RUFD and 3RFD best describe the data. 2RUFD describes the data much better than 3RFD, particularly for the blended double-peaked spectra; this is not the case for the resolved double-peaked spectra.

Table 6.6: *A fraction lines-of-sight with the difference in* χ^2_r *greater than zero*

Faraday Class	2RUFD over 2RFD [%]	3RFD over 2RFD [%]	3RFD over 2RUFD [%]
Single-peaked	82	85	47
Single-peaked + small peaks	86	84	46
blended double-peaked	86	76	32
resolved double-peaked	65	90	75

The wideband data cannot be described by a single Faraday component but requires at least two components. The wideband modelling suggests that unresolved uniform RM-differences are important to these

data (2RUFD). Based on our selection criterion $\chi^2_r < 5$, we find that the models only describe a small fraction ($\sim 50\%$) of the fitted lines-of-sight. These lines-of-sight only represent 20% of the total lines-of-sight across the tails. Therefore, the results suggest that much more complicated models are needed to explain the data.

6.11.5 Reconciling the Estimated Parameters

In this section, we summarise the estimated fitted parameters for our two best-fitting models, namely 2RUFD and 3RFD. We also compare the derived parameters with those obtained from the high-frequency, high-resolution fitting at $0.50''$. We only present results of the lines-of-sight with $\chi^2_r \leq 5$ and fractional errors in the intrinsic fraction polarisation, Faraday separation and Faraday dispersion of 0.1 and RM of 0.5.

Table 6.7 shows a range of the estimated parameters of 2RUFD to lines-of-sight across Hydra A radio galaxy. The stronger component has larger Faraday dispersions, similar to those of Cygnus A but those of Cygnus A are smaller than the dispersions of Hydra A. The components of Hydra A are largely separated in Faraday space – with separations of up to $13\times$ the width of the RMTF. For the case of Cygnus A, the components are separated a maximum by $3\times$ RMTF. The range of uniform RM-difference in Hydra A go up to $\lesssim 4500$ rad m^{-2}, however, it is important to note that in Figure 6.40 RM-difference > 2000 rad m^{-2} are few, thus less reliable.

Table 6.7: *Estimated parameter range of model 2RUFD*

Parameter	Single-peaked	Single-peaked + small peaks	Blended double-peaked	Resolved double-peaked
p_1	$0.075 - 0.45$	$0.06 - 045$	$0.08 - 0.4$	$0.06 - 0.45$
p_2	$0.02 - 0.32$	$0.02 - 0.25$	$0.03 - 0.26$	$0.02 - 0.25$
σ_1	$15 - 450$	$40 - 400$	$10 - 350$	$40 - 110$
σ_2	$5 - 150$	$8 - 175$	$5 - 270$	$0.1 - 230$
$\lvert\phi_1 - \phi_2\rvert$	$20 - 2500$	$20 - 1200$	$60 - 2600$	$8 - 2000$
$\Delta\phi_1$	$15 - 750$	$25 - 1500$	$50 - 1750$	$25 - 2100$
$\Delta\phi_2$	$10 - 1000$	$15 - 1550$	$25 - 2000$	$25 - 1500$

Note: σ, RM separation and $\Delta\phi$ are in units of rad m^{-2}.

Figure 6.44 compares the intrinsic fractional polarisation derived from the wideband data modelling and those from the high-frequency, high-resolution modelling. The left panel is the results of 2RUFD and the right panel is the results of 3RFD. For the wideband modelling, we show the intrinsic fractional polarisation of the strongest component. The estimated intrinsic fractional polarisation of the wideband data modelling are less polarised compared to those at high-frequency modelling. This decrease in polarisation may be attributed to the decrease in resolution from $0.5''$ to $1.5''$.

Figure 6.45 compares the derived RM from the wideband data modelling with those from the high-frequency, high-resolution modelling. The RM from wideband modelling is a weighted sum of the components: $(RM_1 p_1 + RM_2 p_2 + \dots)/(p_1 + p_2 + \dots)$. The RM of 2RUFD and 3RFD are consistent with those from the high-frequency modelling. However, the RM of 3RFD are associated with very large fitting errors;

Table 6.8: *Estimated parameter range of model 3RFD.*

Parameter	Single-peaked	Single-peaked + small peaks	Blended double-peaked	Resolved double-peaked
p_1	$0.05 - 0.4$	$0.08 - 0.5$	$0.125 - 0.4$	$0.075 - 0.25$
p_2	$0.01 - 0.4$	$0.025 - 0.2$	$0.025 - 0.32$	$0.04 - 0.12$
p_3	$0.005 - 0.175$	$0.075 - 0.175$	$0.01 - 0.1$	$0.02 - 0.08$
σ_1	$100 - 950$	$125 - 600$	$75 - 1500$	$140 - 820$
σ_2	$60 - 1000$	$50 - 1000$	$50 - 1250$	$100 - 500$
σ_3	$5 - 450$	$20 - 600$	$30 - 1100$	$75 - 205$
$\lvert\phi_1 - \phi_2\rvert$	$75 - 500$	$100 - 1000$	$10 - 800$	$115 - 1600$
$\lvert\phi_1 - \phi_3\rvert$	$50 - 2500$	$40 - 1500$	$10 - 1000$	$130 - 1750$
$\lvert\phi_2 - \phi_3\rvert$	$10 - 1750$	$10 - 2500$	$30 - 1600$	$60 - 1600$

Note: σ and RM separation are in units of rad m^{-2}.

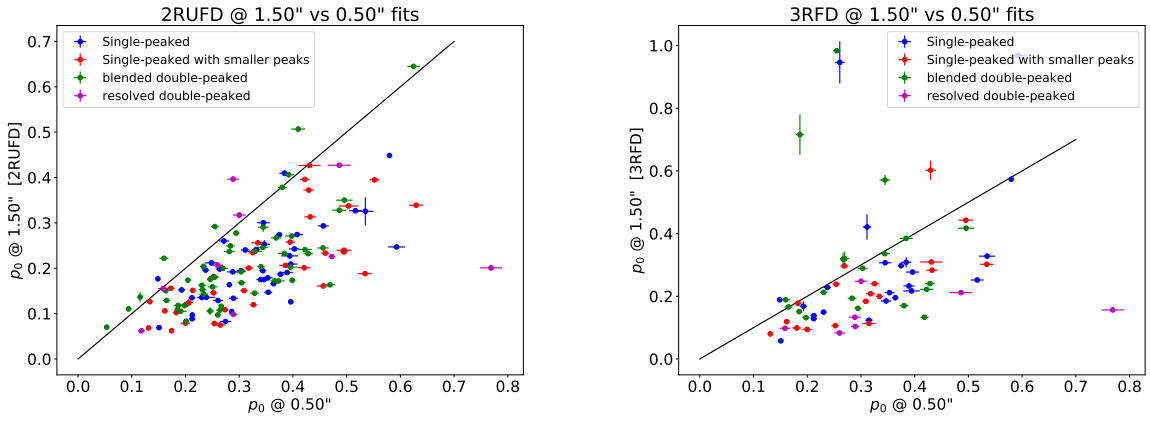

Figure 6.44: *A comparison of the estimated intrinsic fractional polarisation from the wideband data modelling with those from the high-frequency, high-resolution modelling.* The lines-of-sight shown have $\chi^2_r \leq 5$ and the fractional errors in the intrinsic fractional polarisation ≤ 0.1. Left: 2RUFD. Right: 3RFD. The derived intrinsic fractional polarisation from wideband modelling are small compared to those from high-frequency, high-resolution modelling. The observed depolarisation can be attributed to a change in the beam resolution.

that is why there are a few fitted lines-of-sight plotted.

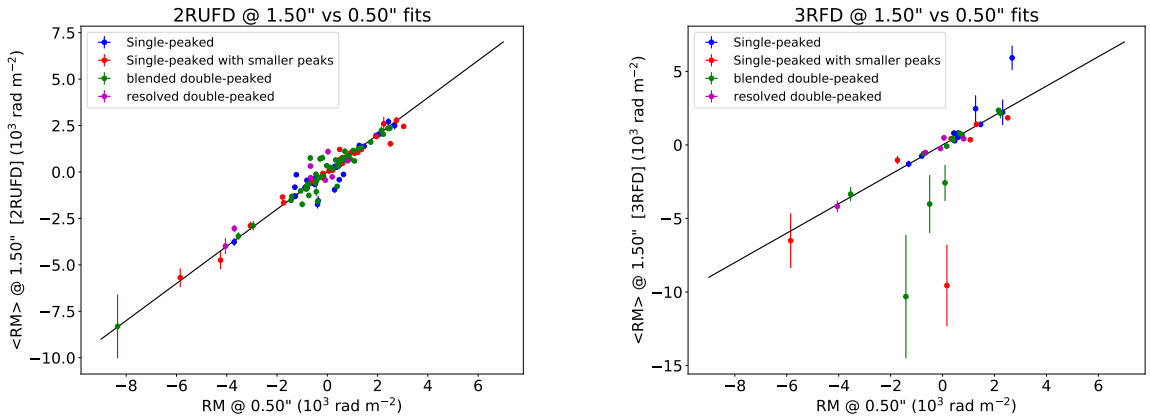

Figure 6.45: *A comparison of the estimated intrinsic fractional polarisation from the wideband data modelling with those from the high-frequency, high-resolution modelling.* RM from wideband modelling is a weighted sum of the components: $(RM_1 p_1 + RM_2 p_2 + \dots)/(p_1 + p_2 + \dots)$. The lines-of-sight shown have $\chi^2_r \leq 5$ and fractional errors ≤ 0.5. RM of 2RUFD and 3RFD are consistent with those of high-frequency modelling. However, the fitting solutions 3RFD is associated with large errors, hence only a few lines-of-sight remain.

Figure 6.46 compares the derived Faraday dispersions from wideband data modelling with those from high-frequency, high-resolution modelling. The Faraday dispersions from the wideband modelling are those of the strong component. The dispersions show no dependence on the Faraday classes and do not correlate. The dispersions from high-frequency, high-resolution solutions are larger than those from wideband data modelling, particularly for 2RUFD. We find that this is always true for all the components. Additionally, the dispersions at higher frequencies range within narrower regions; between $100 - 400$ rad m^{-2}, while for the wideband data the dispersions range between $20 - 400$ rad m^{-2} for 2RUFD and $75 - 5000$ rad m^{-2} for 3RFD. The large dispersions $\gtrsim 2000$ rad m^{-2} are likely not physical. The range of Faraday dispersions of the high-frequency modelling is consistent with those of 2RUFD, while $\sigma_{\rm stdev}$ is consistent with those of 3RFD.

An important question is whether the dispersions $\lesssim 77$ *rad m*$^{-2}$ *and separations* $\lesssim 180$ *rad m*$^{-2}$ *are real? It is not possible to know for certain if these are real or not with our data. We found a similar problem with Cygnus A. We need to include the available L-band data to improve the resolution in Faraday space. However, these lower-frequencies compromise the spatial resolution and since the observed structures are mostly due to spatial fluctuations, we expect the situation to be further complicated. As such, the dispersions and separations larger than these values can be trusted, while those smaller than this must be used with care. One indication of the presence of unresolved components is in the observed Faraday spectra – either through skewness or blended peaks.*

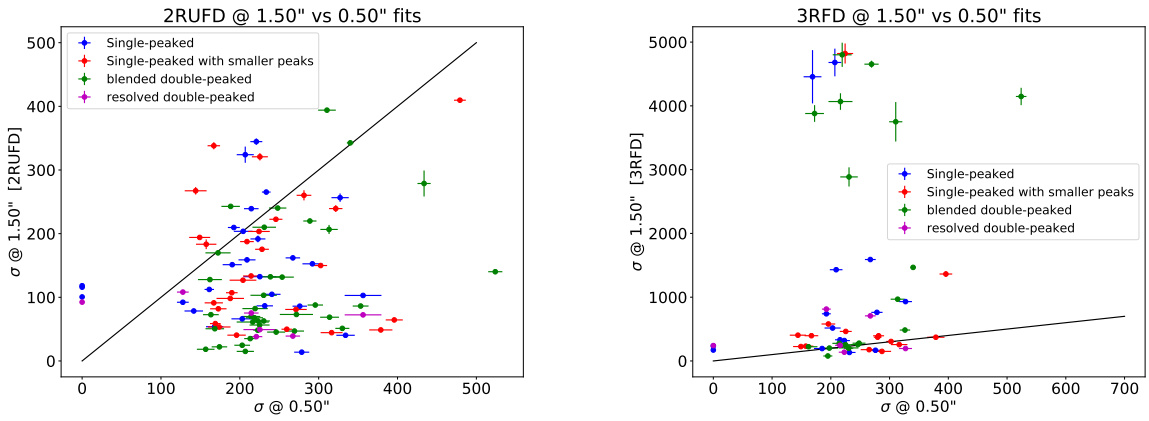

Figure 6.46: *A comparison of the derived Faraday dispersions from wideband data modelling with those from the high-frequency, high-resolution modelling*. The dispersions from the wideband data modelling are those of the strong component. The lines-of-sight shown have $\chi^2_r \leq 5$ and fractional errors ≤ 0.1. The dispersions seem independent of the Faraday classes.

6.12 The overall physical picture

6.12.1 Large-Scale Magnetic Fields

We find RM distribution across the tails ordered on scales ranging between 2 kpc and ~ 30 kpc. We have also shown that there exist field scales $\lesssim 0.5$ kpc. If we assume that these RM spatial scales correspond to magnetic field scales, then we can estimate the magnetic field strength of each scale. We assume an average electron density of ~ 0.04 cm^{-3} across pathlength of 40 kpc (the radial distance estimated from the AGN to end of the mapped tails, see Figure 6.13) and average temperature of 4 keV (see Figure 6.2). This density and temperature results in the thermal gas pressure of $\sim 5 \times 10^{-10}$ dyn cm^{-2}.

Figure 6.47 shows the magnetic field strength as a function of spatial scale (left plot) and β -parameter ($\mathcal{P}_{\mathcal{B}}/\mathcal{P}_T$, right plot). We also show the minimum energy magnetic field strength range ($10 - 70$ μG, Taylor et al. 1990) and the corresponding β in cyan colour. The magnetic fields at small-scales are dynamically important and are most likely to over-pressure the tails.

6.12.2 Unresolved Random-Uniform Magnetic Fields

Our data are in favour of beam-depolarisation as a major contributor to the observed depolarisation. The findings that are consistent with this picture are: i) the presence of double- and multiple-peaked Faraday spectra whose spread is larger than σ, ii) the preference of our wideband modelling towards multi-component models, and iii) the ability of our high-frequency, high-resolution maps to reproduce the observed depolarisation structures. These observational evidence indicates the presence of small-scale fluctuations on scales $\lesssim 0.50'' - 3''$.

Imagine an array of cells of size d across a given pathlength, L. We assume that each cell has an equal electron density, n_t and equal field strength, $\mathcal{B}_t$, with different field orientation. The resulting RM distribu-

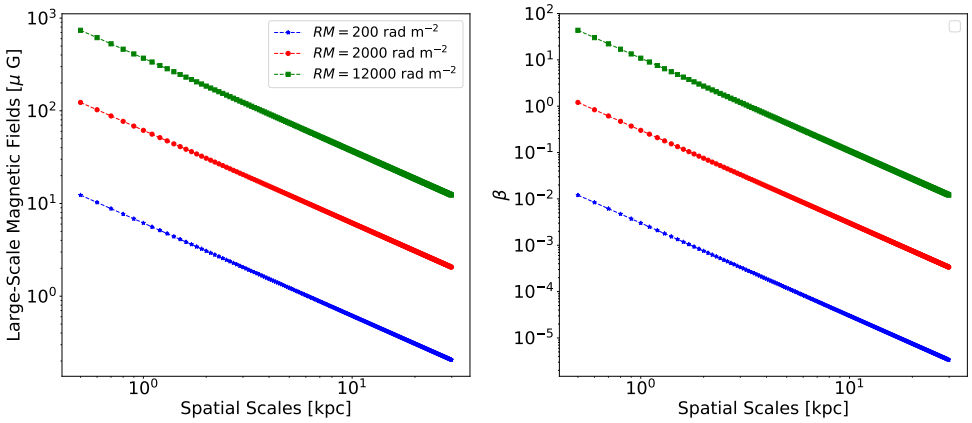

Figure 6.47: *Large-scale magnetic field strengths as a function of spatial scale.* The different colour curves correspond to different RM values. Cyan: A range of minimum energy magnetic field strengths in the tails and the corresponding β-parameter (the ratio of magnetic to thermal pressure in the Faraday rotating gas). We assumed the average electron density of 0.04 cm^{-3} and temperature of 4 keV across 40 kpc pathlength. The scales range between $0.5-30$ kpc. The field strengths at $RM \sim 12000$ rad m^{-2} are comparable to the minimum energy magnetic fields at larger scales and larger towards small-scales.

tion will have a zero mean and dispersion of $\sigma = 812 n_t \mathcal{B}_t d\sqrt{N}$. We assume an average electron density of ~ 0.04 cm^{-3} across a pathlength $L = 40$ kpc. Figure 6.48 shows the estimated random (turbulent) magnetic field strengths (left) and the corresponding β-parameter (right) as a function of spatial scales. The spatial scales range between $0.5-3$ kpc. For the observed Faraday dispersions, the random magnetic field strengths are ≤ 10 µG. The random magnetic fields are not dynamically important.

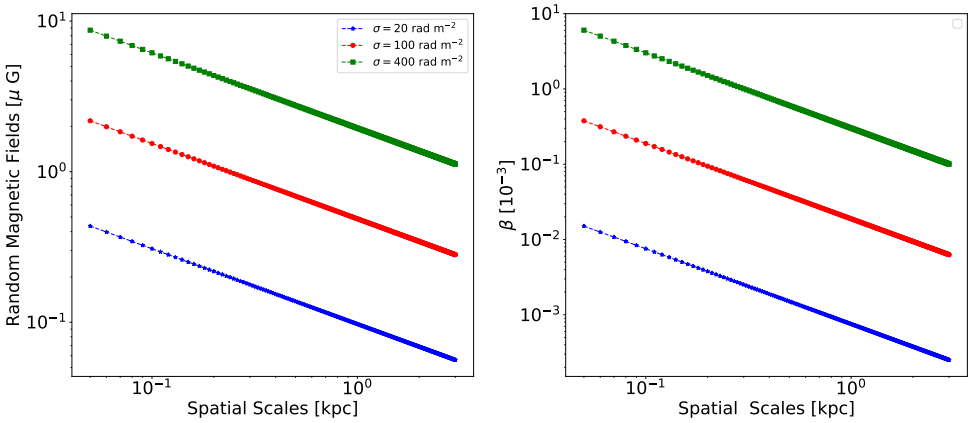

Figure 6.48: *Estimated random magnetic field strengths as a function of spatial scales.* The different colour curves correspond to different Faraday dispersion values. We assume electron density at each spatial scale of 0.04 cm^{-3} and temperature of 4 keV across a pathlength of 40 kpc. We show field estimates for spatial scales ranging from 0.05 kpc to 3 kpc. We chose the lower limit arbitrarily, as we only know that there exists structure < 0.5 kpc. For the observed Faraday dispersions, the random magnetic field strengths are ≤ 10 µG. The random magnetic fields are not dynamically important.

From 2RUFD, we derived unresolved uniform RM-differences that goes up to 2000 rad m^{-2}. The

corresponding uniform field strengths are the same as the red curve in Figure 6.47. Of importance are field values below spatial scale 1 kpc, since these can present unresolved uniform RM-differences. We find that within this region of the graph, the field strengths are larger than the minimum energy magnetic field and are dynamically important.

6.12.3 Mixed Gas

The lack of correlation between Faraday dispersions and RM in Figure 6.15 shows that it is not possible to rule out internal mixing for $RM < 2000$ rad m^{-2}. The derived $\Delta\phi$ from our wideband modelling also suggests a limit for uniform RM-difference is $\lesssim 2500$ rad m^{-2}. Thus, our data are able to rule out mixing for regions with $RM > 2000$ rad m^{-2}. Internal mixing was originally ruled out by Taylor and Perley (1993), using the argument that the observed depolarisation between $5-15$ GHz is too small to result from the "large" Faraday RM. Thus, our physical picture is that the depolarisation in regions with $RM < 2000$ rad m^{-2}, may or may not be due to internal mixing. Using 2000 rad m^{-2} RM value as an upper limit to the contribution from the internally mixed gas, we can estimate the internal electron density of the mixed gas. Taking a path line across the tails to be ~ 15 kpc, and minimum energy magnetic fields in the tails of 17.5 μG (see Table 4 in Taylor et al. 1990), we estimate the internal electron density of 0.009 cm^{-3}.

Our wideband modelling also suggested that a purely mixed gas alone (RUID) is not sufficient to describe the situation in Hydra A, rather, there is always a requirement for a foreground Faraday rotating gas. So there are two possible physical situations: the first is that of a mixed gas within the tails or boundary of the tails responsible for $RM \lesssim 2000$ rad m^{-2} and foreground gas responsible for the rest of the RM and the Faraday dispersions $\lesssim 1000$ rad m^{-2}. The second scenario is that all the depolarisation (uniform and random) and RM originate in a foreground gas. The first scenario implies that most of the depolarisation and RM across the northern tail are internal as well as the inner and outer regions of the southern tail. We are in favour of the latter scenario: unresolved fluctuations and large-scale magnetic fields in an external gas. Our data have demonstrated that the fluctuations (both uniform and random) are important and are responsible for the majority of the depolarisation and that there exists multiple unresolved RM-components.

6.12.4 RM-Components

Our wideband modelling indicates the presence of individual components with the beam. We find that the derived components are always distributed about a mean RM. For Hydra A, the components are separated by a maximum distance of $\sim$ 2500 rad m^{-2} (for 2RUFD). These are largely spread across the Faraday space compared to Cygnus A with maximum separation of 800 rad m^{-2} between the components. These separations are consistent with the derived RM-difference. This possibly implies a significant difference in the RM values across the beam. Additionally, since the components are distributed about the mean, this further implies that their RM values have different signs (both negative and positive). For regions with RM values larger than 2500 rad m^{-2}, an additional external, dominant and common screen is required. The presence of large RM gradients is not far fetched – the RM and Faraday dispersions in Figure 6.13 clearly indicate the presence of gradients. These gradients are most dominant across the southern tail and are most

likely to be responsible for the discontinuities we observe across this tail.

We also find that for our best fitting 2RUFD, the derived Faraday dispersions of the individual components is smaller than the spread of Faraday depths in Faraday space, especially for double- and multiple-peaked spectra. This implies that there is a common depolarising screen in the foreground of the individual components that is responsible for the global width in the Faraday spectra data.

The magnetic field structures within Hydra A cluster system are far from simple. We find that there exists a wide range of spatial scales and field strengths. There is a field scale responsible for the large RM-differences, a magnetic field component responsible for the individual Faraday dispersions (see Section 6.12.2), another component responsible for a common mean RM (see Section 6.12.1) and another responsible for σ_{stdev} – the global depolarising gas.

6.12.5 Possible Locations of the Magnetic Fields

$RM > 2000$ rad m^{-2} most definitely originate in the external screen. However, it must be determined where the screen is located. The only reasonable location is the ambient cluster. The shock due to the expansion of the tails into the cluster occurs at a distance of $200 - 300$ kpc from the cluster centre – too far to have much influence on the region of the mapped source ($\lesssim 30$ kpc radius). The case in Hydra A is unlike that of Cygnus A, where the cocoon-shock can equally account for the observed RM and depolarisation. The $RM < 2000$ rad m^{-2} can originate in either a mixed gas or an external depolarising gas. Our data support the latter.

CHAPTER 7

Summary and Future Work

"When I (Lerato) look at Your heavens, the work of Your fingers, the moon and the stars, which You have set in place, what is man that You are mindful of him, and the son of man that You care for him?"
Psalms 8:3-4

7.1 Our Wideband Study

In this dissertation, we have presented our wideband study of two extended, well-known radio galaxies, namely Cygnus A and Hydra A. We observed these radio galaxies between the year 2014 to 2020, with the VLA radio telescope. Our observations spanned the frequency coverage between $0.2 - 18$ GHz for Cygnus A and $1 - 12$ GHz for Hydra A. We only present the frequency data between $2 - 18$ GHz for Cygnus A and $2 - 12$ GHz for Hydra A, so that we can obtain high spatial resolution while preserving the large bandwidth.

The two radio galaxies are of two different morphologies: Cygnus A is an FR II and Hydra A an FR I. They are the most luminous radio galaxies known of their type and are embedded at the centre of CC dense thermally emitting X-ray clusters. These radio galaxies are also associated with very large Faraday RM ranging between -5000 and $+6400$ rad m^{-2} in Cygnus A and -2000 and $+11900$ rad m^{-2} in Hydra A. The RM distribution across the lobes show large gradients ranging between a few 100 rad m^{-2} arcsec^{-1} up to a few 1000 rad m^{-2} arcsec^{-1}. A decline in the degree of polarisation, referred to as the depolarisation, between two 15 GHz and 5 GHz is observed.

This dissertation aimed to study the structure and origin of the magnetic fields responsible for the observed large Faraday RM, large gradients and depolarisation and study the interplay between the ambient cluster and the radio galaxies. The large Faraday rotations are indicative of large magnetic field strengths and dense gas. The large gradients give information on the spatial structure of the magnetic fields. The depolarisation, on the other hand, is indicative of either i) unresolved small-scale fluctuations (turbulence) in the magnetic fields of the Faraday rotating gas or the synchrotron gas or ii) a mixing of thermal gas with radio synchrotron emitting gas from the lobes/tails. Understanding magnetic fields in clusters is essential because magnetic fields can affect the formation and evolution of the cluster and can also regulate heat conduction, trap or accelerate cosmic particles and can ultimately influence the dynamics of the cluster.

7.2 Results

Below, we summarise significant findings from our wideband polarisation study of the two radio galaxies. For a detailed summary of the results, we refer the reader to the end of each chapter. The summary is as follows:

- The polarisation distribution across the lobes/tails show no spatial correlation with any spatial structure in both radio galaxies. The polarisation distribution is smooth towards higher frequencies and gets clumpier at small-scales – showing ~ 2 kpc-scales at lower frequencies.
- The degree of polarisation of both radio galaxies decreases across the lobes/tails with a decreasing frequency. The inner regions of the lobes/tails (closer to the AGN) depolarise more rapidly than the extreme regions.
- The individual lines-of-sight across the lobes/tails all depolarise with increasing λ^2. The depolarisation also shows structure. For Cygnus A, we classified the depolarisation structure into smooth-decaying, sinc-like and complex. Hydra A lines-of-sight are classified into smooth decaying, oscillatory and complex decaying. Roughly 30% of the classifiable lines-of-sight across Cygnus A are smooth-decays, 12% are sinc-like and 58% are complex. For lines-of-sight across Hydra A, roughly 22% are smooth-decay, 11% oscillatory and 67% are complex.
- We also find a wide range of structure in the Faraday spectra, ranging from a simple single-peaked spectrum to a multiple-peaked spectrum. We classified the Faraday spectra into six categories: single-peaked, single-peaked with smaller peaks, blended and resolved double-peaked spectra and blended and resolved multiple-peaked spectra. We find that 40% of Cygnus A lines-of-sight are single-peaked spectra, with only 10% for Hydra A. Thus, Hydra A spectra data are more structured than those of Cygnus A.
- We also find a significant change in the degree of polarisation with decreasing resolution for both sources. This result suggests that beam-depolarisation is essential to the data. The degree of polarisation does not always increase monotonically with the increasing beam-resolution – as is expected in the presence of a simple randomly fluctuating screen. In most cases, the fractional polarisation changes unpredictably with resolution. Such behaviour is indicative of the complex nature of the media responsible for the depolarisation.
- Using high-frequency, high-resolution Faraday rotation maps, we were able to predict at least $2/3$ of data at low-frequency and low-resolution. These results indicate that most of the depolarisation and depolarisation structure is attributed to unresolved fluctuations in the Faraday rotating screen.
- We convolved Cygnus A data from $0.75''$ to $1.5''$ and for Hydra A from $1.50''$ to $3''$. We found a significant change in the depolarisation pattern and Faraday spectra structure at these two different resolutions. These results further strengthen the importance of beam-depolarisation in our data.
- We do not find any correlation between the observed Faraday RM and Faraday dispersions at higher resolution. The lack of correlation suggests that the Faraday depolarisations are independent of the Faraday rotations. This is another piece of evidence against the internal mixing of ambient thermal gas with the lobes/tails emission. The gas causing the large Faraday rotations must be external.

- We modelled our wideband data using simple analytical models. More specifically, we modelled only four Faraday class spectra; namely, single-peaked, single-peaked with smaller peaks, blended and resolved double-peaked. Our wideband modelling first reveals the complexity in real-life data and the limitation of the available analytical models. Using these ideal models, we show that the data for both sources require at least two or more Faraday components. This multi-component requirement is consistent with the evidence of beam-depolarisation noted above.
  For Cygnus A, we find that the data are best described by three randomly depolarising Faraday components (model 3RFD). In comparison, Hydra A data are better explained by two-components with random fluctuations superimposed on unresolved uniform RM-differences. The wideband data modelling cannot be explained by internal mixing for RM greater than 1000 rad m^{-2} for Cygnus A and 2000 rad m^{-2} for Hydra A; however we cannot rule out internal mixing for lower RM. Using these RM limits, we estimate the electron density within Cygnus A lobes of 7×10^{-4} cm^{-3} at 65 μG and $L = 25$ kpc and $\sim 9 \times 10^{-3}$ cm^{-3} at 18 μG and 15 kpc.
- Our data are consistent with unresolved fluctuations in the magnetised gas. The large RM are external to the synchrotron emitting region. However, we do not know where the turbulent medium is located. Possible locations are the cluster-core or the cocoon-shock for Cygnus A and the cluster-core for Hydra A. These radio galaxies are embedded inside multiscaled magnetic fields ranging between a few 100 pc to ~ 1000 pc.

7.3 Recommendations for Future Observing

The following are recommendations for future observing and analysis:

- To address the location and whether there is any internal mixing, we need higher resolution to resolve the small-scale fluctuations while maintaining the brightness sensitivity. To get a resolution of $0.3''$ at 2 GHz will require baselines longer than 105 km. This baseline is three times longer than the current JVLA baseline at A-configuration. Such baselines are proposed for future instruments. For example, the SKA1-mid array in South Africa will have a baseline of up to 150 km (allowing a resolution of $\sim 0.3''$ at 1.4 GHz) and six times more sensitivity than the JVLA. The SKA phase 2, on the other hand, is planned to have fifty times better sensitivity and ten times better spatial resolution (at 1.4 GHz) than the JVLA. The New Generation of VLA (ngVLA) in the United States is planned to have ten times better sensitivity than the JVLA and baselines thirty times longer than the current VLA, allowing sub-arcseconds to a few milli-arcseconds resolutions. If we obtain higher resolution for resolving out all foreground fluctuations, our need for modelling will be much reduced (although not eliminated). Modelling would then only be necessary for lines-of-sight characterisation.
- In this dissertation, we have attempted to model a wide range of lines-of-sight at once. However, this may not always be ideal, given the complexity in each line-of-sight. The first step into understanding the data better may be to carry out a more detailed analysis of the individual lines-of-sight for specific regions within the source. A further step would be to conduct an in-depth comparison of nearby lines-of-sight to search for any spatial coherences.

- To improve our characterisation using wideband data modelling awaits better and more sophisticated analytical models and simulations. The current models are insufficient to characterise these data more appropriately due to their inherent assumptions, such as Gaussianity and non-spatial correlation. The limitation of the current analytical models was particularly demonstrated with the Hydra A data. These data will provide an excellent basis for testing new, more sophisticated models and simulations.
- We chose to study Cygnus A and Hydra A due to their high surface brightness, which allows high signal-to-noise ratios. The sources are situated in dense environments. It is thus not surprising to see large Faraday rotations and complex depolarisation structures. We recommend similar studies that make use of a broad range of cluster samples.
- Another area of research (though highly technical) would be to develop strategies for classifying depolarisation structures and Faraday spectrum structure in an automated fashion. In this work, we classified the structures in the data manually by eye – which was both time consuming and subject to human biases. Machine learning and deep learning methods may address these issues. Such an automated classification is important for future work, as more such wideband studies are encouraged, and the data are expected to increase significantly.
- As it is now, very little can be learned from the heavily depolarised regions where no fits were possible. There was not enough signal to conduct any meaningful model fitting. The possibility of probing these regions awaits higher sensitivity (larger collecting area especially at high-frequencies) and higher resolutions (longer baselines especially at low-frequencies) for resolving the turbulent screens.
- Another research area of scientific importance may be a detailed comparison of polarisation data with other waveband data such as optical, infrared and X-ray, where available. The specifics of the method for comparing these data still needs to be investigated or invented. We suggest a more obvious image-comparing approach: searching for "spatial correlations" between polarisation maps with X-ray images. When comparing the small-scale structures, although the X-ray images have sufficient resolutions, the images may not have good enough SNR for any meaningful comparison. On the other hand, for large-scale – a few-kpc – spatial comparison may provide some insight. For example, one could investigate whether the few-kpc RM structures and the depolarised regions have any relation to the few-kpc X-ray structures (for example, the ribs in Cygnus A and the irregular structures close to the radio structure in Hydra A). For optical and infrared, it could be that the sub-kpc arises from cool plasma, in such cases, the gas will emit at these frequencies. The challenge is whether modern optical or infrared telescopes have enough sensitivity to detect such faint emissions. We also believe that if such gas is present, the chance of detecting it in Hydra A is higher than in Cygnus A due to the high Galactic latitude of Hydra A (away from significant obscuring dust).igh Galactic lattitude of Hydra A (away from significant obscuring of optical light by dust).
- In the future, it may also be possible to compare polarisation structures of these galaxies with results from MHD simulations. Current MHD simulations are extremely limited in spatial resolution (a few-Mpc) for studying a few kpc-scale structures present in these galaxies. At larger scales (several kpc), existing (or future) MHD simulations can be used to estimate, for example, the magnitude and statistics of RM structures in front of a cluster-centre radio galaxy.

Bibliography

Abell, G. O. (May 1958). “The Distribution of Rich Clusters of Galaxies.” In: *ApJS* 3, p. 211. DOI: 10.1086/190036.

— (Jan. 1965). “Clustering of Galaxies”. In: *ARA&A* 3, p. 1. DOI: 10.1146/annurev.aa.03.090165.000245.

Abell, G. O., H. G. Corwin, and R. P. Olowin (May 1989). “A Catalog of Rich Clusters of Galaxies”. In: *ApJS* 70, p. 1. DOI: 10.1086/191333.

Alexander, P., M. T. Brown, and P. F. Scott (Aug. 1984). “A multi-frequency radio study of Cygnus A.” In: *MNRAS* 209, pp. 851–868. DOI: 10.1093/mnras/209.4.851.

Allen, S. W. et al. (June 1993). “A ROSAT PSPC observation of Abell 478 : the distribution of X-ray absorbing matter in a massive cooling flow.” In: *MNRAS* 262, pp. 901–914. DOI: 10.1093/mnras/262.4.901.

Anderson, C. S., B. M. Gaensler, and I. J. Feain (July 2016). “A Study of Broadband Faraday Rotation and Polarization Behavior over 1.3–10 GHz in 36 Discrete Radio Sources”. In: *ApJ* 825.1, 59, p. 59. DOI: 10.3847/0004-637X/825/1/59. arXiv: 1604.01403 [astro-ph.HE].

Anderson, C. S. et al. (Dec. 2015). “Broadband Radio Polarimetry and Faraday Rotation of 563 Extragalactic Radio Sources”. In: *ApJ* 815.1, 49, p. 49. DOI: 10.1088/0004-637X/815/1/49. arXiv: 1511.04080 [astro-ph.GA].

Anderson, C. S. et al. (Mar. 2018). “Broadband Radio Polarimetry of Fornax A. I. Depolarized Patches Generated by Advected Thermal Material from NGC 1316”. In: *ApJ* 855.1, 41, p. 41. DOI: 10.3847/1538-4357/aaaec0. arXiv: 1802.04812 [astro-ph.HE].

Andrae, R., T. Schulze-Hartung, and P. Melchior (Dec. 2010). “Dos and don’ts of reduced chi-squared”. In: *arXiv e-prints*, arXiv:1012.3754, arXiv:1012.3754. arXiv: 1012.3754 [astro-ph.IM].

Armstrong, J. W., B. J. Rickett, and S. R. Spangler (Apr. 1995). “Electron Density Power Spectrum in the Local Interstellar Medium”. In: *ApJ* 443, p. 209. DOI: 10.1086/175515.

Bacchi, M. et al. (Mar. 2003). “Deep images of cluster radio halos”. In: *A&A* 400, pp. 465–476. DOI: 10.1051/0004-6361:20030044. arXiv: astro-ph/0301206 [astro-ph].

Basu, A. et al. (Nov. 2019). “An In-depth Investigation of Faraday Depth Spectrum Using Synthetic Observations of Turbulent MHD Simulations”. In: *Galaxies* 7.4, p. 89. ISSN: 2075-4434. DOI: 10.3390/galaxies7040089. URL: http://dx.doi.org/10.3390/galaxies7040089.

Bauer, F. E. et al. (June 2005). “The prevalence of cooling cores in clusters of galaxies at z 0.15-0.4”. In: *MNRAS* 359.4, pp. 1481–1490. DOI: 10.1111/j.1365-2966.2005.08999.x. arXiv: astro-ph/0503232 [astro-ph].

Baum, S. A., E. L. Zirbel, and C. P. O’Dea (Sept. 1995). “Toward Understanding the Fanaroff-Riley Dichotomy in Radio Source Morphology and Power”. In: *ApJ* 451, p. 88. DOI: 10.1086/176202.

Baum, S. A. et al. (Dec. 1988). “Extended Optical Line Emitting Gas in Radio Galaxies: Broad-Band Optical, Narrow-Band Optical, and Radio Imaging of a Representative Sample”. In: *ApJS* 68, p. 643. DOI: 10.1086/191301.

Bautz, L. P. and W. W. Morgan (Dec. 1970). “On the Classification of the Forms of Clusters of Galaxies”. In: *ApJ* 162, p. L149. DOI: 10.1086/180643.

Beck, R. and R. Wielebinski (2013). “Magnetic Fields in Galaxies”. In: *Planets, Stars and Stellar Systems. Volume 5: Galactic Structure and Stellar Populations*. Ed. by Terry D. Oswalt and Gerard Gilmore. Vol. 5, p. 641. DOI: 10.1007/978-94-007-5612-0_13.

Begelman, M. C., R. D. Blandford, and M. J. Rees (Apr. 1984). “Theory of extragalactic radio sources”. In: *Reviews of Modern Physics* 56.2, pp. 255–351. DOI: 10.1103/RevModPhys.56.255.

Best, P. N. (Feb. 2009). “Radio source populations: Results from SDSS”. In: *Astronomische Nachrichten* 330.2, pp. 184–189. DOI: 10.1002/asna.200811152.

Bicknell, G. V. (Nov. 1995). “Relativistic Jets and the Fanaroff-Riley Classification of Radio Galaxies”. In: *ApJS* 101, p. 29. DOI: 10.1086/192232. arXiv: astro-ph/9406064 [astro-ph].

Bicknell, G. V., R. A. Cameron, and R. A. Gingold (July 1990). “Rotation Measure Variations across the Lobes of Extragalactic Radio Sources”. In: *ApJ* 357, p. 373. DOI: 10.1086/168928.

Bîrzan, L. et al. (June 2004). “A Systematic Study of Radio-induced X-Ray Cavities in Clusters, Groups, and Galaxies”. In: *ApJ* 607.2, pp. 800–809. DOI: 10.1086/383519. arXiv: astro-ph/0402348 [astro-ph].

Blandford, R. D. and C. F. McKee (Apr. 1982). “Reverberation mapping of the emission line regions of Seyfert galaxies and quasars.” In: *ApJ* 255, pp. 419–439. DOI: 10.1086/159843.

Blanton, E. L. et al. (Sept. 2001). “Chandra Observation of the Radio Source/X-Ray Gas Interaction in the Cooling Flow Cluster Abell 2052”. In: *ApJ* 558.1, pp. L15–L18. DOI: 10.1086/323269. arXiv: astro-ph/0107221 [astro-ph].

Boehringer, H. et al. (Oct. 1993). “A ROSAT HRI study of the interaction of the X-ray emitting gas and radio lobes of NGC 1275.” In: *MNRAS* 264, pp. L25–L28. DOI: 10.1093/mnras/264.1.L25.

Bonafede, A. et al. (Feb. 2009). “Double relics in Abell 2345 and Abell 1240. Spectral index and polarization analysis”. In: *A&A* 494.2, pp. 429–442. DOI: 10.1051/0004-6361:200810588. arXiv: 0810.2223 [astro-ph].

Bonafede, A. et al. (June 2011). “Fractional polarization as a probe of magnetic fields in the intra-cluster medium”. In: *A&A* 530, A24, A24. DOI: 10.1051/0004-6361/201016298. arXiv: 1103.0277 [astro-ph.CO].

Brentjens, M. A. and A. G. de Bruyn (Oct. 2005). “Faraday rotation measure synthesis”. In: *A&A* 441.3, pp. 1217–1228. DOI: 10.1051/0004-6361:20052990. arXiv: astro-ph/0507349 [astro-ph].

Bridle, A. H. and R. A. Perley (Jan. 1984). “Extragalactic Radio Jets”. In: *ARA&A* 22, pp. 319–358. DOI: 10.1146/annurev.aa.22.090184.001535.

Buchner, J. et al. (Apr. 2014). “X-ray spectral modelling of the AGN obscuring region in the CDFS: Bayesian model selection and catalogue”. In: *A&A* 564, A125, A125. DOI: 10.1051/0004-6361/201322971. arXiv: 1402.0004 [astro-ph.HE].

Burbidge, G. (Dec. 1967). “Generation of Radio Sources”. In: *Nature* 216.5122, pp. 1287–1289. DOI: 10.1038/2161287a0.

Burbidge, G. R. (May 1959). “Estimates of the Total Energy in Particles and Magnetic Field in the Non-Thermal Radio Sources.” In: *ApJ* 129, pp. 849–852. DOI: 10.1086/146680.

Burch, S. F. (Feb. 1979). “Multifrequency studies of seven 3CR radio sources - II. Results and interpretation.” In: *MNRAS* 186, pp. 519–553. DOI: 10.1093/mnras/186.3.519.

Burn, B. J. (Jan. 1966). “On the depolarization of discrete radio sources by Faraday dispersion”. In: *MNRAS* 133, p. 67. DOI: 10.1093/mnras/133.1.67.

Burns, J. O. et al. (Mar. 2008). “Why Do Only Some Galaxy Clusters Have Cool Cores?” In: *ApJ* 675.2, pp. 1125–1140. DOI: 10.1086/526514. arXiv: 0708.1954 [astro-ph].

Carilli, C. L. and P. D. Barthel (Jan. 1996). “Cygnus A”. In: *A&A Rev.* 7.1, pp. 1–54. DOI: 10.1007/s001590050001.

Carilli, C. L., J. W. Dreher, and R. A. Perley (1989). “Cygnus a and the Williams Model”. In: *Hot Spots in Extragalactic Radio Sources*. Ed. by Klaus Meisenheimer and Hermann-Josef Roeser. Vol. 327, p. 51. DOI: 10.1007/BFb0036012.

Carilli, C. L., R. A. Perley, and J. H. Dreher (Nov. 1988). “Discovery of the Bow Shock of Cygnus A”. In: *ApJ* 334, p. L73. DOI: 10.1086/185315.

Carilli, C. L., R. A. Perley, and D. E. Harris (Sept. 1994). “Observations of interaction between cluster gas and the radio lobes of Cygnus A.” In: *MNRAS* 270, pp. 173–177. DOI: 10.1093/mnras/270.1.173.

Carilli, C. L. and G. B. Taylor (Jan. 2002). “Cluster Magnetic Fields”. In: *ARA&A* 40, pp. 319–348. DOI: 10.1146/annurev.astro.40.060401.093852. arXiv: astro-ph/0110655 [astro-ph].

Carilli, C. L. et al. (Dec. 1991). “Multifrequency Radio Observations of Cygnus A: Spectral Aging in Powerful Radio Galaxies”. In: *ApJ* 383, p. 554. DOI: 10.1086/170813.

Cho, J. (Dec. 2014). “Origin of Magnetic Field in the Intracluster Medium: Primordial or Astrophysical?” In: *ApJ* 797.2, 133, p. 133. DOI: 10.1088/0004-637X/797/2/133. arXiv: 1410.1893 [astro-ph.CO].

Clarke, T. E. (Dec. 2000). “Probing magnetic fields in clusters of galaxies”. PhD thesis. UNIVERSITY OF TORONTO (CANADA).

— (Dec. 2004). “Faraday Rotation Observations of Magnetic Fields in Galaxy Clusters”. In: *Journal of Korean Astronomical Society* 37.5, pp. 337–342. DOI: 10.5303/JKAS.2004.37.5.337. arXiv: astro-ph/0412268 [astro-ph].

Clarke, T. E., P. P. Kronberg, and H. Böhringer (Feb. 2001). “A New Radio-X-Ray Probe of Galaxy Cluster Magnetic Fields”. In: *ApJ* 547.2, pp. L111–L114. DOI: 10.1086/318896. arXiv: astro-ph/0011281 [astro-ph].

Clegg, A. W. et al. (Feb. 1992). “Rotation Measures of Low-Latitude Extragalactic Sources and the Magnetoionic Structure of the Galaxy”. In: *ApJ* 386, p. 143. DOI: 10.1086/171000.

Colgate, S. A. and H. Li (May 2000). “The Magnetic Fields of the Universe and Their Origin”. In: *Highly Energetic Physical Processes and Mechanisms for Emission from Astrophysical Plasmas*. Ed. by P. C. H. Martens, S. Tsuruta, and M. A. Weber. Vol. 195, p. 255. arXiv: astro-ph/0001418 [astro-ph].

Cooper, B. F. C. and R. M. Price (Sept. 1962). “Faraday Rotation Effects associated with the Radio Source Centaurus A”. In: *Nature* 195.4846, pp. 1084–1085. DOI: 10.1038/1951084a0.

Cornwell, T. J. (Nov. 2008). “Multiscale CLEAN Deconvolution of Radio Synthesis Images”. In: *IEEE Journal of Selected Topics in Signal Processing* 2.5, pp. 793–801. DOI: 10.1109/JSTSP.2008.2006388.

Cornwell, T. J. and P. N. Wilkinson (Sept. 1981). “A new method for making maps with unstable radio interferometers”. In: *MNRAS* 196, pp. 1067–1086. DOI: 10.1093/mnras/196.4.1067.

David, L. P. et al. (June 1990). “Einstein Observations of the Hydra A Cluster and the Efficiency of Galaxy Formation in Groups and Clusters”. In: *ApJ* 356, p. 32. DOI: 10.1086/168812.

David, L. P. et al. (Aug. 2001). “A High-Resolution Study of the Hydra A Cluster with Chandra: Comparison of the Core Mass Distribution with Theoretical Predictions and Evidence for Feedback in the Cooling Flow”. In: *ApJ* 557.2, pp. 546–559. DOI: 10.1086/322250. arXiv: astro-ph/0010224 [astro-ph].

de Vries, M. N. et al. (Aug. 2018). “Detection of non-thermal X-ray emission in the lobes and jets of Cygnus A”. In: *MNRAS* 478.3, pp. 4010–4029. DOI: 10.1093/mnras/sty1232. arXiv: 1805.03114 [astro-ph.HE].

De Young, D. S. and W. I. Axford (Oct. 1967). “Inertial Confinement of Extended Radio Sources”. In: *Nature* 216.5111, pp. 129–131. DOI: 10.1038/216129a0.

Dolag, K., M. Bartelmann, and H. Lesch (Aug. 1999). “SPH simulations of magnetic fields in galaxy clusters”. In: *A&A* 348, pp. 351–363. arXiv: astro-ph/0202272 [astro-ph].

— (May 2002). “Evolution and structure of magnetic fields in simulated galaxy clusters”. In: *A&A* 387, pp. 383–395. DOI: 10.1051/0004-6361:20020241.

Donnert, J. et al. (Jan. 2009). “Cluster magnetic fields from galactic outflows”. In: *MNRAS* 392.3, pp. 1008–1021. DOI: 10.1111/j.1365-2966.2008.14132.x. arXiv: 0808.0919 [astro-ph].

Dreher, J. W. (June 1979). “Polarization maps of Cygnus A at 23 Gigahertz.” In: *ApJ* 230, pp. 687–696. DOI: 10.1086/157127.

Dreher, J. W., C. L. Carilli, and R. A. Perley (May 1987). “The Faraday Rotation of Cygnus A: Magnetic Fields in Cluster Gas”. In: *ApJ* 316, p. 611. DOI: 10.1086/165229.

Duffy, R. T. et al. (June 2018). “The X-ray ribs within the cocoon shock of Cygnus A”. In: *MNRAS* 476.4, pp. 4848–4860. DOI: 10.1093/mnras/sty549. arXiv: 1802.09476 [astro-ph.HE].

Dunbar, Dana S., Robert Selina, and Brad McCreight (Jan. 2019). “Antenna Concept for the Next-Generation Very Large Array”. In: *American Astronomical Society Meeting Abstracts #233*. Vol. 233. American Astronomical Society Meeting Abstracts, p. 361.03.

Dunn, R. J. H. and A. C. Fabian (Dec. 2006). “Investigating AGN heating in a sample of nearby clusters”. In: *MNRAS* 373.3, pp. 959–971. DOI: 10.1111/j.1365-2966.2006.11080.x. arXiv: astro-ph/0609537 [astro-ph].

Dursi, L. J. and C. Pfrommer (Apr. 2008). “Draping of Cluster Magnetic Fields over Bullets and Bubbles—Morphology and Dynamic Effects”. In: *ApJ* 677.2, pp. 993–1018. DOI: 10.1086/529371. arXiv: 0711.0213 [astro-ph].

Dwarakanath, K. S., F. N. Owen, and J. H. van Gorkom (Mar. 1995). “Detection of an H i Disk in Hydra A?” In: *ApJ* 442, p. L1. DOI: 10.1086/187801.

EHT (Apr. 2019). “First M87 Event Horizon Telescope Results. I. The Shadow of the Supermassive Black Hole”. In: *ApJ* 875.1, L1, p. L1. DOI: 10.3847/2041-8213/ab0ec7. arXiv: 1906.11238 [astro-ph.GA].

Eilek, J. A. (Jan. 2002). “The magnetized intracluster plasma”. In: *Highlights of Astronomy* 12, pp. 525–527.

Eilek, J. A. and F. N. Owen (Mar. 2002). “Magnetic Fields in Cluster Cores: Faraday Rotation in A400 and A2634”. In: *ApJ* 567.1, pp. 202–220. DOI: 10.1086/338376. arXiv: astro-ph/0109177 [astro-ph].

Enßlin, T. A. and C. Vogt (Apr. 2003). “The magnetic power spectrum in Faraday rotation screens”. In: *A&A* 401, pp. 835–848. DOI: 10.1051/0004-6361:20030172. arXiv: astro-ph/0302426 [astro-ph].

Ensslin, T. A. et al. (Apr. 1998). “Cluster radio relics as a tracer of shock waves of the large-scale structure formation”. In: *A&A* 332, pp. 395–409. arXiv: astro-ph/9712293 [astro-ph].

Fabbiano, G. et al. (June 1979). “HEAO 1 scanning modulation collimator discovery of an extended X-ray source at Cygnus A.” In: *ApJ* 230, pp. L67–L71. DOI: 10.1086/182963.

Fabian, A. C., E. M. Hu, et al. (Aug. 1981). “The distribution and morphology of X-ray emitting gas in the core of the Perseus cluster.” In: *ApJ* 248, pp. 47–54. DOI: 10.1086/159128.

Fabian, A. C., P. E. J. Nulsen, et al. (July 1981). “The discovery of optical filaments surrounding the central galaxy in A496 - Evidence for a cooling flow”. In: *MNRAS* 196, 35P–37P. DOI: 10.1093/mnras/196.1.35P.

Fabian, A. C. et al. (Nov. 2000). “Chandra imaging of the complex X-ray core of the Perseus cluster”. In: *MNRAS* 318.4, pp. L65–L68. DOI: 10.1046/j.1365-8711.2000.03904.x. arXiv: astro-ph/0007456 [astro-ph].

Fabian, A. C. et al. (Sept. 2003). “A deep Chandra observation of the Perseus cluster: shocks and ripples”. In: *MNRAS* 344.3, pp. L43–L47. DOI: 10.1046/j.1365-8711.2003.06902.x. arXiv: astro-ph/0306036 [astro-ph].

Fanaroff, B. L. and J. M. Riley (May 1974). “The morphology of extragalactic radio sources of high and low luminosity”. In: *MNRAS* 167, 31P–36P. DOI: 10.1093/mnras/167.1.31P.

Feretti, L. (June 2000). “Observational Properties of Diffuse Halos in Clusters”. In: *arXiv e-prints*, astro-ph/0006379, astro–ph/0006379. arXiv: astro-ph/0006379 [astro-ph].

Feretti, L. and G. Giovannini (Jan. 1996). “Diffuse Cluster Radio Sources (Review)”. In: *Extragalactic Radio Sources*. Ed. by Ron D. Ekers, C. Fanti, and L. Padrielli. Vol. 175. IAU Symposium, p. 333.

Feretti, L. et al. (Oct. 1995). “The magnetic field in the Coma cluster.” In: *A&A* 302, p. 680. arXiv: astro-ph/9504058 [astro-ph].

Feretti, L. et al. (Apr. 1999). “The radio galaxies and the magnetic field in Abell 119”. In: *A&A* 344, pp. 472–482. arXiv: astro-ph/9902019 [astro-ph].

Feroz, F. and M. P. Hobson (Feb. 2008). “Multimodal nested sampling: an efficient and robust alternative to Markov Chain Monte Carlo methods for astronomical data analyses”. In: *MNRAS* 384.2, pp. 449–463. DOI: 10.1111/j.1365-2966.2007.12353.x. arXiv: 0704.3704 [astro-ph].

Feroz, F., M. P. Hobson, and M. Bridges (Oct. 2009). “MULTINEST: an efficient and robust Bayesian inference tool for cosmology and particle physics”. In: *MNRAS* 398.4, pp. 1601–1614. DOI: 10.1111/j.1365-2966.2009.14548.x. arXiv: 0809.3437 [astro-ph].

Frick, P. et al. (Jan. 2010). “Wavelet-based Faraday rotation measure synthesis”. In: *MNRAS* 401.1, pp. L24–L28. DOI: 10.1111/j.1745-3933.2009.00778.x. arXiv: 0911.0261 [astro-ph.GA].

Furlanetto, S. R. and A. Loeb (Aug. 2001). “Intergalactic Magnetic Fields from Quasar Outflows”. In: *ApJ* 556.2, pp. 619–634. DOI: 10.1086/321630. arXiv: astro-ph/0102076 [astro-ph].

Gaensler, B. M. et al. (Jan. 2010). “Survey Science with ASKAP: Polarization Sky Survey of the Universe’s Magnetism (POSSUM)”. In: *American Astronomical Society Meeting Abstracts #215*. Vol. 215. American Astronomical Society Meeting Abstracts, p. 470.13.

Gardner, F. F. and J. B. Whiteoak (Jan. 1966). “The Polarization of Cosmic Radio Waves”. In: *ARA&A* 4, p. 245. DOI: 10.1146/annurev.aa.04.090166.001333.

Garrington, S. T., R. G. Conway, and J. P. Leahy (May 1991). “Asymmetry depolarization in double radio sources with one sided jets.” In: *MNRAS* 250, p. 171. DOI: 10.1093/mnras/250.1.171.

Garrington, S. T. et al. (Jan. 1988). “A systematic asymmetry in the polarization properties of double radio sources with one jet”. In: *Nature* 331.6152, pp. 147–149. DOI: 10.1038/331147a0.

Ge, J. P. and F. N. Owen (Mar. 1993). “Faraday Rotation in Cooling Flow Clusters of Galaxies. I. Radio and X-Ray Observations of Abell 1795”. In: *AJ* 105, p. 778. DOI: 10.1086/116471.

Ghisellini, G. and A. Celotti (Nov. 2001). “The dividing line between FR I and FR II radio-galaxies”. In: *A&A* 379, pp. L1–L4. DOI: 10.1051/0004-6361:20011338. arXiv: astro-ph/0106570 [astro-ph].

Giacconi, R. et al. (Dec. 1972). “The Uhuru catalog of X-ray sources.” In: *ApJ* 178, pp. 281–308. DOI: 10.1086/151790.

Giacintucci, S. et al. (Oct. 2009). “A Giant Radio Halo in the Massive and Merging Cluster Abell 1351”. In: *ApJ* 704.1, pp. L54–L57. DOI: 10.1088/0004-637X/704/1/L54. arXiv: 0909.0437 [astro-ph.CO].

Giacintucci, S. et al. (June 2017). “Occurrence of Radio Minihalos in a Mass-limited Sample of Galaxy Clusters”. In: *ApJ* 841.2, 71, p. 71. DOI: 10.3847/1538-4357/aa7069. arXiv: 1701.01364 [astro-ph.HE].

Giovannini, G. et al. (Dec. 2009). “Radio halos in nearby (z < 0.4) clusters of galaxies”. In: *A&A* 507.3, pp. 1257–1270. DOI: 10.1051/0004-6361/200912667. arXiv: 0909.0911 [astro-ph.CO].

Gopal-Krishna and P. J. Wiita (Nov. 2000). “Extragalactic radio sources with hybrid morphology: implications for the Fanaroff-Riley dichotomy”. In: *A&A* 363, pp. 507–516. arXiv: astro - ph / 0009441 [astro-ph].

Govoni, F. and L. Feretti (Jan. 2004). “Magnetic Fields in Clusters of Galaxies”. In: *International Journal of Modern Physics D* 13.8, pp. 1549–1594. DOI: 10.1142/S0218271804005080. arXiv: astro-ph/0410182 [astro-ph].

Govoni, F. et al. (May 2009). “A search for diffuse radio emission in the relaxed, cool-core galaxy clusters A1068, A1413, A1650, A1835, A2029, and Ophiuchus”. In: *A&A* 499.2, pp. 371–383. DOI: 10.1051/0004-6361/200811180. arXiv: 0901.1941 [astro-ph.CO].

Gregory, P. C. (2005). *Bayesian Logical Data Analysis for the Physical Sciences: A Comparative Approach with ‘Mathematica’ Support*.

Greisen, E. W. (2003). “AIPS, the VLA, and the VLBA”. In: *Information Handling in Astronomy - Historical Vistas*. Ed. by André Heck. Vol. 285. Astrophysics and Space Science Library, p. 109. DOI: 10.1007/0-306-48080-8_7.

Greisen, E. W., K. Spekkens, and G. A. van Moorsel (June 2009). “Aperture Synthesis Observations of the Nearby Spiral NGC 6503: Modeling the Thin and Thick H I Disks”. In: *AJ* 137.6, pp. 4718–4733. DOI: 10.1088/0004-6256/137/6/4718. arXiv: 0902.0989 [astro-ph.GA].

Guidetti, D. et al. (May 2010). “Structure of the magnetoionic medium around the Fanaroff-Riley Class I radio galaxy 3C 449”. In: *A&A* 514, A50, A50. DOI: 10.1051/0004-6361/200913872. arXiv: 1002.0811 [astro-ph.CO].

Guidetti, D. et al. (June 2011). “Ordered magnetic fields around radio galaxies: evidence for interaction with the environment”. In: *MNRAS* 413.4, pp. 2525–2544. DOI: 10.1111/j.1365-2966.2011.18321.x. arXiv: 1101.1807 [astro-ph.CO].

Guidetti, D. et al. (June 2012). “The magnetized medium around the radio galaxy B2 0755+37: an interaction with the intragroup gas”. In: *MNRAS* 423.2, pp. 1335–1350. DOI: 10.1111/j.1365-2966.2012.20961.x. arXiv: 1203.4582 [astro-ph.CO].

Gull, S. F. and K. J. E. Northover (July 1973). “Bubble Model of Extragalactic Radio Sources”. In: *Nature* 244.5411, pp. 80–83. DOI: 10.1038/244080a0.

Halbesma, T. L. R. et al. (Mar. 2019). “Simulations of the merging cluster of galaxies Cygnus A”. In: *MNRAS* 483.3, pp. 3851–3864. DOI: 10.1093/mnras/sty3385. arXiv: 1812.05467 [astro-ph.HE].

Hardcastle, M. J. and J. H. Croston (June 2020). “Radio galaxies and feedback from AGN jets”. In: *New A Rev.* 88, 101539, p. 101539. DOI: 10.1016/j.newar.2020.101539. arXiv: 2003.06137 [astro-ph.HE].

Hargrave, P. J. and M. Ryle (Feb. 1974). “Observations of Cygnus A with the 5-km radio telescope.” In: *MNRAS* 166, pp. 305–327. DOI: 10.1093/mnras/166.2.305.

Haverkorn, M. et al. (June 2008). “The Outer Scale of Turbulence in the Magnetoionized Galactic Interstellar Medium”. In: *ApJ* 680.1, pp. 362–370. DOI: 10.1086/587165. arXiv: 0802.2740 [astro-ph].

Heald, G. (Apr. 2009). “The Faraday rotation measure synthesis technique”. In: *Cosmic Magnetic Fields: From Planets, to Stars and Galaxies*. Ed. by Klaus G. Strassmeier, Alexander G. Kosovichev, and John E. Beckman. Vol. 259. IAU Symposium, pp. 591–602. DOI: 10.1017/S1743921309031421.

Heald, G. et al. (July 2020). “Magnetism Science with the Square Kilometre Array”. In: *Galaxies* 8.3, p. 53. DOI: 10.3390/galaxies8030053. arXiv: 2006.03172 [astro-ph.GA].

Heinz, S. et al. (Apr. 2002). “Chandra ACIS-S Observations of Abell 4059: Signs of Dramatic Interaction between a Radio Galaxy and a Galaxy Cluster”. In: *ApJ* 569.2, pp. L79–L82. DOI: 10.1086/340688. arXiv: astro-ph/0201107 [astro-ph].

Hinshaw, G. et al. (Oct. 2013). “Nine-year Wilkinson Microwave Anisotropy Probe (WMAP) Observations: Cosmological Parameter Results”. In: *ApJS* 208.2, 19, p. 19. DOI: 10.1088/0067-0049/208/2/19. arXiv: 1212.5226 [astro-ph.CO].

Hogbom, J. A. (May 1979). “A study of the radio galaxies 3C 111, 192, 219, 223, 315 and 452.” In: *A&AS* 36, pp. 173–192.

Hollins, J. F. et al. (Nov. 2017). “Supernova-regulated ISM. V. Space and Time Correlations”. In: *ApJ* 850.1, 4, p. 4. DOI: 10.3847/1538-4357/aa93e7. arXiv: 1703.05187 [astro-ph.GA].

Hudson, D. S. et al. (Apr. 2010). “What is a cool-core cluster? a detailed analysis of the cores of the X-ray flux-limited HIFLUGCS cluster sample”. In: *A&A* 513, A37, A37. DOI: 10.1051/0004-6361/200912377. arXiv: 0911.0409 [astro-ph.CO].

Hutschenreuter, S. and T. A. Enßlin (Jan. 2020). “The Galactic Faraday depth sky revisited”. In: *A&A* 633, A150, A150. DOI: 10.1051/0004-6361/201935479. arXiv: 1903.06735 [astro-ph.GA].

Jarvis, M. et al. (Jan. 2016). “The MeerKAT International GHz Tiered Extragalactic Exploration (MIGHTEE) Survey”. In: *MeerKAT Science: On the Pathway to the SKA*, p. 6. arXiv: 1709.01901 [astro-ph.GA].

Johnston-Hollitt, M. (Jan. 2004). “The Magnetic Field in A3667”. In: *The Riddle of Cooling Flows in Galaxies and Clusters of galaxies*. Ed. by T. Reiprich, J. Kempner, and N. Soker, p. 51.

Johnston-Hollitt, M., C. P. Hollitt, and R. D. Ekers (Feb. 2004). “Statistical Analysis of Extra-galactic Rotation Measures”. In: *The Magnetized Interstellar Medium*. Ed. by B. Uyaniker, W. Reich, and R. Wielebinski, pp. 13–18. arXiv: astro-ph/0410659 [astro-ph].

Kaczmarek, J. F. et al. (May 2018). “Revealing the Faraday depth structure of radio galaxy NGC 612 with broad-band radio polarimetric observations”. In: *MNRAS* 476.2, pp. 1596–1613. DOI: 10.1093/mnras/sty269. arXiv: 1801.08237 [astro-ph.GA].

Kaiser, C. R. and P. Alexander (Mar. 1997). “A self-similar model for extragalactic radio sources”. In: *MNRAS* 286.1, pp. 215–222. DOI: 10.1093/mnras/286.1.215.

Kaiser, C. R. and P. N. Best (Nov. 2007). “Luminosity function, sizes and FR dichotomy of radio-loud AGN”. In: *MNRAS* 381.4, pp. 1548–1560. DOI: 10.1111/j.1365-2966.2007.12350.x. arXiv: 0708.3733 [astro-ph].

Kale, R. et al. (July 2015). “The Extended GMRT Radio Halo Survey. II. Further results and analysis of the full sample”. In: *A&A* 579, A92, A92. DOI: 10.1051/0004-6361/201525695. arXiv: 1503.02415 [astro-ph.CO].

Kapińska, A. D. et al. (Dec. 2017). “Radio Galaxy Zoo: A Search for Hybrid Morphology Radio Galaxies”. In: *AJ* 154.6, 253, p. 253. DOI: 10.3847/1538-3881/aa90b7. arXiv: 1711.09611 [astro-ph.GA].

Kass, R. E. and A. E. Raftery (June 1995). “Bayes Factor”. In: *Journal of the American Statistical Association* 90, pp. 773–795.

Kawakatu, N., M. Kino, and H. Nagai (June 2009). “On the Origin of Fanaroff-Riley Classification of Radio Galaxies: Deceleration of Supersonic Radio Lobes”. In: *ApJ* 697.2, pp. L173–L176. DOI: 10.1088/0004-637X/697/2/L173. arXiv: 0904.4752 [astro-ph.GA].

Killeen, N. E. B., G. V. Bicknell, and R. D. Ekers (Mar. 1986). “The Radio Galaxy IC 4296 (PKS 1333-22). I. Multifrequency Very Large Array Observations”. In: *ApJ* 302, p. 306. DOI: 10.1086/163992.

Kim, K. -T., Peter C. Tribble, and P. P. Kronberg (Sept. 1991). “Detection of Excess Rotation Measure Due to Intracluster Magnetic Fields in Clusters of Galaxies”. In: *ApJ* 379, p. 80. DOI: 10.1086/170484.

Knuettel, S. et al. (Feb. 2019). “The magnetic field strength of the Faraday screen surrounding the radio galaxy Coma A”. In: *MNRAS* 482.4, pp. 4606–4616. DOI: 10.1093/mnras/sty3018. arXiv: 1811.02844 [astro-ph.GA].

Kronberg, P. P. et al. (Oct. 2001). “Magnetic Energy of the Intergalactic Medium from Galactic Black Holes”. In: *ApJ* 560.1, pp. 178–186. DOI: 10.1086/322767. arXiv: astro-ph/0106281 [astro-ph].

Lacy, M. et al. (Jan. 2020). “The Karl G. Jansky Very Large Array Sky Survey (VLASS). Science Case and Survey Design”. In: *Publications of the Astronomical Society of the Pacific* 132.1009, p. 035001. DOI: 10.1088/1538-3873/ab63eb. URL: https://doi.org/10.1088/1538-3873/ab63eb.

Laing, R. A. (Nov. 1980). “A model for the magnetic-field structure in extended radio sources.” In: *MNRAS* 193, pp. 439–449. DOI: 10.1093/mnras/193.3.439.

— (Jan. 1988). “The sidedness of jets and depolarization in powerful extragalactic radio sources”. In: *Nature* 331.6152, pp. 149–151. DOI: 10.1038/331149a0.

Laing, R. A. et al. (May 2008a). “Multifrequency VLA observations of the FR I radio galaxy 3C 31: morphology, spectrum and magnetic field”. In: *MNRAS* 386.2, pp. 657–672. DOI: 10.1111/j.1365-2966.2008.13091.x. arXiv: 0803.2597 [astro-ph].

Laing, R. A. et al. (Dec. 2008b). “Structures of the magnetoionic media around the Fanaroff-Riley Class I radio galaxies 3C31 and Hydra A”. In: *MNRAS* 391.2, pp. 521–549. DOI: 10.1111/j.1365-2966.2008.13895.x. arXiv: 0809.2411 [astro-ph].

Lane, W. M. et al. (Jan. 2004). “Hydra A at Low Radio Frequencies”. In: *AJ* 127.1, pp. 48–52. DOI: 10.1086/379858. arXiv: astro-ph/0309647 [astro-ph].

Le Roux, E. (Feb. 1961). “Étude théorique du rayonnement synchrotron des radiosources”. In: *Annales d’Astrophysique* 24, p. 71.

Ledlow, M. J. and F. N. Owen (July 1996). “20 CM VLA Survey of Abell Clusters of Galaxies. VI. Radio/Optical Luminosity Functions”. In: *AJ* 112, p. 9. DOI: 10.1086/117985. arXiv: astro-ph/9607014 [astro-ph].

Lee, J. et al. (June 2009). “Detection of Large-Scale Cosmic Magnetic Fields”. In: *arXiv e-prints*, arXiv:0906.1631, arXiv:0906.1631. arXiv: 0906.1631 [astro-ph.CO].

Longair, M. S., M. Ryle, and P. A. G. Scheuer (Jan. 1973). “Models of extended radiosources”. In: *MNRAS* 164, p. 243. DOI: 10.1093/mnras/164.3.243.

Lyutikov, M. (Nov. 2006). “Magnetic draping of merging cores and radio bubbles in clusters of galaxies”. In: *MNRAS* 373.1, pp. 73–78. DOI: 10.1111/j.1365-2966.2006.10835.x. arXiv: astro-ph/0604178 [astro-ph].

Ma, Y. et al. (Aug. 2019). “A broad-band spectro-polarimetric view of the NVSS rotation measure catalogue - I. Breaking the nπ-ambiguity”. In: *MNRAS* 487.3, pp. 3432–3453. DOI: 10.1093/mnras/stz1325. arXiv: 1905.04313 [astro-ph.GA].

Mackay, D. J. C. (2003). *Information Theory, Inference and Learning Algorithms*.

Mathews, W. G. and J. N. Bregman (Sept. 1978). “Radiative accretion flow onto giant galaxies in clusters.” In: *ApJ* 224, pp. 308–319. DOI: 10.1086/156379.

Mazzotta, P. and S. Giacintucci (Mar. 2008). “Do Radio Core-Halos and Cold Fronts in Non-Major-Merging Clusters Originate from the Same Gas Sloshing?” In: *ApJ* 675.1, p. L9. DOI: 10.1086/529433. arXiv: 0801.1905 [astro-ph].

McKinnon, Mark and Rob Selina (Jan. 2018). “The Next-Generation Very Large Array: Technical Overview”. In: *American Astronomical Society Meeting Abstracts #231*. Vol. 231. American Astronomical Society Meeting Abstracts, p. 342.02.

McNamara, B. R. and P. E. J. Nulsen (Sept. 2007). “Heating Hot Atmospheres with Active Galactic Nuclei”. In: *ARA&A* 45.1, pp. 117–175. DOI: 10.1146/annurev.astro.45.051806.110625. arXiv: 0709.2152 [astro-ph].

McNamara, B. R. et al. (May 2000). “Chandra X-Ray Observations of the Hydra A Cluster: An Interaction between the Radio Source and the X-Ray-emitting Gas”. In: *ApJ* 534.2, pp. L135–L138. DOI: 10.1086/312662. arXiv: astro-ph/0001402 [astro-ph].

Meier, D. L. et al. (July 1997). “A magnetic switch that determines the speed of astrophysical jets”. In: *Nature* 388.6640, pp. 350–352. DOI: 10.1038/41034.

Miley, G. (Jan. 1980). “The structure of extended extragalactic radio sources”. In: *ARA&A* 18, pp. 165–218. DOI: 10.1146/annurev.aa.18.090180.001121.

Mingo, B. et al. (Sept. 2019). “Revisiting the Fanaroff-Riley dichotomy and radio-galaxy morphology with the LOFAR Two-Metre Sky Survey (LoTSS)”. In: *MNRAS* 488.2, pp. 2701–2721. DOI: 10.1093/mnras/stz1901. arXiv: 1907.03726 [astro-ph.GA].

Miraghaei, H. and P. N. Best (Apr. 2017). “The nuclear properties and extended morphologies of powerful radio galaxies: the roles of host galaxy and environment”. In: *MNRAS* 466.4, pp. 4346–4363. DOI: 10.1093/mnras/stx007. arXiv: 1701.00919 [astro-ph.GA].

Mitton, S. (Jan. 1971). “Observations of the distribution of polarized emission of Cygnus A at 6-cm wavelength”. In: *MNRAS* 153, p. 133. DOI: 10.1093/mnras/153.2.133.

Miyashita, Y. (July 2019). “Performance Test of QU-Fitting”. In: *Galaxies* 7.3, p. 69. DOI: 10.3390/galaxies7030069.

Miyoshi, M. et al. (Jan. 1995). “Evidence for a black hole from high rotation velocities in a sub-parsec region of NGC4258”. In: *Nature* 373.6510, pp. 127–129. DOI: 10.1038/373127a0.

Molendi, S. and F. Pizzolato (Oct. 2001). “Is the Gas in Cooling Flows Multiphase?” In: *ApJ* 560.1, pp. 194–200. DOI: 10.1086/322387. arXiv: astro-ph/0106552 [astro-ph].

Mukherjee, P., D. Parkinson, and A. R. Liddle (Feb. 2006). “A Nested Sampling Algorithm for Cosmological Model Selection”. In: *ApJ* 638.2, pp. L51–L54. DOI: 10.1086/501068. arXiv: astro-ph/0508461 [astro-ph].

Murgia, M. et al. (Sept. 2004). “Magnetic fields and Faraday rotation in clusters of galaxies”. In: *A&A* 424, pp. 429–446. DOI: 10.1051/0004-6361:20040191. arXiv: astro-ph/0406225 [astro-ph].

Murphy, E. J. and ngVLA Science Advisory Council (Jan. 2021). “New Scientific Frontiers with a next-generation Very Large Array”. In: *American Astronomical Society Meeting Abstracts*. Vol. 53. American Astronomical Society Meeting Abstracts, p. 535.01.

Netzer, H. and B. M. Peterson (1997). “Reverberation Mapping and the Physics of Active Galactic Nuclei”. In: *Astronomical Time Series*. Ed. by D. Maoz, A. Sternberg, and E. M. Leibowitz. Vol. 218, p. 85. DOI: 10.1007/978-94-015-8941-3_8.

Newman, W. I., A. L. Newman, and Y. Rephaeli (Aug. 2002). “Quantification of Uncertainty in the Measurement of Magnetic Fields in Clusters of Galaxies”. In: *ApJ* 575.2, pp. 755–763. DOI: 10.1086/341350. arXiv: astro-ph/0204451 [astro-ph].

Nulsen, P. E. J. et al. (Mar. 2002). “Interaction of Radio Lobes with the Hot Intracluster Medium: Driving Convective Outflow in Hydra A”. In: *ApJ* 568.1, pp. 163–173. DOI: 10.1086/338494. arXiv: astro-ph/0110523 [astro-ph].

Nulsen, P. E. J. et al. (Aug. 2005a). “The Cluster-Scale AGN Outburst in Hydra A”. In: *ApJ* 628.2, pp. 629–636. DOI: 10.1086/430845. arXiv: astro-ph/0408315 [astro-ph].

— (Aug. 2005b). “The Cluster-Scale AGN Outburst in Hydra A”. In: *ApJ* 628.2, pp. 629–636. DOI: 10.1086/430845. arXiv: astro-ph/0408315 [astro-ph].

O’Sullivan, S. P. et al. (Apr. 2012). “Complex Faraday depth structure of active galactic nuclei as revealed by broad-band radio polarimetry”. In: *MNRAS* 421.4, pp. 3300–3315. DOI: 10.1111/j.1365-2966.2012.20554.x. arXiv: 1201.3161 [astro-ph.CO].

O’Sullivan, S. P. et al. (Feb. 2013). “Thermal Plasma in the Giant Lobes of the Radio Galaxy Centaurus A”. In: *ApJ* 764.2, 162, p. 162. DOI: 10.1088/0004-637X/764/2/162. arXiv: 1301.1400 [astro-ph.CO].

Oemler, A. (Nov. 1974). “The Systematic Properties of Clusters of Galaxies. Photometry of 15 Clusters”. In: *ApJ* 194, pp. 1–20. DOI: 10.1086/153216.

Offringa, A. R. et al. (Oct. 2014). “WSCLEAN: an implementation of a fast, generic wide-field imager for radio astronomy”. In: *MNRAS* 444.1, pp. 606–619. DOI: 10.1093/mnras/stu1368. arXiv: 1407.1943 [astro-ph.IM].

Olivares, V. et al. (Nov. 2019). “Ubiquitous cold and massive filaments in cool core clusters”. In: *A&A* 631, A22, A22. DOI: 10.1051/0004-6361/201935350. arXiv: 1902.09164 [astro-ph.GA].

Oppermann, N. et al. (June 2012). “An improved map of the Galactic Faraday sky”. In: *A&A* 542, A93, A93. DOI: 10.1051/0004-6361/201118526. arXiv: 1111.6186 [astro-ph.GA].

Oppermann, N. et al. (Mar. 2015). “Estimating extragalactic Faraday rotation”. In: *A&A* 575, A118, A118. DOI: 10.1051/0004-6361/201423995. arXiv: 1404.3701 [astro-ph.IM].

Owen, F. N. and M. J. Ledlow (Jan. 1994). “The FRI/II Break and the Bivariate Luminosity Function in Abell Clusters of Galaxies”. In: *The Physics of Active Galaxies*. Ed. by Geoffrey V. Bicknell, Michael A. Dopita, and Peter J. Quinn. Vol. 54. Astronomical Society of the Pacific Conference Series, p. 319.

Owen, F. N., M. J. Ledlow, and W. C. Keel (Jan. 1995). “Optical Spectroscopy of Radio Galaxies in abell Clusters. I. Redshifts and Emission-Line Properties”. In: *AJ* 109, p. 14. DOI: 10.1086/117252.

Pasetto, A. et al. (June 2018). “Broadband radio spectro-polarimetric observations of high-Faraday-rotation-measure AGN”. In: *A&A* 613, A74, A74. DOI: 10.1051/0004-6361/201731804. arXiv: 1801.09731 [astro-ph.GA].

Perley, R. A. and B. J. Butler (May 2017). “An Accurate Flux Density Scale from 50 MHz to 50 GHz”. In: *ApJS* 230.1, 7, p. 7. DOI: 10.3847/1538-4365/aa6df9. arXiv: 1609.05940 [astro-ph.IM].

Perley, R. A. and C. L. Carilli (1996). “The structure and polarization of Cygnus A at λ 3.6cm”. In: *Cygnus A – Study of a Radio Galaxy*. Ed. by Christopher L. Carilli and Daniel E. Harris, p. 168.

Perley, R. A., J. W. Dreher, and J. J. Cowan (Oct. 1984). “The jet and filaments in Cygnus A.” In: *ApJ* 285, pp. L35–L38. DOI: 10.1086/184360.

Perley, R. A., H. Roser, and K. Meisenheimer (Dec. 1997). “The radio galaxy PictorA – a study with the VLA”. In: *A&A* 328, pp. 12–32.

Perley, R. A. and G. B. Taylor (May 1991). “VLA Observations of 3C 295—A Young Radio Galaxy?” In: *AJ* 101, p. 1623. DOI: 10.1086/115792.

Perley, R. A. et al. (Sept. 2011). “The Expanded Very Large Array: A New Telescope for New Science”. In: *ApJ* 739.1, L1, p. L1. DOI: 10.1088/2041-8205/739/1/L1. arXiv: 1106.0532 [astro-ph.IM].

Peterson, B. M. and A. Wandel (Sept. 2000). “Evidence for Supermassive Black Holes in Active Galactic Nuclei from Emission-Line Reverberation”. In: *ApJ* 540.1, pp. L13–L16. DOI: 10.1086/312862. arXiv: astro-ph/0007147 [astro-ph].

Rafferty, D. A. et al. (Nov. 2006). “The Feedback-regulated Growth of Black Holes and Bulges through Gas Accretion and Starbursts in Cluster Central Dominant Galaxies”. In: *ApJ* 652.1, pp. 216–231. DOI: 10.1086/507672. arXiv: astro-ph/0605323 [astro-ph].

Rees, M. J. (Jan. 1971). “New Interpretation of Extragalactic Radio Sources”. In: *Nature* 229.5283, pp. 312–317. DOI: 10.1038/229312a0.

Rephaeli, Y. (Jan. 1988). “Magnetic fields in clusters of galaxies.” In: *Comments on Astrophysics* 12, pp. 265–279.

Riseley, C. J. et al. (Jan. 2020). “The POlarised GLEAM Survey (POGS) II: Results from an all-sky rotation measure synthesis survey at long wavelengths”. In: *PASA* 37, e029, e029. DOI: 10.1017/pasa.2020.20. arXiv: 2005.09266 [astro-ph.GA].

Rose, T. et al. (May 2019). “Deep and narrow CO absorption revealing molecular clouds in the Hydra-A brightest cluster galaxy”. In: *MNRAS* 485.1, pp. 229–238. DOI: 10.1093/mnras/stz406. arXiv: 1902.01863 [astro-ph.GA].

Rudnick, L. and K. M. Blundell (May 2003). “Lowering Inferred Cluster Magnetic Field Strengths: The Radio Galaxy Contributions”. In: *ApJ* 588.1, pp. 143–154. DOI: 10.1086/373891. arXiv: astro-ph/0301260 [astro-ph].

Rudnick, L. and F. N. Owen (Feb. 1976). “Head-tail radio sources in clusters of galaxies.” In: *ApJ* 203, pp. L107–L111. DOI: 10.1086/182030.

Ruzmaikin, A. A. and D. D. Sokoloff (Sept. 1979). “The calculation of Faraday rotation measures of cosmic radio sources.” In: *A&A* 78.1, pp. 1–6.

Ruzmaikin, A., D. Sokolov, and A. Shukurov (Nov. 1989). “The dynamo origin of magnetic fields in galaxy clusters.” In: *MNRAS* 241, p. 1. DOI: 10.1093/mnras/241.1.1.

Ryle, M. and M. S. Longair (Jan. 1967). “A possible method for investigating the evolution of radio galaxies”. In: *MNRAS* 136, p. 123. DOI: 10.1093/mnras/136.2.123.

Sakelliou, I. and M. R. Merrifield (Jan. 2000). “The origin of wide-angle tailed radio galaxies”. In: *MNRAS* 311.3, pp. 649–656. DOI: 10.1046/j.1365-8711.2000.03079.x. arXiv: astro-ph/9909511 [astro-ph].

Sanderson, A. J. R., T. J. Ponman, and E. O’Sullivan (Nov. 2006). “A statistically selected Chandra sample of 20 galaxy clusters - I. Temperature and cooling time profiles”. In: *MNRAS* 372.4, pp. 1496–1508. DOI: 10.1111/j.1365-2966.2006.10956.x. arXiv: astro-ph/0608423 [astro-ph].

Sarazin, C. L. (Jan. 1986). “X-ray emission from clusters of galaxies”. In: *Reviews of Modern Physics* 58.1, pp. 1–115. DOI: 10.1103/RevModPhys.58.1.

Savini, F. et al. (Aug. 2018). “First evidence of diffuse ultra-steep-spectrum radio emission surrounding the cool core of a cluster”. In: *MNRAS* 478.2, pp. 2234–2242. DOI: 10.1093/mnras/sty1125. arXiv: 1805.01900 [astro-ph.GA].

Scheuer, P. A. G. (Mar. 1974). “Models of extragalactic radio sources with a continuous energy supply from a central object”. In: *MNRAS* 166, pp. 513–528. DOI: 10.1093/mnras/166.3.513.

Schnitzeler, D. H. F. M., P. Katgert, and A. G. de Bruyn (Feb. 2009). “WSRT Faraday tomography of the Galactic ISM at λ 0.86 m. I. The GEMINI data set at (l, b) = (181°, 20°)”. In: *A&A* 494.2, pp. 611–622. DOI: 10.1051/0004-6361:20078912. arXiv: 0810.4211 [astro-ph].

Schnitzeler, D. H. F. M. et al. (May 2019). “S-PASS/ATCA: a window on the magnetic universe in the Southern hemisphere”. In: *MNRAS* 485.1, pp. 1293–1309. DOI: 10.1093/mnras/stz092. arXiv: 1902.09556 [astro-ph.GA].

Sebokolodi, M. et al. (Sept. 2020). “A Wideband Polarization Study of Cygnus A with the JVLA. I: The Observations and Data”. In: *arXiv e-prints*, arXiv:2009.06554, arXiv:2009.06554. arXiv: 2009.06554 [astro-ph.GA].

Selina, Robert J. et al. (July 2018). “The Next-Generation Very Large Array: a technical overview”. In: *Ground-based and Airborne Telescopes VII*. Ed. by Heather K. Marshall and Jason Spyromilio. Vol. 10700. Society of Photo-Optical Instrumentation Engineers (SPIE) Conference Series, 107001O. DOI: 10.1117/12.2312089. arXiv: 1806.08405 [astro-ph.IM].

Shaw, J. R., M. Bridges, and M. P. Hobson (July 2007). “Efficient Bayesian inference for multimodal problems in cosmology”. In: *MNRAS* 378.4, pp. 1365–1370. DOI: 10.1111/j.1365-2966.2007.11871.x. arXiv: astro-ph/0701867 [astro-ph].

Simard-Normandin, M., P. P. Kronberg, and S. Button (Jan. 1981). “The Faraday rotation measures of extragalactic radio sources.” In: *ApJS* 45, pp. 97–111. DOI: 10.1086/190709.

Simionescu, A. et al. (Mar. 2009). “The large-scale shock in the cluster of galaxies Hydra A”. In: *A&A* 495.3, pp. 721–732. DOI: 10.1051/0004-6361:200811071. arXiv: 0810.0271 [astro-ph].

Skilling, J. (Nov. 2004). “Nested Sampling”. In: *American Institute of Physics Conference Series*. Ed. by Rainer Fischer, Roland Preuss, and Udo Von Toussaint. Vol. 735. American Institute of Physics Conference Series, pp. 395–405. DOI: 10.1063/1.1835238.

Slysh, V. I. (Feb. 1966). “Peculiarities of Polarized Radiation in the Crab Nebula and the Radio Galaxy Cygnus A.” In: *Soviet Ast.* 9, p. 533.

Smith, D. A. et al. (Jan. 2002). “A Chandra X-Ray Study of Cygnus A. III. The Cluster of Galaxies”. In: *ApJ* 565.1, pp. 195–207. DOI: 10.1086/324539. arXiv: astro-ph/0109488 [astro-ph].

Snios, B. et al. (Mar. 2018). “The Cocoon Shocks of Cygnus A: Pressures and Their Implications for the Jets and Lobes”. In: *ApJ* 855.1, 71, p. 71. DOI: 10.3847/1538-4357/aaaf1a. arXiv: 1802.10106 [astro-ph.HE].

Sokoloff, D. D. et al. (Aug. 1998). “Depolarization and Faraday effects in galaxies”. In: *MNRAS* 299.1, pp. 189–206. DOI: 10.1046/j.1365-8711.1998.01782.x.

Spinrad, H. and J. R. Stauffer (July 1982). “Spectroscopic and photographic observations of the Cygnus A group and of the stellar component of the Cygnus A galaxy.” In: *MNRAS* 200, pp. 153–158. DOI: 10.1093/mnras/200.2.153.

Stockton, A. and S. Ridgway (1996). “Optical and near IR observations of Cygnus A”. In: *Cygnus A – Studay of a Radio Galaxy*. Ed. by Christopher L. Carilli and Daniel E. Harris, p. 1.

Stuardi, C. et al. (June 2020). “The LOFAR view of intergalactic magnetic fields with giant radio galaxies”. In: *A&A* 638, A48, A48. DOI: 10.1051/0004-6361/202037635. arXiv: 2004.05169 [astro-ph.GA].

Sun, X. H. et al. (Feb. 2015). “Comparison of Algorithms for Determination of Rotation Measure and Faraday Structure. I. 1100-1400 MHz”. In: *AJ* 149.2, 60, p. 60. DOI: 10.1088/0004-6256/149/2/60. arXiv: 1409.4151 [astro-ph.IM].

Taylor, A. R., J. M. Stil, and C. Sunstrum (Sept. 2009). “A Rotation Measure Image of the Sky”. In: *ApJ* 702.2, pp. 1230–1236. DOI: 10.1088/0004-637X/702/2/1230.

Taylor, G. B. (Oct. 1996). “The Symmetric Parsec-Scale Jets of the Radio Galaxy Hydra A”. In: *ApJ* 470, p. 394. DOI: 10.1086/177874.

Taylor, G. B. and R. A. Perley (Oct. 1993). “Magnetic Fields in the Hydra A Cluster”. In: *ApJ* 416, p. 554. DOI: 10.1086/173257.

Taylor, G. B. et al. (Sept. 1990). “VLA Observations of the Radio Galaxy Hydra A (3C 218)”. In: *ApJ* 360, p. 41. DOI: 10.1086/169094.

Taylor, G. B. et al. (Sept. 2001). “Magnetic fields in the 3C 129 cluster”. In: *MNRAS* 326.1, pp. 2–10. DOI: 10.1046/j.1365-8711.2001.04587.x. arXiv: astro-ph/0104223 [astro-ph].

Terni de Gregory, B. et al. (Dec. 2017). “Narrow head-tail radio galaxies at very high resolution”. In: *A&A* 608, A58, A58. DOI: 10.1051/0004-6361/201730878. arXiv: 1709.00223 [astro-ph.GA].

Thorat, K., L. Saripalli, and R. Subrahmanyan (Oct. 2013). “Environments of extended radio sources in the Australia Telescope Low-Brightness Survey”. In: *MNRAS* 434.4, pp. 2877–2891. DOI: 10.1093/mnras/stt1196. arXiv: 1308.0884 [astro-ph.CO].

Tribble, P. C. (June 1991). “Depolarization of extended radio sources by a foreground Faraday screen.” In: *MNRAS* 250, p. 726. DOI: 10.1093/mnras/250.4.726.

Trotta, R. (June 2007). “Applications of Bayesian model selection to cosmological parameters”. In: *MNRAS* 378.1, pp. 72–82. DOI: 10.1111/j.1365-2966.2007.11738.x. arXiv: astro-ph/0504022 [astro-ph].

Vallee, J. P. (Sept. 1990). “Detecting the Largest Magnets: The Universe and the Clusters of Galaxies”. In: *ApJ* 360, p. 1. DOI: 10.1086/169089.

Van Eck, C. L. et al. (Jan. 2017). “Faraday tomography of the local interstellar medium with LOFAR: Galactic foregrounds towards IC 342”. In: *A&A* 597, A98, A98. DOI: 10.1051/0004-6361/201629707. arXiv: 1612.00710 [astro-ph.GA].

van Weeren, R. J. et al. (Oct. 2010). “Particle Acceleration on Megaparsec Scales in a Merging Galaxy Cluster”. In: *Science* 330.6002, p. 347. DOI: 10.1126/science.1194293. arXiv: 1010.4306 [astro-ph.CO].

Vogt, C. and T. A. Enßlin (Dec. 2003). “Measuring the cluster magnetic field power spectra from Faraday rotation maps of Abell 400, Abell 2634 and Hydra A”. In: *A&A* 412, pp. 373–385. DOI: 10.1051/0004-6361:20031434. arXiv: astro-ph/0309441 [astro-ph].

Waelkens, A. H., A. A. Schekochihin, and T. A. Enßlin (Oct. 2009). “Probing magnetic turbulence by synchrotron polarimetry: statistics and structure of magnetic fields from Stokes correlators”. In: *MNRAS* 398.4, pp. 1970–1988. DOI: 10.1111/j.1365-2966.2009.15231.x. arXiv: 0903.3056 [astro-ph.GA].

Willson, M. A. G. (Jan. 1970). “Radio observations of the cluster of galaxies in Coma Berenices - the 5C4 survey.” In: *MNRAS* 151, p. 1. DOI: 10.1093/mnras/151.1.1.

Wilson, Warwick E. et al. (Sept. 2011). “The Australia Telescope Compact Array Broad-band Backend: description and first results”. In: *MNRAS* 416.2, pp. 832–856. DOI: 10.1111/j.1365-2966.2011.19054.x. arXiv: 1105.3532 [astro-ph.IM].

Wolleben, M. et al. (July 2019). “The Global Magneto-Ionic Medium Survey: Polarimetry of the Southern Sky from 300 to 480 MHz”. In: *AJ* 158.1, 44, p. 44. DOI: 10.3847/1538-3881/ab22b0. arXiv: 1905.12685 [astro-ph.GA].

Xu, H. et al. (June 2009). “Turbulence and Dynamo in Galaxy Cluster Medium: Implications on the Origin of Cluster Magnetic Fields”. In: *ApJ* 698.1, pp. L14–L17. DOI: 10.1088/0004-637X/698/1/L14. arXiv: 0905.2196 [astro-ph.CO].

— (Dec. 2010). “Evolution and Distribution of Magnetic Fields from Active Galactic Nuclei in Galaxy Clusters. I. The Effect of Injection Energy and Redshift”. In: *ApJ* 725.2, pp. 2152–2165. DOI: 10.1088/0004-637X/725/2/2152. arXiv: 1011.0030 [astro-ph.CO].

Xu, H. et al. (Nov. 2012). “Comparisons of Cosmological Magnetohydrodynamic Galaxy Cluster Simulations to Radio Observations”. In: *ApJ* 759.1, 40, p. 40. DOI: 10.1088/0004-637X/759/1/40. arXiv: 1209.2737 [astro-ph.CO].

Young, A. J., A. S. Wilson, and C. G. Mundell (Nov. 2002). “Chandra Imaging of the X-Ray Core of the Virgo Cluster”. In: *ApJ* 579.2, pp. 560–570. DOI: 10.1086/342918. arXiv: astro-ph/0202504 [astro-ph].